



TÉCNICO
LISBOA

**UNIVERSIDADE DE LISBOA
INSTITUTO SUPERIOR TÉCNICO**



Structural Behavior Due to Cascading Earthquake and Tsunami Actions

Cláudia Vanessa Dias Reis

Supervisor: Doctor Mário Manuel Paisana dos Santos Lopes

Co-Supervisors: Doctor Stephane Louis Clain

Doctor Maria Ana Carvalho Viana Baptista

Thesis approved in public session to obtain the PhD Degree in

Civil Engineering

Jury final classification: Pass with Distinction and Honour

2022



TÉCNICO
LISBOA

**UNIVERSIDADE DE LISBOA
INSTITUTO SUPERIOR TÉCNICO**

**Structural Behavior Due to
Cascading Earthquake and Tsunami Actions**

Cláudia Vanessa Dias Reis

Supervisor: Doctor Mário Manuel Paisana dos Santos Lopes
Co-Supervisors: Doctor Stephane Louis Clain
Doctor Maria Ana Carvalho Viana Baptista

Thesis approved in public session to obtain the PhD Degree in

Civil Engineering

Jury final classification: Pass with Distinction and Honour

Jury

Chairperson:

Doctor Eduardo Nuno Brito Santos Júlio, Instituto Superior Técnico, Universidade de Lisboa

Members of the Committee:

Doctor Christophe Berthon, Laboratoire de Mathématiques Jean Leray, Université de Nantes, France

Doctor Daniel Thomas Cox, Oregon State University, USA

Doctor Luís Manuel Henriques Marques Matias, Faculdade de Ciências, Universidade de Lisboa

Doctor Luís Manuel Coelho Guerreiro, Instituto Superior Técnico, Universidade de Lisboa

Doctor Rui Miguel Lage Ferreira, Instituto Superior Técnico, Universidade de Lisboa

Doctor Mário Manuel Paisana dos Santos Lopes, Instituto Superior Técnico, Universidade de Lisboa

Funding Institution

Fundação para a Ciência e a Tecnologia

2022

Acknowledgments

I would like to start by expressing the pleasure that has been to be part of the Civil Engineering Research and Innovation for Sustainability research unit, Department of Civil Engineering, Architecture and Geo-resources of Instituto Superior Técnico, University of Lisbon, supported through Foundation for Science and Technology's funding UIDB/04625/2020. Thank you all for kindly welcoming me in the community.

Financial support was provided by the FCT – Portuguese National Science Foundation through 1) scholarships funding: ULisboa number 571/2017 and SFRH/BD/137531/2018 and 2) project funding: National Funds through FCT - Fundação para a Ciência e Tecnologia, project no. POCI-01-0145-FEDER-028118. An extended acknowledgment to Administração dos Portos de Sines e do Algarve, S.A for promoting the bond between academia and industry through financial sponsorship, support letter for FCT application and sharing structural design details of the port infrastructures.

My sincere appreciation to my advisor Professor Mário Lopes for his constant support, availability and trust along the entire journey. I wish to thank my first co-advisor Professor Stéphane Clain, from the Departamento de Matemática e Centro de Física, Universidade do Minho, Portugal, for his valuable scientific, technological and doctrinal insights. I also would like to thank my second co-advisor Professor Maria Ana Baptista, from Instituto Dom Luiz, Science Faculty of Lisbon University, for her honest feedback, stimulating questions and discussions along the process. The complementary contributions of each member of the team helped me develop an inquisitive and critical scientific mind-set, and, ultimately, as an independent and more confident professional.

I would also like to express my deep gratitude to Professor André R. Barbosa from the School of Civil and Construction Engineering, Oregon State University, United States. His thoughtful guide during the past three years of my work allowed me not only to validate numerical hypothesis and increase the reliability of the thesis, but also helped me open my horizons and built a strong networking with the tsunami engineering community. Another three people played important roles at some part of my investigation path. The first is Professor Jorge Figueiredo from the Departamento de Matemática e Centro de Física, Universidade do Minho, Portugal, whom has been an indispensable dimension of my learning process. The second is Doctor Rachid Omira, a role model scientist, from Instituto Português do Mar e da Atmosfera, whom always instigated my scientific curiosity. The third is Professor Carlos Sousa Oliveira, from Instituto Superior Técnico, for his constant availability.

Thanks to my fellow colleagues, Ricardo Ferreira and Raquel Paula, with whom I had the privilege of becoming friends. Thanks to all my former colleagues, some of them current friends.

Thanks to my friends outside the academia, that helped me kept the balance between professional and social universes along the years.

To my family.

Resumo

Os indicadores urbanísticos e demográficos preveem que a distribuição espacial mantenha a tendência irregular de crescimento privilegiado em zonas costeiras. No entanto, este crescimento coexiste sem particular planeamento dos aglomerados, mesmo em regiões suscetíveis de serem afetadas por perigos de origem natural com potencial catastrófico, como os tsunamis com origem em sismos de elevada magnitude. A resiliência societal e ambiental destas comunidades é, portanto, substancialmente dependente do desempenho das estruturas implementadas ao longo da costa. Todavia, tsunamis recentes com fonte regional ou local demonstraram que as estruturas previamente expostas aos sismos podem perder parcial ou totalmente a sua capacidade de resistência ao subsequente tsunami, evidenciando a escassez de critérios de dimensionamento a considerar o efeito em cascata do sismo e do tsunami. No entanto, a caracterização do fenómeno natural e da respetiva resposta estrutural é complexa e multidisciplinar, envolvendo várias incertezas epistémicas, domínios multi-escala e processos multi-físicos.

O principal objetivo desta dissertação é contribuir para caracterizar o fenómeno natural e o comportamento de estruturas sujeitas ao efeito de cascata das ações do sismo e do tsunami. A conceptualização da metodologia numérica contempla as diferentes etapas do problema, desde a génese do evento até à resposta da estrutura, considerando as variáveis endógenas aos modelos numéricos e exógenas inerentes ao processo físico. Os esquemas numéricos e técnicas de acoplamento usados para modelar as diferentes escalas espaço-temporais foram submetidos a um exaustivo processo de verificação e validação, correlacionando as soluções numéricas com soluções analíticas, dados laboratoriais e registos instrumentais de eventos reais.

A aplicação do conceito tem por objeto a infraestrutura que serve de Terminal de Contentores no porto marítimo de águas profundas em Sines se sujeito à ação em cascata do sismo e tsunami semelhantes ao evento ocorrido em 1755. A estrutura está a ser alvo de um plano de expansão que prevê aumentar o movimento, armazenamento e transporte de carga contentorizada, contribuindo para o aumento da competitividade e visibilidade do Porto de Sines numa perspetiva global. A análise numérica para desenvolver a caracterização da ameaça de multi-perigosidade e respetiva vulnerabilidade estrutural considera a estrutura existente e as previsões de futuras configurações ao longo do plano de expansão, permitindo identificar fatores com potencial para comprometer as atividades correntes e de linha de socorro do porto, respetivamente em casos de funcionamento normal e de emergência. Permite também servir de base para procedimentos de gestão de risco, contribuindo para prever os impactos sociais e ecológicos, assim como a escalabilidade para uma situação *natech*. Das análises são derivadas recomendações de carácter preventivo que se inserem no âmbito do desenvolvimento sustentável de infraestruturas costeiras críticas expostas ao perigo de eventos tsunamigénicos extremos.

Palavras-chave: Multi-perigosidade de sismo e tsunami, Cascata de ações sísmica e de tsunami, Resposta estrutural sucessiva com efeito cumulativo das ações, Caracterização numérica da interação fluido-estrutura

Abstract

The spatial distribution of the world population is uneven with privileged concentration on coastal regions. The trend is expected to continue in both demographic indicators and urban development rate, being many coastal cities in seismic- and tsunami-prone areas built through informal and unplanned settlements, exposing their population and assets to such hazards. The structural performance of the built environment is one of the man-controlled variables that can influence the social, economic and environmental resilience. Nonetheless, recent tsunami events raised the awareness for the threat of earthquake and tsunami cascading effects on coastal structures and highlighted the paucity of structural design criteria considering the cumulative effects of both. By being exposed to the ground-motion, the structures' resistance may decrease and become residual/non-existent to support the incoming tsunami, implying an underestimation of the risk. Yet, the characterization of the natural phenomena and the respective structural response is complex and multidisciplinary, involving various epistemic uncertainties, multi-scale domains and multi-physical processes.

The key objective of this dissertation is to contribute for the characterization of structural behavior due to cascading seismic and tsunami actions. The conceptualization of the numerical methodology considers endogenous variables of the numerical models and exogenous variables intrinsically related to the physical processes along various stages, from the genesis of the tsunamigenic event to the corresponding structural response. Multiple numerical schemes and coupling techniques to model the various spatial-temporal scales were subjected to an exhaustive benchmarking process, correlating numerical solutions with data from analytic, laboratorial and instrumental records of real events.

The proof of concept consists of characterizing the structural behavior of a pile-supported quay serving as terminal container at the Sines deep-water seaport due to the cascading effects of a 1755-alike earthquake and tsunami event. Moreover, the open-type wharf is in expansion phase to increase the cargo capacity and the port competitiveness globally. Multiple configurations resembling the current and future terminal infrastructure(s) were considered along the analyses performed to characterize the multi-hazard effects on the structure and the respective structural vulnerabilities, allowing to identify potential factors that jeopardize the port's activities, such as current operations and lifeline support, and predict both natech scalability and societal and ecologic impacts. From the analyses are inferred structural recommendations of preventive nature towards the sustainable development of critical coastal structures exposed to tsunamigenic hazard.

Keywords: Earthquake and tsunami multi-hazard, Cascade seismic and tsunami loading pattern, Successive structural response accounting cumulative effects, Numerical fluid-structure interaction, Multi-physics, Multi-scales

Contents

| | |
|--|-----------|
| Acknowledgments | vii |
| Resumo | ix |
| Abstract | xi |
| List of Acronyms | xvii |
| List of Tables | xix |
| List of Figures | xxi |
| 1 Introduction | 1 |
| 1.1 Contextualization | 1 |
| 1.2 Objectives | 4 |
| 1.3 Organization | 4 |
| 2 Conceptual Methodology | 7 |
| 2.1 Literature Review | 7 |
| 2.1.1 Risk management | 7 |
| 2.1.2 Disruptive events and governmental responses | 11 |
| 2.1.3 Scientific and Technological Advances and Shortcomings | 16 |
| 2.1.4 Performance of ports on regional-local tsunami-prone regions | 24 |
| 2.1.5 Remarks | 26 |
| 2.2 Conceptual Research Strategy | 26 |
| 2.2.1 Macro-scale: generation and propagation | 27 |
| 2.2.2 Meso-scale: propagation and site-effects | 29 |
| 2.2.3 Micro-scale: loading and structural response | 31 |
| 2.2.4 Remarks | 33 |
| 3 Theoretical models | 35 |
| 3.1 Introduction | 35 |
| 3.2 Characterization of tsunami action | 36 |
| 3.2.1 Lagrangian SPH-based numerical tool to solve NS equations | 37 |
| 3.2.2 Eulerian FV-based numerical tool to solve SW equations | 45 |
| 3.2.3 Coupled model | 52 |
| 3.3 Characterization of seismic action | 52 |

| | | |
|----------|--|-----------|
| 3.3.1 | Notation | 53 |
| 3.3.2 | Ground motion field | 53 |
| 3.3.3 | Ground motion accelerograms based on finite-fault method | 54 |
| 3.3.4 | Design spectra | 55 |
| 3.4 | Characterization of structural behavior | 59 |
| 3.4.1 | Lagrangian FE-based numerical tool to solve motion equations | 59 |
| 4 | Calibration process | 63 |
| 4.1 | SW-FV numerical scheme | 63 |
| 4.1.1 | Analytical benchmark: solitary wave on a sloping beach | 63 |
| 4.1.2 | Field benchmark: Tohoku-Oki, 2011 | 65 |
| 4.1.3 | SW-FV Remarks | 68 |
| 4.2 | NS-SPH numerical scheme | 68 |
| 4.2.1 | Moving boundary condition | 69 |
| 4.2.2 | Open boundary condition | 71 |
| 4.2.3 | Multi-phase | 72 |
| 4.2.4 | Modified dynamic boundary condition | 73 |
| 4.2.5 | NS-SPH Remarks | 74 |
| 4.3 | GMPE models | 75 |
| 4.3.1 | Ground motion fields of PGA | 76 |
| 4.3.2 | Time-histories of acceleration | 77 |
| 4.3.3 | GMPE remarks | 79 |
| 4.4 | FE and constitutive models | 79 |
| 4.4.1 | Constitutive models | 79 |
| 4.4.2 | Soil-structure interaction | 87 |
| 4.4.3 | FE remarks | 89 |
| 5 | Proof of Concept | 91 |
| 5.1 | Experimental data | 91 |
| 5.1.1 | Physical setup | 91 |
| 5.1.2 | Drag coefficient | 94 |
| 5.2 | Numerical data | 96 |
| 5.2.1 | NS-SPH model | 96 |
| 5.2.2 | SW-FV model | 109 |
| 5.2.3 | Coupled model | 110 |
| 5.3 | Physical-numerical correlation study | 110 |
| 5.3.1 | Hydrodynamic quantities | 111 |
| 5.3.2 | Fluid-structure interaction | 113 |
| 5.4 | Remarks | 119 |

| | |
|---|-------------|
| 6 Test-Case | 123 |
| 6.1 Description | 123 |
| 6.2 Methodology | 124 |
| 6.3 Regional and local tsunamigenesis potential | 127 |
| 6.4 Macro- and meso-scales: Cascading multi-hazard | 130 |
| 6.4.1 Baseline solution | 130 |
| 6.4.2 Enhanced solution | 148 |
| 6.5 Cascading multi-hazard remarks | 159 |
| 6.6 Micro-scale: Successive structural analyses | 160 |
| 6.6.1 Structural modeling | 163 |
| 6.6.2 Structural analyses | 167 |
| 7 Conclusions and Recommendations | 181 |
| 7.1 Conclusions | 181 |
| 7.2 Recommendations | 185 |
| 7.3 Future Work | 187 |
| Bibliography | 191 |
| A Eulerian SW-FV benchmarking: Tohoku-oki, 2011 tsunami | A.1 |
| B Coupled Eulerian-Lagrangian benchmarking: OSU experimental campaign | B.5 |
| B.1 Instrumental setup | B.5 |
| B.2 Measurement uncertainty | B.5 |
| B.3 Dirichlet boundary conditions | B.6 |
| C Sines: test-case | C.13 |
| C.1 Container terminal of the Sines deep-water seaport | C.13 |
| C.2 Expansion of the Sines container terminal | C.14 |
| D Sines: cascading seismic and tsunami multi-hazard | D.19 |
| D.1 Parameters of tsunamigenic regional and local sources | D.19 |
| D.2 Influences on tsunami arrival | D.21 |
| E Sines: successive structural response due to seismic and tsunami actions | E.23 |
| E.1 Modal analysis | E.23 |

List of Acronyms

| | |
|----------|--|
| BC | Boundary condition. |
| CFD | Computational fluid dynamics. |
| CFL | Courant Friedrichs Levy condition. |
| CPD | Cell polynomial degree. |
| CWF | Cadiz Wedge fault. |
| DOF | Degree of freedom. |
| GBF | Gorringe Bank fault. |
| GBTVF | Gorringe Bank and Lower Tagus Valley faults. |
| GLET | Great Lisbon earthquake and tsunami. |
| GMPE | Ground motion prediction equations. |
| HSF | Horseshoe fault. |
| HSCFSWIM | Horseshoe, Corner and SWIM region faults. |
| MOOD | Multidimensional Optimal Order Detection technique. |
| MPF | Marquês de Pombal fault. |
| MPHSF | Marquês de Pombal and Horseshoe faults. |
| MPPBF | Marquês de Pombal and Portimão Bank faults. |
| MUSCL | Monotonic Upstream-Centred Scheme for Conservation Laws technique. |
| MPPSF | Marquês de Pombal and Pereira de Sousa faults. |
| PBF | Portimão Bank fault. |
| PGA | Peak ground acceleration. |
| RP | Return period. |
| SVF | Saint Vicent fault. |
| SW | Shallow-water equations. |
| SWIM | Southwest Iberian Margin. |
| NS | Navier-Stokes equations. |
| FV | Finite volume method. |
| FE | Finite element method. |
| SPH | Smoothed particle hydrodynamics method. |
| WIS | Western Iberian Shelf. |
| ZH | Hydrographic zero. |

List of Tables

| | | |
|-----|--|------|
| 3.1 | Regulatory seismic action. Parameters recommended by the national annex for the calibration of the elastic response spectrum for the Portuguese territory [33]. | 56 |
| 3.2 | Regulatory seismic action. Parameters recommended for the calibration of the Eurocode 8 power spectra (adapted from Paola et al. 2017 [359]). | 58 |
| 5.1 | Computational settings for the numerical simulations. | 97 |
| 5.2 | Numerical convergence. Unit: meter. | 109 |
| 5.3 | Physical benchmarking. Average disagreement between recorded physical quantities and numerical solutions of hydrodynamic quantities. | 113 |
| 5.4 | Physical benchmarking. Average disagreement between recorded physical quantities and numerical solutions of forces and pressures exerted on the elevated structure. | 114 |
| 6.1 | Identification of the regional and local tsunamigenic sources. | 130 |
| 6.2 | Peak cascading hazard. Earthquake and tsunami maximum intensity measures for the different structural configurations varying the leading measure (bold font). Identification of the respective triggering source and respective literature reference. | 145 |
| 6.3 | Peak cascading actions. Cascading earthquake and tsunami loading patterns for the different structural configuration cases. | 148 |
| 6.4 | Structural modeling: reinforcement scheme of the horizontal elements. | 161 |
| 6.5 | Structural modeling: soil properties. | 161 |
| 6.6 | Structural analysis: regulatory damage criteria of pile-supported wharves. | 167 |
| 6.7 | Structural analysis: ultimate resistance of cross sections. | 169 |
| 6.8 | Structural analysis: summary behavior of pile-supported quay under cascading earthquake and tsunami actions. | 173 |
| B.1 | Experimental setup: instrumental setup. | B.11 |
| B.2 | Experimental setup: percentage of coefficients of variation of maximum measurements. | B.12 |
| D.1 | Fault parameters of the single tsunamigenic sources: distance from the source to the site, fault geometry (length and width), kinematics (strike, dip, rake and slip), soil rigidity and moment magnitude. A value of 5 km was assumed to model the depth to the top parameter. | D.20 |

D.2 Fault parameters of the composed tsunamigenic sources: fault geometry (length and width), kinematics (strike, dip, rake and slip), soil rigidity and moment magnitude. A value of 5 km was assumed to model the depth to the top parameter D.20

List of Figures

| | | |
|-----|--|----|
| 2.1 | Integrated local-tsunami risk management as a tool for decision-making. Hazard (orange), vulnerability (green) and exposure (blue) factors of risk (red) in pre- and post-event stages. | 10 |
| 2.2 | The 1755 Lisbon earthquake and tsunami event contributed to the development of the earthquake engineering concept, adopted in Lisbon's reconstruction. | 12 |
| 2.3 | The 2004 Sumatra earthquake and Indian Ocean tsunami contributed for the development of tsunami early warning globalisation and guidelines for vertical evacuation preparedness. | 13 |
| 2.4 | Refinement of hazard assessment maps and structural performance criteria were updated after the 2011 Tohoku earthquake and Pacific Ocean tsunami. | 15 |
| 2.5 | Examples of conceptual application of the proposed methodology to Kamaishi port in Iwate prefecture due to the Japan 2011 earthquake and tsunami. The macro-, meso- and micro-scaled frameworks are limited by orange, yellow and green lines, respectively. The interfaces between frameworks are prescribed by boundary conditions, BC, represented in blue. | 27 |
| 2.6 | Schematic representation of the conceptual methodology. Three complementary frameworks, defined in terms of spatial and temporal scales, are proposed to assess a generic structural behavior due to cascading earthquake and tsunami actions. | 34 |
| 3.1 | Discretization of the continuum into discrete elements. Each finite element is an independent geometric region of the domain over which equations with unknown variables are defined using the governing equations of a mathematical model to compute an approximate solution of the variable. | 36 |
| 3.2 | Lagrangian NS-SPH scheme: The principles of the SPH method in plane (left) and elevation (right) views. A physical property of particle a is computed considering the contribution of the neighbouring particles b weighted according to a smoothing-kernel function, $W_{r_{a,b}}$, along a certain area of influence, h . | 38 |
| 3.3 | Eulerian SW-FV: Notation for the shallow-water problem. | 46 |
| 3.4 | Eulerian SW-FV scheme: The principles of the FV method. Notation for the spatial (left) and temporal (right) discretization. | 47 |
| 3.5 | Eulerian SW-FV: Hydrostatic reconstruction for wet-wet with constant bathymetry (left), dry-wet (middle) and wet-wet with linear bathymetry (right). | 49 |
| 3.6 | SW-FV: MUSCL and MOOD techniques. | 49 |

| | | |
|------|--|----|
| 3.7 | Finite fault: notation. | 54 |
| 3.8 | Regulatory seismic action. Generic form of the elastic response spectra. | 56 |
| 3.9 | Regulatory seismic action. Reference acceleration for Portugal mainland regarding earthquakes of type I, inter-plate offshore far-field source (left) and type II, intra-plate inshore near-field source (right). | 57 |
| 3.10 | Regulatory seismic action. Generic form of the power density spectra. | 58 |
| 3.11 | Lagrangian FE scheme: The principles of the FE method. Notation for the spatial discretization. Each finite element is discretized onto a mesh using over which the governing equations of momentum and material constitutive laws are defined to compute the structural response. | 59 |
| 4.1 | Validation of Eulerian SW-FV scheme: propagation of a solitary wave over a sloping beach. Correlation between exact and numerical solutions. | 64 |
| 4.2 | Validation of Eulerian SW-FV scheme: Tohoku-Oki, 2011 tsunami propagation at $t = 1800 s$. Location of the virtual gauges, VG , adopted to perform a numerical convergence analysis, which correspond to deep-ocean DART21418 and coastal GPS806 buoys. . . . | 65 |
| 4.3 | Validation of Eulerian SW-FV scheme: convergence analysis of $\Delta_{x,y} = 1500 m, 700 m$ and $450 m$ resolution grids, using MUSCL, <i>minmod</i> and <i>vanLeer</i> , and MOOD techniques, to assess time series of η at deep-ocean and coastal locations. | 67 |
| 4.4 | Validation of Eulerian SW-FV scheme: correlation between recorded and numerical data using MUSCL, <i>minmod</i> and <i>vanLeer</i> , and MOOD techniques. | 68 |
| 4.5 | Validation of Lagrangian NS-SPH scheme: piston-generated train of waves propagating over a flat and sloping bottom and impacting a vertical wall. | 70 |
| 4.6 | Validation of Lagrangian NS-SPH scheme: inlet zone prescribed at $VG1$ $x = 0.38 m$ using hydrodynamic quantities from full domain simulation. Correlation between wave gauge record and numerical solution of free surface elevation at $VG2$, $x = 1.83 m$ (left) and $VG3$, $x = 3.12 m$ (right) computed with OBC and DBC. | 71 |
| 4.7 | Validation of Lagrangian NS-SPH scheme: geometry of the experimental and instrumental setup. Location of wave-gauges (H) and pressure-gauges (P). Unit: meter. | 72 |
| 4.8 | Validation of Lagrangian NS-SPH scheme: correlation between instrumentally-recorded wave heights and corresponding numerical solutions computed at H1 (left) and H2 (right) using single and multiphase models. | 73 |
| 4.9 | Validation of Lagrangian NS-SPH scheme: correlation between instrumentally-recorded pressure and corresponding numerical solutions computed at P1 (left) and P2 (right) using classic and modified boundary conditions models. | 74 |
| 4.10 | Validation of the peak acceleration: correlation between maps of peak accelerations assembled from the records of the Japan strong motion seismograph networks during the Japan, 2011 earthquake (left), and from synthetic data generated using OpenQuake software (right). | 77 |

| | |
|--|-----|
| 4.11 Validation of the acceleration series: correlation between instrumentally-recorded accelerations and their corresponding synthetically-generated signals, for relatively close (150 Km) and distant (300 Km) locations. | 78 |
| 4.12 Constitutive models. Stress-strain relationship calibrated for C35/45 concrete using Popovic or Mander stress-strain relationship (top). Mander model representing the stress-strain relationship of C35/45 concrete with unconfined and confined sections (bottom). | 80 |
| 4.13 Constitutive models. Constitutive stress-strain relationship calibrated for S355 and S500 steel using Giuffre-Menegotto-Pinto stress-strain relationship. | 82 |
| 4.14 Constitutive models. Behavior of pressure independent and dependent multi-yielding soil materials. | 85 |
| 4.15 Constitutive models. Constitutive relationships for pressure independent and dependent multi-yielding soil materials. | 86 |
| 4.16 Soil-pile interaction model. Response of soil and pile system to a horizontal load applied in the head of the pile. Correlation between solutions using OpenSees and soil elements, and OpenSees using springs to represent the soil (red lines in sub-figures) and L-Pile (blue lines in sub-figures). | 88 |
| 5.1 Experimental setup: overview of geometry and instrumental disposition. All dimensions are in meters. | 92 |
| 5.2 Experimental setup: generation of unbroken- and broken-waves to impact an elevated structure. | 93 |
| 5.3 Experimental calibration of drag coefficient: comparison of recorded and calculated forces exerted on the structure, considering stationary C_d estimated to fit the peak of the wave in the horizontal (left) and vertical (right) directions. Example considering the unbroken wave case. | 95 |
| 5.4 Numerical schemes: schematic summary of the numerical protocols, representing the domains where the SPH and FV solvers are used and the Dirichlet boundary conditions implemented, including transmissive (TBC) for the FV solver, moving (MBC) and open (OBC) for the SPH solver. | 97 |
| 5.5 Physical and numerical NS-SPH models. Visualizations of the numerical model and results are created using Blender. | 98 |
| 5.6 Physical and numerical NS-SPH models. Evaluation of free-surface elevation along the flume due to unbroken wave (WG1 sensor): (a) convergence, and (b) RMSE. Left and right subfigures show 3D and 2D results, respectively. | 100 |
| 5.7 Physical and numerical NS-SPH models. Evaluation of free-surface elevation along the flume due to broken wave (WG1 sensor): (a) convergence, and (b) RMSE. Left and right subfigures show 3D and 2D results, respectively. | 101 |

| | | |
|------|---|-----|
| 5.8 | Physical and numerical NS-SPH models. Evaluation of free-surface elevation near the front of the elevated structure due to unbroken wave (USWG2 sensor): (a) convergence, and (b) RMSE. Left and right subfigures show 3D and 2D results, respectively. | 103 |
| 5.9 | Physical and numerical NS-SPH models. Evaluation of free-surface elevation near the front of the elevated structure due to broken wave (USWG2 sensor): (a) convergence, and (b) RMSE. Left and right subfigures show 3D and 2D results, respectively. | 104 |
| 5.10 | Physical and numerical NS-SPH models. Evaluation of free-surface elevation in the back of the elevated structure due to unbroken wave (USWG6 sensor): (a) convergence, and (b) RMSE. Left and right subfigures show 3D and 2D results, respectively. | 105 |
| 5.11 | Physical and numerical NS-SPH models. Evaluation of free-surface elevation in the back of the elevated structure due to broken wave (USWG6 sensor): (a) convergence, and (b) RMSE. Left and right subfigures show 3D and 2D results, respectively. | 106 |
| 5.12 | Physical and numerical NS-SPH models. Trade-offs between modeling discretization and computational effort. | 108 |
| 5.13 | Physical benchmarking. Correlation between the mean \pm standard deviation (error) laboratorial data and the numerical solution obtained using the Lagrangian NS-SPH, Eulerian SW-FV and coupled Eulerian–Lagrangian modeling configurations. | 112 |
| 5.14 | Physical benchmarking. Correlation between the mean \pm standard deviation (error) laboratorial data and the numerical solution obtained using the Lagrangian NS-SPH, Eulerian SW-FV and coupled Eulerian–Lagrangian modeling configurations. | 114 |
| 5.15 | Physical benchmarking. Correlation between the mean \pm standard deviation (error) laboratorial data and the numerical solution obtained using the Lagrangian NS-SPH, Eulerian SW-FV and coupled Eulerian–Lagrangian modeling configurations. | 115 |
| 5.16 | Physical benchmarking. Correlation between the analytical and the numerical solution obtained using the Lagrangian NS-SPH model. | 117 |
| 6.1 | Test-case: a) global location of Europe, Portugal and Sines, b) location of the deep-water seaport in Sines region and position of the container terminal in the port complex, c) photography of Terminal XXI, d) photography of the constructive solution based on open-topology, and e) two-staged expansions of the cargo hub of Sines deep-water seaport. . . | 125 |
| 6.2 | Test-case: frameworks to characterize the regional/local-tsunami threat in Sines deep-water port, Portugal. Three stages encompassing multi-scale and multi-physics domains are linked by boundary conditions, BC. | 126 |

| | | |
|------|---|-----|
| 6.3 | Topo-bathymetric map with identification of tsunamigenic sources in Gulf of Cadiz region. The solid black line represents a normal fault, while black dashed lines represent the predominant thrust faults of the tectonic complex. White dashed lines represent hypothetical fault ruptures. Acronyms of the tsunamigenic geological mechanisms: GBF - Gorringe Bank fault, MPF - Marquês de Pombal fault, CWF - Cadiz Wedge fault, HSF - Horseshoe fault, SVF - São Vicente fault, PBF - Portimão Bank fault, WIS - Western Iberian Shelf, PS - Pereira de Sousa, TV - Tagus Valley (onshore), CF - Corner fault, HSP - Horseshoe Plain, SWIM - Southwest Iberian Margin. | 128 |
| 6.4 | Peak seismic hazard: range of PGA values for Sines site. The horizontal orange dashed line represents the reference value of PGA derived from the conversion of macro-seismic intensities maps. The horizontal blue dashed lines represent reference values from the national annex of EC8 standards, for type 1 (far-field) events and considering return periods of 1303– (class of importance IV) and 3000–years (return period of a 1755 GLET-alike event). | 135 |
| 6.5 | Peak seismic hazard: PGA values derived from GMPE models considering the attenuation law proposed by Atkinson and Boore 1995 and the multiple sources. Reference values of PGA derived from conversion of macro-seismic intensities maps and from the national annex of EC8 standards, for type 1 (far-field) events and considering return periods of 1303– (class of importance IV) and 3000–years (return period of a 1755 GLET-alike event). | 137 |
| 6.6 | Tsunami hazard: topo-bathymetric variations resembling the future configuration of Sines port with expansion of Terminal XXI (top) and Vasca da Gama Terminal (bottom). Black dots represent virtual gauges. | 138 |
| 6.7 | Peak tsunami hazard: values of free surface elevation due to 1755 GLET-alike tsunami around the cargo hub of Sines port. Reference value of $Z_H = 5\text{ m}$ set to represent the damaging potential of the tsunami hydrostatic effects on the container terminal(s). | 141 |
| 6.8 | Peak tsunami hazard: values of momentum flux due to 1755 GLET-alike tsunami around the cargo hub of Sines port. Reference value of $M_F = 30\text{ m}^3\text{s}^{-2}$ set to represent the damaging potential of the tsunami hydrodynamic effects on the container terminal(s). | 143 |
| 6.9 | Peak seismic action: distribution of PGA from S_{worst} adopting the source rupture of the composite Marquês de Pombal and Pereira de Sousa faults proposed by Terrinha et al. 2003 [449]. | 146 |
| 6.10 | Peak tsunami intensity measures for the different configuration cases. The left column regards maximum free-surface elevation (m), while middle and right columns represent tsunami maximum momenta flux ($m^3\text{s}^{-2}$) during inflow and outflow stages, respectively.) | 147 |
| 6.11 | Dynamic earthquake action: time-histories of seismic acceleration derived from various S_{worst} . Stars representing previously estimated PGA values. | 150 |
| 6.12 | Dynamic earthquake action: correlation between elastic response spectra derived from synthetic accelerograms | 151 |

| | |
|---|-----|
| 6.13 Dynamic tsunami action: modeling of the coupled configuration. | 153 |
| 6.14 Dynamic tsunami action: particle image velocimetry of the three-dimensional NS-SPH simulation of tsunami arrival at the container terminal to characterize the general flow behavior. | 154 |
| 6.15 Dynamic tsunami action: correlation between time-histories of horizontal tsunami force characterized via semi-analytical SW-FV and built-in NS-SPH. | 155 |
| 6.16 Dynamic tsunami action: time-histories of tsunami force on the horizontal direction derived from various S_{worst} and configuration cases. | 157 |
| 6.17 Dynamic tsunami action: time-histories of tsunami force on the vertical direction derived from various S_{worst} and configuration cases. | 158 |
| 6.18 Structural analysis: successive non-linear dynamic analysis. The first to fourth interval corresponds to static loads, seismic acceleration imposed at the bed-rock level (pink), tsunami pressures during inflow stage (blue) and tsunami pressures during outflow stage (green). | 159 |
| 6.19 Structural configuration: constructive design of the container terminal(s). | 162 |
| 6.20 Structural modeling: idealization of pile-supported soil-quay system for FE analysis. Modeling variations include pseudo-3D and 2D domains and configuration of pile-beam connections. Acronyms 'SP' and 'SB' stand for sections along pile or beam/slab, respectively. | 164 |
| 6.21 Structural modeling: ultimate N-M and yielding $M-\theta$ structural capacity of the cross sections of the piles. | 169 |
| 6.22 Structural analysis: modal analysis of the pseudo-3D soil-quay system. Representation of the first six modal periods. | 170 |
| 6.23 Structural modeling: preliminary verification. | 172 |
| 6.24 Successive structural response: main characteristics of structural behavior of the soil-quay system in response to S_{worst} considering GBF triggering source proposed by Grandin et al., 2007. | 176 |
| 6.25 Successive structural response: main characteristics of structural behavior of the soil-quay system in response to S_{worst} considering HSF triggering source proposed by Ribeiro et al., 2007. | 178 |
| 6.26 Successive structural response: behavior of the soil-quay system in response to S_{worst} considering MPPSF triggering source proposed by Terrinha et al., 2007. | 179 |
| A.1 Validation of Eulerian SW-FV scheme: Tohoku-Oki, 2011 tsunami. Location of ocean DART and coastal GPS buoys instruments. | A.1 |
| A.2 Validation of Eulerian SW-FV scheme: correlation between instrumentally recorded data and numerical solutions computed at the correspondent VG using MUSCL, <i>minmod</i> and <i>vanLeer</i> , and MOOD techniques. Cont. \rightarrow | A.2 |

| | | |
|-----|---|------|
| A.3 | Validation of Eulerian SW-FV scheme: correlation between instrumentally recorded data and numerical solutions computed at the correspondent VG using MUSCL, <i>minmod</i> and <i>vanLeer</i> , and MOOD techniques. | A.3 |
| B.1 | Experimental setup: considerations for the benchmarking. Correlation between recorded and filtered data. | B.6 |
| B.2 | Physical benchmarking. Influence of prescribing OBC to initiate partial domains of NS-SPH models. Free surface elevation in the flume, WG2, due to unbroken and broken waves. | B.7 |
| B.3 | Physical benchmarking. Influence of prescribing OBC to initiate partial domains of NS-SPH models. Free surface elevation near the elevated structure, USWG1, due to unbroken and broken waves. | B.8 |
| B.4 | Physical benchmarking. Influence of prescribing OBC to initiate partial domains of NS-SPH models. Free surface elevation after the elevated structure, USWG5, due to unbroken and broken waves. | B.9 |
| C.1 | Terminal XXI during construction works (left) and after conclusion (right). | C.13 |
| C.2 | Global maritime traffic, 2021. | C.14 |
| C.3 | Embryonic plans endeavouring the increase of Sines seaport cargo capacity. Adapted from the parliamentary session at the Portuguese Assembleia da República, in 2014. | C.15 |
| C.4 | Study of the environmental impact assessment for the third and fourth expansion stages of the Sines seaport cargo hub. Adapted from the Environmental Impact Assess developed by Nemus for Administração dos Portos de Sines e do Algarve S.A.. | C.16 |
| C.5 | Presumable design configuration for the thrid and fourth expansion stages of the Sines seaport cargo hub. | C.17 |
| D.1 | Peak tsunami hazard: physical and modeling sources of uncertainty influencing H_{max} profiles acquired at the dry-wet interface of Sines coast, $t = 0 s$ | D.21 |
| E.1 | Structural analysis: modal analysis of 2D soil-wharf system. Representation of the first six modal periods considering SP1 (left) and SP1* (right) configurations. | E.23 |

Chapter 1

Introduction

Historical records from 426 B.C. describe the first correlation between tsunamis and ocean earthquakes by the historian Thucydides in Greece [1].

Chapter 1 is dedicated to contextualize the tsunami engineering subject and outline the objectives and expected outcomes of the dissertation.

1.1 Contextualization

Intensive regional development promoting disparities between coastal and inland regions constitutes an issue in policy making. The global demography in coastal regions highly constrains ecologic, social and economic aspects of sustainability. Moreover, such regions are often prone to unpredictable and destructive natural hazards, potentially evolving to natech hazard, and leading to catastrophic scenarios. The paucity of legislation envisaging a preventive perspective that translates hazard assessments into land management and structural performance criteria jeopardizes the whole concept of sustainable development.

Of all hazards, tsunamis represent one of the hazardous threats for coastal communities. The scenario of settlements concentration in low-lying coastal cities tend to become worst considering the projection of the world population growth, which doubled in the last forty years. Moreover, the statistics used for the tsunami risk management typically address only local inhabitants, missing the large variation posed by tourism contributions [2]. The contribution of science and technology to efficiently characterize tsunami hazard and design more resilient communities is fundamental to stakeholder and politic decision-making.

In response to recent major tsunami disasters, as the 2004 Indonesian and 2011 Japanese, risk management strategies have been developed based on the fundamental principles of land use, emergency management and structural and non-structural countermeasures [3, 4], progressively introducing geographic [5, 6] and demographic inclusive policies, considering physical disabilities, gender or poverty [7, 8]. Field surveys were conducted by expert teams after the events of Indonesia 2004 [9], Chile 2010 [10], Japan 2011 [11], Chile 2015 [12] and Indonesia 2018 [13], providing valuable

insights and data to calibrate physical experiments [14–17] and numerical models [18–21], both used to study past disasters and forecast future ones. Early warning systems [22–24] and evacuation measures and plans [25–29] are being implemented around the globe to mitigate tsunami effects. The tsunami as an action is being studied to define structural performance requirements and increase the resilience of the coastal communities exposed to the tsunami hazard. Both the Japanese [30] and the North American design codes [31, 32] already account for the tsunami action in the loading combination provisions for structural design recommendations. In Europe, the harmonized structural design code [33], Eurocodes, EC, still does not mention the tsunami load. However, a new task-group of International Federation for Structural Concrete is being constituted to provide reliable design and assessment criteria in the field of tsunami engineering in order to improve existing international codes and develop the first guideline for Europe.

Despite the remarkable break-through of the last decades [4], the efficiency of tsunami-risk management policies would benefit from insights of multidisciplinary scientific fields to overcome current drawbacks [34]. One of the challenges to overcome is related with multi-risk perception. Often, natural and anthropogenic risks have inter-dependencies, contributing to increase their disaster potential. The cascading effects of regional/local-tsunamis [35] is one of the multi-hazard cases that continues underappreciated or neglected in the risk assessment and structural design processes [36–41].

However, such extreme events are infrequent which leads to nonexistent or incomplete databases. Moreover, the short temporal interval between the ground-shaking and tsunami-impact makes the characterization and disaggregation of the effects on structures difficult during the field surveys after the tsunami [36, 42]. Experimental and numerical models can provide additional insights on both hazard and structural vulnerability by generating complementary data.

Yet, the experimental simulations are costly, time-consuming, and require accuracy in the scaling relations and appropriate facilities, such as shaking tables, to simulate ground shaking on structures, and large flumes, to generate and propagate tsunami-type long-waves.

The numerical approach became alternative or complementary to physical experiments over the last decades. Nonetheless, the simulation of the natural phenomenon and its interaction with structures require complex models and sophisticated numerical schemes often leading to computationally expensive and time-consuming (or even prohibitive) simulations. Meanwhile, emergent hybrid approaches enable high-performance numerical and physical testing. Real-time multi-directional hybrid simulations on large-scale structural systems using 3D non-linear numerical models combined with large-scale physical models of structural and non-structural components are particularly promising for tsunami-structure interaction and cascading earthquake-tsunami hazards. Hybrid simulations of cascading seismic and tsunami events were recently performed by means of incorporating parametric influences of stiffness, damping, added mass (and natural frequencies) of the structures to their response to seismic effects, and then applying the seismic deformation from the numerical model into the experimental specimen via actuators, followed by the generation of tsunami-like waves propagating along the flume and impacting the specimen.

Despite the mentioned exception towards innovative approaches, the common procedures tend to separate seismic hazard, seismic structural response, tsunami hazard and tsunami structural response, missing the link between them to reduce or be aware of the (large number of) uncertainties inherent to the problem, derived from physical (ex.: source location and rupture mechanism, and aleatory uncertainty in the tsunami wave breaking and the bore formation, which is a chaotic process), numerical (ex.: sophistication of the numerical schemes and quality of data to prescribe initial and boundary conditions) and modeling variables (ex.: simplification of processes assumed on experimental and numerical simulations that effectively compose the physical phenomena).

The coastal structures at risk from tsunami may feel the ground shaking caused by the earthquake, depending on the magnitude and location of the event. An earthquake source, with enough energy to be felt at the location of the structure and to trigger a tsunami, implies the mobilization of the structural resistance to deal with the earthquake action, potentially affecting their performance against the incoming tsunami. Instead of individual actions, it is necessary to characterize the structural response to an adequate cascade loading pattern, combining the seismic displacements and the tsunami forces, otherwise the risk is underestimated compromising sustainable principles and adjacent social and environmental policies. Moreover, literature regarding modeling tsunami effects on coastal structures has been published, but comparatively less attention has been devoted to studying the interaction of fluids with modified [43, 44] or elevated structures [45–48]. In shallow coastal areas, the impact of tsunami-like waves can also have an important vertical hydrodynamic component, which threatens elevated structures such as piloti-type buildings, bridges, wharves with open typology, among others. Similarly, physical and numerical simulations have been privileging the characterization of tsunami effects during inflow over outflow stages. The wave receding after wave impingement can induce negative pressure at the bottom of elevated structure, causing suction effects capable of inducing downward displacement of the structure [49–52].

Moreover, tsunami forces derived from hydraulic components have been favoured over debris [53, 54] and scouring effects [55–57], which represent high damaging potential for the structures [58–60].

Lastly, an enhanced scientific knowledge is particularly valuable if transposed into practical regulatory codes, with potential to influence both stakeholders and technical practices. An optimized design of coastal structures, considering the successive effects of ground-motion and tsunami, must guarantee two main criteria. The first regards requirements of the constructive solution, balancing the demands of flexibility and ductility for earthquake resistance with the demands of stiffness and strength for tsunami resistance. The second regards the trade-off between the economy of the structural solution and the level of structural performance, implying opening the prospects for stakeholders, governments and technicians.

Motivated by the expansion plans of an internationally-sized deep-water port located in a tsunami-prone region, a reflection on the scale of the work needed to perform a multi-risk assessment and the challenges yet to overcome was introduced to emphasize the challenge of combining safety requirements with financial and ecologic concerns. Among tsunami risk mitigation approaches, the conceptual interdisciplinary-based methodology herein proposed focused on the hazard-structural

vulnerability, aiming to support uncertainty-aware, systematic and informed decisions due to structural design.

1.2 Objectives

The cascading earthquake and tsunami loading pattern and the sequential structural response are evaluated by developing a three-stage numeric methodology with characteristic spatial and temporal scales. It takes advantage of the characteristic physics encompassed in the domain, from the genesis of the tectonic phenomena to the infrastructure(s) response, to assess:

1. the adequacy of the numerical schemes to model each domain and the boundary conditions to coupled them;
2. the cascading earthquake and tsunami multi-hazard;
3. the tsunami hydrostatic and hydrodynamic effects on horizontal and vertical directions, during inflow and outflow stages;
4. the distribution of tsunami pressure on vertical, horizontal and over sloping grade elements of the structures directions;
5. the cumulative effects of sequential ground-motion and tsunami loading patterns on structures;
6. the successive behavior of structures with open-typology due to cascading earthquake and tsunami actions.

The key-objective is to contribute for the enhance of scientific knowledge and its transposition to existing or development of new tsunami engineering provisions encompassing the harmonization of tsunami design provisions with existing seismic design provisions, towards safety and operational performance levels. The secondary goal is to raise awareness for more efficient coastal risk management and, ultimately, a sustainable development of tsunami-prone regions. Motivated by the expansion plans of an internationally-sized deep-water port located in a tsunami-prone region, an earthquake and tsunami multi-hazard assessment was performed and the respective successive structural response of an open-typology wharf estimated. Based on the identified structural vulnerabilities with potential to jeopardize the port's activities, current operations and lifeline support, were qualitatively predicted natech situation scalability, societal and ecologic impacts [61]. For these reasons, both the promotion of scientific dissemination and networking with academia and industry represented an ubiquitous aspect along the PhD development.

1.3 Organization

Within the context of the objectives mentioned above, the present dissertation is composed of seven chapters.

Chapter 2 goal is twofold. Section 2.1 is dedicated to reviewing the literature on risk due to tsunami with tectonic origin. The influence of disruptive events on tsunami risk perception that led to the existent mitigation policies, and the advances and gaps in scientific and technological perspectives are integrated to emphasize the challenge of combining safety requirements with financial and ecologic concerns. Section 2.2 introduces a conceptual preventive-based strategy. Taking advantage of the physical characteristics of earthquake ground-motion(s) and tsunami wave(s) on the generation, propagation and site-effects stages, the conceptual methodology was proposed as hypothesis to contribute for tsunami engineering. It encompasses the full domain, from the genesis of the tectonic tsunami to the respective structural behaviour due to cascading earthquake and tsunami actions, considering three interdependent frameworks defined in terms of spatial and temporal scales. The numerical approach aims to promote the awareness of the global uncertainties, physical and numerical, allowing to adapt the sophistication of the risk analysis to its goal, and allowing to support informed and systematic decisions to make safety, financial, ecologic and sustainability criteria compatible. From a technical perspective, implied when promoting the trade-offs between sophistication of the numerical models and computational costs, the simultaneous goal is towards high-quality solutions while controlling computational costs up to a relatively affordable level.

Chapter 3 is devoted to introducing fundamental aspects of numerical methods involved in the characterization of seismic and tsunami natural phenomena and prediction of the respective structural response. Section 3.2 presents the numerical protocols to estimate tsunami hydrodynamic effects on coastal structures while Section 3.3 describes the stochastic procedure to characterize earthquake strong ground motions. Section 3.4 describes the tool for soil-fluid-structure modeling.

Among the vast range of functionalities made available by the numerical tools, a benchmarking process oriented to the main features used on the modeling processes is presented in Chapter 4.

Chapter 5 constitute a proof-of-concept for the tsunami action characterization. It demonstrates the feasibility and practical potential of numerically modelling the tsunami and tsunami-structure interaction phenomena by correlating numerical solutions and instrumentally-recorded data acquired during an experimental campaign performed at the large wave flume of the Hinsdale Wave Research Laboratory, Oregon State University. The correlation includes intensities of hydrodynamic quantities (free-surface elevation and flow velocity) and impacts on an elevated structure (forces and pressures, in both horizontal and vertical directions).

Chapter 6 is assembled to investigate the successive structural behaviour of an open-type wharf due to cascading seismic and tsunami actions. The generic methodology introduced in Chapter 2 is adapted assuming two alternative basic and enhanced forms to investigate the multi-hazard posed by 1755-alike earthquake and tsunami event to the terminal container of Sines deep-water seaport, in Section 6.4. The basic form uses ground motion prediction equations and hydraulic semi-analytic formulation to assess peaks of ground acceleration and tsunami momentum flux, respectively. The enhanced form relies on more sophisticated numerical schemes to characterize the physics of dynamic ground motion and tsunami actions. The respective non-linear dynamic response of the wharf is estimated in Section 6.4.

Chapter 7 compiles the main conclusions drawn along with recommendations for earthquake and

tsunami multi-risk mitigation for critical coastal infrastructures, such as deep-water seaports. The present work constitutes a contribution that would benefit from complementary insights such as those identified for future developments.

Chapter 2

Conceptual Methodology

In 2015, the United Nations for Disaster Risk Reduction defined a 15-year framework to reduce several risks, including the tsunami risk. The distribution of funds recommended by the Sendai Framework [62] include a 90%-share for reconstruction and damage response aspects, while (only) 10% are channeled for preventive actions.

Chapter 2 is dedicated to reviewing the literature on tsunamis with tectonic origin multi-risk management and introducing a generic preventive-based strategy to contribute to designing tsunami-resistant structures towards more resilient coastal communities.

Chapter 2 is based on Reis et al. 2022c [63].

2.1 Literature Review

The spatial distribution of the world population is uneven, with a density of about 40% living in coastal regions. The trend is expected to continue in both demographic indicators and urban development rate, being many coastal cities in seismic- and tsunami-prone regions and built through informal and unplanned settlements, exposing their population and assets to such hazards. Recent tectonic-triggered events raised awareness of the cascading earthquake and tsunami threat and highlighted the paucity of structural design criteria considering the cumulative effects of both. By being exposed to the ground-motion, the structures' resistance may decrease and become residual/non-existent to support the incoming tsunami, implying an underestimation of the risk.

2.1.1 Risk management

In common practice, the risk analysis of different hazards is independently assessed, considering single hazards and undervaluing possible risk interactions. The multi-risk concept is a relatively new approach introduced to overcome the bias present in single-risk evaluations [64–72].

The theoretical concept of multi-hazard/risk and terminology compiled after temporal or causal relationships between hazards has proven to be essential for risk management. The first studies

demonstrating that natural and anthropogenic risks have inter-dependencies that contribute to increasing their potential made use of joint probability distributions of single hazards and probabilistic techniques to integrate the multiple hazards interaction [64–68]. Later, modelling requirements and main issues to be taken into account in the development of simulation tools [69], as well as identification and effects of epistemic physical uncertainties [70], modeling failure uncertainties [73], or even human reaction uncertainties [74] have been investigated, while alternative approaches to deal with data incompleteness and small-sample issues were investigated [75]. The multi-hazard/risk analyses evolution raised into such a level of awareness for the variables involved in the processes that a systematic organization of the inter-dependencies between hazards and respective nomenclature was established to facilitate the harmonization and comprehensiveness of the terms among multi-disciplinary fields of investigation involved in risk-related frameworks [71, 76, 77]. The differentiation between cascading hazards (temporal order in the multi-hazard event) and compound hazards (two or more hazards acting together) establishes hazard interrelationship types: triggering, change condition, compound, independence and mutually exclusive.

In particular the theoretical concept of multi-hazard/risk gained prominence investigating the cascading earthquake and tsunami effects on coastal structures and communities after the 2011 Japan event. The earthquake and tsunami multi-hazard concept started acknowledging a primary earthquake hazard triggering a secondary tsunami effect in a cascading relation, sequential in time, amenable of stochastic, empirical or mechanistic modeling, and deterministic or probabilistic hazard analyses. Earthquake and tsunami multi-hazards triggered by the mega-thrusts of Tohoku and Cascadia were respectively addressed for the Tohoku [38, 78] and Oregon regions [79] using a probabilistic approach. Both studies characterized the local and regional offshore faults capable of triggering tsunamis to generate scenarios. For the Tohoku region, a range of plausible sources was represented by adopting stochastic synthesis of slip distribution, while a probabilistic logic-tree model was assembled to account for the uncertainties of earthquake scenarios for the Oregon region. Seismic and tsunami simulations respectively evaluating ground motion acceleration and tsunami inundation depths were then carried out, while their inherent cumulative distribution functions were calculated to define the exceedance probability and define seismic and tsunami multi-hazard curves. Despite some studies demonstrating the damaging potential of hydrodynamic effects on structures [80, 81], the influence of tsunami flow velocity was disregarded in the aforementioned multi-hazard studies. Lessons learned from the 2011, Japan event also draw attention to another cascading scenario, when M_w7 aftershocks occurred simultaneously with the tsunami [36]. Choi et al., 2015 and 2018 [37, 82] focused on the simultaneous occurrence of tsunamis and aftershocks just after a great subduction earthquake and proposed a loading combination for structural safety verification.

The structural vulnerability due to multi-actions is commonly represented by probabilistic fragility curves relating an intensity measure of hazard to a level of structural performance, except for recent fragility curves developed to account the succession of ground motion and tsunami actions on bridges [83] and portuary building structures [84], most fragility studies developed for coastal structures [40, 85] and multi-risk analyses aiming to evaluate loss for coastal communities subjected to local/regional

tsunami hazard [39, 78, 86–88] are based on joint probability of seismic and hydrostatic tsunami intensity measures affecting buildings [40, 85, 89–93], bridges [83, 94–96], port facilities [84, 97–99] and coastal defense structures [57, 100–105].

The exposure term in the risk equation regards the population, infrastructures and the level of preparedness (warning and evacuation) of the region. The population distribution data is primarily based on statistical data from the census, providing information such as the number of inhabitants per mapping unit and demographic aspects that influence the risk assessment like age, gender, income, education, disabilities and migration. Recent studies on seismic [106–108] and tsunami exposure [109–114] proposed innovative approaches to qualify and quantify the exposure parameter dynamically in space and time. New techniques of exposure data-acquisition, such as remote sensing, laser scanning, mobile apps, drones, and social media tools are being introduced in the framework of risk management [109, 115, 116], skipping a great part of post-event post-processing directly into ready to use information for agencies and population.

The multi-risk assessment, as the product of hazard, vulnerability and exposure, is the ultimate tool to make planned decisions to develop mitigation measures and contribute to resilient coastal communities [28]. However, the earthquake and tsunami multi-risk assessment is simultaneously a recognized important topic and a complex new field to explore the aggregation of the large amount of information, variables and uncertainties in a single model of risk [39, 78, 86, 117, 118, 118–120]. Meanwhile, the path to automated global risk-data, with cloud-based infrastructure is becoming a reality in the framework of harmonized data [116], aiming to provide integrated tools to manage, analyze, understand, and share essential data for natural hazards research and risk management. More complex interpretations, including climate and anthropogenic precedents and/or sequential natech scenarios, are being tackled as influencing conditions in tsunami risk assessments, highlighting the highly complex framework needed to understand and manage tsunami risk [34]. Various approaches to quantify and classify the resilience of communities exposed to natural threats, such as earthquakes [121, 122] and tsunami [123], are emerging while influencing factors, such as land use [124] or citizen preparedness [125], are being investigated [126] as potential catalyst for community resilience building.

Figure 2.1 summarizes the current tsunami risk management procedures. The integrated tsunami risk governance has two distinct phases composing the cycle where post-event data provides simultaneous valuable insights to feed risk models and calibrate pre-event prognostic of risk.

The current risk governance process involving governments, stakeholders, scientists and technicians, civil protection and communities at risk has two primordial perspectives. The preventive perspective is associated with the pre-event stage predicting risk and developing mitigation measures based on understanding and quantification of hazard, eventually considering pre-environmental conditions (physical, environmental, social, economic), plausible hazard interactions (cascading, simultaneous or successive occurrences) and different hazard assessment techniques, such as deterministic or probabilistic approaches, which are function of the purpose it aims to respond. For example, probabilistic approaches are adequate to compose hazard maps while deterministic approaches can represent a complementary targeted, detailed information to evaluate the worst-case

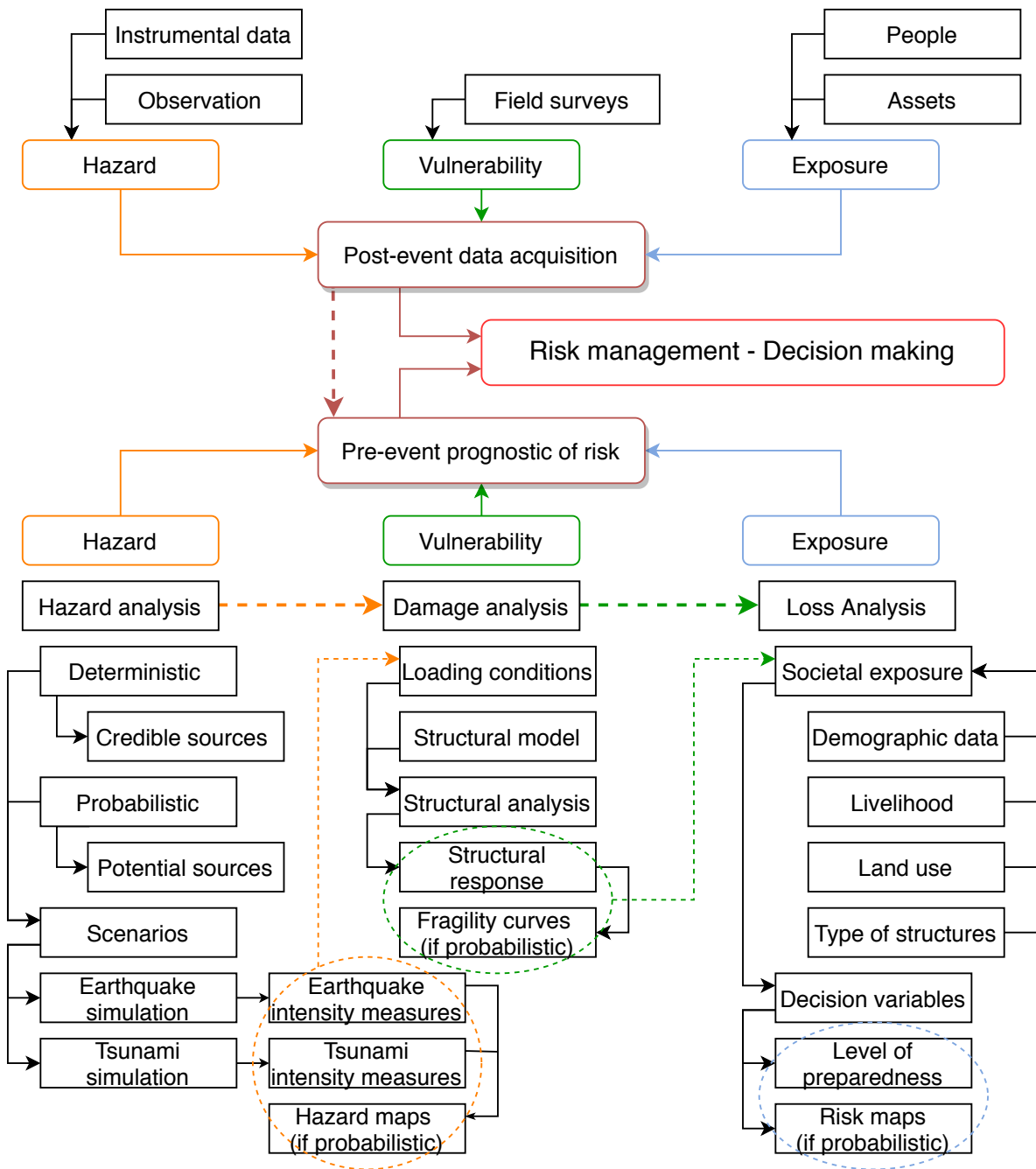


Figure 2.1: Integrated local-tsunami risk management as a tool for decision-making. Hazard (orange), vulnerability (green) and exposure (blue) factors of risk (red) in pre- and post-event stages.

scenario when designing a critical infrastructure [127]. Besides the natural hazard, the risk also depends on man-made influences. The human and assets exposure to risk can determine the amplification or reduction of risk level, while the vulnerability of heritage buildings constrains the resilience of the coastal communities.

The post-event stage is simultaneously a phase of response and an opportunity to refine and redefine strategies for risk governance. Until a recent past, the data from post-events needed analytic interpretations before its incorporation in risk management. However, nowadays' sensor networking composing seismic and tsunami alert systems provide data, almost in real time, that allows early

responses. Additionally, the relief measures taken during the event, namely using recent GIS, mobile apps, drones, and social media tools, are also direct response of risk management authorities. Moreover, data acquisition after an extreme event is essential to calibrate the pre-event analysis, playing a fundamental role in risk management from a prevention perspective.

2.1.2 Disruptive events and governmental responses

Extreme disasters are simultaneously tragic and an opportunity to improve regional and global resilience of communities.

Lisbon, 1755

One of the events that changed the paradigms in the history of earthquake and tsunami disasters was the November 1st 1755, Lisbon event. The $M_w 8.5 \pm 0.3$ earthquake [128] was felt throughout Europe and North Africa and a transoceanic tsunami affecting North Atlantic and Central and South American coasts was observed [129–131].

Many of the most influential thinkers of the European Enlightenment, Kant, Descartes, Rousseau, Voltaire, intervened discussing a disruptive philosophical perspective of earthquake hazard as a scientific matter in detriment of religious interpretations [132, 133]. For the first time a coordinated emergency response was put in place. Despite empirical knowledge on earthquake resistance as part of ancient architectural designs, such as Chinese [134] and Japanese [135] pagoda, and some constructions on the South of Europa, the reconstruction of Lisbon was the first time in the world that an entire city was built to resist future earthquakes

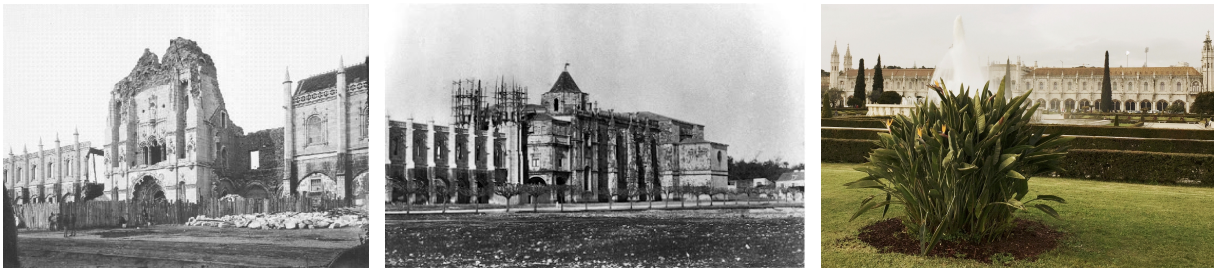
Buildings were re-built grouped in blocks to form an orthogonal grid of streets. Principles of simplicity and uniformity, with anti-seismic concerns and no more than four-stories were adopted. Governed by a prototype of a seismic-resistant code ([136, 137]), the city reconstruction followed the so-called Pombalino construction, consisting of stone masonry and tri-dimensional wood truss made of vertical and horizontal elements braced with diagonals, forming the Saint Andrew's Cross ([138]). Fig. 2.2 depicts the detailed structural solution adopted in the process of reconstruction of the city.

Sumatra, 2004

In 2001, the North American National Tsunami Hazard Mitigation Program [139] had already compiled the seven principles to increase the resilience of coastal communities to tsunami threat. These guidelines were intended for use by local elected, appointed, and administrative officials involved in planning, zoning, building regulation, community redevelopment, and related land use and development functions in coastal communities. The seven basic principles recommended 1) understand the tsunami risk of the region, 2) avoid new development in tsunami run-up areas, 3) locate and configure new development that occurs in tsunami run-up areas, 4) design and construct new buildings to minimize tsunami damage, 5) protect existing development from tsunami losses through



(a) Carmo convent. A memorial of the 1755, Lisbon disaster. The XIV century Gothic structure suffered the ground motion and fire effects.



(b) Jeronimos monastery. From left to right, the XVI century Manueline structure partially survived the ground motion and about 4 m tsunami flow depth [130]. Its reconstruction begun in the early XIX century and, today is one Portuguese tourism reference.



(c) Pombalino constructive solution.



(d) Saint Andrew's Cross.

Figure 2.2: The 1755 Lisbon earthquake and tsunami event contributed to the development of the earthquake engineering concept, adopted in Lisbon's reconstruction.

redevelopment, retrofit, and land reuse plans and projects, 6) take special precautions in locating and designing infrastructure and critical facilities to minimize tsunami damage and 7: evacuation plans.

Yet, the December 26th2004 event in Sumatra, Indonesia marked one of the more recent milestones in the tsunami risk awareness. The M_w 9.1 earthquake is one of the largest instrumentally recorded events [140, 141]. It generated a transoceanic tsunami affecting sixteen countries and recorded by nearly one thousand tide gauges [9, 141]. As one of the deadliest natural disasters ever, it caused more than 200000 casualties, demonstrating the importance of preparedness strategies to mitigate natural threats. The absence of tsunami early warning, proximity of Indonesian coasts to the source and the

difficulty to horizontally evacuate highly densely populated coastal regions, were referred in post-event surveys as the ultimate combination that led to the fatal losses. Strategic land use planning guides, vertical evacuation structures and early warning systems, as the Pacific Ocean already had since the Hawaiian tsunami of 1946, were identified as priority resilience strategies for coastal communities at risk of tsunamis [140, 142, 143].

The United Nations immediately launched the International Early Warning Program planning the creation of a tsunami global warning system. The current extension of the tsunami global warning system covers the Pacific, Indian, NE Atlantic, Mediterranean and connected seas (International Oceanographic Commission, IOC-UNESCO site: <http://neamtic.ioc-unesco.org/>, last accessed: 03Jan2019). The probabilistic hazard assessment for tsunamis generated by earthquakes in the coastlines of the North East Atlantic, the Mediterranean, and connected seas, is available since 2019 aiming to establish a common tsunami-risk management strategy in the region [144]. Fig. 2.3(a) depicts the global coverage of the tsunami global warning system, even if, in certain regions, the effectiveness of the warning system remains constrained by national-scale institutional, budgetary, and maintenance problems [8].

Using insights of structural behavior surveyed in the post-disaster, researchers concentrated their investigations on vertical evacuation buildings. Many of the observed damages in structures show the expected behavior of structures due to ground-motion. However, new and unexpected behavior due to the tsunami impact was observed. Comparatively, the tsunami caused more destruction than the earthquake and made clear the need to consider the tsunami in the structural design of structures, most importantly in structures to be used as vertical shelters [141, 145, 146].

A 2005-result was the “Design Guidelines for Tsunami Shelters” [147], published by the Japan Cabinet Office. The document recommends the location, usage and performance of evacuation buildings, considering the intensity of tsunami pressure on structures as a function of the Froude number. In 2008, the American National Tsunami Hazard Mitigation Program for the Federal Emergency Management Agency, FEMA, published the first edition of “Guidelines for Design of Structures for Vertical Evacuation from Tsunamis”, P-646 report [148], Fig. 2.3(b).



(a) Extension of the current tsunami early warning system.

(b) FEMA P-646, 1st edition.

Figure 2.3: The 2004 Sumatra earthquake and Indian Ocean tsunami contributed for the development of tsunami early warning globalisation and guidelines for vertical evacuation preparedness.

The P-646 report provides guidance on the determination of tsunami hazard, options for vertical evacuation with respective sizes and locations, estimation of tsunami load effects, structural design criteria, and design concepts. The document briefly refers a non-contradictory criteria to design structures to resist an earthquake and the subsequent tsunami. A companion report, “Vertical Evacuation from Tsunamis: A Guide for Community Officials” [149] provide guidance, at a local and state level, for communities to assess the need, plan the design and construction, discuss funding, operation and maintenance issues of vertical evacuation structures.

The USAID Asia prepared guidelines [150] on the resilience of coastal communities in response to the event, including best practices in tsunami risk management that consisted primarily in land use planning based on tsunami inundation and run-up predictions. Additional references to nature-based mitigation solutions are also part of the best practices, including coastal ecosystems, such as mangroves, coastal forests and fringing reefs, that already demonstrated their contribution enhancing coastal resilience during the 2004 tsunami by reducing flow height and velocity, debris blockage and formation of dunes.

Tohoku-Oki, 2011

The March 11th2011, Tohoku, Japan $M_w9.0$ event propelled the concerns on structural performance on tsunami-related disaster risk reduction measures. The conjecture of the pre- and post-disaster boosted the tsunami-related interest in designing resilient communities after holding the status of the world's most costly natural disaster, estimated in 300 billion dollars.

First time modern, well-developed tsunami countermeasures, such as offshore and onshore tsunami barriers, natural planted tree barriers, vertical evacuation buildings, and periodic evacuation training introduced before the 2011 event were put to test during the tsunami [151]. However, the tsunami forecasts were exceeded, unveiling the uncertainty associated to the estimates [112, 151–153]. After the disaster, extensive surveys along more than 600 *km* of coastline were conducted by several national and international teams of experts [11, 154] identifying structural damage patterns due to earthquake and tsunami loading effects, difficult to identify and differentiate. However, about 92% of the fatalities were concentrated in coastal regions and attributed to the tsunami [36, 38, 94, 151, 152].

Lessons learned from the event led the two pioneering countries, North America and Japan, to update and develop new structural design provisions to engineering-based mitigation solutions. The Ministry of Land, Infrastructure, Transport and Tourism of Japan published the “Interim Guidelines on the Structural Design of Tsunami Evacuation Building” [30], aimed at designing vertical shelters and local government-designated high-risk structures, with updated considerations for buoyancy and lateral equivalent hydrostatic load applied to one side of the structure. The flow depth used to calculate the lateral load is derived from tsunami inundation maps provided by the coastal municipalities, which were refined after the demonstration of potential destruction caused by inundation depths over 2 *m* [155], Fig. 2.4(a). The coefficient affecting the lateral force, instead of depending only on the Froude number, as in the previous 2005 document, was rectified to consider the distance to the coast and the dissipation of energy due to the structural orientation. New precautions on scour and debris impact were also

introduced. The Ports and Harbors Bureau of MLIT updated the “Technical standards and commentaries for port and harbour facilities in Japan” [156] after the 2011 event.



(a) Japan inundation warning signal.

(b) ASCE-SEI 7-16 design code.

Figure 2.4: Refinement of hazard assessment maps and structural performance criteria were updated after the 2011 Tohoku earthquake and Pacific Ocean tsunami.

In the United States, a second version of P-646 report [157] was published, while, in 2016, the Tsunami Loads and Effects Subcommittee of the American Society of Civil Engineering prepared the new Chapter 6 - “Tsunami Loads and Effects” to become a part of the ASCE 7 guidelines [32], Fig. 2.4(b). The provisions for tsunami hazard assessments vary between direct derivation from hazard maps and, for critical structures, semi-analytic formulations based hydrodynamic parameters numerically assessed. An empirical equation is recommended for the treatment of the component of tsunami force posed by debris impact. The tsunami chapter briefly refers independent earthquake and tsunami analyses and, for lower-category structures and life safety structural performance, dismisses the tsunami analysis if the lateral framing system maintains 75% of the strength after the ground-motion. For bridges, the the Pacific Earthquake Engineering Research Center, PEER, released recently three reports [158–160] presenting the research results and simplified methodologies for the development of tsunami design guidelines by American Association of State Highway and Transportation Officials, AASHTO, in the USA. It encompasses probabilistic tsunami hazard maps at 1000–year recurrence level, complementary loading equations and geotechnical considerations, and the proposal of simplified and complex 3D investigations of tsunami impact on straight and skewed

bridges, respectively. For harbors, the US National Defense briefly refers the need of considering tsunami action on floating structures located on regions of extremely high seismic risk, and where tsunamis and seiches are anticipated, on the “Unified Facilities Criteria Design: Piers and Wharves”[161]. The US National Tsunami Hazard Mitigation Program developed “Guidelines and Best Practices for Tsunami Hazard Analysis, Planning, and Preparedness for Maritime Communities” addressing minimum requirements to develop consistent and reliable tsunami preparedness products for maritime communities [162]. A committee of the World Association for Waterborne Transport Infrastructure, PIANC, is re-writing the PIANC WG239 document on “Mitigation of Tsunami Hazards in Ports”.

In Europe, the consideration of tsunami as an acting load remains missing in the harmonized structural design code for seismic regions, Eurocode 8 [153, 163]. Nonetheless, the first steps towards tsunami risk are being taken, both from geophysical [164] and engineering perspectives, through the International Federation for Structural Concrete. The second Fib Commission: Analysis and Design recently integrates Task Group 2.13 - Design and assessment for tsunami loading, which is dedicated to characterize tsunami loads acting on structural members for design/assessment of structures and infrastructure. In the future, it aims to introduce reliable design/assessment criteria in the field of tsunami engineering, which will lead to the first guideline for Europe and improvement with respect to existing international codes. It will also address aspects related to the harmonization of tsunami design provisions with existing design provisions for other kind of hazards. Worldwide, Russia is developing rules for assigning the tsunami loads on ports and marine structures [165], while Chile is deriving local guidelines based on the ASCE-16 new tsunami chapter [163].

2.1.3 Scientific and Technological Advances and Shortcomings

Despite the advances of the last decade(s), a better understanding of the tsunami phenomena and its interaction with the coastal structures remains challenging. The development of guidance on structural performance considering the tsunami, from far-field sources, or the cascading ground-motion and tsunami loading pattern, from regional/local sources, is constrained by the seldom occurrence of tsunami events. The data from historical events is circumscribed to geological evidence and/or written testimonials, whereas the instrumentally recorded data from late century events constitute a valuable resource to produce synthetic data and calibrate physical and numerical models.

The design standards provide a set of equation to assess the hydraulic components of tsunami force and the derivative debris and scouring effects. Experimental and numerical studies are being conducted to provide additional insights for the calibration of existing equations or development of new ones. Experimental studies to characterize the tsunami flow impact on coastal structures [17, 166–168], are more numerous than studies on debris transportation and impact [169–171], and scouring effects [56]. Similarly, numerical studies considering the tsunami fluid force exerted on the horizontal direction [166, 172] are more common than on the vertical direction [48, 173], while the computation of debris transportation, damming and impact constitutes a numerical challenge involving laminar and turbulent

flows, interaction between fluid and solids, and randomness of motion and trajectory [54].

However, surveys from past events and recent research have highlighted the hazardous damaging potential of the (so far) less investigated tsunami hydrodynamic pressure exerted on elevated structures, and debris damming and impacts. Experimental and numerical approaches have demonstrated that pressures/forces exerted on the soffit of elevated structures have equal or greater order of magnitude as the ones exerted on the horizontal direction [45, 48, 168, 173–175]. The debris impact on vertical structures can pose violent collisions, while when encountering elevated structures demonstrated to produce generation of significant impulsive loads followed by longer duration damming loads that can lead to structural failure mechanisms [54, 170, 171]. The scouring effects also caused catastrophic geotechnical failures of coastal protection structures, dikes, and quay walls after the Japan, 2011 tsunami [60]. Parametric analyses to determine influencing parameters on scouring effects induced by tsunami have been developed considering different solid geometries, fluid characteristics, and geotechnical conditions of the soil substrate, such as liquefaction potential [176–181].

Physical models

The physical experiments are classic and essential sources of data to study the natural phenomena and the structural behavior. The effects of the earthquake ground-motion on different structures and materials is widely explored in experimental campaigns, typically performed by static cyclic tests and sometimes finalized by shaking-tables tests [182–186].

Tsunami waves have been modeled in laboratory facilities, with initialization conditions resembling the generation phase, while geometrical setup variations are used for the propagation and inundation phases [187, 188]. To model fluid interaction with coastal structures, the costs and scaling ratio of the physical setup increase [168, 189, 190]. These experiments require large facilities equipped with specific flumes only available in a small number of laboratories. Nonetheless, important characterization of tsunami-like waves impacting representative elements [17, 166, 191, 192], buildings [169, 193, 194], elevated structures [168, 175, 195–198], coastal protection structures [199–202], harbours and industrial complexes [167, 203, 204] and pipelines [205, 206] have been investigated along with experiments to assess debris [54, 170, 171, 207], entrapped air [208, 209] and scouring and seepage [56, 176, 177, 179] effects.

Numerical models

Over the last decades, the numerical tools gained emphasis over the more costly and time-consuming experimental approach. Both the earthquake and the tsunami are complex physical phenomena numerically modeled by partial differential equations on which the source of the tsunamigenic earthquake constitutes the initial condition. Commonly, the spatial and temporal discretization of partial into ordinary partial equations is performed before governing equations being utterly solved using classic methods to assess physical quantities and estimate the hazard. The design

parameters of interest for the ground shaking are mainly spectral accelerations and peak values of accelerations, velocities and permanent soil displacements, while for the tsunami, the inundation area, depth and velocity of flow are the most relevant parameters.

Seismic modeling

Alternatively to numerical kinematic earthquake models, more immediate uniform hazard maps with the definition of the design ground-motion by means of acceleration response spectra are present in most design codes for earthquake-prone regions around the world. Yet, the hazard maps have a generalist nature. The employment of hazard-targeted assessment, using broadband or simplified analytic ground-motion prediction equations, can provide detailed, time-dependent data and may represent savings in the design of seismic-resistant buildings without compromising the structural safety [210]. In some regions of EUA, the use of hazard-targeted maps have decreased the seismic forces for the design process up to 30% [211–213]. This effort is particularly interesting for critical structures, such as power-plants, ports or regions encompassing essential infrastructures, such as a Canadian region encompassing 5000 bridges and overpass networks [214]. Moreover, in tsunami-prone regions with moderate tectonic activity the attenuation laws to use in the ground-motion prediction equation models, GMPE, were calibrated with the regional seismicity. Their adequacy to model earthquakes with magnitudes capable to trigger a tsunami is limited [127].

Tsunami modeling

Recently, the tsunami hazard assessment began to be recognized as an essential tool to effectively monitoring risk [215, 216]. The numerical characterization of overall tsunami and particular effects on coastal regions, accounting fluid (hydrostatic and hydrodynamic forces), the all-sized solid elements in the tsunami flow (debris) and geotechnical (scouring) components of the tsunami, have been numerically explored assessed to help understand the (complex) phenomena. Efficient numerical tools are required to model the different tsunami stages, which encompass enormous difference in the spatial and temporal scale.

The tsunami generation and propagation phases take place at a domain with many kilometers and a couple of hours. Tsunami modeling commonly accepts the Shallow Water system as governing equations, SW, while three families of numerical methods are typically used to solve them: finite difference, FD, finite volume, FV, and the finite element, FE. The FD scheme, even though suffering from some limitations (not entirely conservative, not well-balanced and the discontinuities are more difficult to reproduce [217]) was the first to be implemented to perform tsunami simulations due to its inherent simplicity in the implementation on structured grids in comparison with the more complex FV alternatives. COMCOT [218], MOST [219] and TUNAMI [220] are examples of FD scheme implementations widely used by the tsunami science community. The FV overcomes some of the limitations of FD scheme, as it is built-in conservative and, therefore, the solutions of the SWE present a smaller error coefficient [221]. Numerical codes like ANUGA [222] and GEOCLAW [223, 224] use the FV discretization to solve the SW have been used to simulate historical and recent tsunami events. At last, the FE remains the less used numerical scheme to simulate the tsunami propagation governed by the SW due to the lack of local conservation and the difficulties to handle convective terms. To date,

there are few implementations of this scheme with a limited use in the tsunami simulations [225].

Such codes, besides suitable are fast assessing the tsunamigenic potential of large earthquakes and establishing the connection to disaster management agencies for evacuation and mitigation measures [225]. Moreover, to avoid unrealistic emergencies, the computer model evaluations are often combined with historical data of past events to generate precomputed scenarios, further combined with observations from the event itself in order to obtain forecasts and alert levels. Computer models are used by the Tsunami Warning Centres, TWC, at locations that are in high danger of tsunami events, for example, in the Pacific Ocean, but also in Europe in the framework of Tsunami Early Warning Systems [226]. The numerical schemes combining governing equation and numerical methods to solve them constitute valuable tools. Tsunami-prone regions around the globe [227–229], or specific regions, such as Indonesia [230], Northeast Atlantic [231], and Japan [232] have their tsunami hazard estimates, most of them in the form of inundation maps.

Nonetheless, Eulerian mesh-based methods have inherent limitations in the treatment of complex flows and geometries, requiring mathematical transformations that represent additional computational expenses. Additionally, the precise locations of the free surfaces under large deformation, deformable boundaries and moving interfaces within the frame of the fixed Eulerian grid are difficult to handle. Moreover, the eligibility of depth-average SW governing equations is only guaranteed if the wave height is significantly smaller than the wave length, allowing to neglect the modeling of the dispersive component of the wave(s). Otherwise, the hyperbolic system of governing equations is not capable to reproduce the hydraulic phenomena inherent to the flow.

Fluid-solid modeling

While the tsunami simulations of generation and open-ocean propagation phases require an ability to characterize the response at macro-scales, accepting linear equations for a hydrostatic approach as governing equations, the tsunami inundation phase requires complementary high-resolution topobathymetric data and more sophisticated governing equations, such as Navier–Stokes, NS, Reynolds Averaged Navier–Stokes, RANS, Boussinesq or non-linear SW equations, all integrated in depth and taking into account the variations in the vertical direction and the physics of the environment [233, 234]. The Lagrangian mesh-less discretization offers several advantages with respect to classic Eulerian methods when tackling fluid impact or interaction with structures.

The fluid impact on rigid elements [194, 235, 236] have been numerically modeled using solvers of three-dimensional equations, such as (and among others) Eulerian Volume of Fluid method (ex.: OpenFoam [237]) and Lagrangian methods.

One of the Lagrangian methods that had evolved in the last years is the Smoothed Particle Hydrodynamics method, SPH, which was originally developed for astrophysics applications [238, 239], but has been extended to a vast range of problems in both fluid and solid mechanics [240–247]. Being capable of reproducing complex fluid flows, highly non-linear free-surface phenomena, conveniently treating large deformations and handling variable domains in time, such as piston-type wave-makers, makes SPH a promising tool to use in the characterization of tsunami-like waves [225, 244, 248].

Hydraulic phenomena, such as regular, non-regular, solitary, and tsunami waves [249–252], have

demonstrated the capacities of the NS-SPH numerical scheme to reproduce physical phenomena of fluids. Over time, numerical algorithms have been introduced to the original SPH formulation to reproduce a vaster number of physical phenomena [247]. The introduction of static or moving solid boundary conditions to mimic piston-type wave-makers become possible due to reflective properties added to the particles [253, 254], whereas the ghost particles are used when prescribing open boundary conditions to extrapolate or impose hydrodynamic flow quantities [251, 255]. Numerical artifacts have been added to optimize the spatial discretization and treatment of density, viscosity, turbulence and pressure terms [245, 246, 256]. For fluid-solid interactions, complementary treatment of the solid boundary surrounding the structure [257] and air-water interface modeling [258] has been shown to improve numerical predictions of the fluid motion and structural response. Parallel computing and distributed computing algorithms have also been implemented, which have allowed significant reductions in computing time [259, 260]. Lastly, the coupling of SPH to other numerical schemes allows to assemble hybrid models where the SPH method is strictly used on the highly non-linear part of the domain which has been shown to be an effective technique to decrease computational costs [48, 261–265].

The Lagrangian SPH method in association with Navier-Stokes governing equations provides solutions free of numerical dispersion that can reproduce complex hydraulic phenomena, which makes the numerical scheme particularly interesting to use in the framework of coastal engineering research. The scheme has been successfully used in the characterization of waves behavior [45, 249, 252, 266, 267] and their interaction with other fluids [258] and/or solids. Its suitability to model the impact and over-topping effects on vertical [268–271], modified [43, 44] or elevated structures [45–48, 272] have been explored. Parametric studies including various geometric influences, such as aspect ratios (width/depth) [273], orientation [44], openings [274] and elevation [48], and multiphase effects, such as the role of entrapped air on elevated structures [209, 275–277] have been developed.

However, the SPH method suffers from numerical diffusion, has a low convergence rate, needs additional algorithms to model turbulence and presents large pressure fluctuations due to spurious pressure waves in the untreated weakly compressible formulation [245, 246]. Since SPH is a relatively new tool for engineering purposes, additional work is needed to demonstrate the advantages of SPH over the well-established classic mesh-based methods that are computationally cheaper. Recent hybrid techniques have emerged to overcome the inherent limitations associated to the SPH computational costs [48, 261, 263, 264, 268, 278]. By solving the linear(-ish) part of the domain using the comparatively faster but smoother mesh-based approaches, the SPH domain governed by sophisticated systems of equations is reduced, decreasing the computational expense and maintaining the level of detail of the numerical solutions.

Fluid-solid interaction modeling

The fluid-structure interaction problems, that represent the mutual inter-dependence between structure(s) interacting with an internal or surrounding fluid flow, are broadly classified into two approaches: the partitioned approach and the monolithic approach [217].

The partitioned approach treats the fluid and the structure as two computational fields which can be

solved separately with their respective mesh discretization and numerical algorithm [217, 279]. The interface conditions are used explicitly to communicate information between the fluid and structure solutions. This approach takes advantage of the "legacy" codes or numerical algorithms that have been validated [217], assuming identical (Lagrangian-Lagrangian, Eulerian-Eulerian) or different (Eulerian-Lagrangian) discretization methods. One of the most popular methods used to capture the interaction between structure and fluid is the Arbitrary Lagrangian Eulerian method, that makes arbitrary motion of grid/mesh points with respect to their frame of reference compatible [198, 280–283].

The monolithic approach treats the fluid and structure dynamics in a single system equation solved simultaneously by a unified algorithm [18, 95, 284, 285]. For example, Discontinuous Galerkin [286] or the Particle Finite Element Method, PFEM, that since its inception has been shown to be an accurate and versatile numerical method especially for multi-physics problems. Unlike traditional numerical methods for fluid-structure interaction models, such as the Arbitrary Eulerian-Lagrangian, PFEM uses the Lagrangian formulation for both the fluid and structure. The distinguishing feature of PFEM is that the mesh nodes are treated as lumped material particles that can freely move and even separate from a domain. Interactions between particles are facilitated by a finite element mesh and the governing equations are solved in standard FE analysis approach. This allows for a very natural and intuitive coupling of the fluid and solid elements. To prevent mesh distortion, a new mesh is progressively generated at the beginning of each analysis step, making the PFEM numerical scheme efficient for interactions involving free surface flows, breaking waves, and fluid spray. Although representing accuracy for a multidisciplinary problem, it has elevated computational demand and requires modeling expertise. The SPH is simultaneously capable of solving and providing high-quality solutions of FSI while fitting the category of computational demand and high sensibility to modeling parameters [287].

Another general classification of the FSI solution procedures is based upon the treatment of meshes: the conforming mesh methods and non-conforming mesh methods [217, 288]. The conforming mesh methods consider the interface conditions as physical boundary conditions, which treat the interface location as part of the solution, requiring meshes of conventional mesh-based methods, such as FE, FD or FV, or less classic methods, such as Boundary Element Method, that conform to the interface. Owing to the movement and/or deformation of the solid structure, re-meshing (or mesh-updating) is needed as the solution advances [263]. The non-conforming mesh methods treat the boundary location and the related interface conditions as nodal constraints where the approximation of fluid and solid equations conveniently solved independently from each other with their respective referential, and re-meshing is not necessary. On the other hand, non-conforming mesh methods treat the boundary location and the related interface conditions as nodal constraints where the approximation of fluid and solid equations can be conveniently solved and re-meshing is not necessary [263]. Among the non-conforming mesh approaches (mesh-based or mesh-less [289]) are the particle methods [290], such as Molecular Dynamics, Discrete Element Method, SPH, Immersed Particle Method, Lattice Boltzmann Method [291–293].

The characterization of tsunami-driven debris motion and loads can derive from assigning viscosity to the flow density parameter (smaller debris) and/or consider a gravity load impact of a large object

against coastal structures [207, 294]. The characterization depend of the amount of potential debris in the vicinity of the structure. If considering the numerical modeling of debris as fluid-structure interaction problem, it implies a challenging task of modeling of fluid and solids, laminar and turbulent flows, and the capacity to handle the transport of moving bodies in free-surface flow [54]. The large computational cost associated with the numerical processes are unfeasible for common studies, but probably justified when analysing important infra-structure, representing an enhanced solution of solid deformation and inelastic collisions.

Cascading effects

Despite the physical and numerical sophistication of the models, the cascading effects of seismic and tsunami actions remain a topic in need of further characterization and design codes have only obscure references to it. Even academic approaches considering successive structural analyses accounting for cumulative effects of ground motion and tsunami on structures [39, 92, 295] tend to use more simpler GMPE to model ground motion and SW to model tsunami inundation to assess multi-hazard/risk. Commonly, probabilistic approaches involving big data and complex analyses to estimate the likelihood that seismic intensity and tsunami inundation will exceed a certain level during a given time interval were employed to define hazard maps and vulnerability curves for hazard and risk determination, respectively. Earthquake and tsunami multi-hazards triggered by the mega-thrusts of Tohoku [38, 296] and Cascadia [79, 86] were respectively addressed by stochastic approach, considering the conditional contribution of a common physical source for ground-motion and tsunami, rupturing offshore, with an interval of discrete magnitude values capable of triggering tsunamis. Despite their fundamental contribution to risk management, the generalist nature of multi-hazard maps is deemed insufficient to optimize the design of coastal structures located in regional and local tsunami-prone regions.

Deterministic approaches can be conducted to identify different case scenarios, such as maximum or minimum quantities, assess credible and reasonable scenarios, and, based on a premise, eg.: an economic constraint, classify the worst-case scenario. Thus, a scenario-based approach can assume an alternative and complementary role in the probabilistic-deterministic dichotomy. Nonetheless, both followed the global trend (e.g.: [227, 229, 297, 298]) to evaluate the site hazard based on tsunami hydrostatic intensity measures underrating the damage potential of tsunami hydrodynamic effects [80, 299]. Instead of an exclusive focus on potential energy, recent literature has shown the importance of more representative or complementary intensity measures due to kinetic energy when assessing the structural behavior due to tsunami [300, 301]. Moreover, tsunami hazard estimates are commonly developed for uniform hazard maps or target-site peak values, missing the dynamic characterization of the wave interacting with the built environment. The topo-bathymetric variations due to earthquake-induced subsidence and liquefaction, and the presence of coastal protection structures that might collapse due to the previous earthquake or during the tsunami represent hydraulic chocks that may lead to complex reflection, refraction and diffraction phenomena, influencing the structural loading pattern imposed to coastal structures. Complementary insights on the multi-hazard characterization

are deemed necessary to infer realistic loading patterns, particularly for critical infrastructures. The North American design standards define critical infrastructures as *'Buildings and structures that provide services that are designated by federal, state, local, or tribal governments to be essential for the implementation of the response and recovery management plan or for the continued functioning of a community, such as facilities for power, fuel, water, communications, public health, major transportation infrastructure, and essential government operations. Critical facilities comprise all public and private facilities deemed by a community to be essential for the delivery of vital services, protection of special populations, and the provision of other services of importance for that community.'*

In resume, it is necessary to adjust multi-hazard characterization for tsunami engineering purposes, taking into account multiple scales and physics of the phenomena, such as previous seismic ground accelerations anticipating tsunami hydrostatic and hydrodynamic effects, and their conversion to seismic displacements and tsunami forces accounting for environmental influences. Thus, to characterize the physical phenomena, both endogenous variables of the numerical models and exogenous variables of the dynamic environmental conditions are necessary.

Beside hazard characterization, the coastal structures at risk from regional/local tsunami are most likely subjected to the cascading earthquake and tsunami effects, which implies the mobilization of the structural resistance to deal with the earthquake action, potentially affecting their performance against the incoming tsunami. Instead of individual actions, it is necessary to design coastal structures to resist the cascading loading pattern, combining the seismic displacements and the tsunami forces while taking into account the potential cumulative effects if the structure exceeds the threshold of elastic limit.

Despite the enhance of scientific knowledge, it is still lacking its transposition to regulatory codes, with potential to influence both stakeholders and technical practices.

An optimized design of coastal structures, considering the successive effects of ground-motion and tsunami, must guarantee two main criteria. The first regards requirements of the constructive solution, balancing the demands of flexibility and ductility for earthquake resistance with the demands of stiffness and strength for tsunami resistance. Whereas the structural flexibility for the case of earthquakes is very well known, its role on the tsunami-structure interaction is still unexplored, currently constituting one of the most challenging topics related to the micro-scale effects of tsunamis. The role of the structural stiffness/flexibility during the tsunami impact on coastal structures was experimentally tested to show that a more flexible wall witnessed lower tsunami forces than a stiffer one [302], while numerical approaches to model tsunami effects on bridges showed that both the applied tsunami loads and the reaction forces can be magnified if a deck is supported on flexible horizontal and vertical springs and thus a dynamic fluid-structure interaction takes place [303]. Such amplifications of the maximum horizontal force were reduced up to 49% in a bridge superstructure with a flexible horizontal substructure spring. The dynamic fluid-structure interaction is also dependent on the wave type, with unbroken solitary waves interacting with stiff and flexible bridges differently than turbulent bores. The computed time history of the horizontal and vertical loads on the bridge deck, in turn, provide the input to a finite-element model of the bridge structure for capacity comparisons and damage analysis. When investigating a coastal box-girder bridge under earthquake-tsunami sequential events, a two-phase

analysis showed that the prior earthquake has more pronounced effects on stiffness than strength of the bridge columns. The effects of prior earthquake on post-shock bridge tsunami fragility are more pronounced at lower damage levels, whereas the prior earthquake has negligible effects on tsunami fragility at extensive and complete damage states [83]. However, on a study considering a arch support bridge system, the earthquake design specifications of $0.30 g$ and $0.45 g$ provided more than sufficient strength to resist the maximum tsunami horizontal force, while the margin of safety is much smaller for the uplifting force that was considered to be on an acceptable range [304]. A new hybrid simulation was developed to assess the behavior of a vertical-evacuation structure with a breakaway ground floor under hydrodynamic loading, demonstrating the dependence of uplifting load on the bottom slab, the frontal impact force and the overturning moment, on the structure's size and bottom-slab elevation, and the wave's Froude number. With a proper normalization, the force and moment coefficients were generalized to propose a maximum moment coefficient to decide on the overturning stability of the structure [173]. However, the significant differences in the findings of the aforementioned studies (for different coastal structures and wave types) regarding the role of structural flexibility in the case of tsunami impact on structures indicates an elevated complexity of the phenomena.

The second regards the trade-off between the economy of the structural solution and the level of structural performance, implying opening the prospects for stakeholders, governments and technicians.

2.1.4 Performance of ports on regional-local tsunami-prone regions

Past tsunamigenic events in ports around the world have shown that ports have particular damage patterns. The open typology commonly assumes pile-supported wharves designed to act as ductile moment frames with plastic hinge formation at pile-deck and the pile-soil connections. The typical damage pattern of open-type wharves during an earthquake depend on soil-structure interaction and the magnitude of the inertia force relative to the ground displacement. Function of the foundation conditions, the main damages are: 1) for good geotechnical conditions (firm soils): deck pushed seaward due to the seismic inertia force on the rigid deck or excessive bending of the pile heads, and 2) poor geotechnical conditions (loose soils): piles pushed seawards due to soils susceptible to liquefaction, lateral spreading, and differential settlements [305–307].

The primary direct tsunami impacts on ports with open typology have are dominated by the impulsive (hydrodynamic) forces. The hydrodynamic forces resultant from pressures on horizontal and vertical directions at the structure-wave interface induce an overturning moment on wharf components due to an uneven distribution of these forces. Nonetheless, hydrodynamic forces commonly have associate impacts of different origin [80, 308, 309].

On the piles, damage due to hydrodynamic effects can wash away the structure while simultaneous scouring around the base of the foundations occur, increasing the likelihood of structural collapse. On the quay, the lifting of the quay can occur due to buoyancy and hydrodynamic forces on the vertical direction, possibly leading the wash away of the structural components. On the horizontal direction, separation of the quay (or slabs of the quay) from their piles or embankment/footing can occur enabling wash away

of the structural components and sedimentation in-between and beneath the soil-structure system. On the coastal protection structures, seawalls and breakwaters, hydrodynamic forces can induce tilting, rotations, structure or components washed and carried away while scouring around the foundations can potentially increase the likelihood of structural collapse.

On container terminals, lifting, wash away and stocking of the containers can occur while containers inundation and damage can lead to damage and exposition of the cargo, including possible hazardous goods. Cranes can suffer damage due to hydrodynamic forces and failure of the mechanical and electrical control circuits due to inundation. Vessels can collide with structures, structural components other vessels with or without breaking its mooring lines. Breaking of mooring lines due to increased tension from currents intensifies capsizing and sinking of vessels, drifting of vessels inland potentially to becoming large and damaging debris. The vessels damage is highly probable due to potential to ground contact and getting caught in vortexes during currents that typically lasted for up to 24 hours after initial tsunami arrival [309, 310].

Any structures that remain after the preceding earthquake and the initial tsunami arrival are subject to secondary impact from debris. Among structures, structural components, equipment, vessels, containers and remain items composing a portuary complex, the transport and impact of debris constitutes a source of potential failure of individual structural or non-structural elements.

Protocols for tsunami risk mitigation at harbours are emerging and being implemented globally. The International Tsunami Information Center compiled a list of resource material on Marine Ports Guidance (available at:

Nonetheless, anthropogenic and natural (or the combination of both, natech) hazards continues to pose a high risk to the operation of ports all around the globe. The disaster risk management of such critical infrastructures shall ensure that safety and operational performance requirements are kept to minimize adverse social, economic and ecologic consequences. Beside economic losses resulting from port disruptions and the functional recovery following a disaster will be a very time-consuming process, ports also serve as support for providing supplies and humanitarian aid to communities after natural disasters. The resilience of port infrastructures against coastal hazard is function of the hazard threat, their vulnerabilities and the factors controlling recovery. The unpredictability and sometimes infrequent nature of natural hazards increase the uncertainty involved in risk management decisions, typically subjected to divergent performance and economic goals. Regardless the apparent dichotomy between investments policies from policy-makers and risk practitioners is becoming more attenuated. The 2021 report of the European Commission and the World Bank enunciated the benefits of investing in measures to manage the natural risks, quantifies the outweigh the recovery costs in two to ten times higher than the preventive costs and alerts that the metrics between 1980 and 2020, natural disasters affecting nearly 50M people in the European Union, and caused on average an economic loss of 12 billion euros per year, is expected to grow as a result of climate change intensifying the magnitude and frequency of natural disasters [311].

Among the natural hazards threatening Europe, the tsunami risk is comparatively underrated. Mainly after the 2004 Indonesian earthquake and tsunami, tsunami inundation mapping of certain test

sites at Northeast Atlantic [231] and Mediterranean areas [312] helped develop tsunami early warning systems [313, 314] and plan ahead for their modernization [315]. On another mitigation perspective, measures based on structural performance gained attention mainly after the 2011 Japanese earthquake and tsunami. Lessons learned from exhaustive post-disaster surveys revealed the paucity of both design provisions and considerations towards more tsunami resilient infrastructures [11, 154], while expert teams found the disaggregation of structural failures due to earthquake, tsunami or combined effect of both difficult to characterize. Experimental and numerical techniques have been explored to contribute for the characterization of local/regional tsunamis and respective interaction with coastal structures. However, the complexity of (mainly the hydraulic) phenomena requires demanding technical and functional specifications.

2.1.5 Remarks

Recent events boosted the study of the successive earthquake and tsunami effects on threatened structures. Some statements can be derived from field surveys, physical experiments and numerical simulations:

- single vs. multi-hazard effects in structures: cascading hazards imply the successive mobilization of the structural capacity and may induce cumulative effects if the limits of elastic behaviour are exceeded,
- uniform vs. target hazard assessment: the commitment in the quantification of intensity measures represent a trade-off between effort and more accurate actions characterization, potentially representing an optimization in safety-economic relation,
- seismic vs. tsunami design of structures: the forces and deformations induced by a tsunami on a structure are function of the tsunami wave characteristics, height and flow velocity, and exploration of strength and rigidity of the structure, while the forces and deformations induced by an earthquake are function of the ground motion characteristics and depend not only on strength and rigidity but also on mass and exploration of the ductility,
- simple vs. complex analysis: the sophistication of the numerical schemes and the complexity of the structural analysis under successive earthquake and tsunami actions is subjective to the level of the importance of the structure.

2.2 Conceptual Research Strategy

Adopting a preventive perspective, the objective of the conceptual methodology is to contribute for the increase of tsunami resilience in coastal communities. Taking advantage of the physical characteristics of earthquake ground-motion(s) and tsunami wave(s) on the generation, propagation and site-effects stages, three interdependent frameworks composing the methodology are defined in terms of spatial and temporal scales. Each of the interdependent macro-, meso- and micro-scale stages are coupled by

boundary conditions, BC. The meso-scale constitutes a two-way link between the hazard- and structural analysis, allowing a dynamic iterative calibration of the models. Fig. 2.5 schematically represents the three-staged methodology adopting the example of Tohoku-Oki, Japan 2011 earthquake and tsunami at the Kamaishi bay. The following sections detail each stage and identify their inherent physical and numerical uncertainties. The well-known case of Kamaishi bay during the Japan 2011 earthquake and tsunami will serve as illustrative example of application.

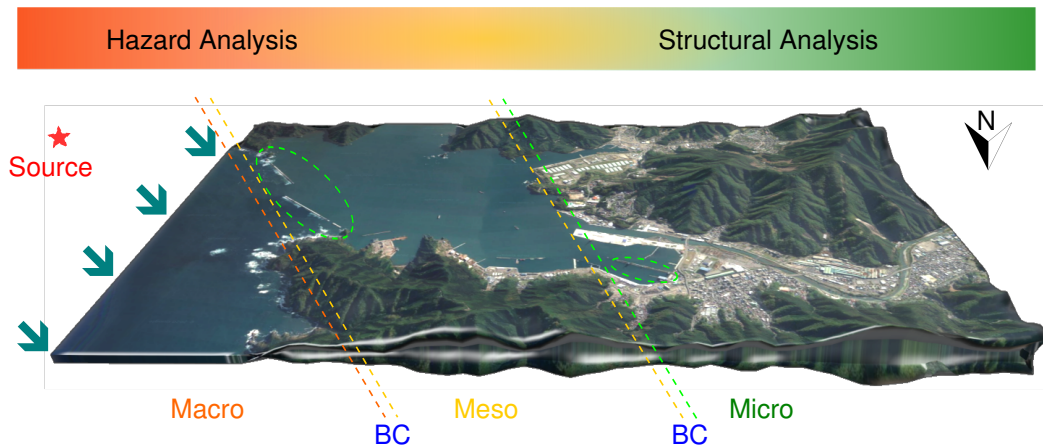


Figure 2.5: Examples of conceptual application of the proposed methodology to Kamaishi port in Iwate prefecture due to the Japan 2011 earthquake and tsunami. The macro-, meso- and micro-scaled frameworks are limited by orange, yellow and green lines, respectively. The interfaces between frameworks are prescribed by boundary conditions, BC, represented in blue.

2.2.1 Macro-scale: generation and propagation

The macro-scale stage concerns the assessment of the earthquake and tsunami multi-hazard of the threatened region (Fig. 2.5). It encompasses the spatial and temporal domain needed for the simulation of the earthquake and tsunami generation and propagation, i.e., hundreds of meters up to about 300 km and from tens of minutes up to about an 1 h .

The more immediate quantification of hazard consists on deriving quantities from real recorded data or hazard maps. The mapping of seismic hazard is often present in most of the world design guidelines, while the United States and Japan also provide tsunami inundation maps. Depending on the importance of the structure, or the absence of hazard uniform data, site-specific characterization of hazards may be required to complement the generalist nature of maps or to overcome the lack of regional information, respectively.

In that case, the initial step of target-hazard assessment is the compilation of all the existent data related to potential tsunamigenic sources and past events to define credible scenario(s), $S_{credible}$. The process requires catalogues constituted by historical and instrumental data, the identification of the active geological faults, geodetic estimates of crustal deformation, seismo-tectonic features and paleo-seismicity information. A twofold criteria is assumed to select sources with potential to generate tsunami, namely, geologic structures located less than 300 km from the site and a minimum moment magnitude

of $Mw7.5$.

Each tsunamigenic source, characterized by geometry (surface area, A , hypocentral depth, d), kinematics (strike, φ , dip, δ , slip, λ and rake, Θ) and soil rigidity, μ , constitutes an inextricable candidate scenario, $S_{candidate}$, for multi-hazard analysis.

The rupture mechanism of each $S_{candidate}$ constitutes the initial conditions for propagation models of earthquake and tsunami waves. The theoretical models adopted to define the initial condition represent the uncertainty of the process and of the model itself, varying between early kinematic point source in a homogeneous and isotropic elastic medium, up to sophisticated dynamic, tri-dimensional circular or rectangular finite faults, distinguishing near- and far-field earthquakes in heterogeneous medium [316]. A common approach to initiate GMPE models is to define the source as a finite-fault identifying the fault location, proximity to sea floor, dimensions and dislocation parameters (dip, slip, rake and strike), and source kinematic parameters (stress drop, rupture velocity and slip distribution). For the tsunami, the co-seismic vertical displacement to initiate the tsunami propagation stage is commonly calculated using the dimensions and dislocation parameters of the focal mechanism, modeled using half-space theory of surface deformation due to shear and tensile faults [317] and the assumption that the free water surface mimics the bottom of the ocean [318].

The reliability of the propagation solutions depend on the sophistication of the methods and detailed knowledge of the bathymetric model considering the environmental conditions. The simulation of tsunami propagation accepts SW governing equations and the quality of the numerical solutions achieve convergence with discretization in the order of few hundred meters [21]. The simulation of ground-motions propagation relies on numerical or stochastic GMPE models. Both approaches require regional crustal properties (geometrical spreading, anelastic structure, and upper crustal amplification and attenuation parameters). The stochastic approach is comparatively more used than the numerical technique. For the tsunami propagation, numerical schemes composed of governing equations, from the fully NS to the simplified hydrostatic SW and solvers using FD, FV or FE methods. Due to the tsunami vertical dimension being much smaller than the horizontal scale, modeling the tsunami propagation under Shallow-Water hyperbolic equations and relatively coarse bathymetric grids is widely accepted in the literature [19].

The results of the macro-scale stage are uniform or target bed-rock seismic motions and tsunami wave(s) height and velocity quantities near the shore.

Example in Fig. 2.5: a vast database of ground-motion records was acquired by more than 1226 accelerographs in Japanese territory only, while tsunami records were obtained by 35 DART and 18 GNSS buoys, 49 OBPs of DONET, and 150 OBPs of S-net [297]. The characterization of the seismic action, for such recent events and well-instrumented region excuse complementary simulations (and reduce uncertainties due to earthquake). Conversely, the paucity of instrumental data from high-magnitude events in regions such as the Northeast Atlantic would require a more demanding approach, involving probabilistic or deterministic numerical tasks to assess the corresponding seismic hazard.

For the tsunami behavior characterization, the instrumentally-recorded data acquired during the

event can play two roles. The first is use the hydrodynamic quantities to initiate tsunami propagation and inundation models limiting the the size of the numerical domain. On one hand, it dismisses the modeling of the source. On the other hand, the source parametrization and modeling (e.g.: using finite-fault models with homogeneous or heterogeneous slip distributions (e.g. [319, 320]) skip the uncertainty associated with the tsunami generation, which potentially influence the quality of the tsunami numerical solutions. The second role is contributing to the development of tsunami databases, which are of utmost importance when calibrating the modeling assumptions and numerical schemes adopted to carry out the simulations.

In the illustrative case, the correlation between data recorded by DART and OBS buoys and numerical data computed at virtual gauges, VG, at the corresponding location would contribute for calibration and validation of the numerical solutions before using VG to capture waves amplitude and flow velocity to constitute the BC for the meso-scale.

2.2.2 Meso-scale: propagation and site-effects

The meso-scale stage encompasses the spatial and time domain needed for the simulation of the earthquake and tsunami considering the strong influence of site-effects, i.e., from few meters up to few hundred meters and up to tens of minutes (Fig. 2.5).

For the ground-motion, the rigidity of the more superficial geological layers and its geometrically irregular configurations on the surface can induce important local amplifications, but other soil characteristics, such as its permeability and liquefaction, subsidence and landslide susceptibility also play an important role when extending the vision to the structural integrity. Typically, the site response is defined in terms of site predominant frequency and amplification effects, expressed by representative static peak values, response spectra or dynamic sets of time-histories.

Similarly, the site-effects strongly influence the tsunami inundation stage. The simpler procedure is to model an increasing onshore bed roughness, which is useful to assess inundation area. The typical treatment adopts numerical schemes including the vertical variation of fluid, which is constrained by topo-bathymetric conditions. High-resolution topo-bathymetric data (at least 10 m resolution grids) are required to capture the site-effects influencing the tsunami flow and dry-wet variations.

Moreover, the inundation phase may also include the fluid interaction with structure(s) by modeling them as immutable rigid bodies, part of topo-bathymetry data, constituting obstacles to the fluid flow. The combination of hydrodynamic quantities captured near the obstacle and empirically-calibrated formulations, as recommended in Japanese and North American design codes, can quantify the hydrostatic and hydrodynamic loading components of tsunami. The technique has two drawbacks (1) it provides static peak-values, and (2) is limited to simple geometries. Another aspect often neglected in tsunami hazard assessment, is the presence of coastal defense structures influencing the characteristics of tsunami waves. Recent lessons from the 2011 Japan event demonstrate unequivocal reduction of waves' height and delay in tsunami travel time [59, 321]. However, if damaged, the coastal protection structure may induce channeling or resonance effects, amplifying the tsunami damaging

potential.

Alternatively to semi-empirical approaches, built-in force assessments overcome time-dependent and fluid-structure-interaction limitations. The particle and coupled methods are promising tools to provide high quality solutions, either modeling the structure as a rigid body and extracting the force for a parallel structural analysis or assigning flexibility to the structure for a two-way interaction. Moreover, the algorithms allow to explore complex and highly non-linear phenomena, such as air entrapment on elevated structures ([208, 209, 275–277]). The trade-offs analysis between the quality of the solutions and the stability and convergence of the solutions, relies on various considerations. The main dichotomy is mainly technical, confronting highly-volatile nature to parametrization and high computational costs with the level of importance of the structure. Yet, the stability and convergence of the solutions is highly-volatile to parametrization and represent high computational costs.

The presence of all-sized solid elements in the tsunami flow constitute another component of tsunami force. The characterization of tsunami-driven debris motion and loads can derive from assigning viscosity to the flow density parameter (smaller debris) and/or consider a gravity load impact of a large object against the coastal structure. The characterization depend of the amount of potential debris in the vicinity of the structure. The US standards recommend an empirical approach to characterize the impact of larger debris. Considering the numerical modeling of debris as fluid-structure interaction problem implies a challenging task of modeling of fluid and solids, laminar and turbulent flows, and the capacity to handle the transport of moving bodies in free-surface flow. The large computational cost associated with the numerical processes are unfeasible for common studies, but probably justified when analysing important infra-structure, representing an enhanced solution of solid deformation and inelastic collisions.

The results of the meso-scale stage are the seismic and tsunami actions exerted on the structure(s). A deterministic assessment provides the maximum static or dynamic values of the actions. For engineering purposes, the premise that different intensity measures can induce the hazardous scenario, S_{worst} , causing devastating damage to structures is assumed, i.e., the assess the maximum seismic ground motion, tsunami free-surface elevation and flow velocity (momentum flux) in both inflow and outflow directions allows to encompass a complete set of loading patterns and characterize the design demand for the structure [127]. The scenario-based approach of of the deterministic approach increases provides realistic considerations for engineering purposes; however, it is important to bear in mind that even the worst-case scenario may be exceeded, like the forecasts of the 2011 Japan event. The probabilistic approach provides a complementary perspective, as all tsunamigenic events are considered to evaluate the probability that a certain level of hazard is exceeded at a given location within a certain recurrence. The probabilistic multi-hazard characterization includes an independent probabilistic characterization of each hazard to generate cumulative distribution functions for the intensity measure of each hazard. The magnitude distribution curves are then multiplied by the rate of occurrence of the seismic events with higher magnitudes than the considered for assembling the curves. The products are hazard curves and/or maps providing the probabilities of exceedance of earthquake-tsunami intensity measures in a specific period of time.

Example: assuming that the seismic action was previously derived from instrumentally-recorded data, the tsunami characterization now requires numerical schemes accounting the vertical component of flow and non-linear terms to consider the environmental influencing parameters, such as variable astronomical tide level, soil subsidence or breakwaters geometrical update due to earthquake effects. Among literature references, the influence of the breakwaters is addressed in terms of tsunami arrival time (delay) and waves amplitude (decrease), but simulations using high-resolution topo-bathymetric data modeling undamaged, total and partially collapsed configurations of the breakwaters would provide complementary data about channeling effects that increase the impact of tsunami hydrodynamic effects. By scattering virtual gauges strategically implemented before the coastal protection structure and inside the Kamaishi bay would benefit the flow behavior characterization and, ultimately, promote the interactive calibration between meso- and micro-stages by dynamically modifying the boundary conditions.

Beside the physical variations, the numerical approach to assess the horizontal and vertical forces on the Kamaishi breakwaters and on port may vary between: (1) a semi-analytical approach adopting the regulation equations together with tsunami inundation depth, to characterize the hydrostatic component, and momentum flux, to characterize the hydrodynamic component of tsunami force, or (2) a built-in approach.

2.2.3 Micro-scale: loading and structural response

The micro-scale regards the spatial and time interval needed to assess the structural response to the cascading seismic and tsunami actions (Fig. 2.5). The spatial domain is set to an interval of centimeters to meters, and the time domain is set to an interval of seconds up to couple of minutes.

The latest and more challenging models to compute the interaction between fluids and structures, i.e., their mutual interdependence, can also be applied to reproduce the physics of a dynamic fluid force triggering movements and deformations in a solid, that, on his turn, influences the characteristics of the flow. Among others, the immediate difficulty of this sophisticated method is the multi-physics discretization of the model. The solids are typically discretized by Lagrangian techniques whereas the fluids follow an Eulerian discretization. Emergent numerical schemes, coupling Lagrangian mesh-less Smoothed Particle Hydrodynamics and mesh-based Finite Element methods are promising algorithms to perform direct computations of fluid-structure interaction problems, but, for now, have a high level of complexity, are volatile to parametrization, and the maintenance of stability and convergence has elevated computational costs.

The more common approach is, after defining both ground accelerations or displacements and tsunami forces, and assuming admissible to consider them acting separately in time, perform individual structural analysis to assess the structural response. To perform the structural analysis, the seismic or tsunami regulations allow design methods based on an elastic analysis of the structure. However, the inelastic response of the structure is required when performing sequential structural analyses accounting for the cumulative effects of the earthquake-tsunami loading pattern. The performance-based design methods, using capacity spectrum, N2, and direct displacement-based

approaches are capable of evaluating the inelastic structural response, in terms of local resistance, ductility and global stability. The structural stability includes settlements, tilting and displacements effects. To verify local safety requirements, the principle of comparison between the capacity and demand is applied. Both capacity and demand can be expressed in terms of static variables, as internal forces and stresses, or by kinematic variables, as displacements, curvatures and strains, imposed by the inherent permanent structural loads and the succession of the ground-motion and tsunami actions. Different levels of complexity can be assigned to perform structural analysis due to cascading earthquake and tsunami actions, from the consideration of geotechnical influences (e.g. scouring) to the complexity of the analysis itself, that can range from the application of static forces to perform pushover analysis, to the prescription of time-histories to perform dynamic analysis, more or less non-linear constitutive models to define materials, two- or three-dimensional models of the prototype, among others.

During the successive analyses, the structure(s): (1) remains in the elastic regime, meaning that the ground-motion would not represent a threat to the tsunami structural resistance (independent structural response); (2) reaches the plastic regime, generating residual stresses and deformations in the structure, affecting its resistance against the incoming tsunami and implying an update of the structural characteristic in the model to take into account the reduction of structural resistance (interdependent structural response) or (3) collapse.

In elevated structures, a correlation between the piles capacity curve and the moment-rotation diagrams can identify which and where the seismic force lead to the development of plastic hinges, more likely to be formed at the top of the pile connecting to the deck, where the largest variation of rotations (curvature) take place, leaving the structure with permanent deformations before it was hit by the tsunami. A comparison between the tsunami hydrodynamic and hydrodynamic effects in the vertical direction and the weight of both the structure and mass of water (time-dependent) represents a reasonable simplified approach to predict the structural performance. However, have been demonstrated that in addition to large uplift forces, tsunami flows also generate significant overturning moment (pitching) both in the case of buildings and bridges, which increases further the risk of failure because it leads to unequal distribution of the uplift forces in the supports, overloading the offshore bearings and columns ([168, 303]). Moreover, the effects of entrapped air between the free-surface and the bottom of the elevated structures constitutes an amplification factor for uplift forces, overturning moment while potentially generating significant three-dimensional effects for coastal decks with beams (jetties, bridges, wharves) due to the tendency of the trapped air to escape in all three directions ([190, 208, 209, 275–277]).

If/when the yielding level is exceeded, the reduction of resistance and stiffness in the structural elements, as well as permanent deformations, due to the earthquake action are transferred as initial boundary conditions to the tsunami structural analysis. Another variable in the micro-scale is the behavior of the foundations and/or adjacent soils. The ground-motion can induce liquefaction or subsidence effects and the tsunami can induce scouring effects which require an additional geotechnical model and respective analysis to be part of the BC interactive calibration.

The result of the micro-scale stage is the characterization of the structural response to cascading ground-motion and tsunami actions. Beside the characterization of the structural behavior, probabilistic fragility curves may be derived representing the probability of exceeding a given damage state (or performance) as a function of an engineering demand parameter of seismic and tsunami actions.

Example: From a macroscopic view, the composite breakwaters depicted in Fig. 2.5 suffered settlements in its rubble mound foundation while the vertical caisson sections were drifted and scattered in both flow directions. A sequential analyses identifying damage or collapse would allow to dynamically update the breakwaters geometry and resistant properties by introducing new BC linking meso- and micro-scale for realistic assessment of induced damage mechanisms on breakwaters and port structures. Due to the time-frame associated with local and regional tsunami, the expert teams that surveyed the structures after the 2011 event found difficult to correlate the structural failures to the earthquake, tsunami or the combined effect of both. From a sequential structural analyses using temporal series of cascading ground motion and tsunami that account time-dependent physical variations as loading pattern it could be possible to withdrawn conclusions about various influencing parameters on structural performance. The main factors are the soil subsidence and or liquefaction that influence the geotechnical conditions of the foundations and the tsunami inundation behavior, the changes of the environmental conditions that modify the topo-bathymetric condition highly constraining tsunami hydraulic phenomena impacting overland built infrastructures, and the structural resistance itself along the time-framed analysis. If the yielding level is exceeded in the seismic analysis, only the residual resistance of the structure should take place in the tsunami simulation.

2.2.4 Remarks

The conceptual methodology herein proposed is composed of three interdependent frameworks established from spatial and temporal similarities. Their interactions are assured by dynamic BC linking the variables within the soil-fluid-structures system. The systematic organization of the variables to include in each framework promote the awareness of the global uncertainties, physical and numerical, allowing to adapt the sophistication of the risk analysis to its goal (e.g. reliability of the cost/benefit of the solutions as a function of the societal importance of the structure). The methodology aims to support informed decisions to make safety, financial, ecologic and sustainability criteria compatible. Fig. 2.6 depicts a simplified resume of the generic methodology.

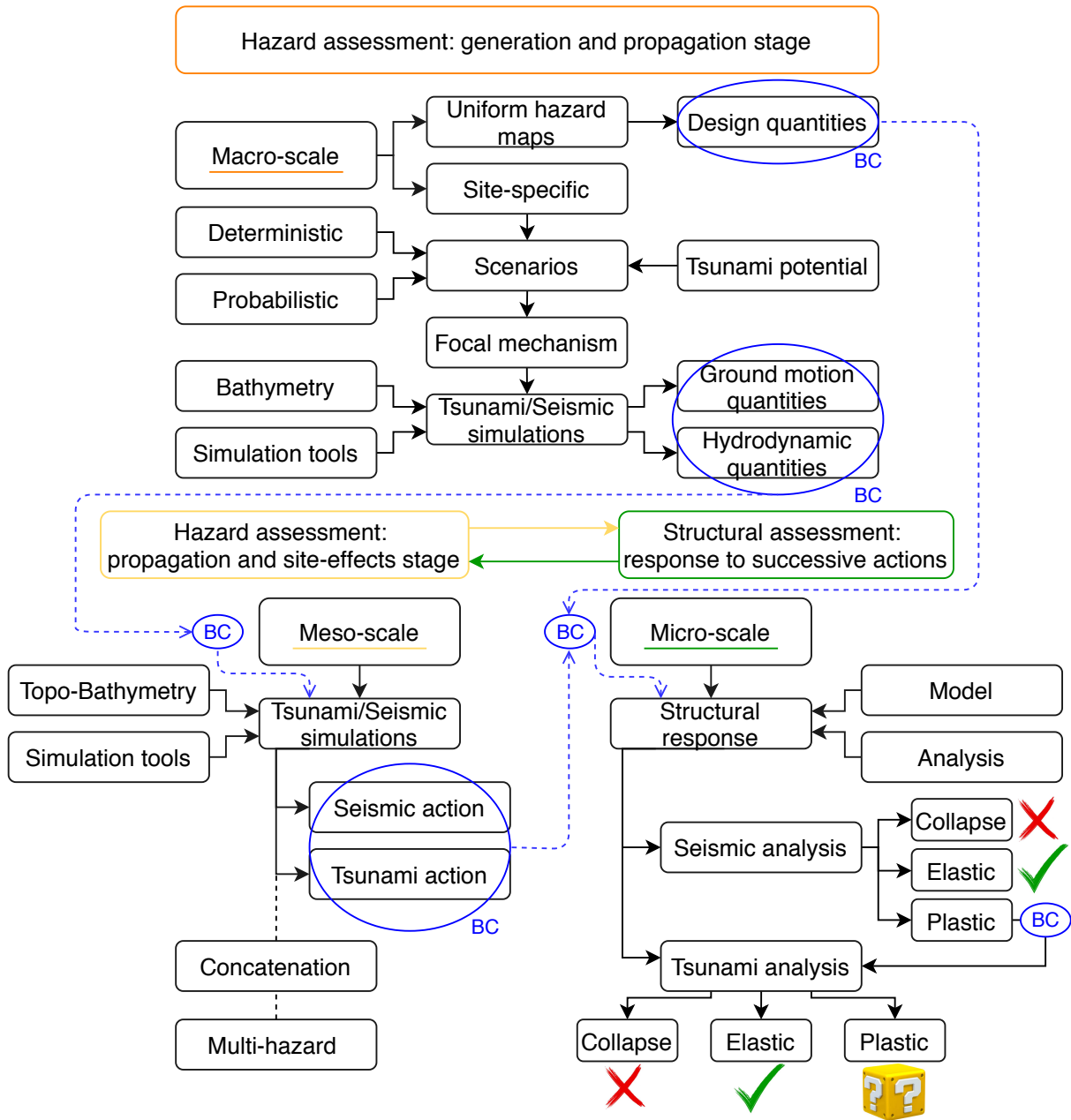


Figure 2.6: Schematic representation of the conceptual methodology. Three complementary frameworks, defined in terms of spatial and temporal scales, are proposed to assess a generic structural behavior due to cascading earthquake and tsunami actions.

Chapter 3

Theoretical models

The earthquake and tsunami phenomena share similar physical stages of generation, propagation and site-effects influencing their waves behavior. The numerical modeling of the tsunamigenic event and its interaction with coastal structures accepts different numerical schemes for each spatio-temporal scale.

Chapter 3 is devoted to introducing the main features of each of the numerical approaches involved in the multidisciplinary analyses.

Chapter 3 is based on Reis et al. 2018, 2021 and 2022b [21, 48, 272].

3.1 Introduction

The corner-stones of engineering are based on probabilistic analyses of systems governed by the Fundamental Laws of Mechanics and the Continuum hypothesis to describe certain physical phenomena:

- First Law of Thermodynamics for energy conservation: a system closed to all transfers energy must remain constant over time.
- Principle of mass conservation: a system closed to all transfers of mass must remain constant over time.
- Newton's Law of Motion for momentum conservation:
 - First law of inertia: in an inertial frame of reference, an object either remains at rest or continues to move at a constant velocity, unless acted upon by a force;
 - Second law of forces: in an inertial frame of reference, the vector sum of the forces on an object is equal to the mass of that object multiplied by the acceleration of the object;
 - Third law of action-reaction: when one body exerts a force on a second body, the second body simultaneously exerts a force equal in magnitude and opposite direction on the first body.

- Continuum hypothesis: the relative free motion of the molecules that compose solids and fluids is imperceptible in the body, being continuously distributed and filling the entire region of space it occupies, allowing to analyse the smooth variation of properties as a continuous medium using constitutive laws that relate stress and strain.

Over the last decades, the numerical approaches gained more emphasis complementing the more costly and time consuming experimental ones to help characterize variables that represent natural or industrial uncertainties. The natural hazards are relatively more challenging to characterize, encompassing complex phenomena only mathematically described by partial differential equations, PDE, expressed as system of governing equations with associated boundary and initial conditions. The typical lack of analytical solutions of PDE can be overcome by numerical solvers. For the numerical treatment, the continuum nature of the domain is discretized into discrete points/nodes framing components/elements over which the governing equations are approximated. Fig. 3.1 represents the spatial discretization of a generic PDE.

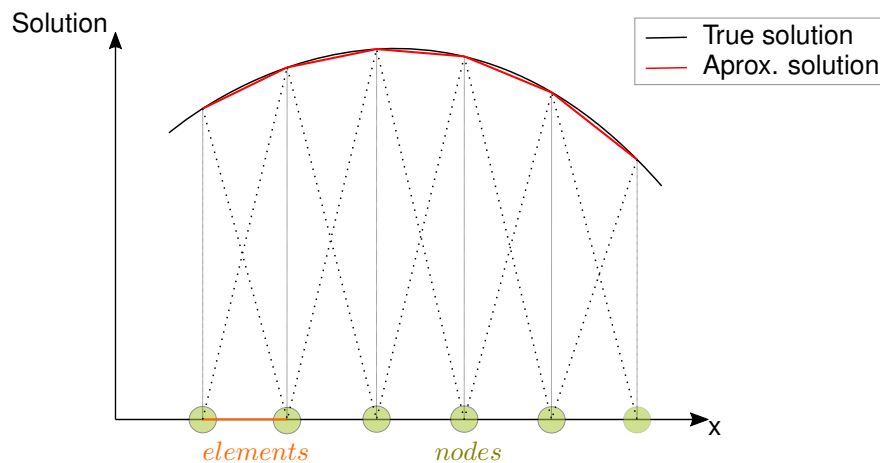


Figure 3.1: Discretization of the continuum into discrete elements. Each finite element is an independent geometric region of the domain over which equations with unknown variables are defined using the governing equations of a mathematical model to compute an approximate solution of the variable.

The spatial discretization is performed using grid-based or mesh-less methods, while the governing equations follow Lagrangian or Eulerian moving or fixed referential, respectively. After the spatial and numerical discretization, the original governing equations are changed into a set of algebraic equations or ordinary differential equations, ODE, that can be solved using time-integration schemes.

The numerical schemes adopted to characterize the cascading tsunami and earthquake actions, and the successive structural response are respectively described along Sections 3.2, 3.3 and 3.4.

3.2 Characterization of tsunami action

The calculation of tsunami wave forces on structures, \vec{F}_T , involves the integration of the external stress distribution over the surface of the structure [322]. The total stress per unit area, $\sigma_{i,j}$, is a combination of inertial (pressure, p) and viscous (tangential shear, τ) stresses, as given by Eq. 3.1:

$$\vec{F}_T = \int_{\partial A_e} \tau_{i,j} n_i dA_e \quad (3.1)$$

where $\tau_{i,j}$ is the stress tensor, n_i is the unit vector representing the direction normal to surface dS and ∂A_e is the net surface of the area exposed to the fluid motion. The integrand in Eq. 3.1 is responsible for the differentiation between the components in normal and tangential directions towards the surface. For most of the flows regime, excepting the at-rest flow regime, determining either the pressure or the tangential shear stresses requires numerical resolution of the fluid motion.

For tsunami-like flows, numerical modeling commonly accepts Navier-Stokes, NS, and Shallow-Water, SW, governing equations, function of the phenomena it aims to reproduce:

- mesh-less particle-based Lagrangian method, considering the fluid as a discrete set of particles drawn by a co-moving observer. The NS system of equations is solved by Smoothed Particle Hydrodynamic, SPH, framework implemented in DualSPHysics open-source code [247, 260], to characterize the tsunami inundation stage and its interaction with coastal structures;
- grid-based Eulerian method, a conservative form considering the continuous fluids drawn by an observer at rest. The non-linear SW system of equations is solved by a well-balanced Finite Volume, FV, method with hydrostatic reconstruction, implemented in-house C++ code [19, 21], to solve the generation and propagation stages of the tsunami;
- coupled Eulerian-Lagrangian modeling configuration, respectively to solve the linear(-ish) part of the domain and the fluid behavior near and impacting the coastal structures, respectively [48].

3.2.1 Lagrangian SPH-based numerical tool to solve NS equations

Fluids are typically governed by the NS equations, derived from three conservation principles of mass, momentum and energy, often complemented by an equation of state to describe the behavior of continuum fluid. To solve the system, the SPH method substitutes the continuum properties of the fluid by a set of discrete interacting particles and locally integrates the NS equations at the location of each particle.

The physical properties of a particle a , such as position, velocity, density, and pressure, are computed by interpolating the values of the neighbouring particles b , within the radius of the smoothing-length, h . The contribution of a b particle inside the n -dimensional domain, Ω , circular if 2D or spherical if 3D, is weighted according to a kernel function, $W_{a,b}$, function of the distance between particles, $r_{a,b}$ [240]. Fig. 3.2 shows a schematic representation of the SPH method principles.

Governing equations

The NS system of equations is derived from three conservation principles of momentum, mass (or continuity). To describe the fluid motion, the NS is complemented by a state equation.

Assuming the fluid is incompressible, the energy equation is dropped since the pressure derives from the free divergence constraint, $\nabla \cdot V = 0$. However, incompressible fluids require the resolution of

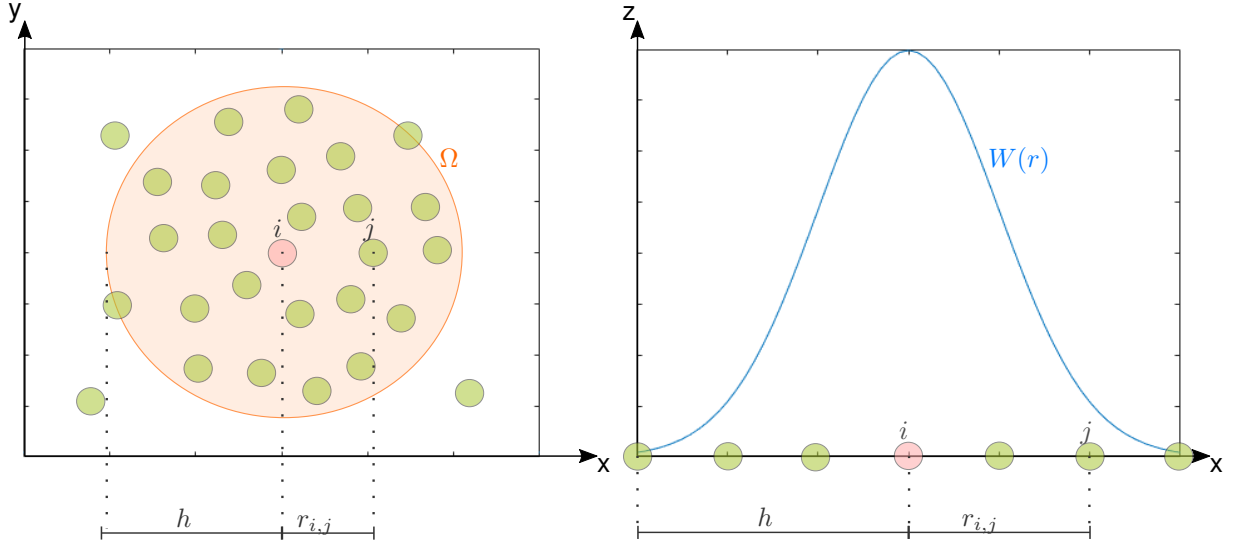


Figure 3.2: Lagrangian NS-SPH scheme: The principles of the SPH method in plane (left) and elevation (right) views. A physical property of particle a is computed considering the contribution of the neighbouring particles b weighted according to a smoothing-kernel function, $W_{r_{a,b}}$, along a certain area of influence, h .

an additional state equation, the Poisson equation, to evaluate the correct pressure that preserves the divergence free property. To avoid the supplementary pressure equations, a popular technique consists of assuming the fluid to be weakly compressible, as a function of density, and solvable by Tait's relation between pressure and density, for the state equation, leading to a strictly hyperbolic system (at least when the diffusion term is canceled). The Lagrangian system of equations, including Tait's formulation [322], follows Eq. 3.2.

$$\begin{cases} \frac{dV}{dt} = -\frac{1}{\rho}\nabla p + g + \Gamma \\ \frac{dr}{dt} = V \\ \frac{d\rho}{dt} = -\rho\nabla V \\ P(\rho) = \beta \left[\left(\frac{\rho}{\rho_0} \right)^\gamma - 1 \right] \end{cases} \quad (3.2)$$

where t is the time, r position, g gravitational acceleration, Γ represents the dissipative term, p and ρ stand for pressure and density, respectively, and velocity $V = (u, v, w)^t$. For Tait's relation, the reference density ρ_0 is usually the gas density at rest, while parameter $\gamma = 7$ is the polytropic constant and $\beta = \rho_0 C_s^2 / \gamma$, where C_s is the speed of sound [260].

The modeling of multi-phase interactions uses a modified version of Tait's equation of state for incompressible and inviscid fluids, Eq. 3.3:

$$P(\rho) = \frac{C_s^2 \rho_0}{\gamma} \left[\left(\frac{\rho}{\rho_0} \right)^\gamma - 1 \right] + \chi - a\rho^2 \quad (3.3)$$

where χ is a constant background pressure and $a\rho^2$ represents the cohesion forces between the

particles of a single phase. The coefficient representing the properties of the water, ρ_w , and air phases, ρ_a , and a characteristic length scale of the problem, L , is given by $a = 1.5g \left(\frac{\rho_w}{\rho_a} \right) L$.

Discretization of spatial and temporal domains

The spatial discretization convert the continuum domain of the fluid into discrete nodal points. The particles are dynamic and influenced by the interactions with neighbouring nodes to guarantee that the velocity of particle a is similar to the average velocity of neighbouring particles b , assuring an ordered flow and preventing penetration between continua.

Cubic Spline and Quintic Wendland kernel functions, both corrected by a shifting algorithm that balances the distribution of the particles in space, assume that neighboring particles that influence computations are within a distance of $2h_{sph}$ to the center of the kernel. Despite their similarities, comparisons between the use of the Cubic Spline kernel and the Quintic Wendland kernel formulations have demonstrated that the Wendland kernel leads to cheaper computational costs while providing more stable and convergent solutions [323, 324]. The Wendland kernel is given by:

$$W_{ab} = \frac{7}{4\pi h_{sph}^2} \left(1 - \frac{q}{2}\right)^4 (2q + 1) \quad (3.4)$$

where b stands for particles that belong to the discrete kernel support of particle a .

The temporal discretization uses numerical schemes to integrate equations of momentum, continuity and state. The more simple two-stage Verlet scheme (Eq. 3.5) is a second order accurate space integrator over a staggered time interval, complemented by a calibration every ten to fifty time steps to avoid divergence of the integrated values thought time. Alternatively, the Symplectic scheme (Eq. 3.6) is symmetric and time-reversible, i. e. step 1 and 3 are exactly the same, providing more stable, but computational more demanding solutions. The variables over time are computed through:

- Verlet scheme:

$$\begin{cases} v_a^{n+1} = v_a^{n-1} + 2\Delta t F_a^n \\ r_a^{n+1} = r_a^n + \Delta t V_a^n + \frac{1}{2}\Delta t^2 F_a^n \\ \rho_a^{n+1} = \rho_a^{n-1} + 2\Delta t D_a^n \end{cases} \Rightarrow \begin{cases} v_a^{n+1} = v_a^n + \Delta t F_a^n \\ r_a^{n+1} = r_a^n + \Delta t V_a^n + \frac{1}{2}\Delta t^2 F_a^n \\ \rho_a^{n+1} = \rho_a^n + \Delta t D_a^n \end{cases} \quad (3.5)$$

- Symplectic scheme:

$$\begin{cases} v_a^{n+1} = v_a^{n+\frac{1}{2}} + \frac{\Delta t}{2} F_a^{n+\frac{1}{2}} \\ r_a^{n+1} = r_a^n + \Delta t V_a^n + \frac{1}{2}\Delta t^2 F_a^n \\ r_a^{n+1} = r_a^{n+\frac{1}{2}} + \frac{\Delta t}{2} v_a^{n+1} \end{cases} \quad (3.6)$$

where Δt is the time step between instant n and $n + 1$.

The speed of sound used in Tait's relation, besides being a parameter to define the compressibility of the fluid (high sound celerity confer a virtual incompressible behaviour to the fluid), also constitutes a parameter that controls the stability of the numerical simulation by influencing the time step. Eq. 3.7 is also designed as the Courant Friedrichs Levy, CFL, condition that control the time step with respect to the space step and the eigenvalues of the system:

$$\Delta t = Cmin \left[\left(\sqrt{\frac{h}{F_a}} \right); \left(\frac{h}{c_0 + max_b \left| \frac{h v_{a,b} r_{a,b}}{r_{a,b}^2} \right|} \right) \right] \quad (3.7)$$

where the constant c is a constant of the order of 10^{-1} and F_a is the force by unit mass applied to the particle. Typically, c_0 assumes an artificial value around ten times the maximum flow speed, restricting the relative density fluctuation [325].

Smoothed Particle Hydrodynamics method

To solve the NS system of equations (Eq. 3.2), the SPH method substitutes the continuum properties of the fluid by a set of discrete interactive particles, a and b , with fluid properties and related employing a kernel function W to mimic the integro-differential operators. The kernel function covers a smoothing length, h_{sph} , featuring a radial smoothed Gaussian-like shape, approximated to a regular and isotropic distribution (see Fig. 3.2).

The integral of the approximation function, f , on the n -dimensional domain, Ω , with respect to the particle position vector, r , is substituted by the average of a discrete summation over all the particles that lie within the radius of the smoothing length (Eq. 3.8):

$$f(r) = \int_{\Omega} f(r') W(r - r', h_{sph}) d\Omega \quad (3.8)$$

where, h_{sph} is the smoothing length defining the influence area of the kernel weighting function, that must fulfill the positivity inside the interaction zone, compact support, normalization and monotonically decreasing value with distance and differentiability [260].

Consequently, for a specific particle a , the discrete average form for the particle approximation follows the formulation (Eq. 3.9):

$$f(r_a) = \sum_b f(r_b) \frac{m_b}{\rho_b} W(r_a - r_b, h_{sph}) \quad (3.9)$$

where a is the particle of interest and b are the neighbouring particles inside the smoothing length, h_{sph} , and affected by a kernel function, $W(r_a - r_b, h_{sph})$, further identified as $W_{a,b}$

Integrating the equations (Eq. 3.2) by parts, using divergence theorem to convert flux into integral of volume (the sum of all sources of the field in a region gives the net flux out of the region), and arguing that the kernel support is compact, the derivatives are now supported by the kernel functions formulated in Eq. 3.10:

$$\left\{ \begin{array}{l} \frac{dv_a}{dt} = - \sum_{b \in N(b)} m_b \left(\frac{p_a + p_b}{\rho_a + \rho_b} + \Pi_{ab} \right) \nabla_a W_{a,b} + g \\ \frac{dr_a}{dt} = v_a \\ \frac{d\rho_a}{dt} = \sum_{b \in N(b)} m_b v_{ab} \nabla_a W_{a,b} \\ P_a = \beta \left[\left(\frac{\rho_a}{\rho_0} \right)^\gamma - 1 \right] \end{array} \right. \quad (3.10)$$

where Π is an additional artificial viscosity term introduced for the sake of stability. The execution parameter describing the viscosity is based on whether the movement is artificial or laminar, respectively in Eq. 3.11:

$$\Pi_{ab} = \begin{cases} \frac{-\alpha c_{ab} \mu_{ab}}{\rho_{ab}} & v_{ab} \cdot r_{ab} < 0 \\ 0 & v_{ab} \cdot r_{ab} \geq 0 \end{cases} \quad (3.11)$$

where $c_{ab} = 0.5(c_a + c_b)$ is the mean speed of sound, $\mu_{ab} = hv_{ab}r_{ab}/(r_{ab}^2 + \eta^2)$, and α is a coefficient used to introduce energy lost through friction to the case, using the coefficient of bottom friction, which represents the ratio between α_{FB} (interaction between fluid and boundary particles) and α_{FF} (interaction between fluid particles). The coefficient of bottom friction is commonly taken as 1, i.e., interactions of fluid–fluid and fluid–boundary particles are equal. Such assumption is admissible for experimental setups where solids are usually composed of smooth surfaces [326]. However, on physical environments the fluid flow is likely to be reduced by the roughness of the contact surfaces. The adjustment of the bottom friction coefficient is deemed necessary to account, for example, with terrain, which influence is commonly associated with the Manning coefficient formulated in Eq. 3.12:

$$v = \frac{1}{n} R^{2/3} \sqrt{S} \quad (3.12)$$

where velocity v is affected by Manning coefficient n , hydraulic radius R and the channel slope S .

Delta-SPH algorithm

Delta-SPH formulation is a density treatment. When the imposed celerity of the sound, used to attribute the compressibility of the fluid, is too high may lead to too small time steps and, consequently, the computation became more expensive. Given that the reference value of sound celerity, c_0 is typically attributed adopting an artificial value of around ten times the maximum flow speed, the computation of the pressure using Tait's state equation in a stiff density field, together with the natural disordering of the Lagrangian particles, also led to computational instability and scattered density distributions. The Delta-SPH algorithm introduces a diffusive term in the continuity equation that reduces density fluctuations (Eq. 3.13):

$$\frac{d\rho_a}{dt} = \sum_b m_b v_{a,b} \cdot \nabla_a W_{a,b} + 2\delta_\Phi h c_0 \sum_b (\rho_b - \rho_a) \frac{r_{a,b} \cdot \nabla_a W_{a,b} m_b}{r_{a,b}^2 \rho_b} \quad (3.13)$$

Shifting algorithm

The disordered spacing of the particles can affect the stability due to the lack of uniform distribution of the particles. The consequences are the misleading of the velocity and pressure fields and the creation of voids in the fluid flow.

The shifting algorithm guarantees an anisotropic spacing of the particles, uniformly balancing areas with high and low concentrations of particles [327].

The shifting distance of the particle, δr , is given by (Eq. 3.14):

$$\delta r = -D \nabla C_a \quad (3.14)$$

where, D is a diffusion coefficient, $D = Ah \|u\|_a \Delta t$, that control the shifting magnitude, being A a dimensionless constant. The particle concentration is estimated by $C_a = \sum_b \frac{m_b}{\rho_b} W_{a,b}$ and the respective gradient approximation, using SPH formulation and kernel approximation, writes as Eq. 3.15:

$$\nabla C_a = \sum_b (C_b - C_a) \frac{m_b}{\rho_b} \nabla W_{a,b} \quad (3.15)$$

The correction imposed by the shifting numerical artifact applies near free-surfaces and implies that the particles motion obeys to Eq. 3.16:

$$\nabla r = \sum_b \frac{m_b}{\rho_b} r_{a,b} \cdot \nabla C_a W_{a,b} \quad (3.16)$$

Boundary conditions

The boundary conditions modeled to mimic a certain behavior are generated by differentiating the particles. The main approaches to enforce solid boundary conditions in SPH method are based on techniques using repulsive forces [240, 253] or fictitious particles to fill the space beyond the boundary interface to mimic the presence of a wall [328, 329]. The method also supports open boundaries in the form of a periodic boundary condition, achieved by allowing particles that are near an open lateral boundary to interact with the fluid particles near the complimentary open lateral boundary on the other side of the domain [254].

- Dynamic Particles - Dynamic Boundary Condition

The solid impermeable boundary conditions [253] are established by particles governed by the same equations of continuity and state as the fluid particles but externally controlled to assume specific positions or motion. This implies that, near the boundary condition, the distance between the fluid and the boundary particles decreases. Consequently, the augmented pressure increases the density of the boundary particles resulting in a repulsive force being exerted on the fluid

particles. A fixed behavior is assigned by imposing the position, which is typically used to model solid objects, such as walls. By imposing motion, according to a motion function, a dynamic behavior can be assigned, which is typically used to mimic gates, floating objects, flap- and piston-type wave-makers [253, 260]. Considering the effect of the boundary exerting a force to the fluid particles, the moving particles of the fluid follows Eq. 3.17:

$$\frac{dv_a}{dt} = - \left(2c^2 \frac{W_{a,b}}{(W_{a,b} + W_0)^2} + m \prod_{ab} \right) \frac{\partial}{\partial z_a} W_{a,b} - g \quad (3.17)$$

where, c is the speed of sound, $W_{a,b}$ is the weight function (or kernel), W_0 is the kernel when the distance between the particles is null, $W_0 = W(r_{ab} = 0)$, \prod_{ab} is the artificial viscosity and g is the gravitational acceleration.

- Dynamic Particles and Ghost Nodes - Modified Dynamic Moving Boundary Condition

The boundary particles are arranged in the same way as the boundary particles in the original dynamic boundary condition, yet is added an additional boundary interface between the fluid and the boundary particles. The interface boundary is composed of ghost nodes mirroring each boundary particle half particle spacing into the fluid by linear extrapolation.

For the density of the boundary particle, ρ_b , the ghost density, ρ_g and its gradient $[\partial_x \rho_g; \partial_y \rho_g; \partial_z \rho_g]$ are computed at the ghost node using a first-order consistent SPH interpolation. The density of the density particle ρ_b is then obtained by means of linear extrapolation with the values derived from the ghost particle, Eq. 3.18:

$$\rho_b = \rho_g + (r_b - r_g) \cdot \nabla \rho \quad (3.18)$$

where r_b and r_g are the position of the boundary particle and associated ghost node.

- Ghost Nodes - Open Boundary Condition

The support kernel of a particle that extends beyond the boundary is continued through the boundary, interacting with the other particles placed on the other side, generating a non-reflective, transmissive behavior [254]. The periodic open boundary conditions [255] are established by promoting the interaction of particles near the frontiers, boundaries or domain edges, allowing to enforce flow conditions.

Ghost particles are used to establish the buffer zones where the physical conditions are imposed or extrapolated from the fluid conditions, handling variable quantities such as velocity, pressure and water depth profiles [255]. The buffer particles and ghost nodes defining the surface are a set of fixed points along the direction normal to the open boundary. In the inlet buffer zone, buffer particles are created to cross the permeable boundary to the fluid domain, allowing to control the free-surface elevation inside the fluid domain. After crossing the buffer interface, the particle becomes a new fluid particle following Eq. 3.19:

$$r_{new} = [r_{fluid} - (r_{fluid} - r_{fixed}) \cdot n_{fixed} - L_b]r_{fixed} \quad (3.19)$$

where r_{fluid} is the positions of the buffer particle converted into a fluid, r_{fixed} is the position of the associated fixed point, L_b is the buffer length and n_{fixed} is the unit vector at the fixed point normal to the fluid-buffer interface inside the fluid domain.

Contrarily, in the outflow buffer zone, the fluid particles become buffer particles that are discarded from the computational domain.

Built-in force computation

The particle impact against a rigid structure is determined by the momentum rate at a discrete time t^n , hitting the wall, by solving the momentum equation taking the interpolation distance $< 2h$ [270, 330]. The computation of the force exerted by the fluid against a solid object at time t^n is then computed as the summation of the momentum variation of each particle b inside the kernel influencing particle a that is in the neighborhood of the solid and experiencing an acceleration (Eq. 3.20):

$$F = \sum_{b \in 2h_{sph}} m_b \left(\frac{dv_{a,b}}{dt} \right) \quad (3.20)$$

where m_b is the mass of particle b and $\frac{dv_{ab}}{dt}$ is the difference in acceleration between particles a and b . Note that the summation is only carried out for the particles that hit the surface of the solid in the time interval $[t^n, t^{n+1}]$.

Application of NS-SPH scheme in coastal engineering problems

The SPH method conceived in the late seventies for modelling astrophysical phenomena [238, 239] has been extended for application to problems of continuum solid and fluid mechanics phenomena [240]. The NS-SPH can tackle fluids impacting or interacting with structures, reproduce complex hydraulic phenomena, conveniently treat large deformations, and handle variable domains in time. The use of boundary conditions to mimic physical reflexive and transmissive behaviors allow to reproduce a large variety of physical phenomena. Over the last decade, coastal engineers have been investigating the applicability and adequacy of the SPH method to characterize fluid behavior and solve fluid-structure interaction problems [244], such as the characterization of non-breaking and breaking waves [252, 331], shallow water coastal flow [250, 251, 332, 333] including tsunami waves [249, 334] and respective overtopping and interaction effects on coastal structures [247, 287].

Multiple studies have been carried out with NS-SPH scheme to model waves impacting coastal structures, such as seawalls [270, 271, 335–338], breakwaters [180, 339–341], buildings [17, 18, 44], bridges [45, 46], piers [47] and more complex and recent approaches considering multi-physics induced by air entrapment [276] or interaction with flexible structures [342].

3.2.2 Eulerian FV-based numerical tool to solve SW equations

The modeling of tsunami behavior commonly accepts the SW as governing equations solved by Eulerian grid-based methods, such as the Finite Elements, Differences and Volume methods.

The grid-based Eulerian FV method is applied as a discretization procedure to represent and numerically solve PDE in the form of algebraic equations. The approximate solution is calculated at discrete places on a meshed geometry by dividing the physical space into contiguous polyhedral control volumes or cells. The surface integral is approximated to the sum of the fluxes crossing the individual faces of the control volume and the flux entering a given volume is identical to that leaving the adjacent volume. The properties of each control volume are calculated at the centroid and interpolated to the surface to be approximated to the volume integral.

Governing equations

The NS equations have simplified derivations combining the fluid properties: compressible or incompressible, viscid or inviscid, laminar or turbulent, etc. One of the most common simplifications is to consider the density constant along the trajectory (incompressible fluid), dispensing the energy equation and simplifying the mass/continuity equation [343].

The Euler approximation, potential governing equations for all fluids, is obtained by the linearization of the NS equations considering the fluid with inviscid and adiabatic properties. The Boussinesq approximation considers the fluid as incompressible and the flow as irrotational, allowing to include frequency dispersion and depth-dependent velocity profile to model breaking and non-breaking waves [344].

The SW, or Saint-Venant equations if unidirectional propagation, are obtained by depth-integrating the NS. The hydrostatic SW treatment of the NS constitutes a suitable and powerful approach to adopt in cases where the horizontal scale is much larger than the vertical scale, like the long-period tsunami waves. Tsunami waves are characteristically long (wave length \gg oceanic depth) and shallow (wave height \ll oceanic depth), allowing to neglect the vertical component of the velocity and acceleration in the system of equations. The SW system of equations is scalable to include non-linear terms, contributing to expanding the solver's adequacy to more models. The SW-FV tool includes numerical artifacts to consider source terms, the built-in conservation property, the capacity to treat discontinuities correctly, and the ability to handle complex bathymetry configurations while preserving some steady state configurations (well-balanced scheme), making the method very efficient.

The 2D SW system of equations modified to include varying bathymetry is given in Cartesian coordinates by Eq. 3.21:

$$\begin{cases} \partial_t h + \partial_x (hu) + \partial_y (hv) = 0 \\ \partial_t (hu) + \partial_x \left(hu^2 + \frac{g}{2} h^2 \right) + \partial_y (huv) = -gh\partial_x b \\ \partial_t (hv) + \partial_x (huv) + \partial_y \left(hu^2 + \frac{g}{2} h^2 \right) = -gh\partial_y b \end{cases} \quad (3.21)$$

where h denotes the water height, u and v are the velocity components along the orthogonal axis, b represents the bathymetry and g is the gravitational acceleration. The free surface, η , is given by the sum of b and h . Fig. 3.3 depicts the SW notation.

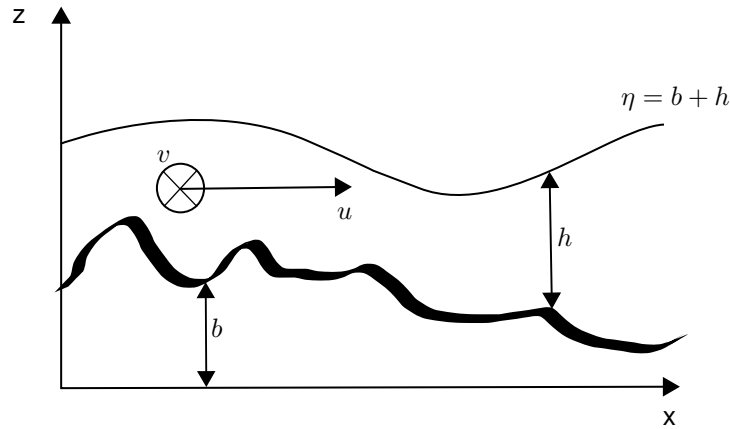


Figure 3.3: Eulerian SW-FV: Notation for the shallow-water problem.

Discretization of spatial and temporal domains

The spatial discretization consists of convert the continuum medium into a numerical domain, $\Omega = [0, L] \times [0, H]$, composed by adjacent discrete cells, $c_{ij} = c_i \times c_j$ with centroid coordinates (x_i, y_j) and interfaces $e_{i \pm \frac{1}{2}, j \pm \frac{1}{2}}$.

The temporal domain is $0 = t^0 < t^1 < \dots < t^n$ until the final prescribed time $t^N = T$. The subdivision of the temporal domain obeys to a non-constant time step $\Delta t^n = t^{n+1} - t^n$ that satisfies the Courant–Friedrichs–Lewy, CFL, condition to guarantee the stability of the simulation and convergence of the solutions by establishing a ration between the distance traveled by the fluid and the distance between elements, guaranteeing that information from a given cell or mesh element must propagate only to its immediate neighbors.

Any function $f = h, \eta, b, u, v$ at time t^n is approximation of the mean value over cell c_{ij} , The surface integrated value, f_{ij}^n , for real numbers $f_{i+\frac{1}{2},j;L}^n$ and $f_{i+\frac{1}{2},j;R}^n$ represent approximations on the left and right side of interface $e_{i+\frac{1}{2},j}$, while $f_{i,j+\frac{1}{2};L}^n$ and $f_{i,j+\frac{1}{2};R}^n$ stand for approximations on the lower and upper side of interface $e_{i,j+\frac{1}{2}}$. Fig. 3.4 depicts the spatial and temporal discretization in FV method, which can be applied to structured cells (rectangular-shape elements with four nodal points in two dimensions or hexahedral-shape elements with eight nodal points in three dimensions) and unstructured meshes (triangle-shape elements in two dimensions or tetrahedron-shape elements in three dimensions).

Finite Volumes method

The numerical scheme is based on the FV method and an uniform grid is used for the discretization of the spatial domain. For the sake of simplicity, the description of the method is introduced for the x -axis, denoting c_i as a cell with center x_i and length Δx .

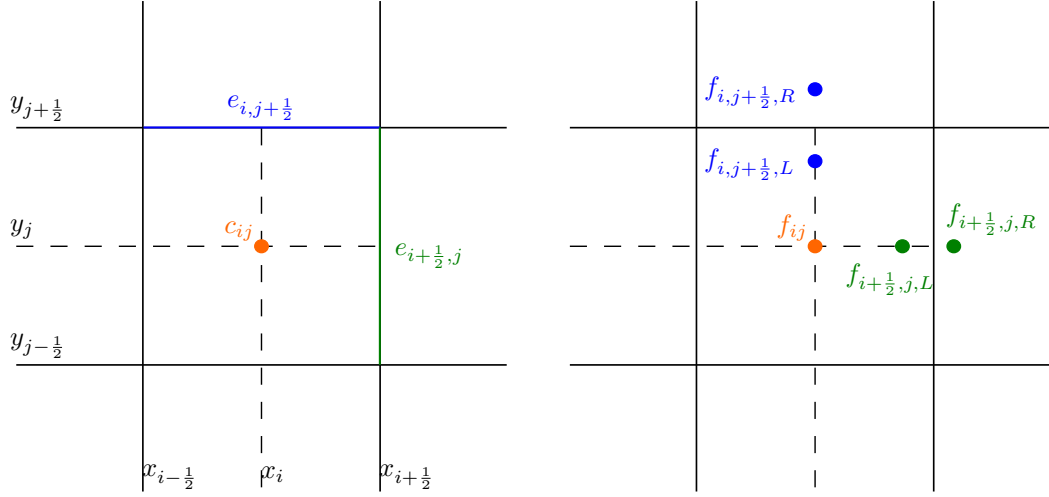


Figure 3.4: Eulerian SW-FV scheme: The principles of the FV method. Notation for the spatial (left) and temporal (right) discretization.

For a generic function, f , its numerical approximation at x_i is denoted by $f_i \approx f(x_i)$, while $f_{i-\frac{1}{2},L}$ and $f_{i+\frac{1}{2},R}$ stand for approximations at the left- and right-hand side of the interface $e_{i+\frac{1}{2}}$.

Assuming that all the state variables are known at time t^n , the values for t^{n+1} are calculated using the explicit FV method. The first-order FV scheme in time follows Eq. 3.22:

$$U_i^{n+1} = U_i^n - \frac{\Delta t}{\Delta x} \left(F_{i+\frac{1}{2}}^n + \varepsilon_{i+\frac{1}{2},L}^n - F_{i-\frac{1}{2}}^n - \varepsilon_{i-\frac{1}{2},R}^n \right) + \Delta t S_i^n \quad (3.22)$$

where, $F_{i+\frac{1}{2}}^n$ is the conservative flux across the interface $x_{i+\frac{1}{2}}$ with $U_i^n = (h_i^n, h_i^n u_i^n)$ as the vector of the conservative variables. The source term, S_i^n represents the discretization of the regular variation of the bathymetry, while $\varepsilon_{i+\frac{1}{2},L}^n$ and $\varepsilon_{i-\frac{1}{2},R}^n$ stand for the non-conservative flux contribution associated to the bathymetry discontinuity across the interface.

To extend the time scheme to a second-order scheme, the forward Euler scheme settings are doubly applied, $U_i^{n+1} = \frac{1}{2} (U_i^n + U_i)$.

To extend to a two-dimensional version, the method derives from a dimensional splitting where each direction is treated separately, using a Cartesian uniform grid as framework, composed of cells centered at point (x_i, y_j) of size $\Delta x \times \Delta y$. The FV for a two-dimensional approach follows Eq. 3.23:

$$U_{ij}^{n+1} = U_{ij}^n - \frac{\Delta t}{\Delta x} \left[F_{i+\frac{1}{2},j}^n + \varepsilon_{i+\frac{1}{2},j,L}^n - F_{i-\frac{1}{2},j}^n - \varepsilon_{i-\frac{1}{2},j,R}^n \right] \\ [10pt] - \frac{\Delta t}{\Delta y} \left[F_{i,j+\frac{1}{2}}^n + \varepsilon_{i,j+\frac{1}{2},L}^n - F_{i,j-\frac{1}{2}}^n - \varepsilon_{i,j-\frac{1}{2},R}^n \right] + \Delta t S_{ij}^n \quad (3.23)$$

An approximation of a function φ at point (x_i, y_j) writes φ_{ij} .

The horizontal conservative fluxes are characterized with $F_{i\pm\frac{1}{2},j}^n$ and the vertical conservative fluxes are set with $F_{i,j\pm\frac{1}{2}}^n$. The same convention applies for the non-conservative fluxes, ε .

The main difficulty is the evaluation of U_i^{n+1} accounting with the influence of discontinuity, steady-state preservation and dry/wet situations. Additional algorithms can complement the SW-FV scheme.

Well-balanced scheme

The non-conservative term $-gh\nabla b$ that accompanies the SW system of equation as written in Eq. 3.21 guarantees the preservation of the steady state configuration (null velocity and constant free surface in wet area). Consequently, the non-conservative term on the right-side of Eq. 3.21 compensates the hydrostatic pressure variation due to bathymetry variations, avoiding non-physical motions after some time-steps of the simulation, such as boiling water effects and erroneous evaluations of numerical approximations.

Hydrostatic reconstruction

The discretization of the source term is performed using the hydrostatic reconstruction proposed by Audusse et al., 2004 [345], that allows to deal with complex flows and dry/wet configurations, preserving the positivity of the water height, which provides robustness to the numerical scheme and accuracy to the computed solutions.

Considering the left and right sides of a cell, $c_{i,j}$, with interfaces $e_{i\pm\frac{1}{2},j\pm\frac{1}{2}}$, the reconstruction is performed at left and right-sides of the interface considering only the water heights involved in the pressure at the interface. Eq. 3.24 presents the generic formulation to set the new hydrostatic reconstruction variables:

$$\left\{ \begin{array}{l} b_e^{*,n} = \max(b_{e,L}, b_{e,R}) \\ h_{e,L}^{*,n} = \max(0, h_{e,L}^n - b_e^{*,n} + b_{e,L}^n) \\ h_{e,R}^{*,n} = \max(0, h_{e,R}^n - b_e^{*,n} + b_{e,R}^n) \\ \eta_{e,L}^{*,n} = h_{e,L}^{*,n} + b_e^{*,n} \\ \eta_{e,R}^{*,n} = h_{e,R}^{*,n} + b_e^{*,n} \\ u_{e,L}^{*,n} = u_{e,L}^n \\ v_{e,R}^{*,n} = v_{e,R}^n \end{array} \right. \quad (3.24)$$

where, $h_{e,L \text{ or } R}^n$ and $b_{e,L \text{ or } R}^n$ are approximations of water height and bathymetry at the side of interface $e_{i\pm\frac{1}{2},j\pm\frac{1}{2}}$. Fig. 3.5 resumes the hydrostatic reconstruction cases.

Limiting techniques

The FV framework may suffer from numerical diffusion, primarily if first-order approximations are performed. Limiting numerical techniques are popular artifacts to reduce the numerical diffusion and provide accuracy and robustness simultaneously.

The code is equipped with two different second-order FV numerical techniques deriving from an a

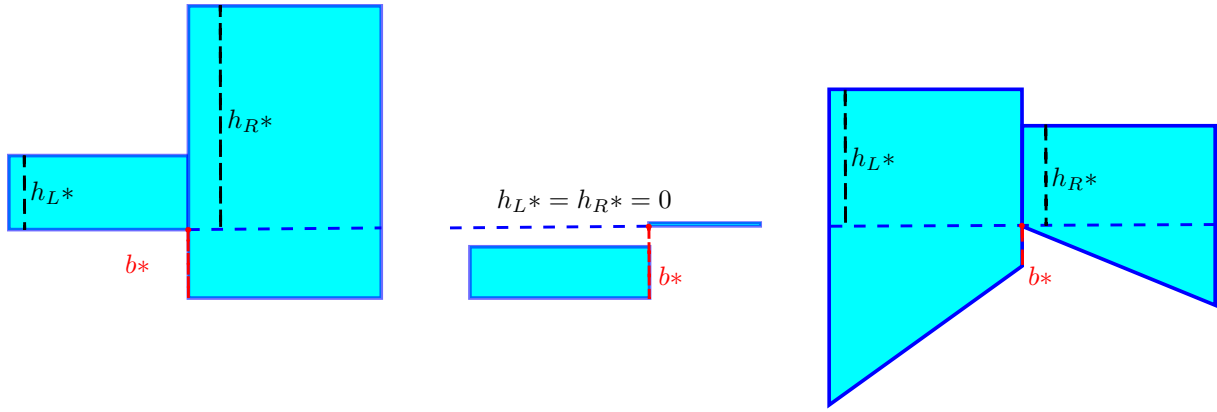


Figure 3.5: Eulerian SW-FV: Hydrostatic reconstruction for wet-wet with constant bathymetry (left), dry-wet (middle) and wet-wet with linear bathymetry (right).

priori or an *a posteriori* limitation procedure, respectively, the Monotonic Upstream-Centred Scheme for Conservation Laws, MUSCL, and the recent Multidimensional Optimal Order Detection, MOOD, techniques (see the discussion in Reis et al., 2018 [21]). Fig. 3.6 shows the fundamentals of MUSCL and MOOD techniques.

MUSCL



MOOD

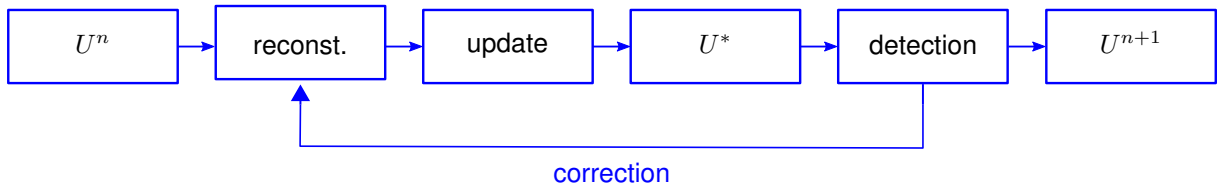


Figure 3.6: SW-FV: MUSCL and MOOD techniques.

MUSCL technique [346] consists of a linear reconstruction controlled by a limiting procedure. It is based on two steps: a local linear reconstruction to achieve the second-order, and a limiting procedure for preventing the solution from generating nonphysical oscillations.

The determination of the first derivative of any function $f = h, \eta, u, v, b$ is calculated by defining the slopes for the x - and y -direction, respectively as $p_{i+\frac{1}{2},j}^n(f) = \frac{f_{i+1,j}^n - f_{ij}^n}{\Delta x}$ and $p_{i,j+\frac{1}{2}}^n(f) = \frac{f_{i,j+1}^n - f_{ij}^n}{\Delta y}$. For a more accurate approximation, is assumed $f_{i-\frac{1}{2},j}^n = f_{ij}^n - \frac{p_{i+\frac{1}{2},j}^n + p_{i+\frac{1}{2},j}^n}{2} \frac{\Delta x}{2}$ on the right side of edge $e_{i-\frac{1}{2},j}$ and $f_{i+\frac{1}{2},j}^n = f_{ij}^n + \frac{p_{i+\frac{1}{2},j}^n + p_{i+\frac{1}{2},j}^n}{2} \frac{\Delta x}{2}$ on the left side of edge $e_{i+\frac{1}{2},j}$.

The reconstruction originates oscillations in the vicinity of a discontinuity leading to the need to implement a non-linear limiting procedure to preserve the monotonicity in each direction. Classical limiter operators implemented in Kotkot are *minmod*, *van Albada* or *van Leer* options.

MOOD technique [347] consists of compute a candidate solution for time t^{n+1} without limiters. After the verification of the admissibility of the solution, the cells are classified by the cell polynomial degree,

CPD. Only the problematic cells are converted to first-order scheme (if $CPD = 1 \Rightarrow \varphi_{i-\frac{1}{2},R} = \varphi_i - \frac{\Delta x}{2} \varphi'_i$ and $CPD = 1 \Rightarrow \varphi_{i+\frac{1}{2},L} = \varphi_i + \frac{\Delta x}{2} \varphi'_i$), being the slope given by $\varphi'_i = \frac{\varphi_{i+1} - \varphi_{i-1}}{2\Delta x}$, or constant value (if $CPD = 0 \Rightarrow \varphi_{i-\frac{1}{2},R} = \varphi_{i+\frac{1}{2},L} = \varphi_i$).

An optimal CPD map of cells at t^n is defined to compute the candidate solution, U^* , that must accomplish the detectors criteria. Detectors are procedures to verify the admissibility of the solution. If the CPD map has been modified, a new computation of the candidate solution is performed, only considering the problematic cells and their neighbor cells. Otherwise, the candidate solution is assumed as the solution at t^{n+1} .

Boundary conditions

Kotkot is prepared to assume two types of boundary conditions: reflective or transmissive. Assuming the edge situated on the right boundary of the domain as $e_{i+\frac{1}{2},j}$ and the reconstructed conservative vector on the left side of the edge, $W_{i+\frac{1}{2},j;L}$, is necessary to define the $W_{i+\frac{1}{2},j;R}$.

For a reflection condition, writes $h_{i+\frac{1}{2},j;R} = h_{i+\frac{1}{2},j;L}$, $b_{i+\frac{1}{2},j;R} = b_{i+\frac{1}{2},j;L}$, $u_{i+\frac{1}{2},j;R} = -u_{i+\frac{1}{2},j;L}$ and $v_{i+\frac{1}{2},j;R} = v_{i+\frac{1}{2},j;L}$.

For a transmission condition, writes $h_{i+\frac{1}{2},j;R} = h_{i+\frac{1}{2},j;L}$, $b_{i+\frac{1}{2},j;R} = b_{i+\frac{1}{2},j;L}$, $u_{i+\frac{1}{2},j;R} = u_{i+\frac{1}{2},j;L}$ and $v_{i+\frac{1}{2},j;R} = v_{i+\frac{1}{2},j;L}$.

The procedure repeats for the edge on the left, upper and lower boundaries, respectively $e_{i-\frac{1}{2},j}$, $e_{i,j+\frac{1}{2}}$ and $e_{i,j-\frac{1}{2}}$. For the upper and lower boundaries, the velocity in the vertical v is modified instead of the horizontal velocity, u .

Semi-analytic force calculation

Based on Bernoulli's Principle, which is related to the conservation of energy, the pressure, flow height and velocity are correlated such that the sum of internal, kinetic and potential energy remains constant along a streamline of the fluid.

The provisions of chapter 6 dedicated to tsunami design loading included in the 2016 edition of the ASCE 7 [32] were adopted to define the hydrostatic and hydrodynamic tsunami effects. The first is intrinsic to inundation depth, whereas the second is directly dependent of the product between the inundation depth by the squared velocity, known as the linear momentum flux [17, 207]. The hydrodynamic quantities are computed by the Eulerian FV scheme solving the system of non-linear SW equations.

Thus, the hydrostatic effects on both the horizontal, $F_{H,static}$, and vertical directions, $F_{V,static}$, are given by Eq. 3.25:

$$\begin{cases} F_{H,static} = \frac{1}{2} \rho b h_{max}^2 \\ F_{V,static} = \rho g V \end{cases} \quad (3.25)$$

where ρ is the density of the fluid, b is the width subject to force, h_{max}^2 is maximum inundation depth, g

is the gravitational acceleration and V is the displaced water volume following Arquimede's principle.

The peak hydrodynamic force is derived from the maximum flux momentum and is given by Eq. 3.26:

$$\begin{cases} F_{H,dynamic} = \frac{1}{2}\rho I_{tsu} C_d C_{cx} B (hu^2)_{max} \\ F_{V,dynamic} = 1.5\rho I_{tsu} Av^2 \end{cases} \quad (3.26)$$

where I_{tsu} is an importance factor for tsunami forces to account for additional uncertainty in estimated parameters varying between 1 and 1.25 depending on risk categories of the structure. C_d is the drag coefficient calibrated by regression to the peak of the first wave, where the most interesting and important results for the forces and pressures exerted on the structure occur. C_d varying between 1.2 and 2.5 depending on the ratio between the width of the structure and the depth, for rectilinear structures, or on the structural element section, for structural components, B is the overall building width (or b is considering a component width perpendicular to the flow). The product of inundation depth with square velocity, hu^2 is the momentum flux, M_F , A is the vertical projected area, and v is the vertical component of tsunami flow velocity. The overall drag force is affected by C_{cx} , which represents the proportion of closure and is determined by Eq. 3.27:

$$C_{cx} = \frac{\sum(A_{col} + A_{wall}) + 1.5A_{beam}}{Bh_{sx}} \quad (3.27)$$

where A stands for the area of the columns, *col*, *wall* and *beam*. The latter, A_{beam} , is the combined vertical projected area of the slab edge facing the flow and the deepest beam laterally exposed to the flow. The height h_{sx} accounts the average height of the stories below the tsunami inundation. In open structures, $C_{cx} \leq 20\%$, the minimum value corresponds to 0.5 and the surge force is negligible.

In the vertical direction, the horizontal slabs with area A located over a sloping grade with angle φ greater than 10° shall be designed for a redirected uplift pressure applied to the soffit of the slab, where $u_v = u \times \tan\varphi$, being u the horizontal flow velocity.

Application of SW-FV scheme in tsunami hazard assessment

The performance of new numerical tools is usually submitted to a benchmarking process before its application to real scenarios. The Long-Wave Run-Up Models Workshops of Catalina Island in California, 1990, Friday Harbor in Washington, 1996, and Catalina Island, 2004, were later compiled by National Oceanic and Atmospheric Administration into a technical memorandum [348] that recommends a battery of verification and validation tests for tsunami simulation tools. Meanwhile, the memorandum was revised by the subcommittee National Tsunami Hazard Mitigation Program, after the NTHMP Model Benchmarking Workshop, redefining the problems and the admissible errors for inundation models used in NTHMP projects [349]. Numerical tools solving the two-dimensional nonlinear SW using FV methods, such as Geoclaw [224] and Tsunami-HySEA [226], have demonstrated their accuracy, reliability and robustness to the benchmarking standards.

3.2.3 Coupled model

Bearing in mind that the FV method is a fast and efficient solver for static domains and regular flows, as long as breaking waves or interaction with complex structures are not involved, together with the fact that SPH is a computationally expensive method that is capable of handling complex hydraulic phenomena and geometries, a coupled simulation represents an intermediate compromise to obtain fast, yet detailed solutions.

Taken into account that: (1) the ultimate goal is the characterization of the wave impact on infrastructure(s), (2) the essential condition when applying the coupling of the models is to guarantee the continuity of the fluid height and horizontal velocity in the neighbouring domains [350], and (3) the simplicity and computational savings are a concern to perform the simulations, the inherent boundary conditions of both Eulerian and Lagrangian methods were explored to couple the models dismissing additional numerical artifacts to the respective computations.

Each numerical method has its intrinsic boundary conditions to replicate the physics involved in the models. Reflection, transmission and open are the boundary conditions supported by SPH [253, 255] and FV methods [19]. The noticeable restriction of FV method is the static nature of the boundary interface, limiting the modeling of gates, flaps and pistons. The SPH method overcomes the limitation taking advantage of its variable domain length in time, characteristic of the Lagrangian discretization.

The modeling technique uses the SPH and FV capacity to capture physical quantities of the fluid in a virtual position. By imposing Dirichlet boundary conditions inherent to each model, the frontiers where the data exchange occurs are prescribed in a natural manner:

- the transition from NS-SPH to SW-FV domain is achieved by computing the hydrodynamic quantities at a virtual position coinciding with the location of the TBC used to initiate the FV domain. The SPH treats the quantities summing the relevant properties of all the particles inside the influence of the smoothing length, $2h_{sph} \approx 4\Delta p$, where Δp is the initial particle inter-distance. Then, the time-histories of the flow velocity are assigned in the horizontal direction, while the time-history of the free-surface elevation is imposed by assuming the height as a function of the highest particle position;
- the transition from SW-FV to NS-SPH domain is obtained by capturing the free-surface elevation and flow velocity at the cell that immediately precedes the position that coincides with the location of the OBC used to initiate the SPH domain. The OBC [255] is prescribed by a buffer layer of particles with a chosen width of $6\Delta p$ in the normal direction of the OBC.

3.3 Characterization of seismic action

The lack of real high magnitude earthquake records is often complemented by synthetic generation of data adopting different mathematical, empirical or hybrid approaches [351]. The generated data varies between discrete peak values or time-histories of seismic quantities, such as acceleration.

Numerical methods based on Ground Motion Prediction Equations, GMPE, are valuable tools to infer seismic quantities required for earthquake engineering purposes:

- peak values, using an open-source software, OpenQuake [352], written in the python programming language to generate the distribution of peak ground acceleration into a ground motion field;
- time-histories, using an open-source EXSIM code [353] written in FORTRAN based on stochastic finite-fault modeling to assess site response.

3.3.1 Notation

A finite fault seismologic modeling constitutes a representation of the spatial extent, hypocentral depth, d , kinematic parameters and geotechnical characterization of the rupture process, the propagation path, R and the site-effects influencing the seismic waves. The geometric parameters of the source include the width and length of the rupture area, and the focal mechanism (of instrumentally recorded events) or kinematic parameters (of fault ruptures). The kinematic parameters include strike, φ , dip, δ , slip, λ and rake, Θ) and rigidity of the propagation medium, μ . Fig. 3.7 depicts the finite fault notation. O represents the hypocenter (at h depth) or its projection on the surface, epicenter. Strike, φ , is the fault trace direction in decimal degrees ($0^\circ - 360^\circ$) relative to the North. Rake, Θ is the direction of the hanging wall moves during rupture in decimal degrees ($-180^\circ - 180^\circ$) relative to the fault strike. $\Theta > 0$ represents a thrust or reverse fault whereas $\Theta < 0$ represents a normal fault. Dip, δ , is the angle of the fault in decimal degrees ($0^\circ - 90^\circ$) relative to the horizontal. Slip is the relative displacement of formerly adjacent points on opposite sides of a fault, measured on the fault surface.

3.3.2 Ground motion field

The OpenQuake tool is an open-source hazard and risk modelling software developed by Global Earthquake Model, GEM [352], structured as a Python-based module for modelling earthquake ruptures and calculating hazard results such as hazard curves, stochastic event sets, ground motion fields of peak ground intensities (hosted on GitHub: github.com/gem/eq-engine).

The generation of ground motion fields is typically governed by equations that follow a form of logarithmic function of spectral accelerations and its associated uncertainty at a given site. A GMPE relates a ground-motion intensity measure to a set of explanatory variables describing the source, wave propagation path and site response [354]. The functional form of the generic GMPE reads as Eq. 3.28:

$$\ln Y = F_E + F_z + F_\gamma + F_S + C, \quad (3.28)$$

where $\ln Y$ is the logarithmic expression of a ground-motion intensity measure, peak ground acceleration, PGA, for the present study. The F_E , F_z , F_γ and F_S represent functions for earthquake source, attenuation along the path, geometrical and anelastic, and site-effects, respectively.

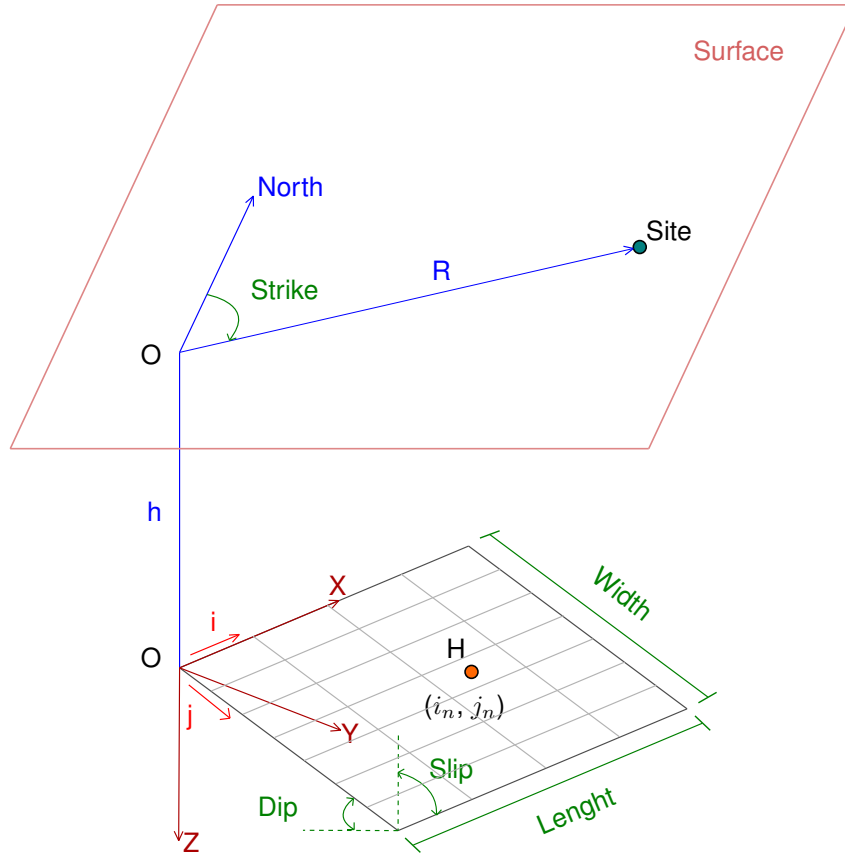


Figure 3.7: Finite fault: notation.

3.3.3 Ground motion accelerograms based on finite-fault method

The EXSIM is an open-source stochastic finite-fault simulation algorithm relying on dynamic corner frequency that generates the time-series of the earthquake's ground motion [353]. The routine is hosted in Github github.com/GFZ-Centre-for-Early-Warning/exsim/blob/master/EXSIM12.for.

The fundamental concept is the fault modeling into sub-faults, where each sub-fault is considered a small point source, calculated by stochastic point-source method [355]. The contributions of each of the N sub-faults are then normalized and a time adjustment is applied to control high and low frequency amplitudes. The sum of the various contributions gives the total seismic signal at the site (see Fig. 3.7), as in Eq. 3.29:

$$A(t) = \sum_{i=1}^{nl} \sum_{j=1}^{nw} H_{ij} \times A_{ij}(t - \Delta t_{ij}) \quad (3.29)$$

where, nl and nw are the number of sub-faults along the length and width of the main fault, H_{ij} is a normalization factor for the ij^{th} sub-fault that aims to conserve energy, and Δt_{ij} is the relative time delay for the radiated wave from the ij^{th} sub-fault to reach the observation point, P in Fig. 3.7.

The model of the total radiation is based on the spectrum of the ground motion at a specific site with the contributions of the complementary physical processes of seismic source generation, path propagation and site effects, as defined by Boore [355, 356] (Eq. 3.30):

$$A(M_0, R, f) = S(M_0, f) \cdot P(R, f) \cdot G(f) \cdot I(f) \quad (3.30)$$

where $S(M_0, f)$ is the displacement source spectrum, in the seismic source, reflecting the source geometry and spectral characteristics in the source vicinity, the $P(R, f)$ reflect the path influences, the $G(f)$ regards the site effects and $I(f)$ the instrument or type of motion considered, where f is frequency of the seismic wave.

The source spectrum is commonly modeled using the Ω -square approach [357], that relates the seismic moment, M_0 , and the corner frequency, f_0 , assuming $M_0 f^3 = constant$. The constant is related to the stress drop parameter, $\Delta\sigma$, to establish Eq. 3.31:

$$f_0 = 4,9 \times 10^6 \beta^3 \sqrt{\frac{\Delta\sigma}{M_0}} \quad (3.31)$$

The current EXSIM algorithm version considers a f_c in function of time. The tool normalizes the sub-faults contributions and applies the time adjustments to control high and low frequency amplitudes and summed them to obtain the total seismic signal at the site. For each sub-fault, seismic moment, $M_{0,ij}$, corner-frequency, $f_{c,ij}$, and normalization factor H_{ij} are derived from the total moment, M_0 , and slip distributions among the ij^{th} sub-faults, s_{ij} . The $M_{0,ij}$ reads as Eq. 3.32:

$$M_{0,ij} = \frac{M_0 \times s_{ij}}{\sum_{i=l}^{nl} \sum_{j=l}^{nw} s_{ij}} \quad (3.32)$$

Mathematically, $f_{c,ij}$ is given by Eq. 3.33:

$$f_{c,ij} = 4.9 \times 10^6 \beta \left[\frac{\Delta\sigma}{\min(N_R/N, F_{pulse}) \times M_0} \right]^{(1/3)} \quad (3.33)$$

where N_R is the number of sub-faults and F_{pulse} is the maximum fraction of the fault area.

The normalization factor, H_{ij} , representing the delay associated to a sub-fault, is given by Eq. 3.34:

$$H_{ij} = \frac{M_0}{M_{0,ij}} \sqrt{\frac{\sum_k \left(\frac{f_0^2 f_k^2}{f_0^2 + f_k^2} \right)^2}{N \sum_k \left(\frac{f_{0,ij}^2 f_k^2}{f_{0,ij}^2 + f_k^2} \right)^2}} \quad (3.34)$$

where f_0 and M_0 are respectively the corner frequency and seismic moment of the whole fault, while f_k is the k^{th} frequency ordinate.

3.3.4 Design spectra

The European normative, Eurocode 8 [33], recommends a simplified representation of the earthquake motion at a given point on the surface by an elastic ground acceleration response spectrum, which represents the frequency/period of an oscillator with a certain damping, function of the peak horizontal acceleration at the bedrock and type of soil where it is implemented, following the expression in Eq. 3.35:

$$\left\{ \begin{array}{ll} S_e(T) = a_g \cdot S \cdot \left[1 + \frac{T}{T_B} \cdot (\eta \cdot 2.5 - 1) \right] & \text{if } 0 \leq T \leq T_B \\ S_e(T) = a_g \cdot S \cdot \eta \cdot 2.5 & \text{if } T_B \leq T \leq T_C \\ S_e(T) = a_g \cdot S \cdot \eta \cdot 2.5 \cdot \frac{T_C}{T} & \text{if } T_C \leq T \leq T_D \\ S_e(T) = a_g \cdot S \cdot \eta \cdot 2.5 \cdot \left[\frac{T_C \cdot T_D}{T^2} \right] & \text{if } T_D \leq T \leq 4(s) \end{array} \right. \quad (3.35)$$

where, $S_e(T)$ is the elastic response spectrum, T the vibration period of a linear single-degree-of-freedom system, a_g is design ground acceleration, T_B is the lower limit of the period of the constant spectral acceleration branch, T_C is the upper limit of the period of the constant spectral acceleration branch, T_D is the value defining the beginning of the constant displacement response range of the spectrum, S factor to account soil influence; $\eta = \sqrt{10/(5 + \xi)} \geq 0.55$ is the damping correction factor with reference value of $\eta = 1$ for $\xi = 5\%$, being ξ the percentage of viscous damping ratio of the structure.

Fig. 3.8 shows the generic shape of the spectrum, while Table 3.1 provides T_B , T_C , T_D and S to define the ordinates and shapes of various spectra for the Portuguese territory. The S parameter depends of the shear waves velocity or N_{SPT} value. Type A soil has average shear velocity below the ground surface greater than 800 m/s and represents rocky soils, while the poorer soil, non-cohesive type E soil, has average shear velocities up to 180 m/s .

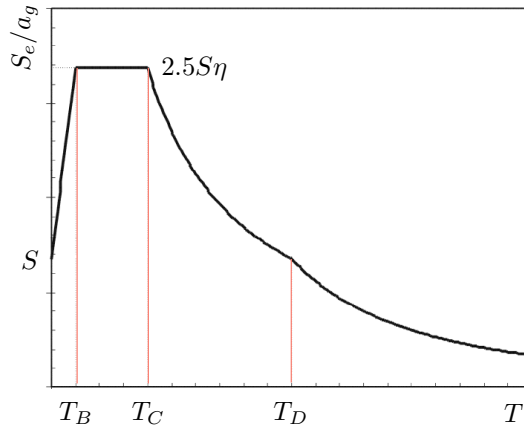


Figure 3.8: Regulatory seismic action. Generic form of the elastic response spectra.

| Soil | S | Earthquake type I | | | Earthquake type II | | |
|------|------|-------------------|-----------|-----------|--------------------|-----------|-----------|
| | | T_B [s] | T_C [s] | T_D [s] | T_B [s] | T_C [s] | T_D [s] |
| A | 1.00 | 0.1 | 0.6 | 2.0 | 0.1 | 0.25 | 2.0 |
| B | 1.35 | 0.1 | 0.6 | 2.0 | 0.1 | 0.25 | 2.0 |
| C | 1.60 | 0.1 | 0.6 | 2.0 | 0.1 | 0.25 | 2.0 |
| D | 2.00 | 0.1 | 0.8 | 2.0 | 0.1 | 0.30 | 2.0 |
| E | 1.80 | 0.1 | 0.6 | 2.0 | 0.1 | 0.25 | 2.0 |

Table 3.1: Regulatory seismic action. Parameters recommended by the national annex for the calibration of the elastic response spectrum for the Portuguese territory [33].

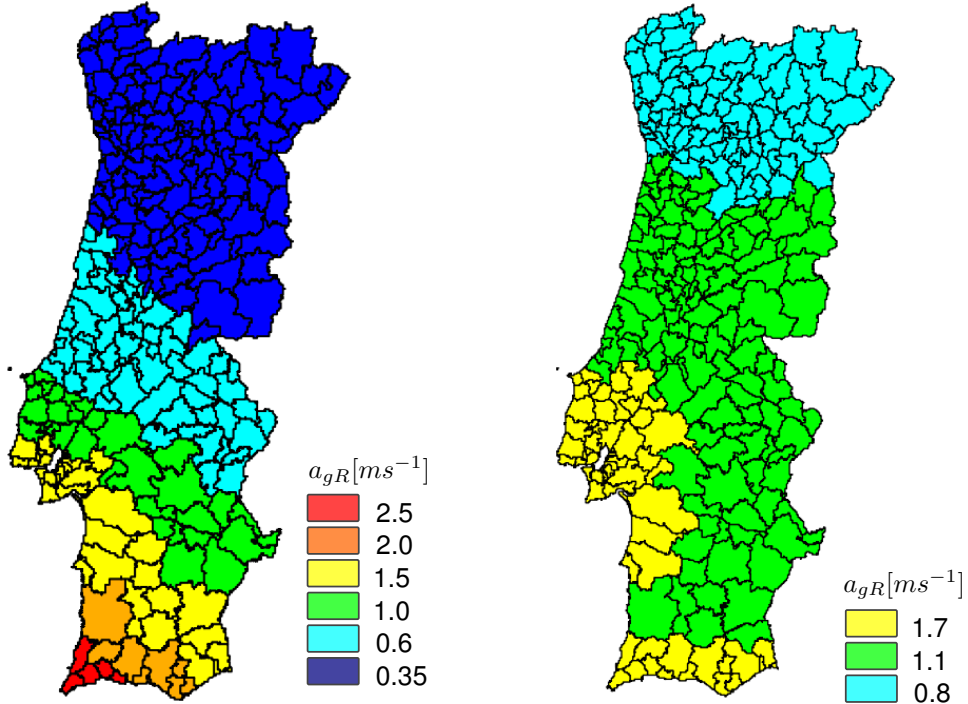


Figure 3.9: Regulatory seismic action. Reference acceleration for Portugal mainland regarding earthquakes of type I, inter-plate offshore far-field source (left) and type II, intra-plate inshore near-field source (right).

The design ground acceleration, a_g , product of $\gamma_1 \cdot a_{gR}$, may also constitute an amplification of the spectra, function of the class of importance of the structure. Fig. 3.9 depicts the reference horizontal acceleration on the bed-rock, a_{gR} , recommended for the different seismic zones and both type of earthquakes, type I and II, far- and near-field-source, respectively.

The a_{gR} has annual probability of occurrence of 1/475 years and is recommended for class of importance II structures (office and housing buildings). The γ_1 parameter allows to adapt a_{gR} for the different structural classes of importance using Eq. 3.36:

$$\gamma_1 = \left(\frac{RP}{475} \right)^{\frac{1}{K}} \quad (3.36)$$

where γ_1 is the importance factor, RP is the return period and K adopts a value of 1.5 or 2.5 respectively for type I and II earthquakes. The RP adopts 243, 475, 821 and 1303 for classes of importance I, II, III and IV, respectively. Thus the values of γ_1 for the different classes of importance are 0.65, 1.00, 1.45 and 1.95, for type I earthquakes, and 0.75, 1.00, 1.25 and 1.50, for type II earthquakes. Eurocode also prescribes the use of Eq. 3.36 to increase the RP value for critical infrastructures.

Assuming that the response spectra is an overlapping of multiple stochastic accelerograms [358], the generation of an artificial accelerogram is based on the design power spectra through a stochastic process that overlaps harmonic series using Eq. 3.37:

$$X(t) = \sum_{k=1}^N \sqrt{2S_x(\omega_k) \Delta\omega} \cos(\omega_k t + \phi_k) \quad (3.37)$$

where $S_x(\omega_k)$ is the bandwidth frequency, assuming the bandwidth as $\omega = k - \frac{1}{2}\Delta\omega$, and ϕ_k is a phase angle at interval $[0 : 2\pi]$ to insert the randomness factor in the generation of the harmonic series.

The random broadband signal is then characterized using a power spectral density function, $G_z(\omega)$. The $G_z(\omega)$ is defined after applying an auto-correlation function and Fourier transform to the various signals. Each signal is perceived as a stochastic process with an inherent power. Using a best fit procedure, Paola et al. 2007 [359] derived a power spectral density function coherent to the Eurocode 8. The analytical form of Eq. 3.38 reads:

$$\left\{ \begin{array}{ll} G_z(\omega) = \beta \left(\frac{\omega}{\omega_D}\right)^{2.52} & \text{if } 0 \leq \omega \leq \omega_D \\ G_z(\omega) = \beta + (\gamma - \beta) \frac{\omega - \omega_D}{\omega_C - \omega_D} & \text{if } \omega_D \leq \omega \leq \omega_C \\ G_z(\omega) = \gamma \left(\frac{\omega_C}{\omega}\right)^{1.33} & \text{if } \omega_C \leq \omega \leq \omega_B \\ G_z(\omega) = \gamma \left(\frac{\omega_C \omega_B}{\omega^2}\right)^{1.33} & \text{if } \omega \geq \omega_B \end{array} \right. \quad (3.38)$$

where $\beta = \beta_0 a_g^2$, $\gamma = \gamma_0 a_g^2$ and in which the values of ω_B , ω_C , ω_D , γ_0 and β_0 depend on the soil type. Fig. 3.8 shows the generic shape of the power spectrum, while Table 3.2 provides β_0 , γ_0 , ω_D , ω_C and ω_B , function of the type of soil [359] to generate a set of artificial signals from the design response spectra of EC8 for the Portuguese territory, varying the type of soil, and distance from the source (near- and far-field generation).

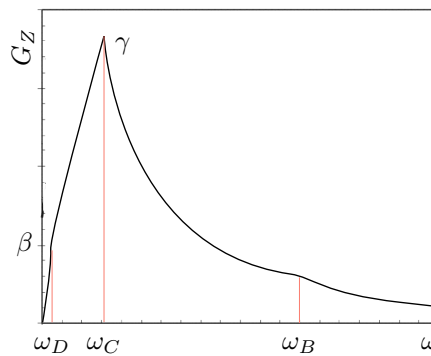


Figure 3.10: Regulatory seismic action. Generic form of the power density spectra.

| Soil | β_0 [s] | γ_0 [s] | ω_D [s^{-1}] | ω_C [s^{-1}] | ω_B [s^{-1}] |
|------|---------------|----------------|-------------------------|-------------------------|-------------------------|
| A | 842 | 2619 | π | 5π | $40\pi/3$ |
| B | 1896 | 4935 | π | 4π | $40\pi/3$ |
| C | 2507 | 5710 | π | $10\pi/3$ | 10π |
| D | 6141 | 11080 | π | $5\pi/2$ | 10π |
| E | 2580 | 6717 | π | 4π | $40\pi/3$ |

Table 3.2: Regulatory seismic action. Parameters recommended for the calibration of the Eurocode 8 power spectra (adapted from Paola et al. 2017 [359]).

3.4 Characterization of structural behavior

The open-source Open System for Earthquake Engineering Simulation, Opensees [360, 361], is an object-oriented framework, using TCL string-based command language associated with procedures written in $C++$ language, suitable for structural and geotechnical modeling. The framework is based on Finite Elements method, FE, and is hosted in Github: github.com/OpenSees/OpenSees. A detailed description of the OpenSees commands can be found at opensees.berkeley.edu/wiki/index.php/Main_Page.

3.4.1 Lagrangian FE-based numerical tool to solve motion equations

The grid-based Lagrangian approach using the FE method is the procedure that substitutes the continuum into discrete elements to numerically evaluate nodes (force-displacement), elements (force-deformation), sections (moment-curvature) and fibers (material stress-strain) of the domain. Fig. 3.11 shows a schematic representation of FE method principles.

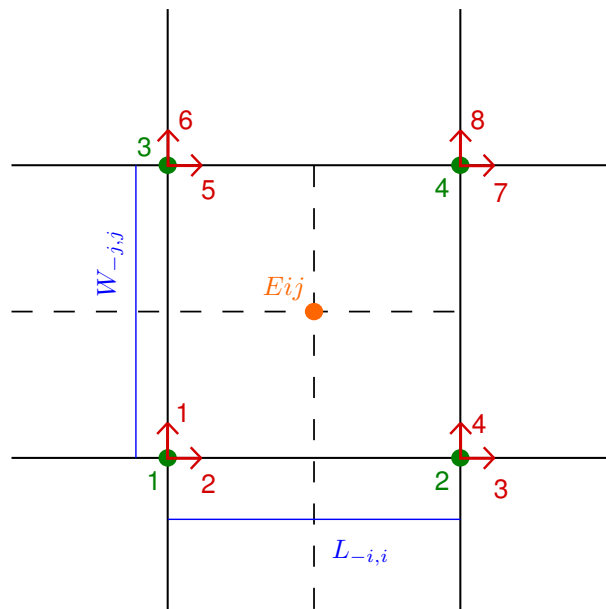


Figure 3.11: Lagrangian FE scheme: The principles of the FE method. Notation for the spatial discretization. Each finite element is discretized onto a mesh using over which the governing equations of momentum and material constitutive laws are defined to compute the structural response.

Governing equations

The governing equations follow the classic Newton's laws of motion complemented by D'Alembert's principle that extends the principle of virtual work from static to dynamic systems.

For the sake of simplicity, the equation of motion of a single-degree-of-freedom, SDOF, linear oscillator system subjected to ground excitation is based on Newton's law (Eq. 3.39):

$$m\ddot{u} + c\dot{u} + ku = m\ddot{u}_g \quad (3.39)$$

where, m is a single mass, attached to the ground by a linear spring of stiffness k , and a linear viscous damper of constant c . The relative displacement between the mass and ground is $u = u_t - u_g$, being u_t the total displacement of the mass and u_g the displacement of the ground due to motion. Therefore, \dot{u} is the velocity across the viscous damper and \ddot{u} the acceleration on the mass. The external force applied to the system, $f = m\ddot{u}$ is positive in the direction of the motion u .

For a multiple-degree-of-freedom, MDOF, the number of motion equations is equal to the number of degrees of freedom. The equation has the general form as in Eq. 3.40

$$M\ddot{u} + C\dot{u} + Ku = f \quad (3.40)$$

where, $u = (u_1, u_2)^T$ is the vector containing the degrees of freedom of the system (displacements, rotations, or generalized coordinates, depending on the way the model has been built), M is the mass matrix, K is the stiffness matrix and C is the viscous damping matrix. The theoretical concepts on dynamic behavior of structures are detailed in [362].

Discretization of spatial domain

The spatial discretization is a function of the dimensions of the domain and the respective degrees of freedom. A domain with one spatial dimension has one degree of freedom per node, two-dimensional has three degrees of freedom per node and three-dimensional has six degrees of freedom per node.

Accordingly, single- or multi-dimensional elements are used to assemble the model, from zero-length elements to tetrahedrons, delimited by nodes (see Fig. 3.11). The nodes accept the definition of single- or multi-points constraints that prescribe the movement (typically 0) of a single degree of freedom at a node or defined by the movement of certain degrees of freedom at another node, respectively.

Object-oriented Finite Elements method

The FE-based algorithm in OpenSees is an object-oriented framework that uses TCL string-based command language to assign a set of procedures. It is written in C++ language to carry out FE analysis. The procedures (called commands or objects) to TCL are grouped into five categories: modeling, misc, analysis, output and database.

The modeling of the domain is the aggregation of geometrical entities (point, line, surface, volume), elements (elastic, force-based or displacement-based beam-column, truss, quad, brick), sections (elastic, fiber, plate), materials (uniaxial for stress-strain or force-deformation relationships, multi-dimensional representing the stress-strain relationship at the gauss-point of a continuum element), single-point constraints prescribing the movement of a single DOF at a node (fix translation and/or rotation), multi-point constraint defining the relationship between the movement of certain DOF as a function of the DOF at another node (equal DOF, rigid diaphragm, rigid link).

The misc commands are used to generate elements or modify properties of elements, such as adding masses, or assign Rayleigh damping to the model. Thus, the model comprises coordinates definitions of nodes and elements, supporting additional mass and Rayleigh damping specifications.

The elements accept geometric transformations to transform single-element stiffness and resisting force from the local system to the global coordinate system, such as P-delta effects. Different materials from a vast OpenSees library provide complementary characteristics to the model. Friction models are also available, which specifies the coefficient of friction in terms of the absolute sliding velocity and the pressure on the contact area, such as Coulomb friction or dependent of velocity, normal force, or multi-linear velocity.

Besides the implemented libraries of elements, materials and analysis, new ones can be user-defined to perform linear and nonlinear structural and geotechnical models, adopting linear or non-linear, static or dynamic analysis.

The static-based analyses include linear, non-linear monotonic (pushover) and non-linear reversed cyclic. The transient-based analyses include uniform or multiple support excitation (pattern or time-series). Eigenvalue analyses can be set and combined with all other analysis types.

Static and dynamic analyses are assembled based on a system of equations. A constrain handler controls how the constraint equations are enforced in the analysis and how it handles the boundary conditions and imposed displacements, while the number of degrees of freedom defines the mapping between equation numbers and degrees of freedom. The time integrator determines the predictive step for time $t + \Delta t$, whereas the solution algorithm determines the sequence of steps taken to solve the equation at the current time step. The solver adopted defines how to tackle the system of equations in the analyses and how to store them. The convergence of the solutions is continuously tested.

Recorder object(s) monitor the nodes, elements, sections and fibers during the analysis to generate the numerical solutions after a convergent static or transient analysis step. The nodal records are capable to provide displacement, velocity, acceleration, incremental displacement, eigenvector for mode i , nodal reaction and damping forces, for the response of a number of nodes at every converged step, envelope the min, max and absolute max of a number of nodal response quantities or the drift between two nodes. The drift is taken as the ratio between the prescribed relative displacement and the specified distance between the nodes. The element recorder type records the response or envelope response of a number of elements at every converged step. The response recorded is element-dependent, varying among forces, local forces, stresses, stiffness, deformations, inflection point, tangent drifts, integration points and weights, friction, etc. OpenSees also allows verifying the state of the model and response quantities in real time during the simulation, including nodal displacement, velocity and acceleration, returning the current time in the domain.

Application in coastal engineering

The OpenSees open-source tool has been widely used to perform seismic structural analyses of multiple geometries and materials and eventual soil-structure and fluid-structure interactions, demonstrating its potential for geotechnical [363], structural and interactive models. Moreover, graphical interfaces connecting the text-only solver to graphical pre/post processors are emerging (e.g. GiD platform [364]). OpenSees has been used to model and perform seismic analysis of piles [365, 366] and pile-supported wharves [367, 368], some of them considering the soil-structure

interaction effects [369–371].

The structural response of buildings under exclusive seismic action [372–374] and earthquake and tsunami cascading actions [40, 92, 295, 375] has been investigated using OpenSees. Bridges were also analysed, as a structure [376, 377] or considering the bridge-foundation-ground system [378, 379]. Recently, the effects of storm waves [197] and tsunami-waves on bridges superstructures was evaluated [18, 380, 381]. Successive analyses of earthquake and tsunami actions on bridges were performed using non-linear materials [95, 382] to investigate cumulative effects of the successive nature of the analysis, quantify soil-fluid-structures interaction and evaluate the efficiency of retrofitting processes.

Chapter 4

Calibration process

Chapter 4 presents benchmarking and calibration processes of numerical schemes and modeling assumptions for the test-case.

Chapter 4 is based on Reis et al. 2018 [21].

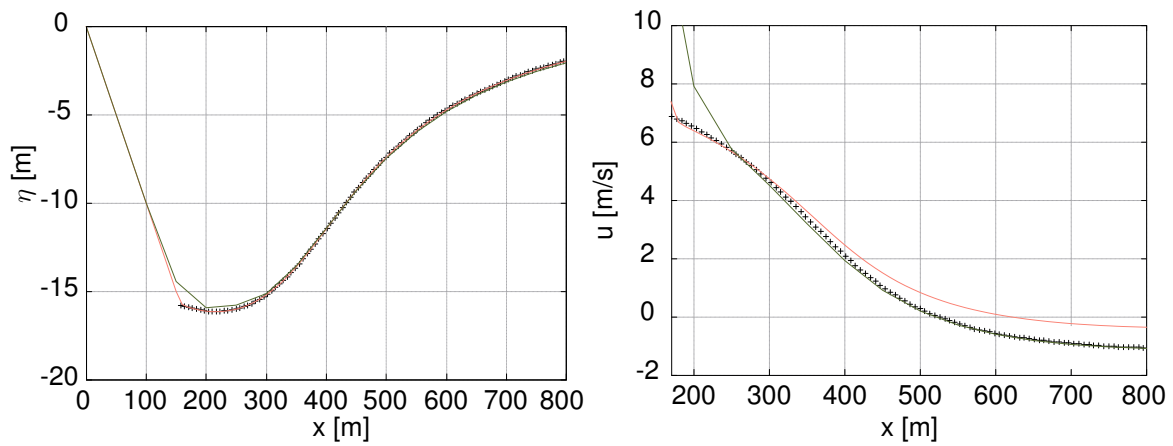
4.1 SW-FV numerical scheme

The performance of the SW-FV tool has been validated through an exhaustive benchmarking process, composed of verification (mass conservation, stability and convergence) and validation tests using data from different provenience, including analytic, experimental and recorded data [19, 21, 383]. For the sake of conciseness and avoiding redundancy with Reis et al., 2018 [21], two representative cases of the tests battery were selected to demonstrate the performance of the tool. The numerical solutions of a 1D solitary wave propagation over a sloping beach and 2D train of waves from the Tohoku-Oki, 2011 event were correlated with analytical and instrumentally-recorded data, respectively.

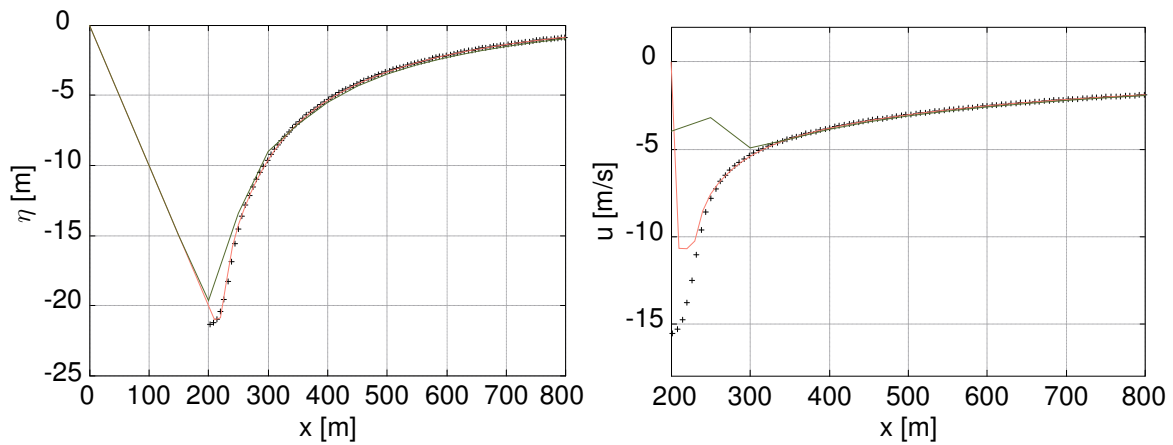
4.1.1 Analytical benchmark: solitary wave on a sloping beach

The 1-D analytical benchmark represents the propagation of a solitary wave over a constant-slope beach [384, 385]. The initial conditions include the initial profile of a leading-depression N wave and null velocity. The beach conditions encompass a 1/10-constant slope along $x = [-200\text{ m}, 49800\text{ m}]$ domain, with initial shoreline position at $x = 0\text{ m}$ (dry-wet interface).

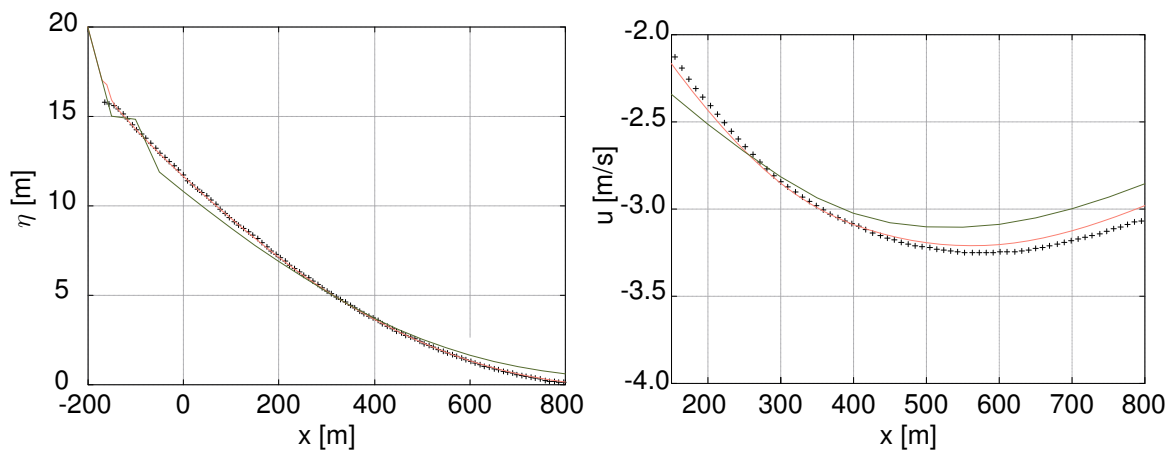
The numerical solutions of η and u were computed using MUSCL (*minmod* and *vanLeer* limiters) and MOOD limiting techniques for $t = 160\text{ s}$ (Fig. 4.1(a)), $t = 175\text{ s}$ (Fig. 4.1(b)) and $t = 220\text{ s}$ (Fig. 4.1(c)). The convergence of the numerical solutions was investigated over five uniform meshes with $\Delta x = 50\text{ m}$, $\Delta x = 20\text{ m}$, $\Delta x = 10\text{ m}$ and $\Delta x = 5\text{ m}$ discretization. Fig. 4.1 depicts a representative correlation between exact and numerical solutions using MUSCL *vanLeer* technique and adopting coarser and finer mesh discretizations, 50 cm and 5 cm , respectively.



(a) Free surface elevation (left) and flow velocity (right) at $t = 160 s$.



(b) Free surface elevation (left) and flow velocity (right) at $t = 175 s$.



(c) Free surface elevation (left) and flow velocity (right) at $t = 220 s$

KEY: + Exact solution — $\Delta x=0.05m$ — $\Delta x=0.50m$

Figure 4.1: Validation of Eulerian SW-FV scheme: propagation of a solitary wave over a sloping beach. Correlation between exact and numerical solutions.

Although the code better performance predicting the free-surface elevation, the convergence of the solutions was also verified for the solutions of flow velocity. The numerical solutions from simulations using the MOOD technique presented the more accurate results, followed by the MUSCL limiter with *vanLeer* limiter technique. The MUSCL with *minmod* limiter represents the third best-solution in terms of accuracy, yet the technique confers the higher robustness to the code.

4.1.2 Field benchmark: Tohoku-Oki, 2011

The SW-FV tool described in Section 3.2.2 was tested to reproduce the Tohoku-Oki, Japan, 2011 tsunami propagation. Fig. 4.2 depicts the arrival of the Japan, 2011 tsunami at two representative locations. One corresponds to the location of a DART buoy, 500 Km far from the epicentre, 650 Km from the coast and 6 Km-deep ocean (DART21418), while the other corresponds to the location of a coastal GPS buoy (GPS806), about 20 Km from the shoreline, implemented in a 100 m-shallow area.

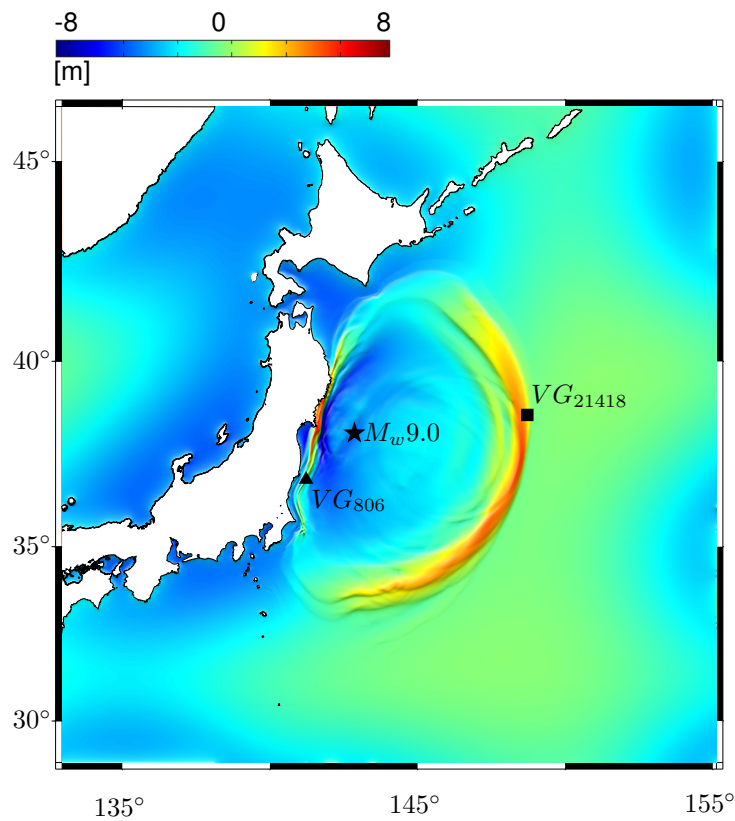


Figure 4.2: Validation of Eulerian SW-FV scheme: Tohoku-Oki, 2011 tsunami propagation at $t = 1800 s$. Location of the virtual gauges, VG , adopted to perform a numerical convergence analysis, which correspond to deep-ocean DART21418 and coastal GPS806 buoys.

The initial condition of the simulation was selected from various source rupture parameters proposed after the event [21], which had their vertical co-seismic deformation, with homogeneous and heterogeneous slip distribution, calculated using Mirone software [386]. The solutions of tsunami propagation induced by the different seafloor vertical displacements were computed with SW-FV tool using a coarse grid of 1500 m. Then, the solutions were compared with records from deep-ocean DART and a near-shore GPS buoys, showing that the rupture proposed by Fujii et al. 2011 [319] lead to more

promising fittings than the remaining initial conditions.

Thus, the 2-D propagation of the Tohoku-Oki tsunami event was calculated using the aforementioned initial deformation on the SW-FV code equipped with the techniques MUSCL, with the *minmod* and van Leer limiters, and MOOD. A transmission condition was prescribed on the outward limit of the computational domain. Considering the duration of the event, the physical time of the numerical simulation was set to $t_f = 9200\text{ s}$ to include the first tsunami manifestation acquired by the different oceanic instrumentation.

The numerical convergence was studied at the two representative locations identified in Fig. 4.2. The uniformly-space grids used to assess the numerical convergence had $\Delta x = \Delta y = 1500\text{ m}$, $\Delta x = \Delta y = 700\text{ m}$ and $\Delta x = \Delta y = 450\text{ m}$ resolution. The 1500 m and 700 m spaced grids were obtained from the GEBCO site (<https://www.gebco.net/>). To create the 450 m -spaced grid, the GEBCO data was complemented with data provided by the Japan Oceanographic Data Center. The numerical simulations were carried out using the different MUSCL and MOOD techniques. Fig. 4.3 depicts the qualitative convergence analysis of the numerical solutions using different grid resolutions at open ocean and coastal locations.

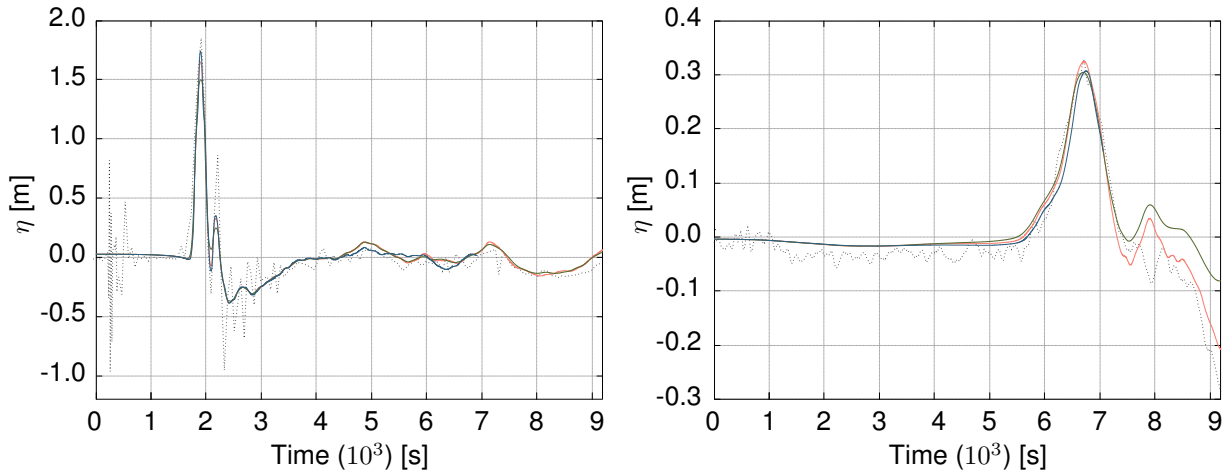
The convergence analysis showed that the comparison of solutions calculated from 700 m and 1500 m grids represent a more evident improvement than the comparison observed on solutions calculated from 700 m and 450 m grids due to the 450 m grid construction using data from a different data source, while 1500 m - and 700 m -grids shared a common GEBCO database.

Adopting $\Delta x = \Delta y = 700\text{ m}$, the free-surface elevation was then calculated for the various virtual positions corresponding to instrumented locations represented in Fig. A.1, Annex A. The numerical simulations were computed adopting MUSCL and MOOD techniques to assess their influence in the quality of the numerical solutions. Fig. 4.4 shows the comparison between instrumentally-recorded data and numerical solutions assessed at DART21418 and GPS806. The entire range of correlations performed for the other eleven locations is presented in Annex A.

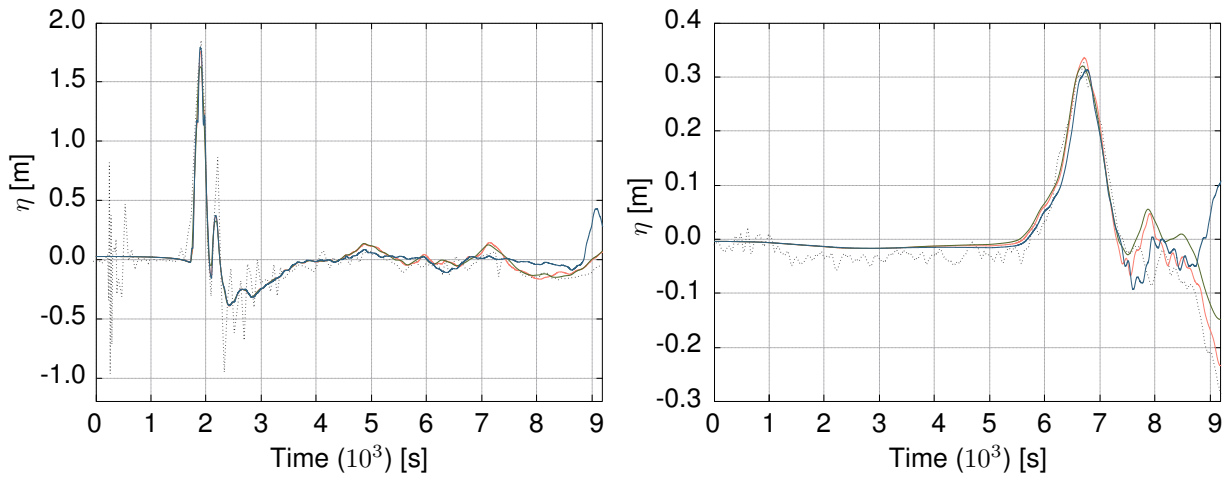
The first corresponds to the location of a DART buoy, 500 Km far from the epicentre, 650 Km from the coast and 6 Km -deep ocean (DART21418), measuring η quantities up to 2 m . The second corresponds to the location of a coastal GPS buoy (GPS806), about 20 Km from the shoreline, implemented in a 100 m -shallow area, which recorded a 0.30 m -wave arrival, after being subjected to a series of reflection and refraction phenomena due to topo-bathymetric influences (oceanic floor and coastal morphology geometries).

In general, the numerical results reproduce the recorded measures and waveforms, for both far- and near-field gauges. Since convergence and parametric studies considering the different techniques and limiters were performed, the observable discrepancies between recorded data and numerical solutions were mostly associated to the initial condition prescribed to the SW-FV system and the resolution of the topo-bathymetric data over which the simulations were carried out. Another possible influencing factor is the lack of the dispersion effect in the shallow-water model.

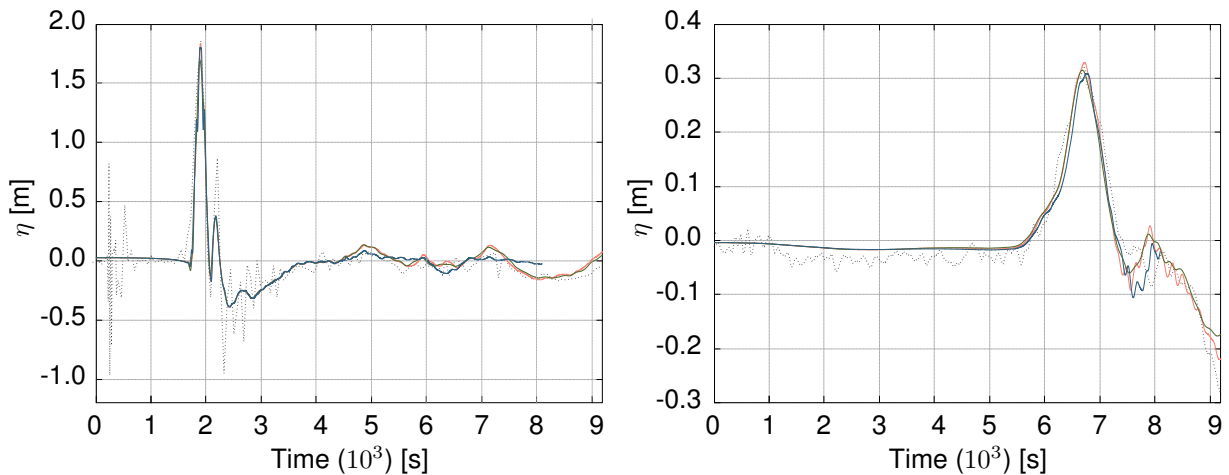
Relatively to the numerical scheme, the MOOD simulations presented the best performance, eight out of the thirteen fitting estimates achieve errors below 10%. Yet, the less diffusive MOOD technique



(a) Correlation between instrumentally recorded data and numerical solutions computed with MUSCL *minmod* technique over various resolution grids for deep-ocean (left) and coastal (right) locations.



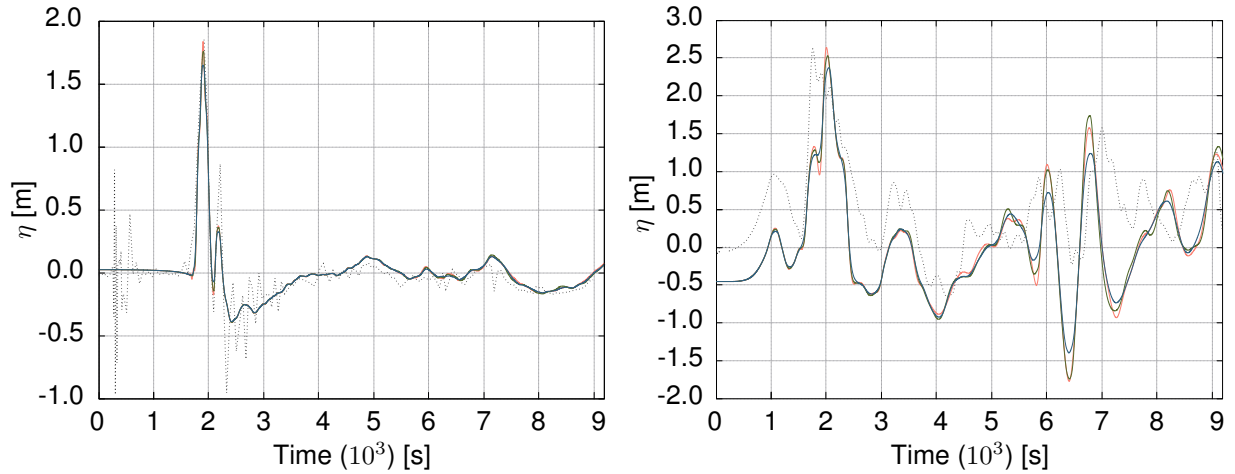
(b) Correlation between instrumentally recorded data and numerical solutions computed with MUSCL *van Leer* technique over various resolution grids for deep-ocean (left) and coastal (right) locations.



(c) Correlation between instrumentally recorded data and numerical solutions computed with MOOD technique over various resolution grids for deep-ocean (left) and coastal (right) locations.

KEY: Recorded — $\Delta x, y = 700 m$ — $\Delta x, y = 1500 m$ — $\Delta x, y = 450 m$

Figure 4.3: Validation of Eulerian SW-FV scheme: convergence analysis of $\Delta_{x,y} = 1500 m$, $700 m$ and $450 m$ resolution grids, using MUSCL, *minmod* and *vanLeer*, and MOOD techniques, to assess time series of η at deep-ocean and coastal locations.



(a) Left: oceanic DART21418 record and VG_{21413} solution. Right: coastal GPS806 Fukushima record and VG_{806} solution.

Figure 4.4: Validation of Eulerian SW-FV scheme: correlation between recorded and numerical data using MUSCL, *minmod* and *vanLeer*, and MOOD techniques.

tends to amplify the uncertainties of the parameters in opposition with the solutions obtained with the more diffusive MUSCL technique, which may lead to overestimates of η . The *vanLeer* limiter represents the second-best performance while the MUSCL equipped with the *minmod* limiter represents the more robust scheme, conversely to MOOD.

4.1.3 SW-FV Remarks

In general, the validation of the SW-FV tool, with resolution up to second-order, hydrostatic reconstruction, well-balanced property and two high-order numerical techniques, MUSCL and MOOD, shows a good performance. The results show that the MUSCL limiters influence the numerical solution. The *minmod* limiter provides robustness to the solution, the *vanLeer* limiter achieves increased accuracy, but the MOOD technique gives the solution with better quality in terms of accuracy. The source model and the topo-bathymetric data play an essential role in the quality of the numerical solution. The source modeling variables were associated with influencing factors of the tsunami propagation in deep-ocean, while solutions near the shore showed additional sensitivity to the resolution of the topo-bathymetric mesh.

4.2 NS-SPH numerical scheme

The NS-SPH scheme implemented in DualSPHysics code has been gaining popularity among various fields of investigation, such as coastal engineering. Over the last decade, the code has been adapted to tackle a wider range of physical phenomena. To model tsunami-like waves and tsunami interaction with coastal infrastructures, complementary algorithms have been added to the original numerical scheme. The benchmarking of NS-SPH tool was oriented to study some algorithms applicable to coastal engineering problems (and the case-test in particular), including boundary

conditions, solid-fluid and fluid-fluid interactions.

4.2.1 Moving boundary condition

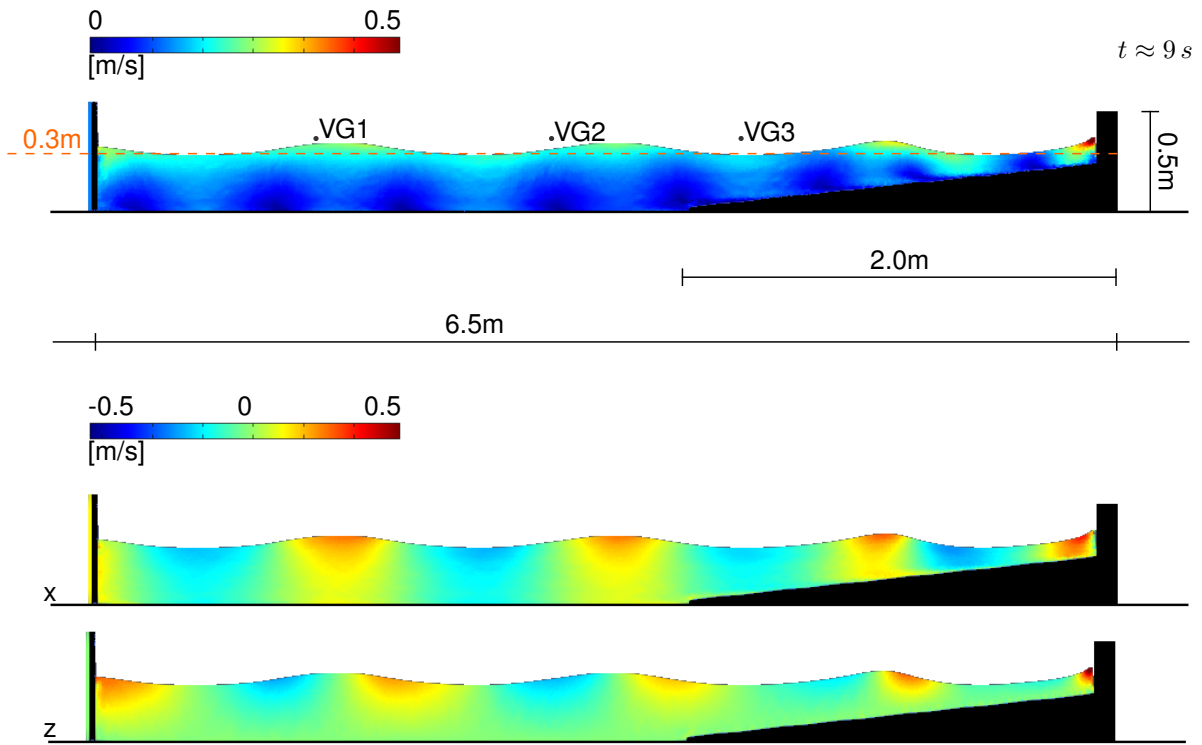
DualSPHysics allows to generate theoretical regular and irregular waves or other types of waves, such as tsunami-like waves, using a piston-type wave-maker. The type of wave is generated by varying the level of the fluid at rest and introducing the horizontal displacements of the piston. The feature is particularly interesting to model waves generated in physical facilities to carry out experimental simulations, typically involving tanks and singular or articulated paddles.

An experimental case developed at Universitat Politècnica de Catalunya [247] was considered to test the numerical modeling of moving boundary conditions. The physical experiment consists of a train of waves generated by the horizontal motion of a piston wave-maker propagating over a 4.5 m-flat and 2.0 m-sloping bottom of a 7.0 m-long tank with 1.0 m of height. A vertical wall of 0.5 m of height was implemented at the end of the 1 : 8.5 sloping section of the tank. Fig. 4.5(a) depicts the general configuration of the experimental setup.

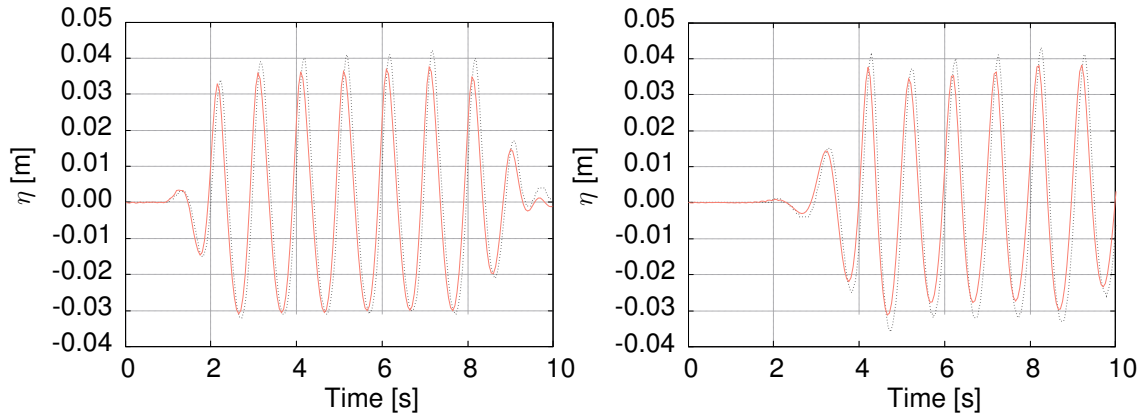
The objective of the case study is to reproduce the wave free-surface elevation measured at three different locations ($x = 0.38\text{ m}$, $x = 1.83\text{ m}$ and $x = 3.12\text{ m}$) and characterize the force exerted on the frontal surface of the vertical wall. Numerically, the initial conditions of the system were prescribed using external data containing the horizontal displacement of the piston, which follows a 10 s-long sinusoidal function, period of 1 s, varying between -0.025 m and 0.025 m . The time of the numerical simulation was set to $t_f = 11.5\text{ s}$, adopting an initial inter-particle distance of $\Delta p = 0.005\text{ m}$. Fig. 4.5 depicts the numerical solutions of horizontal and vertical flow velocity at representative $t = 9\text{ s}$, correlation between the free surface elevations instrumentally recorded and the numerical solutions, and forces numerically estimated at the frontal surface of the wall.

Despite a slight underestimation of the water free surface and compression of the wave, the correlation between recorded data and numerical solutions showed a high performance of the NS-SPH scheme assessing hydrostatic quantities. The lack of experimental measures of flow velocity conditioned the evaluation of the numerical performance assessing hydrodynamic quantities. Nonetheless, the numerical flow velocity induced by a piston-type wave-maker estimated by Altomare et al., 2017 [387] was validated against theoretical second-order Stokes waves showing a good agreement for regular and irregular waves, but also demonstrated that adding a damping parameter to model the active wave absorption constitutes an improvement to reflection coefficient estimates (the ratio between the amplitude of the reflected wave and the amplitude of the incident wave).

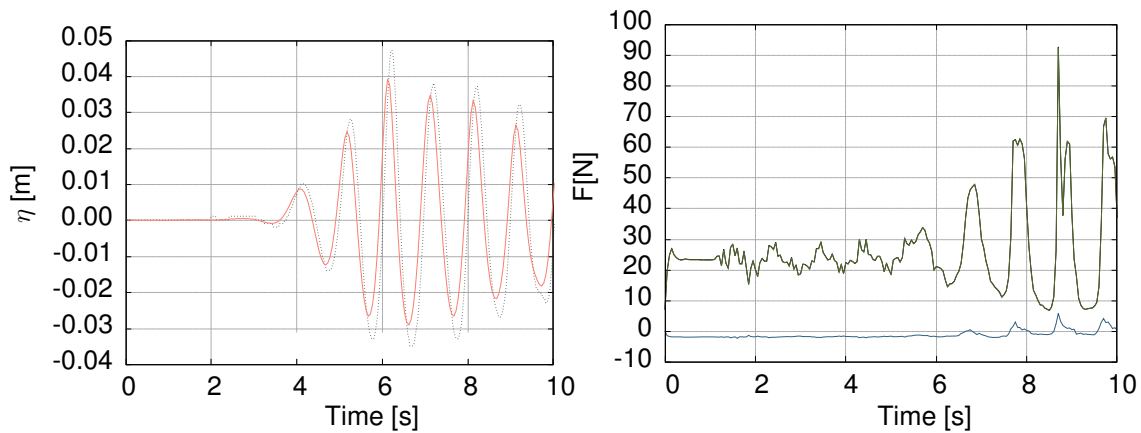
The force built-in assessment based on simple summations of the product between the mass and acceleration of the neighbouring particles of a solid (derivative of relative position and velocity), was capable to characterize both normal and tangential components of fluid forces, i.e. pressure and the frictional stress, respectively.



(a) Dimensions of the 2D domain and magnitude of flow velocity. Vectorial flow velocity in both horizontal and vertical directions.



(b) Correlation between wave gauge record and numerical solution of free surface elevation at VG1, $x = 0.38\text{ m}$ (left) and VG2, $x = 1.83\text{ m}$ (right).



(c) Correlation between wave gauge record and numerical solution of free surface elevation at VG3, $x = 3.12\text{ m}$ (left). Normal and tangential forces exerted on the front of the vertical wall (right).

KEY:Recorded — Numerical — Normal force — Tangential force

Figure 4.5: Validation of Lagrangian NS-SPH scheme: piston-generated train of waves propagating over a flat and sloping bottom and impacting a vertical wall.

4.2.2 Open boundary condition

The inlet-outlet simultaneously represent a relatively simple form of controlling computational costs inherent to NS-SPH simulations and a versatile approach suitable to model various engineering applications, involving the capabilities of enforcing unsteady velocity and pressure profiles and/or pressure and velocity gradients along a given direction, prescribe variable free-surface elevation of flow entering and exiting the computational domain and generate common engineering shapes buffer geometries. The feature is particularly interesting to model large domains, such as coastal engineering problems, reducing cost computation demand and becoming accessible to local computing clusters while maintaining the level of detail of the numerical solutions.

The setup represented in Fig. 4.5(a), was adopted to test the prescription of an open boundary condition at VG1 ($x = 0.38\text{ m}$) location. The hydrodynamic quantities adopted to prescribe the OBC were assessed in Section 4.2.1. Fig. 4.6 depicts the correlations between recorded data and computed solutions of free surface elevation at locations VG2 ($x = 1.83\text{ m}$) and VG3 ($x = 3.12\text{ m}$) using two initial conditions. The first corresponds to a moving boundary condition and full model of the domain while the second reduces the domain to a partial geometry and was initiated by hydrodynamic quantities imposed at ghost particles adopting hydrodynamic quantities from the full model captured at VG1 ($x = 0.38\text{ m}$).

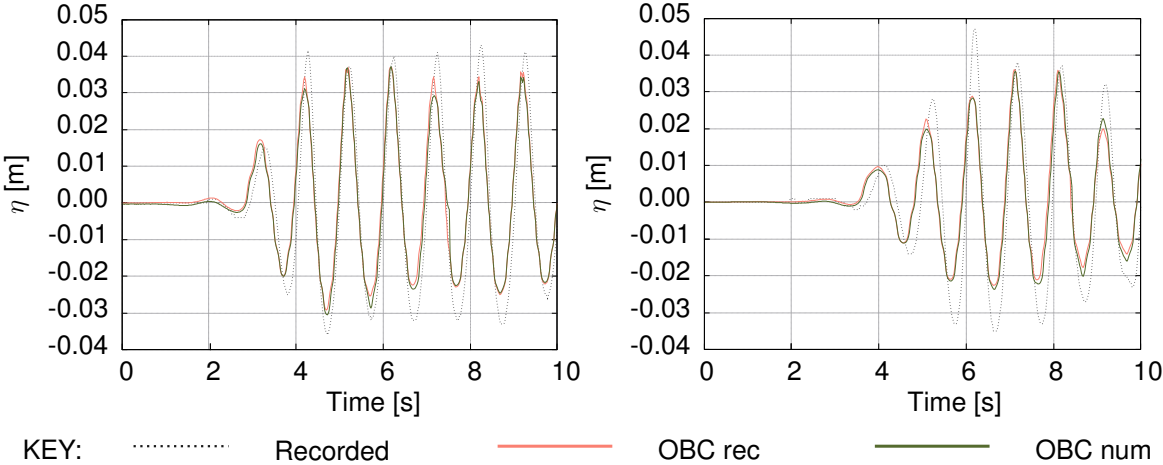


Figure 4.6: Validation of Lagrangian NS-SPH scheme: inlet zone prescribed at VG1 $x = 0.38\text{ m}$ using hydrodynamic quantities from full domain simulation. Correlation between wave gauge record and numerical solution of free surface elevation at VG2, $x = 1.83\text{ m}$ (left) and VG3, $x = 3.12\text{ m}$ (right) computed with OBC and DBC.

The correlation of different initial conditions adopted to initiate the simulations allowed to assess the influence of using a boundary condition in the quality of the solutions and quantify the potential computational optimization for larger models. Regarding the quality of the solutions, the slight underestimation of the water free surface verified in Section 4.2.1 was amplified by imposing an OBC, showing that the physical quantities used to establish the boundary conditions and the number of Dirichlet conditions modeling the domain of the problem influence the quality of the solution. The numerical solution using laboratorial recordings of free-surface elevation and numerically assessed flow velocity to impose the OBC provided better predictions of free-surface elevation on the subsequent points of virtual acquisition. The latter numerical solution also presented better predictions than the

solution composed of two boundary conditions (piston initiation, data acquisition and OBC prescription at VG1 using numerically assessed flow hydraulic quantities, flow height and velocity).

Regarding the computational cost, lacks expression due to minimal differences in terms of geometry (reduction of 5.8% of the full domain) and number of initial particles discretizing the 2D model, 53777 for full domain and 53337 for partial domain. For this benchmarking case, the run-time per physical second was in fact higher for the partial domain (52.42 s) than for the full domain (44.77 s) due to the generation of new particles in the inlet zone, which lead to a total of 61730 particles in the end of the simulation.

4.2.3 Multi-phase

Recently, DualSPHysics includes an algorithm to simultaneously account multiple fluids, such as air-water interactions. The feature is particularly interesting when modeling mixing and violent free-surface hydrodynamic interactions.

A dam breaking is a well-known benchmark for demonstrating the robustness of many SPH schemes and testing its suitability to impulsively-started, rapidly-evolving free-surface flows. Based on an experiment performed at the Maritime Research Institute Netherlands [388], a 3D numerical setup of an obstacle being impacted by a wave generated by a dam breaking was assembled to investigate the influence of single- and multi-phase algorithms on the quality of the free-surface elevation estimates.

On the experiment, the dam break effect was physically reproduced by a lock gate with instantaneous movement holding a quiescent volume of water that was then released into the tank. The length, width and height dimensions the experiment were respectively $3.22\text{ m} \times 1\text{ m} \times 1\text{ m}$ for the tank, $1.22\text{ m} \times 1\text{ m} \times 0.55\text{ m}$ for the volume of water and $0.16\text{ m} \times 0.40\text{ m} \times 0.16\text{ m}$ for the solid obstacle. Wave gauges were located in the middle of y -direction at H1: $x = 0.56\text{ m}$ (reservoir) and H2: $x = 2.22\text{ m}$ (tank), while pressure gauges were implemented in the middle frontal and top surfaces of the solid obstacle. Fig. 4.7 represents the geometry of the setup and the positions of the wave-gauges.

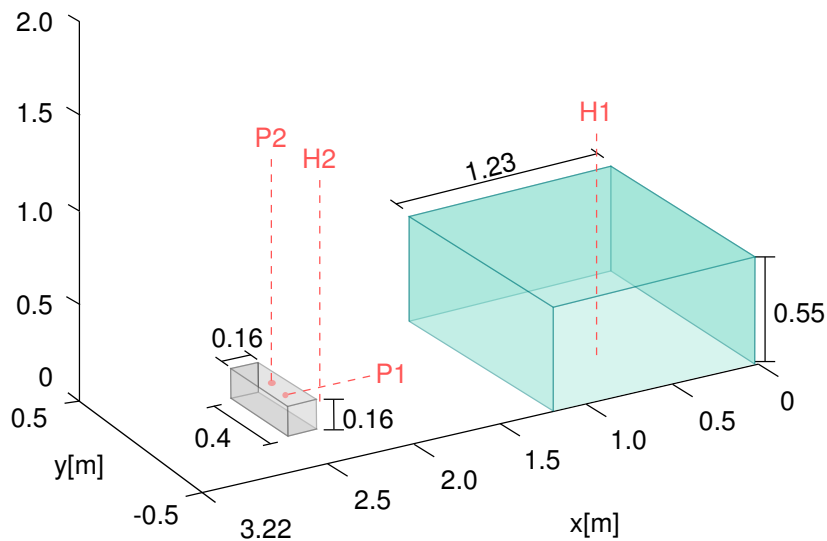


Figure 4.7: Validation of Lagrangian NS-SPH scheme: geometry of the experimental and instrumental setup. Location of wave-gauges (H) and pressure-gauges (P). Unit: meter.

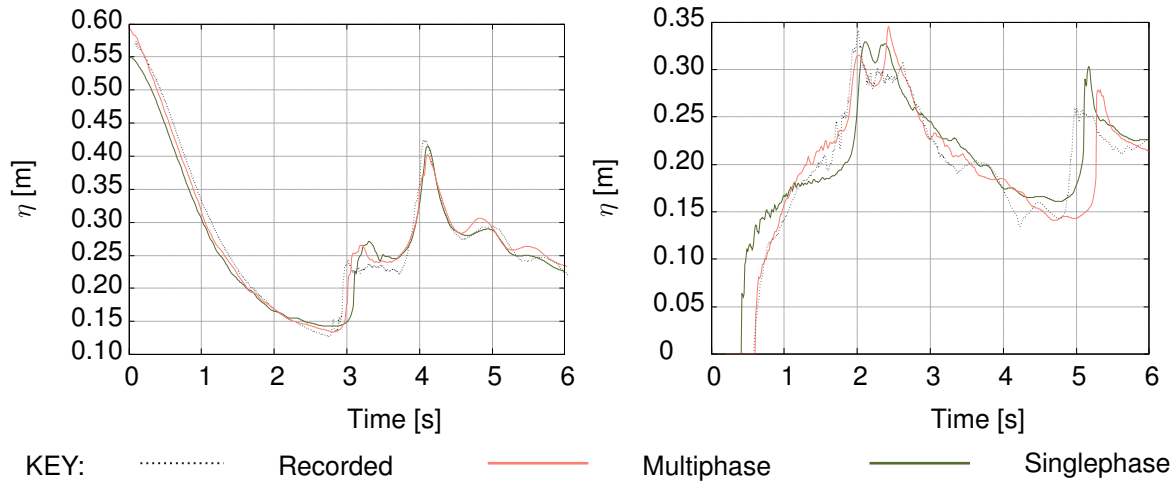


Figure 4.8: Validation of Lagrangian NS-SPH scheme: correlation between instrumentally-recorded wave heights and corresponding numerical solutions computed at H1 (left) and H2 (right) using single and multiphase models.

The corresponding numerical setup was modeled to mimic the experiment, except for the tank definition. Instead of a 1 m open roof tank, the model adopts a 2 m-height tank and a zero normal pressure gradient imposed on the top boundary. The material properties for liquid-gas flows considered density of the water $\rho_{water} = 1000 \text{ kg/m}^3$, polytropic constant $\gamma = 7$, speed of sound $c = 30 \text{ m/s}$, for the water, and $\rho_{air} = 1/800\rho_{water}$, polytropic constant $\gamma = 1.4$, speed of sound $c = 200 \text{ m/s}$, for the air. The model was discretized using $\Delta p = 0.02 \text{ m}$ and the simulation time was set to 6 s. Fig. 4.8 depicts the correlation between recorded and computed data, using single- and multiphase algorithm.

The solutions using multiphase fluid-gas showed a slightly improved fitting between the recorded and numerical solutions of free-surface elevation, more evident in H2 position closer to the obstacle. However, the run-time of single- and multiphase simulations was quite different. Using the same GPU GeForce RTX 2060 and Δp , the simulation of single-phased model including 145093 particles was about 225 s, while the computation of the multiphase simulation including 460472 particles took 43914 s.

4.2.4 Modified dynamic boundary condition

Despite the dynamic boundary condition being accepted as an adequate approach to model coastal engineering problems due to its capability of discretizing complex 3D geometries without the need of implementing complex mirroring techniques or semi-analytical wall boundary conditions, recent works [329] drawn attention for its over dissipation, finding difficult to preserve steady-states, and failing to capture the condition for low resolutions leading to higher than expected velocities close to the boundary and throughout the flow. Recently, a modified moving boundary condition was implemented in DualSPHysics, which was found to be more accurate than using the zero-velocity approach of the original dynamic boundary condition [329]. However, the technique requires the use of ghost nodes between the boundary interface and, consequently, represents additional computational costs. The feature was indicated as particularly interesting to characterize time-series of pressure/forces exerted against obstacles. The numerical setup presented in Section 4.2.3 was re-modeled to a single-phase

problem ($\Delta p = 0.01 m$) and re-computed using classic and modified dynamic boundary conditions. Fig. 4.9 presents the correlation between experimental data and numerical solutions of normal and tangential pressures at P1 ($x = 2.389 m, y = 0 m, z = 0.025 m$) and P2 ($x = 2.487 m, y = 0 m, z = 0.165 m$).

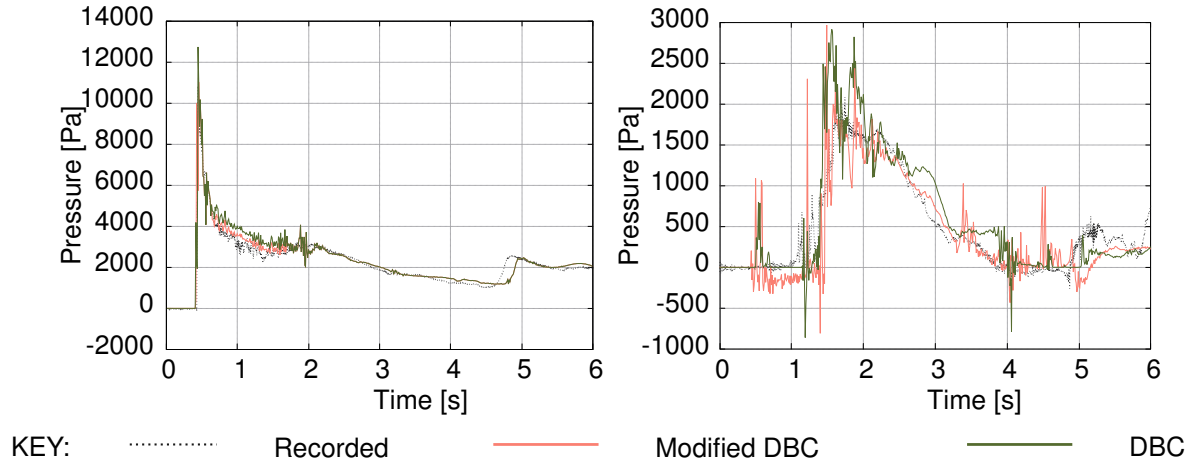


Figure 4.9: Validation of Lagrangian NS-SPH scheme: correlation between instrumentally-recorded pressure and corresponding numerical solutions computed at P1 (left) and P2 (right) using classic and modified boundary conditions models.

The solutions obtained with classic and modified dynamic boundary conditions showed relatively identical solutions of pressure assessed in the frontal surface of the obstacle, yet presenting a better fitting of the solution calculated using the modified version of the dynamic boundary condition between $t = 0.5 s$ and $t = 2 s$, which corresponds to fluid impact and transition to steady-state. The pressure assessment on the top surface of the obstacle was probably influenced an insufficient Δp , leading to the generation of spikes along the virtual acquisition of the time-series. Despite lacking a clear evidence of advantages using the modified version of the dynamic boundary condition, the solution presented slightly better fitting with the recorded data than the solution obtained using the classic dynamic boundary condition.

In face of the correlation, the run-times using the same GPU GeForce RTX 2060, Δp and number of particles, were about $2510 s$ for the model with dynamic boundary condition and $3014 s$ for the model with modified dynamic boundary condition.

4.2.5 NS-SPH Remarks

In general, NS-SPH was capable of reproducing complex hydraulic phenomena. Yet, the convergence of the solutions was sensitive to physical and numerical parameters used during the modeling process, requiring complementary algorithms to guarantee convergence, stability and accuracy of the numerical solutions, such as particles rearrangement towards an uniform distribution and multiphase interaction of fluids to adapt the particles behavior to the physics they aim to model. The computational costs and low convergence rates still constitute drawbacks of the SPH method when compared to less demanding mesh-based methods.

Although the case-sensitive nature of NS-SPH scheme inhibits the development of general

modeling guidelines, the evaluation of the influence played by complementary algorithms, such as dynamic- and open-boundary conditions, particles shifting and the multiphase interface, was investigated. In general, multi-directional and multi-dimensional models allowed to characterize free-surface, normal and tangential components of pressures and forces being exerted on solids. Such capacities are of particular interest reproducing natural hydraulic phenomena and their effects on coastal structures. Moreover, coupling techniques, such as inlet-outlet buffer zones prescribed by open boundary conditions composed of ghost particles, demonstrated to constitute a suitable approach to reduce NS-SPH numerical domains strictly to highly non-linear regions, helping transpose the computational costs challenge. Conversely to other boundary conditions, the buffer zones in the open boundaries accept physical information from linear and non-linear wave theories, external numerical models such as CFD models, or even measurement data. Nonetheless, it is important to underline that the additional modeling effort to prescribe the OBC in order to reduce the computational demand is only efficient when the sum of initial and new generated particles at the buffer zone of a partial-domain model exceeds the number of particles of the full-domain model.

Similarly, a careful analysis considering the use of single- or multiphase is deemed necessary to assess the trade-offs among the level of required accuracy, the modeling challenge and the associated computational costs. For example, the comparison between single and multiphase cases presented in Section 4.2.3 respectively showed 10 steps per second *versus* 200 steps per second, while the run-time of the simulations were increased by an order of 100, requiring 12.5 MB CPU and 24.5 MB GPU *versus* 39.6 MB CPU and 67.3 MB GPU memory, and storage of 2.6 GB *versus* 20.3 GB.

Another analysis regarding classical and modified dynamic boundary conditions showed a slight improvement on the pressure characterization using the modified version, that helped remove some of the pressure noise at the boundary and allowed to obtain less spikes in the time-series of pressure being exerted against the obstacle. The computational costs of acquiring solutions using classical or modified dynamic boundary conditions represent a difference of about 20% in run-times.

4.3 GMPE models

Commonly, the location and importance of the infrastructures dictates the required level of structural performance under seismic action. Function of static or dynamic structural analyses, the characterization of the ground motion data varies between discrete peak values or time-histories of seismic quantities, inferred from probabilistic or deterministic approaches, targeting regions, sites or the infrastructure itself.

The 2011, Tohoku-Oki, Japan earthquake was the most recorded event in history. Data recorded from the Japanese seismic network were considered to perform a brief validation of the open-source tools characterizing seismic actions. OpenQuake [352] was one of the elected tools to determine the distribution of peak ground accelerations, and EXSIM [353] was the complementary tool to characterize time-histories of acceleration. The validation was performed for two location of the 1225 records acquired from K-NET (three data channels that correspond to three components of a seismograph) and Kik-net (six data channel where the first three correspond to three components of a borehole seismograph and

the other three correspond to those of a surface seismograph), which are available at <https://www.kyoshin.bosai.go.jp/>. The hypo-centre of the Mw9.1 earthquake was identified off the Sanriku coast, northeast Japan, at geographical coordinates 38.1035°N in latitude and 142.861°W , and about 15 m in depth. Multiple finite-fault models were proposed by different authors for the rupture of the reverse fault type with WNW-ESE compressional axis that triggered the 2011 Tohoku-Oki earthquake. They used inversion techniques to infer the co-seismic slip distribution from seismic data [389], GPS data [390], tsunami data [319], or a combination of different types of data [391]. Most models proposed heterogeneous co-seismic slip distributions varying between 40 m around the epicentre to values under 1 m in the edges of the $400\text{ Km} \times 200\text{ Km}$ fault, including the Japan Meteorological Agency and the United States Geological Survey. Moreover, the relatively long time separating similar peak amplitudes on near-field accelerograms were alternatively associated to the rupture of two close sources [392]. Considering the uncertainties associated with the source parameters, and for the sake of simplicity, a homogeneous and random slip distribution was herein assumed to model geometry and rupture of a single fault.

4.3.1 Ground motion fields of PGA

The source modeling assumed a single planar rupture with middle top surface aligned with the hypocenter. The fault parameters include a $400\text{ Km} \times 200\text{ Km}$ rupture geometry, with $\Theta = 20^{\circ}$, $\varphi = 30^{\circ}$ and $\delta = 18^{\circ}$. The 5 m -resolution grids were defined between longitude 130°W and 150°W , and latitude between 28°N and 43°N . The propagation of the seismic waves was modeled using several attenuation laws developed for the Japanese territory [393–396]. For the benchmarking process, the solution obtained with the GMPE model proposed by Abrahamson et al., 2014 [394] was adopted. The site geotechnical conditions assumed a rigid soil, with $V_{s,30} = 760\text{ m/s}$. The GMPE model was set to calculate the distribution of PGA along the Northeast coast of Japan due to the Mw9.0 2011, Tohoku-Oki earthquake. Fig. 4.10 depicts the correlation between the map of PGA recorded by the seismic network covering the Japanese territory and the synthetic map of PGA obtained from the aforementioned GMPE model. The PGA values estimated at IWT023 - Kamaishi station, Iwate prefecture, and IBRH17 - Kasumigaura station, Ibaraki prefecture, were also verified against recorded data.

From a qualitative perspective, the maps of PGA distribution in the Northeast regions of the Japanese territory demonstrated a general agreement between recorded and numerical data. The seismographs of the Japanese networks recorded the higher PGA values at Iwate, Miyagi, Fukushima and Ibaraki prefectures, from Northeast to Southwest direction. The simulations show a similar PGA distribution at the corresponding locations, maintaining a similar pattern of attenuation. Qualitatively, the range of values numerically obtained were comparatively smaller than the range of values recorded by some of the Miyagi and Ibaraki stations (represented in dark-red in Fig. 4.10). After analysis, was verified that the abrupt peaks recorded by these stations were underestimated probably due to the homogeneous characterization of the site conditions and/or attenuation law and site conditions adopted in the GMPE

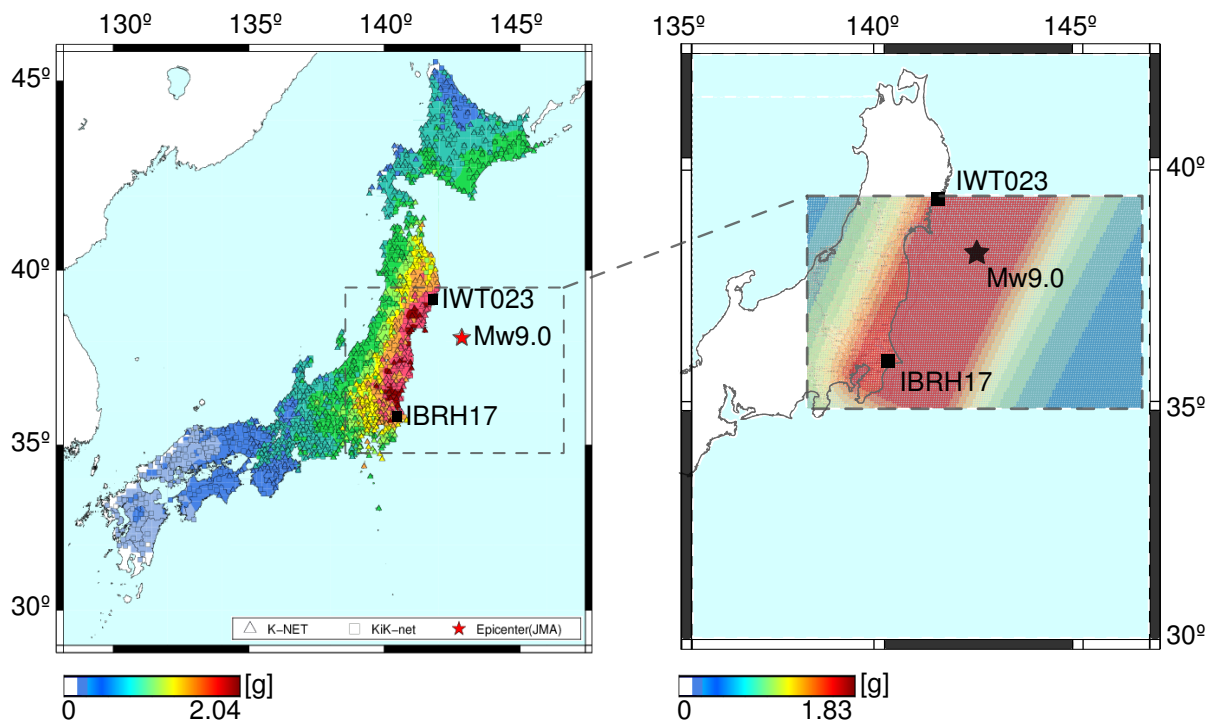


Figure 4.10: Validation of the peak acceleration: correlation between maps of peak accelerations assembled from the records of the Japan strong motion seismograph networks during the Japan, 2011 earthquake (left), and from synthetic data generated using OpenQuake software (right).

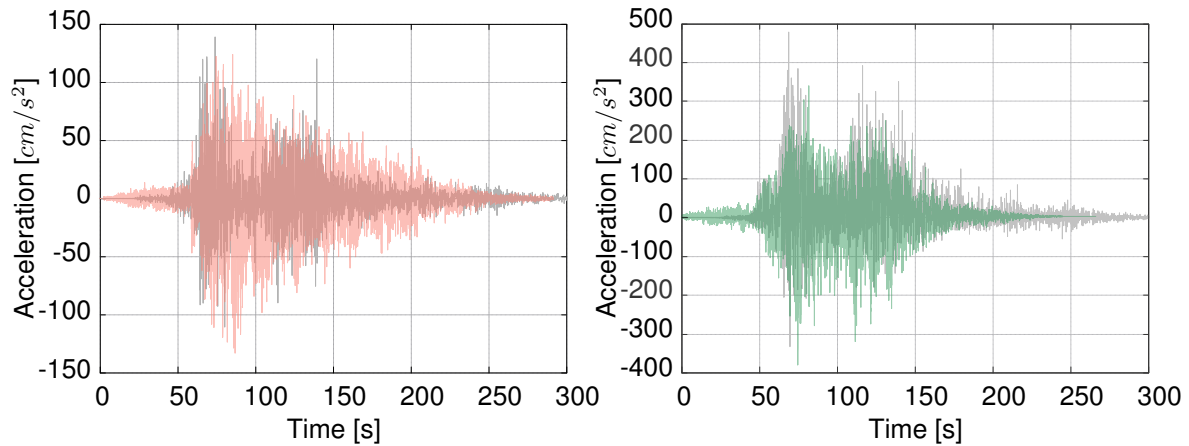
model, leading to a more uniform distribution of PGA in the synthetic map.

The additional verification at locations corresponding to IWT023 and IBRH17 stations were respectively estimated in $0.42 g$ and $0.51 g$, representing a close approximation to the PGA values acquired by the referred stations ($\approx 0.5 g$). Nonetheless, detailed source and site characterizations are likely to lead to more realistic results. Meanwhile, attenuation laws developed for Japan are being updated using records from the Japan 2011 earthquake, contributing for the calibration of the GMPE to forecast extreme events that occur in subduction systems, up to $Mw9.1$ and distances to the fault of less than $300 km$ [397].

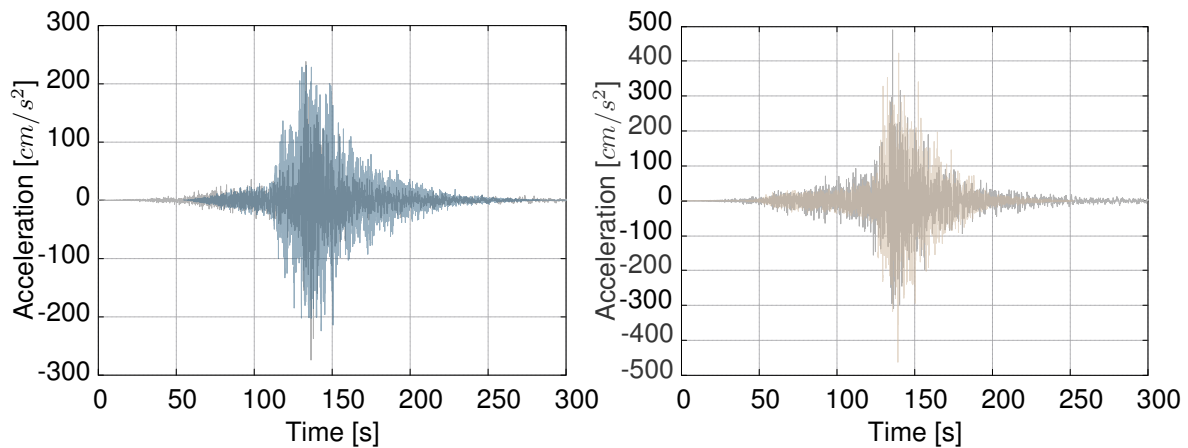
4.3.2 Time-histories of acceleration

The generation of synthetic motions by EXSIM software were correlated with real records from kiK-net seismic network (502 available records), at borehole and surface levels. The mathematical generation of various accelerograms assumed a single-event source rupture, adopting representative values of $400 Km \times 150 Km$ for source geometry, random slip distribution, $15 MPa$ of stress drop, 200° -strike, 18° -dip and $18 Km$ -depth as input parameters for the stochastic simulations [398]. The reference velocity for bedrock level is $760 m/s$, while $k_0 = 0.03 s$. Simulations for two different sites and twenty trials for each case were carried out using attenuation law for the path propagation, with and without site amplification. Fig. 4.11 depicts the correlation between recorded signals at an Iwate prefecture station (IWT023 - Kamaishi, about $150 Km$ distance from the epicenter, which recorded two distinct trains/phases of strong ground motions) and at an Ibaraki prefecture (IBRH17 - Kasumigaura,

about 300 Km distance from the epicenter and indistinct predominance of phases).



(a) Acceleration at Iwate prefecture, Kamaishi station location, at the borehole (left) and surface (right) levels.



(b) Acceleration at Ibaraki prefecture, Kasumigaura station location, at the borehole (left) and surface (right) levels.

KEY: — Recorded — IWT023 Hole — IWT023 Surface — IBRH17 Hole — IBRH17 Surface

Figure 4.11: Validation of the acceleration series: correlation between instrumentally-recorded accelerations and their corresponding synthetically-generated signals, for relatively close (150 Km) and distant (300 Km) locations.

The simulations of the Mw9.1 2011, Tohoku-Oki, Japan earthquake presented a relatively good fitting with the data recorded by the seismic network. However, and despite recent advances of EXSIM, the determination of low frequencies remains a challenging task. For example, a relatively high stress parameter ($\approx 150 MPa$) was adopted to match the high frequencies shown in Fig. 4.11. Nonetheless, in terms of wave arrival time and high frequencies, the generated results depicted in Fig. 4.11 were considered globally satisfactory. Comparatively, the correlation carried out for the IBRH17 station location (about 300 Km from the epicenter) demonstrated a better fitting than the correlation for the closer IWT023 station (about 150 Km away from the epicenter), that was a bi-peak train of phases difficult to reproduce using a single event with homogeneous distribution. In the literature [398], was demonstrated that a source modeling considering a multiple-event with heterogeneous slip distribution was capable to differentiate the two distinctive trains of accelerations. However, the same study assigned the compatibility between recorded and synthetic signals to asperities influencing the radiated waves. Because the distribution of asperities is only known after the event, using generic models of rupture generation or developed from suites of past events was assumed reasonable to develop

dynamic characterizations of site accelerations.

4.3.3 GMPE remarks

The peak and dynamic characterization of seismic acceleration constitutes a reliable approach to predict ground motions at a wider and a target-specific location. The quality of the synthetically-generated data relies on the level of modeling detail and amount of uncertainty along the modeling process of source, path and site components influencing the waveform of the signals. Moreover, GMPE models are case-sensitive, which represents a challenging task modeling high magnitude events in regions with moderate seismic activity. The lack of data from high magnitude events constraints not only the calibration of GMPE, but also the validation of synthetically generated solutions.

4.4 FE and constitutive models

The finite element method is the prevalent and long-term validated technique used over the last decades to perform structural analysis [399, 400]. The fundamental principles in structural analysis are: 1) equilibrium: internal forces or stresses counteracting external loads; 2) constitutive laws: relationship between the stress and strain in the structure members material; 3) compatibility: continuity or consistency conditions on strains and deflections.

4.4.1 Constitutive models

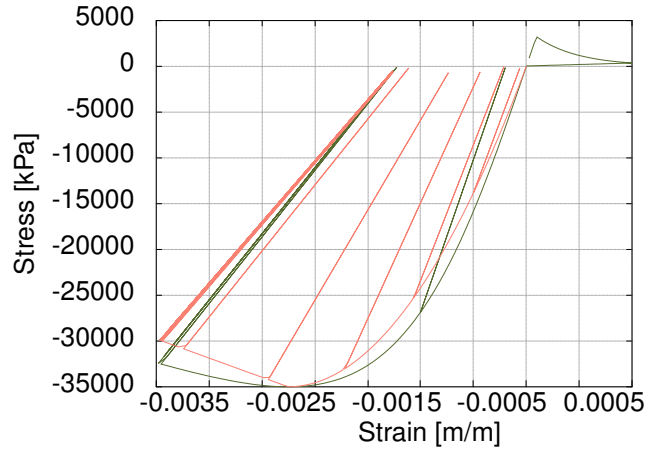
Multiple stress-strain constitutive relationships of concrete, steel and cohesive soils are available on OpenSees library. The following sections present the calibration process of the constitutive relationships adopted to model non-linear behavior of the materials used on the case-test.

Concrete model

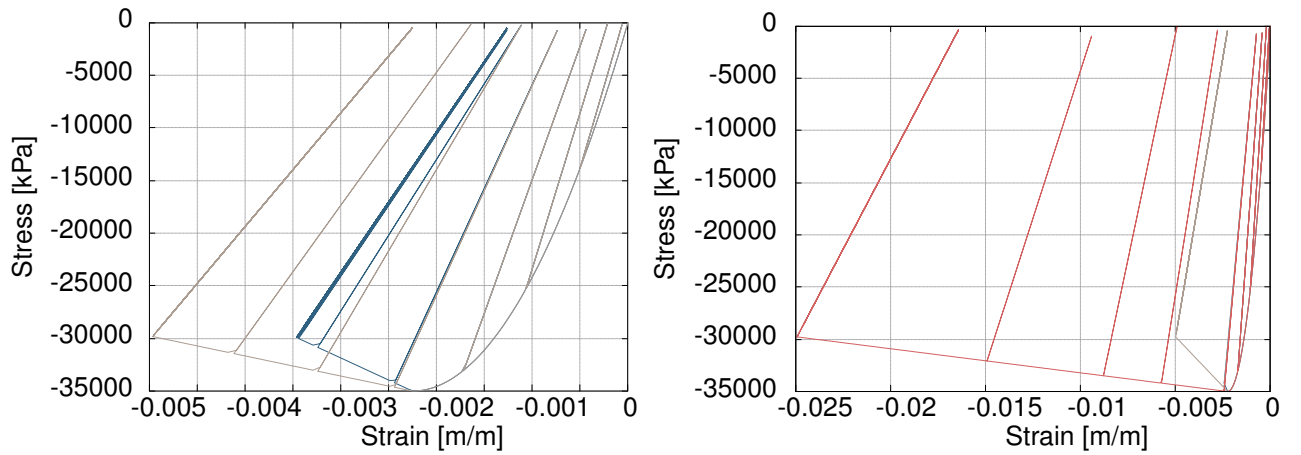
The form of the stress-strain curve was adapted from the experimentally-calibrated model proposed by Popovics [401] and modified by Mander [402]. The constitutive relationship consists of a three-parameter controlled curve encompassing compressive strength, modulus of elasticity and concrete ultimate strain to represent the behavior of an uniaxial concrete material with degraded linear unloading/reloading stiffness and tensile strength with exponential decay, while the simplification introduced by Mander withdrawn tensile strength capacity from concrete response.

Fig. 4.12(a) shows the hysteric behavior of an unconfined C35/45 strength grade concrete (concrete material of the test-case) subjected to a cyclic strain history ranging from 0 to -0.005 in intervals of 0.001. The curves were obtained using Popovic and Mander models to highlight the similarities of both models and the effect of dropping the small contribution of concrete resisting tensile strength.

The longitudinal compressive concrete stress f_c for a quasi-static strain rate and monotonic loading suggested by Popovics [401] is given by Eq. 4.1:



(a) Popovic and Mander constitutive model for an unconfined C35/45 concrete.



(b) Stress-strain relationship of C35/45 concrete using Mander constitutive model at unconfined $\varepsilon_{co} = 3.5e^{-3}$ and low confined $\varepsilon_{cu} = 5.0e^{-3}$ pressures (left), and at low $\varepsilon_{co} = 5.0e^{-3}$ and high $\varepsilon_{cu} = 25.0e^{-3}$ confinement pressures (right).

KEY: — Mander — Popovic — Unconfined — Confined — H-Confined

Figure 4.12: Constitutive models. Stress-strain relationship calibrated for C35/45 concrete using Popovic or Mander stress-strain relationship (top). Mander model representing the stress-strain relationship of C35/45 concrete with unconfined and confined sections (bottom).

$$f_c = \frac{f'_{cc} x r}{r - 1 + x'} \quad (4.1)$$

where f'_{cc} is compressive strength of confined concrete following Eq. 4.2:

$$f'_{cc} = f'_{c0} \left(-1.254 + 2.254 \sqrt{\frac{1 + 7.94 f'_i}{f'_{c0}}} - 2 \frac{f'_i}{f'_{c0}} \right) \quad (4.2)$$

being f'_{c0} the compressive strength of unconfined concrete.

Assuming that the ultimate deformation corresponds to the ultimate concrete compressive strain of a section at first hoop fractures, Mander [402] added the effective lateral confining stress on the concrete, f'_i , in Eq.4.3:

$$f'_i = \frac{1}{2} k_e R_s f_{yh} \quad (4.3)$$

where R_s is the ratio of the volume of transverse confining steel to the volume of confined concrete core, k_e is confinement effectiveness coefficient of transverse reinforcement and f_{yh} is yield strength of the transverse reinforcement.

The x parameter in Eq. 4.1 is the ratio between longitudinal compressive strain, ε_c and strain at maximum concrete stress, $\varepsilon_{cc} = 1 + 5\left(\frac{f'_{cc}}{f'_{c0}} - 1\right)$.

The model allows considering rectangular or circular geometries, and unconfined or confined sections by increasing the compressive strength and strain at crushing strength, ε_{cu} . Eurocode 8 [33] prescribe Eq. 4.4 to determine the ultimate strain of confined concrete:

$$\varepsilon_{cu} = 0.004 + 1.4\rho_s \frac{\sigma_{yp}\varepsilon_{su}}{\sigma_{cc}} \quad (4.4)$$

where, ρ_w is the volumetric ratio of transverse reinforcement, which is given by $\rho_w = 4A_{sp}/d_s S$ and $\rho_w = 2\rho_w$ for circular and rectangular sections, respectively; σ_{yp} and ε_{su} are the yield strength and ultimate strain of the transverse steel respectively and σ_{cc} is the confined concrete strength. According to Mader et al. 1988 [402], the latter is given combining the properties of unconfined and confined concrete using Eq. 4.5:

$$\sigma_{cc} = \sigma_{co} \left(-1.254 + 2.254 \sqrt{1 + \frac{7.94\sigma_l}{\sigma_{co}}} - 2 \frac{\sigma_l}{\sigma_{co}} \right) \quad (4.5)$$

where σ_{co} is the strain at crushing strength for unconfined concrete $\varepsilon_{co} = 3.5e^{-3}$ and σ_l is the lateral confinement pressure to account for non-uniform distribution of the pressure on the transverse sections due to the reinforcement spacing. Mander et al. 1988 [402] suggested a two-folded assumption for the calculation of effective confinement pressure being: 1) the product of an uniform distribution of the lateral pressure and the ratio between effective confined area and concrete core area, and 2) a function of the maximum strain of the transverse reinforcement steel determined by circumferential equilibrium ($p_{radial} = radius \times F_{circumferential}$). Thus, the σ_l for a circular section is given by Eq. 4.6:

$$\sigma_l = 1/2 k_e \rho_s \sigma_{yp} \quad (4.6)$$

where k_e is the coefficient of confinement efficient. For circular and spiral distribution of transverse reinforcement, k_e is respectively given by Eq. 4.7:

$$\begin{cases} k_e = \frac{1 - \frac{s'}{2d_s}}{1 - \rho_{cc}} & \text{circular} \\ k_e = \frac{1 - \frac{s'}{2d_s}}{1 - \rho_{cc}} & \text{spiral} \end{cases} \quad (4.7)$$

Figure 4.12(b) depicts the constitutive relationship of concrete materials adopted to model the test-case, using Mander model for unconfined and confined C35/45, ε_{cu} prescribed by Eurocode 8 recommendation (unconfined, $\varepsilon_{cu}=5\%$, beam confinement, $\varepsilon_{cu}=5\%$), and piles highly confined, $\varepsilon_{cu} = 25\%$).

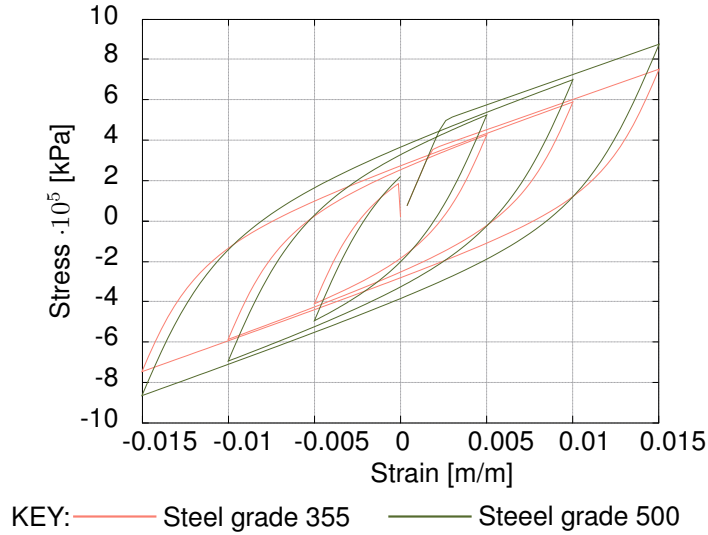


Figure 4.13: Constitutive models. Constitutive stress-strain relationship calibrated for S355 and S500 steel using Giuffre-Menegotto-Pinto stress-strain relationship.

Steel model

The stress-strain constitutive relationship to model steel is based on the uniaxial Giuffre-Menegotto-Pinto steel material object with isotropic strain hardening [403].

For example, Fig. 4.13 shows the hysteric behavior of steel grades S355 and S500 (steel materials of the test case) subjected to a cyclic loading, constructed based on the an uniaxial Giuffre-Menegotto-Pinto steel material object with isotropic strain hardening.

The normalized analytical form of the stress-strain relationship in Eq. 4.8:

$$f^* = b\varepsilon^* + \frac{(1-b)\varepsilon^*}{(1+|\varepsilon^*|^R)^{1/R}} \quad (4.8)$$

have ε^* being the normalized strain and f^* the normalized stress. The normalize stress is given by Eq. 4.9:

$$\begin{cases} \varepsilon^* = \frac{\varepsilon - \varepsilon_r}{\varepsilon_0 - \varepsilon_r} \\ f^* = \frac{f - f_r}{f_0 - f_r} \end{cases} \quad (4.9)$$

The formula is composed of two linear asymptotic branches with slope E_0 and $E_1 = b \times E_0$ respectively predicting the elastic and post-yielding response of the material. The origin is at the reversal point (ε_r, f_r) , while the yield point is denoted as ε_0, f_0 . The transition curve between the linear asymptotes is a smooth curvature defined by variable R dependent on the strain amplitude between the latest yield point and the maximum plastic strain in the loading direction after the reversal [404]. The effect of isotropic hardening is assumed as a parallel shift of the post-yield linear asymptote by a stress f_{st} depending on the maximum strain in either tension and compression loading direction [404].

Soil

The soil response due to monotonic or cyclic loading is based on elastic-plastic constitutive relationships for cohesive and cohesion-less materials. On one of the models the plasticity is independent of confinement changes, following governing equations based on the [405] yield criterion, while the other model is sensitive to pressure variations, assuming a multi-yield criteria proposed by [406].

The pressure independent elastic-plastic material exclusively introduces deviatoric stress-strain in plastic response neglecting volumetric changes, which represents advantages representing materials with behavior insensitive to confinement changes, such as organic soils or clay under fast undrained loading conditions. The hyperbolic backbone curve representing shear stress τ strain γ relation is defined by Eq. 4.10:

$$\tau = G \frac{\gamma}{1 + \gamma/\gamma_r \cdot (p'_r/p')^d} \quad (4.10)$$

where G represents shear modulus, p' instantaneous effective confinement and d defines ratio between shear G and Bulk B moduli. The peak shear strength τ_f given by Eq. 4.11 is function of the soil friction angle and cohesion, c :

$$\tau_f = \frac{2\sqrt{2}\sin\varphi}{3 - \sin\varphi} \cdot p'_i + \frac{2\sqrt{2}}{3} \cdot c \quad (4.11)$$

In case of automatic surface generation reference γ_r follows the condition described in Eq. 4.12:

$$\tau_f = \frac{2\sqrt{2}\sin\varphi}{3 - \sin\varphi} \cdot p'_i + \frac{2\sqrt{2}}{3} \cdot c = G_r \frac{\gamma_{max}}{1 + \gamma_{max}/\gamma_r} \quad (4.12)$$

Otherwise, OpenSees allows to define yield surfaces of independent elastic-plastic material based on shear modulus reduction by providing pairs of shear strain and desired shear modulus reduction.

The pressure dependent elastic-plastic material reproduces the behavior of pressure sensitive materials, such as sands and silts, accounting dilating (shear-induced volume contraction or dilation) and non-flow liquefaction (cyclic mobility) properties. The octahedral curve representing shear stress strain relation is identically defined by Eq. 4.10. However, for the dependent elastic-plastic materials, the peak shear strength τ_f given by Eq. 4.13 is function of the soil friction angle which is dependent of effective confinement:

$$\tau_f = \frac{2\sqrt{2}\sin\varphi}{3 - \sin\varphi} \cdot p' \quad (4.13)$$

In case of automatic surface generation reference γ_r follows the condition described in Eq. 4.14 at p'_r :

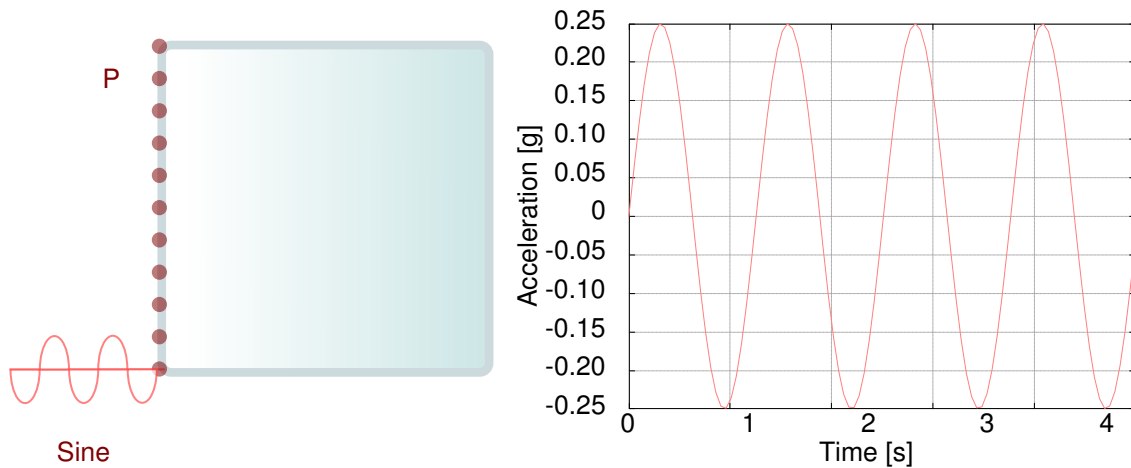
$$\tau_f = \frac{2\sqrt{2}\sin\varphi}{3 - \sin\varphi} \cdot p'_r = G_r \frac{\gamma_{max}}{1 + \gamma_{max}/\gamma_r} \quad (4.14)$$

A brief parametric analysis was performed varying the constitutive relationships (pressure

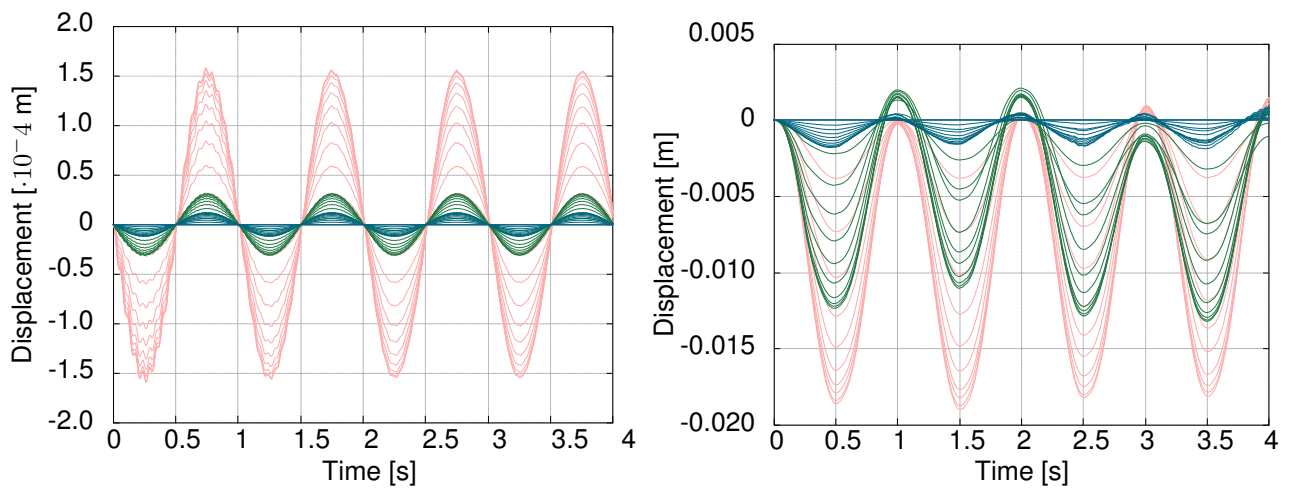
independent- and dependent multi-yielding material), types of soil (clay or sand), and soil resistance (soft/stiff clay and loose/dense sand). The soil was modeled as a two-dimensional 1 m quad element with 1 m thickness, fixed on the base in $x-$ and $y-$ directions. A sine load was applied during 4 s , with 1 g of acceleration amplitude and 1 s of period. The soil element was discretized into an uniform 0.1 m quadrilateral mesh. The horizontal displacement was measured on the nodes points (P) of the left edge while the stress-strain curves were capture at the bottom, middle and top points. Fig. 4.14 represents the 2D setup and the soil responses.

A supplementary dynamic analysis of a three-dimensional model of soil was conducted to characterize the non-linear response of pressure independent and dependent soils under a real recorded signal. Fig. 4.15(a) represents the 3D unitary volume soil and initial boundary conditions, including the loading corresponding to Loma Prieta earthquake. Figs. 4.15(b) and 4.15(c) depict the corresponding displacement-stress relationship evaluated at point P (identified in Fig. 4.15(a)), respectively illustrating the response of pressure independent and dependent multi-yielding materials.

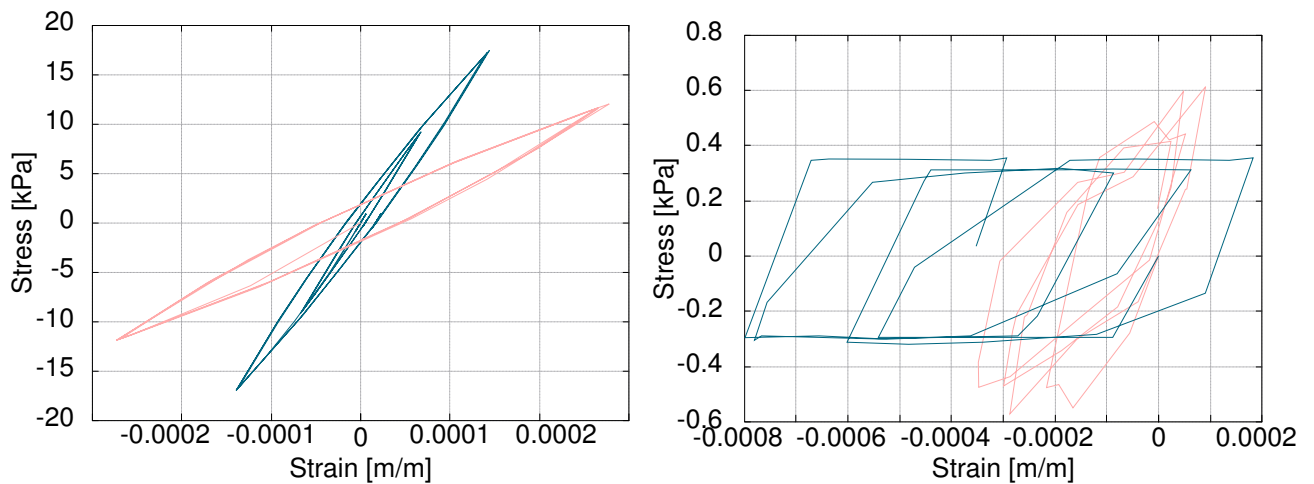
Along the loading-unloading cycle is possible to identify energy dissipation, which indicates the models capacity to reproduce plastic behavior of the soil materials. The soils displacements due to the $M_w6.9$ Loma Prieta earthquake are relatively small, less than 1 mm , yet the energetic damping dissipation is observable, mostly in loose sand and soft clay soils. Regarding confinement effects on the soil response, the pressure dependent model used to model cohesion-less material is adequate to capture such effect, particularly in loose sand, whereas (and as expected) dense sand shows minimal confinement influence in its response. The curves of unconfined and confined clay using pressure independent material are overlapped, confirming the constitutive model limitation to predict pressure influences on soils response to cyclic loading.



(a) Two-dimensional numerical setup (left) and cyclic sine loading function (right).



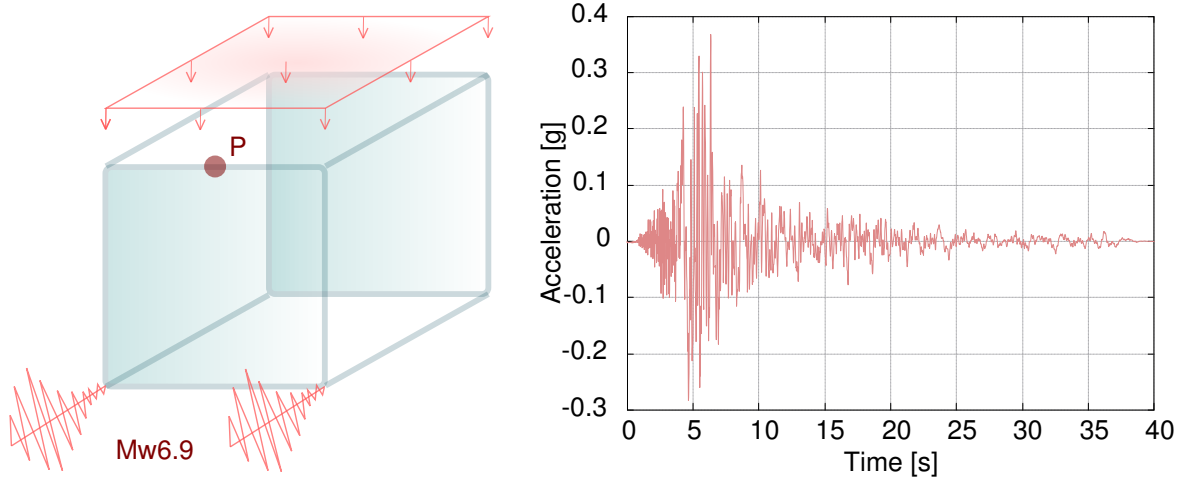
(b) Histories of horizontal displacement of pressure independent (left) and dependent (right) materials under cyclic load. Measures at different P along the left edge of the soil element.



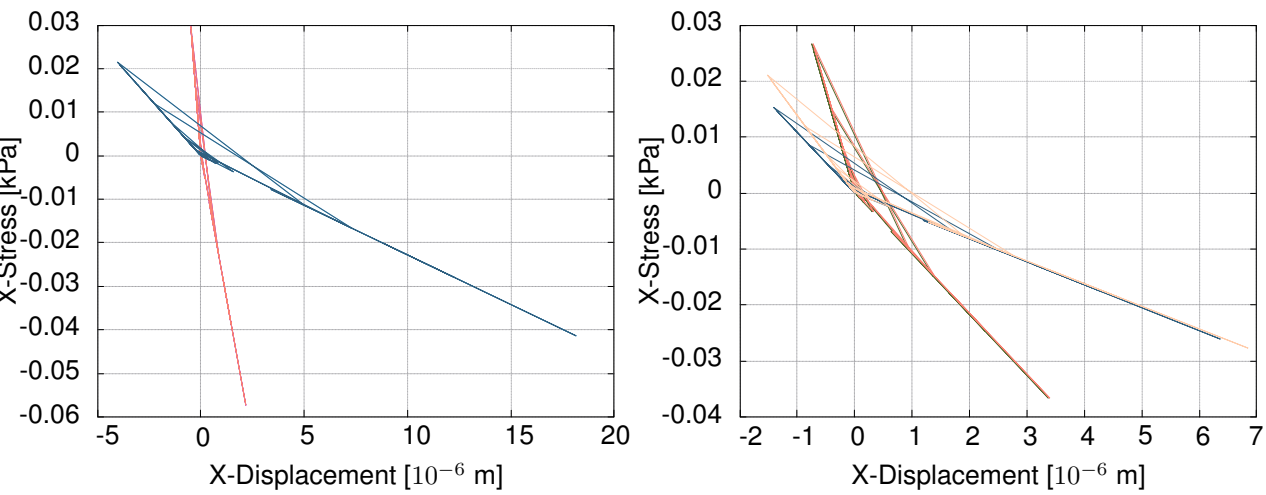
(c) Strain-stress response of pressure independent (left) and depended (right) materials under to cyclic load. Measured at top left node of the soil element.

KEY: — Soft/loose clay/sand — Medium clay/dense — Stiff/dense clay/sand

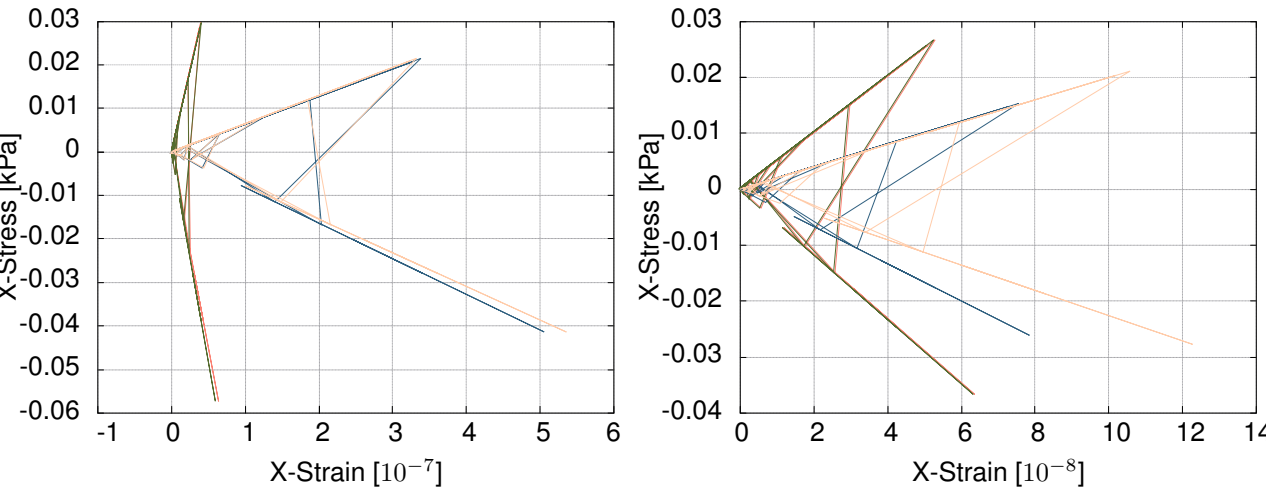
Figure 4.14: Constitutive models. Behavior of pressure independent and dependent multi-yielding soil materials.



(a) Three-dimensional unitary volume of soil subjected to uniform -5 kNm pressure (left) and time-series of ground motion acceleration recorded during $Mw6.9$ Loma Prieta, 1989 earthquake (right).



(b) Displacement-stress response of unconfined and confined pressure independent (left) and dependent (right) materials due to dynamic load.



(c) Strain-effective stress response of unconfined and confined pressure independent (left) and dependent (right) materials due to dynamic load.

KEY: — Confined stiff clay/dense sand — Unconfined stiff clay/dense sand
 — Confined soft clay/loose sand — Unconfined soft clay/loose sand

Figure 4.15: Constitutive models. Constitutive relationships for pressure independent and dependent multi-yielding soil materials.

4.4.2 Soil-structure interaction

Laterally loaded pile foundation

Coupled geotechnical and structural displacement-based design combines inertial (demand on structure due to seismic ground accelerations acting on its mass) and kinematic (load imposed on a structure by movement of soil) effects. The soil-structure interaction accepts discrete and continuum modeling approaches. Considering one example of OpenSees library (available at https://opensees.berkeley.edu/wiki/index.php/OpenSees_User), both approaches were tested and correlated.

The model using discrete soil representation consists of a beam on a nonlinear Winkler foundation using beam elements and springs representing the vertical and lateral response of surrounding soil subjected to a 3500 kN load applied in the positive x -direction at the head of the pile. The 1 m -diameter pile is 21 m long, 20 m of which are embedded. The definition of the elastic section of the pile is based on cross-sectional area and moments of inertia, while modulus of elasticity, $E = 25\text{ GPa}$, and shear modulus, $G = 9.615385\text{ GPa}$, defined the material. Soil springs were modeled using zero-length elements connecting the fixed and slave nodes in both horizontal and vertical directions. The soil elastic properties were defined using unit weight $\gamma = 17\text{ kN/m}^{-3}$, internal friction angle $\phi = 36^\circ$ and shear modulus of $G_{soil} = 150\text{ MPa}$. A static analysis was conducted to obtain the displacements at the pile nodes extracting the deflection of the pile, the reaction forces in the p-y springs visualizing the lateral soil response, and the shear and moment along the elements of the pile.

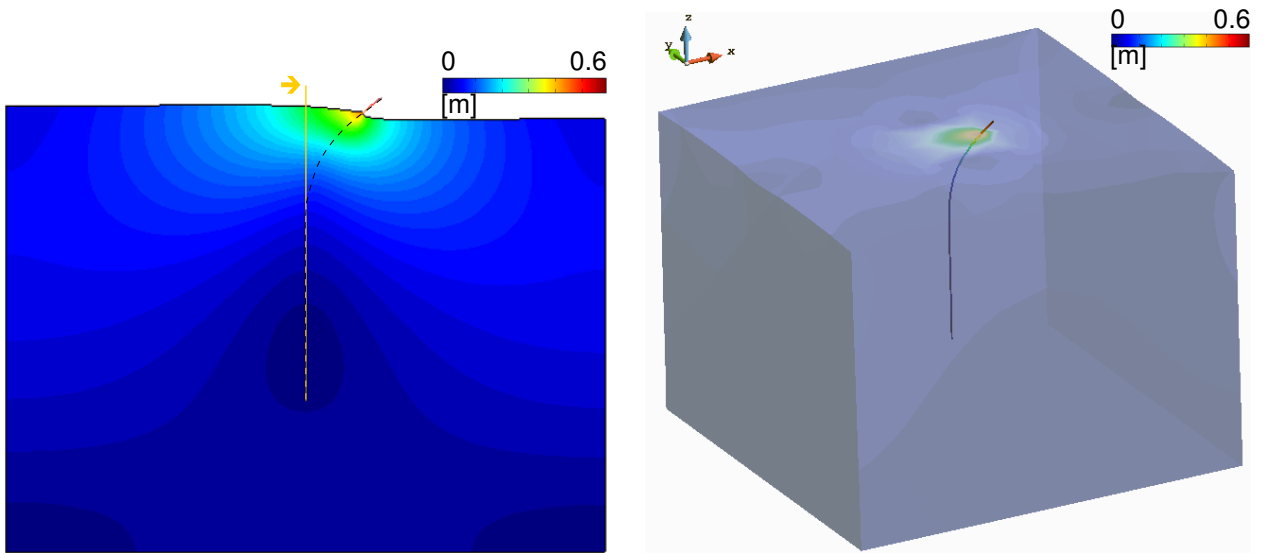
The model using continuum soil adopted three-dimensional elements surrounding the pile. The connection soil-pile was set using nodes sharing equal degrees of freedom over the embedded length of the pile.

Fig. 4.16 depicts the deflection, bending moment and shear force on the pile, and respective soil reaction after application of the horizontal loading force at the head of the pile.

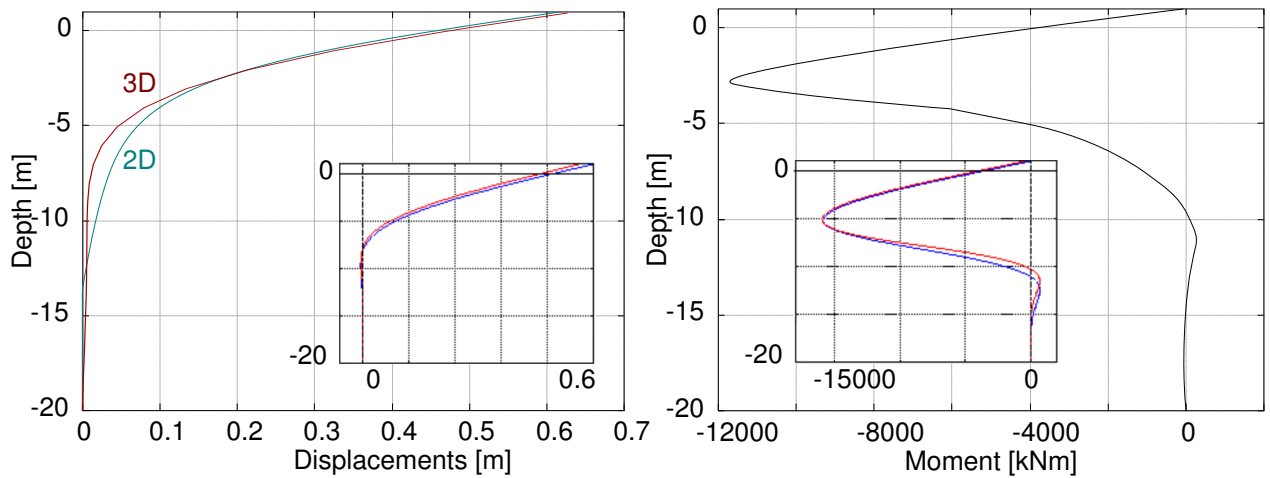
In the example, the results obtained with OpenSees were verified against the solutions of another commercial software, LPILE, showing an overall agreement while minor discrepancies were attributable to differences between the two analysis methods.

In general, the OpenSees model using soil elements provides a close approach of the quantities assessed in the test-case. The displacement in the head of the pile is close to the test-case, yet it shows an expanded interaction of the pile-soil system in the vertical interface, i.e., the pile deflection is observed up to -10 m in depth against the -8 m -depth of the test-cases. In comparison with the test-case, the maximum bending moment of the pile is about 20% underestimated. The shear force solution matches the evaluation of the test-case approaches.

Such differences are most-likely due to the lack of data to assign the soil parameters required in a pressure dependent multi-yielding constitutive model of the soil. In opposition to elastic or even elastic-plastic materials, the number of parameters to model soil elements are comparatively higher. Moreover, the elements to establish the soil-structure interaction are intrinsically different. The discrete/nodal springs are distributed in depth while soil elements are governed by continuum



(a) Deflection of pile-structure interaction system on two- (left) and three-dimensional (right) models.



(b) Displacement (left) and bending moment (right) along the pile.

Figure 4.16: Soil-pile interaction model. Response of soil and pile system to a horizontal load applied in the head of the pile. Correlation between solutions using OpenSees and soil elements, and OpenSees using springs to represent the soil (red lines in sub-figures) and L-Pile (blue lines in sub-figures).

mechanics, allowing to share effects induced by the pile and among soil elements.

4.4.3 FE remarks

The stress-strain relationships used to model concrete and steel materials are widely used in nonlinear modeling of reinforced concrete components. Soil constitutive models allow to model various soil materials elastic and elastic-plastic response to monotonic and cyclic loading. The behavior of organic soils or clay under fast (undrained) loading conditions is governed by constitutive model of pressure independent multi-yielding material ([405] yield surface), while pressure dependent multi-yielding is appropriate to model sands and silts ([406] yield surface).

A correlation between discrete and continuum approaches to model soil-structure interaction shows different levels of modeling demand. On one hand, springs are often used to resemble the soil influence on the structural foundation due to simplicity and quantity of data required to assign the soil properties. On the other hand, the continuum approach requires more and more detailed characterization of the soil parameters, their calibration is challenging, and represents higher computational costs. Yet, it is capable to reproduce complex soil and soil-structure interaction phenomena, such as the effects of soil confinement, interaction between interfaces of different soils, liquefaction, and shear-induced volume contraction or dilation.

Chapter 5

Proof of Concept

Chapter 5 constitutes the proof-of-concept for numerical tsunami action characterization by correlating numerical solutions and instrumentally-recorded data acquired during an experimental campaign performed at the large wave flume of the Hinsdale Wave Research Laboratory, Oregon State University. The correlation includes intensities of hydrodynamic quantities (free-surface elevation and flow velocity) and impacts on an elevated structure (forces and pressures, in both horizontal and vertical directions).

Chapter 5 is based on Reis et al. 2021 and 2022b [48, 272].

5.1 Experimental data

An experimental campaign conducted at the large wave flume at Hinsdale Wave Research Laboratory, Oregon State University was carried out to provide laboratory data to assess the impact of waves on elevated structures.

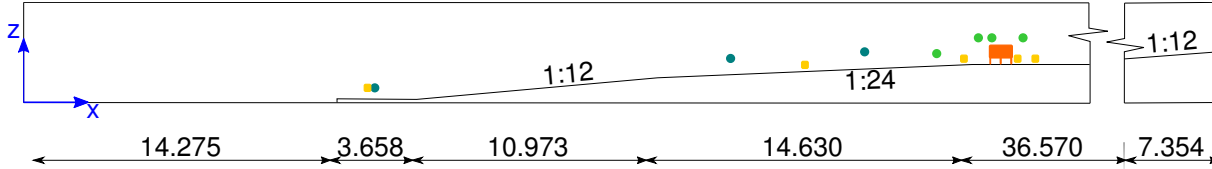
The experiment consisted in the generation of tsunami-like waves, which propagated in a variable sloping tank, and interacted with an elevated structure. By varying the still water level and the piston velocity, the flow generated resembles tsunami bores and quasi-steady flow and are further identified as unbroken and broken wave cases, respectively.

The objective of the experiment was to develop a dataset of measures concerning: (1) water height and velocity due to unbroken and broken (bore) tsunami-like waves, and (2) forces and pressures exerted on an elevated structure resembling a scaled two-story building. The experiment was instrumentally monitored and physical data was recorded.

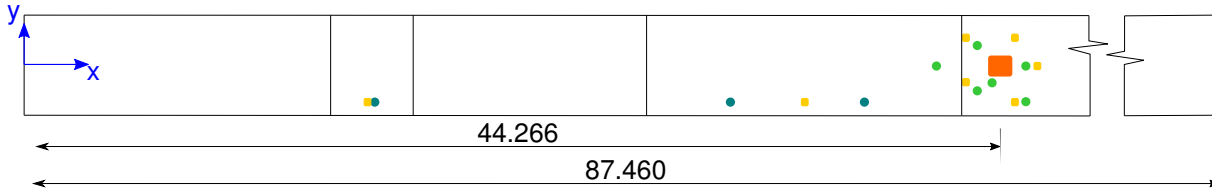
5.1.1 Physical setup

Figure 5.1 depicts the setup, including an elevation and a plan view of the flume with the instrumentation. The experimental setup was assembled on a flume with a length, width, and depth of 87.430 m, 3.660 m and 4.572 m, respectively. The bathymetry of the channel includes (1) a flat base slab

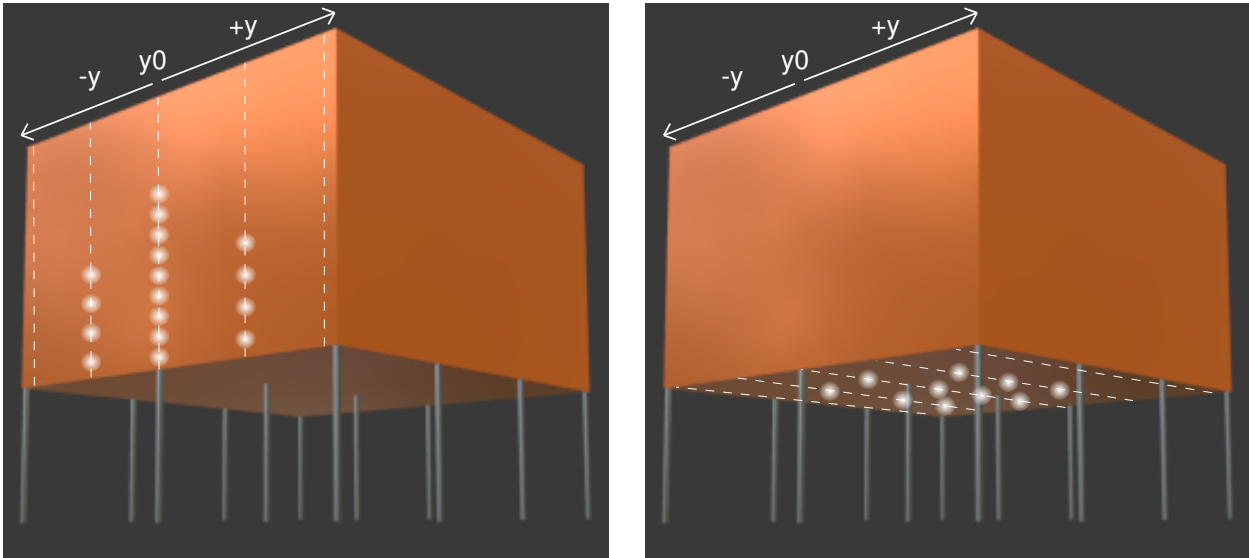
from 0 m to 14.250 m, (2) a slab elevated 0.150 m, relative to the base slab, between 14.250 m and 17.907 m, (3) a 1/12 slope with a projected horizontal length of 10.971 m followed by (4) a 1/24 slope with a projected horizontal length of 14.628 m, (5) a flat extension of 36.570 m, and (6) a final 1/12 slope with projected horizontal length of 7.354 m. An elevated structure was positioned at $x = 44.266$ m, $y = 0.002$ m and $z = 2.002$ m, relative to the coordinate system.



(a) Elevation view.



(b) Plan view.



(c) Pressure gauges layout in both horizontal (left) and vertical (right) direction. Dot lines are 0.250 m-spaced.

KEY: ■ Specimen ● Wave Gauge ● Ultrasonic wave gauge ● Velocimeter

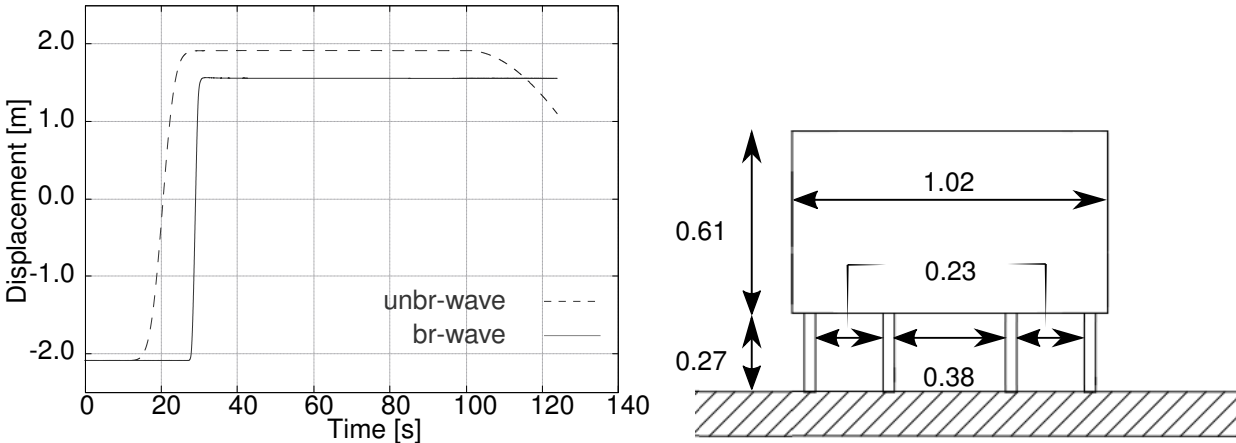
Figure 5.1: Experimental setup: overview of geometry and instrumental disposition. All dimensions are in meters.

The flume is equipped with a piston-type wave-maker with a hydraulic actuator assembly of 4.2 m maximum stroke and 4 m s^{-1} maximum velocity. The wave-maker is capable of producing regular, irregular and solitary waves, with periods ranging between 0.8 s to 12^+ s. The at-rest position of the piston defines the null state of the coordinate system. The initial position of the paddle was set to -2.060 m. The piston operated under displacement control, for the generation of unbroken and broken long-waves. The still water level was set at $z = 2.00$ m for the unbroken wave case and $z = 1.85$ m for the broken case, which resulted in models without and with an air gap between the still water level and the bottom of the structure, respectively. The two waves cases were thus quite distinct. The shape of

the unbroken wave was nonturbulent, with an approximate duration of 25 s, average height of 30 cm and 1.5 m s^{-1} velocity. The shape of the broken wave was steep and abrupt, with half the duration, circa of $1\text{ m} \pm 20\text{ cm}$ height and the velocity measuring around 2.5 m s^{-1} . Fig. 5.2 depicts the horizontal displacements of the wave-maker. An elevated structure resembling a two-story building supported by piles was implemented in the model. The specimen (in Fig. 5.2(b)) of the scaled elevated structure was 1.016 m square in plan, had a height of 0.615 m, and had twelve protruding square columns that had a cross-section of 0.254 m^2 .



(a) Photograph of unbroken- (left) and broken-waves (right) induced by the horizontal displacement of the piston wave-maker and different initial free-surface elevations, respectively of 2.00 m and 1.85 m.



(b) Horizontal displacement of the piston wave-maker for the generation of unbroken- and broken-waves (left). Dimensions of the specimen resembling an elevated structure (right), in meters.

Figure 5.2: Experimental setup: generation of unbroken- and broken-waves to impact an elevated structure.

The instrumentation of the experimental campaign included three wave gauges (WG) and five ultrasonic wave gauges (USWG) to record the water free-surface along the flume and surrounding the structure, respectively. Seven acoustic doppler velocimeters (ADV) recorded the velocities along the flume and near the structure. Nine load cells (LC) measured stream-wise, transverse, and vertical wave forces. Fourteen pressure gauges (PG) recorded the horizontal and vertical pressure exerted against the structure using a layout disposition to map the pressure distributions on the structure. The instrumental setup is resumed in Table B.1, Appendix B. The tests and data acquisition were

repeatedly trialed for each wave case. The data obtained from instrumental acquisition is represented by the mean laboratorial data complemented by standard deviation of the the physical data derived from the trials that composed the experimental campaign. The corresponding coefficient of variation (COV) of the recorded quantities is resumed in Table B.2, Appendix B.

5.1.2 Drag coefficient

In fluid mechanics, the hydrodynamic force is the product of the momentum flux affected by a dimensionless coefficient known as drag coefficient, C_d , that represents the behavior of a quasi-steady flow against a fully submerged solid. In tsunami literature, it also applies to partially submerged objects and moderate to high tsunami velocity [50, 407]. Over the years, extensive and numerous physical experiments were performed to assess the influence of several parameters, such as the shape of the object, bore height, Reynolds number characterizing laminar or turbulent flow, Froude number characterizing sub- or supercritical flow, ratio between water depth and object width, and blockage coefficient considering the width of the tank and of the column. Most authors agree on the sensitivity of C_d and on the difficulty to calibrate it [17, 169, 195, 273, 407–413], demonstrating that C_d is not a function of any single non-dimensional grouping, but strongly depends of a combination including the Froude number, ratio between the widths of the propagation channel and of the obstacle, and the shape of the object.

Aiming to contribute for the formulation of gravity-controlled free-surface flow, the C_d of tsunami-like unbroken- and broken-waves traveling over an inundated bed is briefly tackled. Moreover, due to its case-sensitiveness nature, C_d characterization is required to quantify hydrodynamic force values, which are obtained by regression to best-fit the peak of the first wave, where the most interesting and important results for the forces and pressures exerted on the structure occur.

The characterized of C_d considers the analytical Eq. 3.26, where $\rho = 1000 \text{ kg/m}^3$ is the density of the water, the characteristic width of the solid subjected to the action of the fluid is $B = 1.016 \text{ m}$ and hu^2 is the momentum flux, which was calculated using records of USWG6 and ADV7 instruments for the stream-wise direction, while records from ADV3 to ADV6 were considered for the calculation in the vertical direction.

The coefficient for the horizontal direction was valued in $C_d = 1.1$, for the unbroken-wave case, and $C_d = 1.3$, for the broken-wave case. Both values are lower than the provisions from the ASCE 7 standard, that recommends $C_d = 2.0$ depending on the ratios of width to depth and width to height of the submerged surface area. However, C_d estimates are simultaneously reasonable due to the elevated geometry of the obstacle and are in agreement with some studies performed for rectangular-shaped columns [166, 273] and studies involving circular-shaped [378, 414, 415] that logically induce smaller values of resistance to the flow than pointy objects. Other studies on rectangular columns lead to estimated values ranging from $C_d = 2.0$ to $C_d = 4.0$ [201, 415, 416].

In the vertical direction, for the unbroken wave case, the obtained $C_d = 2.0$ is smaller than the recommendation of the Federal Emergency Management Agency (FEMA) guidelines ($C_d = 3.0$) [157].

For the broken wave case, the greater turbulence of the flow and magnitude of the stream-wise force promoted a significant reduction of the uplifting force that is the result of the sum between front and back loads with opposite signs. The value of $C_d = 0.2$ is similar to under-unity values assessed for aerodynamic problems, reinforcing the assumption that the hydrodynamic force equation recommended by FEMA [157] and ASCE [32] adopting a static drag coefficient is relatively adequate to evaluate the net fluid force on a body in a quasi-steady flow [50, 407], but inadequate to estimate the hydrodynamic load when the tsunami flow makes the transition from laminar to turbulent flow, usually at Reynold's number of the order of $Re \approx 10^5$.

Figure 5.3 illustrates the potential time dependency influence when defining the tsunami design loading. The semi-analytic formulation (adequate to determine peak values) is adopted to calculate time-series for the force exerted on an elevated structure, using the hydrodynamic quantities measured by the laboratorial instruments, USWGs and ADVs, and the C_d values previously quantified for peak values of the unbroken-wave case. The curves are compared to recorded forces measured by LC5, for the horizontal directions, and the sum of LC6 to LC9, for the vertical direction.

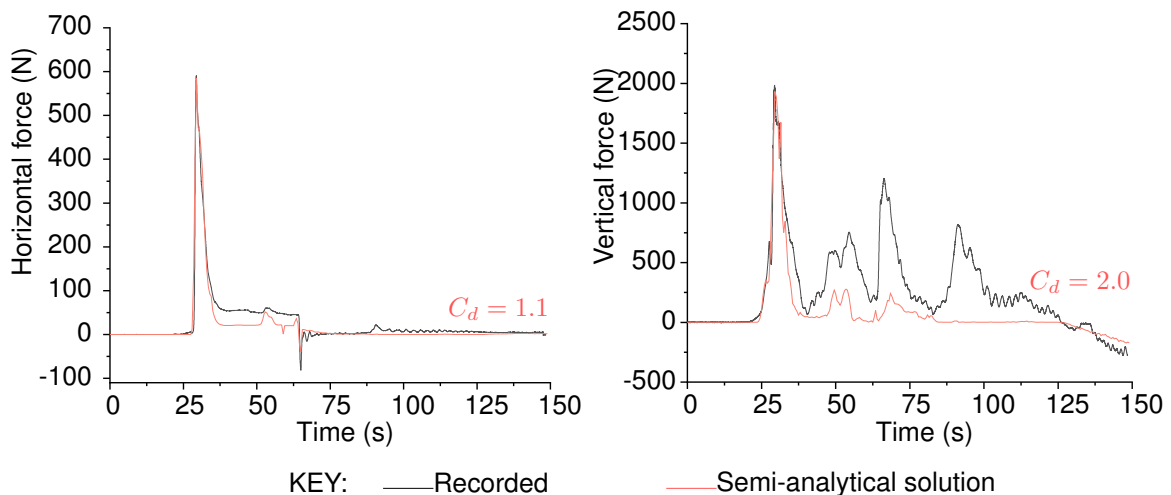


Figure 5.3: Experimental calibration of drag coefficient: comparison of recorded and calculated forces exerted on the structure, considering stationary C_d estimated to fit the peak of the wave in the horizontal (left) and vertical (right) directions. Example considering the unbroken wave case.

As expected, the fitting between recorded and calculated curves displays a good agreement for the first wave since the C_d was calibrated by regression to reproduce the peak of the first wave. For the horizontal direction, the variations after the first wave may be acceptable to design lateral tsunami-resistant systems. Conversely, a significant underestimation of the vertical force exerted on the bottom of the structure occurs, partially neglecting its intensity over time. As depicted in Fig. 5.3, the hydrodynamic effect in the vertical direction (at right) has an important expression over time, with the peaks of the first four waves being greater than the maximum peak value in the horizontal direction (at left). The optimistic characterization of the tsunami hydrodynamic effect in the vertical direction represents a strong potential contribution to under-design structural resisting systems of elevated structures. Moreover, Fig. 5.3 only represents the more predictable nonturbulent unbroken-wave case. A brief incursion on the broken wave case, adopting Eq. 3.26, hydrodynamic quantities instrumentally recorded near the

structure and $C_d = 3.0$, demonstrates less accentuated waves following the first bore. Adopting a slightly conservative value of C_d potentially represents a procedure to avoid a dynamic characterization of the tsunami hydrodynamic effects in the vertical direction, simplifying the structural design for such cases.

5.2 Numerical data

The assessment of the hydrodynamic effects of the tsunami-like wave impacting the elevated structure is performed considering three distinct numerical configurations:

- built-in numerical computation on Lagrangian NS system using the SPH framework introduced in Section 3.2.1 and implemented in open-source DualSPHysics software[247];
- semi-analytic quantification using the computation of the tsunami-like hydrodynamic quantities by Eulerian discretization scheme that considers the SW equations in a fixed reference system, solved in FV-based scheme implemented using the C++ code introduced in Section 3.2.2 [19, 21]. Forces and pressures exerted on the structure are calculated using equations 3.25 and 3.26;
- coupled Eulerian SW-FV and Lagrangian NS-SPH introduced in Section 3.2.3 to simulate the tsunami propagation and inundation phases, respectively.

To mimic the stages of the experiment, the whole domain has been divided into three zones: generation of the wave, followed by reflections and rarefactions, and ended with a slow energy decay. Fig. 5.4 depicts the sub-domains and the numerical configurations used to perform the simulations, including two different solvers (SPH and FV) and three different Dirichlet boundary conditions, which are transmissive (TBC), for the FV, and moving (MBC) and open (OBC), for the SPH. The models using a MBC resembling the physical displacement of the piston, “P”, or the models using TBC imposing hydrodynamic quantities are flagged by a “Y”(es) or “N”(o) symbol. The following sections describe the numerical assumptions used to assemble the configurations and the modeling conditions prescribed to perform the numerical simulations.

5.2.1 NS-SPH model

The first modeling configuration adopted uses the Lagrangian SPH method to solve the Navier-Stokes equations, as introduced in Chapter 3, 3.2.1. To reproduce the three-dimensional physical setup, the flume and elevated structure were created in the open-source Blender [417] (see Fig. 5.5(a)), while the remaining setup was pre-processed in DesignSPHysics [418]. The numerical model fluid motion is prescribed by a moving boundary condition, at $x = 0\text{ m}$, which mimics the horizontal displacement of the piston. The time-histories of two different displacements of the wave-maker, resembling an unbroken and a broken wave, are provided by an external data file. A two-dimensional model was derived from the 3D original model by taking a longitudinal section cut along the center axis of the flume ($y = 0$).

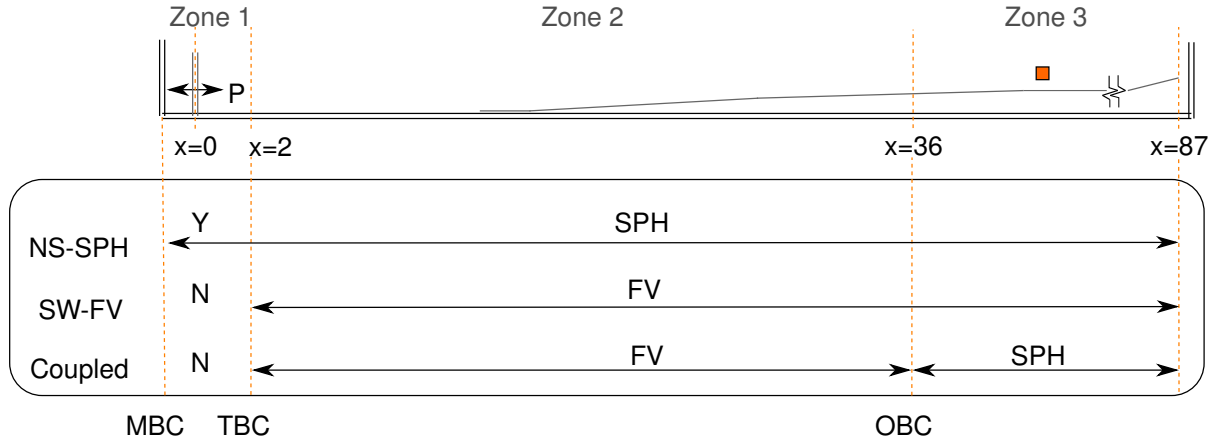


Figure 5.4: Numerical schemes: schematic summary of the numerical protocols, representing the domains where the SPH and FV solvers are used and the Dirichlet boundary conditions implemented, including transmissive (TBC) for the FV solver, moving (MBC) and open (OBC) for the SPH solver.

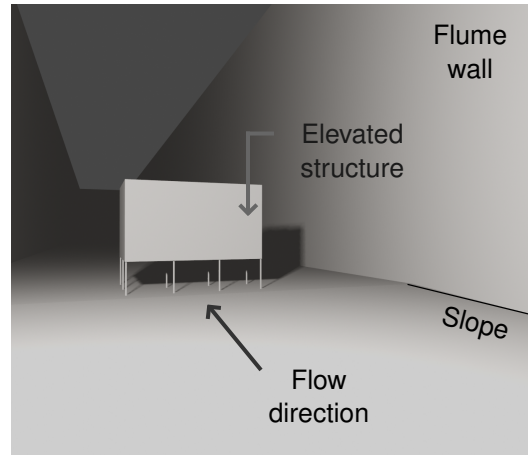
Simulations for both unbroken- and broken-wave cases were carried with the DualSPHysics v5.0 software running on a single graphics processing unit, GPU, CUDA driver version 11, 64 CUDA cores per 30 multiprocessors, card NVIDIA GeForce RTX 2060, @2.6 GHz, with 2 GB of memory. DualSPHYSICS v5.0 is compiled with CUDA library version 9.2. Table 5.1 lists the numerical conditions used in the simulations. The fluid density, smoothing kernel, assumption of weakly compressible and near irrotational flows are common parameters to all models. The temporal domain of the simulations was set to $t_f = 100 s$, with a time-step of $\Delta t = 0.05 s$ to guarantee an adequate approximation to Courant–Friedrichs–Lewy coefficient, $CFL = 0.20$. Virtual sensors were implemented in the numerical model at the corresponding locations of WG, USWG, LC, and PG instruments (see Fig. 5.1) to perform the convergence study and the physical-numerical correlation for both unbroken (Fig. 5.5(b)) and broken wave cases (Fig. 5.5(c)).

The convergence and calibration study was performed for values of initial inter-particle distance Δp varying from $0.10 m$ to $0.02 m$ in the 3D models and from $0.10 m$ to $0.005 m$ in the 2D models. The range of Δp is constrained by the computational capacities, i.e., by the RAM memory, GPU capacity, and data storage of the desktop computer used to perform the simulations.

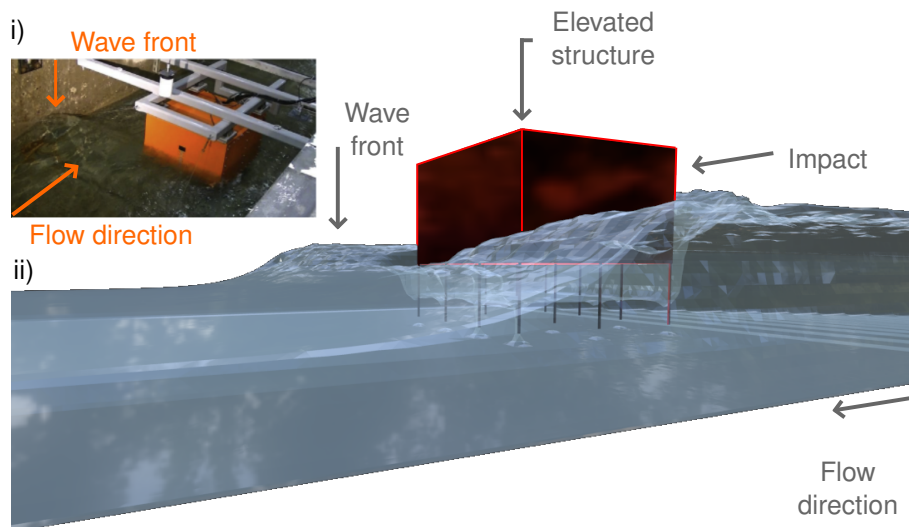
Table 5.1: Computational settings for the numerical simulations.

| Assembly Attribute | Values |
|--------------------------------------|--------------------------------|
| Kernel function | Wendland |
| Temporal discretization | Symplectic algorithm |
| CFL coefficient | 0.2 |
| Spatial discretization | Wendland kernel |
| Coefficient for artificial viscosity | 0.01 (near irrotational flows) |
| Reference fluid density | $1000 kg/m^2$ |
| Time of simulation | 100 s |

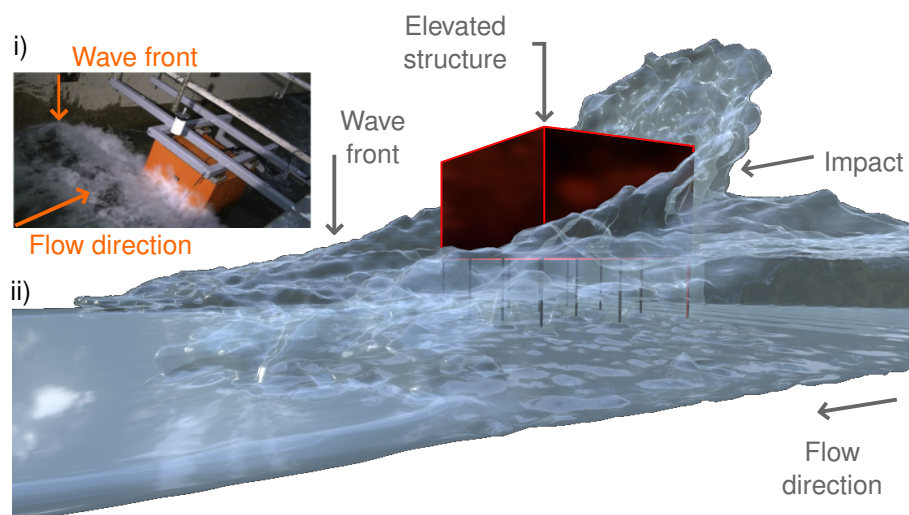
As one of SPH's drawbacks is the low rate of convergence, a convergence study on the 3D vs. 2D modeling assumption, using different Δp influencing the solutions of free surface elevation was



(a) NS-SPH model: photograph of the physical setup (left) and numerical model of the empty flume with wave-facing view of the elevated structure (right).



(b) Simulation of the tsunami-like unbroken wave case (quasi-steady state): i) photograph of the wave impacting the elevated structure and ii) sample numerical solution during the fluid-structure interaction.



(c) Simulation of the tsunami-like broken wave case (bore): i) photograph of the wave impacting the elevated structure and ii) sample numerical solution during the fluid-structure interaction.

Figure 5.5: Physical and numerical NS-SPH models. Visualizations of the numerical model and results are created using Blender.

performed to verify that the models show convergence for smaller inter-particle initial distances and to determine the admissible largest particle initial spacing that is capable of capturing the hydrodynamic flow conditions while controlling computational costs.

The convergence of the numerical solutions is assessed using the Root-Mean-Square-Error (RMSE) of the free-surface elevation measured at each considered location in the flume including sensors located in the vicinity of the structure. The RMSE represents the quadratic mean of the variance between the reference solution, E , and the parameterized numerical solutions, S , (Eq. 5.1),

$$RMSE_T = \sqrt{\frac{\sum_{i=1}^n (S_i - E_i)^2}{n}} \text{ with } n \text{ such that } t_n = T \quad (5.1)$$

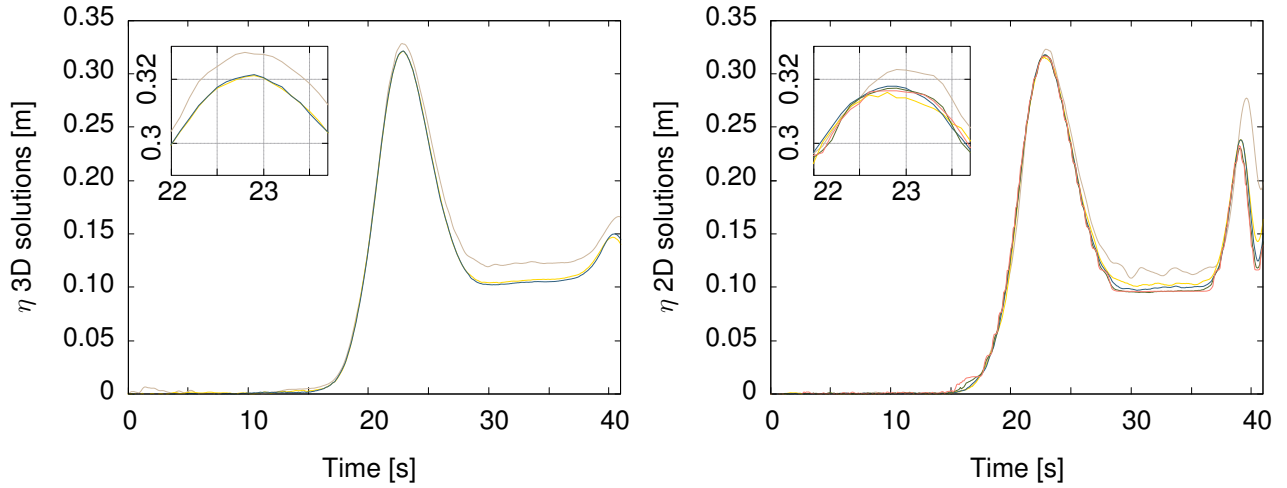
where S_i is the value of the numerical solution S at a given time-step i , E_i the corresponding value of the reference solution, and n the number of time-steps for the interval of time considered in the $RMSE_T$ calculations. The reference solutions, E , are the simulation results obtained using an inter-particle distance of $\Delta = 0.005 \text{ m}$ for the 2D models and $\Delta p = 0.02 \text{ m}$ in the 3D models, respectively. Variables considered include sensor locations (WG1, USWG2, USWG6), wave cases (unbroken and broken), model dimensions (3D and 2D), discretization (Δp varied between 0.005 m and 0.10 m in the 2D models, and between 0.02 m and 0.10 m in the 3D models), and time of the analysis (t_{1wave} , t_{2wave} , t_{final} , which are time to first wave, second wave, and final, respectively).

From the analysis of $RMSE_T$ varying the identified parameters are inferred the advisable ratios between H and Δp , $\frac{H}{\Delta p}$, which is a dimensionless number comparatively more useful in terms of practical modeling application than Δp . To aid on the determination of $\frac{H}{\Delta p}$ ratio, two criteria were assumed to establish the admissible error. The first is quantitative by considering a maximum error of 5%, which is a reasonable physical discrepancy and represents half the reference value for the validation of tsunami inundation models [226, 419]. The second is qualitatively derived from the correlation between visually inspected convergence and RMSE, e_{conv} . The results inferred from the analyses of numerical convergence of Δp and the $\frac{H}{\Delta p}$ ratio are detailed in the following subsections.

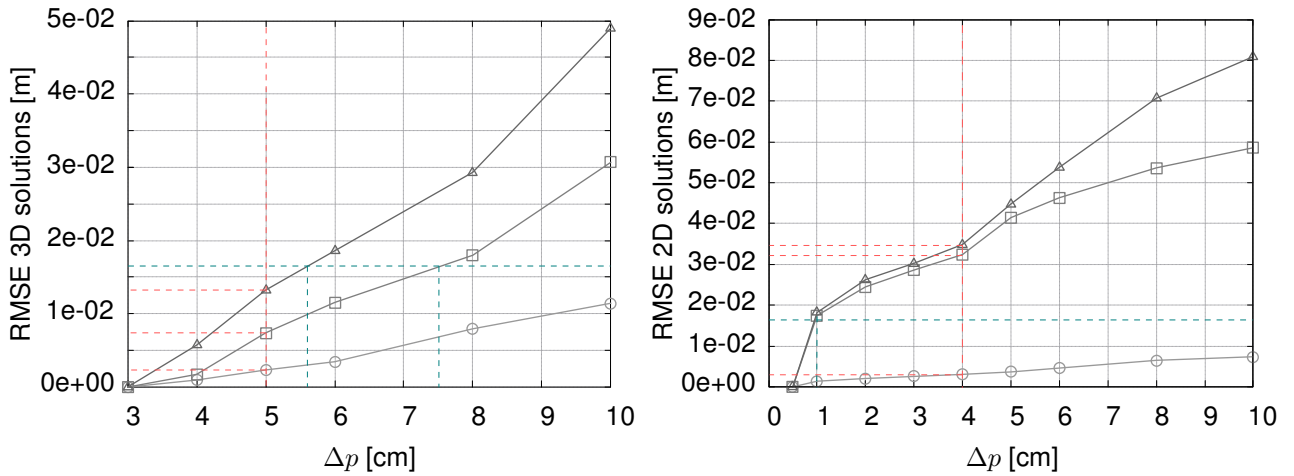
Free-surface along the flume

Figure 5.6 and Figure 5.7 depict the results of the free-surface elevation at WG1, for the unbroken and broken wave cases, respectively. In addition, the $RMSE_T$ metrics are plotted as a function of Δp for the 3D and 2D models, where T is taken as t_{1wave} , t_{2waves} , and t_{final} . From inspection of the graphs, the $e_{5\%}$ is evaluated as 1.6 cm and 7.5 cm for the unbroken and for the broken wave cases, respectively.

For both the unbroken and broken wave cases, the 3D and 2D solutions of the first wave, t_{1wave} , present minimal variations, tending to a numerical convergence at $\Delta p \leq 5 \text{ cm}$, where it can be seen that the maximum $RMSE$ is inferior to 5 mm in the t_{1wave} analysis. Moreover, the 3D and 2D numerical solutions derived from the same Δp present equivalent time-spatial gradients of free surface quantities, which indicate that neglecting the third dimension does leads to negligible errors on flows running on symmetrical configurations. However, such hypothesis is jeopardise after the interactions of the first wave with the elevated structure, where the influence of Δp and the dimensional aspect of the model



(a) Convergence of 3D solutions (left) and 2D solutions (right) assessed for a simulation time corresponding to the first and second waves ($t_{2waves} = 60$ s).



(b) RMSE of 3D solutions (left) and 2D solutions (right) calculated for simulation times corresponding to the first wave ($t_{1wave} = 35$ s), first and second waves ($t_{2waves} = 60$ s) and final ($t_{final} = 100$ s).

KEY:

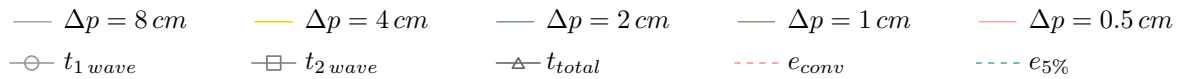
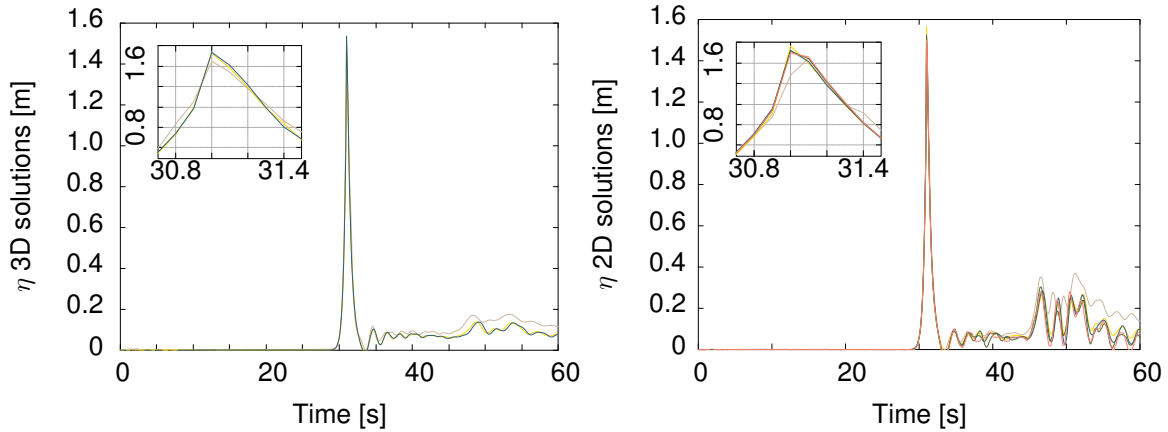
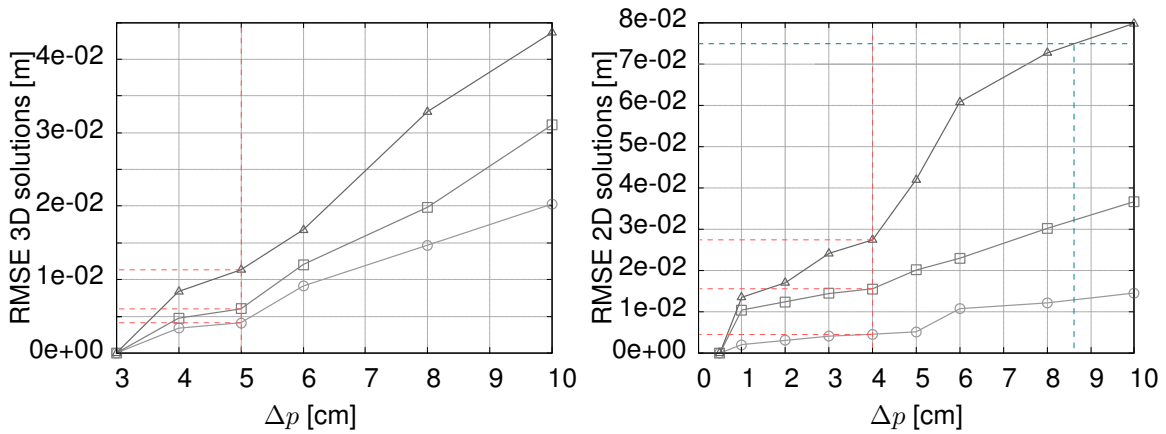


Figure 5.6: Physical and numerical NS-SPH models. Evaluation of free-surface elevation along the flume due to unbroken wave (WG1 sensor): (a) convergence, and (b) RMSE. Left and right subfigures show 3D and 2D results, respectively.



(a) Convergence of 3D solutions (left) and 2D solutions (right) assessed for a simulation time corresponding to the first and second waves ($t_{2waves} = 60$ s).



(b) RMSE of 3D solutions (left) and 2D solutions (right) calculated for simulation times corresponding to the first wave ($t_{1wave} = 35$ s), first and second waves ($t_{2waves} = 60$ s) and final ($t_{final} = 100$ s).

KEY:

— $\Delta p = 8$ cm — $\Delta p = 4$ cm — $\Delta p = 2$ cm — $\Delta p = 1$ cm — $\Delta p = 0.5$ cm
 ○ t_{1wave} □ t_{2wave} △ t_{total} - - - e_{conv} - - - $e_{5\%}$

Figure 5.7: Physical and numerical NS-SPH models. Evaluation of free-surface elevation along the flume due to broken wave (WG1 sensor): (a) convergence, and (b) RMSE. Left and right subfigures show 3D and 2D results, respectively.

become more evident.

For the unbroken wave case, the convergence of 3D and 2D solutions is observed graphically at Δp between 8 cm and 4 cm (Figs. 5.6(a) and 5.7(a)), respectively. Complementary e_{conv} , relating Δp and the error counterpart, and $e_{5\%}$ representing an error threshold value, at the same Δp shows that e_{conv} is below $e_{5\%}$ in the 3D solutions with $\Delta p < 6\text{ cm}$ and 2D solutions considering exclusively $RMSE_{1wave}$. Considering the maximum free-surface elevation of the unbroken wave case, $\eta_{max} = 0.32\text{ m}$, the $\frac{H}{\Delta p}$ ratio is about 7 and 8 respectively for 3D and 2D models, which is less than the 10 particles per height indicated in the literature [260, 331, 387, 420], but a reasonable quantification due to the relatively low complexity of the models.

For the broken wave case, where the maximum free-surface elevation of the wave is $\eta_{max} = 1.50\text{ m}$, and assuming the convergence at the same $\Delta p = 5\text{ cm}$ for the 3D model and $\Delta p = 4\text{ cm}$ for the 2D model, the ratio $\frac{H}{\Delta p}$ increases to 30 and 38, respectively, which corresponds to an increase of about 4.5 times in the number of particles when simulating broken wave versus unbroken wave cases.

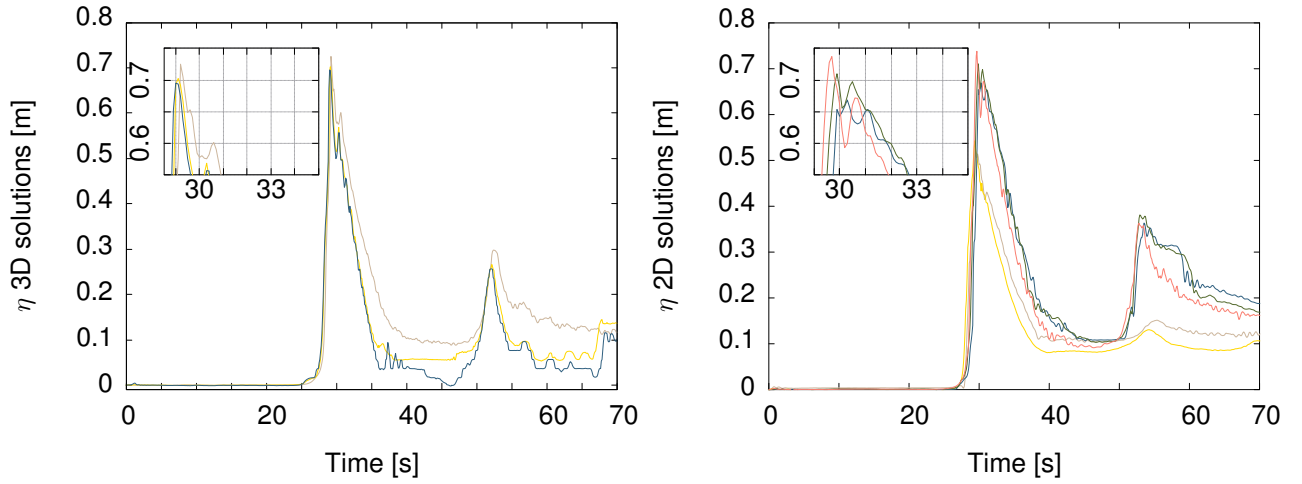
Free-surface near the elevated structure

Figures 5.8 to 5.11 depict the simulation time-series results and $RMSE_T$ of the free-surface elevation results assessed near the elevated structure for the 3D and 2D simulations of the unbroken and broken wave cases. Results are reported for the USWG2 and USWG6, multiple values of Δp , and time intervals t_{1wave} , t_{2waves} , and t_{final} . For the USWG2 location, the $e_{5\%}$ of waves impacting the structure is evaluated as 3.5 cm and 8.5 cm for the unbroken and broken wave cases, respectively, while for the USWG6 location the value of $e_{5\%} = 1.6\text{ cm}$ and $e_{5\%} = 2.5\text{ cm}$.

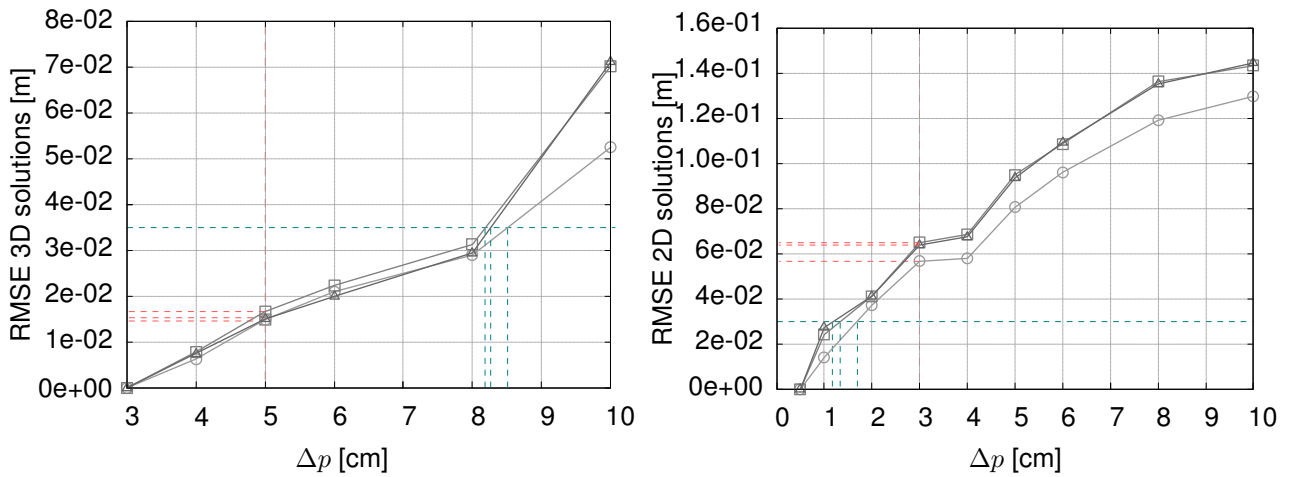
Near the structure, due to highly non-linear phenomena occurring during a tsunami-like wave impacting an elevated structure, the RMSE quantities for intervals t_{1wave} , t_{2waves} and t_{final} , are significantly closer than what was observed for the solutions along the flume. For the unbroken wave cases, the e_{conv} values are similar to results for the WG1 location, but the $e_{5\%}$ analyses show a comparatively quicker degradation of the quality of the solutions, especially in the 2D models (see Figs. 5.8(b) and 5.10(b)). For the broken wave cases, parts of the domain are characterized by higher gradients, where 3D modeling assumptions lead to smaller errors and increased convergence (see Figs. 5.9(b) and 5.11(b)).

The fluid structure interaction impacts the maximum values of Δp that can be used. For the 3D simulations of the unbroken wave cases at USWG2, the $\Delta p = 5\text{ cm}$ discretization is sufficient to ensure the convergence of the solutions while keeping e_{conv} below $e_{5\%}$, leading to a ratio of $\frac{H}{\Delta p} = 14$. For the 2D simulations, the previous $\Delta p = 4\text{ cm}$ for wave propagation at WG1 is insufficient when analysing the fluid interaction with the elevated structure, leading to a $\Delta p = 3\text{ cm}$ and a corresponding ratio $\frac{H}{\Delta p} = 23$. For the free surface elevation due to broken wave that over-tops the elevated structure, the solutions converge but present some numerical diffusion for the 2D solutions, also translated in the error quantification. A $\Delta p = 4\text{ cm}$ for both the 3D and 2D is considered admissible due to the significantly higher wave height, leading to $\frac{H}{\Delta p} = 43$.

The numerical solutions of the free surface elevation at USWG6 show important spurious oscillations



(a) Convergence of 3D solutions (left) and 2D solutions (right) assessed for a simulation time corresponding to the first and second waves ($t_{2waves} = 60 s$).

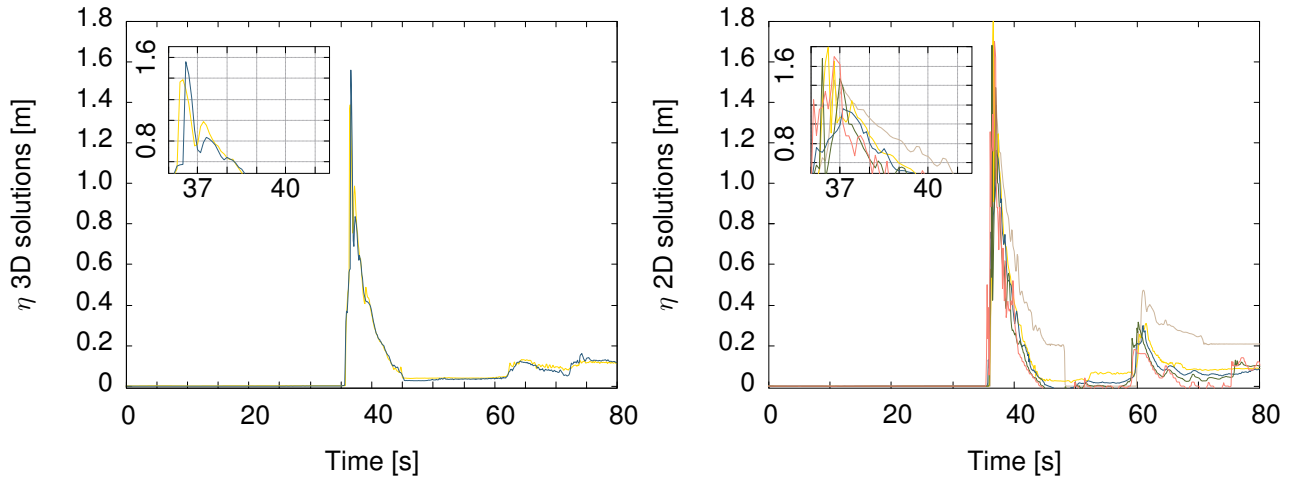


(b) RMSE of 3D solutions (left) and 2D solutions (right) calculated for simulation times corresponding to the first wave ($t_{1wave} = 35 s$), first and second waves ($t_{2waves} = 60 s$) and final ($t_{final} = 100 s$).

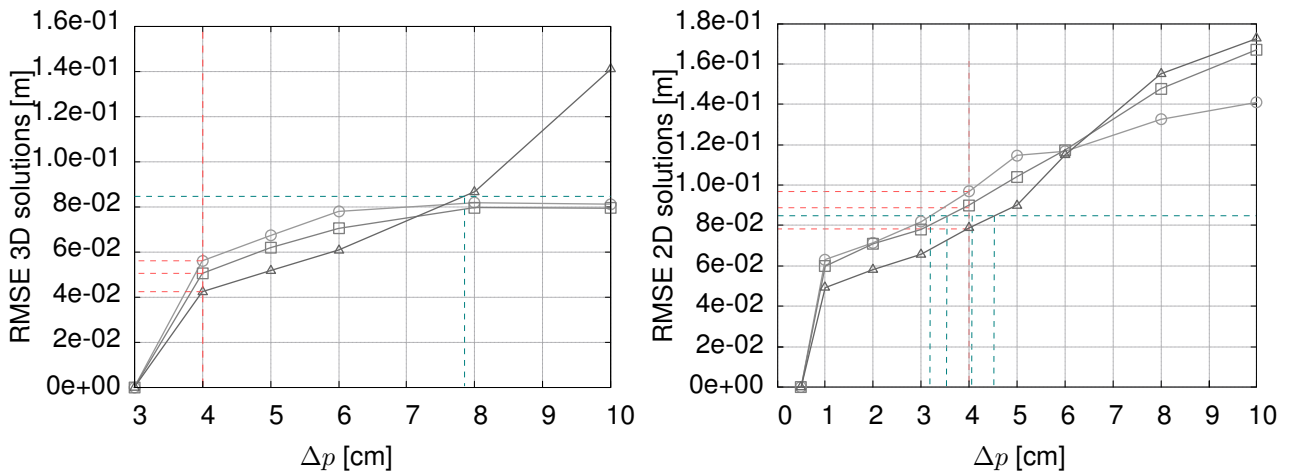
KEY:

- $\Delta p = 8 cm$ — $\Delta p = 4 cm$ — $\Delta p = 2 cm$ — $\Delta p = 1 cm$ — $\Delta p = 0.5 cm$
- $t_{1 wave}$ □ $t_{2 wave}$ △ t_{total} - - - e_{conv} - - - $e_{5\%}$

Figure 5.8: Physical and numerical NS-SPH models. Evaluation of free-surface elevation near the front of the elevated structure due to unbroken wave (USWG2 sensor): (a) convergence, and (b) RMSE. Left and right subfigures show 3D and 2D results, respectively.



(a) Convergence of 3D solutions (left) and 2D solutions (right) assessed for a simulation time corresponding to the first and second waves ($t_{2waves} = 60$ s).

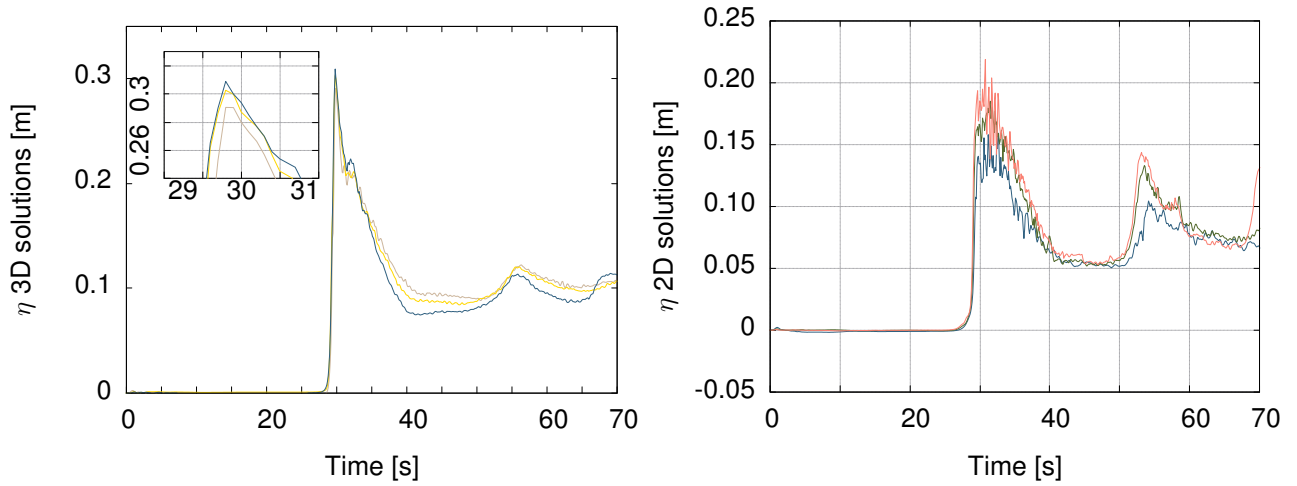


(b) RMSE of 3D solutions (left) and 2D solutions (right) calculated for simulation times corresponding to the first wave ($t_{1wave} = 35$ s), first and second waves ($t_{2waves} = 60$ s) and final ($t_{final} = 100$ s).

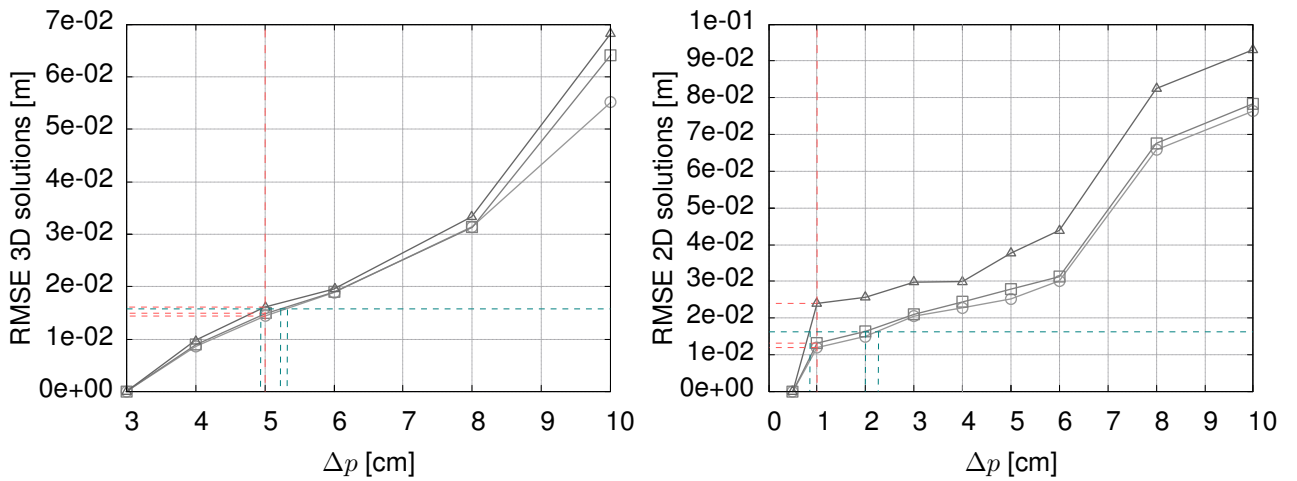
KEY:

- $\Delta p = 8$ cm — $\Delta p = 4$ cm — $\Delta p = 2$ cm — $\Delta p = 1$ cm — $\Delta p = 0.5$ cm
- t_{1wave} □ t_{2wave} △ t_{total} - - - e_{conv} - - - $e_{5\%}$

Figure 5.9: Physical and numerical NS-SPH models. Evaluation of free-surface elevation near the front of the elevated structure due to broken wave (USWG2 sensor): (a) convergence, and (b) RMSE. Left and right subfigures show 3D and 2D results, respectively.



(a) Convergence of 3D solutions (left) and 2D solutions (right) assessed for a simulation time corresponding to the first and second waves ($t_{2waves} = 60$ s).

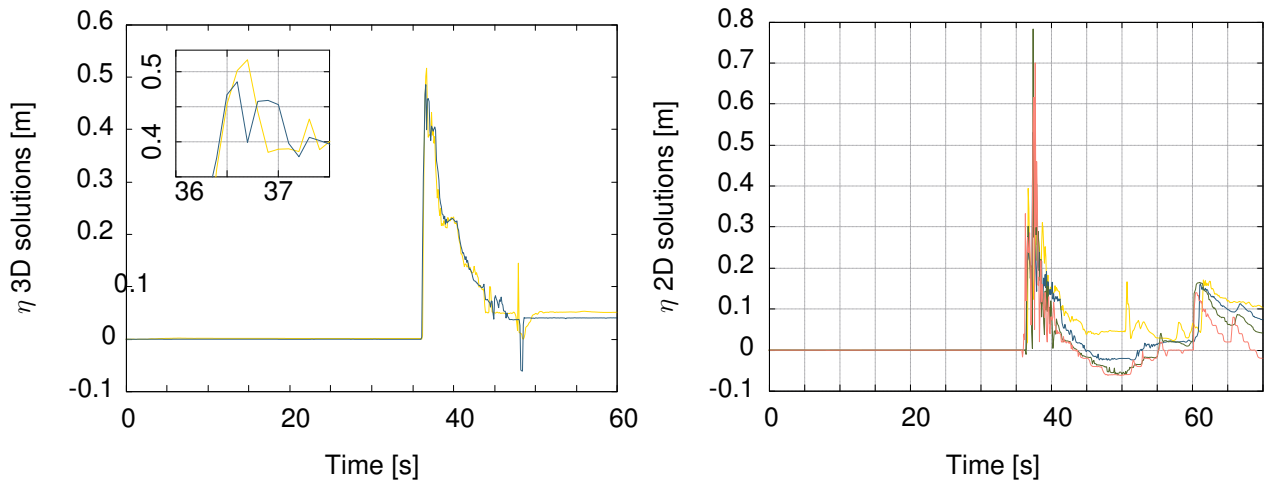


(b) RMSE of 3D solutions (left) and 2D solutions (right) calculated for simulation times corresponding to the first wave ($t_{1wave} = 35$ s), first and second waves ($t_{2waves} = 60$ s) and final ($t_{final} = 100$ s).

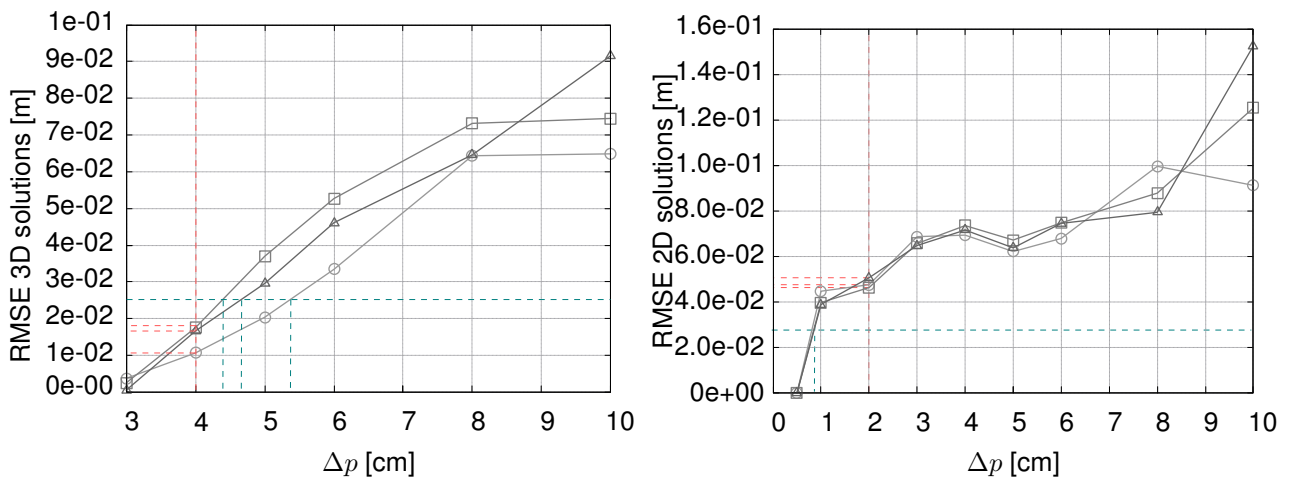
KEY:

- $\Delta p = 8$ cm — $\Delta p = 4$ cm — $\Delta p = 2$ cm — $\Delta p = 1$ cm — $\Delta p = 0.5$ cm
- t_{1wave} □ t_{2wave} △ t_{total} - - - e_{conv} - - - $e_{5\%}$

Figure 5.10: Physical and numerical NS-SPH models. Evaluation of free-surface elevation in the back of the elevated structure due to unbroken wave (USWG6 sensor): (a) convergence, and (b) RMSE. Left and right subfigures show 3D and 2D results, respectively.



(a) Convergence of 3D solutions (left) and 2D solutions (right) assessed for a simulation time corresponding to the first and second waves ($t_{2waves} = 60$ s).



(b) RMSE of 3D solutions (left) and 2D solutions (right) calculated for simulation times corresponding to the first wave ($t_{1wave} = 35$ s), first and second waves ($t_{2waves} = 60$ s) and final ($t_{final} = 100$ s).

KEY:

- $\Delta p = 8$ cm — $\Delta p = 4$ cm — $\Delta p = 2$ cm — $\Delta p = 1$ cm — $\Delta p = 0.5$ cm
- t_{1wave} □ t_{2wave} △ t_{total} - - - e_{conv} - - - $e_{5\%}$

Figure 5.11: Physical and numerical NS-SPH models. Evaluation of free-surface elevation in the back of the elevated structure due to broken wave (USWG6 sensor): (a) convergence, and (b) RMSE. Left and right subfigures show 3D and 2D results, respectively.

for the 2D simulations, constraining a detailed view of the peak of the first wave (Figs. 5.10(a) and 5.11(a)). For the unbroken wave case, despite the RMSE 2D curves tending to horizontal after $\Delta p = 4\text{ cm}$ (Fig. 5.10(b)), the $\Delta p = 1\text{ cm}$ discretization is the one close to the reference solution in Fig. 5.10(a), which leads to $\frac{H}{\Delta p} \approx 30$. The 3D solutions obtained from simulations carried out using $\Delta = 5\text{ cm}$ show a higher peak of the first wave and have RMSE estimates close to $e_{5\%}$, but a clearer convergence of the solutions indicate $\frac{H}{\Delta p} < 10$. For the broken wave case, $\Delta p = 4\text{ cm}$ and $\Delta p = 2\text{ cm}$ discretization of the 3D and 2D modeling respectively lead to 13 and 25 as minimum values for the $\frac{H}{\Delta p}$ ratio. The 3D simulations convergence seems more reliable, providing numerical solutions with e_{conv} below $e_{5\%}$. The RMSE estimates of the 2D solutions (Fig. 5.10(b)) show an inexplicable variability in the curves that is probably induced by the aforementioned oscillations of the numerical solution shown in 2D solutions of Fig. 5.10(a).

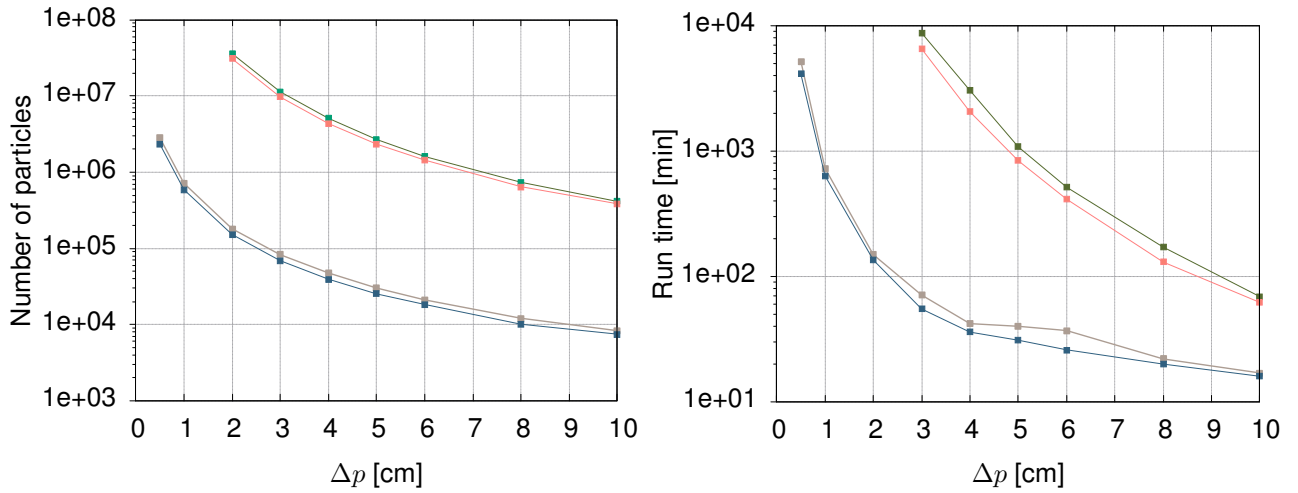
Computational costs

Figure 5.12 shows the influence of Δp discretization in terms of number of particles, run-time, and data storage requirements for the simulations performed in this study. In addition, the bottom right figure shows the log-linear trend between the number of particles in the model and the run-time. While it was shown that clearly the 3D simulations were able to achieve improved accuracy, these are obtained at greatly increased computational costs. For example, in this study, the 2D modeling corresponds to a reduction of 100 times in the number of particles, being on the order of thousands in 2D models and millions in 3D models, representing exponential savings in the time to perform the simulations and amount of data storage needed. In the following section, a physical-numerical correlation is performed with 3D and 2D solutions illustrating the different dichotomy accuracy-demand when adopting the same $\Delta p = 3\text{ cm}$ in 3D and 2D modeling.

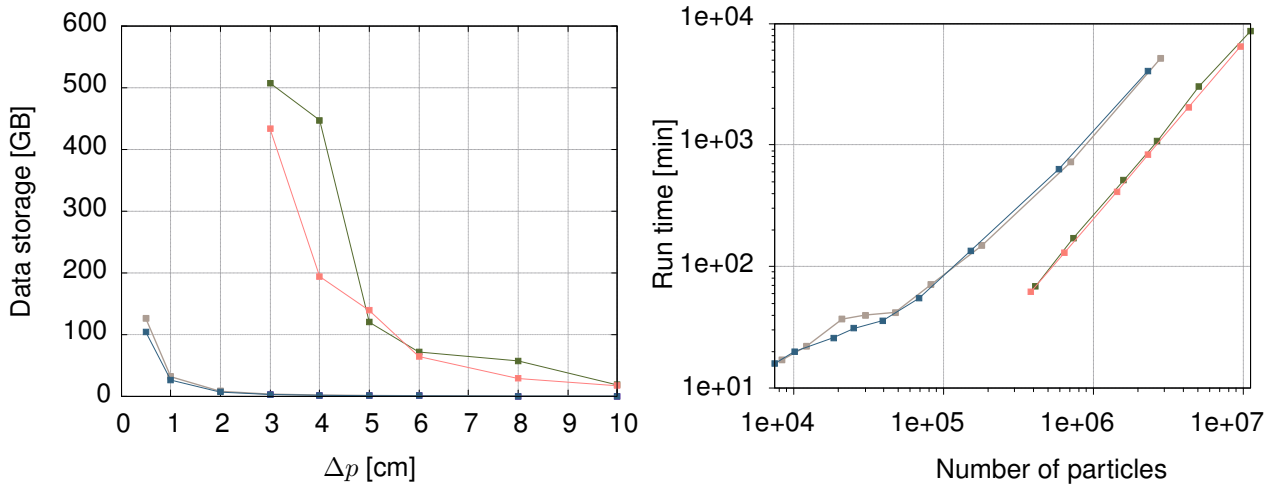
Modeling and calibration remarks

Qualitatively, the numerical convergence was globally verified while quality of the numerical solutions is improved by smaller domain discretization. To model the propagation of tsunami-like waves along a simple bathymetry and assess the peak of the first wave even near the structure, 2D models were deemed sufficient to produce converged solutions, whereas to model tsunami-like flows impacting an elevated structure, the 2D models provide important preliminary information but the 3D models provide complementary detailed information.

Quantitatively (see Table 5.2), the solutions tended to converge approximately at $\Delta p = 3\text{ cm}$, influencing the minimum values required for $\frac{H}{\Delta p}$ and the computational demand for the different cases. For the 3D and 2D models with $\Delta p = 3\text{ cm}$, the numbers of particles were about 11.3 million versus 82.5 thousand, respectively, with the corresponding simulation time equal to 150 hours versus 1.5 hours, and data for storage requirements equal to 500 GB versus less than 4 GB, for each simulation. In terms error metrics, the 3D solutions represent an improvement with respect to the 2D ones in the free-surface elevation after the structure as well as the vertical forces when considering



(a) Influence of the Δp discretization on the number of particles (left) and simulation run-time (right).



(b) Influence of the Δp discretization on the storage space required (left) and ratio relation between the number of particles and the simulation run-time (right).

KEY: ■ 2D unbr-case ■ 2D br-case ■ 3D unbr-case ■ 3D br-case

Figure 5.12: Physical and numerical NS-SPH models. Trade-offs between modeling discretization and computational effort.

Table 5.2: Numerical convergence. Unit: meter.

| VG | Case | η | $e_{5\%}$ | Model | Δp | $\frac{H}{\Delta p}$ | e_{conv} | | |
|-------|------|--------|-----------|-------|------------|----------------------|-------------|--------------|-------------|
| | | | | | | | t_{1wave} | t_{2waves} | t_{total} |
| WG1 | unbr | 0.32 | 1.6E-02 | 2D | 0.04 | 8 | 4.0E-03 | 3.2E-02 | 3.5E-02 |
| | | | | 3D | 0.05 | 7 | 2.5E-03 | 7.5E-03 | 1.5E-02 |
| | br | 1.60 | 7.5E-02 | 2D | 0.04 | 38 | 4.5E-03 | 1.6E-02 | 2.8E-02 |
| | | | | 3D | 0.05 | 30 | 4.5E-03 | 6.0E-03 | 1.2E-02 |
| USWG2 | unbr | 0.70 | 3.5E-02 | 2D | 0.03 | 24 | 5.5E-02 | 6.2E-02 | 6.3E-02 |
| | | | | 3D | 0.05 | 14 | 1.4E-02 | 1.5E-02 | 1.6E-02 |
| | br | 1.70 | 8.5E-02 | 2D | 0.04 | 43 | 8.0E-02 | 9.0E-02 | 9.7E-02 |
| | | | | 3D | 0.04 | 43 | 4.1E-02 | 5.0E-02 | 5.8E-02 |
| USWG6 | unbr | 0.30 | 1.6E-02 | 2D | 0.01 | 30 | 1.3E-02 | 1.4E-02 | 2.2E-02 |
| | | | | 3D | 0.05 | 6 | 1.3E-02 | 1.5E-02 | 6.1E-02 |
| | br | 0.5 | 2.5E-02 | 2D | 0.02 | 25 | 7.0E-02 | 7.4E-02 | 7.6E-02 |
| | | | | 3D | 0.04 | 13 | 2.0E-02 | 2.7E-02 | 2.8E-02 |

$t = 100 s$. For the unbroken wave case, trade-offs between accuracy gains and computational costs indicate that for 2D models with $\frac{H}{\Delta p} \approx 10$ particles are of interest, which is similar to the values proposed in the literature for wave propagation [260, 331, 387, 420]. For the broken wave case, the simulations using different Δp clearly indicated that the use of 2D models with $\frac{H}{\Delta p}$ in the range of 30 to 40 particles and 3D models would represent a reasonably improved solutions. These $\frac{H}{\Delta p}$ values are in line with the values in the literature that report $\frac{H}{\Delta p}$ equal to 36 to 40 for waves impacting a vertical wall [337], 42 when reproducing sea waves interacting with a pier [47], a value of at least 60 when modeling complex hydraulic phenomena of wave over-topping a rubble-mound breakwater [421].

Moreover, for simulations performed by relatively affordable computers, the total time-to-solution, and the computational efforts, in terms of allocated memory and data storage are contributing factors to perform a cost-benefit analysis to determine which Δp discretization is particularly suited for an application. For the benchmarking process, the 3D effects, although more representative near the elevated structure and mostly in the broken wave case, were considered negligible due to the symmetric nature of the setup. The 2D models computed with $\Delta p = 0.03 m$, which represents a $H/\Delta p = 23$, for the unbroken wave case, and $H/\Delta p = 43$, for the broken wave case, was deemed sufficient to yield converged solutions and results with a reasonable discrepancy between peak values.

5.2.2 SW-FV model

The second modeling configuration adopted uses the Eulerian FV method to solve the non-linear SW equations, as introduced in Chapter 3, 3.2.2. The set of simulations was carried out on a laptop with an AMD Ryzen5 2500U @1.8GHz CPU using around 27000 cells. The code to solve the SW equations uses a second-order approximation in space, with well-balanced fluxes, and the second-order Heun scheme in time [19, 21]. A parametric study on the refinement of the structured mesh was performed using different cell sizes. For the benchmark simulations, $\Delta x = 0.12 m$ and $\Delta y = 0.15 m$, in x -direction and y -direction, respectively. An additional parametric study considering the limiting

techniques was performed showing overlying curves, with minor differences between them when varying the MUSCL, minmod and van Leer, and MOOD techniques. The latter was selected to compute the numerical solutions for the benchmarking process. The simulation time is $t_f = 150\text{ s}$ with time-steps around $\Delta t = 0.01\text{ s}$ controlled by a $CFL = 0.45$ to guarantee the numerical stability. Due to the inherent limitation of the present FV discretization to deal with variable domains in time, the initial condition is prescribed by a TBC, at $x = 2\text{ m}$, using hydrodynamic quantities computed by SPH.

5.2.3 Coupled model

The third modeling configuration adopted aims to provide an efficient, yet simple and low-cost, alternative configuration to perform the simulation. Considering the simplified, but fast nature of SW-FV and the sophisticated, but computationally demanding, nature of NS-SPH, this configuration uses the inherent characteristics and boundary conditions of each scheme to perform the simulation, as introduced in Chapter 3, 3.2.3. To avoid the piston-type wave generation, the left-most Eulerian SW-FV part of the simulation is initiated by a TBC prescribed using time-histories captured in the Lagrangian NS-SPH simulation, at $x = 2\text{ m}$. The simulation of the area where the structure is implemented is performed by the Lagrangian NS-SPH, initiated by an OBC prescribed using time-histories captured in the Eulerian SW-FV simulation, at $x = 36\text{ m}$.

An additional verification regarding the source feeding the Dirichlet boundary condition was carried out to assess the influence of introducing BC, as referred in Section 4.2.2. Different time-histories of flow height and velocity were adopted to prescribe an OBC at $x = 13\text{ m}$. The first used the NS-SPH numerical solution, aiming to assess the influence of introducing a OBC by comparing a fully and two-partial SPH solutions, while the second and third respectively used instrumentally-recorded data from WG1 and ADV1, and the hydrodynamic quantities of the SW-FV solutions. The latter two aimed to assess the influence of the data used to prescribe the initial conditions on the quality of the numerical solutions. The analysis was developed using solutions of free surface elevation in the flume, WG2, near the structure, USWG1, and after the structure, USWG5. The correlation between the various solutions is detailed in Appendix B, showing that, as expected, the physical hydrodynamic quantities used to establish the boundary conditions and the number of interpolations in the form of Dirichlet BC influence the quality of the solution.

5.3 Physical-numerical correlation study

The mean value and standard deviation of the physical data recorded in the experimental campaign are used to draw correlations between the numerical simulation results and their experimental counterparts.

Considering the large amount of data involved, only one record of each type of measure, including USGW6 and ADV7, for water elevation and flow velocity, respectively. In addition, the stream-wise force was measured by load cell LC5, while the total vertical forces were measured as the sum of

forces measured by LC6 to LC9 sensors and these are used for correlation of the numerically obtained horizontal and vertical forces with the experimental results. Horizontal and vertical pressures are also compared for PG4 and PG11 sensors and corresponding locations, respectively.

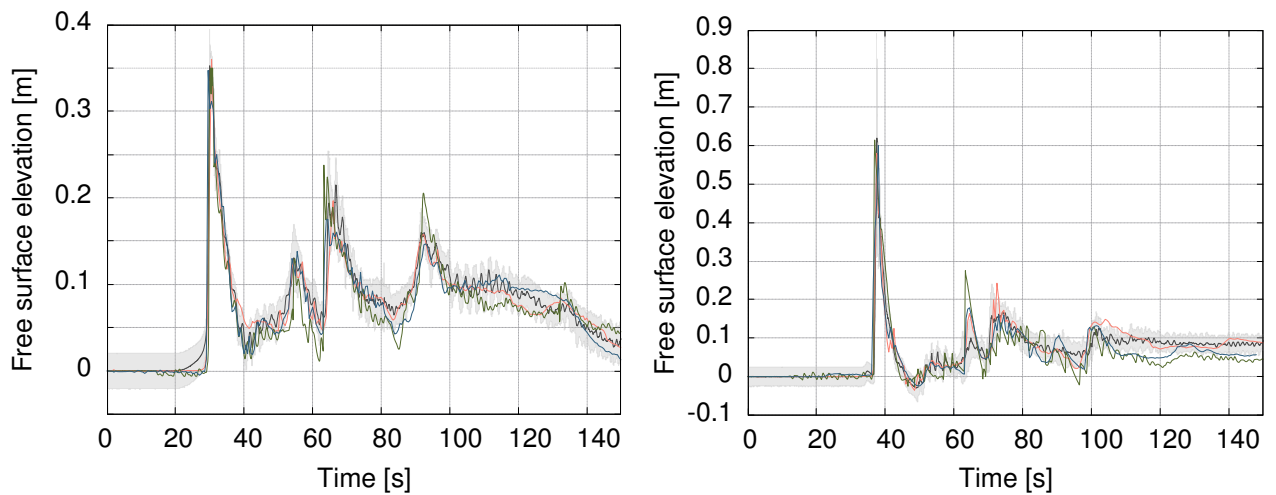
Results are shown for the unbroken and broken wave cases including a comparison of water elevation, flow velocity, horizontal and vertical forces and pressures exerted on the elevated structure, where the colourful curves represent the numerical solutions and the black lines represent the mean laboratorial data complemented by standard deviation of the the physical data derived from the trials that composed the experimental campaign, represented in shaded grey and identified as “Error”. The vertical forces and pressures, in both unbroken and broken wave cases, are exclusively characterized by Lagrangian NS-SPH scheme (i.e. first and third numerical configurations) due to the depth-averaged nature of the SW-FV scheme, which limits the assessment of the hydrodynamic quantities to supply the analytical formulation as suggested by the North American ASCE code.

5.3.1 Hydrodynamic quantities

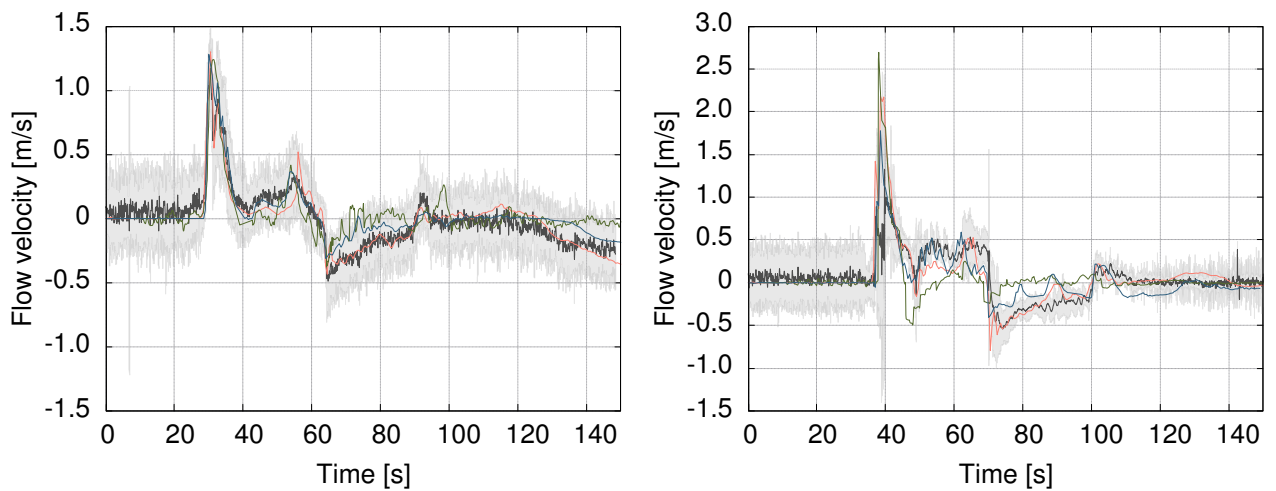
Figure 5.13 depicts the experimental data and data from the numerical solutions for the free-surface elevation and flow velocity after the structure for the unbroken and broken wave cases.

From a qualitative perspective, the time series of the numerical solutions fit the mean value and standard deviation of the physical data curves in most representations of Fig. 5.13. As expected, among the experimental-numerical data correlation the NS-SPH approach is associated with the numerical solutions with better accuracy, while the SW-FV approach provides the smoother solutions and shows the inherent limitations to reproduce some phenomena, such as the characterization of vertical geometries, i.e., the elevated structure is interpreted as a full obstacle to the flow whereas NS-SPH can mimic the partial obstacle of an elevated structure. The coupled Eulerian-Lagrangian modeling configuration provides numerical solutions with intermediate quality. The SW-FV scheme in the first part of the modeling configuration influences the overall quality of the solutions, capturing well the first peak, but not as well secondary peaks, mainly for the broken-wave case which involves highly non-linear phenomena. Nonetheless, from an overall appreciation of the modeling assumptions, the 2D modeling configurations with the numerical parameters calibrated in Sections 5.2.1 to 5.2.3 demonstrate their ability to generically reproduce the hydrodynamic quantities involved in the experimental setup.

From a quantitative perspective, a most conservative criterion is adopted to evaluate the fitting of the curves, considering exclusively the comparison between mean values of the recorded laboratorial data and the corresponding numerical solution for the total simulation time. The percentage of fitting discrepancy of the different experiment to numerical result correlations is set to the average percentage of the comparison between 300 points (time-steps of 0.5 s) and is calculated using the root mean square error approach. Table 5.3 lists the average fitting disagreement of the numerical solutions regarding the hydrodynamic quantities. In the absence of other numerical validation criteria, the adequacy of the models is based on the reference value for the validation of tsunami inundation models, which require



(a) Free surface elevation after the elevated structure, USWG6, for unbroken (left) and broken wave (right) cases.



(b) Flow velocity after the elevated structure, ADV7, for unbroken (left) and broken wave (right) cases.

KEY: — Recorded — NS-SPH — SW-FV — Coupled

Figure 5.13: Physical benchmarking. Correlation between the mean \pm standard deviation (error) laboratorial data and the numerical solution obtained using the Lagrangian NS-SPH, Eulerian SW-FV and coupled Eulerian–Lagrangian modeling configurations.

Table 5.3: Physical benchmarking. Average disagreement between recorded physical quantities and numerical solutions of hydrodynamic quantities.

| Simulation | | NS-SPH | SW-FV | Coupled |
|------------|------|--------------------------|-------|---------|
| Sensor | Case | Fitting disagreement [%] | | |
| USWG6 | unbr | 2.50 | 4.62 | 3.57 |
| | br | 2.04 | 4.75 | 3.94 |
| ADV7 | unbr | 7.73 | 10.48 | 9.27 |
| | br | 8.99 | 10.93 | 9.98 |

deviations below 10% [226, 422], which is verified in both wave cases.

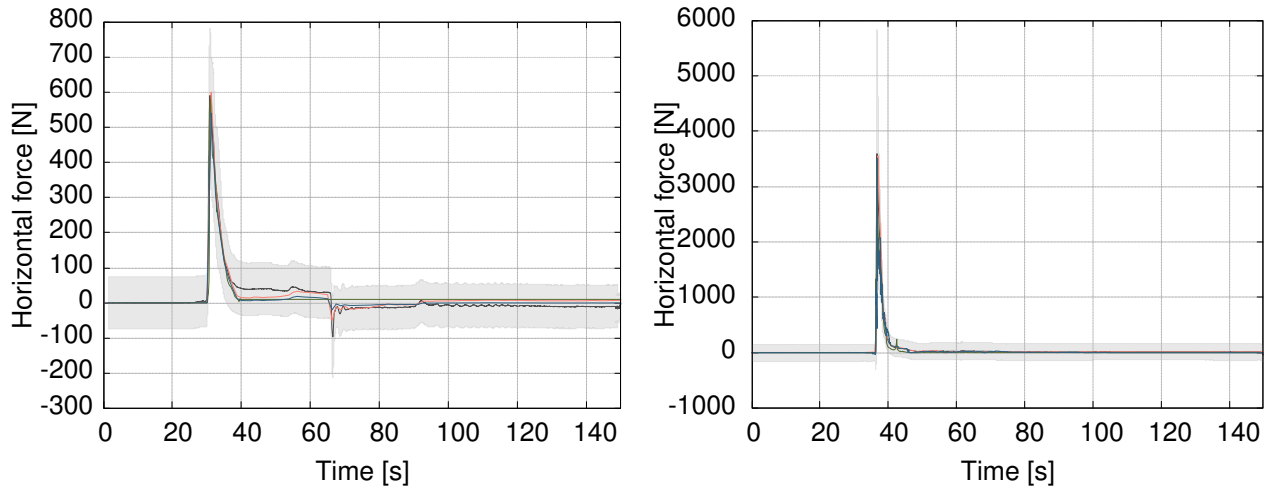
5.3.2 Fluid-structure interaction

Figures 5.14 and 5.15 depict the experimental data and data from the numerical solutions for forces and pressures exerted on the elevated structure in both horizontal and vertical directions for the unbroken and broken wave cases.

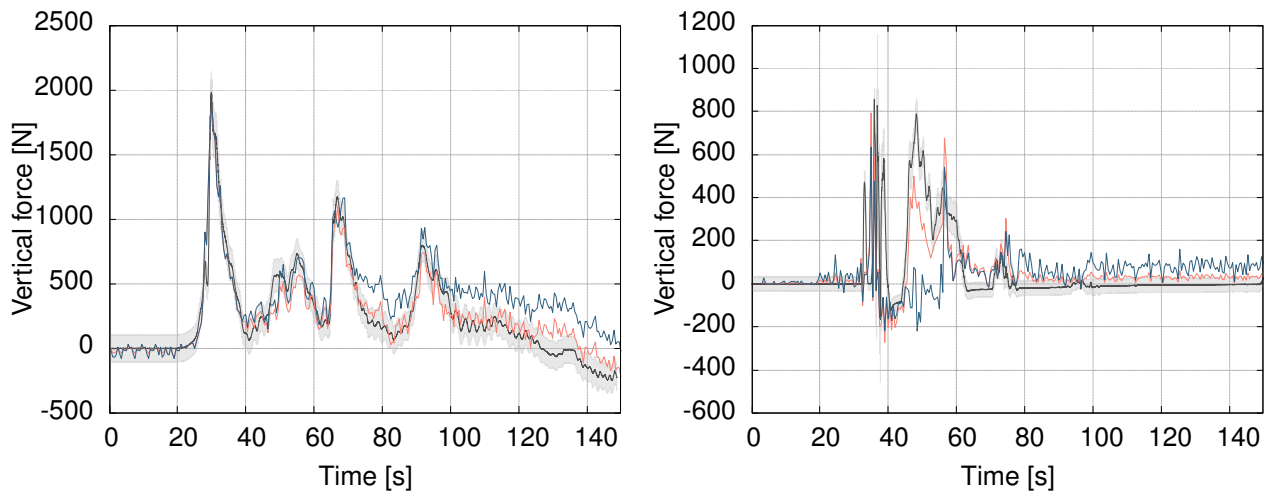
From a qualitative perspective, the NS-SPH is capable of providing the better characterization of forces and pressures, while the SW-FV approach provides the smoother solutions and it is not yielding results for the assessment of vertical force/pressure. Capturing the vertical force induced by the broken wave proved the most challenging task, involving bore-like hydraulic phenomena and non-free surface, where a multi-phase air–water algorithm could possibly represent the difference in the accuracy of the solutions. From an overall appreciation of the modeling assumptions, the 2D modeling configurations with the numerical parameters calibrated in Sections 5.2.1 to 5.2.3 demonstrate their ability to reproduce horizontal forces and pressures exerted on the elevated structure. In the vertical direction, the coupled scheme reasonably predicts vertical force and pressure induced by an unbroken wave, but the inherent nature of SW feeding the OBC is deemed insufficient for the characterization of these quantities in the broken wave case.

The quantitative appreciation, resumed in Table 5.4 reiterates the qualitative observations. The fitting between recorded and numerical data regarding vertical force LC69 exceeds the percentage considered admissible. The the vertical pressure in PG11 for the unbroken wave case is close to the admissible upper limit while presenting a good fitting percentage for the broken wave case due to the shape of the curve, null until an accentuated peak around 40 *s* followed by an almost null value for the remain time of simulation.

Nonetheless, the average fitting estimates tend to normalize the error in time and, possibly, in spatial distribution. Thus, a complementary correlation including 3D models were performed to evaluate in more detail the characterization of pressures exerted on the elevated structure, in both horizontal and vertical directions. For the unbroken wave case, the 3D model consists of more than 11.3 million particles, whereas the 2D model consists of approximately 82.5 thousand particles. For the broken wave case, the 3D model has a total close to 9.7 million particles, and the 2D model has around 69 thousand particles. The numerical results of maximum pressures in the horizontal and vertical directions are



(a) Horizontal force exerted on the elevated structure, LC5, for unbroken (left) and broken wave (right) cases.



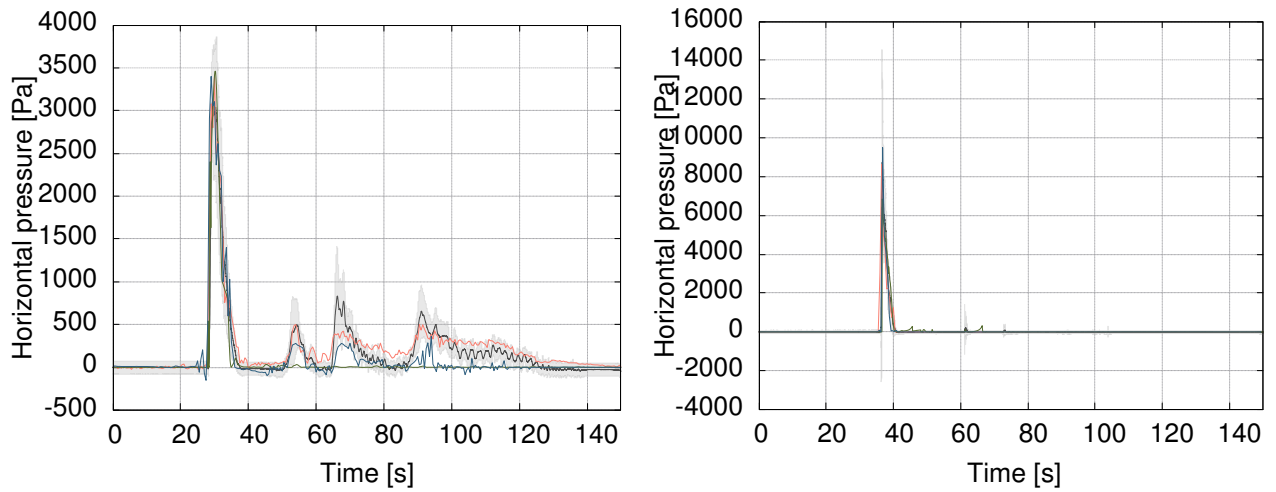
(b) Vertical force exerted on the elevated structure, LC69, for unbroken (left) and broken wave (right) cases.

KEY: — Recorded — NS-SPH — SW-FV — Coupled

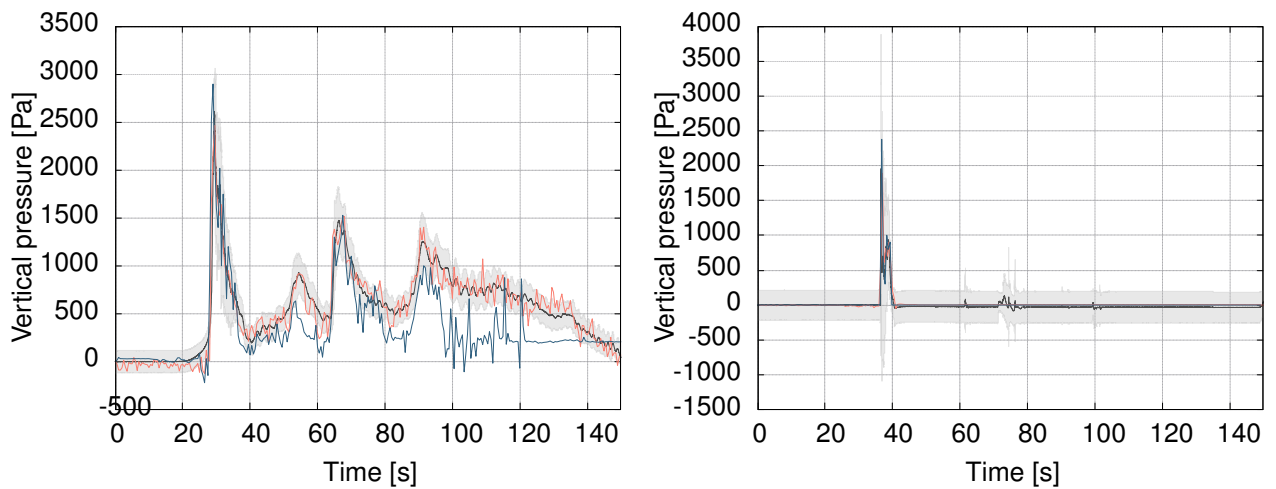
Figure 5.14: Physical benchmarking. Correlation between the mean \pm standard deviation (error) laboratorial data and the numerical solution obtained using the Lagrangian NS-SPH, Eulerian SW-FV and coupled Eulerian–Lagrangian modeling configurations.

Table 5.4: Physical benchmarking. Average disagreement between recorded physical quantities and numerical solutions of forces and pressures exerted on the elevated structure.

| Simulation | | NS-SPH | SW-FV | Coupled |
|------------|------|--------------------------|-------|---------|
| Sensor | Case | Fitting disagreement [%] | | |
| LC5 | unbr | 1.87 | 3.20 | 1.80 |
| | br | 1.50 | 1.68 | 0.72 |
| LC6-9 | unbr | 4.25 | - | 10.54 |
| | br | 9.02 | - | 23.27 |
| PG4 | unbr | 2.88 | 4.01 | 3.65 |
| | br | 0.98 | 0.73 | 1.22 |
| PG11 | unbr | 3.65 | - | 9.69 |
| | br | 1.88 | - | 2.08 |



(a) Horizontal pressure exerted on the elevated structure, PG4, for unbroken (left) and broken wave (right) cases.



(b) Vertical force exerted on the elevated structure, LC69, for unbroken (left) and broken wave (right) cases.

KEY: — Recorded — NS-SPH — SW-FV — Coupled

Figure 5.15: Physical benchmarking. Correlation between the mean \pm standard deviation (error) laboratorial data and the numerical solution obtained using the Lagrangian NS-SPH, Eulerian SW-FV and coupled Eulerian–Lagrangian modeling configurations.

compared with analytical expressions proposed by [168] for the maximum pressures obtained in the experimental program.

The analytical expressions are based on a multiple linear regression with interaction effects. The analytical expressions for the horizontal and vertical directions are given in Eqs. 5.2 and 5.3, respectively:

$$\frac{p(y, z)}{\rho g h_w} = \beta_{0,h} + \beta_{1,h} \frac{y}{b} + \beta_{2,h} \frac{z}{h} + \beta_{3,h} \frac{yz}{bh} \quad (5.2)$$

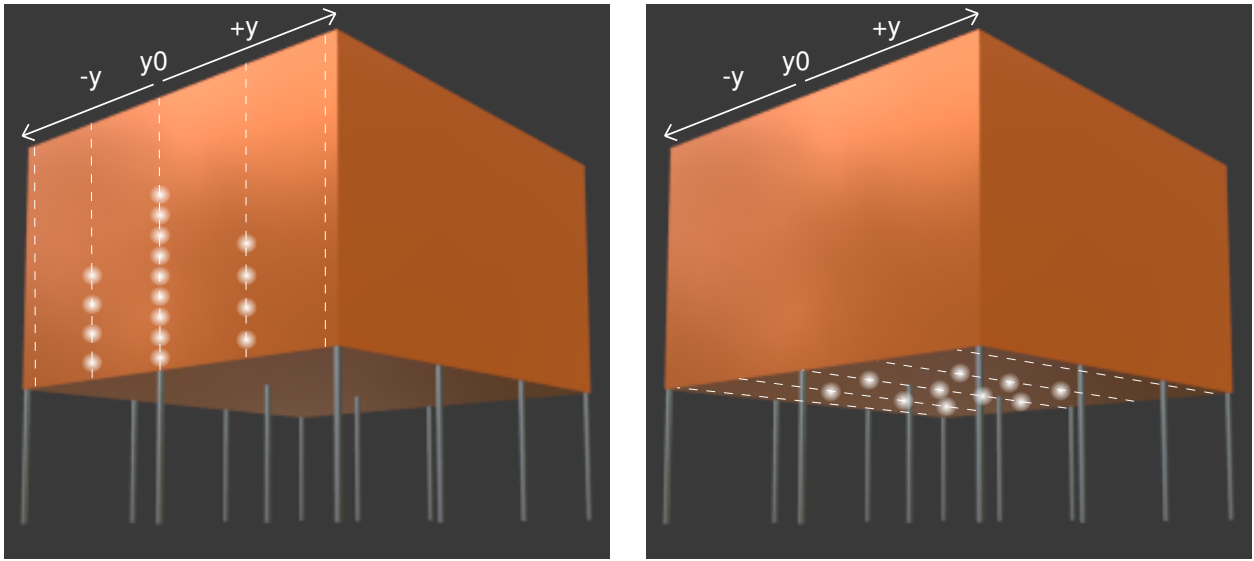
where h_w is the mean free-surface elevation, y and b are the horizontal local axis along the specimen in the transverse and perpendicular direction of the flow, and z along the vertical direction; h is the height of the specimen. The multiple linear regression coefficients of the surface to maximum pressure data are $\beta_{0,h} = 0.739$, $\beta_{1,h} = -0.003$, $\beta_{2,h} = -1.347$ and $\beta_{3,h} = -0.014$, for the unbroken wave case, and $\beta_{0,h} = 0.779$, $\beta_{1,h} = -0.046$, $\beta_{2,h} = -0.217$ and $\beta_{3,h} = -0.003$, for the broken wave case. The values of h_w values are 0.55 m and 1.30 m respectively for the unbroken and broken wave cases.

$$\frac{p(y, x)}{\rho g h_w} = \beta_{0,v} + \beta_{1,v} \frac{y}{b} + \beta_{2,v} \frac{x}{w} + \beta_{3,v} \frac{yx}{bw} \quad (5.3)$$

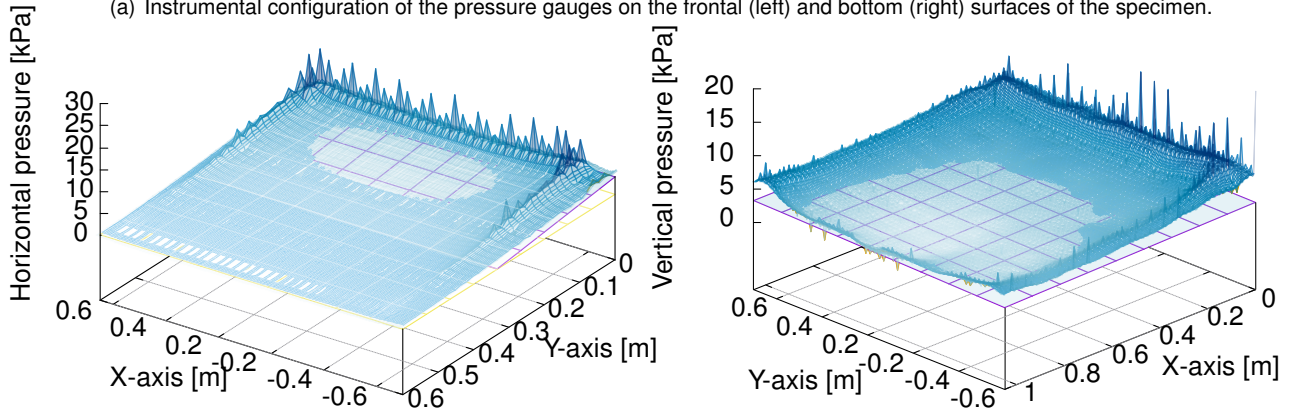
where the multiple linear regression coefficients assume values of $\beta_{0,v} = 0.624$, $\beta_{1,v} = -0.069$, $\beta_{2,v} = -0.083$ and $\beta_{3,v} = -0.123$, for the unbroken wave case, and $\beta_{0,v} = 1.528$, $\beta_{1,v} = -0.168$, $\beta_{2,v} = -1.072$ and $\beta_{3,v} = 0.447$, for the broken wave case. The values of h_w values are 0.48 m and 0.95 m respectively for the unbroken and broken wave cases. Note that there are slight variations in some of the parameters when compared to the model in [168] since slight errors were identified by the second author following the publication of [168].

Fig. 5.16 depicts the correlation between the maximum pressure obtained numerically for the model with $\Delta p = 3 \text{ cm}$, calculated for points located at a distance of 0.01 m apart, where pressure gauges were located in the experimental setup. The correlation between analytical and numerical results show good agreement for pressures on both the horizontal and vertical directions at the middle portions of the front and soffit of the specimen, respectively; while the slightly asymmetrical distribution of pressures seen in the analytical expressions is also captured numerically. However, the SPH solutions near the edges of the of the front and bottom faces are notable, particularly near the edges of the front face of the structure that is first impacted by the bore, due to small nonphysical gap between the fluid and solid boundaries, affecting the accuracy of pressures measured on the boundary. Recent functionalities, such as modified dynamic boundary conditions, help to remove the pressure noise at the boundary and allow calculating pressures without the spikes, yet it would imply additional computational costs. Depending on the number and distribution of particles in the interface between solid and fluid, the execution time may increase up to 25% due to extra interpolation carried on the ghost nodes projected from the boundary particles into the fluid domain [329], which would fail to address the goal of SPH modeling optimization for simulations performed by relatively affordable computers.

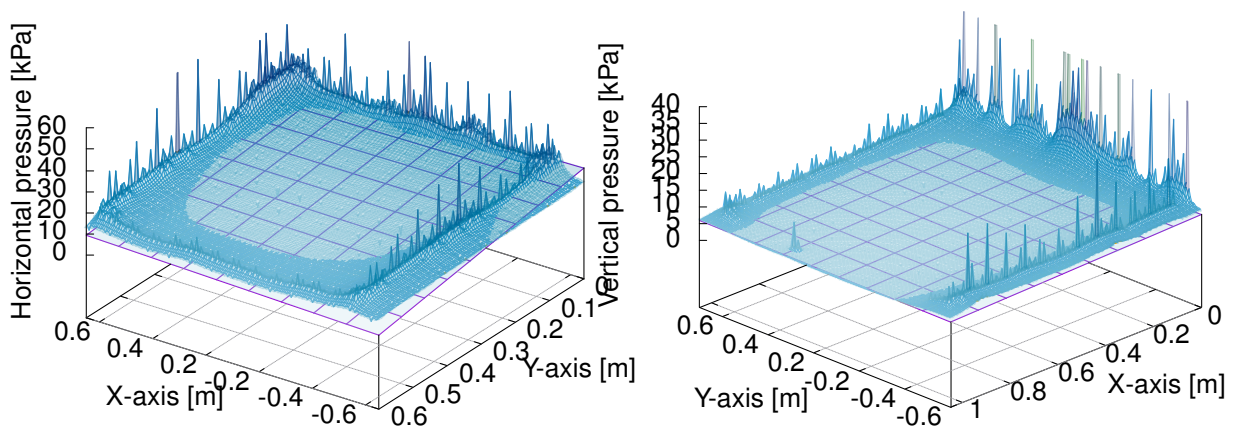
There can be various reasons for notable differences observed in analytical and numerical solutions shown in Fig. 5.16. On the one hand, the analytical expressions were derived using pressure gauges



(a) Instrumental configuration of the pressure gauges on the frontal (left) and bottom (right) surfaces of the specimen.



(b) Distribution of the maximum horizontal (left) and vertical (right) pressures exerted on the frontal surface of the elevated structure, for unbroken case.



(c) Distribution of the vertical pressure exerted on the soffit of the elevated structure, for unbroken (left) and broken wave (right) cases.

KEY: — Recorded — NS-SPH — SW-FV — Coupled

Figure 5.16: Physical benchmarking. Correlation between the analytical and the numerical solution obtained using the Lagrangian NS-SPH model.

installed during the experiments, which did not include any sensors near edges or corners, except a central one at the near the bottom edge of the front face (see Fig. 5.16(a)), which means that the multi-linear regression does not model experimental values at those locations. On the other hand, the numerical solutions of the maximum pressures show significant spikes, particularly near corners and edges of the front and bottom face. These spikes are related to the need in the SPH method in definition of an artificial viscosity to treat these spurious pressure fluctuations [245, 423]. However the lack of experimental data limits the validation that can be performed and indicates that future experimental programs should include a denser array of pressure gauges to capture better the actual physical pressure measurements near corners and edges of the front and bottom face of the structure. Lastly, another possible reason for the discrepancy between analytical and numerical solutions is related to the adequacy of $\frac{H}{\Delta p}$ ratio recommended based on the convergence study performed in Section 5.2.1.

The horizontal and vertical pressure distribution in three different slices of the specimen (0.3 m apart in the y -direction as depicted in Fig. 5.16(a)) show the asymmetry of pressure distributions observed in the experimental data and analytical model. In the horizontal direction, the numerical solutions at $y = 0\text{ m}$ and $y \pm 0.3\text{ m}$ are relatively in agreement with the indicative analytical solution, showing that the $\frac{H}{\Delta p}$ ratio recommended based on the convergence study of the free-surface elevation is adequate to also characterize horizontal pressure quantities, whereas in the vertical direction, the selected $\frac{H}{\Delta p}$ is leading to larger differences between the numerical and analytical models.

This correlation of the numerical solutions with the experimental and analytical solutions is representative of the inherent limitations of weakly-compressive SPH method and its application in this study. The first limitation of the work is related to the limitations of the SPH method in treating contact discontinuities. However, even though some smoothing algorithms exist which limit could limit the spikiness of the pressure simulation results shown, limited data exists to validate wave induced pressures, especially closest to the edges and corners of the elevated structure. The second limitation of the work performed is related to the modeling of the water only and not the multi-phase air-water interface and flow modeling, which may also contribute to the discrepancies shown, especially in the vertical direction [258, 323]. Multi-phase (air-water) modeling requires a multi-phase air-water algorithm handling the discontinuity of some physical proprieties (such as density, sound speed, etc.). Such a multi-phase algorithm for treatment of the air-water interface was recently implemented in DualSPHysics; however, the modeling complexity and costs grow exponentially and such modeling options will be evaluated in the future but resorting to large supercomputers and data storage capabilities.

Overall, it is worth noting that even with the discrepancies observed in peak pressures and despite the lack of further refinements in the discretization and multi-phase modeling of the non-free surface of the fluid impacting the bottom of the elevated structure, the characterization of the peak forces showed good agreement with the experimental data for the tsunami-like wave loading studied herein, especially since the first wave impact controlled the force responses.

5.4 Remarks

The experimental-numerical data correlation demonstrated that NS-SPH approach is associated with the numerical solutions with better accuracy, while the SW-FV approach provides the smoother solutions and shows the inherent limitations to reproduce some phenomena, such as the characterization of vertical velocities (due to the SW simplification), not yielding results for the assessment of force/pressure in the vertical direction. The coupled Eulerian-Lagrangian modeling configuration provides numerical solutions with intermediate quality. The SW-FV scheme in the first part of the modeling configuration influences the overall quality of the solutions, capturing well the peak, but not as well secondary peaks.

The interpretation of the results are based on the intrinsic characteristics of the governing equations and numerical schemes. Due to the nature of the governing equations, the SW equations are an averaging approach of the NS equations with respect to the vertical coordinate, neglecting the viscosity effects. It is also worth mentioning that the SW finite volume code used here suffers from the limitation of disregarding the breaking wave in shallow water domain. Such a wave behavior frequently occurring when approaching the shoreline could have a great importance in assessing the impact of long-wave phenomena (i.e, storm and tsunami) on coastal structures [248]. Moreover, the hyperbolic SW system presents some shock waves corresponding to breaking waves that are hardly reproduced by the model. For gravitational waves meeting the SW assumption, such a dissipation is quite low and the non-dissipative SW-FV system is eligible. On the other hand, turbulent flows require a large amount of viscous dissipation that cannot be directly produced using SW equations unless additional dissipation terms are introduced in the SW-FV tool, as the one used in the present benchmarking process, making possible the correct assessment of the flow behavior. On the contrary, the NS-SPH approach considers an empirical artificial viscosity term in its formulation, enabling the reproduction of the hydrodynamic effects, but the scheme tends to produce extra numerical diffusion that may be translated in a discrete overestimation of the physical viscosity.

The numerical treatment of the elevated structure is constrained by the nature of Eulerian and Lagrangian methods. In the experimental three-dimensional (3D) setup, the structure is a partial occlusive obstacle corresponding to an elevated specimen, which allows water to flow under and around it, but in which, due to symmetry, the lateral flow has a negligible effect. In the 2D numerical models, the fluid is prevented from flowing around the structure, leading to slight over predictions of the quantities of interest, when compared to the range of the experimentally recorded data. The FV method, considering the structure as a z -elevation of a solid, assumes the structure to be a full obstacle with no space for the fluid to flow underneath, increasing the dam effect. Less mass flow crossing the obstacle leads to an increase of reflected and retained fluid, respectively before and after the structure. The velocity profile is thus slightly reduced but with sharper shocks, higher amplitude and shorter duration. These observations are in accordance with the well-known feature of FV to treat simple free-surfaces with no breaking waves. On the contrary, the NS-SPH scheme models the space between the elevated structure and the flume based and walls into account, enabling the fluid to flow out numerically. This demonstrates the capacity of the NS-SPH model to reproduce the full geometry of

the structure, reinforcing the acknowledgment of its adequacy to treat more complex free-surfaces and interaction with solids.

The solutions are also affected by the complexity of the modeling configuration, measured in terms of prescribed boundary conditions. Despite the complementary function of Lagrangian scheme to initiate characteristically fixed-domain in Eulerian simulation, each transition from one model to another adds some deviations and an accumulation of numerical approximations, reducing the overall accuracy of the solution. The velocity in the vertical direction is exclusively quantified by the Lagrangian approach, i.e. the time series used to prescribe Dirichlet boundary condition in the different domains account exclusively for the free surface position and horizontal velocity.

Besides the intrinsic constraints posed by the nature of the numerical schemes influencing the quality of the final solutions, the characterization of force and pressure is also influenced by the numerical approach adopted to quantify them, built-in computation using NS-SPH scheme or analytic formulation using the hydrodynamic quantities computed by Eulerian SW-FV scheme. The latter Eulerian SW-FV approach introduces additional approximations in the quantification of force and pressure quantities due to (1) the semi-empirical nature of the hydrodynamic equation with the C_d value calibrated to match the peak value of the first wave, neglecting the time-dependency of C_d at leads to an under-estimation of the quantities after the first wave and (2) the position of the virtual gauges where the hydrodynamic quantities are measure is relocated for the cell that immediately precedes the one on which the fluid impacts the solid, to avoid the limitation of Eulerian SW-FV scheme to deal with fluids interacting with solids. Depending on the mesh discretization, such procedure can represent a difference of some centimeters with respect to the position occupied by the instruments in the experimental setup, representing additional uncertainty in the quantification of forces/pressures exerted on the structure.

Despite the enhanced performance of NS-SPH approach, the calibration and convergence of solutions depend on modeling assumptions and are sensitive to user-defined parameters [245]. Moreover, computational costs and low convergence rates still constitute drawbacks of the SPH method when compared to less demanding mesh-based methods [48, 245, 246]. A trade-offs between the quality of the solutions and the computational costs is useful to assume modeling approaches to explore the NS-SPH potential to solve complex hydraulic phenomena and fluid-structure interactions, as long as keeping in mind that $\frac{H}{\Delta p}$ relations are a function of the flow regime and complexity of the hydraulic phenomena being simulated. Depending on the importance of the infrastructure, additional multi-phase air-water interface and modified dynamic boundary conditions can potentially increase the accuracy of the pressure numerical solutions yet compromising computational costs.

Finally, numerical results can complement the results obtained from experimental studies. This work highlights that additional instruments should be placed at strategic locations in future experimental programs to further validate local numerical responses, such as pressures near the edges and corners of structures. Details of pressure distributions are especially important if numerical models are to be used in the validation of analytical expressions and methods to be used in future guidelines for tsunami design of overland built infrastructure, such as buildings, bridges, and ports, that may be subjected to

tsunami loading.

Chapter 6

Test-Case

Chapter 6 is assembled to investigate the successive structural behaviour of an open-type wharf due to cascading seismic and tsunami actions. The conceptual methodology introduced in Chapter 2 was adapted to investigate the successive response of the Sines container terminal(s) subjected to a cascading 1755-alike earthquake and tsunami event. The multi-hazard was characterized via two alternative basic and enhanced numerical approaches, considering current and future configurations due to expansion plans of the port of Sines container terminal(s).

Chapter 6 is based on Reis et al. 2019, 2021, 2022a,b,c [21, 48, 63, 127, 272].

6.1 Description

Seaports play an essential role in the policies of sustainable mobility as critical links allowing the transfer of goods and passengers, helping to increase the functionality and efficiency of the general system of transportation. Furthermore, seaports represent priority entry points into an area affected by an earthquake, playing a crucial lifeline role in rescue operations. However, ports represent a multi-component system in which each element has its structural response to dynamic actions. A potential disruption of one element may trigger a domino effect compromising the performance of the entire system. Therefore, the critical nature of such infrastructures represents demanding structural design to fulfill elevated safety and operational performance requirements.

The Sines -28 mZH deep-water seaport has more than 2000 *ha* of maritime, industrial and logistic zones. The infrastructure is geo-strategically implemented at the south of the capital, Lisbon, on the crossing the leading international maritime routes, having a high expansion potential both in infrastructures and road and rail accessibility. Composed of liquid bulk, petrochemical, fishing and leisure, multipurpose, natural gas and container terminals, the port plays a fundamental role as an energetic supplier for the country (crude and its derivatives, coal and natural gas) and in the trade of general and containerized cargo. The container terminal of the 40-years old Sines port started operating in 2004, with an approximate 300 *m*-length quay. The constructive solution was based on a closed typology adopting gravity caissons. Conversely, the second constructive phase adopted an

open typology to extend the container terminal up to about 1 km of length. The pile supported quay of the wharf started to operate in 2013. Fig. 6.1 depicts the current configuration of the Sines port complex, adopting Google maps of Sines region (earth.google.com/web/, last access: October 2021), data available from Administração dos Portos de Sines e do Algarve S.A. (<https://www.apsinesalgarve.pt/>, last access: October 2021) and private photography of the container terminal (Lopes, M. *personal collection*.)

Recent manifestations of interest demonstrated by the Energy Department of the United States government and China COSCO Shipping Company are associated with plans to expand the liquid natural gas terminal and build a mega container terminal. The port administration reports a ten-years (2020 – 2030) plan to develop its competitiveness in the global maritime trade based on port efficiency, maritime and hinterland connectivity strategies (<http://www.apsinesalgarve.pt/en/>, last access: October 2021). The third stage of the container terminal expansion consists of enlarging the current Terminal XXI infrastructure up to 1950 m , projecting an increase in the annual handling capacity from 2.3 to 4.1 million TEU. The fourth stage aims for the construction of a modern open deep water wharf, Vasco da Gama terminal, with predicted storage area of 46 ha and capacity to handle another 3.0 million TEU of cargo per year, allowing the accommodation of three large ships simultaneously and house a 1370 m -long quay wall. Fig. 6.1 represents the container terminal(s) configuration after the expansion phases, modeled after environmental impact assessment documents [424, 425] and data provided by the Administração dos Portos de Sines e do Algarve S.A.. Detailed information regarding third and fourth expansion phases planned for increasing the cargo capacity of Sines cargo hub be found in Section C.2, Appendix C.

A detailed characterization of the design actions constitutes a fundamental base to guarantee the best trade-off between demanding criteria and constructive costs. Yet, the procedure is particularly challenging when characterizing the ones derived from natural hazards. The Portuguese region has moderate tectonic activity due to inland and offshore geological structures [426, 427]. Nevertheless, catastrophic seismic and tsunami events occurred in the past, mostly triggered at the south and southwest offshore Iberian regions, such as the 1755 Great Lisbon Earthquake and Tsunami (GLET) event, which had magnitudes estimated between $Mw8.0$ and $Mw - 9.0$ [109, 128, 428]. The oscillations induced by such energetic seismic and tsunami waves can excite the port and lead to the disruption of functions and damage to structures, moored ships and elements of the cargo systems, such as cranes [429]. Moreover, extreme events such as the 1755 GLET event have the potential to compromise the lifeline role played by the portuary complex in case of post-event emergency.

6.2 Methodology

The generic and conceptual methodology introduced in Section 2.2 was adapted to model the 1755 GLET event and the structural response of the container terminal of Sines port. Fig. 6.2 depicts the macro-, meso- and micro-stages that are part of the numerical domain, from the genesis of the natural phenomena to the response of the man-made structure. It raises uncertainty awareness regarding

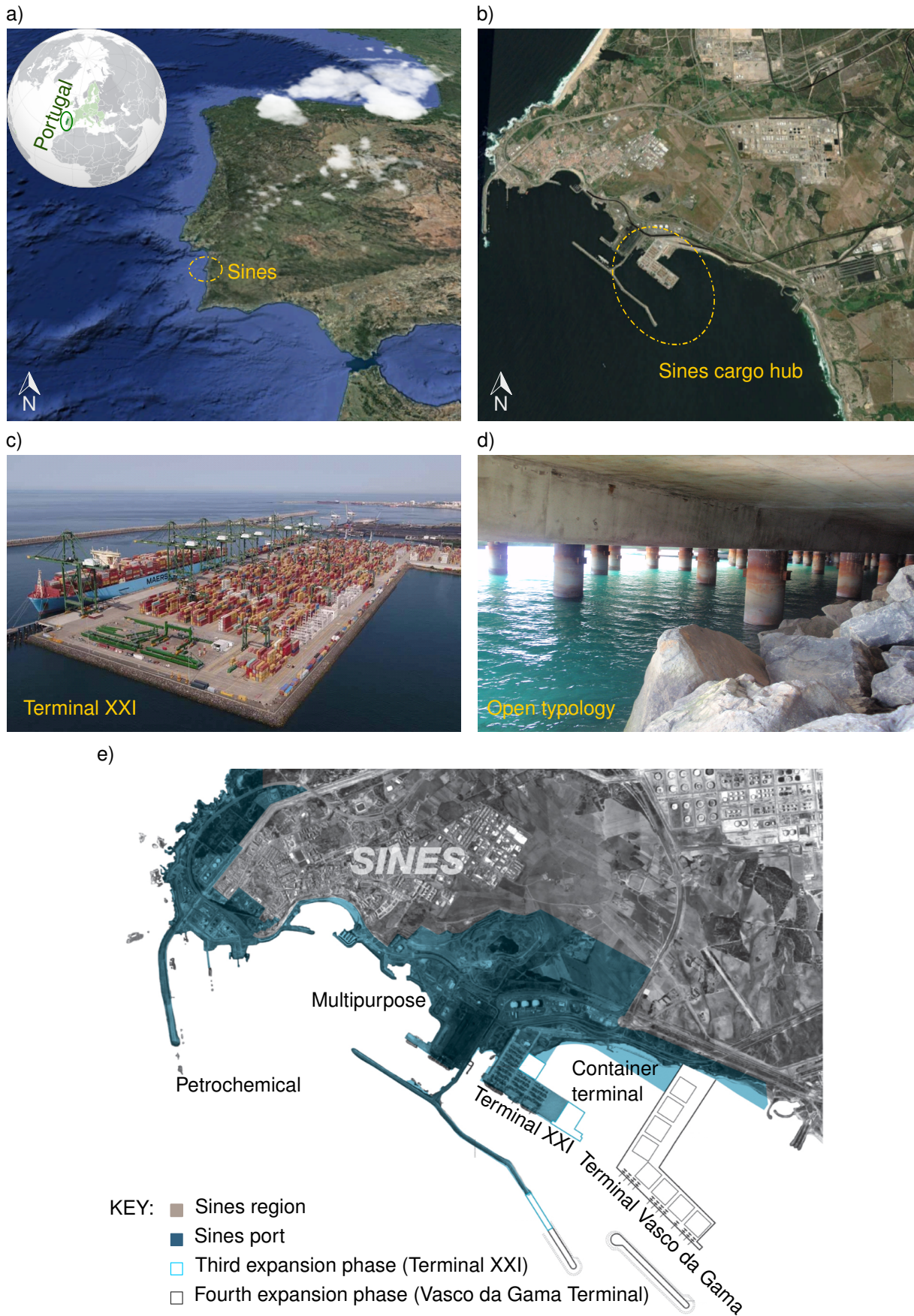


Figure 6.1: Test-case: a) global location of Europe, Portugal and Sines, b) location of the deep-water seaport in Sines region and position of the container terminal in the port complex, c) photography of Terminal XXI, d) photography of the constructive solution based on open-typology, and e) two-staged expansions of the cargo hub of Sines deep-water seaport.

physical and numerical variables while maintain a sense of trade-offs between the level of accuracy of the solutions and the computational demand, contributing to informed decisions on multi-risk management function of the goal of structural performance.

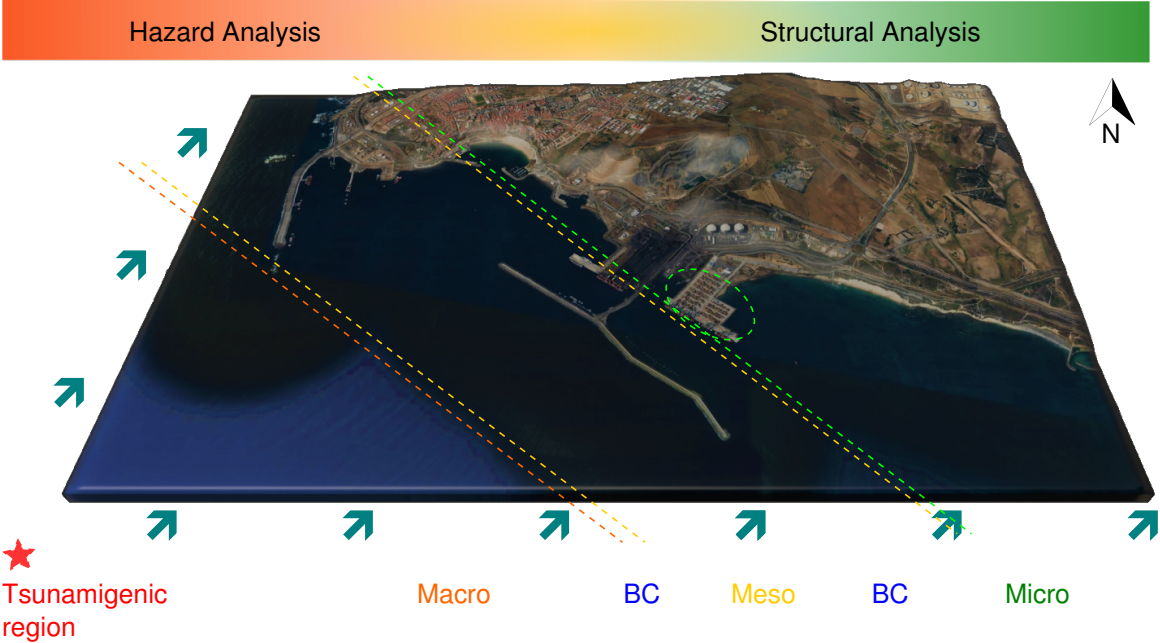


Figure 6.2: Test-case: frameworks to characterize the regional/local-tsunami threat in Sines deep-water port, Portugal. Three stages encompassing multi-scale and multi-physics domains are linked by boundary conditions, BC.

Risk mitigation strategies are evolving towards preventive multi-hazard risk management. The assessment of cascading seismic and tsunami multi-hazards is commonly pursued following probabilistic approaches involving big data and complex analyses to estimate the likelihood that seismic intensity and tsunami inundation will exceed a certain level during a given time interval. Despite their fundamental contribution to risk management, the generalist nature of multi-hazard maps is deemed insufficient to optimize the design of coastal structures located in regional and local tsunami-prone regions. However, the probabilistic-deterministic dichotomy of hazard assessment constitutes an exaggerated differentiation, hence that each study is initiated with credible sources that should be chosen according to the nature of the project, varying quantity and quality of the data available to characterise the physical processes. Scenario-based evaluations can provide complementary key insights of relevance to design critical facilities [127]. Thus, an alternative deterministic analysis was explored to characterize the cascade seismic and tsunami multi-hazard of a 1755 GLET-alike event oriented to the container terminal of Sines deep-water seaport. Section 6.3 identifies and combines the plausible local and regional tsunamigenic sources constituting candidate scenarios, $S_{candidate}$, to assess the cascading effects of a 1755 GLET-alike event impacting the structure(s) serving as container terminal(s) in Sines port. Based on the conceptual methodology described in Section 2.2, which encompasses modeling hypothesis, two modeling approaches varying

the level of numerical sophistication were performed to characterize 'baseline' and 'enhance' solutions.

The baseline target-hazard assessment, in Section 6.4.1, assumed a simplified approach based on GMPE and non-linear SW system equations solved by FV method to characterize discrete values of ground motion acceleration and tsunami hydrostatic and hydrodynamic quantities as explanatory variables, respectively. The intensity measures inherent to each of the inextricable $S_{candidate}$ were characterized over 864 seismic and 144 tsunami simulations and then compared to key-thresholds to identify the scenarios with damaging potential, $S_{eligible}$. The quantities of each $S_{eligible}$ were assessed varying the earthquake and tsunami intensity measures as leading measures to define a set of combined worst-case scenarios for the infrastructure, S_{worst} . The cascading loading patterns for structural design purposes were then derived for the S_{worst} following the acceleration assessed from deterministic scenarios and tsunami forces determined using the semi-analytical formulation of the North American regulation with hydraulic quantities numerically assessed using SW-FV scheme.

The enhanced target-hazard assessment, in Section 6.4.2, adopted more sophisticated numerical schemes to determine dynamic ground motions and tsunami forces via built-in approach based on NS-SPH scheme to use in the successive structural non-linear dynamic analysis of the soil-wharf system using an open-source FE software.

All numerical schemes used to model the test-case were introduced in Chapter 3 and validated in Chapters 4 and 5.

6.3 Regional and local tsunamigenesis potential

The 1755 GLET is one of the most studied events, but its source remains under scientific debate, mainly due to the complex network of thrust faults in the southwest Iberia margin (SWIM), Gulf of Cadiz region and slow convergence in the boundaries of the African and Eurasian plates [430–438].

The SWIM region, considered responsible for the generation of 1755 GLET and other important tsunamis, such as the more recent 1969 earthquake and tsunami, is a region of slow lithospheric deformation between the Eurasian and African plates. The Eurasia plate moving in oblique NW–SE convergence towards the African plate represents a purely strike-slip domain to the west ending in the convergent arcs of the Gulf of Cadiz to the east [427]. The SWIM region is predominantly composed of NNE–SSW thrust faults, such as the Gorringe Bank, Marquês de Pombal and Horseshoe faults, while the thrust faults in the Gulf of Cadiz have a NE–SW orientation, such as the Portimão Bank fault [426]. Figure 6.3 depicts the location of the main geological structures with tsunamigenic potential identified in SWIM and Gulf of Cadiz regions.

The epicentral estimates of the 1755 GLET in the Atlantic Ocean, western coast of Portugal, have almost two centuries and were initially based on tsunami travel-time data justifying the epicentral location relatively close to Lisbon [439, 440]. Further isoseismical regression analyses located the epicenter around the Saint Vicent fault [430, 441], whereas studies based on damage reports relocated the epicenter close to the Gorringe Bank region [428, 442].

A conjoint source based on classical location proposal estimates and modern data suggests the

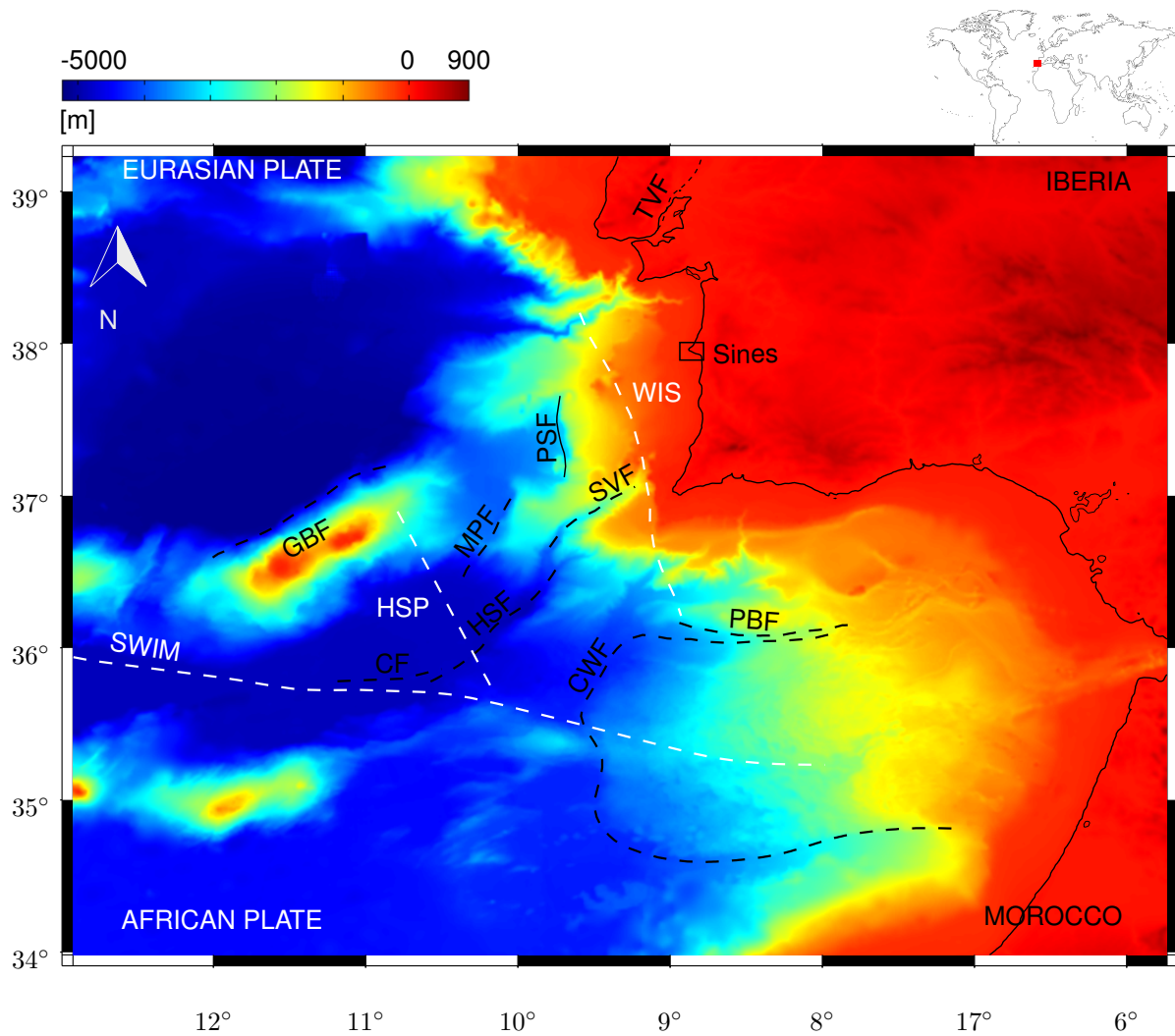


Figure 6.3: Topo-bathymetric map with identification of tsunamigenic sources in Gulf of Cadiz region. The solid black line represents a normal fault, while black dashed lines represent the predominant thrust faults of the tectonic complex. White dashed lines represent hypothetical fault ruptures. Acronyms of the tsunamigenic geological mechanisms: GBF - Gorringe Bank fault, MPF - Marquês de Pombal fault, CWF - Cadiz Wedge fault, HSF - Horseshoe fault, SVF - São Vicente fault, PBF - Portimão Bank fault, WIS - Western Iberian Shelf, PS - Pereira de Sousa, TV - Tagus Valley (onshore), CF - Corner fault, HSP - Horseshoe Plain, SWIM - Southwest Iberian Margin.

composite offshore Gorringer Bank thrust fault triggering the rupture of the inland Lower Tagus Valley fault [443]. Meanwhile, the advances of instrumental and computational capacities led to the proposal of new focal mechanisms. Tsunami simulations were carried out to test the hypotheses of an incipient subduction zone along the Western Iberian shelf, and the composite rupture of a L-shaped mechanism composed of Marquês de Pombal and Portimão Bank faults [444–447]. The interpretation of multi-channel seismic reflection data showed the Marques de Pombal Fault [448], or composite ruptures of the Marquês de Pombal and Pereira de Sousa faults [449], or Horseshoe fault [450, 451], as candidate sources for the 1755 GLET event. Moreover, data from seismic tomographic imaging allowed to add the Cadiz Wedge fault [452, 453], to the list of possible sources.

Later, multiple comparative analyses accounting for the single and composite rupture mechanisms were performed [22, 454–458]. Some of them proposed modified versions of the original rupture mechanisms [426]. Shreds of evidence of seismogenic activity in the form of strike-slip displacement in the encounter between the Eurasian and African Plate of the Southwest Iberian Margin and the northwest thrust system encompassing the Horseshoe and Corner thrust faults were proposed as a new rupture mechanism [459]. The Portimão Bank fault [22] was individually modeled to assess its tsunamigenic potential, while a rupture encompassing kinematic parameters of the Gorringer Bank, Marquês de Pombal and Horseshoe faults was assembled into an alternative NW-SE fault in the center of the Horseshoe plain and perpendicular to Gorringer Bank [457], herein referred and simulated as a variation of Horseshoe Plain.

To discuss the credibility/reliability of the latter Horseshoe Plain and the Western Iberian Shelf triggering sources, it is highlighted that the rupture at the Horseshoe Plain was proposed by Barkan et al. 2009 [457] to justify far-field observations of tsunami heights in the Caribbean. However, the only known tectonic structure at Horseshoe Plain with the NW–SE strike orientation is the ancient Paleo Iberia–Africa Boundary formed during the opening of the central Atlantic ocean in the Late-Jurassic–Early Cretaceous era. Thus, the author [457] acknowledged the need of further investigations to test if the structure is currently active.

Regarding the Western Iberian Shelf, although the first proposals of 1755 GLET source were off the western coast of Portugal [440], the rupture of the compressive structures of the Gorringer Bank fault was proposed in the late twentieth century [428] to overcome some inconsistencies, yet remained incompatible with tsunami research. Baptista et al. 1998 [446] re-evaluated a seismic rupture closer to the western coast of Portugal and extended it further north toward Lisbon. Such mechanism was utterly corroborated in a phenomenological reconstruction of the 1755 GLET assuming $M_w 9.0$ due to an extended rupture of a 350 km times 150 km area in Western Iberian Shelf [456]. The configuration of the co-seismic faulting proposed by Wood et al. 2008 [456] was based on a full range of contemporary observations of macro-seismic impacts, effects of far-field sources elongating period, near-field and far-field tsunami heights and travel times, evidence for associated deformation, and accompanying regional stress changes. However, it lacks geological evidences to support the hazardous hypothesis of rupture at the Western Iberian Shelf. For the present work, both faults were simulated to play a disclaimer role, raising awareness for the possibility of hazard exceedance in the future. However, the multi-hazard

Table 6.1: Identification of the regional and local tsunamigenic sources.

| Acronym | Identification | Authors |
|---------------|--|-------------------------------|
| 1 - GBF | Gorringe Bank | [22, 426, 428, 455–458] |
| 2 - MPF | Marquês de Pombal | [22, 426, 448, 454, 456, 458] |
| 3 - CWF | Cadiz Wedge | [22, 452, 453, 455, 456, 458] |
| 4 - HSF | Horseshoe | [22, 426, 454, 458] |
| 5 - SVF | Saint Vicent | [454] |
| 6 - PBF | Portimão Bank | [22] |
| 7 - WIS | Western Iberian Shelf | [446, 456] |
| 8 - MPPSF | Marquês de Pombal and Pereira de Sousa | [449, 455] |
| 9 - MPPBF | Marquês de Pombal and Portimão Bank | [447] |
| 10 - MPHFSF | Marquês de Pombal and Horseshoe | [426, 450, 451, 458] |
| 11 - GBTVF | Gorringe Bank and Lower Tagus Valley | [443] |
| 12 - HSCFSWIM | Horseshoe, Corner and SWIM | [459] |

assessment neglects the quantities derived from these two source rupture proposals.

Table lists the $S_{candidate}$, respectively encompassing single or composite fault ruptures with magnitudes ranging between $Mw8$ and $Mw9$, and epicentral distances from $D \approx 120 km$ to $D \approx 300 km$. Detailed description of the parameters defining the initial conditions of each $S_{candidate}$ can be found in Section D.1, Appendix D.

6.4 Macro- and meso-scales: Cascading multi-hazard

6.4.1 Baseline solution

Description

The multiple $S_{candidate}$ were addressed as single ground motion and tsunami physical processes, considering the source, propagation and site uncertainties. Due to rocky geotechnical conditions of the site [424, 425], the seismic and tsunami analyses respectively neglect soil liquefaction and debris transportation. The independent earthquake and tsunami simulations were carried out to quantify seismic PGA and tsunami free-surface elevation, η and momentum flux M_F to assess the scenarios with damaging potential, $S_{eligible}$.

Assuming the source parameters of the identified $S_{candidate}$, the seismic simulations are carried out using the GMPE implemented in OpenQuake software library [352] (available at <https://www.globalquakemodel.org/>), described in Section 3.3.2. A GMPE model relates the ground-motion intensity measure to a set of variables describing the source, wave propagation path and site conditions [354]. Its generic functional form reads as Eq. 3.28, encompassing functions for earthquake source, attenuation along the path, and geometrical and anelastic site-effects, respectively. Due to the infrequent nature of large magnitude events in the region of the case-study, the GMPE models were assembled considering source and propagation uncertainties, while the site amplification and liquefaction potential were neglected due to site geotechnical conditions, with relatively shallow layer of rocky soil. The simulations of each scenario are repeatedly carried out varying the sources

parameters and the attenuation laws to generate multiple ground motion fields concerning the distribution of the PGA at the site of interest.

The tsunami initial condition assumed that the free-surface elevation at instant $t = 0$ s mimics the ocean floor displacements [318]. The computation of the co-seismic displacements followed the Okada's theory [317], implemented in Mirone software [386]. The multiple tsunami simulations were then carried out using the in-house SW-FV numerical tool described in Section 3.2.2 and validated in Section 4.1.

The simulations of each scenario were repeatedly carried out varying the site conditions resembling the multiple infrastructures configurations along the expansion phase (Fig. 6.1). The tsunami simulations assessed tsunami free-surface elevation, η , flow velocity and momentum flux, M_F . The tsunami hazard was addressed for both the site and the target structure by scattering fifteen virtual gauges, VG , along the coast.

The tsunami quantities captured by the various VG were adopted to characterize the tsunami force impacting the coastal structure using semi-empirically calibrated equations. The determination of fluid forces exerted on a stationary rigid body followed Eq. 3.1 the component normal to the surface, pressure exerted on the surface, and the tangent component to the surface, shear stress. Yet, for engineering estimates, the North American design codes from Federal Emergency Management Agency, FEMA P646 [31], and American Society of Civil Engineers, ASCE7-16 [32], recommend the decomposition of \vec{F} into hydrostatic and hydrodynamic loads calculated via Eqs. 3.25 and 3.26, respectively.

Once this process was complete, various combinations considering the seismic and tsunami intensity quantities as a leading measure were considered to set the S_{worst} and the derivative cascading loading pattern for the structure. The cornerstone to establish the inter-dependency condition between the seismic and tsunami individual processes was to consider inextricable $S_{candidate}$, i.e., each scenario derives from a common triggering source. To identify the $S_{eligible}$, the earthquake and tsunami intensity measures assessed for each of the $S_{candidate}$ are correlated with reference values representing potential damage for the structure, Eq. 6.1:

$$S_{eligible} = \begin{cases} PGA \geq IM_{ground-motion} \\ \eta \geq IM_{hydrostatic} \\ M_F \geq IM_{hydrodynamic} \end{cases} \quad (6.1)$$

PGA is the horizontal peak ground acceleration, η is the free surface elevation, and M_F the momentum flux assessed for the site/target structure, while IM represents values of ground-motion, and tsunami hydrostatic and hydrodynamic intensity measures referred in the literature as thresholds of damaging potential for the coastal structures and likely to prevent the serviceability of the port.

A set of S_{worst} was characterized by adopting the various earthquake and tsunami intensity quantities and varying the leading measure to infer the initial conditions that promote the hazardous scenarios in terms of seismic acceleration and tsunami hydrostatic and hydrodynamic values during the inflow and outflow stages for the different infrastructure configurations. The cascade earthquake and tsunami loading pattern for each structural configuration was established considering the set with:

- leading earthquake action: the source that promoted the maximum PGA and respective tsunami

quantities;

- leading tsunami hydrostatic action: the source that promoted the highest η and respective PGA and M_F quantities;
- leading tsunami hydrodynamic action (for both tsunami inflow and outflow): the source that promoted the highest M_F and respective PGA and η .

Seismic hazard

Each of the presumable fault ruptures proposed in the literature constituting a $S_{candidate}$ represented a source source term in the GMPE model (Table 6.1). The parameters defining the source conditions of each $S_{candidate}$ were introduced in OpenQuake tool [352] to investigate the seismic hazard in Sines region. Besides the source parameters, the GMPE model assumed various attenuation laws for path propagation. The site characteristics was identically modelled for all $S_{candidate}$.

The GMPE are strongly dependent on ground motion attenuation models. However, the probable regions for the generation of a 1755 GLET-alike event are geographically located at the confluence of distinct crustal types, both in terms of rheology and tectonics, which limits the straightforward application of attenuation models developed for a specific tectonic profile. To assess the adequacy of existing attenuation laws for the eastern coast of North America to model seismic activity at Western Iberia, Vilanova et al. 2012 [460] correlated results of GMPE with instrumental and historical seismic data from Western Iberia. The attenuation models developed to model stable continental crust regions of eastern North America are deemed adequate to predict results for both onshore and offshore Iberian events, while the models developed for the active shallow crustal regions tend to underestimated the seismic accelerations. Moreover, the adequacy of attenuation models that apply to eastern North America was corroborated by the common origin of both eastern North America and western Iberia margins that were separated in the Mesozoic period by intra-continental rifting [460]. These recommendations were adopted by Silva et al. [461, 462] to assess the ground shaking throughout mainland Portugal using Atkinson and Boore 2006 [463] and Akkar and Bommer 2010 [464] attenuation equations. However, the referred attenuation models were calibrated with low-to-moderate magnitude events due to the characteristic tectonic activity of the region, lacking the regional data to calibrate the scaling laws for larger magnitude events, such as the 1755 GLET. Therefore the adequacy of an attenuation law to model a large magnitude event triggered in the Gulf of Cadiz region was investigated considering models derived from data of intra- and inter-plate scenarios and moderate to large magnitude ground motion records acquired at North American and European regions. Twenty-four attenuation laws from the vast OpenQuake library [465] were adopted to model the propagation stage of the earthquake, such as Atkinson and Boore 1995 [466], Toro et al. 1997 [467] modified in 2002 [468], Campbell 2003 [469], Atkinson and Boore 2003, 2006 and 2011 [393, 463, 470], Atkinson 2008 [471], Boore and Atkinson 2008 [472], Chiou and Youngs 2008 [473], Abrahamson and Silva 2008 [474], Atkinson and Macias 2009 [475], Akkar and Bommer 2010 [464], Bindi et al. 2014 [476], Akkar et al. 2014 [477], Abrahamson et al. 2014, 2016 and 2018

[394, 478, 479], Chiou and Youngs 2014 [480] and Cauzzi et al. 2015 [481].

To model the site effects, and since the soil site conditions are close to reference site conditions, hard soil, the site scaling in the GMPE barely constitutes an influence. Moreover, several authors described very low attenuation for large magnitude earthquakes in the southwest Iberia region [427, 455] and references therein. Thus, the near-surface ($\approx 30\text{ m}$) shear-wave velocity representing site effects was defined assuming a value compatible with hard soils, $V_{s,30} = 800\text{ m/s}$ [33, 462, 482].

The seismic simulations combining 36 sources and 24 attenuation laws were carried out over 2 km -resolution grids. The 864 simulations generated ground motion fields of PGA intensity measure. The interval of the PGA values in Sines is wide, between 0.034 g and 1.115 g , requiring a general framework. The contextualization of the PGA solutions used macro-seismic intensity data estimated for the 1755 GLET event and design provisions from Eurocode 8 regulation complemented by the Portuguese annex [33].

Macro-seismic intensity data is typically more abundant than strong-motion recordings or even exclusive when considering historical events. Thus, empirical relationships are commonly adopted to adjust the qualitative and quantitative aspects of seismic data. The conversion of the intensity degrees of the macro-seismic scale into PGA values follows the generic form in Eq. 6.2:

$$\log PGA = A + B \cdot I \quad (6.2)$$

where the logarithmic value of PGA is adjusted to the seismic intensity, I , using A and B coefficients, which are function of the seismicity of the region. Grandin et al. 2007 [455] identified similarities between the 1755 GLET event and the parameters proposed by Trifunac and Brady 1975 [483], calibrated with instrumental data from the western United States region, suggesting values of $A = 0.014$ and $B = 0.3$, while Pro et al. 2020 [484] recommended the use of the conversion equation proposed by Faenza and Michelini 2010 [485] for $I \geq 7$. Zanini et al. 2019 [486] and Capera et al. 2020 [487] compared several conversion equations to investigate the uncertainty associated with the conversion process. Their study demonstrated an equivalent slope of the Trifunac and Brady 1975 [483] and Faenza and Michelini 2010 [485] regressions for the $8 < I \leq 9$. The 1755 GLET at Sines region was estimated in $I = IX$ by Elmrabet et al. 1989 [488]. Recently updated maps of seismic maximum intensity derived from deterministic observation compiled by Teves-Costa et al. 2019 [435] and corroborated by Buforn et al. 2020 [489] confirm the estimate. Making use of Eq. 6.2 with A and B coefficients suggested by Trifunac and Brady 1975 [483], the quantitative PGA value was evaluated in 0.265 g .

Despite the European standards does not include port structures, a complementary correlation between the PGA solutions and EC8 design recommendations was developed to provide a probabilistic framework for the seismic PGA values. Whenever a region has no seismic codes or standards for designing port structures, the local codes applicable to that particular region or the guidelines of the World Association for Waterborne Transport Infrastructure, PIANC [305], may be used as a basis to develop a new seismic design standard. The seismic design guidelines for port structures are intended to be performance-based, allowing a certain degree of damage depending on the specific functions

and response characteristics of the port structure and the probability of earthquake occurrence in the region. To this end, PIANC code defines two levels of performance. The first represents an earthquake motion with a probability of exceedance of 10% during the 50 years of theoretical life-span of a port structure, which corresponds to a return period of 475 years. The second represents an earthquake motion with a 2% probability of exceedance during the theoretical life-span of the structure, representing a 2475 years return period.

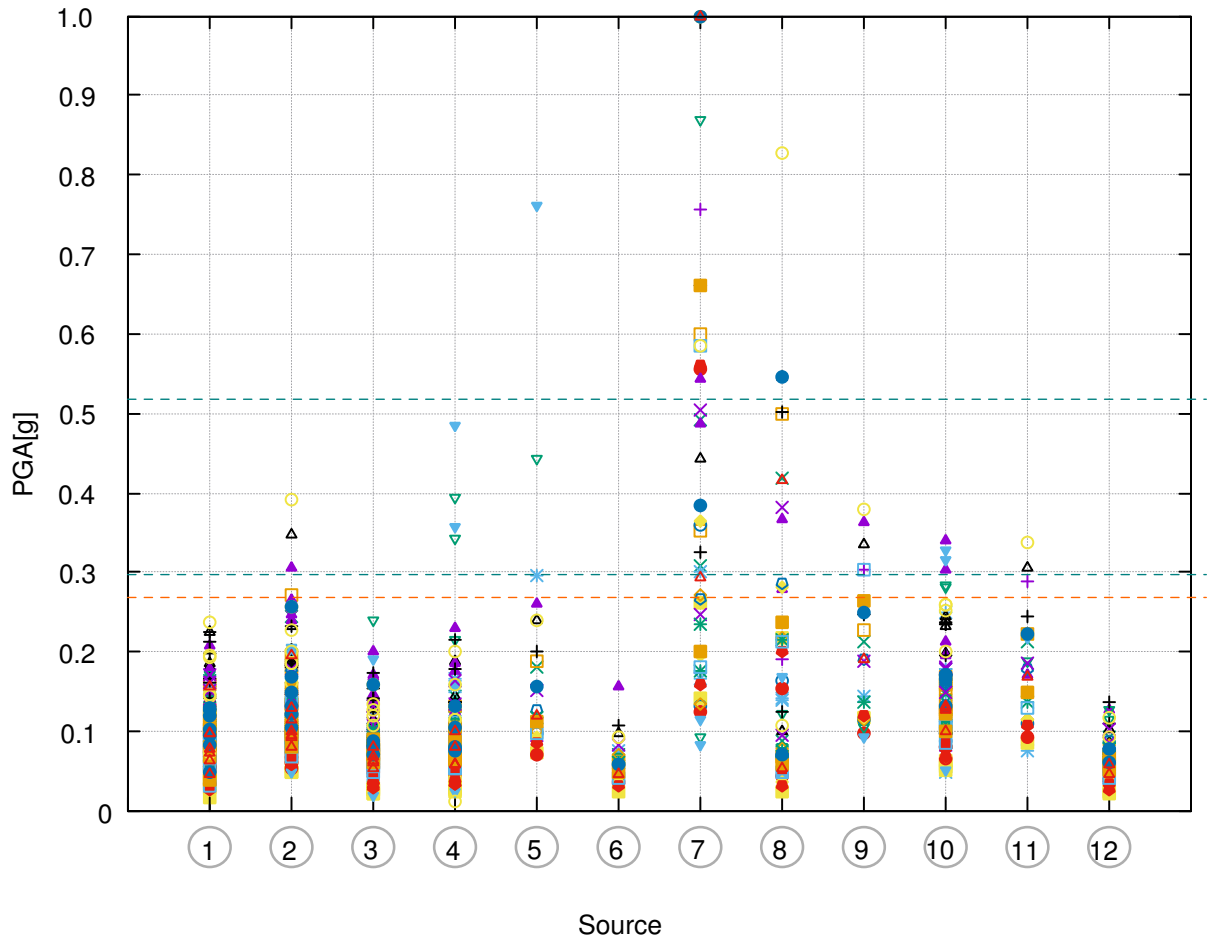
The transposition of PIANC recommendations to the EC8 guidelines was possible by adapting the reference earthquake to the performance level of structures having different classes of importance. The EC8 reference earthquake has a probability of annual occurrence of one in 475 years and is recommended for office and housing buildings (class of importance II). The Portuguese annex of Eurocode 8 provides Eq. 3.36 (Section 4.3) to adapt the reference acceleration for the different structural classes of importance modifying the RP and K adopting values of 1.5 or 2.5 for far- or near-field earthquakes, respectively.

The design reference PGA values for Sines, at the bedrock level, are $a_{gR} = 0.153 g$ and $a_{gR} = 0.173 g$ for far- and near-field earthquakes. The container terminal of Sines port was assumed to fit class IV level of importance structure due to their societal and environmental importance. For class of importance IV, associated with 1303-years return periods, the Portuguese national document recommends amplifying the far- and the near-field earthquakes in 95% and 50%, leading to PGA values of $0.298 g$ and $0.260 g$, respectively. Moreover, according to Matias et al. 2013 [426], the Gulf of Cadiz region can potentially trigger magnitude 8 events every 700 year and $Mw8.7$ earthquakes up to 3500 years. In accordance with Eq. 3.36, a 3000-years return period earthquake would generate PGA of $0.523 g$ and $0.362 g$ for far- and near-field sources, respectively. Considering a simplified definition of far-field earthquake concept [490], all $S_{candidate}$ are located within $D \geq 50 km$ and represent far-field scenarios. The comparison between spectral accelerations for the main periods of vibration for the transverse direction of the quay would be similar, as all values vary proportionally if it is assumed that the shape of the response spectrum does not change.

Figure 6.4 depicts the PGA values derived from 874 GMPE models encompassing the source and path uncertainties. The solutions are correlated to PGA values derived from the macro-seismic intensity maps and the design recommendations adopted from the national annex of EC8 for class of importance IV infrastructures considering a type 1 (far-field) event with return periods of one in 1303 years, which are relatively similar, $0.265 g$ and $0.298 g$, and return periods of one in 3000 years of return period event, $0.523 g$.

From the 864 simulations, 806 solutions presented PGA values below the inferior reference ($0.265 g$) while 21 had values above the upper PGA reference value ($0.523 g$) and 47 scenarios led to solutions with values between $0.3 g$ and $0.5 g$. The attenuation laws that generated the 55 solutions with PGA value exceeding the lower design reference ($0.298 g$) were then analysed to assess their adequacy to model a 1755 GLET-alike event.

The GMPE model with 8 out of the 55 solutions exceeding the lower design reference used Atkinson and Boore 1995 attenuation law [466], which was derived for direct calibration using eastern North



Scenarios

- ① GBF ② MPF ③ CWF ④ HSF ⑤ SVF ⑥ PBF
 ⑦ WIS ⑧ MPPSF ⑨ MPPBF ⑩ MPHSF ⑪ GBTVF ⑫ HSCFSWIM

Attenuation laws

- | | | | | | |
|---|-----------------------------|---|-------------------------------|---|-----------------------|
| + | Abrahamson et al. 2014 | ▲ | Atkinson and Boore 1995 | × | Campbell 2013 Share |
| × | Abrahamson et al. 2015Inter | ▼ | Atkinson and Boore 2003 Inter | * | Cauzzi et al. 2014 |
| * | Abrahamson et al. 2015Intra | ▼ | Atkinson and Boore 2003 Intra | □ | Chiou and Youngs 2008 |
| □ | Abrahamson et al. 2018Inter | ◇ | Atkinson and Boore 2006 | ■ | Chiou and Youngs 2014 |
| ■ | Abrahamson et al. 2018Intra | ◇ | Atkinson and Macias 2009 | ○ | Toro et al. 1999 |
| ○ | Akkar and Bommer 2010 | ◊ | Bindi et al. 2014 | ● | Toro 2002 |
| ● | Akkar et al. 2014 | ● | Boore and Atkinson 2008 | ▲ | Toro 2002 Share |
| ▲ | Atkinson 2008 | + | Campbell 2013 | | |

Figure 6.4: Peak seismic hazard: range of PGA values for Sines site. The horizontal orange dashed line represents the reference value of PGA derived from the conversion of macro-seismic intensities maps. The horizontal blue dashed lines represent reference values from the national annex of EC8 standards, for type 1 (far-field) events and considering return periods of 1303– (class of importance IV) and 3000–years (return period of a 1755 GLET-alike event).

America data, while the Atkinson and Boore 2003 law [356], developed for the subduction zones with $5.0 < M_w < 8.3$, respectively for inter-plate and intra-plate earthquakes, led to 6 of the solutions each. The fault modeling of these GMPE models are based on circular or rectangular fault, but both have a uniform attenuation along the propagation path. On the one hand, another 6 solutions derived from the GMPE model using the Toro et al. 1997 [467] law showed an extended plateau of the values observed near the source occupying longer distances. Half the referred solutions exceeded the upper $0.5g$ PGA reference. The Toro et al. 2002 [468] modifications for large magnitude and short distance events generated 3 solutions each. The attenuation law proposed by Atkinson 2008 [471] assuming a higher plateau near the source and an abrupt attenuation after about 100 km also produced 6 out of the 55 solutions. The attenuation laws by Abrahamson et al. 2014, 2015 and 2018 for inter-plate triggered events [394, 478, 479] generated 3 solutions each, while the calibration for intra-plate events generated 2 solutions each. The attenuation laws that also generated 3 out of the 55 solutions each were based on Bindi et al. 2014 [476] calibrated with data from pan-European database, Campbell 2003 [469] based on the hybrid empirical method estimating strong ground motion near large-magnitude earthquakes of western North America, and Toro et al. 2002 [468] calibrated for Central and Eastern America regions. The attenuation laws proposed by Atkinson and Macias 2009 [475] developed for the Cascadia subduction, and Campbell 2003 using SHARE database [469], generated 2 solutions each. The Atkinson and Boore [463] for northeastern America, Akkar and Bommer 2010 [464], calibrated with data from pan-European databases ($4.0 < M_w < 8.0$), and Akkar et al. 2014 [477] for Europe and Middle East, Boore and Atkinson 2008 [472] developed for average horizontal accelerations, and Chiou and Youngs 2008 and 2014 [473, 480] in the framework of the Next Generation Attenuation model developed by the Pacific Earthquake Engineering Research Center generated a single solution each, but all having in common the same triggering source, the WIS with an extensive rupture area. The latter attenuation laws and the remain that lead to PGA values lower than the seismic references were considered inadequate to assess seismic quantities for designing structures to resist a large magnitude 1755 GLET-alike event.

Considering the path analysis, the PGA assessment was conducted using GMPE models adopting the Atkinson and Boore 1995 [466] attenuation law, which was considered a reasonable and reliable assumption to evaluate the influence of the source parameters on the PGA solutions. Figure 6.5 depicts the PGA values derived from each source.

As expected, the fault parameters promoting more significant magnitude events and epicentral location closer to the site of interest were found to be more likely to generate the higher PGA values at Sines site. Magnitudes equal or greater than 8.3 and distances below 250 km suggested a favorable combination to achieve PGA values around the EC8 indicative value, while $M_w > 8.5$ and $D < 200\text{ km}$ lead to more hazardous scenarios. The higher PGA values were derived from the sources originally proposed in the literature with rupture areas capable of justifying the historical tsunami observations, such as MPHSF and MPPBF, and the MPPSF proposed after data acquisition from a research cruise on the SW Portuguese Continental Margin using multiple seismic profiler equipment. The WIS fault generated seismic acceleration exceeding and diverging the framework of values derived from all the

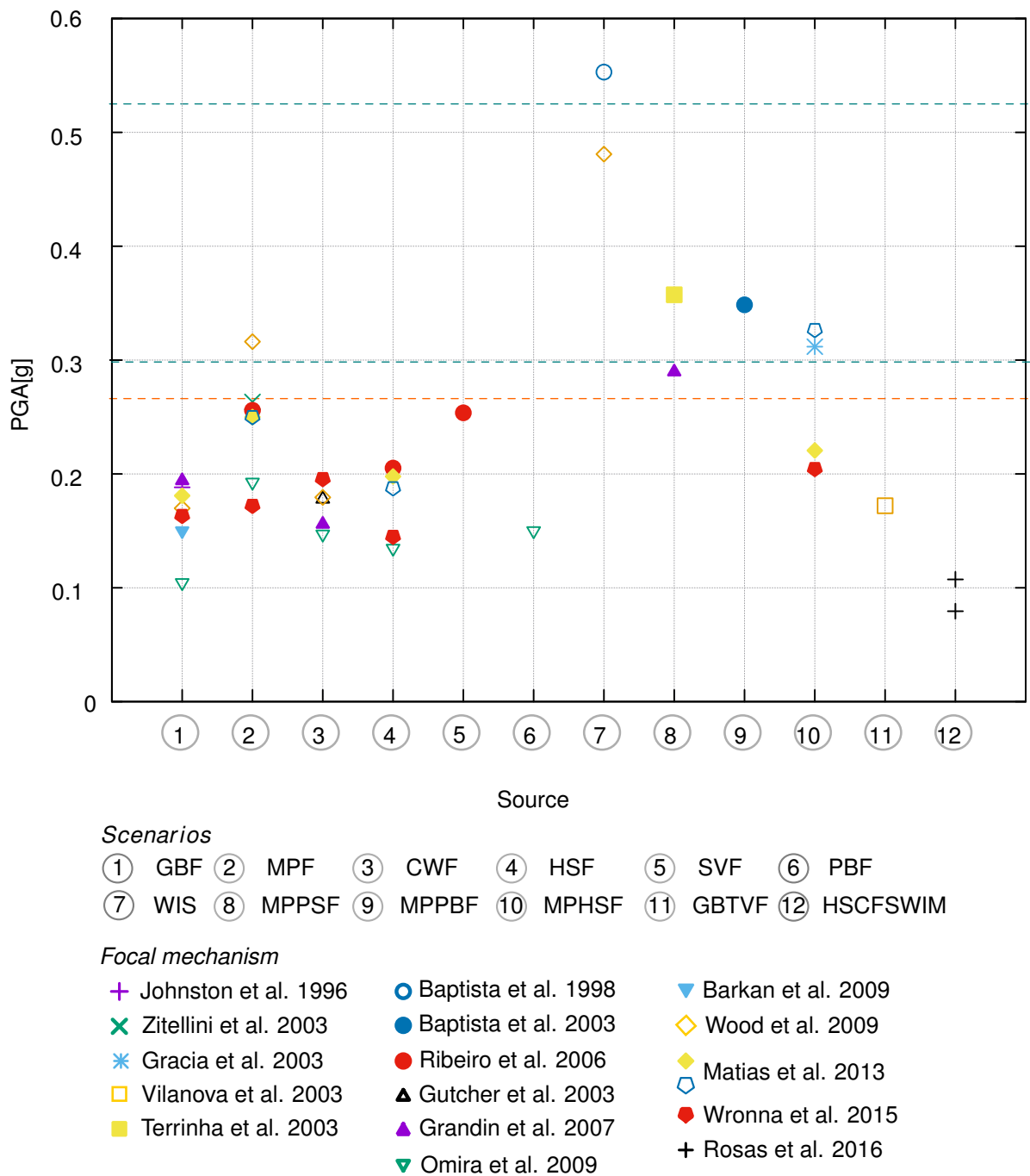


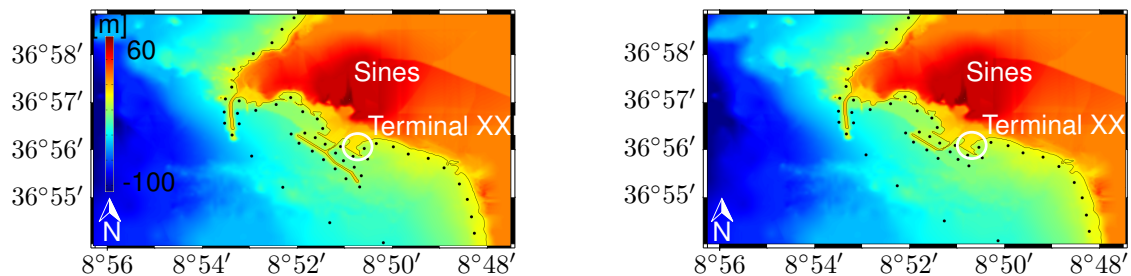
Figure 6.5: Peak seismic hazard: PGA values derived from GMPE models considering the attenuation law proposed by Atkinson and Boore 1995 and the multiple sources. Reference values of PGA derived from conversion of macro-seismic intensities maps and from the national annex of EC8 standards, for type 1 (far-field) events and considering return periods of 1303– (class of importance IV) and 3000–years (return period of a 1755 GLET-alike event).

other sources.

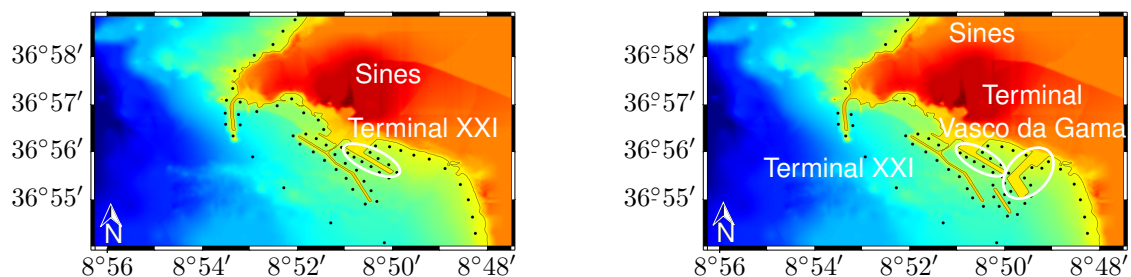
Considering the seismic hazard key threshold equals to the national regulation to design infrastructures of class of importance IV, the single and composed MPF were considered $S_{eligible}$. In the literature [489, 491], one can find references corroborating estimates of PGA values exceeding the national design recommendations.

Tsunami hazard

The tsunami initial conditions were generated from the fault parameters of the various $S_{candidate}$ using Mirone software [386]. The initial conditions were imposed in the form of grids overlapping the $15\text{ arc} - \text{sec}$ resolution topo-bathymetric, available at the General Bathymetric Chart of the Oceans site (GEBCO, gebco.net, last accessed: 30 October 2020). For the inundation modeling, the GEBCO grid was complemented with 1 m high-resolution topo-bathymetric data from a digital elevation map around the Sines coast [458] (Fig. 6.6(a)). The high-resolution topo-bathymetric grid was adapted to resemble three configurations of the cargo area of the Sines port. One of the grids was modified to assess the influence of the coastal protection structure assuming the collapse of the breakwater (Fig. 6.6(a)), which is a reasonable assumption since the structure was originally design to withstand less energetic storm waves. Other two grids were modified to resemble the future third and fourth expansions phases of the port, respectively including the enlargement of Terminal XXI and respective breakwater, and the construction of the new Vasco da Gama container terminal (Fig. 6.6(b)). Environmental time-dependent effects, such as sea-level variations due to tides or climate changes, and subsidence due to prior earthquake were not accounted on the analysis.



(a) Case A1 (left) - current configuration of Terminal XXI and undamaged breakwater. Original grid of digital terrain model. Case A2 (right) - current configuration of Terminal XXI and collapsed breakwater due to previous seismic action. Modified topo-bathymetry.



(b) Case B1 (left) - future configuration of terminal after enlargement of Terminal XXI and extension of breakwater. Case B2 (right) - future configuration of terminal container(s) after construction of Vasco da Gama terminal. Modified topo-bathymetry.

Figure 6.6: Tsunami hazard: topo-bathymetric variations resembling the future configuration of Sines port with expansion of Terminal XXI (top) and Vasca da Gama Terminal (bottom). Black dots represent virtual gauges.

The tsunami simulations were set for $t_{simulation} = 7200 s$ and carried out using the in-house well-balanced SW-FV to obtain:

- spatial distribution: profiles of peak wave heights, h_{max} , along 30 km (cases A) and 40 km (cases B) of the Sines coast acquired at the initial position of the dry-wet interface,
- temporal variations of tsunami hydrodynamic quantities, free-surface elevation, η , and flow velocity, u and v , to calculate the corresponding momentum flux, M_F , acquired at 50 virtual gauges scattered along the Sines coast.

Hydrostatic effects

The first observation withdrawn from the correlation between h_{max} profiles along the Sines coast and time-histories of η acquired around the container terminal was the complementary nature of both analyses when assessing the hazard posed by the tsunami in terms of hydrostatic quantities.

Depending on the source characteristics, the tsunami propagation and arrival at Sines coast followed a preferential orientation. Considering the implementation of the Sines port on the Portuguese coast, the waves propagation towards the coastline induced privileged wave impacts on the north or south shores, depending on the alignment of the sources of each $S_{candidate}$. The scenarios derived from $S_{candidate}$ located in $\Theta \leq 60^\circ$, which are GBF, MPF, HSF, SVF and MPHSF, tend to promote higher waves on the north shore (above $37^\circ 57' - N$ and between $8^\circ 53' - 8^\circ 52' - E$), whereas scenarios CWF, PBF, WIS, MPPSF, MPPBF and HSCFSWIM have higher h_{max} below $37^\circ 57' - N$ and between $8^\circ 53' - 8^\circ 48' - E$. As expected, the multiple variations of topo-bathymetric conditions representing the configuration cases (Fig. 6.6) also influenced h_{max} estimated for each $S_{candidate}$. A brief parametric analysis demonstrating parameters that influence the tsunami arrival on coastal sites is showed in Section D.2, Annex D.

The h_{max} analysis highlighted the influence of considering site or target hazard evaluations. The SVF source with the fault parameters proposed by Ribeiro et al. 2006 [454] promoted the higher wave at the north shore of Sines ($\approx 25 m$), while the scenarios adopting the parameters proposed in Baptista et al. 1998 [446] and Wood et al. 2009 [456] induced the higher waves at the container terminal (15 m to 17 m function of the structural configuration). Moreover, the h_{max} profiles show abrupt variations, quantified in more than 50% in intervals of a few meters, i.e. the evaluation of discrete η values, even computed in virtual gauges implemented less than a 0.5 km apart, are slightly inferior than the peaks obtained from the h_{max} calculated for the initial position of the dry-wet interface. The discrete acquisition of tsunami quantities at virtual gauges may skip one of the abrupt variations of h_{max} around the quay, misleading quantities that constitute the basis of hazard mitigation measures (e.g. for structural design).

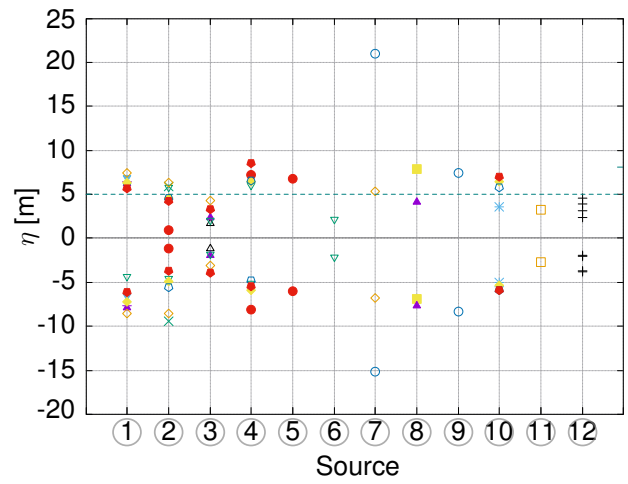
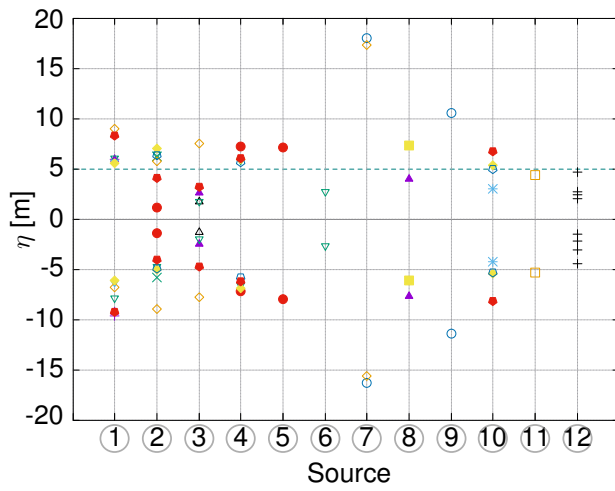
A time-dependent perspective derived from the complementary η analyses provided essential details for the tsunami hazard assessment, such as the shape of the leading N-waves that presented similar (or even higher) negative counterparts. Such characterization constitutes a fundamental insight when designing tsunami-resistant structures by identifying the highest wave during the train of waves that compose the tsunami. The tsunami simulations showed that SVF is the only $S_{candidate}$ presenting an unequivocal higher first wave, while the remaining scenarios have higher η values at or after the 3rd wave. The ASCE 7 standard recommends a minimum of two tsunami inflow and outflow cycles, which, in the

case study herein tackled, would mislead energetic waves impacting the infra-structure, leading to under-designed structures to resist a 1755 GLET-like tsunami constituted by a train of waves representing a successive load pattern potentially contributing for a gradual lost of structural resistance.

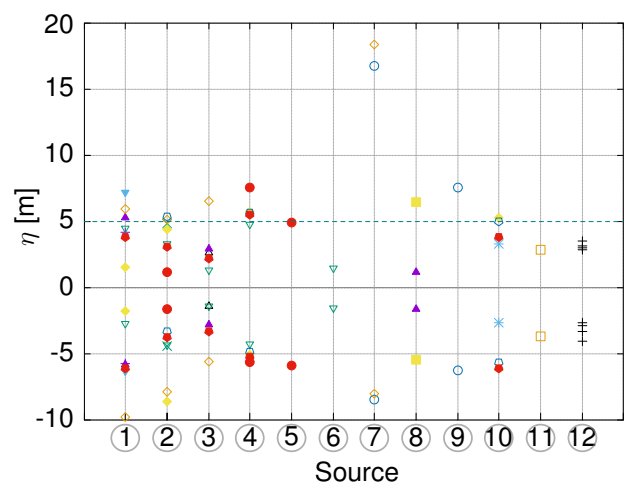
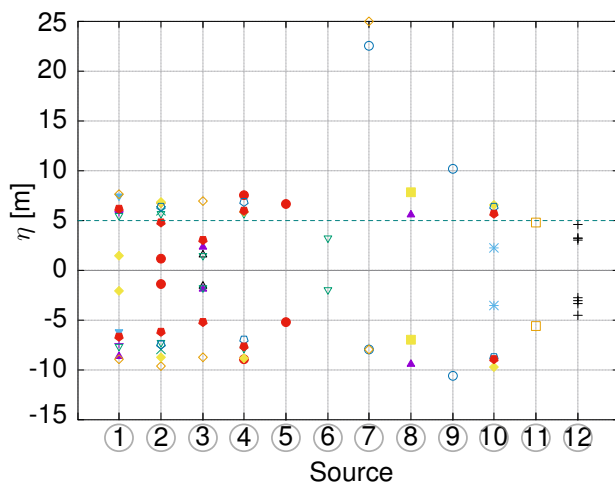
For the sake of consistency, Fig. 6.7 depicts the maximum and minimum values of η assessed for the different scenarios and configurations of the container terminal structure(s). The reference value of η in Fig. 6.7 represents a value derived from field observations of structural behavior in response to the Japan 2011 tsunami. Suppasri et al. 2015 [492] verified that $\eta \geq 2\text{ m}$ is likely to induce damage on buildings with different structural materials, being amplified in ria coasts where the topo-bathymetric conditions increased the flow velocity, comparatively to plain coasts. Chua et al. 2020 [84] recently compiled the damage induced on ports, demonstrating that $\eta > 5\text{ m}$ represents a 90% probability of damage preventing serviceability of the port.

The influence of breakwater in the tsunami flow propagation was assessed by evaluating the hydrostatic quantities at the virtual sensors implemented in the location corresponding to the front of the breakwater and the pile-supported quay for the different infrastructure configurations. The values of η were particularly reduced in scenarios with comparatively small waves arriving at the terminal container area due to the reflection of the wave to the seaward direction (e.g. CWF, PBF, GBTVF and some of the GBF, MPF and HSF scenarios). The correlations between Case A2 and the other cases demonstrated more pronounced differences of η (up to 2.5 m) during the first wave and a delay of 3 min in the tsunami arrival to the wharf structure.

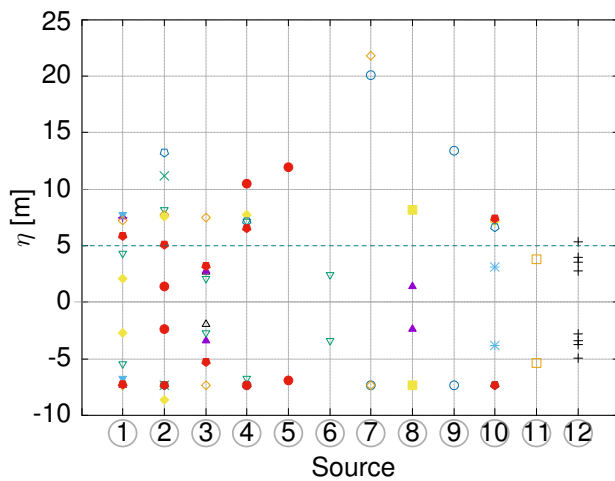
In the interval between the back of the breakwater and the container terminal, corresponding to the shipping area, the values of η were influenced by phenomena more complex than single reflection. Considering the different structural configurations, the time-histories of η tend to have increasing values during the simulation due to subsequent higher waves, water circumventing the coastal protection structure raising the inundation in the shipping region and resonance effects between the breakwater and the terminal structures. In agreement with over-topping phenomena on the breakwater, the polarity of the waves in MPPSF, MPPBF and MPHSF scenarios follow a close (but with temporal shift) shape of case A2 time-histories, tending to mimic the shape of the waves captured in front of the breakwater. In contrast, in GBF, MPF, HSF and SVF scenarios, the absence of the negative counterpart of the first wave peak appeared to represent a partial over-topping of the breakwater and a further flooding behavior after contouring the breakwater, explaining the higher delay of the tsunami arrival at the container terminal. In Case B2, the values of η assessed at Terminal XXI were relatively smaller than the ones quantified for the cases without the new Terminal Vasco da Gama, that was found to limit the tsunami inflow and outflow at the shipping region of Terminal XXI while delaying the tsunami arrival. The temporal shifting referred is more evident on the arrival of the first wave but attenuated along the simulation time, tending to become closer (magnitudes and temporal distribution) to the time histories of Cases A1 and B1, indicating smaller wave periods likely in association with the resonance effects mentioned above and probably amplified by the presence of the new infrastructures. In the future Vasco da Gama terminal, Case C, η tends to exceed the values evaluated for the existing Terminal XXI structure, mainly for MPF, HSF, SVF and MPPBF scenarios.



(a) Current configuration. Case A1 (left) - Terminal XXI with undamaged breakwater. Case A2 (right) - Terminal XXI assuming the collapse of the breakwater.



(b) Future configurations. Case B1 (left) - enlargement of Terminal XXI and respective breakwater. Case B2 (right) - Terminal XXI after construction of Vasco da Gama terminal.



- Focal mechanisms*
- | | |
|---|---|
| + | ▲ |
| × | ▲ |
| * | ▼ |
| □ | ▼ |
| ■ | ◇ |
| ○ | ◇ |
| ● | ◻ |
| ● | ◆ |
| | + |

(c) Future configurations. Case C - Terminal Vasco da Gama.

Scenarios

- | | | | | | |
|---|---|---|---|---|---|
| ① | ② | ③ | ④ | ⑤ | ⑥ |
| ⑦ | ⑧ | ⑨ | ⑩ | ⑪ | ⑫ |

Figure 6.7: Peak tsunami hazard: values of free surface elevation due to 1755 GLET-alike tsunami around the cargo hub of Sines port. Reference value of $Z_H = 5\text{ m}$ set to represent the damaging potential of the tsunami hydrostatic effects on the container terminal(s).

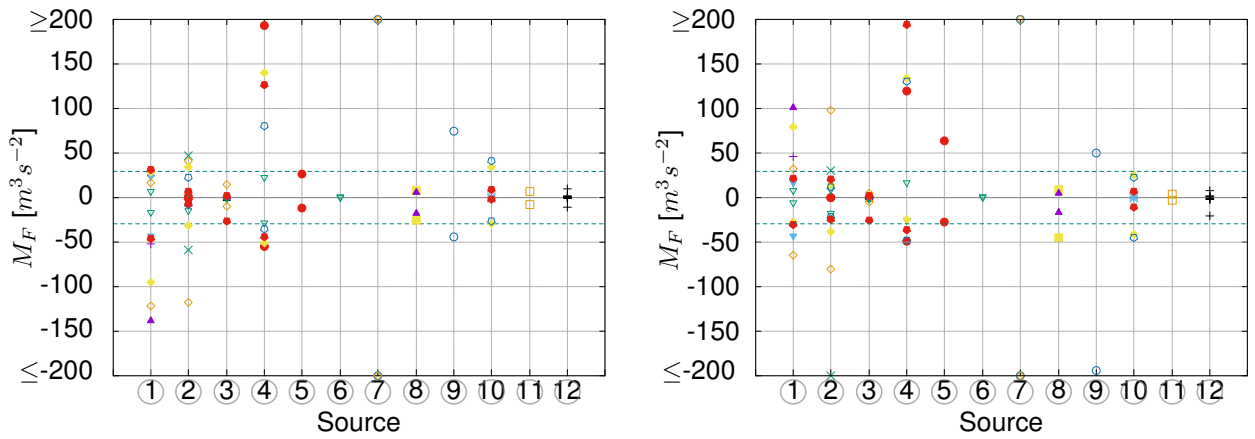
The $S_{candidate}$ that meet the $\eta \geq 5 m$ criteria in all configurations were considered $S_{eligible}$. For Terminal XXI, Cases A2 and B2 presented slightly hazardous quantities due to the lack of the breakwater protection structure and the resonance effects promoted by the new container terminal, respectively. The solutions for the configuration Cases A1 and B1 presented relatively similar hydrostatic values. The quantities evaluated at the Vasco da Gama terminal location, Case C, tend to exceed the values assessed for Terminal XXI. The GBF, MPF (except sources of Ribeiro et al. 2006 and Wronna et al. 2015), HSF, SVF, WIS, MPPSF using initial condition of Terrinha et al. 2003, MPPBF and MPHSF (except source from Gracia et al. 2003) were elected $S_{eligible}$.

Hydrodynamic effects

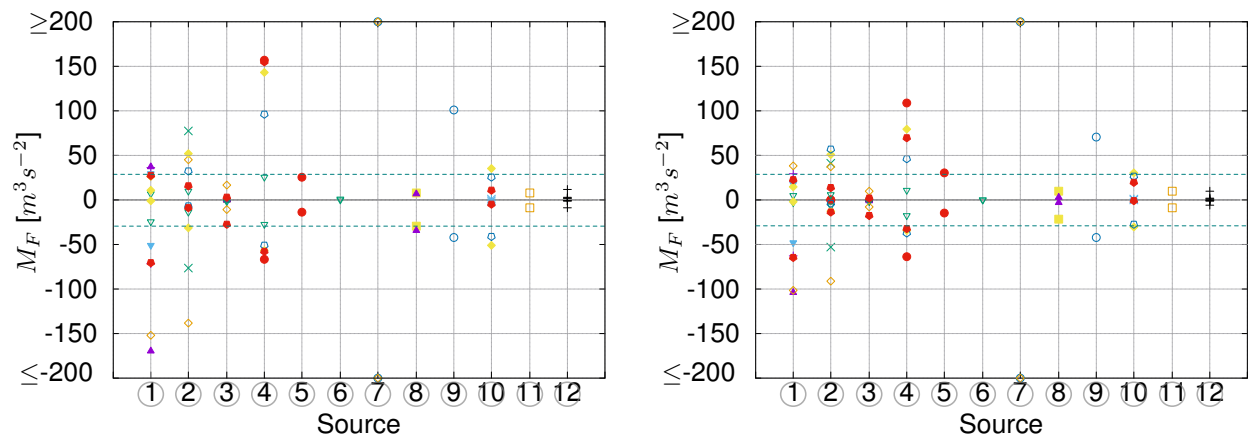
Besides the common tsunami hazard characterisation based on hydrostatic intensity measures, late developments show the significant role played by flow velocity when characterising the structural response to tsunami threats. The momentum flux, $M_F = hv^2$, provides a composed representation of tsunami effects on coastal structures capturing physical characteristics of hydrodynamic forces acting on structures during tsunamis [50]. Park et al. 2013 [14] investigated the importance of hydrodynamic effects in tsunami inundation models and, later applied the experimental-numerical correlation to developed fragility curves for wood and reinforced concrete buildings on seaside Oregon exposed to a tsunami generated in the Cascadia subduction zone [196]. For wood buildings, a 90% probability of collapse was associated to $\eta \geq 5 m$ and $M_F \geq 10 m^3 s^{-2}$, whereas for reinforced concrete buildings the M_F value to induce 80% probability of moderate to extensive damage varied between $80 m^3 s^{-2}$ and $250 m^3 s^{-2}$, depending on the number of storeys (1 to 6 storeys). The work of Song et al. 2018 [493] showed that $\eta \approx 5 m$ and $M_F = 30 m^3 s^{-2} = 100\%$ probability of major up to complete damage for coastal and ria regions. Fig. 6.8 depict the M_F values of the multiple scenarios and configurations of the Sines port. The reference value represents a compromise between the values mentioned above for reinforced concrete, $M_F = 30 m^3 s^{-2}$, and the level of performance demand required for critical structures, such as the Sines port.

Most scenarios presented an asymmetric distribution of M_F quantities due to tsunami inflow and outflow stages. In most scenarios, the collapse of the breakwater influencing the propagation towards Terminal XXI, resembled in Case A2, and the tsunami impact on the future Vasco da Gama terminal, in Case C, tended to promote a more symmetric distribution of positive and negative M_F values. In Cases A1, B1 and B2, the assymetry of the waves' peaks tended to become more accentuated mainly after the first cycle. The 6th chapter of the ASCE code recommends considering two complete tsunami cycles when assessing tsunami forces. From the present 1755 GLET-alike tsunami simulations, set to $t = 7200 s$, the critical values or flow height and velocity were verified at or after the third wave, which shows the need to adjust the bi-cyclic recommendation to account the energetic succession of tsunami train of waves.

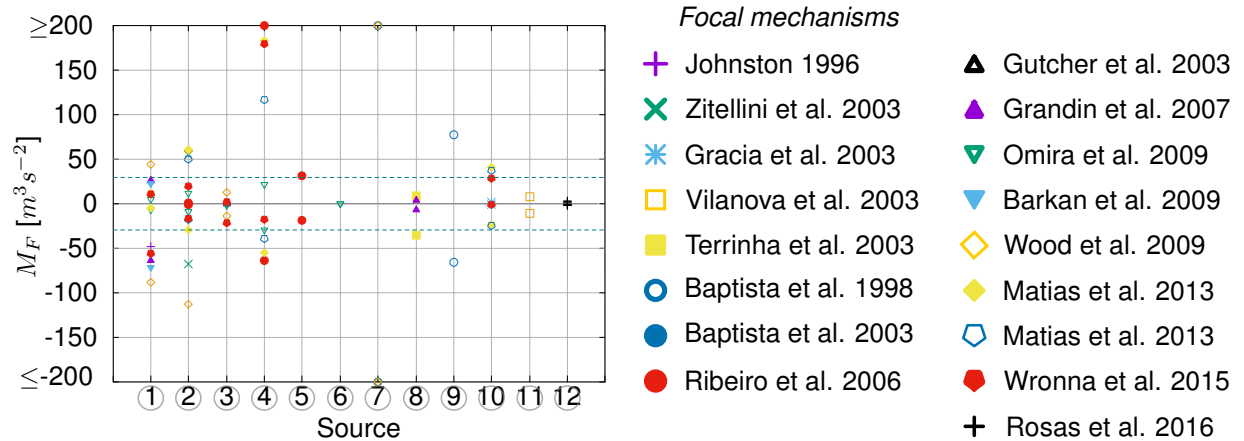
Moreover, the predominance of positive and negative momenta flux, M_F^+ and M_F^- , induce different structural actions and, consequently, different structural responses. The asymmetric distribution privileging a positive momentum flux, M_F^+ , showed higher tsunami hydrodynamic quantities during the inflow phase, when the horizontal hydrodynamic force pushes the quay against the embankment while



(a) Current configuration. Case A1 (left) - Terminal XXI with undamaged breakwater. Case A2 (right) - Terminal XXI assuming the collapse of the breakwater.



(b) Future configurations. Case B1 (left) - enlargement of Terminal XXI and respective breakwater. Case B2 (right) - Terminal XXI after construction of Vasco da Gama terminal.



(c) Future configurations. Case C - Terminal Vasco da Gama.

Scenarios

- | | | | | | |
|-------|---------|---------|----------|---------|------------|
| ① GBF | ② MPF | ③ CWF | ④ HSF | ⑤ SVF | ⑥ PBF |
| ⑦ WIS | ⑧ MPPSF | ⑨ MPPBF | ⑩ MPHFSF | ⑪ GBTVF | ⑫ HSCFSWIM |

Figure 6.8: Peak tsunami hazard: values of momentum flux due to 1755 GLET-alike tsunami around the cargo hub of Sines port. Reference value of $M_F = 30 \text{ m}^3 \text{ s}^{-2}$ set to represent the damaging potential of the tsunami hydrodynamic effects on the container terminal(s).

in the vertical directions induces an uplifting effect at the soffit of the slab, which was designed to withstand downward forces. The effects of M_F^+ were particularly evident on the HSF scenarios solutions. Conversely, the GBF and MPF scenarios tended to present predominant M_F^- effects corresponding to the outflow phase, that potentially induces seaward displacement of the elevated structure.

The scenarios and configurations that meet the $\|M_F\| \geq 30 \text{ m}^3 \text{ s}^{-2}$ criteria in the container terminal(s) were considered $S_{eligible}$. During the tsunami inflow phase, the HSF (except scenarios derived from Omira et al. 2009 source parameters), WIS and MPPBF scenarios were elected, while WIS, GBF with source parameters proposed by Wood et al. 2009, the MPF with initial conditions of Zitellini et al. 2001 and Wood et al. 2009, and HSF from Ribeiro et al. 2006 were considered $S_{eligible}$ of the tsunami outflow phase.

Cascading seismic and tsunami hazard

The individual $S_{eligible}$ of seismic and tsunami processes indicated hazardous intensity measures derived from the WIS scenarios. However, an issue regarding the credibility/reliability of the triggering source was previously raised to discussed its contribution on the multi-hazard assessment. Although the first proposals of 1755 GLET source were off the western coast of Portugal [440], the rupture of the compressive structures of the GBF was proposed only in the late twentieth century [428]. Nonetheless, the tsunami quantities were incompatible with tsunami research. The WIS rupture hypothesis considering that the seismic rupture was closer to the western coast of Portugal and extended farther north toward Lisbon [446] explained the tsunami observations. The WIS mechanism was utterly corroborated in a phenomenological reconstruction of the 1755 GLET [456], assuming $Mw9.0$, an extended rupture of a 350 km -length times 150 km -width projected area, displacement parameters of $\varphi = 350^\circ$, $\delta = 25^\circ$, $\lambda = 20 \text{ m}$ and $\Theta = 60^\circ$ and the soil rigidity, $\mu = 4 \times 10^{10} \text{ Pa}$ [456]. The configuration of the co-seismic faulting was based on a full range of contemporary observations of macro-seismic impacts, effects of far-field sources elongating period, near-field and far-field tsunami heights and travel times, evidence for associated deformation, and accompanying regional stress changes [456]. Yet, among the parameters lacks the geological evidence to support the existence of the hypothetical WIS fault. Moreover, Figs. 6.5, 6.7 and 6.8 show the solutions calculated from WIS source diverging from all the PGA framework from all the other sources. Thus, the WIS scenarios were maintained in the present study to play a disclaimer role, raising awareness for the possibility of hazard exceedance in the future, but were dismissed from the list of $S_{eligible}$.

From the credible $S_{eligible}$, listing sets of earthquake and tsunami intensity measures together, were selected the hazardous ones in terms of ground motion acceleration, tsunami height and momentum flux influential quantities. Table 6.2, complementary of Figs. 6.9 and 6.10, resumes the intrinsic values of each hazardous scenario when considering different leading intensity measures, PGA, η and M_F , in both tsunami flow conditions.

Keeping in mind design criteria considerations, the different leading intensity were combined to establish loading pattern respecting the scenarios integrity, i.e., maintaining the inextricable condition of

Table 6.2: Peak cascading hazard. Earthquake and tsunami maximum intensity measures for the different structural configurations varying the leading measure (bold font). Identification of the respective triggering source and respective literature reference.

| Str. Case | Lead IM | Scenario | | η [m] | M_F^+ [m ³ s ⁻²] | M_F^- [m ³ s ⁻²] | PGA <i>g</i> |
|--------------|------------|----------|----------------------------|---------------|--|--|-----------------|
| | | Source | Literature | | | | |
| A1 | η | MPPBF | Baptista et al. 2003 [447] | 11 | 75 | -45 | 0.35 |
| | M_F^+ | HSF | Ribeiro et al. 2006 [454] | 7 | 193 | -55 | 0.21 |
| | M_F^- | GBF | Grandin et al. 2007 [455] | 6 | 27 | -139 | 0.20 |
| A2 | η | HSF | Wronna et al. 2015 [458] | 9 | 194 | -37 | 0.16 |
| | M_F^+ | HSF | Wronna et al. 2015 [458] | 9 | 194 | -37 | 0.16 |
| | M_F^- | MPF | Zitellini et al. 2001[448] | 6 | 30 | -252 | 0.27 |
| B1 | η | MPPBF | Baptista et al. 2003[447] | 10 | 100 | -42 | 0.35 |
| | M_F^+ | HSF | Ribeiro et al. 2006 [454] | 8 | 156 | -67 | 0.21 |
| | M_F^- | GBF | Grandin et al. 2007 [455] | 6 | 37 | -170 | 0.20 |
| B2 | η | MPPBF | Baptista et al. 2003 [447] | 8 | 75 | -47 | 0.35 |
| | M_F^+ | HSF | Ribeiro et al. 2006 [454] | 8 | 108 | -63 | 0.21 |
| | M_F^- | GBF | Grandin et al. 2007 [455] | 5 | 22 | -101 | 0.20 |
| C | η | MPPBF | Baptista et al. 2003 [447] | 14 | 77 | -66 | 0.35 |
| | M_F^+ | HSF | Ribeiro et al. 2006 [454] | 11 | 242 | -64 | 0.21 |
| | M_F^- | MPF | Wood et al. 2009 [456] | 8 | 60 | -113 | 0.32 |
| Site | PGA | MPPSF | Terrinha et al. 2003 [449] | ≈ 8 | <50 | >-50 | 0.37 |

the source that defined the combined scenario. Thus, from the $S_{eligible}$ list were identified the hazardous seismic and tsunami sets of potential S_{worst} for the structure by combining the higher leading intensity measure (varying between PGA, η , M_F^+ and M_F^-) with the respective intensity measures obtained for the same triggering source. The higher PGA value was derived from the MPPSF scenario adopting Terrinha et al. 2003 source and attenuation parameters proposed by Atkinson and Boore 1995 (Fig. 6.9). The corresponding tsunami hydrostatic quantities posed a significant buoyancy hazard for the infrastructure, 8 m against the 5 m reference value for the elevated structure, while the assessed momenta flux were below the damaging reference value. Apart from the MPPBF scenario, the scenarios triggering the hazardous tsunami quantities presented PGA values below the EC8 recommendation. On the one hand, the great uncertainty associated with the PGA estimates might have prevented the accurate prediction of a strong ground motion event in the seismically moderate region. On the other hand, under an optimistic perspective on the accuracy of the PGA predictions, the Sines port designed as a structure of class of importance III, would be capable to resist most of the earthquakes estimates, keeping itself in elastic regime during the earthquake and prepared to withstand the incoming tsunami.

Regarding the structural response of the resisting system to the tsunami action, hydrostatic and hydrodynamic considerations, flow phases, inflow and outflow stages, and loading direction, horizontal and vertical, were considered design influencing factors. Figure 6.10 depicts the S_{worst} intensity measures for each of the infrastructure configurations.

The S_{worst} considering the hydrostatic tsunami effects on the structure led to two different scenarios, depending on the configuration case. For configurations Cases A1, B1, B2 and C, the MPPBF fault

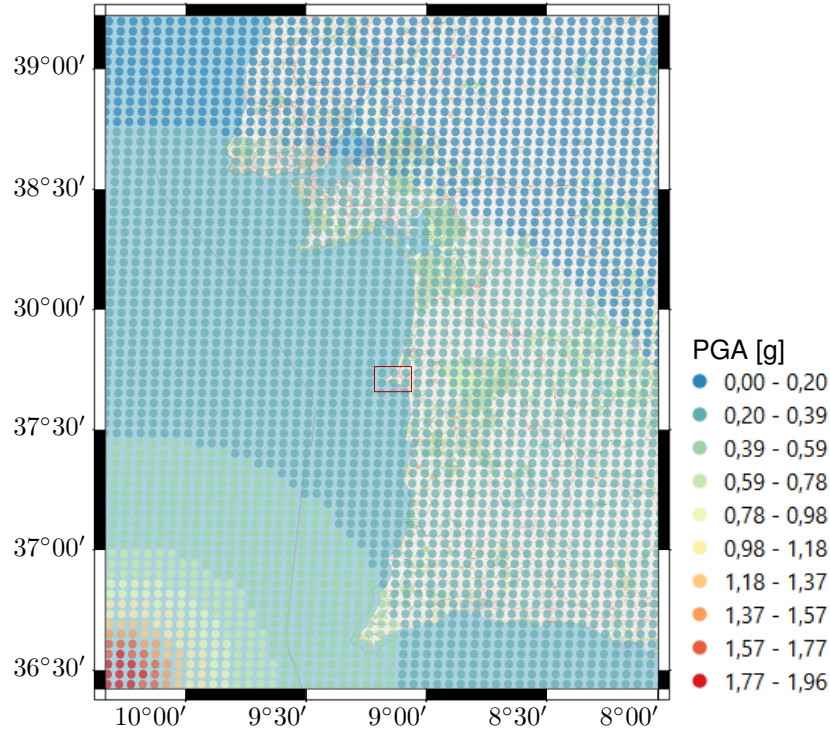


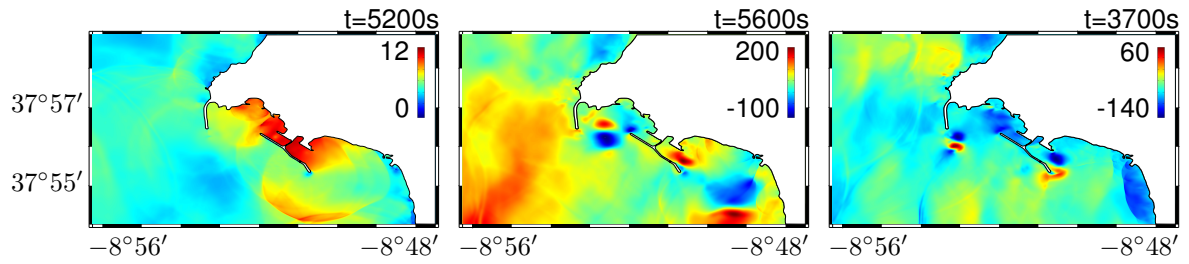
Figure 6.9: Peak seismic action: distribution of PGA from S_{worst} adopting the source rupture of the composite Marquês de Pombal and Pereira de Sousa faults proposed by Terrinha et al. 2003 [449].

parameters proposed by Baptista et al. 2003 triggered the higher waves, while for Case A2, the higher wave was promoted by HSF scenario with Wronna et al. 2015 initial conditions.

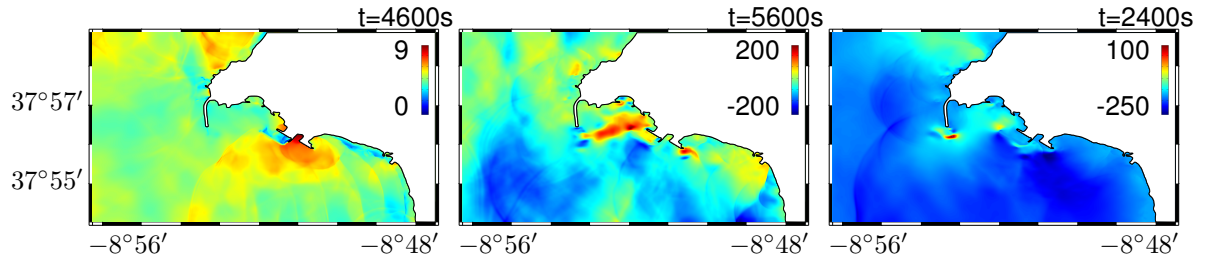
The M_F quantities demonstrate significant variability depending on the flow direction. For M_F^+ , the HSF scenario with a source characterization using the parameters proposed by Ribeiro et al. 2006 represented the S_{worst} for all configuration cases excepting Case A2, which shares the HSF common source that triggers the higher wave. The GBF source with source parameters of Grandin et al. 2007 was found to be the S_{worst} for Cases A1, B1 and B2. The rupture of MPF represented the hazardous scenario when considering the absence of the breakwater, Case A2, and for the new Vasco da Gama terminal, Case C, respectively derived from the Zitellini et al. 2001 and Wood et al. 2009 proposals of source parameters.

Peak loading patterns

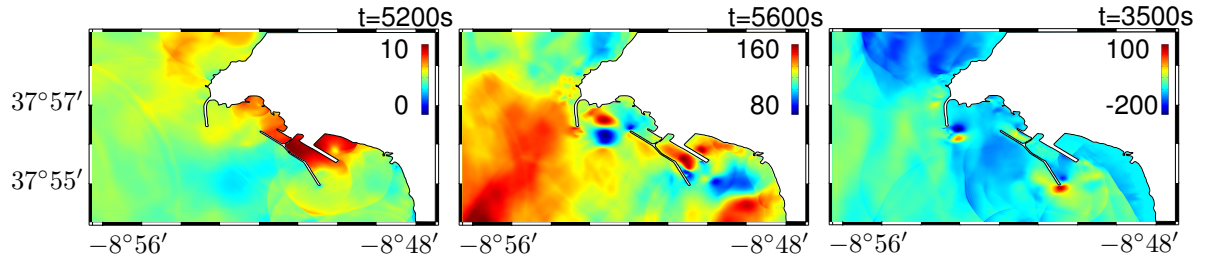
The corresponding design forces were then estimated for the set of S_{worst} using the sum of Eqs. 3.25 and 3.26 introduced in Section 3.2.2 assuming $\gamma_s = 11kN/m^3$, $\rho_s = 1.1kg/m^3$, $I_{tsu} = 1.25$ and $C_d = 2$. The hydrodynamic quantities feeding the equations were capture by virtual gauges located at the cell of fluid immediately before the cell containing the structure. The horizontal and vertical forces exerted on the pile-supported infrastructure were calculated for a transverse 12 m-width section corresponding to one module of the structure that repeats itself along the longitudinal direction. Using the pseudo-3D module allows to mimic the configuration of the piles, 2 piles and 5 piles every 6 m, and adopt the design recommendations for open structures, i.e., a structure in which the portion within the inundation depth



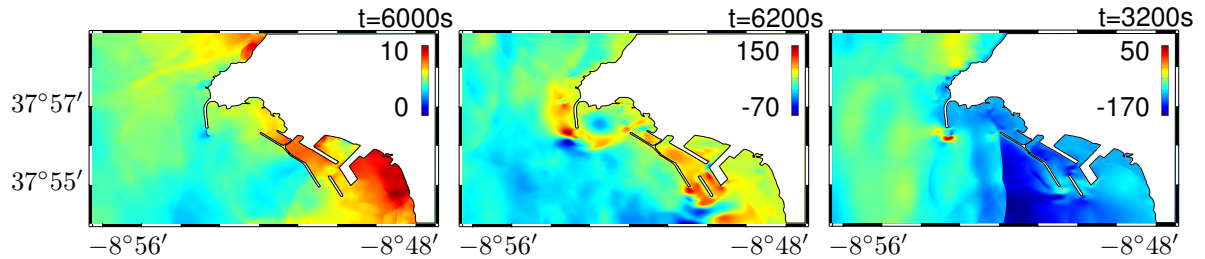
(a) Case A1: maxima η (left), M_F^+ (middle) and M_F^- (right) and respective elapsed times after $t_{sim} = 0 s$, using the fault parameters proposed by Baptista et al. 2003 [447] for the composite Marquês de Pombal and Portimão Bank faults, Ribeiro et al. 2006 [454] for the Horseshoe fault and Grandin et al. 2007 [455] for the Gorringe Bank fault.



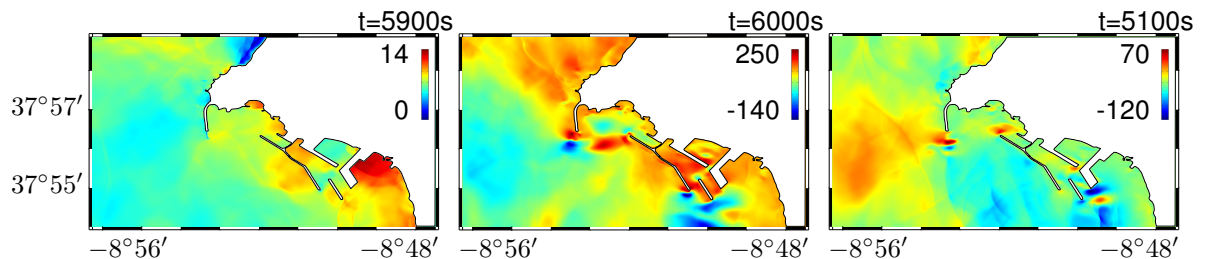
(b) Case A2: maxima η (left), M_F^+ (middle) and M_F^- (right) and respective elapsed times after $t_{sim} = 0 s$, using the fault parameters proposed by Wronna et al. 2015 [458] for the Horseshoe fault and Zitellini et al. 2001 [448] for the Marquês de Pombal fault.



(c) Case B1: maxima η (left), M_F^+ (middle) and M_F^- (right) and respective elapsed times after $t_{sim} = 0 s$, using the fault parameters proposed by Baptista et al. 2003 [447] for the composite Marquês de Pombal and Portimão Bank faults, Ribeiro et al. 2006 [454] for the Horseshoe fault and Grandin et al. 2007 [455] for the Gorringe Bank fault.



(d) Case B2: maxima η (left), M_F^+ (middle) and M_F^- (right) and respective elapsed times after $t_{sim} = 0 s$, using the fault parameters proposed by Baptista et al. 2003 [447] for the composite Marquês de Pombal and Portimão Bank faults, Ribeiro et al. 2006 [454] for the Horseshoe fault and Grandin et al. 2007 [455] for the Gorringe Bank fault.



(e) Case C: maxima η (left), M_F^+ (middle) and M_F^- (right) and respective elapsed times after $t_{sim} = 0 s$, using the fault parameters by Baptista et al. 2003 [447] for the composite Marquês de Pombal and Portimão Bank faults, Ribeiro et al. 2006 [454] for the Horseshoe fault and Wood et al. 2009 [456] for the Marquês de Pombal fault.

Figure 6.10: Peak tsunami intensity measures for the different configuration cases. The left column regards maximum free-surface elevation (m), while middle and right columns represent tsunami maximum momenta flux (m^3s^{-2}) during inflow and outflow stages, respectively.)

has no greater than 20% of closure ratio, not having interior partitions or contents preventing flow from passing through and exiting the structure as unimpeded waterborne debris [32]. In this case, $C_{cx} = 0.5$. The slopping grade under the slab was set to 36 : 25. Table 6.3 resumes tsunami horizontal and vertical forces inferred from the set of S_{worst} . Considering the long-term forecast for the construction of Vasco da Gama terminal, an additional exercise of comparing tsunami forces for an open- or closed-typologies was performed, cases C1 and C2. respectively. For the sake of simplicity, the results are presented in kN per meter in the longitudinal direction (perpendicular to shoreline).

Table 6.3: Peak cascading actions. Cascading earthquake and tsunami loading patterns for the different structural configuration cases.

| Str. Case | Lead IM | PGA [g] | Horizontal force [kN/m] | | Vertical force [kN/m] | |
|-----------|---------|---------|-------------------------|---------|-----------------------|---------|
| | | | Inflow | Outflow | Inflow | Outflow |
| A1 | η | 0.35 | 335.53 | 282.68 | 1 070.23 | 249.68 |
| | M_F^+ | 0.21 | 277.50 | 168.28 | 3 439.40 | 240.30 |
| | M_F^- | 0.20 | 231.89 | 158.78 | 677.15 | 161.55 |
| | PGA | 0.37 | 242.02 | 197.98 | 1 005.36 | 244.99 |
| A2 | η | 0.16 | 332.94 | 231.20 | 2 752.64 | 257.18 |
| | M_F^+ | 0.16 | 332.94 | 231.20 | 2 752.64 | 257.18 |
| | M_F^- | 0.27 | 178.21 | 54.01 | 862.66 | 55.62 |
| | PGA | 0.37 | 246.43 | 193.57 | 1 148.06 | 235.62 |
| B1 | η | 0.35 | 319.04 | 256.50 | 1 433.46 | 252.49 |
| | M_F^+ | 0.21 | 288.71 | 190.49 | 2 517.97 | 229.05 |
| | M_F^- | 0.20 | 181.30 | 90.13 | 995.85 | 132.49 |
| | PGA | 0.37 | 242.02 | 197.98 | 1 005.36 | 244.99 |
| B2 | η | 0.35 | 253.03 | 199.30 | 1 362.11 | 247.80 |
| | M_F^+ | 0.21 | 267.57 | 192.25 | 1 833.02 | 232.80 |
| | M_F^- | 0.20 | 147.19 | 93.02 | 794.17 | 197.18 |
| | PGA | 0.37 | 242.02 | 197.98 | 1 005.36 | 244.99 |
| C1 | η | 0.35 | 418.91 | 355.93 | 919.74 | 229.99 |
| | M_F^+ | 0.21 | 409.08 | 274.31 | 2 803.37 | 231.87 |
| | M_F^- | 0.32 | 246.43 | 170.23 | 1 148.06 | 185.93 |
| | PGA | 0.37 | 242.02 | 197.98 | 1 005.36 | 291.87 |
| C2 | η | 0.35 | 875.87 | 781.40 | - | - |
| | M_F^+ | 0.21 | 902.38 | 700.22 | - | - |
| | M_F^- | 0.32 | 699.64 | 585.35 | - | - |
| | PGA | 0.37 | 259.64 | 180.36 | - | - |

6.4.2 Enhanced solution

Description

The deterministic approach of multi-hazard assessment provided peak quantities combining ground motion, and tsunami hydrostatic and hydrodynamic effects on the container terminal of Sines deep-water seaport. From the same S_{worst} was inferred the extended characterization of corresponding dynamic loading patterns.

The EXSIM tool described in Section 3.3.3, was adopted to determine the time-story of seismic accelerations. Tsunami dynamic forces were determined using the coupled methodology described in Section 3.2.3 and validated in Chapter 5.

Seismic hazard

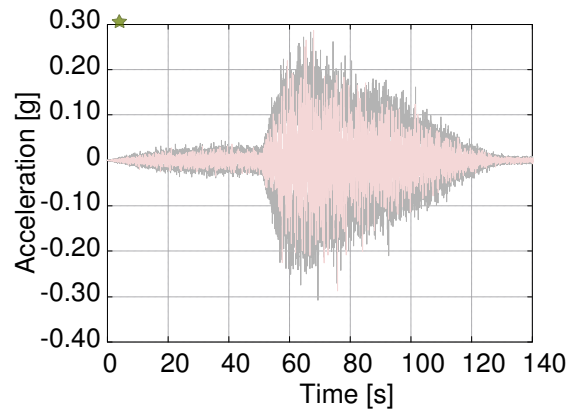
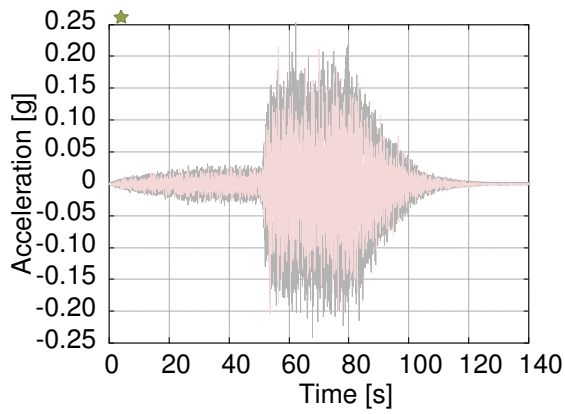
The peak values of ground acceleration provided an important insight for structural design methods based on non-linear static analysis. However, a complementary characterization of the seismic action in time domain was pursued for further non-linear dynamic analyses. The S_{worst} were re-evaluated adopting the routine implemented in EXSIM [353]. Each of the S_{worst} were modeled to include geometry, kinematics and geotechnical parameters, as resumed in Section D.1, Appendix D. In addition, EXSIM requires complementary data such as magnitude, stress drop, type of fault, fault length and width, stress_{ref}, hypocenter location in along fault and down dip distance from the fault, geometric spreading, quality factor, damping of response spectra, number of frequencies, frequencies, crustal amplification filter for frequencies, site amplification for frequencies, slip weight for sub-faults, seed and number of trials, number and location of sites to compute the accelerations.

An overall and broad region of distributed deformation under NNW-SSE compressive stress-fields were reported for Portugal mainland and adjacent West Iberia region [494–496]. A value of 100 *bar* were indicated as an upper boundary for the local stress, yet with a disclaimer considering it as an overestimation by Ribeiro et al. 1996 [494]. Zonno et al. 2005 [495] adopted values of 50 *bar* for offshore sources and 120 *bar* for inland sources, while Carvalho et al. 2009 estimated 101 *bar* for intraplate and 66 *bar* for interplate ruptures. Values between 90 *bar* and 130 *bar* were later estimated for the Azores region [497]. For the EXSIM parametrization, the stress drop parameter was defined with a value of 65 *bar*.

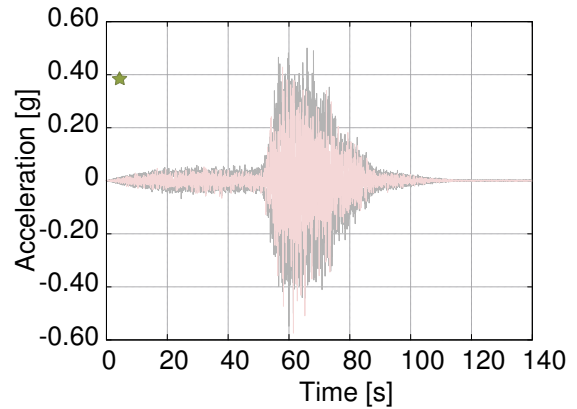
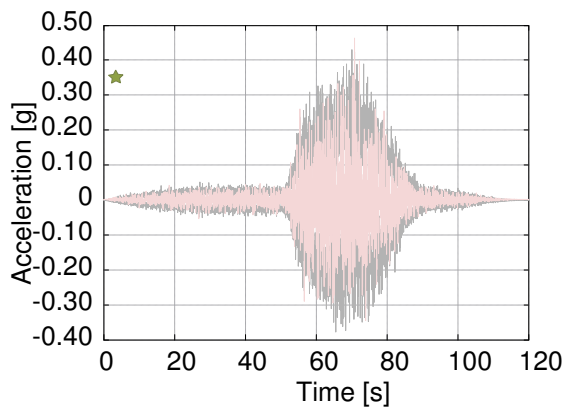
The hypocenter location along fault and down dip distance from the fault reference point (an upper corner) was assumed with a random location. The geometric spreading was modeled following bi-linear relationship with transition at the average value of 34.5 *km*, between 37.5 *km* given in Zonno et al. 2005 [495] and 31.0 *km* given in Carvalho et al. 2009 [496]. The quality factor, $Q = \max(Q_{min}; Q_0 F \eta)$, used $Q_0 = 239$ and $\eta = 1.06$. The crustal amplification filter relating frequency and amplification follows Atkinson and Boore 2006 [463] relation for hard rock, while the site amplification filter file considers no amplification for the Sines port case due to its implementation of good geotechnical conditions. Random slip weights were assigned to all sub-faults.

Given the inherent variability in earthquake ground motions, design standards typically require analyses for multiple ground motions to provide statistically robust measures of the demands. Twenty accelerograms were generated for each of the S_{worst} . Fig. 6.11 shows the time-stories of design seismic acceleration for the various S_{worst} . For the sake of readability, one time-history and its complementary standard variation is shown in the accelerograms.

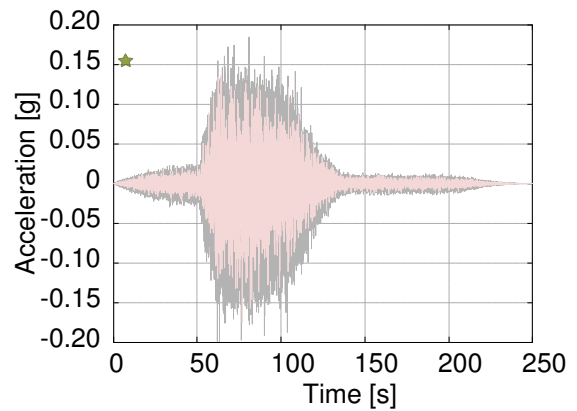
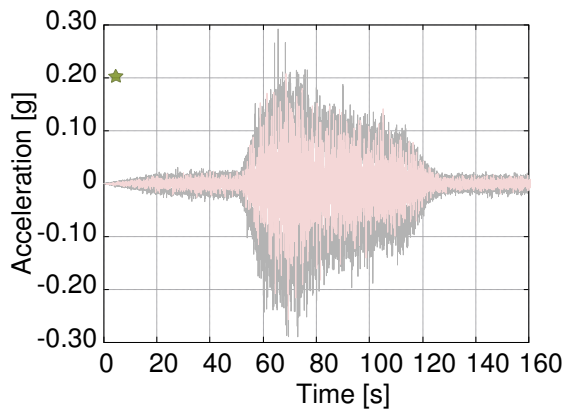
The maxima accelerations estimated from dynamic characterization are in general agreement with PGA assessed in Section 6.4.1. Moreover, the synthetic time series generated by means of a non-stationary stochastic method were converted into spectrum responses with damping of 5% to check



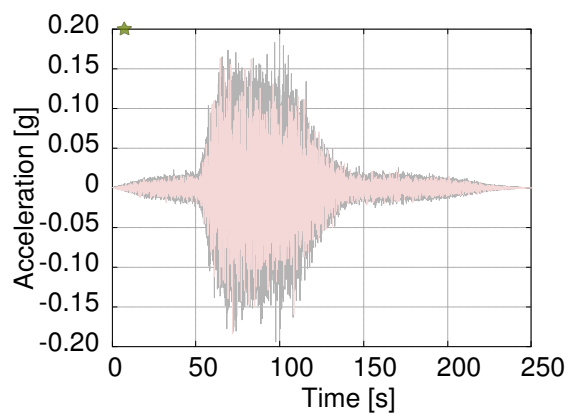
(a) Marquês de Pombal sources proposed by Zitellini et al. 2001 [448] (left) and Wood et al. 2009 [456] (right).



(b) Marquês de Pombal and Portimão Bank source proposed by Baptista et al. 2003 [447] (left) and Marquês de Pombal and Pereira de Sousa source proposed by Terrinha et al. 2015 [449] (right).



(c) Horseshoe source proposed by Ribeiro et al. 2006 [454] (left) and Wronna et al. 2015 [458] (right).



(d) Gorrige Bank source proposed by Grandin et al. 2007 [455].

Figure 6.11: Dynamic earthquake action: time-histories of seismic acceleration derived from various S_{worst} . Stars representing previously estimated PGA values.

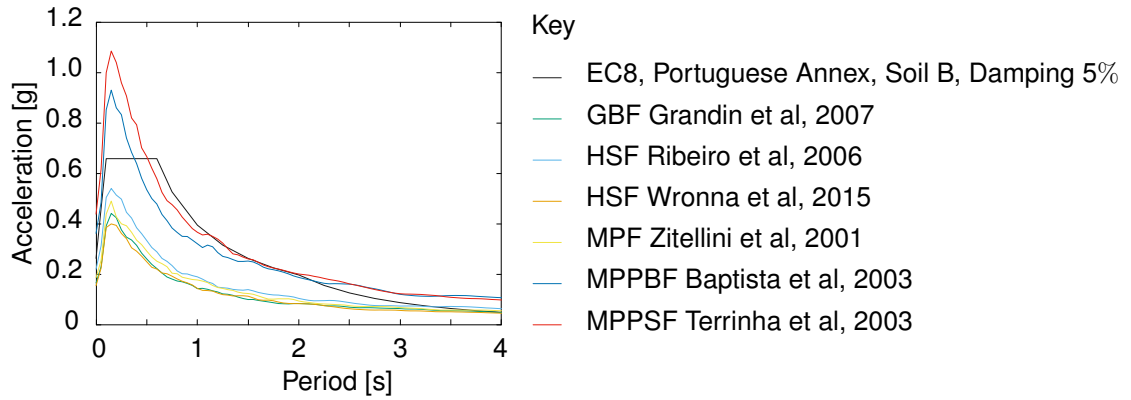


Figure 6.12: Dynamic earthquake action: correlation between elastic response spectra derived from synthetic accelerograms

the compatibility with the recommendations of the Portuguese target design spectrum recommended in Eurocode 8, which was introduced in Section 3.3.4. Each elastic response spectrum of S_{worst} was represented as an average of its twenty generated response spectra, considering a viscous damping of 5%. The regulatory elastic response spectra was calculated for the Sines region and soil B. Fig. 6.12 shows the correlation between the synthetic and regulatory elastic response spectra.

In general, the correlation reveals variability among the generated and the regulatory elastic response spectra. In terms of shape form, the average generated spectra missed the representation of the constant spectral acceleration (interval between regulatory T_B and T_C), mostly due to the results each of the generated or design spectra yield to represent. Whereas the response spectrum represents the response to a specific earthquake, the design spectrum represents the predicted response to an earthquake having the same PGA [498–500]. The S_{worst} corresponding to composed fault ruptures scenarios, MPPSF proposed by Terrinha et al. 2003 [449] and MPPBF proposed by Baptista et al. 2003 [447], once again exceeded the regulatory constant spectral acceleration branch. The predominant period for the synthetic ground motions of 1755-alike earthquakes was evaluated between 0.2 s and 0.4 s, which indicates the a relevant presence of high-frequency content. The contents of branch of constant of velocity (interval between regulatory T_C and T_D) and constant displacement (after T_D) presented similarities with the regulatory elastic response spectra.

Tsunami hazard

The forces and pressures induced by S_{worst} of a 1755-alike tsunami in the container terminal of Sines deep-water seaport were characterized using a coupled Eulerian SW-FV and Lagrangian NS-SPH configuration. The first part of the numerical domain encompassing the tsunami propagation, from the source of each S_{worst} up to tens of kilometers after the coastline, was modeled using SW-FV scheme to characterize inundation behavior. The simulations were identical to the ones carried out to determine the peak quantities assessment described in Section 5.2.2. Virtual gauges were strategically implemented within 50 m from the breakwater (perpendicular to structure) and repeated every 100 m (parallel to structure), VG_A . A second row of virtual gauges was placed in the vicinity of the quay, VG_B . The second part of the coupled domain was modeled using NS-SPH scheme to capture gradients of

vertical variation, encompassing the final 850 m of tsunami arrival up to the dry-wet interface and about 1250 m after the initial position of the shoreline, corresponding to the average limits of tsunami inundation area estimated from the various S_{worst} . Fig. 6.13(a) show the schematic representation of the various VG implemented in the cargo hub region.

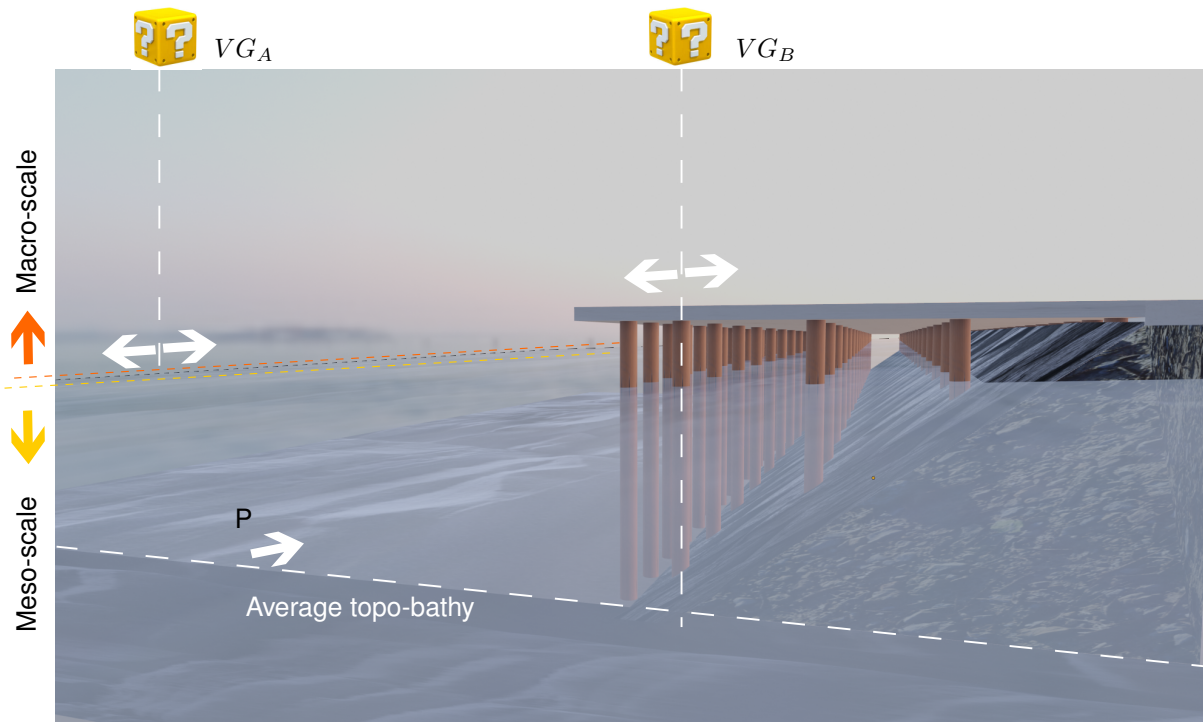
The topo-bathymetric conditions assigned to the NS-SPH model were derived from average approximation of the high-resolution grids, from which were extracted transverse profiles every 100 m in the longitudinal direction (perpendicular to shoreline). Fig. 6.13(b) depicts the various profiles and average sloping conditions, where $x = 0$ m marks the position before the breakwater in landward direction. The domain was set to cover the average limit of tsunami inundated area ($x \approx 1.25$ km). The average bathymetry and the soil-quay system were modeled using Blender [417], which is an open-source rendering engine capable of exporting .stl format files that can be read by DualSPHysics (see Fig. 6.13(a)).

The prototype of the cargo/shipping hub was reduced to geometrical scale of 1 : 10 in conjunction with temporal scale of 1 : $10^{1/2}$, based on the Froude similitude using Buckingham's theorem. For example, a wave with free surface elevation of $\eta = 8$ m and period of $T = 12$ s in real scale values corresponds to $\eta = 0.8$ m and $T = 3.80$ s when converted into reduced-scaled model. The effects of scouring, air entrapment between the fluid and the soffit of the quay slab, and debris impact and damming were neglected.

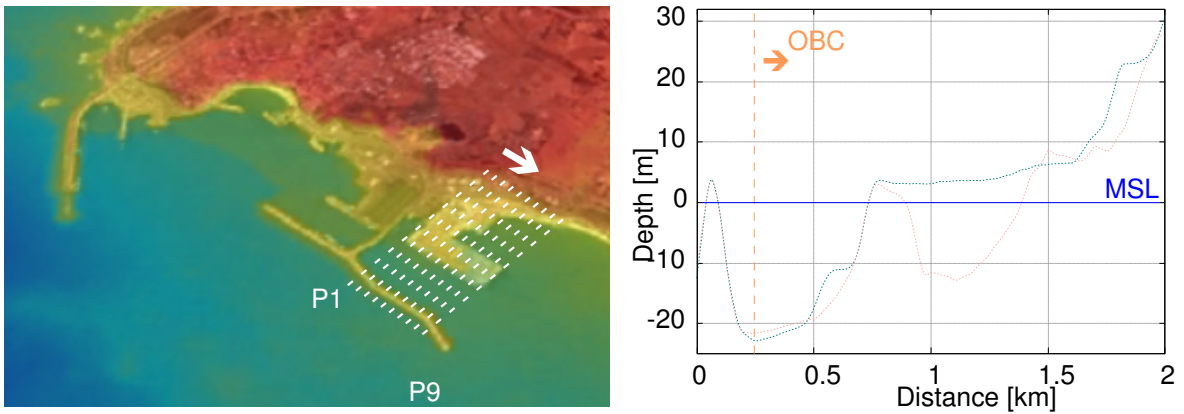
In the prototype, the distance between the breakwater and the quay is about 850 m while the inundated area extends between $x = 0$ m and $x = 1250$ m, corresponding to a 200 m-long domain in the scaled model. The local water depth considering mean-sea level condition was set to $y = 0$ m. The interface between Eulerian SW-FV and Lagrangian NS-SPH, where the data-exchange occurs, was prescribed using Dirichlet boundary condition. The transition from SW-FV to NS-SPH was imposed by OBC using free-surface elevation and flow velocity quantities captured at the cell that immediately precedes the position of the OBC VG_A (see Fig. 6.13(a)). The OBC was prescribed by a buffer layer of particles with width of $8\Delta p$ in the normal direction of the OBC, at $x = 800$ m and $y = -23.5$ m. The inlet-outlet configuration was set to convert the new particles into fluid particles while allowing reverse flow to mimic tsunami wave outflow on the seaward direction. The prototype was initially modeled to assess tri-dimensional hydraulic influences. Representative 12 m-width pseudo 3D module and 2D models were created after the original 3D model.

A brief convergence analysis of both 3D and 2D models discretization was perform using a representative OBD with initial $\eta = 1.0$ m and constant flow velocity $u = 1.6$ m/s², corresponding to $\eta = 10.0$ m and $u = 5.0$ m/s² in the prototype. The values of $\frac{H}{\Delta p}$ varied among the ratios assessed in the convergence analysis described in Section 5.2.1, Chapter 5, i.e. $\frac{H}{\Delta p} \approx 20$ to 40. The simulations were carried out using computational resources identical the ones described in Section 5.2.1. For the 3D model, $\Delta p = 0.2$ m discretization lead to convergence, resulting in more than 4.2M of initial particles and near 124 h of GPU simulation run-time, while an equivalent 2D model was discretized within $\Delta p = 0.05$ m resulting in 58K initial particles and simulation run-time of about 1 h.

The 3D NS-SPH simulations corroborated the main aspects observed in the SW-FV solutions, such



(a) Overview of the numerical model.



(b) Modeling of topo-bathymetric conditions for the NS-SPH model.

Figure 6.13: Dynamic tsunami action: modeling of the coupled configuration.

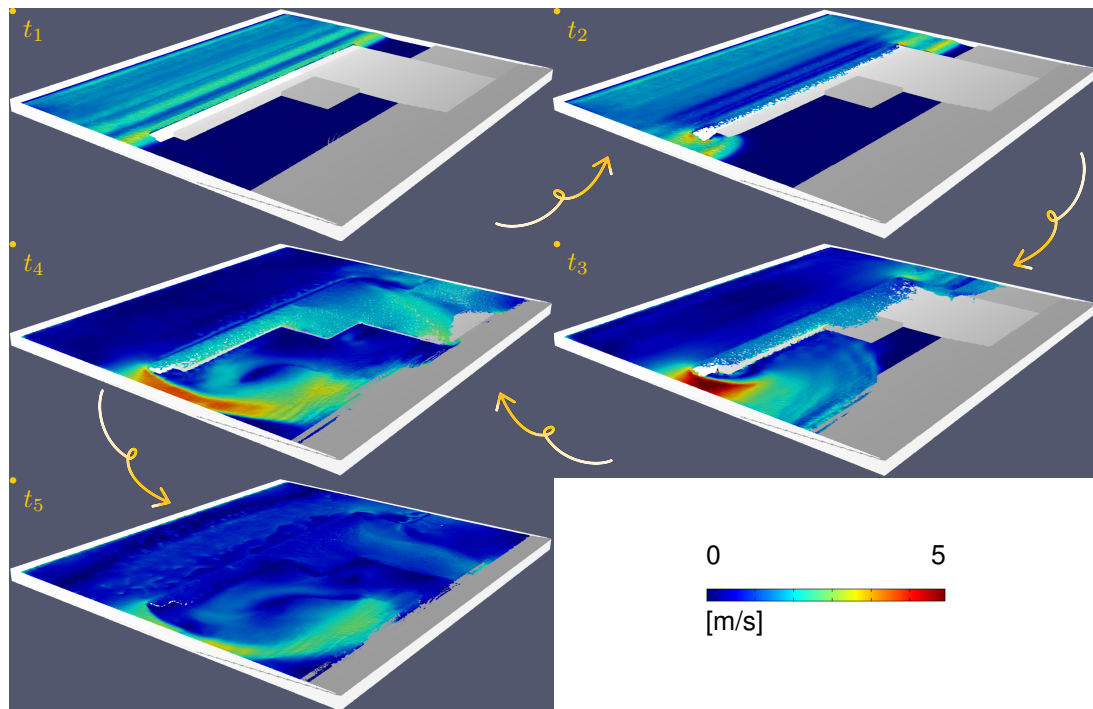
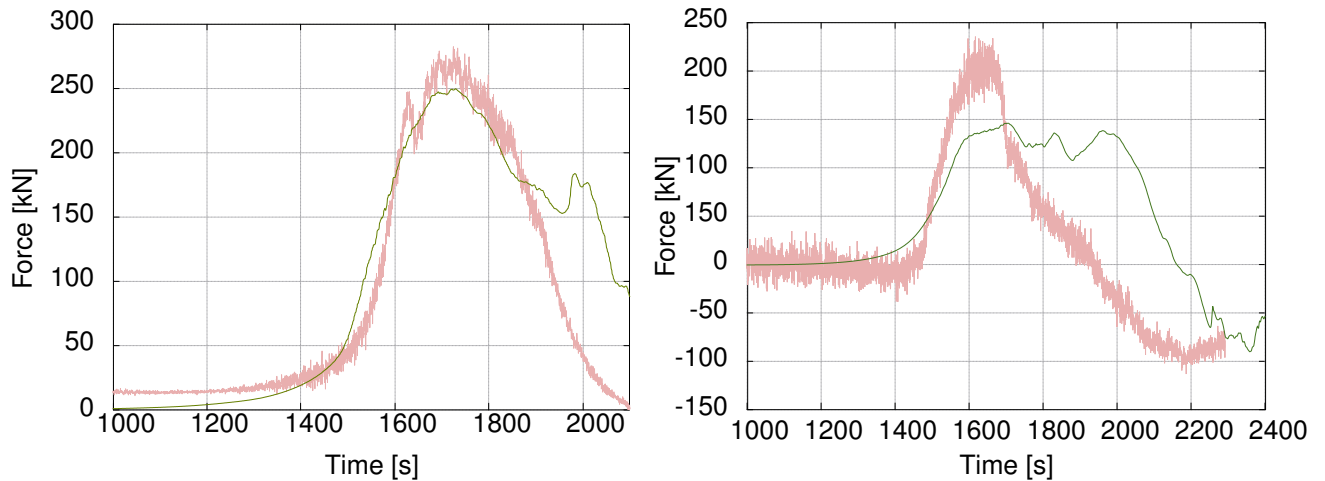


Figure 6.14: Dynamic tsunami action: particle image velocimetry of the three-dimensional NS-SPH simulation of tsunami arrival at the container terminal to characterize the general flow behavior.

as the impact and inundation patterns of the flow. Fig. 6.14 represents the numerical solutions at different times of interaction with the rigid quay. At instant t_1 the wave generated after the breakwater arrived at the quay immediately occupying the space between the free-surface level and the soffit of the quay slab due the combination of flow current itself and sloping grade of the embankment. The wave propagating towards the frontal 2.5 m -height docking region of the quay induced a seaward reflection effect. Instant t_2 shows the referred reflection effect becoming more evident when observing the position of the inundation above the quay and the limit of the lateral flow propagation towards the shoreline, i.e. the advance of the wave was faster on the lateral sides of the quay. The flow circumventing the structure developed a more accentuated response due to drag phenomenon near the sharp edges of the quay (as discussed in Section 5.1.2). The concentration of high flow velocities near the quay edges represented the main highlight observed at t_3 . A logical discussion on the origin of such amplification might consider two possible hypothesis, drag effects or channeling effects due the numerical modeling (relatively narrow space between quay and domain lateral limit). However, making use of the SW-FV solutions previously computed over wider domain was verified that same local amplifications pointing to the likelihood of being associated with drag effects posed by the obstacle. At t_4 the tsunami long-waves kept being compressed against the structure and the sloping coast wide-spreading the pathway. For example, in the wharf section designed with closed typology the impact of the flow occurred against the frontal surface perpendicular to the tsunami but the inundation of the quay started behind that point, at the lateral region near the dry-wet interface of the coastline. At instant t_5 , the shipping and storage areas were totally inundated.

Considering the SPH sensitive nature to user-defined parameters and the absence of data to



(a) Horizontal force exerted on the pile-supported quay due to tsunami first wave generated at representative S_{worst} MPPBF (left) and MPPSF (right).

KEY: — Semi-analytical SW-FV — Built-in NS-SPH

Figure 6.15: Dynamic tsunami action: correlation between time-histories of horizontal tsunami force characterized via semi-analytical SW-FV and built-in NS-SPH.

perform modeling calibration and validation, the numerical solutions were correlated with the results obtained using the long time-used and validated SW-FV tool. The initial conditions were assigned using two representative S_{worst} corresponding to the rupture of the MPPSF proposed by Terrinha et al., 2003 [449]) and MPPBF proposed by Baptista et al., 2003. The quantities were collected at the secondary set of virtual gauges implemented within 1 m from the container terminal(s), V_{GB} (see Fig. 6.13(a)). As discussed along Section 5.2, the non-linear FV-SW and NS-SPH schemes share equivalent capacity to reproduce tsunami-like waves propagation. Aiming for a fair comparison, the time of simulation was to $t \approx 650\text{ s}$ ($t \approx 2200\text{ s}$ in the prototype) order to capture the arrival of the wave while avoiding the influence of more complex hydraulic phenomena after the impact against the elevated structure. An overall fitting of the free-surface elevation curves at V_{GB} locations was verified, which contributed to increase the confidence level of using the coupled numerical protocol. The forces exerted on the quay were estimated by SW-FV and NS-SPH numerical schemes using analytical and built-in approaches, respectively. Due to SW-FV inherent characteristics, tsunami forces on the vertical direction were exclusively estimated by NS-SPH. Fig. 6.15 shows both solutions of horizontal tsunami forces exerted on the pile supported quay considering MPPSF and MPPBF scenarios and configuration case A1 (current conditions at Terminal XXI).

Moreover, the computational costs of 3D, pseudo 3D and 2D simulations were analysed on a cost-benefit perspective to evaluate the advantages of having local tri-dimensional effects (full 3D model) or pursuing simulations with more detailed geometry and refined particle discretization of the pile-supported quay (pseudo 3D model) or simplified 2D representations. The uniformity of tsunami flow impacting the quay (large infrastructure) along the longitudinal direction (parallel to shoreline) contributed to validate the assumption of a 2D model over full 3D model would provide advantageous reasonable characterization of tsunami pressures and forces exerted on the quay. The simulations of 2D models were carried out using $\Delta p = 0.05\text{ m}$, for intervals of time corresponding to the reduced

temporal scale of the tsunami $t = 7200 \text{ s} : 10^{1/2} \approx 2280 \text{ s}$. Figures 6.16 and 6.17 depict tsunami horizontal and vertical forces deduced from S_{worst} , considering current and future structural configurations. On the horizontal direction, positive forces represent fluid pushing the structure on sea-to land-ward direction. On the vertical direction, positive forces represent tsunami uplifting effects.

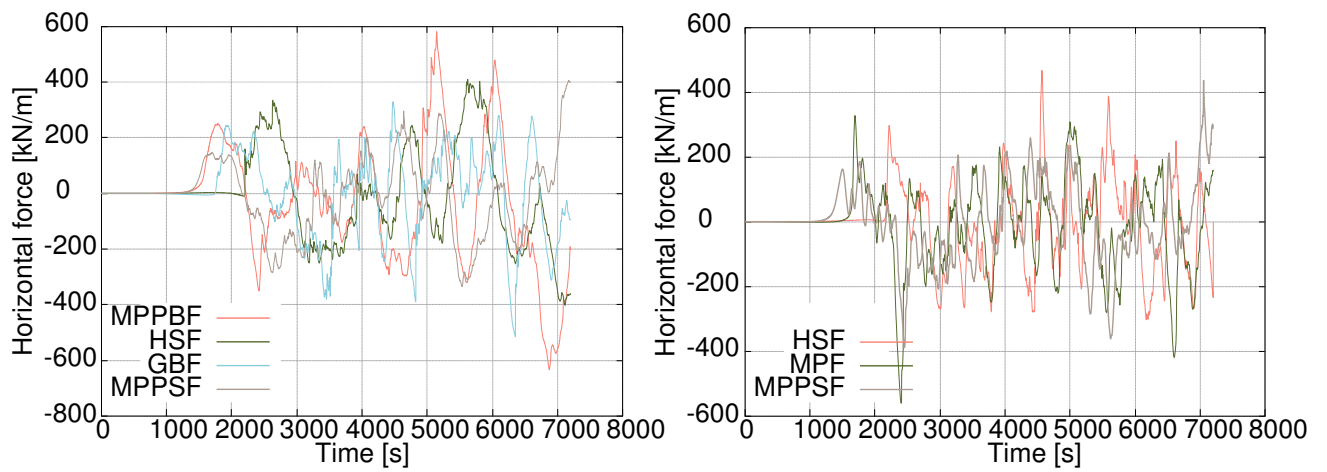
Dynamic loading patterns

The sets of dynamic loading patterns derived from each of the S_{worst} encompass time-histories of seismic acceleration and tsunami pressure in horizontal and vertical directions. Fig. 6.18 represents the general application of cascading loading patterns, and the particular set of designing loads for the various configuration cases.

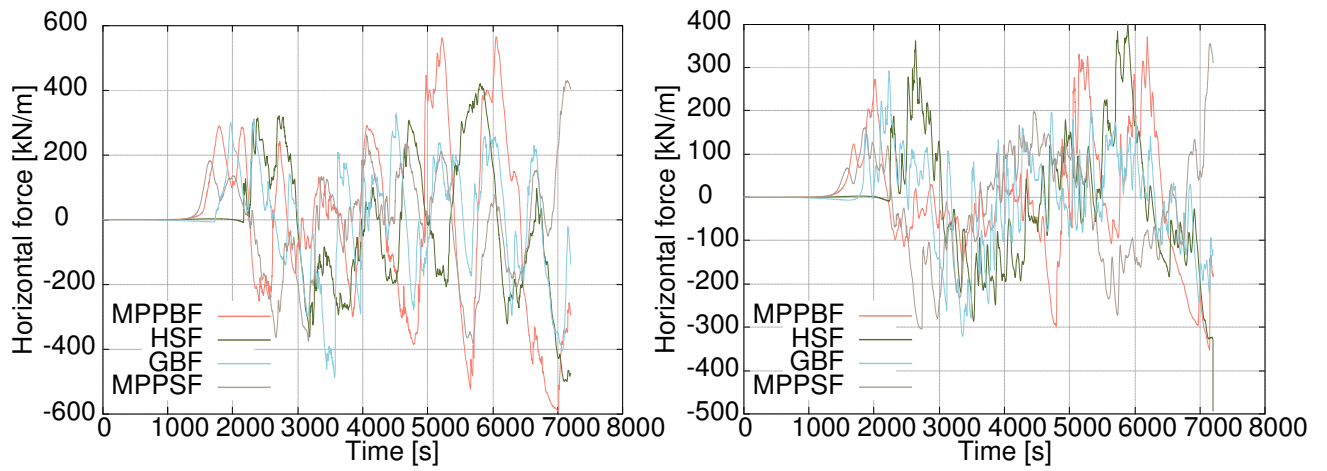
Earthquake accelerations were applied at the foundation level while tsunami forces were applied as uniform forces on the infrastructure elements. The loading combination followed the previously identified inextricable S_{worst} . Function of the configuration case, the loading pattern composition consists of seismic acceleration and tsunami horizontal and vertical effects derived from the rupture of S_{worst} . For example, for case A1 (current configuration of the cargo hub) loading cases included MPPBF proposed by Baptista et al., 2003, HSF proposed by Ribeiro et al., 2007, GBF proposed by Grandin et al., 2007 and MPPSF proposed by Terrinha et al., 2003.

The uncertainty about the most suitable distribution pattern for the representation of the hydrodynamic forces remains in the literature [501], varying among triangular and trapezoidal patterns or literature referring that the use of different distribution patterns provided similar results [502]. Regarding pressure characterization, modified the Goda equations originally developed for wave pressures on a vertical caisson breakwater were experimentally calibrated for elevated structures [503]. However, the pressure distribution was exclusively calibrated for the horizontal direction. Another work by Reis et al., 2022 [272] numerically predicted the pressure distribution on an elevated structure in both horizontal and vertical directions. However the surfaces of the elevated structure had regular surfaces, whereas the soffit of the quay has irregular geometry. Thus, the application of the tsunami action in the structural model would benefit from the multi-phase advantages of NS-SPH to study the tsunami pressure distribution under the quay. Moreover, a better characterization of drag effects among the piles is deemed necessary to infer channeling and force reduction due to relative positioning of the piles in the group. The NS-SPH showed that the first pile being impacted by the tsunami absorbed most of the wave impact.

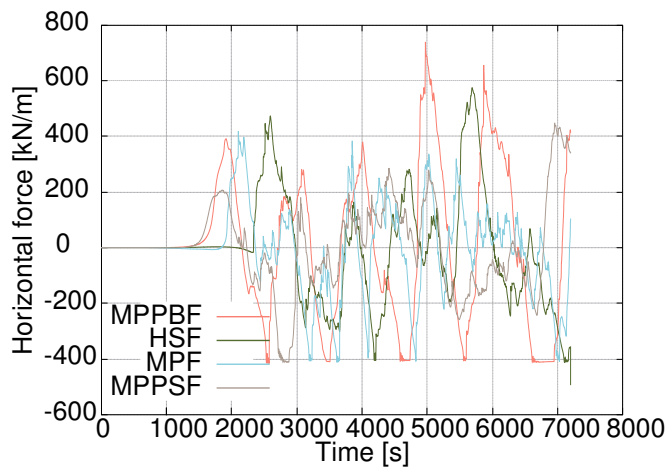
Nonetheless, the modeling followed a more sophisticated approach than what is envisioned on international regulatory codes. The NS-SPH models showed that tangential forces on the quay during inflow and outflow represent less than 10% of the loads exerted perpendicularly to the piles, while the ratio between horizontal and vertical forces was estimated in approximately 70%. An average proportion was adopted to characterize the percentage of total horizontal force being uniformly applied on the piles. Total force was considered for the first pile, 80% for the second, an reductions of 10% for the after piles. On the vertical direction, a harmonization of the highly non-linear phenomena occurring under the quay was adopted to linearly define the tsunami uplifting force.



(a) Configuration cases A1 (left) and A2 (right).

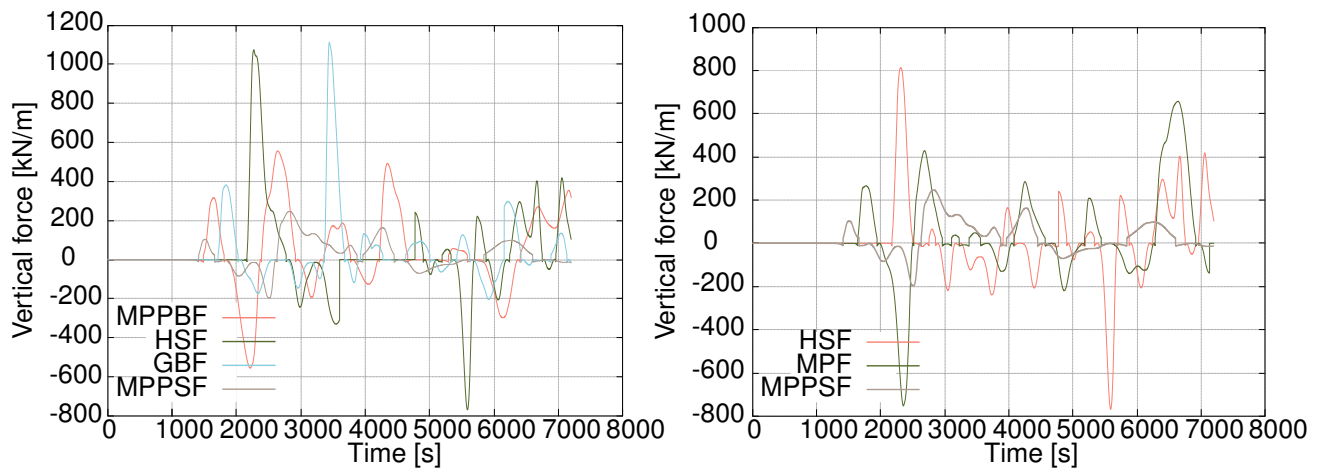


(b) Configuration cases B1 (left) and B2 (right).

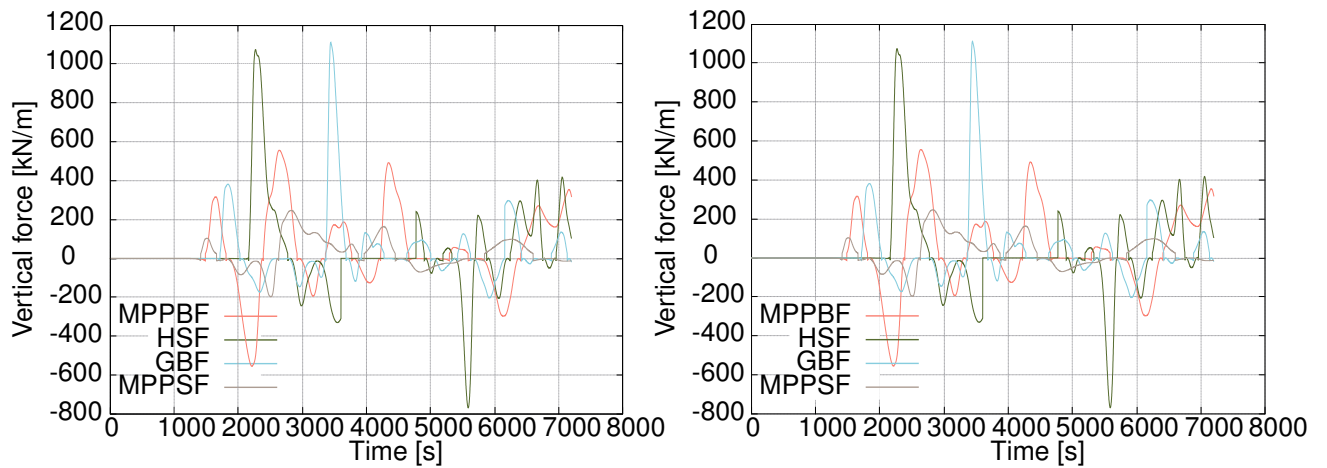


(c) Configuration cases C1.

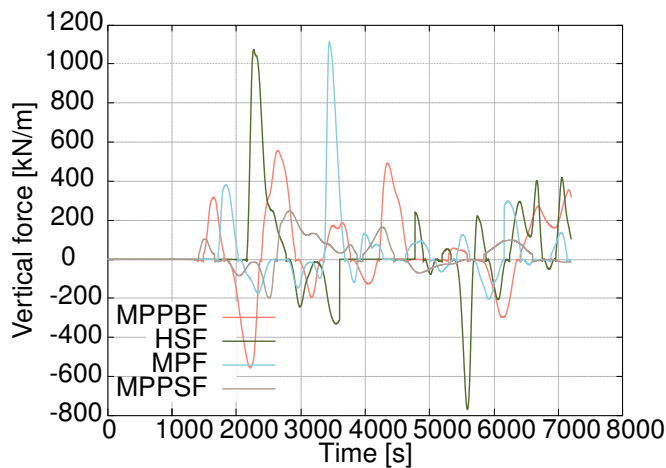
Figure 6.16: Dynamic tsunami action: time-histories of tsunami force on the horizontal direction derived from various S_{worst} and configuration cases.



(a) Configuration cases A1 (left) and A2 (right).



(b) Configuration cases B1 (left) and B2 (right).



(c) Configuration cases C1.

Figure 6.17: Dynamic tsunami action: time-histories of tsunami force on the vertical direction derived from various S_{worst} and configuration cases.

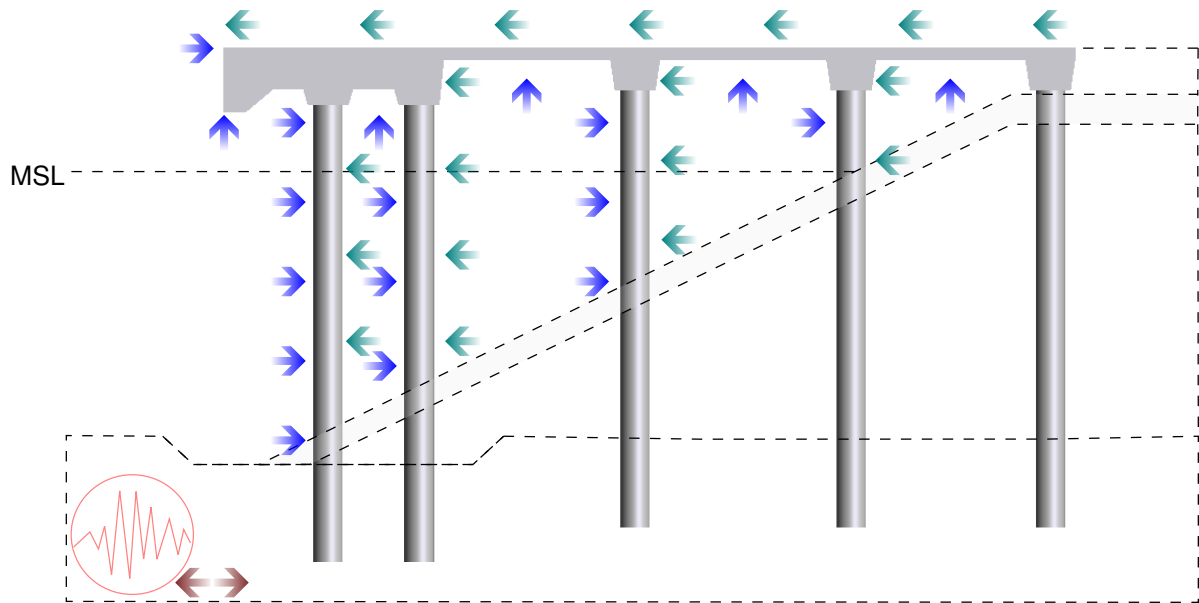


Figure 6.18: Structural analysis: successive non-linear dynamic analysis. The first to fourth interval corresponds to static loads, seismic acceleration imposed at the bed-rock level (pink), tsunami pressures during inflow stage (blue) and tsunami pressures during outflow stage (green).

6.5 Cascading multi-hazard remarks

Hazard maps provide powerful and immediate data for engineering purposes, while having an intrinsic generalist nature. The design of critical coastal structures benefit from complementary assessment of cascading seismic and tsunami multi-hazard targeting the infrastructure. Probabilistic or scenario based approaches to characterize seismic actions are comparatively more abundant than tsunami hazard estimates. The main focus of the developed work was about the performance and capacities of numerical schemes to reproduce hydraulic phenomena associated with tsunami.

Over the 864 simulations using OpenQuake software [352], at least 7 out of the 36 focal mechanism had potential to generate seismic accelerations exceeding the recommendation by the Portuguese national annex of EC8 for structures of class of importance IV ($0.298g$). Over 144 simulations of tsunami using SW-FV scheme showed that the hazardous seismic and tsunami scenarios were triggered by different sources. The hazardous seismic scenario induced $PGA = 0.37g$, while the hazardous tsunami scenario depended on the intensity measure and structural configuration of the terminal, where the corresponding PGA values varied from $0.16g$ to $0.35g$. Hydrostatic and hydrodynamic tsunami maxima quantities also derived from different scenarios and flow stages (inflow or outflow). The simulations demonstrated that, depending on the scenario, the higher hydraulic quantities were inferred between second and fifth waves, which corroborates literature mentions about the first wave of the 1755 tsunami not being the most impressive [129].

The role of coastal protections structures designed to withstand storm waves were found beneficial reducing the tsunami wave height in some of the scenarios. However, in other scenarios the presence of the breakwater led to resonance effects between the protection and the quay infrastructures. In most scenarios, the flow circumventing the edge of the breakwater led to amplification of the flow velocity

towards the quay.

Depending on the structural configuration, the hydrostatic design quantities varied from 8 m to 11 m, at Terminal XXI, and 14 m at the future Vasco da Gama terminal. The range of estimated values of positive momenta flux varied between $100 \text{ m}^3 \text{ s}^{-2}$ and $200 \text{ m}^3 \text{ s}^{-2}$, for Terminal XXI, and $M_F^+ \approx 240 \text{ m}^3 \text{ s}^{-2}$, for Vasco da Gama terminal. During the outflow stage, the negative momenta flux was quantified as $100 \text{ m}^3 \text{ s}^{-2}$ to $250 \text{ m}^3 \text{ s}^{-2}$, for Terminal XXI, $M_F^- \approx 110 \text{ m}^3 \text{ s}^{-2}$ for Vasco da Gama terminal.

Accordingly, the tsunami forces in horizontal and vertical directions were calculated using the basic and the enhance approaches for a 6 m pseudo 3D module.

The basic approach adopted the analytical recommendations of the North American standards. Average values of horizontal forces in front of the quay during the inflow were estimated in $F_h \approx 300 \text{ kN/m}$ for open typologies and double to triple values if considering a close typology for the new Vasco da Gama terminal. In the vertical direction, the tsunami forces show a wide range of values, from $F_v \approx 700 \text{ kN/m}$ to $F_v \approx 3000 \text{ kN/m}$. During the outflow, $F_h \approx 200 \text{ kN/m}$ and $F_h \approx 700 \text{ kN/m}$ for open and closed typologies, respectively, while $F_v \approx 200 \text{ kN/m}$.

The enhanced approach was conducted using the coupled numerical scheme to perform the simulations. The horizontal and vertical forces exerted on the pile-supported quay were computed using a built-in algorithm. The time histories of tsunami horizontal forces showed maxima values varying between $F_h \approx 400 \text{ kN/m}$ and $F_h \approx 800 \text{ kN/m}$, and minima between $F_v \approx -200 \text{ kN/m}$ and $F_v \approx -800 \text{ kN/m}$.

The dynamic characterizations of ground motion accelerations provided values matching the PGA estimates for the various S_{worst} . The dynamic characterization of horizontal tsunami forces showed relatively higher values than the peak estimates from the baseline solutions. However, the main differences were observed when correlating values of vertical forces. On the enhanced solutions the force was effectively quantified along the quay, while the numerical quantities adopted on the semi-analytical approach of the baseline solution were obtained from virtual gauges positioned at the last cell before the fluid-soil interaction. Moreover, the inherent simplification of SW-FV numerical scheme limits the fluid flow characterization on the vertical direction (as discussed in Section 5).

The dynamic characterization demonstrated negligible three-dimensional effects along the quay longitudinal direction, but concentrated amplifications near the unprotected pointy edges facing the waves flow. Similarly, the distribution of the pressure in the vertical direction has a tendentious exponential growth near the edges of the quay. As discussed in Chapter 5, the noisy results of pressure fields distribution accentuated on the edges are due to the inherent SPH challenge of tuning physical and numerical dissipation.

6.6 Micro-scale: Successive structural analyses

Starting from the extreme north, the current 946 m-long quay serving as container terminal is supported by RC caissons along the first 230 m and piles along the subsequent 716 m further north.

| Section | Principal reinforcement | |
|---------|-------------------------|---------------------------------|
| SB1 | Superior | $\phi 25//0.20 + \phi 20//0.20$ |
| | Inferior | 0 |
| SB2 | Inferior | $\phi 16//0.20 + \phi 20//0.20$ |
| | Superior | 0 |
| SB3 | Superior | $\phi 16//0.20 + \phi 20//0.20$ |
| | Inferior | 0 |
| SB4 | Superior | $\phi 16//0.20 + \phi 20//0.20$ |
| | Inferior | 0 |
| SB5 | Inferior | $\phi 16//0.20 + \phi 20//0.20$ |
| | Superior | 0 |
| SB6 | Superior | $\phi 20//0.10$ |
| | Inferior | 0 |
| SB7 | Superior | $\phi 20//0.10$ |
| | Inferior | 0 |
| SB8 | Inferior | $\phi 20//0.10$ |
| | Superior | 0 |
| SB9 | Both/each | $\phi 20//0.10$ |

Table 6.4: Structural modeling: reinforcement scheme of the horizontal elements.

The open typology is expected to be extrapolated for the future 204 m and 600 m expansion phases of the container terminal, as well as for the construction of the new Vasco da Gama terminal. Fig. 6.19 depicts the schematic constructive design of the container terminal(s) [504]. Further on, longitudinal and transverse directions of the soil-quay system stand for parallel and perpendicular orientation towards the shoreline, respectively.

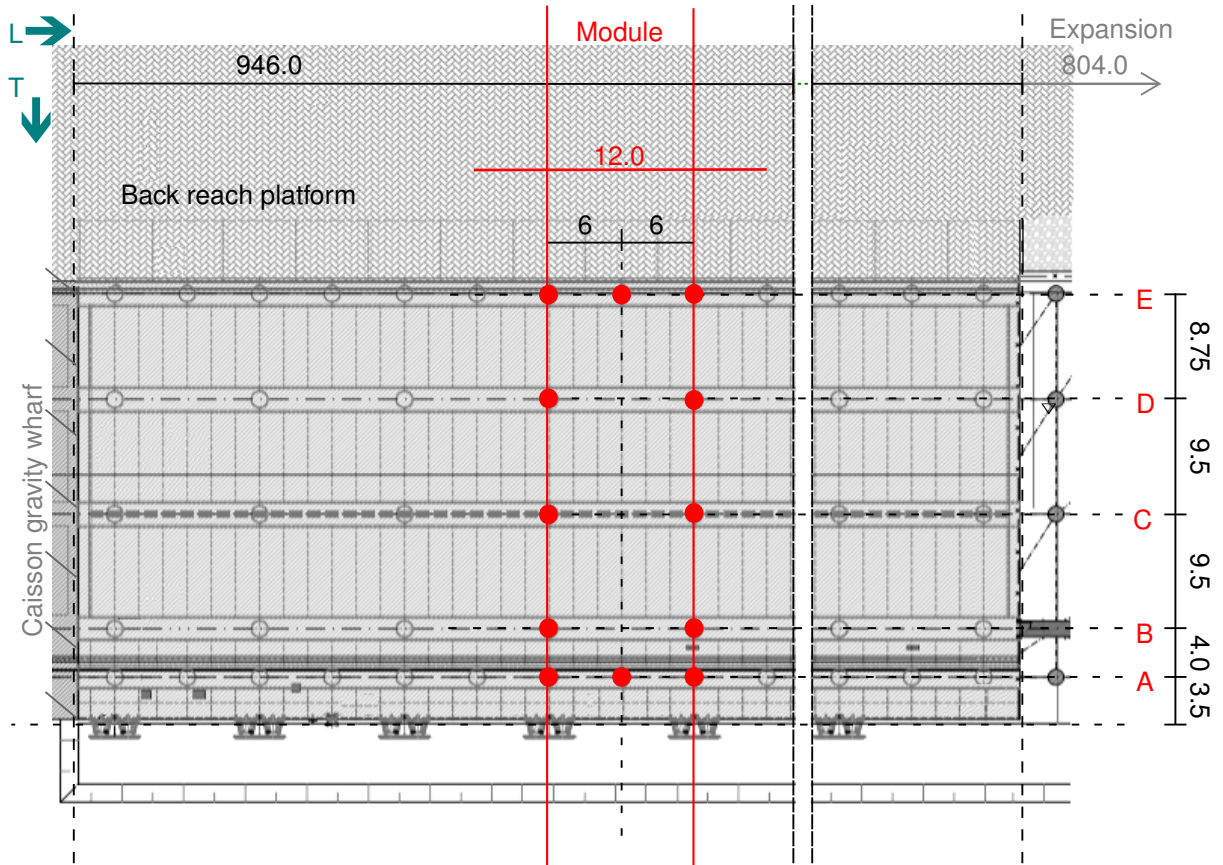
The RC deck relies on longitudinal and transverse beams defining 100 m modules, where pre-cast channel elements and cast-in-place RC slabs using C35/45 concrete and A500 NR SD reinforcing steel materials (cover thickness ≈ 6 cm) have thickness of 2.5 m in the front (seaward) and 0.45 m in back (landward) of the quay. Table 6.4 resumes the scheme of reinforcement of the various sections composing the horizontal elements (see Fig. 6.20 for detail and identification of the sections).

The modules are supported by rows of five and two vertical cast-in-site RC piles in intervals of 6 m, directly transmitting the loads to the soil. The piles have circular cross-sections of 1.3 m diameter, accounting with the S355 JR tube with 11 mm-thickness adopted to driving the piles during the construction works which was left as lost form-work. The length of the piles in alignments A and B is 26 m while in alignments C, D and E is 24,5 m. All piles are 4 m-embedded deep into bedrock foundation, above which is deposited an artificial triangular rock-filled embankment of quarry material. The soil parameters characterized via geotechnical prospection are listed in Table 6.5 [504].

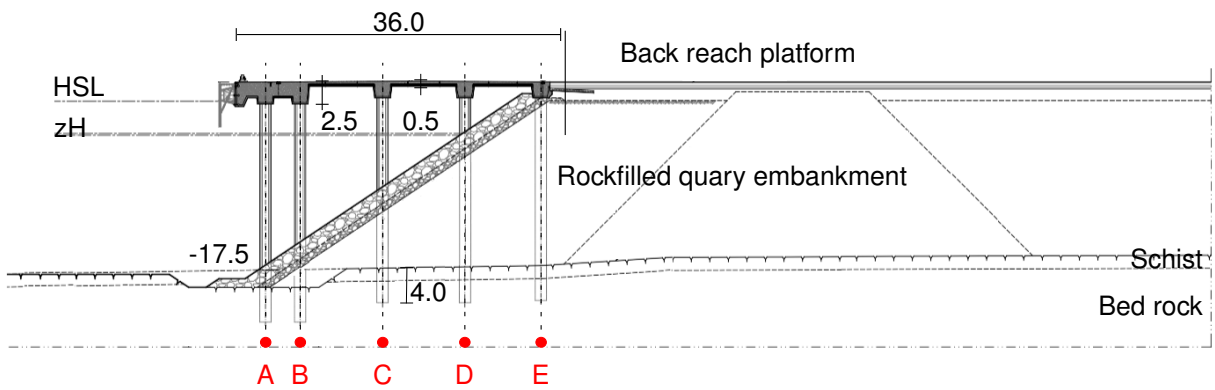
| Drained Soil | Name | γ_{unsat} [kN/m ³] | γ_{sat} [kN/m ³] | ν | E_{ref} [kN/m ²] | c_{ref} [kN/m ²] | ϕ ° |
|--------------|------------------|--|--|-------|-----------------------------------|-----------------------------------|-------------|
| 1 | Bedrock | 24.4 | 26.0 | 0.20 | 8.5E6 | 10.0 | 30.0 |
| 2 | Modified bedrock | 26.1 | 27.5 | 0.33 | 1.5E6 | 8.0 | 28.0 |
| 3 | Quarry run fill | 18.0 | 20.0 | 0.30 | 0.5E6 | 0.0 | 40.0 |
| 4 | Rock fill | 18.0 | 20.0 | 0.27 | 0.8E6 | 0.0 | 45.0 |

Table 6.5: Structural modeling: soil properties.

The relationship between time-histories of intensity measures quantified in Section 6.4.2 and structural demand were characterized via successive seismic and tsunami non-linear dynamic analysis. The demand of interest for the open-type soil-quay system consists of horizontal displacement,



(a) Plan view.



(b) Transverse view.

Figure 6.19: Structural configuration: constructive design of the container terminal(s).

bending moment and shear force along quay and piles, axial force on piles, moment-rotation diagrams on pile-slab and pile-foundations connections, and soil stresses.

6.6.1 Structural modeling

Models with 2D and pseudo-3D discretization that repeat themselves along the longitudinal direction were adopted to represent the soil-structure system. The fibre modelling approach employed in the current endeavour inherently accounts for geometric and material non-linearities. Fig. 6.20 depicts the numerical model of the soil-quay system.

The multi-layered soil, encompassing bedrock foundations and rock-fill composing the embankment, was modeled using 3D brick and 2D quad elements with non-linear properties. The various layers of soil material were defined based on characteristic properties acquired during geotechnical prospection, resumed in Table 6.5. The soil tensile strength was set to zero.

For the pseudo-3D model, the dimensions of the soil medium were set to approximately 250 m in the transverse direction, 36 m in the longitudinal direction and 60 m in depth. For the 2D model, the soil medium dimensions were set to approximately 435 m and 60 m in transverse and vertical directions with thickness (longitudinal dimension) of 12 m . Beside the dimensions assumed to mimic free field conditions, the surfaces limiting the soil massif in the transverse direction were defined to have identical horizontal displacements enforcing an approximate shear-type horizontal response for the soil substrate.

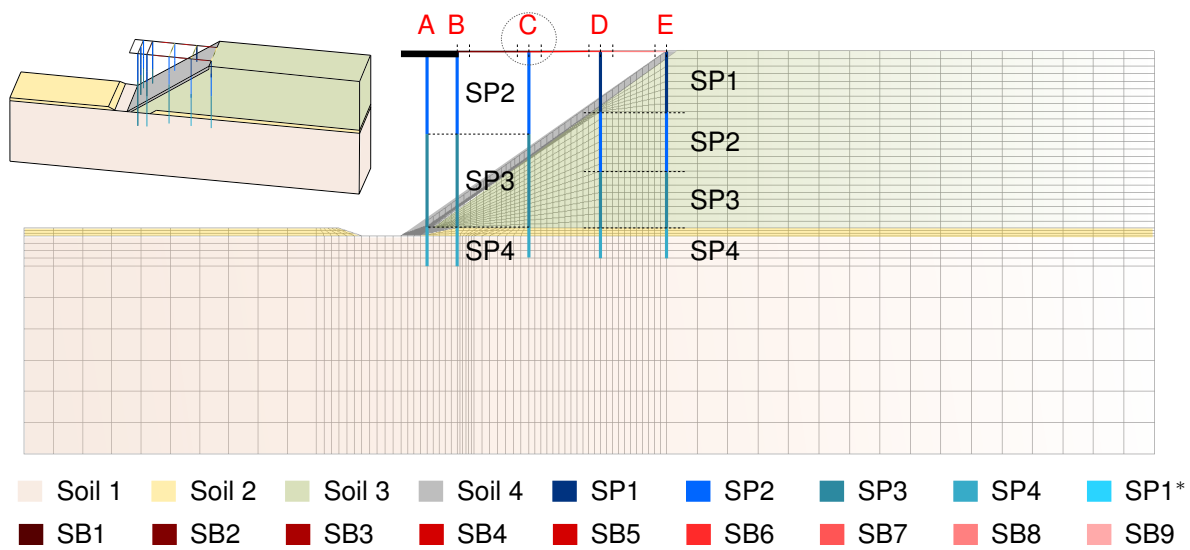
The conditions to guarantee the interaction between the soil and the structure were imposed between nodes with identical coordinates assigning a infinitely rigid constraint. This assignment kinematically connected the structure and soil substrates.

The RC structure consisting of a quay deck supported by circular piles was modeled as a frame adopting Displacement-based Beam-Column elements with non-linear distributed plasticity assembled by Force-Deformation fiber sections defined in terms of materials and geometry.

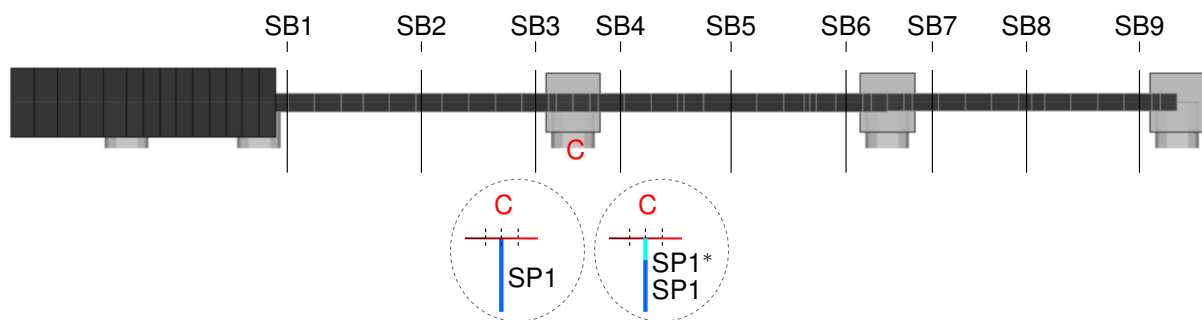
The materials adopted to model the RC frame include core and cover concrete for strength class C35/45 following Mander [402] unified stress-strain model considering degraded linear unloading/reloading stiffness. The steel constitutive material follows Giuffre-Menegotto-Pinto steel model with isotropic strain hardening [403], for class of resistance A500. The constitutive relationships of the materials are described in Section 4.4.1.

The pseudo-3D model was defined using elements with full and half sections to model the central and lateral rows of piles and beams in the transverse direction of the module (see representation of the module in Fig. 6.19), while the 2D model was modeled using the full sections of beams and piles overlapping elements representing piles A and E to resemble the frame spacing (rows of two or five piles spaced 6 m apart).

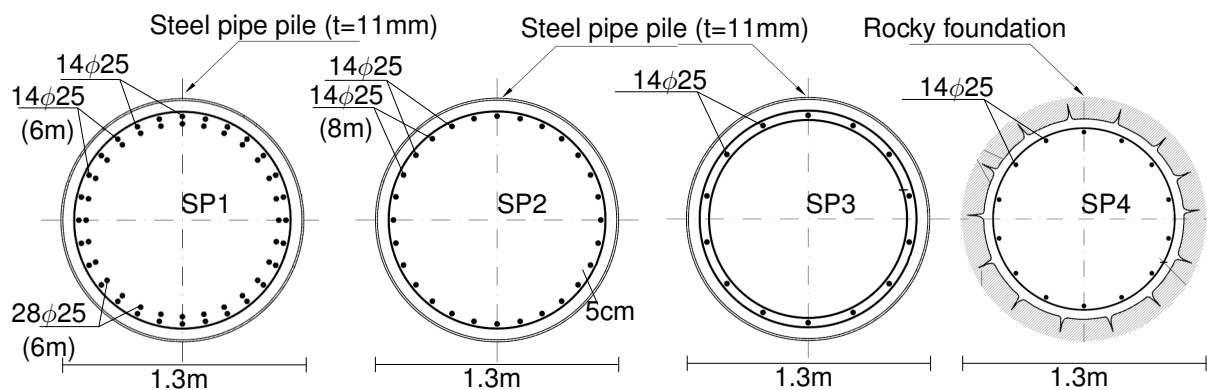
The A335 metallic tube used to drive the piles into the foundation was kept as lost form-work in the prototype. In the model, the A355 steel tube was represented as an equivalent area of A500 steel and converted into reinforcing bars of 25 mm diameters in the sections of the piles. The mean yielding strength of A500 steel is $f_{yd,500} = 553\text{ MPa}$, while A355 is $f_{yd,355} = 382\text{ MPa}$. The conversion of the



(a) General overview of 2D and pseudo-3D models.



(b) Modeling details: horizontal elements. Configurations SP1 and SP1* at the connection between pile and longitudinal beam (example on point C).



(c) Modeling details: vertical elements.

Figure 6.20: Structural modeling: idealization of pile-supported soil-quay system for FE analysis. Modeling variations include pseudo-3D and 2D domains and configuration of pile-beam connections. Acronyms 'SP' and 'SB' stand for sections along pile or beam/slab, respectively.

A355 tube into A500 bars was done by assigning to the bars that represent the tube the same yield capacity as the area of the tube. The area of a hollow 11 mm tube is $A_{tube} = 0.0445 m^2$, representing a yielding strength of $F_{s,tube} = A_{tube} f_{yd,355} = 13720 kN$. Each ϕ_{25} A500 bar has an yielding strength of $F_{s,1bar} = 213 kN$. Thus, an equivalent number of 64 ϕ_{25} -bars of A500 steel were added to the external perimeter of the pile section.

The piles were then subdivided along their length depending on the reinforcement configurations, and free or embedded sections (variable due to embankment slope and rocky foundation). Various fiber-sections were assembled to model the section of the piles, 'SP' in Fig. 6.20. To SP1, SP2, SP3 and SP4 were respectively assigned 120, 92, 78 and 14 ϕ_{25} -bars of A500 steel. Piles in row D and E have SP1 along 6 m followed by another 6 m of SP2, transitioning to SP3 until the last 4 m of SP4, which represents the section directly embedded into rocky soil. Piles in rows A, B and C have a 8 m SP2 on the connection to the quay, SP3 with 12 m length and the same 4 m of SP4 on the rocky foundation.

Vertical pile-supported quay structures are usually designed to act as ductile moment frames with plastic hinge formation during earthquakes at the connection to the quay deck and possibly a second hinge may form below the surface of the soil. However the positioning of the piles' tube edging the beams prevents the development and spreading of the plastic hinge at the strategic location. To avoid an over-conservative characterization of the structural behavior of the pile-supported quay with a plastic hinge of almost zero length, the connection of the tube edging the beam was alternatively modeled adopting a sectional transition between SP1 and the longitudinal beams to enforce the spreading of plastic hinge in the length where the steel stress is between yielding and ultimate values. Because in this case the model was incapable of accounting the spreading length of the plastic hinge, the transitional section was modeled based on Eurocode 2 (EC2) recommendations to determine the anchorage length of the longitudinal reinforcement aiming to assure that bond forces are safely transmitted to the concrete avoiding longitudinal cracking or spalling. The design anchorage length, l_0 , to model the top section of the piles was calculated accounting for the basic required anchorage length, $l_{b,rqd}$, affected by coefficients to account the influences of the form of the bars, α_1 , concrete minimum cover, α_2 , confinement by transverse reinforcement, α_3 , welded transverse bars along the anchorage length, α_4 , and pressure transverse to the plane of splitting along the anchorage length, α_5 . The product needs to be equal or greater than the minimum anchorage length, $l_{0,min}$, as in Eq. 6.3:

$$l_0 = \alpha_1 \alpha_2 \alpha_3 \alpha_4 \alpha_5 \frac{\phi \tau_{sd}}{4 f_{bd}} \geq l_{0,min} \quad (6.3)$$

where, τ_{sd} is steel design yield stress and $f_{bd} = 2.25 \eta_1 \eta_2 f_{ctd}$ is the ultimate bond stress. The values of α and η coefficients are tabled in EC2. Except for $\alpha_2 = 0.94$, the contribution of the effects all α coefficients was found negligible. For the pile-slab connection, $\eta_1 = \eta_2 = 1$ respectively represented good quality of the bond condition due to concreting process and bar diameter inferior to 32 mm, resulting in $f_{bd} = 7.4 MPa$. The design anchorage length was quantified as $l_0 = 2.5/4 \cdot 0.94 \cdot 435/7.4 = 34.5 cm$.

The $l_{0,min}$ for anchorages in tension assume the maximum of $0, 3/l_{b,rqd}; 10\varphi$ or 100 mm, while for anchorages in compression $max 0, 6/l_{b,rqd}; 10\varphi; 100 mm$, where φ is creep coefficient. Thus, the circa

35 *cm* of anchorage length represents the zone where the ultimate capacity is reduced up to zero (elastic regime). To assign the characteristic plastic hinge function, the spreading length exclusively corresponds to the zone encompassing ultimate to yielding capacity. Assuming a 1.22 ratio between ultimate and yielding capacity of steel bars [505], the $l_0 \cdot (1.22 - 1) = 34.5 \cdot (1.22 - 1) = 7.6 \text{ cm}$. Since l_0 is estimated conservatively, the real value is less than 7.6 *cm*. As the plastic hinge spreads in both direction (beam and pile) from the cross-section of maximum stress in the pile reinforcement, a 10 *cm* length of plastic hinge was assumed and modelled. Fig. 6.20(b) depicts the two configurations, SP1 and SP1* with a lower 10 *cm* position of the tube (exclusively considering the steel bars at the top of the piles).

Beside the tube, the contribution of the transverse reinforcement composed of 12 *mm* diameter spiral stirrups spaced 100 *mm*, for SP1, and 200 *mm* for the other sections, was introduced as a confinement parameter changing the ultimate strain to $\varepsilon_{cu} = 0.025$ in the concrete constitutive relationship model (following calibration procedure introduced in Section 4.4.1). Twenty and ten fibers were considered for the discretization of the cross section of the piles on circumferential and radial directions, respectively.

For the pseudo-3D the longitudinal beams in A, B, C, D and E rows have 1.8 *m* height and average 1.5 *m* width, while slab weight was added on the quay diaphragm. For the 2D model, the slabs of BC, CD and DE spans, were modeled as horizontal elements of 0.45 *m* in height and 1.0 *m* in width, in the transverse direction. Nine fiber sections, SB, were defined to assign the reinforcement conditions. Eighteen and ten fibers were considered for the discretization of the cross section of the beams on vertical and horizontal directions, respectively. On both pseudo-3D and 2D models, AB sections/beams were modeled as elastic C35/45 RC concrete sections with 2.5 *m* in height. A condition uniforming the quay horizontal displacement in the transverse direction was imposed via diaphragm option.

The frame model was discretized into 0.5 *m* bars. To obtain better results near the elements edges, where plasticity is typically concentrated, while keeping the numbers of elements low, reducing the computational time, a refined mesh concentration was applied. The soil model was discretized into 4.0 *m* hexahedral or quadrilateral elements, refined to 1.0 *m* in the vicinity of the soil-quay interface. The pseudo-3D model was discretized into a composition of 2412 line elements, 53040 soil hexahedral elements and 60604 nodes, while the 2D model discretization led to 488 line elements, 6147 quadrilateral element and 6834 nodes.

The static loading included weight of the structure and live loads, -10 kN/m on the quay and -30 kN/m on back-reach platform corresponding to cargo storage (see Fig. 6.1). The dynamic loading included seismic and tsunami actions assessed in Section 6.4.2. The time series of seismic acceleration were prescribed as uniform uni-directional excitation in x -direction at the rocky foundation. In the 2D model, the tsunami loading was imposed as horizontal and vertical forces, while in the pseudo-3D model adopted forms of horizontal and vertical distributed pressures along the structural elements. Loads associated with cranes, reach stacker, rubber defenses and mooring were neglected. For time steps of $\Delta t = 0.01 \text{ s}$, the simulations of pseudo-3D and 2D models required run-times of circa 96 *h* and 8 *h*, respectively.

6.6.2 Structural analyses

Regulatory damage limitation

Working Group 34 of the International Navigation Association (PIANC) [305] gives specifications of damage, established on the basis of the serviceability and ultimate states, for the different types of quay structures. For pile-supported wharves, the level of structural damage relies on damage criteria resumed in Table 6.6:

| Level of damage | | Serviceable | Repairable | Near collapse | Collapse |
|-----------------|-----------------------------------|-----------------------|-------------------|---------------|----------|
| Deck | Differential settlement quay-soil | $\leq 0.3 \text{ m}$ | N/A | N/A | N/A |
| | Residual tilting | 0.0524 rad | N/A | N/A | N/A |
| Dike | Horizontal displacement | $\leq 0.15 \text{ m}$ | N/A | N/A | N/A |
| Pile | Peak response | Elastic | Limited inelastic | Plastic | Beyond |

Table 6.6: Structural analysis: regulatory damage criteria of pile-supported wharves.

Regarding load bearing capacity, it represents a combination of the piles capacity to transmit (mainly) axial forces, into the foundations and the surrounding soil capacity to absorb the load. Eurocode 7 (EC7) provides outline guidance on the embedded depth, $z \geq 3D_{pile}$ and $z \geq 5 \text{ m}$, or reduced up to $z \geq 2 \text{ m}$ when favorable geologic conditions were determined via geological studies, which is the case of the pile-supported quay of Sines port.

The design situations in EC7 (Part I) include geotechnical failure by compression, tension and transverse loading, and structural failure by buckling, shear and bending. The limit state design, based on ultimate and serviceability limit states, is based on the simplification of performance criteria into a single safety criteria associated with ultimate limit state, ULS, for piles bearing in medium to dense soils (as in Sines port). The ULS encompasses verification of soil and structure capacities to provide resistance, R_d , for the design actions, E_d , such that $R_d \geq E_d$ requirement is verified. The determination of R_d admitted in Section 7 of EC7-I includes alternative principles based on static load tests, empirical or analytical calculation methods, dynamic load test results, and observation of the behavior of comparable pile foundations in similar soil conditions.

In Sines, an exhaustive geotechnical campaign was carried out to provide geotechnical profiles of soil, which identified a lithostratigraphic profile composed of deorite gabbro and microgabbro, argillaceous and carbonaceous shale. From field Standard Penetration Tests, SPT, and laboratorial static load tests was determined the soil capacity (maximum vertical load) for the piles. In particular for alignment of piles A, B, C, D and E were quantified values of 5714 kN , 7976 kN , 7122 kN , 6958 kN and 7971 kN , respectively [504].

Part 2 of EC7 allows to calculate the compressive resistance of a single pile from profiles of ground tests or directly from ground parameters. The evaluation of the pile ultimate bearing capacity to support axial loading, R_{ult} , was determined using a theoretical formulation based on soil parameters encompassing contributions of load capacity at the end of the pile, q_b , and friction along the pile embedded on the layer(s) of soil i , $q_{s,i}$. The base R_b and shaft R_s resistances are expressed in Eq. 6.4:

$$\begin{cases} R_b = A_b \cdot q_b \\ R_s = A_{s,i} \cdot q_{s,i} \end{cases} \quad (6.4)$$

where A_b is the nominal plan area of the base of the pile and $A_{s,i}$ is the nominal surface area of the pile on soil layer i .

The unit base resistance $q_b = \sigma_c \cdot k_{sq} \cdot d_r$, where σ_c is soil compressive strength, k_{sq} is a factor depending on the quality of the soil following Rock Quality Designation for rock core taken from boreholes ($k_{sq} = 0.8$ for high quality rock) and d_r is a factor depending on the embedded length of the pile in the rock, l , which follows $d_r = 1 + 0.4 \cdot l/D$, where D is the the diameter of the pile.

The unit shaft resistance in soil layer $q_{s,i} = P \cdot \tau_{ult}$, where P is the perimeter of the pile and τ_{ult} is the ultimate resistance to friction on piles driven into rock, directly depending on the uniaxial σ_c of soil and indirectly on the rock mass, N_σ following $\tau_{ult} = \sigma_c \cdot N_\sigma$. In absence of EC7 guidelines, AASHTO manual recommends $\tau_{ult} = (0.21 \sim 0.26) \cdot \sigma_c^k$, where $k = 0.5$.

Assuming piles driven into rocky soil with an average $\sigma_c^b = 7000^{0.5} \text{ kNm}$, the ultimate bearing capacity of the piles $R_{ult} \approx 10000 \text{ kN}$. For design resistance, R_d is affected by two safety factors to reduce base, γ_b and friction γ_s capacities to assess the allowable bearing load, q_a . The values of γ_b and γ_s are given in EC7-1, Annex A, Table A6 ($\gamma_b = \gamma_s = 1.3$). The design pile capacity $R_d = 7690 \text{ kN}$.

Resistance capacity

A fiber-based approach was adopted to model the quay elements. The design process still relies on the $R_d \geq E_d$ requirement based on design action affects (axial and shear load, N and V, and bending moment, M). The N-M diagrams for ultimate and yielding bearing capacity of the pile cross section were calculated using an in-house code. Fig. 6.21 depicts N-M diagrams of each section and the yielding capacity of the sections with likelihood of plastic hinges development, at pile-quay and pile-rocky foundation connections. Positive values on y-axis represent tensile axial force. Fig. 6.21 shows the correlation between yielding capacity (moment-curvature relationship) of SP1 and SP1*, for axial loading of 2000 kN , 5000 kN and 10000 kN , while the yielding capacity of SP4 exhibiting a longer hardening phase was adjusted to be coherent with values of admissible ultimate resistance, 1000 kN , 2000 kN and 5000 kN . The resistance given by the M-N diagrams of the sections encapsulated by the tube, S1, S2 and S3, were found similar, while SP1* and S4 presented values with smaller order of magnitude.

For the horizontal elements, the ultimate resistance of 12 m -width cross sections of S1 to S9 was estimated for bending and shear. Table 6.7 summarizes the estimated values of resistance.

Preliminary analysis

Bearing in mind the computational costs associated with pseudo-3D and 2D analysis, the first verification was the similarities of the numerical solutions, presumably accepting a two-dimensional modeling approach (lack or minimal out of the plane effects). Moreover, modal analysis of both models

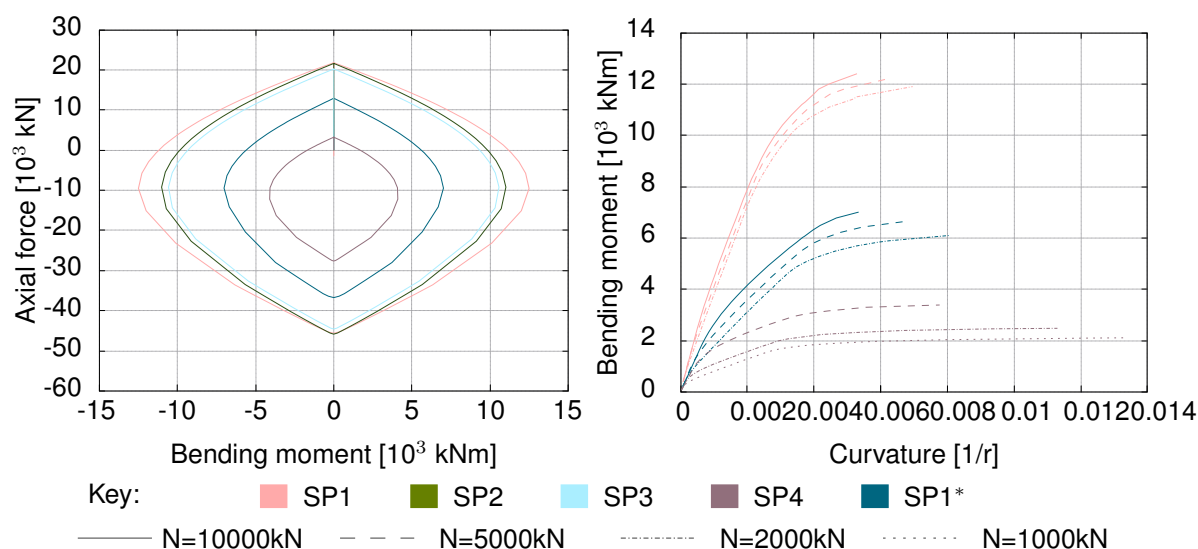


Figure 6.21: Structural modeling: ultimate N-M and yielding M- θ structural capacity of the cross sections of the piles.

| | | | | |
|-------------------------------------|--------------|--------------|--------------|--------------|
| Elements, compressive strength | N_{rd}^- | | | |
| | [kN] | | | |
| Soil: alignment of piles A | 5714 | | | |
| Soil: alignment of piles B | 7976 | | | |
| Soil: alignment of piles C | 7122 | | | |
| Soil: alignment of piles D | 6958 | | | |
| Soil: alignment of piles E | 7971 | | | |
| Piles | 7690 | | | |
| Cross-sections: vertical elements | $N_{rd,max}$ | $N_{rd,min}$ | $M_{rd,max}$ | $M_{rd,min}$ |
| | [kN] | [kN] | [kNm] | [kNm] |
| SP1 | 26684 | -50500 | 12453 | -12453 |
| SP1* | 12927 | -36744 | 7463 | -7463 |
| SP2 | 21601 | -45829 | 11001 | -11001 |
| SP3 | 20220 | -44554 | 10557 | -10557 |
| SP4 | 3232 | -27619 | 4091 | -4091 |
| Cross-sections: horizontal elements | V_{rd} | M_{rd} | | |
| | [kN] | [kNm] | | |
| SB1 | 2112 | -7932 | | |
| SB2 | 2112 | 5256 | | |
| SB3 | 2112 | -5256 | | |
| SB4 | 2112 | -5256 | | |
| SB5 | 2112 | 5700 | | |
| SB6 | 2112 | -5568 | | |
| SB7 | 2112 | -5568 | | |
| SB8 | 2112 | 5568 | | |
| SB9 | 2112 | -5568 | | |

Table 6.7: Structural analysis: ultimate resistance of cross sections.

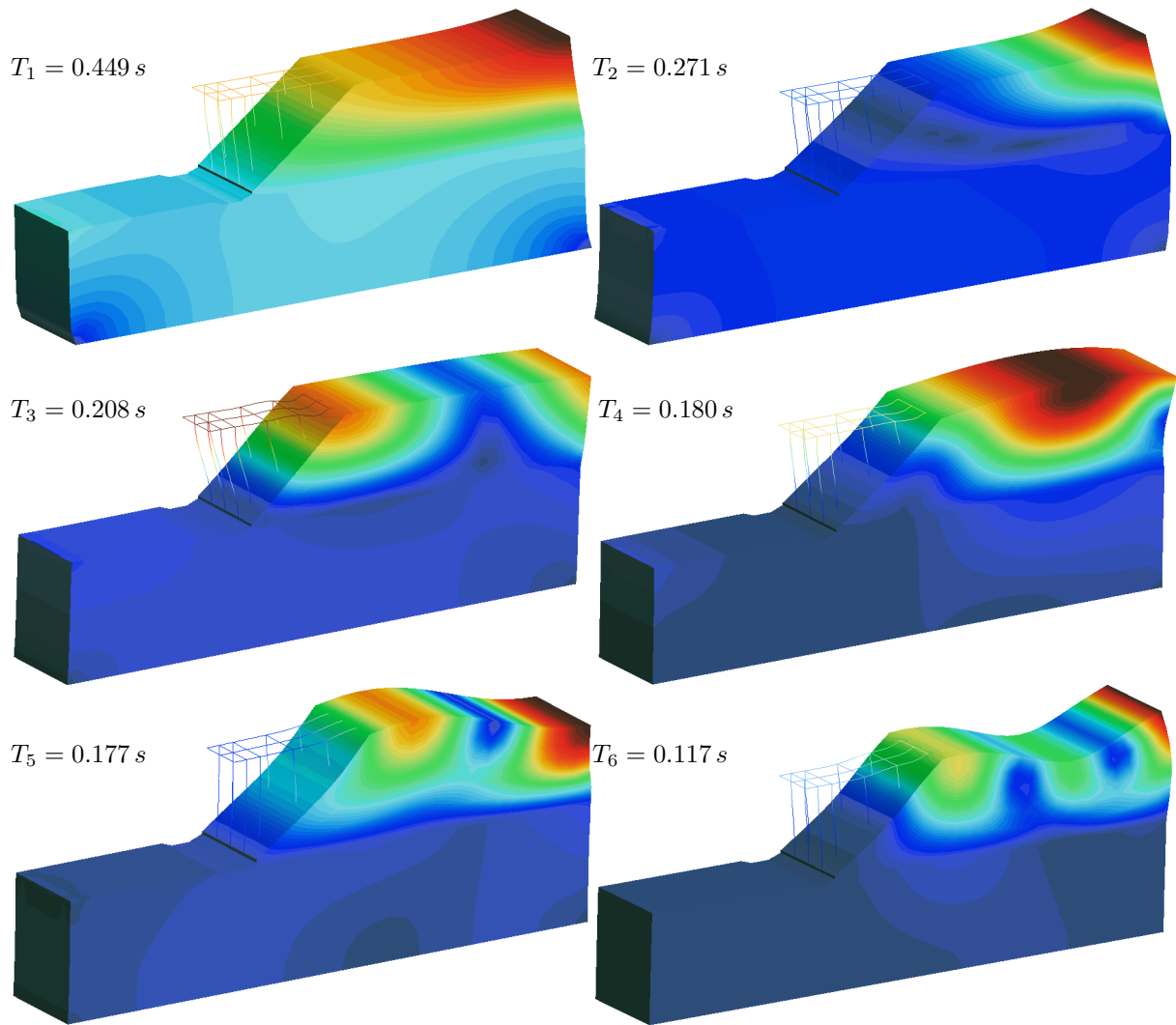


Figure 6.22: Structural analysis: modal analysis of the pseudo-3D soil-quay system. Representation of the first six modal periods.

were performed to characterize the first six modal periods and determine the Rayleigh damping matrix for the following successive analyses of the system. The modal analyses included a brief parametric study including pseudo-3D and 2D domains, and SP1 and SP1* configurations. The Static analysis with Load-Control integrator interval was governed by the UmPack system of equations solved by Krylov-Newton algorithm. The load application followed ten incremental steps (10% per step). The norm displacement criterion was set to 10^{-5} tolerance to verify convergence of the results in each step, allowing a maximum of 500 iterations per step.

Figure 6.22 depicts the results of the modal analysis for the pseudo-3D model. The results for the 2D models can be found at Section E.1, Annex E. In general, modal analyses showed minimal variations on the natural periods of the system, varying between $T_1 \approx 0.4 \text{ s}$ and $T_6 \approx 0.1 \text{ s}$. The comparison between 2D models with SP1 and SP1* connections showed (slightly) higher vibration periods of the model with SP1* configuration, indicating a (slightly) more flexible behavior of SP1* configuration, which was the configuration adopted to conduct the successive structural analyses.

The preliminary stage of the analysis also allowed to verify modeling and calibration assumptions,

such as soil-structure interaction and non-linearity of soil-quay system responses. The 2D model of the soil-quay system with SP1* configuration was subjected to a static $\pm 10000kN$ horizontal load applied with an increasing 20% load factor on the quay. Fig. 6.23 depicts the preliminary results.

As expected, the displacements of quay and soil massif at the connection between both are equal due to soil-structure sharing equal DOF and imposed diaphragm condition applied on the quay. The movement of the soil-quay system was privileged when pushed on the seaward direction due to both soil geometry and its non-linear behavior, which typically resists compressive but not tensile stresses. For the same load magnitude, the soil exhibited about 0.0012 m of horizontal displacement and 22 kPa of soil stress for positive load (landward), while the negative load (seaward) induced higher 0.0066 m displacements and 42 kPa stress. The solicitation of the soil volume required in each loading case also corroborated the theoretical expectations, i.e., the soil stress distribution along the embankment length was related with the loading direction with concentrated stress in the embankment region being observed for the seaward loading case, while a larger part of the embankment contributed to resist the loads applied on the landward direction.

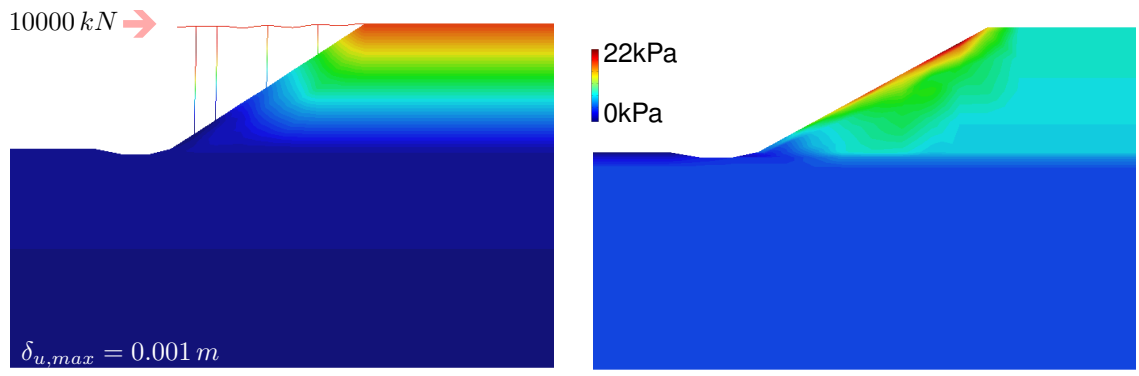
Successive structural analyses

The Rayleigh damping for the purpose of dynamic analyses was assigned by a damping matrix expressed as a linear combination of mass and stiffness matrices. The Rayleigh damping parameters, $c = \alpha m + \beta k$, where m and k represent mass and stiffness matrices, were automatically calculated from the periods of the most relevant vibration modes and assuming material damping ratio of $\xi = 5\%$ (slightly conservative for the soil which has good geotechnical properties). All successive transient analyses were performed considering the dumping matrix on the UmfPack system of equations solved by Krylov-Newton algorithm.

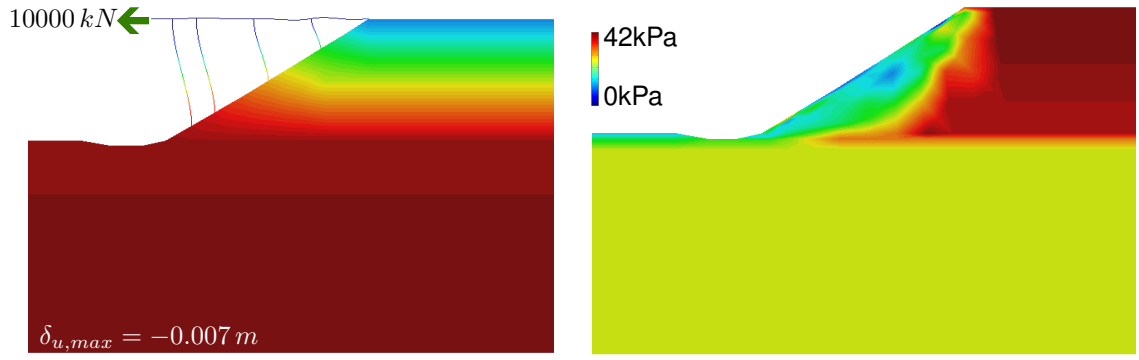
The first-staged static analysis was performed to assess the static effects of dead and live loads. The effects of each stage were set as initial conditions for the following stages, so stage Interval 2 continues from the end of the static analysis and stage interval 3 due to tsunami continues from the end of seismic stage 2. The successive structural analyses were then carried out for the various set of dynamic cascading loading patterns (Fig. 6.18).

The second stage, a non-linear transient analysis, was performed to characterize the behavior of the soil-quay system under seismic accelerations. The Transient analysis used Newmark integration scheme. The convergence was tested with Norm Displacement Increment with tolerance of 10^{-3} verified along the maximum of 500 interactions/step. The duration of the analyses were set to match the duration of each accelerogram, to cover up the stages from rest to excited to rest stages, plus an unloading phase carried out over a time lapse sufficient to ensure that the structure is fully at rest. The ground motion was imposed at the bed-rock level as an uniform excitation given by the various accelerograms, in x -direction (horizontal excitation). The seismic analysis showed the responses of the soil-quay system to the different accelerograms imposed at the bedrock level.

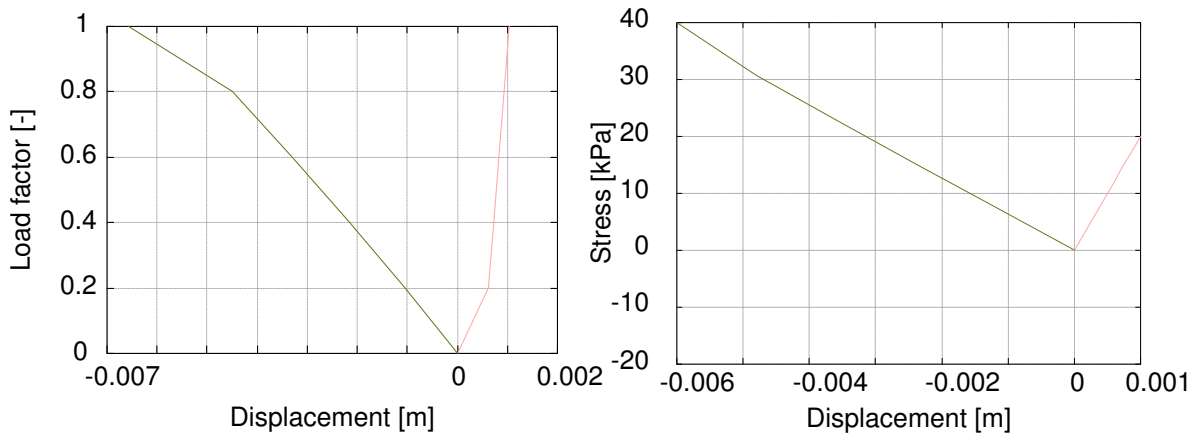
The third stage, a non-linear transient analysis, was performed to characterize the soil-quay system under tsunami effects. Each analysis was initialized with cumulative effects kept from the previous ones.



(a) Static load on landward direction: total displacement (right) and soil stress (left).



(b) Static load on seaward direction: total displacement (right) and soil stress (left).



(c) Soil non-linear behavior under static load: horizontal displacements (right) and soil displacement-stress relationship (left). Pink and green lines correspond to cases of load applied on the land- and sea-ward directions, respectively.

Figure 6.23: Structural modeling: preliminary verification.

| Scenario | Loading | EQ Displacements | | Residual | Regime |
|-----------|---------------|------------------|-------------|------------------|---------------------|
| | EQ [g] | Landward [m] | Seaward [m] | Displacement [0] | EQ |
| MPF zit | -0.24 - 0.25 | 0.030 | -0.030 | 0.003 | Failure SP1* Pile E |
| MPF woo | -0.30 to 0.28 | 0.024 | -0.030 | -0.002 | Plastic SP1* Pile E |
| MPPBF bap | -0.38 to 0.45 | 0.027 | -0.037 | -0.003 | Failure SP1* Pile E |
| MPPSF ter | -0.59 to 0.52 | 0.042 | -0.058 | -0.003 | Failure SP1* Pile E |
| HSF rib | -0.30 to 0.29 | 0.015 | -0.025 | -0.002 | Plastic SP1* Pile E |
| HSF wro | -0.20 to 0.18 | 0.015 | -0.017 | 0 | Elastic |
| GBF grd | -0.20 to 0.20 | 0.015 | -0.015 | 0 | Elastic |

| Scenario | Loading | | TSU Displacements | | Regime |
|-----------|--------------|--------------|-------------------|-------------|--------------------|
| | TSU H [kN/m] | TSU V [kN/m] | Landward [m] | Seaward [m] | TSU |
| Scenario | -580 to 320 | -760 to 650 | - | - | Failure |
| MPF zit | -400 to 400 | -200 to 1100 | 0.008 | -0.033 | Failure SP1* |
| MPF woo | -610 to 590 | -580 to 580 | - | - | Failure |
| MPPBF bap | -320 to 400 | -200 to 250 | - | - | Failure |
| MPPSF ter | -400 to 400 | -780 to 1050 | 0.007 | -0.017 | Failure S9 Slab BC |
| HSF rib | -480 to 300 | -860 to 1050 | 0.030 | -0.022 | Failure S1 Slab BC |
| HSF wro | -510 to 300 | -200 to 1100 | 0.003 | -0.007 | Failure S1 Slab BC |
| GBF grd | -500 to 490 | -200 to 1050 | 0.007 | -0.033 | Failure S2 Slab BC |

Table 6.8: Structural analysis: summary behavior of pile-supported quay under cascading earthquake and tsunami actions.

The tsunami pressures were applied using a pattern of unitary nodal forces controlled by a function representing the tsunami imposed variations (see Fig. 6.18).

Structural response

The seismic responses of the soil-quay system were systematically computed for the various set of loading patterns derived from S_{worst} of the 1755 GLET-alike event.

From the seismic analysis, the overall qualitative soil displacement pattern demonstrated a quite similar response for the various S_{worst} . The largest lateral displacements of the soil occurred in the upper layers due to geometry and likelihood of shear deformation associated with geotechnical conditions of soil type 3. The maximum lateral displacement of the soil occurred at the top layer of soil (type 3), corresponding to the location where the quay links the back-reach embankment. In the slope region of the embankment where the piles are embedded, the lateral displacements extend to the deeper soil, from near the dike toe up to the transition of embankment-rocky foundation layers. The non-linear properties assigned to the soil material and the difference in the volume of soil in the transverse direction (perpendicular to shoreline), led to higher displacements on the seaward direction. Table 6.8 resumes maxima horizontal displacements induced by seismic and successive tsunami actions, respectively. Positive and negative values represent land- and sea-ward directions, respectively.

Table 6.8 resumes the main characteristics of the structural behavior of the soil-pile supported quay under loading patterns of cascading seismic and tsunami actions from S_{worst} .

Quantitatively, the seismic analyses of the various S_{worst} showed a range of quay horizontal displacements between $\|\delta_x = 0.015\text{ m}\|$ and $\|\delta_x = 0.058\text{ m}\|$, land- and sea-ward directions respectively. Except S_{worst} derived from GBF proposed by Grandin et al., 2007 and HSF proposed by Wronna et al., 2015, the seismic analyses of all other scenarios solutions demonstrated a residual displacement after

the ground motions. Such observation implied a transition from elastic to plastic regime and likeliness to evolve to structural failure due to limited ductility of the system (slab without confinement reinforcement and pile with small plastic hinge lengths).

To ascertain the location of plastic hinges development, values of bending moment, axial and shear forces were determined at instant of time corresponding to maxima displacements of the quay on both land- and sea-ward directions. Then, values of design and resistance capacity were correlated to infer the status of the section: elastic (below yielding level capacity), plastic (between yielding and ultimate capacity) or collapse (above ultimate capacity). Such approach considering static quantities was adopted to determine the location of structural vulnerability.

Among the results, three possible cases were denoted. One corresponds to seismic actions inducing structural response remaining under structural yielding threshold, which is equivalent of having a hypothetical scenario of distant tsunami on which the infrastructures are minimally exposed or unaffected by seismic accelerations, keeping original resistance to withstand the incoming tsunami (for example GBF scenario proposed by Grandin et al., 2007). Another two cases represent a typical regional/local tsunami, on which the structure is previously affected by seismic action, transitioning from elastic to plastic regime (for example HSF scenario proposed by Ribeiro et al., 2007) and possibly evolving to collapse (for example MPPSF scenario proposed by Terrinha et al., 2003). Figs. 6.24, 6.25 and 6.26 depict the identified three representative cases. In addition, Fig.6.25 representing structural failure due to seismic action also presents an independent analysis exclusively considering tsunami action. The aim was to highlight possible consequences of skipping dependence effects when characterizing structural responses individually (and conducting risk analyses).

The S_{worst} generated by GBF with rupture parameters proposed by Grandin et al., 2007 (Fig. 6.24) generated seismic accelerations and tsunami forces that induced a structural behavior characterized by:

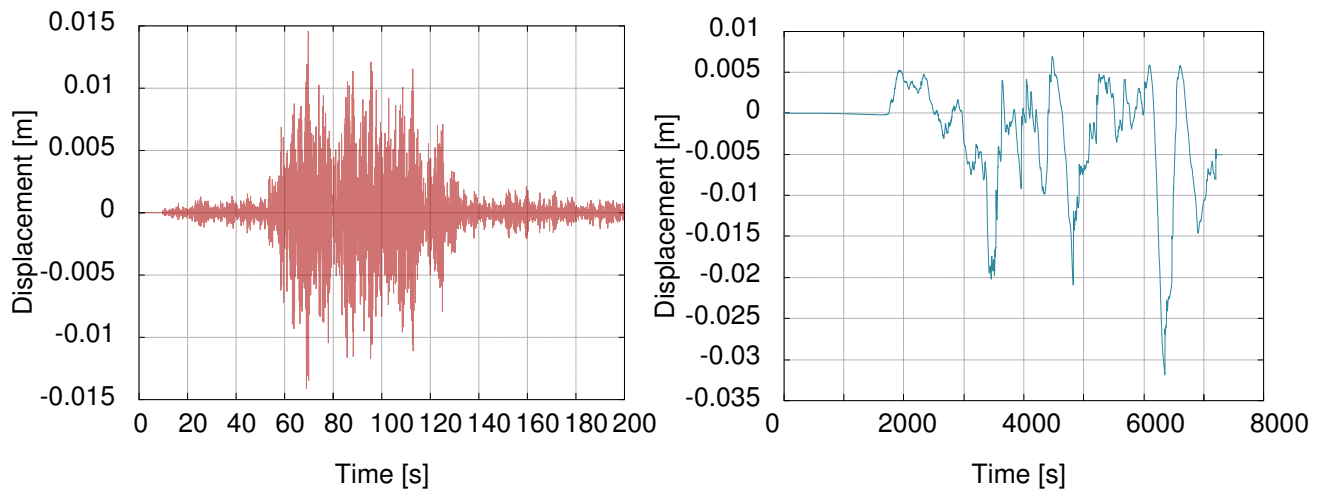
- horizontal displacements induced on the soil-quay system due to seismic accelerations (Fig. 6.24(a)) of $\delta_{u,x} \approx -0.015\text{ m}$ at $t = 62.94\text{ s}$ (seaward direction), and $\delta_{u,x} \approx 0.015\text{ m}$ at $t = 74.64\text{ s}$ (landward direction),
- the geometry of soil-quay system remained unchanged after the seismic analysis, probably indicating that the system kept its initial resistance without exceeding yielding levels,
- nonetheless, to assure that design forces of the structural elements were under the yielding capacity limit, diagrams of M_{sd} , N_{sd} and V_{sd} were computed at time-steps of maxima displacements. Fig. 6.24(b) shows higher design forces at SP1* on pile E, section S9 of the slab connecting to head of pile E and at the transition from SP3 to SP4 on the embedded piles,
- Fig. 6.24(c) depicts the corresponding M- Θ diagram showing $M_{sd,SP1^*}$ between $\approx -600\text{ kNm}$ and $\approx 1000\text{ kNm}$ which is about six times smaller than $\|M_{yield,SP1^*}\| \approx 6500\text{ kNm}$, confirming elastic regime of the infrastructure after seismic accelerations up to 0.20 g ,
- the successive tsunami loading led to horizontal displacements of the quay (Fig. 6.24(a)) evaluated in $\delta_{u,x} \approx -0.032\text{ m}$ at $t = 6348.40\text{ s}$ (seaward direction), and $\delta_{u,x} \approx 0.007\text{ m}$ at $t = 4475.37\text{ s}$

(landward direction),

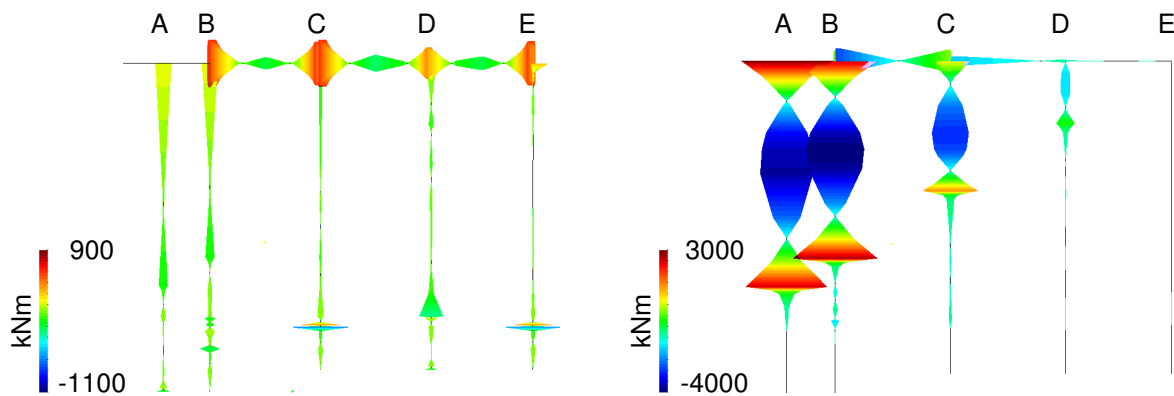
- maxima bending moment values were identified at sections SP2 on piles A and B (middle section along the piles' free length), and S2 on the slab between piles B and C (Fig. 6.24(b)),
- corresponding M- Θ diagrams (Fig. 6.24(c)) of the referred sections showed $M_{sd,SP2}$ between $\approx -3000 \text{ kNm}$ and $\approx 2000 \text{ kNm}$, below $\leq \|M_{yield,SP2}\| \approx 8000 \text{ kNm}$. For the slab section S2, reinforced for positive moments, $M_{sd,S2} \approx -1800 \text{ kNm}$ induce structural failure associated with an upward vertical displacement of $\delta_{u,x} \approx 0.014 \text{ m}$ during tsunami inflow, at $t = 4440 \text{ s}$,
- a brief verification of axial design force at SP1* on pile A showed $N_{sd,SP1^*} = -8000 \text{ kN} < N_{rd,max} = 36740 \text{ kN}$ and shear design force of $V_{sd,S9} = 1650 \text{ kN} < N_{rd,max} = 2112 \text{ kN}$,
- for GBF scenario, the slab between piles B and C was the first element exhibiting structural failure due to tsunami uplifting forces exerted on the soffit of the quay, partially due to the lack of superior reinforcement.

The S_{worst} generated by HSF with rupture parameters proposed by Ribeiro et al., 2003 (Fig. 6.25) generated seismic accelerations and tsunami forces that induced a structural behavior characterized by:

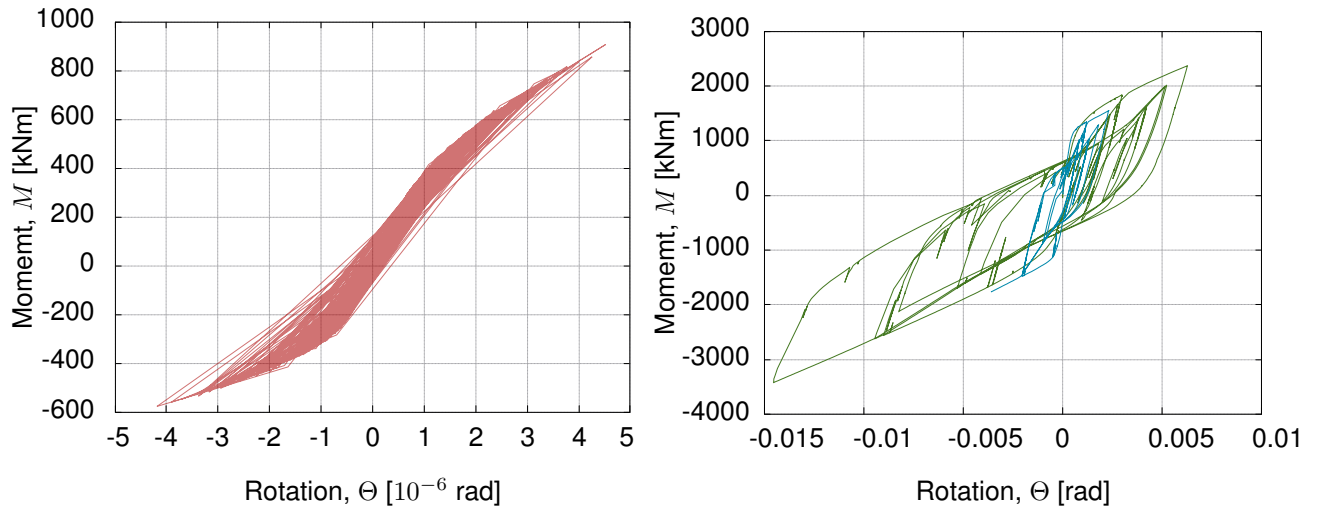
- horizontal displacements induced on the soil-quay system due to seismic accelerations (Fig. 6.25(a)) of $\delta_{u,x} \approx -0.030 \text{ m}$ at $t = 62.94 \text{ s}$ (seaward direction), and $\delta_{u,x} \approx 0.015 \text{ m}$ at $t = 74.64 \text{ s}$ (landward direction),
- the seismic analysis showed one millimetre residual displacement of the quay on the land-ward direction after $t \approx 70 \text{ s}$, coincident with the second transposition of the yielding threshold during the peak displacement on landward direction. The first yielding level transposition occurred during the peak displacement on seaward direction,
- at identified times of maxima displacements (Fig. 6.25(b)), the section most likely to constitute a structural vulnerability was SP1* on the head of pile E. The corresponding M- Θ diagram (Fig. 6.25(c)) demonstrated that the design bending moment on head of pile E reached a value of $M_{sd,SP1^*} = 7250 \text{ kNm}$, which is close to ultimate resistance capacity, $\|M_{rd,SP1^*}\| = 7463 \text{ kNm}$, and clearly above the yielding capacity,
- the head of the piles have higher resistance capacity than the corresponding connected sections of the slabs. However, the soil partially restraints the rotation on head of pile E. A verification at the slab sections connecting to piles D, C and B showed $M_{sd} < M_{rd}$,
- the residual rotation of $1 \cdot 10^{-4} \text{ rad}$ on the head of pile E transitioned to the successive tsunami analysis,
- horizontal displacements of the soil-quay system due to tsunami force (Fig. 6.24(a)) promoted $\delta_{u,x} \approx -0.0026 \text{ m}$ at $t = 5532.10 \text{ s}$ (seaward direction), and $\delta_{u,x} \approx 0.0012 \text{ m}$ at $t = 7168.60 \text{ s}$ (landward direction),



(a) Horizontal displacements of the quay due to seismic acceleration (left) and tsunami force (right).



(b) Bending moments due to seismic acceleration (left) and tsunami force (right) at time-steps corresponding to maxima values.



(c) Diagrams of moment-rotation generated for the sections subjected to higher moments due to seismic (left) and tsunami (right) actions. Red, green and blue lines represent SP1* on pile E during earthquake excitation, SP2 on frontal piles and S1 on slab between piles B and C, respectively.

Figure 6.24: Successive structural response: main characteristics of structural behavior of the soil-quay system in response to S_{worst} considering GBF triggering source proposed by Grandin et al., 2007.

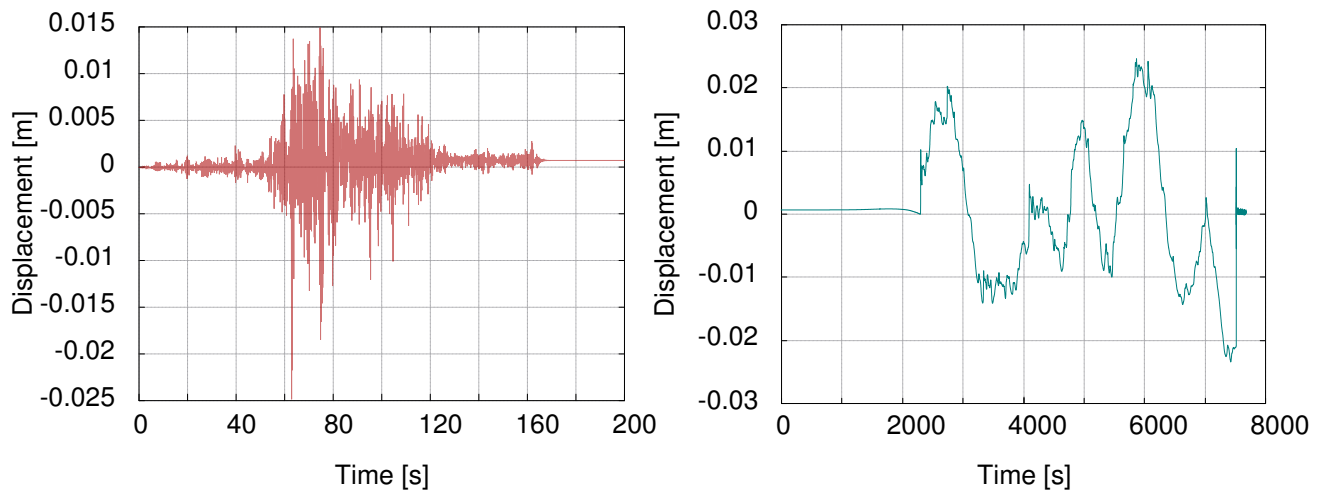
- the higher design moments occurred at sections SP1* on piles B and D, and slab sections S2 and S5 (Fig. 6.25(b)),
- corresponding M- Θ diagram (Fig. 6.24(c)) showed $M_{sd,SP2}$ under $\|M_{rd,SP2}\| = 11001 \text{ kNm}$, while slab sections S2 and S5 matched the ultimate resistance capacity ($M_{rd,s2} = 5246 \text{ kNm}$ and $M_{rd,s5} = 5700 \text{ kNm}$) at $t \approx 7000 \text{ s}$,
- however, temporal series of axial and shear design forces showed that earlier, at $t \approx 5500 \text{ s}$ corresponding to minimum value of tsunami forces during outflow stage, both $N_{sd,S9}$ and $V_{sd,S9}$ matched their corresponding tensile and shear ultimate resistance capacity at section S9 (Table 6.7),
- for HSF scenario, there was structural failure associated with slab S9 due to weight and drag effects of a $\eta = 7 \text{ m}$ wave withdrawal on seaward direction. Moreover, the top of pile E on which slab S9 connects suffered previous reduction of its resistance capacity under the earthquake action. The resistance to this failure mode can be increased, for example, anchoring the transverse beam to embankment or rocky soil in order to guarantee the required resistance.

The S_{worst} generated by MPPSF with rupture parameters proposed by Terrinha et al., 2003 (Fig. 6.26) generated seismic accelerations and tsunami forces that induced a structural behavior characterized by:

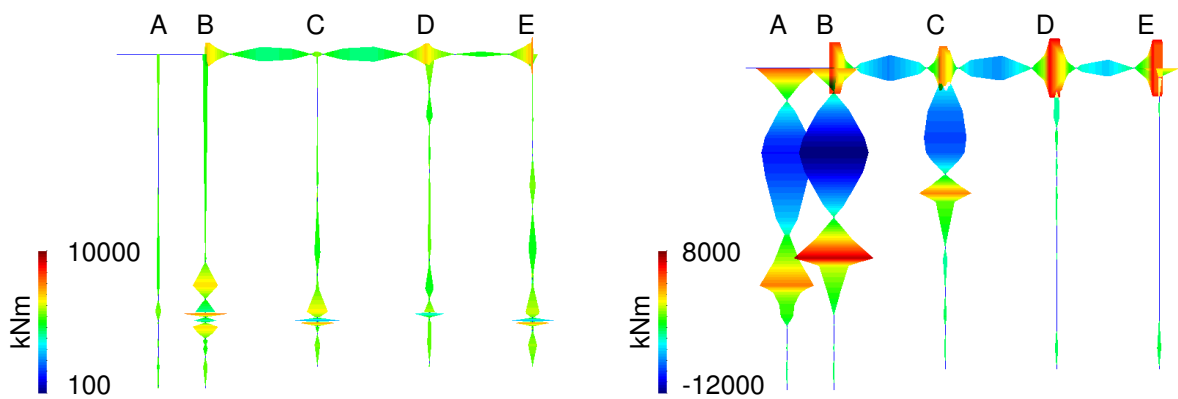
- horizontal displacements induced on the soil-quay system due to seismic accelerations (Fig. 6.26(a)) of $\delta_{u,x} \approx -0.058 \text{ m}$ at $t = 58.46 \text{ s}$ (seaward direction), and $\delta_{u,x} \approx 0.042 \text{ m}$ at $t = 65.25 \text{ s}$ (landward direction),
- the seismic analysis showed a resultant residual displacement of circa -0.003 m on the sea-ward direction after $t \approx 63 \text{ s}$,
- at identified times of maxima displacements, SP1* of pile E was the section experiencing higher bending moment,
- corresponding M- Θ diagram (Fig. 6.25(c)) showed $M_{sd,SP1^*}$ exceeding $M_{yield,SP1^*} \approx 6000 \text{ kNm}$ rapidly evolving to match $M_{rd,SP1^*} = 7463 \text{ kNm}$,
- if tsunami action was considered individually, the correlation between design and resistance capacity showed $M_{sd,sb1} < M_{rd,sb1} = -7932 \text{ kNm}$ and $M_{sd,sb2} < M_{rd,sb2} = -5256 \text{ kNm}$ on the slab between piles B and C. Similarly, tsunami effects were insufficient to induce damage on the piles supporting the quay.

Successive structural response remarks

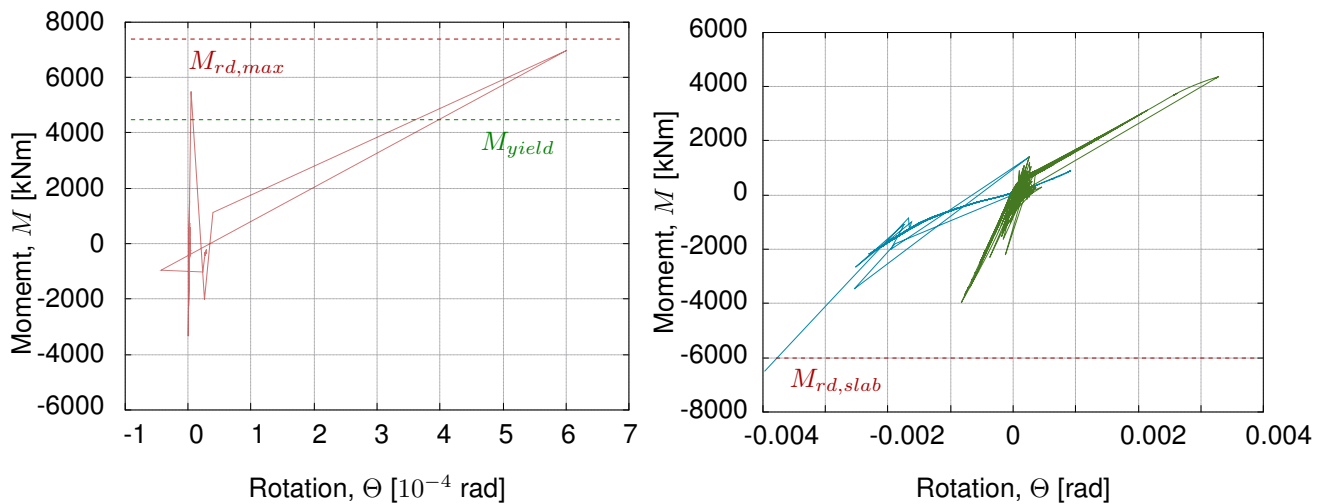
The incidence of damaging pattern due to seismic actions indicated vulnerabilities at pile-quay connection. Diagrams of M- Θ at the SP1* demonstrated considerable higher values at piles in alignment E (shorter pile). Moreover, the seismic action induced concentrated stresses at the transition



(a) Horizontal displacements of the quay due to seismic acceleration (left) and tsunami force (right).



(b) Bending moments due to seismic acceleration (left) and tsunami force (right) at time-steps corresponding to maxima values.



(c) Diagrams of moment-rotation generated for the sections subjected to higher moments due to seismic (left) and tsunami (right) actions. Red, green and blue lines represent SP1* on pile E during earthquake excitation, SP2 on frontal piles and S1 on slab between piles B and C, respectively.

Figure 6.25: Successive structural response: main characteristics of structural behavior of the soil-quay system in response to S_{worst} considering HSF triggering source proposed by Ribeiro et al., 2007.

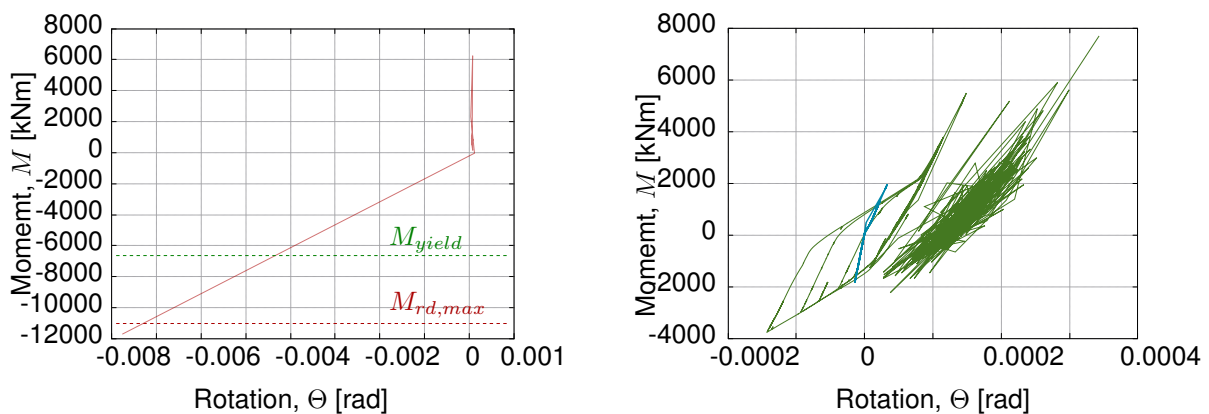
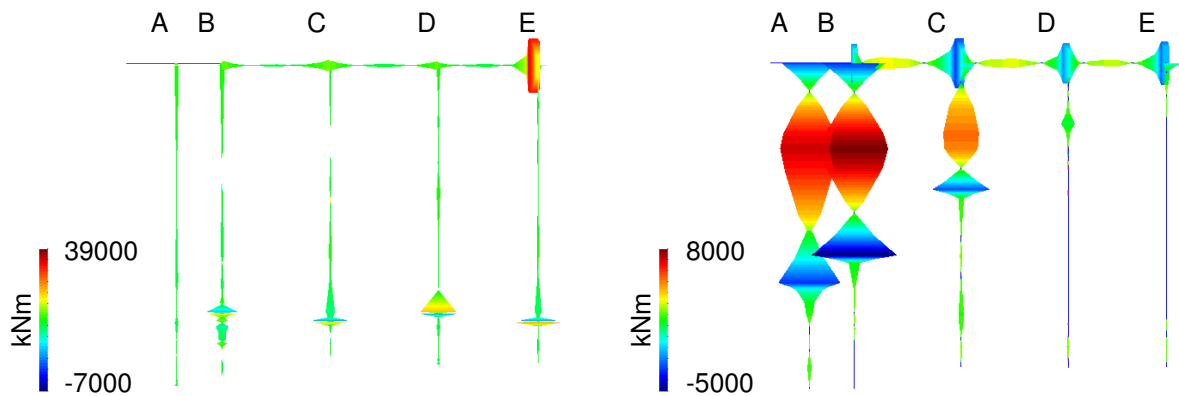
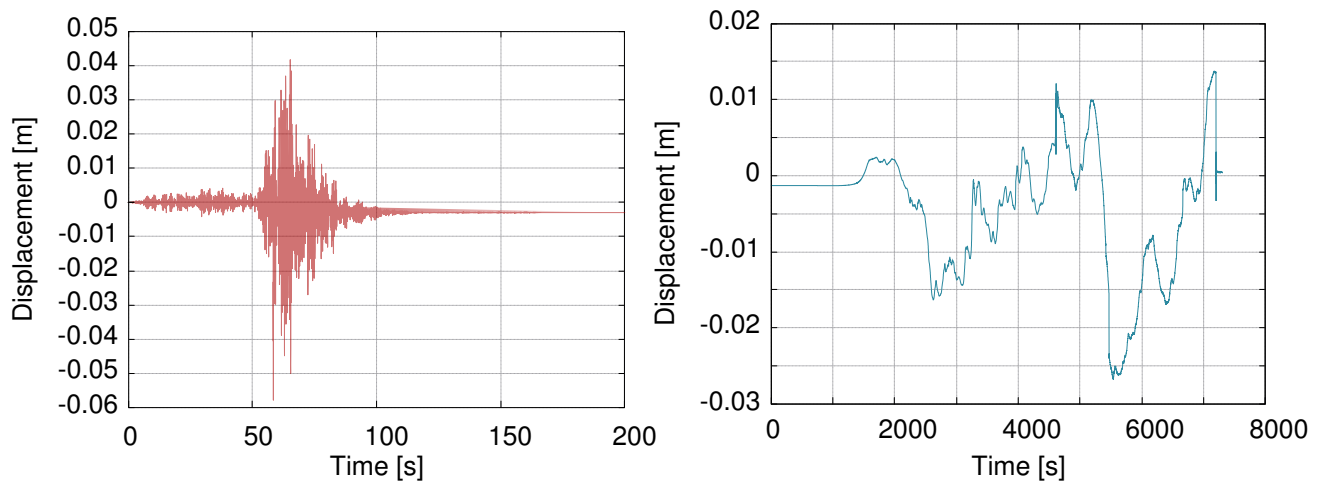


Figure 6.26: Successive structural response: behavior of the soil-quay system in response to S_{worst} considering MPPSF triggering source proposed by Terrinha et al., 2007.

from the embedded SP3 to SP4, due to soil layer variation and the tube interruption at the interface with rocky foundation.

The tsunami action on the horizontal direction posed main structural effects at free part of piles A and B, more exposed to the bore effects, and highlighted a point of fragility at the slab near pile E due to tensile forces. The effects on the embedded part of the piles when subjected to tsunami action was significantly reduced in comparison with seismic action.

The vertical component of the tsunami-quay interaction showed high likelihood of tsunami hydrostatic and hydrodynamic effects generating uplifting phenomena on the slender (0.45 m -height) slabs. The weight of the quay per meter was calculated as 50 kN/m and 12.5 kN/m , for the different slab thickness (2.5 m on 7 m transverse length on the front facing ocean and 0.45 m on 30 m close to back-reach). Except for MPPSF S_{worst} (scenario corresponding to maximum seismic acceleration and structural failure previous to tsunami), the lower value of tsunami effects on the vertical direction was quantified from $F_v \approx 19\text{ kN/m}$ to $F_v \approx 55\text{ kN/m}$.

Chapter 7

Conclusions and Recommendations

Chapter 7 compiles the major conclusions drawn along with recommendations derived for earthquake and tsunami multi-risk management for critical coastal infrastructures, such as deep-water seaports. The present work constitutes a contribution that might benefit from complementary insights such as the ones herein identified as future works.

7.1 Conclusions

The multi-disciplinary nature of the thesis allowed to withdraw contributions towards advances in the fields of numerical, geophysical and structural engineering investigation on regional/local tsunami risk management. Particular design recommendations were formulated for critical ports with open typology, which accumulate everyday activities with lifeline support services in case of disaster.

Regarding the adequacy of modeling approaches:

- Section 2.2 - the earthquake and tsunami phenomena share similar physical stages of generation, propagation and site-effects influencing their waves behavior. Taking advantage of the physical characteristics of earthquake ground-motion(s) and tsunami wave(s) on the generation, propagation and site-effects stages, three interdependent frameworks composing the proposed methodology are defined in terms of spatial and temporal scales. Each of the interdependent macro-, meso- and micro-scale stages are coupled by boundary conditions.
 - macro-scale stage encompasses the spatial and temporal domain needed for the simulation of the earthquake and tsunami generation and propagation, i.e., hundreds of meters up to about 300 *km* and from tens of minutes up to about an 1 *h*. The results of the macro-scale stage are uniform or target bed-rock seismic motions, and tsunami nearshore hydrodynamic quantities.
 - meso-scale stage includes the spatial and time domain needed for the simulation of earthquake and tsunami phenomena considering the strong influence of site-effects, i.e., from few meters up to few hundred meters and up to tens of minutes. The results of the

meso-scale stage are the seismic and tsunami actions exerted on the structure(s).

- micro-scale involves the spatial and time interval needed to assess the structural response to the cascading seismic and tsunami actions. The spatial domain is set to an interval of centimeters to meters, and the time domain is set to an interval of seconds up to couple of minutes.
- The sophistication of the numerical schemes adopted to solve each domain composing the proposed methodology should be function of the importance of the structure(s)/region.
- Section 4.1 - non-linear Shallow Water system of governing equations (SW) solved by classic Eulerian Finite Volume method (FV) constitutes a fast and efficient approach to characterize tsunami propagation and inundation where the treatment of complex flows and geometries is negligible. Source modeling and resolution of the topo-bathymetric mesh were identified as major influencing parameters on the quality of the numerical solutions.
- Section 4.2 - scheme composed of Navier-Stokes system of governing equations (NS) solved by Lagrangian Smoothed Particle Hydrodynamics method (SPH) is capable of tackling fluid impact or interaction with structures, reproducing complex fluid flows, highly non-linear free-surface phenomena, conveniently treating large deformations and handling variable domains in time, such as piston-type wave-makers. Yet, NS-SPH is highly sensitive to physical and numerical parameters, embodies simulations with high computational costs and the solutions have low convergence rates. In some cases, additional algorithms are required to guarantee stability and quality of the solutions increasing computational demand. In such cases, the trade-offs between the improved accuracy of the solutions and computational costs involved to compute them should be target of analysis.
- Section 3.2.3 - taking advantage of both numerical schemes later demonstrated, in Chapter 5, its promising contribution reducing computational costs while providing enhanced quality of the numerical solutions, by means of a coupling technique between Eulerian SW-FV and Lagrangian NS-SPH schemes based on Dirichlet boundary conditions.
- Section 4.3 - GMPE models implemented in OpenQuake and EXSIM open-source tools have demonstrate their capacity of generating maps of PGA distribution and predict time-histories of ground motions in relatively accordance with seismic quantities recorded by instrumental networks.

From a numerical perspective, Chapter 5 was entirely dedicated to an exhaustive proof-of-concept to characterize forces and pressures induced by tsunami-like waves on an elevated coastal structure. The numerical solutions of three numerical protocols were calibrated (Section 5.2) and validated (Section 5.3) by correlation with experimental data acquired from an experimental campaign performed at the large wave flume of the Hinsdale Wave Research Laboratory, Oregon State University. The correlations between the experimental data and the numerical solutions highlight the following advantages and disadvantages of the simulation protocols:

- built-in numerical computation on Lagrangian NS system using the SPH framework implemented in DualSPHysics. The convergence of 3D and 2D solutions tend to $\Delta p = 3\text{ cm}$, which represents about 11.3 million versus 82.5 thousand particles, respectively, with the corresponding simulation time equal to 150 *hours* versus 1.5 *hours*, and data for storage requirements equal to 500 *GB* versus less than 4 *GB*, for each simulation. In terms error metrics, the 3D solutions represent an improvement with respect to the 2D ones in the free-surface elevation after the structure as well as on the computation of the vertical force. The use of 2D models to represent flow phenomena and interaction with the structures is eligible due to flow and symmetry conditions. Keeping in mind the control of computational costs, the accuracy of 2D models with $\frac{H}{\Delta p} \approx 10$ particles for the unbroken wave case and $\frac{H}{\Delta p} \approx 40$ for the broken wave case had guaranteed convergent and reliable solutions.
- semi-analytic quantification force equations recommended by the North American standards using the computation of the tsunami-like hydrodynamic quantities by Eulerian SW-FV using a C++ code. The simulations of unbroken and broken wave cases took less than 10 *m* of run-time and provided solutions of flow propagation along the flume showing accurate estimates of the hydrodynamic quantities when compared with instrumentally-acquired data. Yet, inherent characteristics of the scheme represent limitations when dealing with fluids interacting with solids and assessing quantities in the vertical direction. For reference, the ASCE code recommendation to estimate the tsunami hydrodynamic effects on the vertical direction is based on trigonometric decomposition of horizontal flow velocity for sloping grades over 10° . The semi-empirical nature of the hydrodynamic equation with the C_d value calibrated to match the peak value of the first wave prevent a time-dependent characterization of tsunami force.
- new coupled Eulerian SW-FV and Lagrangian NS-SPH configuration via Dirichlet boundary conditions. The characterization of the linear(-ish) part of the domain using the comparatively faster but smoother mesh-based approaches contributes to reduce the SPH domain governed by sophisticated systems of equations, decreasing the computational expense and maintaining the level of detail of the numerical solutions.
- NS-SPH solutions are comparatively better than the SW-FV solutions, while coupling both numerical schemes represents a good compromise.
- Eulerian SW-FV and Lagrangian NS-SPH are complementary. The Lagrangian NS-SPH proved able to handle complex and realistic geometries, but requiring considerable computational efforts. The SW-FV is definitively faster, but unable to compute complex flows. The coupled solution takes advantage of both Eulerian and Lagrangian methods reducing the SPH domain to the highly non-linear regions, which represents a promising approach to balance the computational costs and keep the accuracy of the numerical solutions.
- The modeling of the laboratorial setup with the reduction of the SPH domain for less than a half about 50% of computation time saving. In real coastal engineering problems, the scale of the

tsunami propagation phase is much larger than the inundation and fluid-interaction phases of the experimental campaign, leading to a greater expression of the advantages of the coupled configuration.

After the calibration and validation of the numerical schemes, the impact of a 1755 GLET-alike event on the container terminal of the Sines deep-water seaport was investigated. The study considered the current and future configurations of the cargo hub (container terminal). The characterization of the cascading earthquake and tsunami multi-hazard was performed adopting a baseline approach to quantify peak seismic and tsunami intensity measures, and an enhance approach to characterize their dynamic nature. The main multi-hazard conclusions are:

- cascading earthquake and tsunami multi-hazard inferred from different intensity measures provide sets of coherent loading patterns for structural design:
 - different sources trigger the hazardous seismic and the tsunami scenarios. The hazardous seismic scenario is derived from the MPPSF source proposed by Terrinha et al. 2003 ($PGA = 0.37 g$), while the hazardous tsunami scenario depends on the intensity measure and structural configuration of the terminal, where the corresponding PGA values vary from $0.16 g$ to $0.35 g$,
 - the tsunami hazardous scenarios were derived from HSF and MPF single and composed source ruptures,
 - hydrostatic and hydrodynamic tsunami effects during the inflow stage can induce landward displacements and uplift of the quay slab. Depending on the configuration of the cargo hub (current or future configuration of the terminal container), the hydrostatic design quantities vary from $8 m$ to $11 m$, for Terminal XXI and $14 m$ for the Vasco da Gama terminal. Accordingly, positive momenta flux were quantified between $100 m^3 s^{-2}$ and $200 m^3 s^{-2}$, for Terminal XXI and $M_F^+ \approx 240 m^3 s^{-2}$, for Vasco da Gama,
 - the hydrodynamic tsunami quantities during the outflow stage, associated with seaward displacement of the structure, were quantified as negative momenta flux varying between $100 m^3 s^{-2}$ to $250 m^3 s^{-2}$ for Terminal XXI and $M_F^- \approx 110 m^3 s^{-2}$ for Vasco da Gama terminal.
- for engineering purposes, tsunami hazard assessment encompassing both the hydrostatic and the hydrodynamic components of tsunami represents a paradigm shifting on the assessment of damaging potential associated with the extreme phenomena,
- dynamically, in most scenarios the first tsunami wave was not representing the hazardous wave, in terms of hydraulic quantities and forces exerted on the target structure. The momenta flux quantities of a tsunami may be composed of a train of equally energetic waves during several hours. The current design recommendations referring two cycles of in-outflow balancing free-surface elevation and flow velocity quantities neglect these possible scenarios. Awareness should be raised to upgrade structural design recommendations in function of the region tectonics by linking rupture parameters with tsunami development towards the continental margins,

- peak and dynamic multi-hazard characterization have complementary functions determining design loading patterns. The time-dependent multi-hazard characterization corroborated most of the peak quantities while providing content and duration insights for structural designing processes,
- the level of numerical sophistication should be adapted to structural performance requirements.

Regarding the successive structural response of the soil-wharf system due to extreme local tsunami, S_{worst} :

- from the S_{worst} , the seismic accelerations around $0.3g$ showed capacity to exceed M_{yield} levels on head of the shorter pile E, while accelerations near $0.4g$ conducted to structural failure,
- for the successive tsunami, the structural damaging pattern was identified at:
 - middle section of the first two piles facing the ocean due to tsunami horizontal forces varying between $-30 kNm$ and $15 kNm$ and inducing displacements between $-0.033 m$ and $0.018 m$,
 - slender slabs (mainly the one between piles BC) due to tsunami vertical forces from $-20 kNm$ and $37 kNm$ on sections lacking superior and inferior reinforcement, respectively.

For other $S_{eligible}$, the cascading earthquake and tsunami loading pattern may represent innocuous effects on the structure, such as the ones derived from triggering sources located on the Cadiz Wedge, while others also have potential to (at least) induce damage that represent interruptions of the port activities. Considering the structural importance of Sines port, risk management should encompass a demand of structural performance that would allow the port to provide post-disaster lifeline support and, shortly after, resume to daily activities.

7.2 Recommendations

Risk management can benefit from reinforcing the ties between natural hazards and engineering practitioners, linking science and industry, and promoting dialogue between risk analysts and policy-makers. Based on the present work, the cornerstone is to raise awareness for the various factors influencing multi-risk management. For the Sines port, the promotion of pre-event actions, such as multi-hazard assessment considering the critical nature of the infrastructures, would lead to informed decisions towards the required level of structural performance, ultimately enhancing risk management. Moreover, the multi-hazard assessed for the harbour have the potential to evolve for a natech multi-risk situations. The characterization of cascading multi-risk should rely on targeting the critical infrastructure, accounting for the surrounding built environment and accounting the cumulative effects of cascading (natural and anthropogenic) effects.

Some of the primordial recommendations to maintain the port operational during an extreme event including elevated cascading seismic accelerations and tsunami hydrodynamic effects are:

- the design of the pile-supported quay should consider seismic accelerations with $PGA = 0.5g$ due to the critical nature of the infrastructure,
- asymmetry of the embankment geometry and non-linear properties of the materials privileged the horizontal displacements on the seaward direction. Anchoring the quay to embankment or rocky foundation, depending on the soil characteristics, can control the horizontal displacements,
- the relative position of the tube to the soffit of the beam limits the spreading of the plastic hinge formation. The embedded dowel connection of the tube edging the beam constitutes a fragility zone as plasticity starts developing at the weakest section of the pile-beam interface with very limited spreading length of the plastic due to adjacent sections with higher resistance capacity. Therefore, it is expected a rapidly evolution to collapse after exceedance of the yielding capacity. To increase the interval between yielding and ultimate resistance capacity, the distance between the top of the tube and the soffit of the quay beam should be increased to approximately the same value as the pile diameter. To provide a confinement close to the tube ($\varepsilon_{cu} = 25.0e^{-3}$), an equivalent transverse reinforcement should be considered,
- to control the location of plastic hinges development (favorably on the piles' head, easier to repair than the slabs, if needed), the sum of the resistance capacity of the slabs' sections should be higher than at each node of the section representing the head of the piles,
- partially extending the metallic tube into rocky foundation would reduce the differences between on the piles' sections at the interface where the tube ends, additionally accompanying the transition of soil layers,
- for adequate tsunami structural performance, slab sections should include superior and inferior reinforcement accounting tsunami buoyancy and uplifting effects to provide flexural capacity for negative moments at slab middle spans and for positive moments at the sections adjacent to the piles,
- the reduction of slabs area exposed to tsunami vertical effects, for example using pressure relief openings on quay slab, would contribute to reduce the effects of tsunami on the vertical direction. The design of the future container terminal should perform a cost-benefit analysis on the options of increase slab reinforcement and/or include pressure relief openings on the slabs,
- the role of coastal protection structures was briefly accounted by assuming the presence or absence of the breakwater due to its design to withstand less energetic and shorter duration storm waves. Higher values of flux momentum were verified around the end of the breakwater while, in some scenarios, resonance effects between the breakwater and the container terminal were identified. Function of future work insights identifying locals more exposed/vulnerable to stronger tsunami currents, reflection and refraction of the waves and resonance effects, the breakwater should be adequately armored with natural rock-fill or artificial blocks to anticipate scouring issues,

- globally, the risk response should be integrated with entire port complex prioritizing infrastructures with lifeline supporting roles and responsibilities (hinterland network and energy provision).

From a risk management perspective, the inextricable loading patterns of the $S_{candidate}$ would benefit from a complementary characterization of tsunami loading considering other effects that were out of the scope of the present work, such as debris interaction with the built environment, with potential of increasing tsunami effects on the terminal container. Instead, a preventive measure of debris control could be adopted based on the strategic implementation of structures engineered for good performance during tsunami inundation near potential debris sources that can represent an obstruction to the flow, reduce the dispersal of debris, and control the debris transportation into pre-defined paths avoiding critical impacts and dam effects (function of future work insights).

The effects of vessels moored at the container terminal should be further investigated. The considerations to account the tsunami interaction with large ships should consider tsunami inflow and outflow stages. The vessel impacts the wharf during inflow. During outflow, if the ship is at berth, the flow can induce elevated tensions in the mooring lines (which can break or exert an additional contribution for the quay wash-away on seaward direction). The development of port emergency protocol in case of tsunami warning alert (due to strong earthquake or issued by the authorities) is recommended and should provide plans for terrestrial and maritime evacuation. In case of strong earthquake or tsunami warning issued, the best practice is to stay offshore, if the vessel is at the sea, or in case the vessel is in the harbour should be assessed if it is possible the withdrawal of the ships for a safety distance away from the wharves. In case of short notice of the alert, which is more probable for Sines region, a secure and short-length mooring of the ship to the mooring bollard would minimize the amplification of berthing effects against the structure.

7.3 Future Work

At the macro-scale, the multi-hazard/risk assessment would benefit from considering probabilities associated with uncertainties influencing the explanatory variables. For example, physical uncertainties for the generation phase include geometry and rupture parameters, such as the effects of earthquake spatial slip correlation on variability of earthquake and tsunami potential energy and intensities. For the earthquake propagation phase, the calibration of attenuation laws for elevated magnitude earthquakes at moderate seismicity regions need further investigation. For the tsunami, variables for the site influences encompass (re-)definition of tsunami hazard considering climate change impact (the areas at risk of tsunami will increase as global mean sea level rises), directivity and polarity of the waves would contribute to decrease the level of uncertainty associated with the risk assessment.

At the meso-scale, due to complex hydraulic phenomena under the slab, mainly the tsunami force on the vertical directions would benefit from more detailed characterization, only possible using more sophisticated numerical schemes, such as the SPH method solving the NS system of equations equipped with a multiphase algorithm. Such numerical schemes can theoretically contribute to the characterization of other tsunami effects on the structures that remain unexplored, such as berthing

and mooring effects of ships, tsunami during the outflow developing suction effects on elevated structures and multi-phase phenomena due to air entrapped under elevated structures with irregular geometry, such as the soffit of quays. Moreover, the tsunami hazard characterization would benefit from considering the effects induced by various coastal defense configurations. Beside the presence/absence of the breakwater (as considered in the present analyses), intermediary configurations of horizontal and vertical partial collapse can induce channeling and wave height amplification towards the container terminal. Other effects, such as geotechnical failures, topo-bathymetric variations due to subsidence from the previous ground motion, identification of surrounding elements becoming debris, and vessels and cranes interaction with the quay should also be made part of the tsunami hazard assessment. Similarly to physical aspects, numerical aspects associated with the sophistication of the modeling and numerical schemes used to perform the numerical simulations also pose uncertainty for hazard/risk assessments. An approach targeting the critical infrastructure(s) and accounting for the uncertainties associated with physical and modelling would contribute to provide variability to thresholds levels of damage/collapse and, ultimately, contribute to more informed decisions. A detailed risk evaluation should allow to predict the scalability to a natech situation.

The characterization of tsunami forces application (ex.: analytical design recommendations) would benefit from further investigation on the adequacy of assuming generic uniform, triangular or trapezoidal distribution on the structural surface. Complementary data regarding pressures' distribution, for example by correlating data from physical and numerical simulations along impacted surfaces to update the analytical formulations, on both horizontal and vertical directions would allow to improve design guidelines. Simulations (physical and/or numerical) can also investigate the effects of the spacing among the group of piles, i.e., distance between piles affecting drag forces.

At the micro-scale, balance the demands of flexibility and ductility for earthquake resistance with the demands of stiffness and strength for the tsunami resistance remains unexplored. The role of structural flexibility for the case of earthquakes is already well known, however, its role on the tsunami-structure interaction constitutes one of the most challenging topics related to the micro-scale effects of tsunamis. Its characterization could contribute to develop non-contradictory engineered-based recommendations.

The characterization of successive structural response would benefit from using kinematic quantities, such as moment-curvature diagrams, allowing to quantitatively detail the damage status of the sections between yielding and ultimate resistance capacity levels.

For coherence of micro-scale analysis sophistication, the structural response to tsunami would benefit from modeling a 3D or pseudo-3D two-way fluid-structure interaction. The capacity of introducing flexibility on the structure as a function of the non-linear properties of the materials might simultaneously represent a better characterization of the tsunami pressures being exerted on horizontal and vertical surfaces of the structure, as well as the corresponding deformation of the infrastructure. Numerical schemes encompassing Lagrangian-based discretization of fluid and solids are being investigated to become capable to assign distortion and fracture algorithms, such as the Peridynamic method using the well established fracture theory of Griffith. So far, SPH method relies on

hourglass control algorithm to assign fracture models to the materials. Yet, resultant stress fields on solid mechanics are noisy, similarly to pressure fields distribution of fluid mechanics, due to the inherent challenge of tuning physical and numerical dissipation. In the future, particle methods integrating non-linear properties on solids interacting with fluids and other various additional effects on a single model, such as mooring and berthing of vessels simulated by MoorDyn, and debris transportation and impact using motion on solids algorithm, will assure realistic numerical characterization of highly complex physical phenomena.

Globally, from macro- to micro-scale, the generation of synthetic data covering a range of possible combinations of various explanatory variables would allow to encompass a wider perspective on probabilistic multi-risk assessment. However, the prediction process implies big data generation and respective analysis, which could rely on innovative tools based on machine learning and artificial intelligence to make the process systemic and significantly more expedite.

Bibliography

- [1] C. F. Smith. *Thucydides: History of the Peloponnesian War*. Harvard University Press, books i an edition, 1919. ISBN 9780141909394.
- [2] T. Takabatake, M. Esteban, I. Nistor, T. Shibayama, and S. Nishizaki. Effectiveness of hard and soft tsunami countermeasures on loss of life under different population scenarios. *International Journal of Disaster Risk Reduction*, 45:101491, 2020. ISSN 22124209. doi: 10.1016/j.ijdr.2020.101491.
- [3] E. N. Bernard, H. O. Mofjeld, V. V. Titov, C. E. Synolakis, and F. I. González. Tsunami: Scientific frontiers, mitigation, forecasting and policy implications. *Philosophical Transactions of the Royal Society A: Mathematical, Physical and Engineering Sciences*, 364(1845):1989–2007, 2006. ISSN 1364503X. doi: 10.1098/rsta.2006.1809.
- [4] K. Satake. Advances in earthquake and tsunami sciences and disaster risk reduction since the 2004 Indian ocean tsunami. *Geosciences Letters*, 1(15):1–13, 2014. doi: 10.1186/s40562-014-0015-7.
- [5] P. Shi, T. Ye, Y. Wang, T. Zhou, W. Xu, J. Du, J. Wang, N. Li, C. Huang, L. Liu, B. Chen, Y. Su, W. Fang, M. Wang, X. Hu, J. Wu, C. He, Q. Zhang, Q. Ye, C. Jaeger, and N. Okada. Disaster risk science: A geographical perspective and a research framework. *International Journal of Disaster Risk Science*, 11(4):426–440, 2020. ISSN 21926395. doi: 10.1007/s13753-020-00296-5. URL <https://doi.org/10.1007/s13753-020-00296-5>.
- [6] R. Maletta and G. Mendicino. A methodological approach to assess the territorial vulnerability in terms of people and road characteristics. *Georisk*, 0(0):1–14, 2020. ISSN 17499526. doi: 10.1080/17499518.2020.1815214. URL <https://doi.org/10.1080/17499518.2020.1815214>.
- [7] L. M. Stough and D. Kang. The Sendai framework for disaster risk reduction and persons with disabilities. *International Journal of Disaster Risk Science*, 6(2):140–149, 2015. ISSN 20950055. doi: 10.1007/s13753-015-0051-8.
- [8] B. Wisner. Five years beyond Sendai - Can we get beyond frameworks? *International Journal of Disaster Risk Science*, 11(2):239–249, 2020. ISSN 21926395. doi: 10.1007/s13753-020-00263-0. URL <https://doi.org/10.1007/s13753-020-00263-0>.

- [9] J. C. Borrero, C. E. Synolakis, and H. M. Fritz. Northern Sumatra field survey after the December 2004 Great Sumatra earthquake and Indian ocean tsunami. *Earthquake Spectra*, 22(S3):93–104, 2006. doi: 10.1193/1.2206793.
- [10] H. M. Fritz, C. M. Petroff, P. A. Catalán, R. Cienfuegos, P. Winckler, N. Kalligeris, R. Weiss, S. E. Barrientos, G. Meneses, C. Valderas-Bermejo, C. Ebeling, A. Papadopoulos, M. Contreras, R. Almar, J. C. Dominguez, and C. E. Synolakis. Field survey of the 27 february 2010 Chile tsunami. *Pure and Applied Geophysics*, 168(11):1989–2010, 2011. ISSN 00334553. doi: 10.1007/s00024-011-0283-5.
- [11] A. Pomonis, K. Saito, S. Fraser, S. C. Chian, K. Goda, J. Macabuag, M. Offord, A. Raby, P. Sammonds, E. Gavanski, M. Koyama, H. Murakami, T. Rossetto, D. Grant, and J. E. Alarcon. EEFIT Field Report: The Mw9.0 Tōhoku Earthquake and Tsunami of 11th March. Technical Report March, Earthquake Engineering Field Investigation Team, United Kigdom, 2011.
- [12] R. Aránguiz, G. González, J. González, P. A. Catalán, R. Cienfuegos, Y. Yagi, R. Okuwaki, L. Urra, K. Contreras, I. Del Rio, and C. Rojas. The 16 September 2015 Chile Tsunami from the Post-Tsunami Survey and Numerical Modeling Perspectives. *Pure and Applied Geophysics*, 173(2): 333–348, 2016. ISSN 14209136. doi: 10.1007/s00024-015-1225-4.
- [13] R. Omira, G. G. Dogan, R. N. Hidayat, S. Husrin, G. Prasetya, A. Annunziato, C. Proietti, P. Probst, M. A. Paparo, M. Wronna, A. Zaytsev, P. Pronin, A. Giniyatullin, P. S. Putra, D. Hartanto, G. G. Ginanjar, W. Kongko, E. Pelinovsky, and A. C. Yalciner. The September 28th, 2018, tsunami in Palu-Sulawesi, Indonesia: A post-event field survey. *Pure and Applied Geophysics*, 176(4): 1379–1395, 2019. ISSN 14209136. doi: 10.1007/s00024-019-02145-z.
- [14] H. Park, D. T. Cox, P. J. Lynett, D. M. Wiebe, and S. Shin. Tsunami inundation modeling in constructed environments: A physical and numerical comparison of free-surface elevation, velocity, and momentum flux. *Coastal Engineering*, 79:9–21, 2013. ISSN 03783839. doi: 10.1016/j.coastaleng.2013.04.002.
- [15] M. Esteban, T. Glasbergen, T. Takabatake, B. Hofland, S. Nishizaki, Y. Nishida, J. Stolle, I. Nistor, J. D. Bricker, H. Takagi, and T. Shibayama. Overtopping of coastal structures by tsunami waves. *Geosciences*, 7(4):121, 2017. ISSN 2076-3263. doi: 10.3390/geosciences7040121.
- [16] S. Schimmels, S. Venkatachalam, and I. Didenkulova. Tsunami generation in a large scale experimental facility. *Coastal Engineering*, 110:32–41, 2016. ISSN 03783839. doi: 10.1016/j.coastaleng.2015.12.005.
- [17] O. Farahmandpour, A. K. Marsono, P. Forouzani, M. M. Tap, and S. Abu Bakar. Experimental simulation of tsunami surge and its interaction with coastal structure. *International Journal of Protective Structures*, 11(2):258–280, 2020. ISSN 2041420X. doi: 10.1177/2041419619874082.

- [18] M. Zhu and M. H. Scott. Modeling fluid-structure interaction by the particle finite element method in OpenSees. *Computers and Structures*, 132:12–21, 2014. ISSN 00457949. doi: 10.1016/j.compstruc.2013.11.002.
- [19] S. Clain, C. Reis, R. Costa, J. Figueiredo, M. A. Baptista, and J. M. Miranda. Second-order finite volume with hydrostatic reconstruction for tsunami simulation. *Journal of Advances in Modeling Earth Systems*, 8(4):1691–1713, 2016. ISSN 19422466. doi: 10.1002/2015MS000603.
- [20] B. Bonev, J. S. Hesthaven, F. X. Giraldo, and M. A. Kopera. Discontinuous Galerkin scheme for the spherical shallow water equations with applications to tsunami modeling and prediction. *Journal of Computational Physics*, 362:425–448, 2018. ISSN 10902716. doi: 10.1016/j.jcp.2018.02.008.
- [21] C. Reis, J. Figueiredo, S. Clain, R. Omira, M. A. Baptista, and J. M. Miranda. Comparison between MUSCL and MOOD techniques in a finite volume well-balanced code to solve SWE. The Tohoku-Oki, 2011 example. *Geophysical Journal International*, 2018. doi: 10.1093/gji/ggy472.
- [22] R. Omira, M. A. Baptista, L. Matias, J. M. Miranda, C. Catita, F. Carrilho, and E. R. Toto. Design of a sea-level tsunami detection network for the Gulf of Cadiz. *Natural Hazards and Earth System Science*, 9(4):1327–1338, 2009. ISSN 16849981. doi: 10.5194/nhess-9-1327-2009.
- [23] D. Jin and J. Lin. Managing tsunamis through early warning systems: A multidisciplinary approach. *Ocean and Coastal Management*, 54(2):189–199, 2011. ISSN 09645691. doi: 10.1016/j.ocecoaman.2010.10.025.
- [24] T. Maeda, K. Obara, M. Shinohara, T. Kanazawa, and K. Uehira. Successive estimation of a tsunami wavefield without earthquake source data A data assimilation approach toward real-time tsunami forecasting. *Geophysical Research Letters*, 42:7923–7932, 2015. doi: 10.1002/2015GL065588.
- [25] A. Pimanmas, P. Joyklad, and P. Warnitchai. Structural design guideline for tsunami evacuation shelter. *Journal of Earthquake and Tsunami*, 4(4):269–284, 2010. doi: 10.1142/S1793431110000868.
- [26] Y. Nakano. Structural design requirements for tsunami evacuation buildings in Japan. *American Concrete Institute, ACI Special Publication*, 2017-Janua(SP 313):1–12, 2017.
- [27] E. Meilianda, B. Pradhan, Syamsidik, L. K. Comfort, D. Alfian, R. Juanda, S. Syahreza, and K. Munadi. Assessment of post-tsunami disaster land use/land cover change and potential impact of future sea-level rise to low-lying coastal areas: A case study of Banda Aceh coast of Indonesia. *International Journal of Disaster Risk Reduction*, 41(August):101292, 2019. ISSN 22124209. doi: 10.1016/j.ijdrr.2019.101292.
- [28] A. Buylova, C. Chen, L. A. Cramer, H. Wang, and D. T. Cox. Household risk perceptions and evacuation intentions in earthquake and tsunami in a Cascadia Subduction Zone. *International*

- Journal of Disaster Risk Reduction*, 44:101442, 2020. ISSN 22124209. doi: 10.1016/j.ijdr.2019.101442.
- [29] F. Kitamura, D. Inazu, T. Ikeya, and A. Okayasu. An allocating method of tsunami evacuation routes and refuges for minimizing expected casualties. *International Journal of Disaster Risk Reduction*, 45:101519, 2020. ISSN 22124209. doi: 10.1016/j.ijdr.2020.101519.
- [30] Ministry of Land Infrastructure Transportation and Tourism. Interim guidelines on structural requirements for tsunami evacuation buildings considering the Great East Japan Earthquake. Annex to the Technical Advice. Technical report, Housing Bureau, Building Guidance Division, Ministry of Land, Infrastructure, Transportation and Tourism, 2011.
- [31] Federal Emergency Management Agency. Guidelines for design of structures for vertical evacuation from tsunamis. Third edition. Technical report, Applied Technology Council, Federal Emergency Management Agency, National Oceanic and Atmospheric Administration, 2019.
- [32] American Society of Civil Engineers. *ASCE/SEI 7-16 Minimum design loads and associated criteria for buildings and other structures*. American Society of Civil Engineers, Reston, Virginia, United States, 2016.
- [33] Eurocodes. NP EN 1998-1: Eurocódigo 8 - Projecto de Estruturas para resistência aos sismos. Parte 1: Regras gerais, acções sísmicas e regras para edifícios. *Instituto Português da Qualidade*, 2010.
- [34] I. Rafliana, F. Jalayer, A. Cerase, L. Cugliari, M. Baiguera, D. Salmanidou, Ö. Necmioğlu, I. A. Ayerbe, S. Lorito, F. Løvholt, A. Babeyko, M. A. Salgado-Gálvez, J. Selva, R. D. Risi, M. B. Sørensen, J. Behrens, Í. Aniel-Quiroga, M. Del, S. Belliazzi, I. R. Pranantyo, A. Amato, and U. Hancilar. Tsunami risk communication and management: Contemporary gaps and challenges. *International Journal of Disaster Risk Reduction*, page 102771, 2022. ISSN 2212-4209. doi: 10.1016/j.ijdr.2021.102771. URL <https://doi.org/10.1016/j.ijdr.2021.102771>.
- [35] UNESCO-IOC. Tsunami glossary. Technical Report 85, UNESCO, 2016. URL http://ioc3.unesco.org/itic/files/tsunami_glossary_small.pdf.
- [36] T. Sugano, A. Nozu, E. Kohama, K. I. Shimosako, and Y. Kikuchi. Damage to coastal structures. *Soil and Foundations*, 54(4):883–901, aug 2014. ISSN 00380806. doi: 10.1016/j.sandf.2014.06.018.
- [37] B. Choi, A. Nishida, T. Itoi, and T. Takada. Load combination of aftershocks and tsunami for tsunami-resistant design. In *12th International Conference on Applications of Statistics and Probability in Civil Engineering*, pages 12–15, Vancouver, Canada, jul 2015. doi: 10.14288/1.0076105.
- [38] R. De Risi and K. Goda. Probabilistic earthquake–tsunami multi-hazard analysis: Application to the Tohoku Region, Japan. *Frontiers in Built Environment*, 2(25), 2016. ISSN 2297-3362. doi: 10.3389/fbuil.2016.00025.

- [39] J. Bonacho and C. Sousa Oliveira. Multi-hazard analysis of earthquake shaking and tsunami impact. *International Journal of Disaster Risk Reduction*, 31(October 2017):275–280, 2018. ISSN 22124209. doi: 10.1016/j.ijdrr.2018.05.023.
- [40] M. S. Alam, A. R. Barbosa, M. H. Scott, D. T. Cox, and J. W. van de Lindt. Development of physics-based tsunami fragility functions considering structural member failures. *Journal of Structural Engineering*, 144(3):04017221, 2018. ISSN 0733-9445. doi: 10.1061/(ASCE)ST.1943-541X.0001953.
- [41] J. Palacios, M. Diaz, and J. Morales. Analysis of structural performance of existing rc building designated as tsunami evacuation shelter in case of earthquake-tsunami scenarios in Lima city. *Tecnia*, 29(2):109–124, 2019. ISSN 0375-7765. doi: 10.21754/tecnica.v29i2.704.
- [42] I. Charvet, J. Macabuag, and T. Rossetto. Estimating tsunami-induced building damage through fragility functions: Critical review and research needs. *Frontiers in Built Environment*, 3(August): 1–22, 2017. ISSN 22973362. doi: 10.3389/fbuil.2017.00036.
- [43] D. Wüthrich, M. Pfister, and A. J. Schleiss. Hydrodynamic impact of water waves on buildings. *Houille Blanche*, 2020-March(1):34–41, 2020. ISSN 00186368. doi: 10.1051/lhb/2020007. URL <https://doi.org/10.1051/lhb/2020007>.
- [44] G. Pringgana, L. S. Cunningham, and B. D. Rogers. Influence of orientation and arrangement of structures on tsunami impact forces: Numerical investigation with Smoothed Particle Hydrodynamics. *Journal of Waterway, Port, Coastal, and Ocean Engineering*, 147(3):04021006, 2021. ISSN 0733-950X. doi: 10.1061/(asce)ww.1943-5460.0000629.
- [45] Z. Wei, R. A. Dalrymple, A. Héroult, G. Bilotta, E. Rustico, and H. Yeh. SPH modeling of dynamic impact of tsunami bore on bridge piers. *Coastal Engineering*, 104:26–42, 2015. ISSN 03783839. doi: 10.1016/j.coastaleng.2015.06.008.
- [46] M. Sarfaraz and A. Pak. SPH numerical simulation of tsunami wave forces impinged on bridge superstructures. *Coastal Engineering*, 121(November 2016):145–157, 2017. ISSN 03783839. doi: 10.1016/j.coastaleng.2016.12.005.
- [47] C. Altomare, A. Tafuni, J. M. Domínguez, A. J. C. Crespo, X. Gironella, and J. Sospedra. SPH simulations of real sea waves impacting a large-scale structure. *Journal of Marine Science and Engineering*, 8(10):1–21, 2020. ISSN 20771312. doi: 10.3390/jmse8100826.
- [48] C. Reis, S. Clain, J. Figueiredo, A. R. Barbosa, M. A. Baptista, and M. Lopes. Experimentally validated numerical models to assess tsunami hydrodynamic force on an elevated structure. *Engineering Structures*, 249(September), 2021. ISSN 18737323. doi: 10.1016/j.engstruct.2021.113280.
- [49] M. Tirindelli, G. Cuomo, W. Allsop, and A. Lamberti. Wave-in-deck forces on jetties and related structures. In *Proceedings of the International Offshore and Polar Engineering Conference*, pages 2812–2819, Honolulu, Hawaii, 2003. The International Society of Offshore and Polar Engineers.

- [50] H. Yeh, A. R. Barbosa, H. T. S. Ko, and J. G. Cawley. Tsunami loadings on structures: review and analysis. *Coastal Engineering*, 1(34):1–13, 2014. ISSN 01613782. doi: <http://dx.doi.org/10.9753/icce.v34.currents.4>.
- [51] P. N. Sun, M. Luo, D. Le Touzé, and A. M. Zhang. The suction effect during freak wave slamming on a fixed platform deck: Smoothed particle hydrodynamics simulation and experimental study. *Physics of Fluids*, 31(11), 2019. ISSN 10897666. doi: 10.1063/1.5124613. URL <https://doi.org/10.1063/1.5124613>.
- [52] V. Sivagamasundari and S. A. Sannasiraj. Experimental study of vertical wave-in-deck force and pressure on a thin plate due to regular and focused waves. *Journal of Ocean Engineering and Marine Energy*, 6(2):199–210, 2020. ISSN 21986452. doi: 10.1007/s40722-020-00169-5. URL <https://doi.org/10.1007/s40722-020-00169-5>.
- [53] G. Y. K. Chock. Design for tsunami loads and effects in the ASCE 7-16 standard. *Journal of Structural Engineering*, 142(11), 2016. doi: DOI:10.1061/(ASCE)ST.1943-541X.0001565.
- [54] I. Nistor, N. Goseberg, and J. Stolle. Tsunami-driven debris motion and loads: A critical review. *Frontiers in Built Environment*, 3(January):1–11, 2017. ISSN 2297-3362. doi: 10.3389/fbuil.2017.00002. URL <http://journal.frontiersin.org/article/10.3389/fbuil.2017.00002/full>.
- [55] R. Jayaratne, A. Abimola, T. Mikami, S. Matsuba, M. Esteban, and T. Shibayama. Predictive model for scour depth of coastal structure failures due to tsunamis. *Coastal Engineering Proceedings*, 1(34):56, 2014. ISSN 2156-1028. doi: 10.9753/icce.v34.structures.56. URL <https://journals.tdl.org/icce/index.php/icce/article/view/8039>.
- [56] B. E. Larsen, L. K. Arbøll, S. F. Kristoffersen, S. Carstensen, and D. R. Fuhrman. Experimental study of tsunami-induced scour around a monopile foundation. *Coastal Engineering*, 138(April): 9–21, 2018. ISSN 03783839. doi: 10.1016/j.coastaleng.2018.04.007.
- [57] T. Matsuda, K. Maeda, M. Miyake, J. Miyamoto, H. Sumida, and K. Tsurugasaki. Instability of a caisson-type breakwater induced by an earthquake–tsunami event. *International Journal of Geomechanics*, 16(5):1–19, feb 2016. doi: 10.1061/(ASCE)GM.1943-5622.0000619.
- [58] M. J. Olsen, K. F. Cheung, Y. Yamazaki, S. Butcher, M. Garlock, S. C. Yim, S. McGarity, I. Robertson, L. Burgos, and Y. L. Young. Damage assessment of the 2010 Chile earthquake and tsunami using terrestrial laser scanning. *Earthquake Spectra*, 28(SUPPL.1), 2012. ISSN 87552930. doi: 10.1193/1.4000021.
- [59] S. Fraser, A. Raby, A. Pomonis, K. Goda, S. C. Chian, J. Macabuag, M. Offord, K. Saito, and P. Sammonds. Tsunami damage to coastal defences and buildings in the March 11th 2011 Mw9.0 Great East Japan earthquake and tsunami. *Bulletin of Earthquake Engineering*, 11:2015–239, 2013. ISSN 1570761X. doi: 10.1007/s10518-012-9348-9.

- [60] H. Hazarika, K. Kasama, D. Suetsugu, S. Kataoka, and N. Yasufuku. Damage to geotechnical structures in waterfront areas of Northern Tohoku due to the March 11, 2011 tsunami disaster. *Indian Geotechnical Journal*, 43(2):137–152, 2013. ISSN 00468983. doi: 10.1007/s40098-012-0021-7.
- [61] G. S. G. Dwarakish and A. M. Salim. Review on the role of ports in the development of a nation. *Aquatic Procedia*, 4(Icwrcoe):295–301, 2015. ISSN 2214241X. doi: 10.1016/j.aqpro.2015.02.040. URL <http://linkinghub.elsevier.com/retrieve/pii/S2214241X15000413>.
- [62] United Nations Office for Disaster Risk Reduction. Sendai framework for disaster risk reduction 2015-2030. Technical report, United Nations Office for Disaster Risk Reduction. UNISDR, Sendai, Japan, 2015.
- [63] C. Reis, M. Lopes, M. A. Baptista, and S. Clain. Towards an integrated framework for the risk assessment of coastal structures exposed to earthquake and tsunami hazards. *Resilient Cities and Structures*, Submitted, 2022.
- [64] W. Marzocchi, A. Garcia-Aristizabal, P. Gasparini, M. L. Mastellone, and A. D. Ruocco. Basic principles of multi-risk assessment: A case study in Italy. *Natural Hazards*, 62(2):551–573, 2012. ISSN 0921030X. doi: 10.1007/s11069-012-0092-x.
- [65] J. Selva. Long-term multi-risk assessment: Statistical treatment of interaction among risks. *Natural Hazards*, 67(2):701–722, 2013. ISSN 0921030X. doi: 10.1007/s11069-013-0599-9.
- [66] A. Mignan, S. Wiemer, and D. Giardini. The quantification of low-probability-high-consequences events: Part I. A generic multi-risk approach. *Natural Hazards*, 73(3):1999–2022, 2014. ISSN 0921030X. doi: 10.1007/s11069-014-1178-4.
- [67] Z. Liu, F. Nadim, A. Garcia-Aristizabal, A. Mignan, K. Fleming, and B. Q. Luna. A three-level framework for multi-risk assessment. *Georisk: Assessment and Management of Risk for Engineered Systems and Geohazards*, 9(2):59–74, 2015. ISSN 17499526. doi: 10.1080/17499518.2015.1041989.
- [68] X. Ming, W. Xu, Y. Li, J. Du, B. Liu, and P. Shi. Quantitative multi-hazard risk assessment with vulnerability surface and hazard joint return period. *Stochastic Environmental Research and Risk Assessment*, 29(1):35–44, 2015. ISSN 14363259. doi: 10.1007/s00477-014-0935-y.
- [69] G. Zuccaro, D. De Gregorio, and M. F. Leone. Theoretical model for cascading effects analyses. *International Journal of Disaster Risk Reduction*, 30(May):199–215, 2018. ISSN 22124209. doi: 10.1016/j.ijdr.2018.04.019.
- [70] K. J. Beven, S. Almeida, W. P. Aspinall, P. D. Bates, S. Blazkova, E. Borgomeo, J. Freer, K. Goda, J. W. Hall, C. Phillips, Jeremy, M. Simpson, D. B. Stephenson, T. Wagener, M. Watson, and K. L. Wilkins. Epistemic uncertainties and natural hazard risk assessment – Part 1: A review of the

- issues. *Natural Hazards and Earth System Sciences*, 18:2741–2768, 2018. ISSN 2195-9269. doi: 10.5194/nhessd-18-2741-2018.
- [71] D. Alexander. A magnitude scale for cascading disasters. *International Journal of Disaster Risk Reduction*, 30(March):180–185, 2018. ISSN 22124209. doi: 10.1016/j.ijdr.2018.03.006.
- [72] P. A. Korswagen, S. N. Jonkman, and K. C. Terwel. Probabilistic assessment of structural damage from coupled multi-hazards. *Structural Safety*, 76:135–148, 2019. ISSN 0167-4730. doi: 10.1016/j.strusafe.2018.08.001. URL <https://doi.org/10.1016/j.strusafe.2018.08.001>.
- [73] Y. Ben-Haim. Cascading failures in hierarchical networks with unity of command: An info-gap analysis. *International Journal of Disaster Risk Reduction*, 41(101291), 2019. ISSN 22124209. doi: 10.1016/j.ijdr.2019.101291. URL <https://doi.org/10.1016/j.ijdr.2019.101291>.
- [74] S. Mizrahi. Cascading disasters, information cascades and continuous time models of domino effects. *International Journal of Disaster Risk Reduction*, 49(101672), 2020. ISSN 22124209. doi: 10.1016/j.ijdr.2020.101672. URL <https://doi.org/10.1016/j.ijdr.2020.101672>.
- [75] Z. Gong, Y. Wang, G. Wei, L. Li, and W. Guo. Cascading disasters risk modeling based on linear uncertainty distributions. *International Journal of Disaster Risk Reduction*, 43(101385), 2020. ISSN 22124209. doi: 10.1016/j.ijdr.2019.101385. URL <https://doi.org/10.1016/j.ijdr.2019.101385>.
- [76] G. Pescaroli and D. Alexander. Understanding compound, interconnected, interacting, and cascading risks: A holistic framework. *Risk Analysis*, 38(11):2245–2257, 2018. ISSN 15396924. doi: 10.1111/risa.13128.
- [77] A. Tilloy, B. D. Malamud, H. Winter, and A. Joly-Laugel. A review of quantification methodologies for multi-hazard interrelationships. *Earth-Science Reviews*, 196(June):102881, 2019. ISSN 00128252. doi: 10.1016/j.earscirev.2019.102881. URL <https://doi.org/10.1016/j.earscirev.2019.102881>.
- [78] K. Goda and R. De Risi. Multi-hazard loss estimation for shaking and tsunami using stochastic rupture sources. *International Journal of Disaster Risk Reduction*, 28(February):539–554, 2018. ISSN 22124209. doi: 10.1016/j.ijdr.2018.01.002.
- [79] H. Park, D. T. Cox, M. S. Alam, and A. R. Barbosa. Probabilistic seismic and tsunami hazard analysis conditioned on a megathrust rupture of the Cascadia subduction zone. *Frontiers in Built Environment*, 3(June):1–19, 2017. ISSN 2297-3362. doi: 10.3389/fbuil.2017.00032.
- [80] J. C. Borrero, P. J. Lynett, and N. Kalligeris. Tsunami currents in ports. *Philosophical Transactions Royal Society A*, 373(20140372), sep 2015. ISSN 1364503X. doi: <http://dx.doi.org/10.1098/rsta.2014.0372>.

- [81] R. De Risi, K. Goda, T. Yasuda, and N. Mori. Is flow velocity important in tsunami empirical fragility modeling? *Earth-Science Reviews*, 166:64–82, 2017. ISSN 00128252. doi: 10.1016/j.earscirev.2016.12.015.
- [82] B. Choi, A. Nishida, T. Itoi, and T. Takada. Engineering applications using probabilistic aftershock hazard analyses: Aftershock hazard map and load combination of aftershocks and tsunamis. *Geosciences (Switzerland)*, 8(1), 2018. ISSN 20763263. doi: 10.3390/geosciences8010001.
- [83] J. G. Xu, G. Wu, D. C. Feng, and J. J. Fan. Probabilistic multi-hazard fragility analysis of RC bridges under earthquake-tsunami sequential events. *Engineering Structures*, 238(March):112250, 2021. ISSN 18737323. doi: 10.1016/j.engstruct.2021.112250. URL <https://doi.org/10.1016/j.engstruct.2021.112250>.
- [84] C. T. Chua, A. D. Switzer, A. Suppasri, L. Li, K. Pakoksung, D. Lallemand, S. F. Jenkins, I. Charvet, T. Chua, and A. Cheong. Tsunami damage to ports : Cataloguing damage to create fragility functions from the 2011 Tohoku event. *Natural Hazard and Earth Sciences*, in review(October): 1–37, 2020. doi: 10.5194/nhess-2020-355.
- [85] S. Park, J. W. Van De Lindt, D. T. Cox, R. Gupta, and F. Aguiniga. Successive earthquake-tsunami analysis to develop collapse fragilities. *Journal of Earthquake Engineering*, 16(6):851–863, 2012. ISSN 13632469. doi: 10.1080/13632469.2012.685209.
- [86] H. Park, M. S. Alam, D. T. Cox, A. R. Barbosa, and J. W. van de Lindt. Probabilistic seismic and tsunami damage analysis (PSTDA) of the Cascadia Subduction Zone applied to Seaside, Oregon. *International Journal of Disaster Risk Reduction*, 35(October 2018):101076, 2019. ISSN 22124209. doi: 10.1016/j.ijdrr.2019.101076.
- [87] C. Y. Lam and T. Shimizu. A network analytical framework to analyze infrastructure damage based on earthquake cascades: A study of earthquake cases in Japan. *International Journal of Disaster Risk Reduction*, 54(102025), 2021. ISSN 22124209. doi: 10.1016/j.ijdrr.2020.102025. URL <https://doi.org/10.1016/j.ijdrr.2020.102025>.
- [88] A. Suppasri, E. Maly, M. Kitamura, G. Pescaroli, D. Alexander, and F. Imamura. Cascading disasters triggered by tsunami hazards: A perspective for critical infrastructure resilience and disaster risk reduction. *International Journal of Disaster Risk Reduction*, 66(102597), 2021. ISSN 2212-4209. doi: 10.1016/j.ijdrr.2021.102597. URL <https://doi.org/10.1016/j.ijdrr.2021.102597>.
- [89] P. Rao, S. Reddy, and K. Rao. Response of coastal buildings subjected to seismic and tsunami forces. *International Journal of Engineering Science and Technology*, 2(11):6195–6203, 2010.
- [90] M. Mück, H. Taubenböck, J. Post, S. Wegscheider, G. Strunz, S. Sumaryono, and F. A. Ismail. Assessing building vulnerability to earthquake and tsunami hazard using remotely sensed data. *Natural Hazards*, 68(1):97–114, 2013. ISSN 0921030X. doi: 10.1007/s11069-012-0481-1.

- [91] S. Nayak, M. H. O. Reddy, R. Madhavi, and S. C. Dutta. Assessing tsunami vulnerability of structures designed for seismic loading. *International Journal of Disaster Risk Reduction*, 7 (January):28–38, 2014. ISSN 22124209. doi: 10.1016/j.ijdrr.2013.12.001. URL <http://dx.doi.org/10.1016/j.ijdrr.2013.12.001>.
- [92] C. Petrone, T. Rossetto, and K. Goda. Fragility assessment of a RC structure under tsunami actions via nonlinear static and dynamic analyses. *Engineering Structures*, 136:33–56, 2017. ISSN 18737323. doi: 10.1016/j.engstruct.2017.01.013.
- [93] T. Rossetto, C. Petrone, I. Eames, C. De La Barra, A. Foster, and J. Macabuag. Advances in the assessment of buildings subjected to earthquakes and tsunami. In K. Pitilakis, editor, *Geotechnical, Geological and Earthquake Engineering*, volume 46, chapter 23, pages 545–562. Springer International Publishing AG, part of Springer Nature 2018., 2018. ISBN 9783319757414. doi: 10.1007/978-3-319-75741-4_23.
- [94] T. J. Carey, H. B. Mason, A. R. Barbosa, and M. H. Scott. Modeling framework for soil-bridge system response during sequential earthquake and tsunami loading. *NCEE 2014 - 10th U.S. National Conference on Earthquake Engineering: Frontiers of Earthquake Engineering*, pages 1 – 10, 2014. doi: 10.4231/D3J96098C.
- [95] K.-H. Kim, B. Andrawes, and C. A. Duarte. Behavior of FRP retrofitted bridge timber piles under earthquake and tsunami loading. In *Structures Congress 2017: Bridges and Transportation Structures - Selected Papers from the Structures Congress 2017*, pages 340–352, Denver, United States, apr 2017. ISBN 9780784480403. doi: 10.1061/9780784480403.029.
- [96] H. Ishibashi, M. Akiyama, D. M. Frangopol, S. Koshimura, T. Kojima, and K. Nanami. Framework for estimating the risk and resilience of road networks with bridges and embankments under both seismic and tsunami hazards. *Structure and Infrastructure Engineering*, 0(0):1–21, 2020. ISSN 17448980. doi: 10.1080/15732479.2020.1843503. URL <https://doi.org/10.1080/15732479.2020.1843503>.
- [97] G.-C. Kang, D.-S. Kim, and T.-H. Kim. Quay wall stability considering earthquake and tsunami overtopping forces together in the active condition. *Natural Hazards Review*, 15(4), 2014. ISSN 1527-6988. doi: 10.1061/(ASCE)NH.1527-6996.0000151.
- [98] K.-H. Lee, D.-S. Kim, and T.-H. Kim. Extreme case study of quay wall stability under earthquake and tsunami. *Marine Georesources and Geotechnology*, 33(6):504–520, 2015. ISSN 1064-119X. doi: 10.1080/1064119X.2014.954177.
- [99] S. V. Karafagka, S. D. Fotopoulou, and K. D. Pitilakis. Tsunami fragility curves for seaport structures. In *1st International Conference on Natural Hazards and Infrastructure*, pages 28–30, 2016.

- [100] D. Choudhury and S. S. Nimbalkar. Pseudo-dynamic approach of seismic active earth pressure behind retaining wall. *Geotechnical and Geological Engineering*, 24(5):1103–1113, 2006. ISSN 09603182. doi: 10.1007/s10706-005-1134-x.
- [101] D. Choudhury and S. M. Ahmad. Design of waterfront retaining wall for the passive case under earthquake and tsunami. *Applied Ocean Research*, 29(1-2):37–44, sep 2007. ISSN 01411187. doi: 10.1016/j.apor.2007.08.001.
- [102] S. M. Ahmad and D. Choudhury. Stability of waterfront retaining wall subjected to pseudo-dynamic earthquake forces and tsunami. *Journal of Earthquake and Tsunami*, 2(2):107–131, 2008. ISSN 00298018. doi: 10.1016/j.oceaneng.2007.03.005.
- [103] D. Chakraborty and D. Choudhury. Stability of non-vertical waterfront retaining wall supporting inclined backfill under earthquake and tsunami. *Ocean Engineering*, 78:1–10, 2014. doi: 10.1016/j.oceaneng.2013.11.024.
- [104] B. Chaudhary, H. Hazarika, I. Ishibashi, and A. Abdullah. Sliding and overturning stability of breakwater under combined effect of earthquake and tsunami. *Ocean Engineering*, 136:106–116, 2017. ISSN 00298018. doi: 10.1016/j.oceaneng.2017.03.021.
- [105] B. G. Rajesh and D. Choudhury. Seismic stability of seawalls under earthquake and tsunami forces using a modified pseudodynamic method. *Natural Hazards Review*, 19(3):1–12, 2018. doi: 10.1061/(ASCE)NH.1527-6996.0000289.
- [106] W. Qi, G. Su, L. Sun, F. Yang, and Y. Wu. “Internet+” approach to mapping exposure and seismic vulnerability of buildings in a context of rapid socioeconomic growth: a case study in Tangshan, China. *Natural Hazards*, 86(s1):107–139, 2017. ISSN 15730840. doi: 10.1007/s11069-016-2581-9.
- [107] G. Pavić, M. Hadzima-Nyarko, B. Bulajić, and Ž. Jurković. Development of seismic vulnerability and exposure models-A case study of Croatia. *Sustainability (Switzerland)*, 12(3), 2020. ISSN 20711050. doi: 10.3390/su12030973.
- [108] F. Rivera, T. Rossetto, and J. Twigg. An interdisciplinary study of the seismic exposure dynamics of Santiago de Chile. *International Journal of Disaster Risk Reduction*, 48(February):101581, 2020. ISSN 22124209. doi: 10.1016/j.ijdr.2020.101581.
- [109] N. J. Wood and J. W. Good. Vulnerability of port and harbor communities to earthquake and tsunami hazards: The use of GIS in community hazard planning. *Coastal Management*, 32(3): 243–269, 2004. ISSN 08920753. doi: 10.1080/08920750490448622.
- [110] M. Rokhis Khomarudin, G. Strunz, R. Ludwig, K. Zoßeder, J. Post, W. Kongko, and W. S. Pranowo. Hazard analysis and estimation of people exposure as contribution to tsunami risk assessment in the west coast of sumatra, the south coast of Java and bali. *Zeitschrift fur Geomorphologie*, 54 (May 2014):337–356, 2010. ISSN 03728854. doi: 10.1127/0372-8854/2010/0054S3-0031.

- [111] S. Park, J. W. Van De Lindt, D. T. Cox, and R. Gupta. Concept of community fragilities for tsunami coastal inundation studies. *Natural Hazard Review*, 14(4):220–228, 2013. doi: doi10.1061/(ASCE)NH.1527-6996.0000092.
- [112] F. Lovholt, N. J. Setiadi, J. Birkmann, C. B. Harbitz, C. Bach, N. Fernando, G. Kaiser, and F. Nadim. Tsunami risk reduction - are we better prepared today than in 2004?, 2014. ISSN 22124209.
- [113] J. L. Canales, M. V. Rio, and A. Gubler. Increasing tsunami risk through intensive urban densification in metropolitan areas: A longitudinal analysis in Viña del Mar, Chile. *International Journal of Disaster Risk Reduction*, 41:101312, 2019. ISSN 22124209. doi: 10.1016/j.ijdr.2019.101312.
- [114] D. Mardiatno, M. N. Malawani, and R. M. rifatun Nisaa'. The future tsunami risk potential as a consequence of building development in Pangandaran Region, West Java, Indonesia. *International Journal of Disaster Risk Reduction*, 46(January):101523, 2020. ISSN 22124209. doi: 10.1016/j.ijdr.2020.101523.
- [115] K. Poljanšek, T. De Groeve, M. M. Ferrer, and I. Clark. *Science for disaster risk management 2017: Knowing better and losig less*. Publications Office of te European Union, Luxembourg, 2017. ISBN 9789279606786. doi: 10.2788/688605.
- [116] J. P. Pinelli, M. Esteva, E. M. Rathje, D. Roueche, S. J. Brandenberg, G. Mosqueda, J. Padgett, and F. Haan. Disaster risk management through the DesignSafe cyberinfrastructure. *International Journal of Disaster Risk Science*, 11(6):719–734, 2020. ISSN 21926395. doi: 10.1007/s13753-020-00320-8. URL <https://doi.org/10.1007/s13753-020-00320-8>.
- [117] M. S. Alam, A. R. Barbosa, M. H. Scott, D. T. Cox, and J. W. Van De Lindt. Multi-hazard earthquake-tsunami structural fragility assessment framework. In *13th International Conference on Applications of Statistics and Probability in Civil Engineering, ICASP 2019*, pages 1–8, Seoul, South Korea, 2019.
- [118] N. Attary, J. W. Van De Lindt, A. R. Barbosa, D. T. Cox, and V. U. Unnikrishnan. Performance-based tsunami engineering for risk assessment of structures subjected to multi-hazards: tsunami following earthquake. *Journal of Earthquake Engineering*, 0(00):1–20, 2019. ISSN 13632469. doi: 10.1080/13632469.2019.1616335.
- [119] R. J. Murnane, G. Allegri, A. Bushi, J. Dabbeek, H. de Moel, M. Duncan, S. Fraser, C. Galasso, C. Giovando, P. Henshaw, K. Horsburgh, C. Huyck, S. Jenkins, C. Johnson, G. Kamihanda, J. Kijazi, W. Kikwasi, W. Kombe, S. Loughlin, F. Lovholt, A. Masanja, G. Mbongoni, S. Minas, M. Msabi, M. Msechu, H. Mtongori, F. Nadim, M. O'Hara, M. Pagani, E. Phillips, T. Rossetto, R. Rudari, P. Sangana, V. Silva, J. Twigg, G. UHINGA, and E. Verrucci. Data schemas for multiple hazards, exposure and vulnerability. *Disaster Prevention and Management: An International Journal*, 28(6):752–763, 2019. ISSN 09653562. doi: 10.1108/DPM-09-2019-0293.

- [120] F. Imamura, S. P. Boret, A. Suppasri, and A. Muhari. Recent occurrences of serious tsunami damage and the future challenges of tsunami disaster risk reduction. *Progress in Disaster Science*, 1(June):100009, 2019. ISSN 25900617. doi: 10.1016/j.pdisas.2019.100009.
- [121] N. Blagojević and B. Stojadinović. A demand-supply framework for evaluating the effect of resource and service constraints on community disaster resilience. *Resilient Cities and Structures*, 1(1):13–32, 2022. ISSN 27727416. doi: 10.1016/j.rcns.2022.03.001.
- [122] J. G. S. Castillo, M. Bruneau, and N. Elhami-Khorasani. Seismic resilience of building inventory towards resilient cities. *Resilient Cities and Structures*, 1(1):1–12, 2022. ISSN 27727416. doi: 10.1016/j.rcns.2022.03.002.
- [123] P. Sooriyaarachchi, A. L. Sandika, and N. Madawanarachchi. Coastal community resilience level of tsunami prone area: A case study in Sri Lanka. *Procedia Engineering*, 212:683–690, 2018. ISSN 18777058. doi: 10.1016/j.proeng.2018.01.088. URL <https://doi.org/10.1016/j.proeng.2018.01.088>.
- [124] M. G. H. Lunecke and P. Villagra. Community resilience and urban planning in tsunami-prone settlements in Chile. *Disasters*, 44(1):103–124, 2020. ISSN 14677717. doi: 10.1111/disa.12369.
- [125] E. E. Doyle, E. Lambie, C. Orchiston, J. S. Becker, L. McLaren, D. Johnston, and G. Leonard. Citizen science as a catalyst for community resilience building: A two-phase tsunami case study. *Australasian Journal of Disaster and Trauma Studies*, 24(1):23–49, 2020. ISSN 11744707.
- [126] R. S. Oktari, Syamsidik, R. Idroes, H. Sofyan, and K. Munadi. City resilience towards coastal hazards: An integrated bottom-up and top-down assessment. *Water (Switzerland)*, 12(10), 2020. ISSN 20734441. doi: 10.3390/w12102823.
- [127] C. Reis, M. A. Baptista, M. Lopes, C. S. Oliveira, S. Clain, C. Sousa Oliveira, S. Clain, C. S. Oliveira, and S. Clain. Cascade earthquake and tsunami hazard assessment : A deterministic perspective for engineering purposes. *International Journal of Disaster Risk Reduction*, submitted (102952), 2022. doi: 10.1016/j.ijdr.2022.102952.
- [128] J. M. M. Solares and A. L. Arroyo. The great historical 1755 earthquake. Effects and damage in Spain. *Journal of Seismology*, 8(2):275–294, 2004. ISSN 13834649. doi: 10.1023/B:JOSE.0000021365.94606.03.
- [129] M. A. Baptista and J. M. Miranda. Revision of the Portuguese catalog of tsunamis. *Natural Hazards Earth Systems*, 9(1):25–42, jan 2009.
- [130] M. A. Baptista, J. M. Miranda, R. Omira, and C. Antunes. Potential inundation of Lisbon downtown by a 1755-like tsunami. *Natural Hazards and Earth System Science*, 11(12):3319–3326, 2011. ISSN 15618633. doi: 10.5194/nhess-11-3319-2011.
- [131] S. Allgeyer, C. Daubord, H. Hébert, A. Loevenbruck, F. Schindelé, and R. Madariaga. Could a 1755-Like Tsunami Reach the French Atlantic Coastline? Constraints from Twentieth Century

- Observations and Numerical Modeling. *Pure and Applied Geophysics*, 170(9-10):1415–1431, 2013. ISSN 00334553. doi: 10.1007/s00024-012-0513-5.
- [132] R. R. Dynes. The Lisbon earthquake in 1755: the first modern disaster. Technical report, Department of Sociology and Criminal Justice, University of Delaware, 2003.
- [133] Á. S. Pereira. The opportunity of a disaster: The economic impact of the 1755 Lisbon earthquake. *Journal of Economic History*, 69(2):466–499, 2009. ISSN 00220507. doi: 10.1017/S0022050709000850.
- [134] H. Shiping. Earthquake resistant properties of chinese traditional architecture. *Earthquake Spectra*, 7(3):355–389, 1991.
- [135] K. Fujita, K. Chiba, N. Kawai, M. Koshihara, C. Minowa, and T. Hanazato. Earthquake response analysis of traditional Japanese timber pagoda. *10th World Conference on Timber Engineering 2008*, 3:1329–1336, 2008.
- [136] M. Paz. *International handbook of earthquake engineering: codes, programs and examples*. Springer Science and Business Media, Louisville, Kentucky, US, 1st editio edition, 1994. ISBN 978-1-4613-5859-6. doi: 10.1007/978-1-4615-2069-6.
- [137] J. E. Daniell. Global view of seismic code and building practice factors. In Michael Beer, I. A. Kougoumtzoglou, E. Patelli, and I. S.-K. Au, editors, *Encyclopedia of Earthquake Engineering*, pages 1–12. Springer-Verlag Berlin Heidelberg, Berlin Heidelberg, 1st editio edition, 2015. ISBN 9783642361975. doi: 10.1007/978-3-642-36197-5.
- [138] M. Lopes, H. Meireles, S. Cattari, R. Bento, and S. Lagomarsino. Pombalino constructions: Description and seismic assessment. In A. G. Costa, J. Guedes, and H. Varum, editors, *Building Pathology and Rehabilitation, Vol 2*, pages 187–233. Springer-Verlag Berlin Heidelberg, Berlin, Heidelberg, 2014. ISBN 978-3-642-39686-1. doi: 10.1007/978-3-642-39686-1_7.
- [139] N. T. H. M. P. NTHMP. Designing for tsunamis: seven principles for planning and designing for tsunami hazards. Technical report, NOAA, USGS, FEMA, NSF., US, 2001.
- [140] S. Stein and E. A. Okal. The 2004 Sumatra earthquake and Indian Ocean tsunami: What happened and why? *Visual Geosciences*, 10(1):21–26, 2005. ISSN 16102924. doi: 10.1007/s10069-005-0025-x.
- [141] A. Ghobarah, M. Saatcioglu, and I. Nistor. The impact of the 26 december 2004 earthquake and tsunami on structures and infrastructure. *Engineering Structures*, 28(2):312–326, 2006. ISSN 01410296. doi: 10.1016/j.engstruct.2005.09.028.
- [142] C. E. Synolakis and L. Kong. Runup measurements of the December 2004 Indian Ocean tsunami. *Earthquake Spectra*, 22(S3):67–91, jun 2006.

- [143] C. E. Synolakis and E. N. Bernard. Tsunami science before and beyond Boxing Day 2004. *Philosophical Transactions of the Royal Society A: Mathematical, Physical and Engineering Sciences*, 364(1845):2231–2265, aug 2006. ISSN 1364-503X. doi: 10.1098/rsta.2006.1824.
- [144] R. Basili, B. Brizuela, A. Herrero, S. Iqbal, S. Lorito, F. E. Maesano, S. Murphy, P. Perfetti, F. Romano, A. Scala, J. Selva, M. Taroni, M. M. Tiberti, H. K. Thio, R. Tonini, M. Volpe, S. Glimsdal, C. B. Harbitz, F. Løvholt, M. A. Baptista, F. Carrilho, L. M. Matias, R. Omira, A. Babeyko, A. HOechner, M. Gurbuz, O. Pekcan, A. C. Yalciner, M. Canals, G. Lastras, A. Agalos, G. Papadopoulos, I. Triantafyllou, S. Bencheekroun, H. A. Jaouadi, S. B. Abdallah, A. Bouallegue, H. Hamdi, F. Oueslati, A. Amato, A. Armigliato, J. Behrens, G. Davies, D. D. Bucci, M. Dolce, E. Geist, J. M. G. Vida, M. Gonzalez, J. M. Sánchez, C. Meletti, C. O. Sozdinler, M. Pagani, T. Parsons, J. Polet, W. Power, M. B. Sørensen, and A. Zaytsev. The making of the NEAM tsunami hazard model 2018 (NEAMTHM18). *Frontiers in Earth Science: Geohazards and Georisks*, 8: 1–29, 2021. doi: 10.3389/feart.2020.616594.
- [145] H. B. Kaushik and S. K. Jain. Impact of Great December 26, 2004 Sumatra earthquake and tsunami on structures in Port Blair. *Journal of Performance of Constructed Facilities*, 21(2):128–142, 2007. ISSN 0887-3828. doi: 10.1061/(ASCE)0887-3828(2007)21:2(128).
- [146] F. Leone, F. Lavigne, R. Paris, J. C. Denain, and F. Vinet. A spatial analysis of the december 26th, 2004 tsunami-induced damages: Lessons learned for a better risk assessment integrating buildings vulnerability. *Applied Geography*, 31(1):363–375, jan 2011. ISSN 01436228. doi: 10.1016/j.apgeog.2010.07.009.
- [147] Japanese Cabinet Office. Guideline for structural design of tsunami evacuation buildings (in Japanese). Technical report, JCO,2005, Tokyo, Japan, 2005. URL <http://www.bousai.go.jp/oshirase/h17/050610/guideline.pdf>.
- [148] Federal Emergency Management Agency. Design of structures for vertical evacuation from tsunamis. First edition. Technical report, Federal Emergency Management Agency; National Oceanic and Atmospheric Administration, 2008.
- [149] Federal Emergency Management Agency. Vertical evacuation from tsunamis: A guide for community officials. Technical Report P-646A, Federal Emergency Mngement Administration, 2009.
- [150] U. A. f. I. D. USAID. Global climate change in the Asia-Pacific Region: An analysis and road map for USAID regional development mission for Asia. Technical Report July, Summary for Policymakers. Climate Change 2007: The Physical Science Basis. Contribution of Working Group I to the Fourth Assessment Report of the Intergovernmental Panel on Climate Change, 2008.
- [151] N. Mori, T. Takahashi, T. Yasuda, and H. Yanagisawa. Survey of 2011 Tohoku earthquake tsunami inundation and run-up. *Geophysical Research Letters*, 38(18), 2011. ISSN 00948276. doi: 10.1029/2011GL049210.

- [152] H. M. Fritz, D. A. Phillips, A. Okayasu, S. Takenori, H. Liu, F. Mohammed, V. Skanavis, C. E. Synolakis, and T. Takahashi. The 2011 Japan tsunami current velocity measurements from survivor videos at Kesenuma Bay using LiDAR. *Geophysical Research Letters*, 39(7), 2012. doi: 10.1029/2011GL050686.
- [153] A. Raby, J. Macabuag, A. Pomonis, S. Wilkinson, and T. Rossetto. Implications of the 2011 Great East Japan Tsunami on sea defence design. *International Journal of Disaster Risk Reduction*, 14: 332–346, 2015. ISSN 22124209. doi: 10.1016/j.ijdr.2015.08.009.
- [154] J. Tsuru and S. Murakami. Summary of the field survey and research on the 2011 off the Pacific coast of Tohoku earthquake. Technical report, National Institute for Land and Infrastructure Management, NILIM, Japan, 2011.
- [155] A. Suppasri, I. Charvet, J. Macabuag, T. Rossetto, N. Leelawat, P. Latcharote, and F. Imamura. Building damage assessment and implications for future tsunami fragility estimations. In *Handbook of Coastal Disaster Mitigation for Engineers and Planners*, chapter 9, pages 147–178. Elsevier Inc., 2015. ISBN 9780128012703. doi: 10.1016/B978-0-12-801060-0.00009-5.
- [156] Overseas Coastal Area Development Institute of Japan. Technical standards and commentaries for port and harbour facilities in Japan. Technical report, The Overseas Coastal Area Development Institute of Japan, OCDI, Tokyo, Japan, 2002.
- [157] F. E. M. A. FEMA. Guidelines for design of structures for vertical evacuation from tsunamis. Second edition. Technical Report P646, Federal Emergency Management Agency, 2012.
- [158] P. J. Lynett, H. K. Thio, M. H. Scott, T. Murphy, T. Shantz, and J.-D. Shen. Validation of tsunami design guidelines for coastal bridges - Final report of project TPF5/307. Technical report, Oregon Department of Transportation, Washington DC, 2021.
- [159] D. Istrati and I. G. Buckle. Tsunami loads on straight and skewed bridges. Part 1: Experimental investigation and design recommendations. Technical report, Oregon Department of Transportation, Oregon, EUA, 2021.
- [160] D. Istrati and I. G. Buckle. Tsunami loads on straight and skewed bridges – Part 2 : Numerical investigation and design recommendations. Technical Report March, Oregon Department of Transportation, Oregon, EUA, 2021.
- [161] Unified Facilities Criteria. UFC 4-152-01, Design: piers and wharves. Technical report, US Department of Defense, 2017.
- [162] N. National Tsunami Hazard Mitigation Program. Guidelines and best practices for tsunami hazard analysis , planning , and preparedness for maritime communities. Technical report, United States National Tsunami Hazard Mitigation Program, Washington, 2015.
- [163] J. Macabuag, A. Raby, A. Pomonis, I. Nistor, S. Wilkinson, and T. Rossetto. Tsunami design procedures for engineered buildings: A critical review. *Proceedings of the Institution of Civil*

Engineers: Civil Engineering, 171(4):166–178, 2018. ISSN 17517672. doi: 10.1680/jcien.17.00043.

- [164] A. Babeyko, S. Lorito, F. Hernandez, J. Lauterjung, F. Løvholt, A. Rudloff, M. B. Sørensen, A. Androsov, Í. Aniel-Quiroga, A. Armigliato, M. A. Baptista, E. Baglione, R. Basili, J. Behrens, B. Brizuela, S. Bruni, M. D. Cambaz, J. Cantavella-Nadal, F. Carrilho, I. Chandler, D. Chang-Seng, M. Charalampakis, L. Cugliari, C. Denamiel, G. G. Dogan, G. Festa, D. R. Fuhrman, A.-A. Gabriel, P. Galea, S. J. Gibbons, M. Gonzalez, L. Graziani, M.-A. Gutscher, S. Harig, H. Hebert, C. Ionescu, F. Jalayer, N. Kalligeris, U. Kânoğlu, P. Lanucara, J. M. Sánchez, S. Murphy, Ö. Necmioğlu, R. Omira, G. A. Papadopoulos, R. Paris, F. Romano, T. Rossetto, J. Selva, A. Scala, R. Tonini, K. Trelopoulos, I. Triantafyllou, R. Urgeles, R. Vallone, I. Vilibić, M. Volpe, and Ahmet C. Yalciner. Towards the new thematic core service tsunami within the EPOS research infrastructure. *Annals of Geophysics*, 65(2), 2022. doi: 10.4401/ag-8762. URL <https://drive.google.com/file/d/1NxWLC3S7etv1CqqFPAazJJZwjEIzGemR/view>.
- [165] M. Klyachko, I. Nudner, V. Maximov, and V. Filkov. On standard “Building, structures and areas. Safety requirements under tsunami impact”. In *10th U.S. National Conference on Earthquake Engineering*, pages 1 – 11, Alaska, United States, 2014. doi: 10.4231/D3TB0XW0V.
- [166] S. Shafiei, B. W. Melville, and A. Y. Shamseldin. Experimental investigation of tsunami bore impact force and pressure on a square prism. *Coastal Engineering*, 110:1–16, 2016. ISSN 03783839. doi: 10.1016/j.coastaleng.2015.12.006.
- [167] C. Chen, B. W. Melville, N. A. K. Nandasena, A. Y. Shamseldin, and L. W. Wotherspoon. Experimental study of uplift loads due to tsunami bore impact on a wharf model. *Coastal Engineering*, 117:126–137, nov 2016. ISSN 03783839. doi: 10.1016/j.coastaleng.2016.08.001.
- [168] M. S. Alam, A. O. Winter, G. Galant, K. Shekhar, A. R. Barbosa, M. R. Motley, M. O. Eberhard, D. T. Cox, P. Arduino, and P. Lomonaco. Tsunami-like wave-induced lateral and uplift pressures and forces on an elevated coastal structure. *Journal of Waterway, Port, Coastal and Ocean Engineering*, 146(4):1–18, 2020. doi: 10.1061/(ASCE)WW.1943-5460.0000562.
- [169] Y. Nouri, I. Nistor, D. Palermo, and A. Cornett. Experimental investigation of tsunami impact on free standing structures. *Coastal Engineering Journal*, 52(1):43–70, 2010. ISSN 2166-4250. doi: 10.1142/S0578563410002117.
- [170] R. B. Haehnel and S. F. Daly. Maximum impact force of woody debris on floodplain structures. *Journal of Hydraulic Engineering*, 130(2):112–120, 2004. ISSN 0733-9429. doi: 10.1061/(asce)0733-9429(2004)130:2(112).
- [171] M. Ikeno, D. Takabatake, N. Kihara, H. Kaida, Y. Miyagawa, and A. Shibayama. Improvement of collision force formula for woody debris by airborne and hydraulic experiments. *Coastal Engineering Journal*, 58(4), 2016. ISSN 17936292. doi: 10.1142/S0578563416400222.

- [172] S. Marras and K. T. Mandli. Modeling and simulation of tsunami impact: A short review of recent advances and future challenges. *Geosciences (Switzerland)*, 11(1):1–19, 2021. ISSN 20763263. doi: 10.3390/geosciences11010005.
- [173] P. Xie and V. H. Chu. The impact of tsunami wave force on elevated coastal structures. *Coastal Engineering*, 162(May):103777, 2020. ISSN 03783839. doi: 10.1016/j.coastaleng.2020.103777. URL <https://doi.org/10.1016/j.coastaleng.2020.103777>.
- [174] M. Percher, W. Bruin, S. E. Dickenson, M. Eskijian, Y. Oritatsu, and W. Rudolph. Performance of port and harbor structures impacted by the march 11, 2011 Great Tohoku earthquake and tsunami. *Ports 2013*, pages 610–619, 2013. doi: 10.1061/9780784413067.063. URL <http://ascelibrary.org/doi/abs/10.1061/9780784413067.063>.
- [175] M. R. Motley, M. O. Eberhard, P. Arduino, and A. R. Barbosa. Probabilistic assessment of tsunami forces on coastal structures. Technical report, DesignSafe, 2019.
- [176] S. Tonkin, H. Yeh, F. Kato, and S. Sato. Tsunami scour around a cylinder. *Journal of Fluid Mechanics*, 496:165–192, 2003. ISSN 00221120. doi: 10.1017/S0022112003006402.
- [177] H. Takahashi, S. Sassa, Y. Morikawa, D. Takano, and K. Maruyama. Stability of caisson-type breakwater foundation under tsunami-induced seepage. *Soils and Foundations*, 54(4):789–805, 2014. ISSN 00380806. doi: 10.1016/j.sandf.2014.07.002. URL <http://dx.doi.org/10.1016/j.sandf.2014.07.002>.
- [178] D. Wang, S. Li, T. Arikawa, and H. Gen. ISPH simulation of scour behind seawall due to continuous tsunami overflow. *Coastal Engineering Journal*, 58(3):104–115, 2016. ISSN 17936292. doi: 10.1142/S0578563416500145.
- [179] N. Takegawa, Y. Sawada, K. Murai, and T. Kawabata. Influence of liquefaction on scour behind coastal dikes due to tsunami overflow. *International Journal of Geotechnical Engineering*, 12(1): 40–45, 2018. ISSN 19387879. doi: 10.1080/19386362.2016.1246216. URL <http://dx.doi.org/10.1080/19386362.2016.1246216>.
- [180] A. Yeganeh-bakhtiary, H. Houshang, and S. Abolfathi. Lagrangian two-phase flow modeling of scour in front of vertical breakwater. *Coastal Engineering Journal*, 00(00):1–15, 2020. ISSN 2166-4250. doi: 10.1080/21664250.2020.1747140. URL <https://doi.org/10.1080/21664250.2020.1747140>.
- [181] H. Li, S. Wang, X. Chen, C. Hu, and J. Liu. Numerical study of scour depth effect on wave-induced seabed response and liquefaction around a pipeline. *Marine Georesources and Geotechnology*, 39(2):188–199, 2021. ISSN 15210618. doi: 10.1080/1064119X.2019.1689588. URL <https://doi.org/10.1080/1064119X.2019.1689588>.
- [182] N. Johnson, R. T. Ranf, M. S. Saiidi, D. Sanders, and M. Eberhard. Seismic testing of a two-span reinforced concrete bridge. *Journal of Bridge Engineering*, 13(2):173–182, 2008. ISSN 1084-0702. doi: 10.1061/(asce)1084-0702(2008)13:2(173).

- [183] A. F. Naser, H. A. Mohammed, and A. A. Mohammed. Seismic design assessment of bridge piers location effect on the structural capacity of supports under earthquake action. *International Journal of Safety and Security Engineering*, 11(2):143–153, 2021. ISSN 2041904X. doi: 10.18280/ijssse.110203.
- [184] E. A. Flores-Johnson, B. A. Company-Rodríguez, J. F. Koh-Dzul, and J. G. Carrillo. Shaking table test of U-shaped walls made of fiber-reinforced foamed concrete. *Materials*, 13(11):1–17, 2020. ISSN 19961944. doi: 10.3390/ma13112534.
- [185] D. Skokandić, A. D. Vlašić, M. K. Marić, M. Srbić, and A. M. Ivanković. Seismic assessment and retrofitting of existing Road bridges: State of the art review. *Materials*, 15(7), 2022. ISSN 19961944. doi: 10.3390/ma15072523.
- [186] N. Bianchini, N. Mendes, C. Calderini, P. X. Candeias, M. Rossi, and P. B. Lourenço. Seismic response of a small-scale masonry groin vault: experimental investigation by performing quasi-static and shake table tests. *Bulletin of Earthquake Engineering*, 20(3):1739–1765, 2022. ISSN 15731456. doi: 10.1007/s10518-021-01280-0. URL <https://doi.org/10.1007/s10518-021-01280-0>.
- [187] M. J. Briggs, C. E. Synolakis, G. S. Harkins, and D. R. Green. Laboratory experiments of tsunami runup on a circular island. *Pure and Applied Geophysics*, 144(3-4):569–593, 1995. ISSN 00334553. doi: 10.1007/BF00874384.
- [188] H. Yeh, P. L. F. Liu, and C. E. Synolakis. Long-wave runup models: Friday Harbor, USA, 12-17 September 1995. *World Scientific*, 1996.
- [189] M. Shito, I. Inuzuka, I. Amaya, H. Saito, and J. Kurata. Numerical simulations and experiments on tsunami for the design of coastal and offshore structures. *IHI Engineering Review*, pages 0–4, 2011.
- [190] D. Istrati, I. G. Buckle, A. Itani, P. Lomonaco, and S. C. Yim. Large-Scale Fsi Experiments on Tsunami-Induced Forces in Bridges. In *16th World Conference on Earthquake, 16WCEE*, page Paper N° 2579, Santiago, Chile, jan 2017.
- [191] C. Jiang, X. Liu, Y. Yao, B. Deng, and J. Chen. Numerical investigation of tsunami-like solitary wave interaction with a seawall. *Journal of Earthquake and Tsunami*, 2016. doi: 10.1142/S1793431117400061.
- [192] A. Silva and S. Araki. Investigating the behavior of an onshore wall and trench combination ahead of a tsunami-like wave. *Geosciences (Switzerland)*, 10(8):1–22, 2020. ISSN 20763263. doi: 10.3390/geosciences10080310.
- [193] J. W. van de Lindt, R. Gupta, R. A. Garcia, and J. Wilson. Tsunami bore forces on a compliant residential building model. *Engineering Structures*, 31(11):2534–2539, 2009. ISSN 01410296. doi: 10.1016/j.engstruct.2009.05.017.

- [194] R. Triatmadja and A. Nurhasanah. Tsunami force on buildings with openings and protection. *Journal of Earthquake and Tsunami*, 6(4):1–17, 2012. ISSN 17934311. doi: 10.1142/S1793431112500248.
- [195] T. Honda, Y. Oda, K. Ito, M. Watanabe, and T. Takabatake. An experimental study on the tsunami pressure acting on piloti-type buildings. *Proceedings of the Coastal Engineering Conference*, 2014-Janua(February 2016), 2014. ISSN 01613782. doi: 10.9753/icce.v34.structures.41.
- [196] H. Park, D. T. Cox, and A. R. Barbosa. Comparison of inundation depth and momentum flux based fragilities for probabilistic tsunami damage assessment and uncertainty analysis. *Coastal Engineering*, 122:10–26, 2017. ISSN 03783839. doi: 10.1016/j.coastaleng.2017.01.008.
- [197] I. M. Qeshta, M. J. Hashemi, R. Gravina, and S. Setunge. Review of resilience assessment of coastal bridges to extreme wave-induced loads. *Engineering Structures*, 185(June 2018):332–352, 2019. ISSN 18737323. doi: 10.1016/j.engstruct.2019.01.101. URL <https://doi.org/10.1016/j.engstruct.2019.01.101>.
- [198] T. Xiang, D. Istrati, S. C. Yim, I. G. Buckle, and P. Lomonaco. Tsunami loads on a representative coastal bridge deck: Experimental study and validation of design equations. *Journal of Waterway, Port, Coastal, and Ocean Engineering*, 146(5):04020022, 2020. ISSN 0733-950X. doi: 10.1061/(asce)ww.1943-5460.0000560.
- [199] S. Rahman, S. Akib, M. T. R. Khan, and S. M. Shirazi. Experimental study on tsunami risk reduction on coastal building fronted by sea wall. *The Scientific World Journal*, 2014(March), 2014. ISSN 1537744X. doi: 10.1155/2014/729357.
- [200] S. C. Hsiao and T. C. Lin. Tsunami-like solitary waves impinging and overtopping an impermeable seawall: Experiment and RANS modeling. *Coastal Engineering*, 57(1):1–18, 2010. ISSN 03783839. doi: 10.1016/j.coastaleng.2009.08.004. URL <http://dx.doi.org/10.1016/j.coastaleng.2009.08.004>.
- [201] A. Foster, T. Rossetto, and W. Allsop. An experimentally validated approach for evaluating tsunami inundation forces on rectangular buildings. *Coastal Engineering*, 128(November 2016):44–57, 2017. ISSN 03783839. doi: 10.1016/j.coastaleng.2017.07.006.
- [202] K. Yoshida, S. Maeno, T. liboshi, and D. Araki. Estimation of hydrodynamic forces acting on concrete blocks of toe protection works for coastal dikes by tsunami overflows. *Applied Ocean Research*, 80(September):181–196, 2018. ISSN 01411187. doi: 10.1016/j.apor.2018.09.001. URL <https://doi.org/10.1016/j.apor.2018.09.001>.
- [203] S. Dan, C. Altomare, T. Suzuki, T. Spiesschaert, and T. Verwaest. Reduction of wave overtopping and force impact at harbor quays due to very oblique waves. *Journal of Marine Science and Engineering*, 8(598):1–26, 2020. ISSN 20771312. doi: 10.3390/jmse8080598.

- [204] N. Kihara, T. Arikawa, T. Asai, M. Hasebe, T. Ikeya, S. Inoue, H. Kaida, H. Matsutomi, Y. Nakano, Y. Okuda, S. Okuno, T. Ooie, Y. Shigihara, G. Shoji, T. Tateno, C. Tsurudome, and M. Watanabe. A physical model of tsunami inundation and wave pressures for an idealized coastal industrial site. *Coastal Engineering*, 169(December 2020):103970, 2021. ISSN 03783839. doi: 10.1016/j.coastaleng.2021.103970. URL <https://doi.org/10.1016/j.coastaleng.2021.103970>.
- [205] B. Ghodoosipour, J. Stolle, I. Nistor, A. Mohammadian, and N. Goseberg. Experimental study on extreme hydrodynamic loading on pipelines. Part 1: Flow hydrodynamics. *Journal of Marine Science and Engineering*, 7(8):1–20, 2019. ISSN 20771312. doi: 10.3390/jmse7080251.
- [206] B. Ghodoosipour, J. Stolle, I. Nistor, A. Mohammadian, and N. Goseberg. Experimental study on extreme hydrodynamic loading on pipelines part 2: Induced force analysis. *Journal of Marine Science and Engineering*, 7(8), 2019. ISSN 20771312. doi: 10.3390/jmse7080262.
- [207] A. Como and H. Mahmoud. Numerical evaluation of tsunami debris impact loading on wooden structural walls. *Engineering Structures*, 56:1249–1261, 2013. ISSN 01410296. doi: 10.1016/j.engstruct.2013.06.023.
- [208] A. Cornett. Extreme wave pressures and loads on a pile-supported wharf deck - Influences of air gap and wave direction. *Coastal Engineering Proceedings*, 36(5), 2018. ISSN 0589-087X. doi: 10.9753/icce.v36.waves.5.
- [209] D. Istrati and I. Buckle. Role of trapped air on the tsunami-induced transient loads and response of coastal bridges. *Geosciences (Switzerland)*, 9(4), 2019. ISSN 20763263. doi: 10.3390/geosciences9040191.
- [210] J. Žižmond and M. Dolšek. Risk-targeted force-based design and performance check by means of nonlinear analysis. In *10th Pacific Conference on Earthquake Engineering*, pages 1–8, Sydney, Australia, 2015. doi: 10.1177/0269216310366390.
- [211] N. Luco, B. R. Ellingwood, R. O. Hamburger, J. D. Hooper, J. Kimball, and C. A. Kircher. Risk-targeted versus current seismic design maps for the conterminous United States. In *Structural Engineers Association of California*, pages 1–13, Squaw Creek, California, United States, 2007.
- [212] S. K. Ghosh. Significant changes from ASCE 7-05 to ASCE 7-10, part 1: Seismic design provisions. *PCI Journal*, 59(1):60–82, 2014. ISSN 08879672. doi: 10.15554/pcij.01012014.60.82.
- [213] A. Gkimprixis, E. Tubaldi, and J. Douglas. Comparison of methods to develop risk-targeted seismic design maps. *Bulletin of Earthquake Engineering*, 17(7):3727–3752, 2019. ISSN 15731456. doi: 10.1007/s10518-019-00629-w. URL <https://doi.org/10.1007/s10518-019-00629-w>.
- [214] A. Farzam, M. J. Nollet, and A. Khaled. Integration of site condition information using geographic information system for seismic risk reduction for bridge network. *Georisk*, 0(0):1–14, 2021. ISSN 17499526. doi: 10.1080/17499518.2021.1952609. URL <https://doi.org/10.1080/17499518.2021.1952609>.

- [215] R. De Risi and K. Goda. Probabilistic earthquake-tsunami hazard assessment: The first step towards resilient coastal communities. *Procedia Engineering*, 198(September 2016):1058–1069, 2017. ISSN 18777058. doi: 10.1016/j.proeng.2017.07.150.
- [216] K. Goda, T. Rossetto, N. Mori, and S. Tesfamariam. Editorial: Mega Quakes: Cascading earthquake hazards and compounding risks. *Frontiers in Built Environment*, 4(8):5–7, 2018. doi: 10.3389/fbuil.2018.00008.
- [217] G. Hou, J. Wang, and A. Layton. Numerical methods for fluid-structure interaction - A review. *Communications in Computational Physics*, 12(2):337–377, 2012. ISSN 18152406. doi: 10.4208/cicp.291210.290411s.
- [218] P. L. F. Liu, S. B. Woo, and Y. S. Cho. COMCOT Computer program for tsunami propagation and inundation. Technical report, Cornell University, New York, 1998.
- [219] V. V. Titov and F. I. González. Implementation and testing of the method of splitting tsunami (MOST) model. Technical Report Contribution No. 1927 from NOAA/Pacific Marine Environmental Laboratory, NOAA, Seattle, 1997.
- [220] F. Imamura, A. C. Yalciner, and G. Ozyurt. Tsunami modelling manual. Technical report, UNESCO IOC international training course on Tsunami Numerical Modelling., 2006.
- [221] A. M. Salah, E. J. Nelson, and G. P. Williams. Tools and algorithms to link horizontal hydrologic and vertical hydrodynamic models and provide a stochastic modeling framework. *Journal of Advances in Modeling Earth Systems*, 2(4):14, 2010. doi: 10.3894/james.2010.2.12.
- [222] S. G. Roberts, O. Nielsen, D. Gray, and J. Sexton. ANUGA User Manual. Technical report, Commonwealth of Australia (Geoscience Australia) and the Australian National University, Canberra, Australia, 2010.
- [223] M. J. Berger, D. L. George, R. J. LeVeque, and K. T. Mandli. The GeoClaw software for depth-averaged flows with adaptive refinement. *Advances in Water Resources*, 34(9):1195–1206, 2011. ISSN 03091708. doi: 10.1016/j.advwatres.2011.02.016.
- [224] R. J. Leveque, D. L. George, and M. J. Berger. Tsunami modelling with adaptively refined finite volume methods. *Acta Numerica*, 20:211–289, 2011. ISSN 09624929. doi: 10.1017/S0962492911000043.
- [225] J. Behrens and F. Dias. New computational methods in tsunami science. *Philosophical Transactions of the Royal Society A: Mathematical, Physical and Engineering Sciences*, 373(2053), 2015. ISSN 1364503X. doi: 10.1098/rsta.2014.0382.
- [226] J. Macías, M. J. Castro, S. Ortega, C. E. Sánchez, and J. M. González-Vida. NTHMP benchmarking of Tsunami-HySEA model for propagation and inundation. The 2011 NTHMP model benchmarking workshop. Technical Report November, University of Malaga. Project:

- Development of efficient hydrodynamic and morphodynamic simulators for risk assessment and forecasting (SIMURISK), Malaga, Spain, 2016.
- [227] F. Lovholt, S. Glimsdal, C. B. Harbitz, N. Zamora, F. Nadim, P. Peduzzi, H. Dao, and H. Smebye. Tsunami hazard and exposure on the global scale. *Earth-Science Reviews*, 110(1-4):58–73, 2012. ISSN 00128252. doi: 10.1016/j.earscirev.2011.10.002.
- [228] F. Lovholt, S. Glimsdal, C. B. Harbitz, N. Horspool, H. Smebye, A. de Bono, and F. Nadim. Global tsunami hazard and exposure due to large co-seismic slip. *International Journal of Disaster Risk Reduction*, 10(PB):406–418, 2014. ISSN 22124209. doi: 10.1016/j.ijdr.2014.04.003.
- [229] A. Grezio, A. Babeyko, M. A. Baptista, J. Behrens, A. Costa, G. Davies, E. L. Geist, S. Glimsdal, F. I. González, J. Griffin, C. B. Harbitz, R. J. LeVeque, S. Lorito, F. Lovholt, R. Omira, C. Mueller, R. Paris, T. Parsons, J. Polet, W. Power, J. Selva, M. B. Sørensen, and H. K. Thio. Probabilistic tsunami hazard analysis: Multiple sources and global applications. *Reviews of Geophysics*, 55(4):1158–1198, 2017. ISSN 19449208. doi: 10.1002/2017RG000579.
- [230] N. Horspool, I. Pranantyo, J. Griffin, H. Latief, D. H. Natawidjaja, W. Kongko, A. Cipta, B. Bustaman, S. D. Anugrah, and H. K. Thio. A probabilistic tsunami hazard assessment for Indonesia. *Natural Hazards and Earth System Sciences*, 14(11):3105–3122, 2014. ISSN 16849981. doi: 10.5194/nhess-14-3105-2014.
- [231] R. Omira, M. A. Baptista, and L. Matias. Probabilistic tsunami hazard in the Northeast Atlantic from near- and far-field tectonic sources. *Pure and Applied Geophysics*, 172(3-4):901–920, 2015. ISSN 14209136. doi: 10.1007/s00024-014-0949-x.
- [232] J. Woessner and R. Jalali. Tsunami inundation hazard across Japan. *International Journal of Disaster Risk Reduction*, 49(March), 2020. ISSN 2212-4209. doi: 10.1016/j.ijdr.2020.101654.
- [233] H. Xiao, W. Huang, J. Tao, and C. Liu. Numerical modeling of wave-current forces acting on horizontal cylinder of marine structures by VOF method. *Ocean Engineering*, 67:58–67, 2013. ISSN 00298018. doi: 10.1016/j.oceaneng.2013.01.027. URL <http://dx.doi.org/10.1016/j.oceaneng.2013.01.027>.
- [234] X. Qin, M. R. Motley, R. J. LeVeque, F. I. González, and K. Mueller. A comparison of a two-dimensional depth averaged flow model and a three-dimensional RANS model for predicting tsunami inundation. *Natural Hazard and Earth Sciences*, 18:2489–2506, 2018. ISSN 16849981. doi: 10.5194/nhess-18-2489-2018.
- [235] H. Yeh. Design tsunami forces for onshore structures. *Journal of Disaster Research*, 2(6):531–536, 2007.
- [236] K. Qu, X. Ren, S. Kraatz, and E. Zhao. Numerical analysis of tsunami-like wave impact on horizontal cylinders. *Ocean Engineering*, 145(58):316–333, 2017. ISSN 00298018. doi: 10.1016/j.oceaneng.2017.09.027.

- [237] H. G. Weller, G. Tabor, H. Jasak, and C. Fureby. A tensorial approach to computational continuum mechanics using object-oriented techniques. *Computers in Physics*, 12(6):620, 1998. ISSN 08941866. doi: 10.1063/1.168744.
- [238] L. B. Lucy. A numerical approach to the testing of the fission hypothesis. *The astronomical journal*, 82(12):1013–1024, 1977. ISSN 0949-1775.
- [239] R. A. Gingold and J. J. Monaghan. Smoothed particle hydrodynamics: theory and application to non-spherical stars. *Monthly Notices of the Royal Astronomical Society*, 181:375–389, 1977.
- [240] J. J. Monaghan. Smoothed particle hydrodynamics. *Annual review of astronomy and astrophysics*, 30(1):543–574, 1992.
- [241] Y. Liu and M. Lin. Hydrodynamic coefficients induced by waves and currents for submerged circular cylinder. *Procedia Engineering*, 4:253–261, 2010. doi: 10.1016/j.proeng.2010.08.029.
- [242] D. Violeau and B. D. Rogers. Smoothed particle hydrodynamics (SPH) for free-surface flows: Past, present and future. *Journal of Hydraulic Research*, 54(1):1–26, 2016. ISSN 00221686. doi: 10.1080/00221686.2015.1119209. URL <https://doi.org/10.1080/00221686.2015.1119209>.
- [243] M. Shadloo, G. Oger, and D. Le Touzé. Smoothed particle hydrodynamics method for fluid flows, towards industrial applications: Motivations, current state, and challenges. *Computers and Fluids*, 136:11–34, 2016. ISSN 00457930. doi: 10.1016/j.compfluid.2016.05.029.
- [244] H. Gotoh and A. Khayyer. On the state-of-the-art of particle methods for coastal and ocean engineering. *Coastal Engineering Journal*, 60(1):79–103, 2018. ISSN 17936292. doi: 10.1080/21664250.2018.1436243. URL <https://doi.org/10.1080/21664250.2018.1436243>.
- [245] S. J. Lind, B. D. Rogers, and P. K. Stansby. Review of smoothed particle hydrodynamics: towards converged Lagrangian flow modelling. *Proceedings of the Royal Society A: Mathematical, Physical and Engineering Sciences*, 476(2241):20190801, 2020. ISSN 1364-5021. doi: 10.1098/rspa.2019.0801.
- [246] R. Vacondio, C. Altomare, M. De Leffe, X. Hu, D. Le Touzé, S. Lind, J. C. Marongiu, S. Marrone, B. D. Rogers, and A. Souto-Iglesias. Grand challenges for Smoothed Particle Hydrodynamics numerical schemes. *Computational Particle Mechanics*, 2020. ISSN 21964386. doi: 10.1007/s40571-020-00354-1.
- [247] J. M. Domínguez, G. Fourtakas, C. Altomare, R. B. Canelas, A. Tafuni, O. García-Feal, I. Martínez-Estévez, A. Mokos, R. Vacondio, A. J. C. Crespo, B. D. Rogers, P. K. Stansby, and M. Gómez-Gesteira. State-of-the-art SPH solver DualSPHysics: from fluid dynamics to multiphysics problems. *Computational Particle Mechanics*, pages 1–29, 2021. doi: 10.1007/s40571-021-00404-2. URL <http://arxiv.org/abs/2104.00537><http://dx.doi.org/10.1007/s40571-021-00404-2>.

- [248] M. MacCabe, P. K. Stansby, L. S. Cunningham, and B. D. Rogers. Modelling the impact of tsunamis on coastal defences in the UK. *Coastal Engineering Proceedings*, 34:36–36, 2014.
- [249] B. D. Rogers and R. A. Dalrymple. SPH modeling of tsunami waves. In *Advanced Numerical Models for Simulating Tsunami Waves and Runup*, chapter Chapter 3, pages 75–100. World Scientific, 2008. ISBN 9789812790910. doi: 10.1142/9789812790910.
- [250] M. D. Lefte, D. L. Touzé, and B. Alessandrini. SPH modeling of shallow-water coastal flows. *Journal of Hydraulic Research*, 48(SUPPL. 1):118–125, 2010. ISSN 00221686. doi: 10.1080/00221686.2010.9641252.
- [251] C. Altomare, B. Tagliafierro, J. M. Domínguez, T. Suzuki, and G. Viccione. Improved relaxation zone method in SPH-based model for coastal engineering applications. *Applied Ocean Research*, 81(May):15–33, 2018. ISSN 01411187. doi: 10.1016/j.apor.2018.09.013.
- [252] J. M. Domínguez, C. Altomare, J. González-Cao, and P. Lomonaco. Towards a more complete tool for coastal engineering: solitary wave generation, propagation and breaking in an SPH-based model. *Coastal Engineering Journal*, 61(1):15–40, 2019. ISSN 17936292. doi: 10.1080/21664250.2018.1560682.
- [253] A. J. C. Crespo, M. Gómez-Gesteira, and R. A. Dalrymple. Boundary conditions generated by dynamic particles in SPH methods. *Computers, Materials and Continua*, 5(3):173–184, 2007. ISSN 15462218.
- [254] M. Gómez-Gesteira, B. D. Rogers, A. J. C. Crespo, R. A. Dalrymple, M. S. Narayanaswamy, and J. M. Domínguez. SPHysics - development of a free-surface fluid solver - Part 1: theory and formulations. *Computers and Geosciences*, 48:289–299, 2012. ISSN 00983004. doi: 10.1016/j.cageo.2012.02.029.
- [255] A. Tafuni, J. M. Domínguez, R. Vacondio, and A. J. C. Crespo. A versatile algorithm for the treatment of open boundary conditions in Smoothed particle hydrodynamics GPU models. *Computer Methods in Applied Mechanics and Engineering*, 342:604–624, 2018. ISSN 00457825. doi: 10.1016/j.cma.2018.08.004.
- [256] Y. You, A. Khayyer, X. Zheng, H. Gotoh, and Q. Ma. Enhancement of δ -SPH for ocean engineering applications through incorporation of a background mesh scheme. *Applied Ocean Research*, 1 (November 2020):102508, 2021. ISSN 01411187. doi: 10.1016/j.apor.2020.102508.
- [257] M. Gómez-Gesteira and R. A. Dalrymple. Using a three-dimensional Smoothed Particle Hydrodynamics method for wave impact on a tall structure. *Journal of Waterway, Port, Coastal, and Ocean Engineering*, 130:63–69, 2004. ISSN 0733-950X. doi: 10.1061/(asce)0733-950x(2004)130:2(63).
- [258] A. Colagrossi and M. Landrini. Numerical simulation of interfacial flows by smoothed particle hydrodynamics. *Journal of Computational Physics*, 191(2):448–475, 2003. ISSN 00219991. doi: 10.1016/S0021-9991(03)00324-3.

- [259] D. V. Balderas, J. M. Domínguez, B. D. Rogers, and A. J. Crespo. Towards accelerating smoothed particle hydrodynamics simulations for free-surface flows on multi-GPU clusters. *Journal of Parallel and Distributed Computing*, 73(11):1483–1493, 2013. ISSN 07437315. doi: 10.1016/j.jpdc.2012.07.010.
- [260] A. J. C. Crespo, J. M. Domínguez, B. D. Rogers, M. Gómez-Gesteira, S. Longshaw, R. J. F. B. Canelas, R. Vacondio, A. Barreiro, and O. García-Feal. DualSPHysics: Open-source parallel CFD solver based on Smoothed Particle Hydrodynamics (SPH). *Computer Physics Communications*, 187:204–216, 2015. ISSN 00104655. doi: 10.1016/j.cpc.2014.10.004.
- [261] M. S. Narayanaswamy, A. J. C. Crespo, M. Gómez-Gesteira, and R. A. Dalrymple. SPHysics-FUNWAVE hybrid model for coastal wave propagation. *Journal of Hydraulic Research*, 48(SUPPL. 1):85–93, 2010. ISSN 00221686. doi: 10.1080/00221686.2010.9641249.
- [262] C. Altomare, J. M. Domínguez, A. J. C. Crespo, T. Suzuki, I. Caceres, and M. Gómez-Gesteira. Hybridization of the wave propagation model SWASH and the meshfree particle method SPH for real coastal applications. *Coastal Engineering Journal*, 57(04):1550024, 2015. ISSN 0578-5634. doi: 10.1142/S0578563415500242.
- [263] K. Wu, D. Yang, and N. Wright. A coupled SPH-DEM model for fluid-structure interaction problems with free-surface flow and structural failure. *Computers and Structures*, 177:141–161, 2016. doi: 10.1016/j.compstruc.2016.08.012.
- [264] S. Marrone, A. Di Mascio, and D. Le Touzé. Coupling of Smoothed Particle Hydrodynamics with Finite Volume method for free-surface flows. *Journal of Computational Physics*, 310(November): 161–180, 2016. ISSN 10902716. doi: 10.1016/j.jcp.2015.11.059.
- [265] T. Verbrugghe, J. M. Domínguez, C. Altomare, A. Tafuni, P. Troch, and A. Kortenhaus. Application of open boundaries within a two-way coupled SPH model to simulate non-linear wave-structure interactions. *Coastal Engineering Proceedings*, 1(36):14, 2019. ISSN 0589-087X. doi: 10.9753/icce.v36.papers.14.
- [266] R. A. Dalrymple and B. D. Rogers. Numerical modeling of water waves with the SPH method. *Coastal Engineering*, 53:141–147, 2006. ISSN 03783839. doi: 10.1016/j.coastaleng.2005.10.004.
- [267] R. Lowe, M. L. Buckley, C. Altomare, D. Rijnsdorp, Y. Yao, T. Suzuki, and J. D. Bricker. Numerical simulations of surf zone wave dynamics using Smoothed Particle Hydrodynamics. *Ocean Modelling*, 144(June):101481, 2019. ISSN 14635003. doi: 10.1016/j.oceomod.2019.101481. URL <https://doi.org/10.1016/j.oceomod.2019.101481>.
- [268] C. Altomare, A. J. C. Crespo, J. M. J. M. Domínguez, M. Gómez-Gesteira, T. Suzuki, and T. Verwaest. Applicability of Smoothed Particle Hydrodynamics for estimation of sea wave impact on coastal structures. *Coastal Engineering*, 96:1–12, 2015. ISSN 03783839. doi: 10.1016/j.coastaleng.2014.11.001. URL <http://dx.doi.org/10.1016/j.coastaleng.2014.11.001>.

- [269] G. Pringgana, L. S. Cunningham, and B. D. Rogers. Modelling of tsunami-induced bore and structure interaction. *Proceedings of the Institution of Civil Engineers - Engineering and Computational Mechanics*, 169(3):109–125, 2016. ISSN 1755-0777. doi: 10.1680/jencm.15.00020. URL <http://www.icevirtuallibrary.com/doi/10.1680/jencm.15.00020>.
- [270] J. González-Cao, C. Altomare, A. J. C. Crespo, J. M. Domínguez, M. Gómez-Gesteira, and D. Kisacik. On the accuracy of DualSPHysics to assess violent collisions with coastal structures. *Computers and Fluids*, 179:604–612, 2019. ISSN 00457930. doi: 10.1016/j.compfluid.2018.11.021.
- [271] B.-I. Dang, H. Xuan, and M. Abdel. Numerical study on wave forces and overtopping over various seawall structures using advanced SPH-based method. *Engineering Structures*, 226(111349): 1–9, 2021. ISSN 0141-0296. doi: 10.1016/j.engstruct.2020.111349.
- [272] C. Reis, A. R. Barbosa, J. Figueiredo, S. Clain, M. Lopes, and M. A. Baptista. Smoothed Particle Hydrodynamics modeling of elevated structures impacted by tsunami-like waves. *Engineering Structures*, 270(114851), 2022. doi: 10.1016/j.engstruct.2022.114851.
- [273] N. Asadollahi, I. Nistor, and A. Mohammadian. Numerical investigation of tsunami bore effects on structures , part 1 : Drag coefficients. *Natural Hazards*, 96(1):285–309, 2018. ISSN 1573-0840. doi: 10.1007/s11069-018-3542-2.
- [274] D. Ghosh, A. K. Mittal, and S. K. Bhattacharyya. Multiphase modeling of tsunami impact on building with openings. *Journal of Computational Multiphase Flows*, 8(2):85–94, 2016. ISSN 17574838. doi: 10.1177/0010836716653881.
- [275] C. Fragassa, M. Topalovic, A. Pavlovic, and S. Vulovic. Dealing with the effect of air in fluid structure interaction by coupled SPH-FEM methods. *Materials*, 12(7), 2019. ISSN 19961944. doi: 10.3390/ma12071162.
- [276] T. Fonty, M. Ferrand, A. Leroy, and D. Violeau. Air entrainment modeling in the SPH method: A two-phase mixture formulation with open boundaries. *Flow, Turbulence and Combustion*, 105: 1149–1195, 2020. ISSN 15731987. doi: 10.1007/s10494-020-00165-7. URL <https://doi.org/10.1007/s10494-020-00165-7>.
- [277] M. Luo, M. Rubinato, and X. Zhao. Experimental investigation of freak wave actions on a floating platform and effects of the air gap. *Ocean Engineering*, 253(111192), 2022. doi: 10.1016/j.oceaneng.2022.111192.
- [278] T. Verbrugge, V. Stratigaki, C. Altomare, J. M. Domínguez, P. Troch, and A. Kortenhaus. Implementation of open boundaries within a two-way coupled SPH model to simulate nonlinear wave–structure interactions. *Energies*, 12(4), 2019. ISSN 19961073. doi: 10.3390/en12040697.
- [279] R. van Loon, P. D. Anderson, F. van de Vosse, and S. J. Sherwin. Comparison of various fluid-structure interaction methods for deformable bodies. *Computers and Structures*, 85(11-14):833–843, 2007. ISSN 00457949. doi: 10.1016/j.compstruc.2007.01.010.

- [280] J. Donea, S. Giuliani, and J. P. Halleux. An arbitrary lagrangian-eulerian finite element method for transient dynamic fluid-structure interactions. *Computer Methods in Applied Mechanics and Engineering*, 33(1-3):689–723, 1982. ISSN 00457825. doi: 10.1016/0045-7825(82)90128-1.
- [281] S. Marrone, A. Colagrossi, L. Chiron, M. D. Lefte, and D. L. Touzé. High-speed water impacts of flat plates in different ditching configuration through a Riemann-ALE SPH model. *Journal of Hydrodynamics*, 30(1):38–48, 2018. ISSN 18780342. doi: 10.1007/s42241-018-0004-y.
- [282] K. Abe, K. Murotani, and K. Watanabe. Development of Mpm-Mps coupling method and numerical analysis of scouring of embankment caused by overflow. *Journal of Japan Society of Civil Engineers, Ser. A2 (Applied Mechanics (AM))*, 76(2):205–216, 2020. doi: 10.2208/jscejam.76.2_i_205.
- [283] A. Hasanpour, D. Istrati, and I. Buckle. Coupled sph–fem modeling of tsunami-borne large debris flow and impact on coastal structures. *Journal of Marine Science and Engineering*, 9(10), 2021. ISSN 20771312. doi: 10.3390/jmse9101068.
- [284] T. Richter. A fully eulerian formulation for fluid-structure-interaction problems. *Journal of Computational Physics*, 233(1):227–240, 2013. ISSN 10902716. doi: 10.1016/j.jcp.2012.08.047. URL <http://dx.doi.org/10.1016/j.jcp.2012.08.047>.
- [285] X. Wang, K. Kamrin, and Chris Rycr. An incompressible Eulerian method for fluid-structure interaction with mixed soft and rigid solids.pdf. *Physics of fluids*, 34(033504), 2022. doi: 10.1063/5.0082233.
- [286] P. Antonietti, M. Verani, C. Vergara, and S. Zonca. Numerical solution of fluid-structure interaction problems by means of a high order Discontinuous Galerkin method on polygonal grids. *Finite Elements in Analysis and Design*, 159(September 2018):1–14, 2019. ISSN 0168874X. doi: 10.1016/j.finel.2019.02.002. URL <https://doi.org/10.1016/j.finel.2019.02.002>.
- [287] M. Liu and Z. Zhang. Smoothed particle hydrodynamics (SPH) for modeling fluid-structure interactions. *Science China: Physics, Mechanics and Astronomy*, 62(8):0–38, 2019. ISSN 18691927. doi: 10.1007/s11433-018-9357-0.
- [288] R. J. F. B. Canelas, M. Brito, O. García-Feal, J. M. Domínguez, and A. J. C. Crespo. Extending DualSPHysics with a Differential Variational Inequality: modeling fluid-mechanism interaction. *Applied Ocean Research*, 76(December 2017):88–97, 2018. ISSN 01411187. doi: 10.1016/j.apor.2018.04.015.
- [289] V. P. Nguyen, T. Rabczuk, S. Bordas, and M. Duflo. Meshless methods: A review and computer implementation aspects. *Mathematics and Computers in Simulation*, 79(3):763–813, 2008. ISSN 03784754. doi: 10.1016/j.matcom.2008.01.003.
- [290] M. Luo, A. Khayyer, and P. Lin. Particle methods in ocean and coastal engineering. *Applied Ocean Research*, 114:102734, 2021. ISSN 01411187. doi: 10.1016/j.apor.2021.102734. URL <https://doi.org/10.1016/j.apor.2021.102734>.

- [291] M. Geveler, D. Ribbrock, G. Dominik, and S. Turek. Lattice-Boltzmann simulation of the shallow-water equations with fluid-structure interaction on multi- and manycore processors, 2010. ISSN 03029743.
- [292] M. S. Glessmer and C. F. Janßen. Using an interactive lattice Boltzmann solver in fluid mechanics instruction. *Computation*, 5(3):35, 2017. ISSN 2079-3197. doi: 10.3390/computation5030035. URL <http://www.mdpi.com/2079-3197/5/3/35>.
- [293] B. Dorschner, S. S. Chikatamarla, and I. V. Karlin. Fluid-structure interaction with the entropic lattice Boltzmann method. *Physical Review E*, 97(2):1–12, 2018. ISSN 24700053. doi: 10.1103/PhysRevE.97.023305.
- [294] E. Majtan, L. S. Cunningham, and B. D. Rogers. Experimental and numerical investigation of floating large woody debris impact on a masonry arch bridge.pdf. *Journal of Marine Science and Engineering*, 10(911), 2022. doi: 10.3390/jmse10070911.
- [295] T. Rossetto, C. De la Barra, C. Petrone, J. C. De la Llera, J. Vásquez, and M. Baiguera. Comparative assessment of nonlinear static and dynamic methods for analysing building response under sequential earthquake and tsunami. *Earthquake Engineering and Structural Dynamics*, 48(8):867–887, 2019. ISSN 10969845. doi: 10.1002/eqe.3167.
- [296] K. Goda, R. De Risi, F. D. Luca, A. Muhammad, T. Yasuda, and N. Mori. Multi-hazard earthquake-tsunami loss estimation of Kuroshio town, Kochi prefecture, Japan considering the Nankai-Tonankai megathrust rupture scenarios. *International Journal of Disaster Risk Reduction*, 2020.
- [297] I. E. Mulia and K. Satake. Developments of tsunami observing systems in Japan. *Frontiers in Earth Science*, 8(May):1–7, 2020. ISSN 22966463. doi: 10.3389/feart.2020.00145.
- [298] B. Aydın, N. Sharghivand, and Ö. Bayazıtöğlü. Potential tsunami hazard along the southern Turkish coast. *Coastal Engineering*, 158(March), 2020. ISSN 03783839. doi: 10.1016/j.coastaleng.2020.103696.
- [299] P. J. Lynett, J. C. Borrero, R. Weiss, S. Son, D. Greer, and W. Renteria. Observations and modeling of tsunami-induced currents in ports and harbors. *Earth and Planetary Science Letters*, 327-328: 68–74, 2012. ISSN 0012821X. doi: 10.1016/j.epsl.2012.02.002. URL <http://dx.doi.org/10.1016/j.epsl.2012.02.002>.
- [300] J. Macabuag, T. Rossetto, I. Ioannou, A. Suppasri, D. Sugawara, B. Adriano, F. Imamura, I. Eames, and S. Koshimura. A proposed methodology for deriving tsunami fragility functions for buildings using optimum intensity measures. *Natural Hazards*, 84(2):1257–1285, 2016. ISSN 15730840. doi: 10.1007/s11069-016-2485-8.
- [301] Y. Xiong, Q. Liang, H. Park, D. T. Cox, and G. Wang. A deterministic approach for assessing tsunami-induced building damage through quantification of hydrodynamic forces. *Coastal Engineering*, 144(November):1–14, 2019. ISSN 03783839. doi: 10.1016/j.coastaleng.2018.

- 11.002. URL <https://doi.org/10.1016/j.coastaleng.2018.11.002><https://linkinghub.elsevier.com/retrieve/pii/S0378383918301820>.
- [302] D. Linton, R. Gupta, D. Cox, J. van de Lindt, M. E. Oshnack, and M. Clauson. Evaluation of tsunami loads on wood-frame walls at full Scale. *Journal of Structural Engineering*, 139(8):1318–1325, 2013. ISSN 0733-9445. doi: 10.1061/(asce)st.1943-541x.0000644.
- [303] D. Istrati, I. G. Buckle, P. Lomonaco, and S. C. Yim. Deciphering the tsunami wave impact and associated connection forces in open-girder coastal bridges. *Journal of Marine Science and Engineering*, 6(148):1–36, 2018. doi: 10.3390/jmse6040148.
- [304] S. C. Yim, Y. Wei, M. Azadbakht, S. Nimmala, and T. Potisuk. Case study for tsunami design of coastal infrastructure: Spencer creek bridge, Oregon. *Journal of Bridge Engineering*, 20(1):1–12, 2015. doi: 10.1061/(ASCE)BE.1943-5592.0000631.
- [305] PIANC Working Group 34. Seismic design guidelines for port structures - Report of Working Group No.34. Technical report, World Association for Waterborne Transport Infrastructure, 2001.
- [306] S. Iai. Seismic performance-based design of port structures and simulation techniques. Technical Report 1, PARI, Port and Airport Research Institute, 2001.
- [307] T. Nagao and P. Lu. A simplified reliability estimation method for pile-supported wharf on the residual displacement by earthquake. *Soil Dynamics and Earthquake Engineering*, 129(October 2019):105904, 2020. ISSN 02677261. doi: 10.1016/j.soildyn.2019.105904. URL <https://doi.org/10.1016/j.soildyn.2019.105904>.
- [308] J. C. Borrero, D. G. Goring, S. D. Greer, and W. L. Power. Far-Field tsunami hazard in New Zealand ports. *Pure and Applied Geophysics*, 172(3-4):731–756, 2015. ISSN 14209136. doi: 10.1007/s00024-014-0987-4.
- [309] J. M. Turnbull and M. W. Hughes. Anticipating tsunami impacts in Port Marlborough: implications for port operation and harbour navigability. Technical report, University of Canterbury, New Zealand, 2017. URL https://www.marlborough.govt.nz/repository/libraries/id:1w1mps0ir17q9sgxanf9/hierarchy/Documents/Services/EM-EngineeringLifelinesList/Anticipating_Tsunami_Impacts_In_Port_Marlborough.pdf.
- [310] A. Muhari, I. Charvet, F. Tsuyoshi, A. Suppasri, and F. Imamura. Assessment of tsunami hazards in ports and their impact on marine vessels derived from tsunami models and the observed damage data. *Natural Hazards*, 78(2):1309–1328, 2015. ISSN 15730840. doi: 10.1007/s11069-015-1772-0.
- [311] W. B. Group. Investment in Disaster Risk Management in Europe Makes Economic Sense. Technical report, Funded by European Union, Washington DC, 2021.
- [312] G. A. Papadopoulos and A. Fokaefs. Strong tsunamis in the mediterranean sea: A re-evaluation. *ISSET Journal of Earthquake Technology*, 42(4):159–170, 2005. ISSN 09720405.

- [313] G. A. Papadopoulos, E. Lekkas, and K.-n. Katsetsiadou. GeoHazards tsunami alert efficiency in the Eastern Mediterranean. *GeoHazards*, 2:44–60, 2020. doi: 10.3390/geohazards1010005.
- [314] L. Matías, M. A. Baptista, R. Omira, A. Annunziato, G. Franchello, and F. Carrilho. Third generation tsunami scenario matrix for the Portuguese tsunami early warning system. In *15th World Conference on Earthquake Engineering*, Lisbon , Portugal, 2012.
- [315] L. Matias, F. Carrilho, V. Sá, R. Omira, M. Niehus, C. Corela, J. L. Barros, and Y. Omar. The contribution of submarine optical fiber telecom cables to the monitoring of earthquakes and tsunamis in the NE Atlantic. *Frontiers in Earth Science*, 9(686296):1–17, 2021. ISSN 22966463. doi: 10.3389/feart.2021.686296.
- [316] R. Madariaga. *Seismic Source Theory*, volume 4. Elsevier B.V., 2015. ISBN 9780444538031. doi: 10.1016/B978-0-444-53802-4.00070-1. URL <http://dx.doi.org/10.1016/B978-0-444-53802-4.00070-1>.
- [317] Y. Okada. Surface deformation due to shear and tensile faults in a Half-Space. *Bulletin of the seismological Society of America*, 75(4):1135–1154, 1985.
- [318] K. Kajiura. Tsunami source, energy and directivity of wave radiation. *Bulletin of the Earthquake Research Institute*, 48:835–869, 1970.
- [319] Y. Fujii, K. Satake, S. Sakai, M. Shinohara, and T. Kanazawa. Tsunami source of the 2011 off the Pacific Coast of Tohoku earthquake. *Earth, Planets, Space*, 63(7):815–820, sep 2011.
- [320] K. Satake, Y. Fujii, T. Harada, and Y. Namegaya. Time and space distribution of coseismic slip of the 2011 Tohoku earthquake as inferred from tsunami waveform data. *Bulletin of the Seismological Society of America*, 103(2B):1473–1492, may 2013. doi: 10.1785/0120120122.
- [321] A. Suppasri, N. Shuto, F. Imamura, S. Koshimura, E. Mas, and A. C. Yalciner. Lessons learned from the 2011 Great East Japan Tsunami: Performance of tsunami countermeasures, coastal buildings, and tsunami evacuation in Japan. *Pure and Applied Geophysics*, 170(6-8):993–1018, 2013. ISSN 00334553. doi: 10.1007/s00024-012-0511-7.
- [322] G. K. Batchelor. An introduction to fluid dynamics. Cambridge University Press, 1967. ISSN 00319228.
- [323] K. Gong, S. Shao, H. Liu, B. Wang, and S. K. Tan. Two-phase SPH simulation of fluid-structure interactions. *Journal of Fluids and Structures*, 65:155–179, 2016. ISSN 10958622. doi: 10.1016/j.jfluidstructs.2016.05.012. URL <http://dx.doi.org/10.1016/j.jfluidstructs.2016.05.012>.
- [324] W. Dehnen and H. Aly. Improving convergence in smoothed particle hydrodynamics simulations without pairing instability. *Monthly Notices of the Royal Astronomical Society*, 425(2):1068–1082, 2012. ISSN 00358711. doi: 10.1111/j.1365-2966.2012.21439.x.
- [325] R. J. F. B. Canelas. *Numerical modeling of fully coupled solid-fluid flow*. Phd thesis, Universidade de Lisboa, 2015.

- [326] M. Gormley and S. Macleod. Towards a solid particle hydrodynamic (Sph)-based solids transport model applied to ultra-lowwater usage sanitation in developing countries. *Water (Switzerland)*, 13(4), 2021. ISSN 20734441. doi: 10.3390/w13040441.
- [327] A. Mokos, B. D. Rogers, and P. K. Stansby. A multi-phase particle shifting algorithm for SPH simulations of violent hydrodynamics with a large number of particles. *Journal of Hydraulic Research*, 55(2):143–162, 2017. ISSN 00221686. doi: 10.1080/00221686.2016.1212944.
- [328] S. Marrone, M. Antuono, A. Colagrossi, G. Colicchio, D. Le Touzé, and G. Graziani. δ -SPH model for simulating violent impact flows. *Computer Methods in Applied Mechanics and Engineering*, 200(13-16):1526–1542, 2011. ISSN 00457825. doi: 10.1016/j.cma.2010.12.016. URL <http://dx.doi.org/10.1016/j.cma.2010.12.016>.
- [329] A. English, J. M. Domínguez, R. Vacondio, A. J. Crespo, P. K. Stansby, S. J. Lind, L. Chiapponi, and M. Gómez-Gesteira. Modified dynamic boundary conditions (mDBC) for general-purpose smoothed particle hydrodynamics (SPH): application to tank sloshing, dam break and fish pass problems. *Computational Particle Mechanics*, 2021. ISSN 21964386. doi: 10.1007/s40571-021-00403-3. URL <https://doi.org/10.1007/s40571-021-00403-3>.
- [330] E. Didier and M. G. Neves. A semi-infinite numerical wave flume using smoothed particle hydrodynamics. *International Journal of Offshore and Polar Engineering*, 22(3):193–199, 2012. ISSN 10535381.
- [331] S. Lee, K. Ko, and J.-w. Hong. Comparative study on the breaking waves by a piston-type wavemaker in experiments and SPH simulations. *Coastal Engineering Journal*, 00(00):1–18, 2020. ISSN 2166-4250. doi: 10.1080/21664250.2020.1747141.
- [332] Swapnadip De Chowdhury and S. A. Sannasiraj. SPH simulation of shallow water wave propagation. *Ocean Engineering*, 60:41–52, 2013. ISSN 00298018. doi: 10.1016/j.oceaneng.2012.12.036.
- [333] T. Verbrugge, J. M. Domínguez, A. J. C. Crespo, C. Altomare, V. Stratigaki, P. Troch, and A. Kortenhaus. Coupling methodology for smoothed particle hydrodynamics modelling of non-linear wave-structure interactions. *Coastal Engineering*, 138(April):184–198, 2018. ISSN 03783839. doi: 10.1016/j.coastaleng.2018.04.021.
- [334] R. Guandalini, G. Agate, A. Amicarelli, S. Manenti, M. Gallati, and S. Sibilla. SPH Modelling of a 3D Tsunami Test Case. *Development and Applications of Oceanic Engineering*, 3(1), 2014. URL www.daooe-journal.org.
- [335] J. H. Pu and S. Shao. Smoothed particle hydrodynamics simulation of wave overtopping characteristics for different coastal structures. *The Scientific World Journal*, 2012, 2012. ISSN 1537744X. doi: 10.1100/2012/163613.

- [336] A. Barreiro, A. J. C. Crespo, and J. M. Domínguez. Smoothed Particle Hydrodynamics for coastal engineering problems. *Computers and Structures*, 120:96–106, 2013. ISSN 0045-7949. doi: 10.1016/j.compstruc.2013.02.010. URL <http://dx.doi.org/10.1016/j.compstruc.2013.02.010>.
- [337] E. Didier, D. R. C. B. Neves, R. Martins, and M. G. Neves. Wave interaction with a vertical wall: SPH numerical and experimental modeling. *Ocean Engineering*, 88:330–341, 2014. ISSN 00298018. doi: 10.1016/j.oceaneng.2014.06.029.
- [338] X.-y. Ni, W.-b. Feng, and D. Wu. Numerical simulations of wave interactions with vertical wave barriers using the SPH method. *International Journal for Numerical Methods in Fluids*, 76(4): 223–245, 2014. ISSN 10970363. doi: 10.1002/flid.3933.
- [339] D. D. Meringolo, F. Aristodemo, and P. Veltri. SPH numerical modeling of wave-perforated breakwater interaction. *Coastal Engineering*, 101:48–68, 2015. ISSN 03783839. doi: 10.1016/j.coastaleng.2015.04.004.
- [340] C. Altomare, A. J. Crespo, B. D. Rogers, J. M. Dominguez, X. Gironella, and M. Gómez-Gesteira. Numerical modelling of armour block sea breakwater with smoothed particle hydrodynamics. *Computers and Structures*, 130:34–45, 2014. ISSN 00457949. doi: 10.1016/j.compstruc.2013.10.011. URL <http://dx.doi.org/10.1016/j.compstruc.2013.10.011>.
- [341] F. Zhang, A. J. C. Crespo, C. Altomare, J. M. Domínguez, A. Marzeddu, S. P. Shang, and M. Gómez-Gesteira. Dualsphysics: A numerical tool to simulate real breakwaters. *Journal of Hydrodynamics*, 30(1):95–105, 2018. ISSN 18780342. doi: 10.1007/s42241-018-0010-0.
- [342] J. O'Connor and B. D. Rogers. A fluid-structure interaction model for free-surface flows and flexible structures using Smoothed Particle Hydrodynamics on a GPU. *Journal of Fluids and Structures*, 104(Under Review):103312, 2021. ISSN 0889-9746. doi: 10.1016/j.jfluidstructs.2021.103312. URL <https://doi.org/10.1016/j.jfluidstructs.2021.103312>.
- [343] P. Birken. *Numerical methods for the unsteady compressible Navier-Stokes equations*. PhD thesis, Universitat Kassel, 2012.
- [344] J. L. Lara, I. J. Losada, M. Del Jesus, G. Barajas, and R. Guanche. IH-3VOF: A three-dimensional navier-stokes model for wave and structure interaction. *Proceedings of the Coastal Engineering Conference*, 1(January 2010):55, 2010. ISSN 01613782. doi: 10.9753/icce.v32.waves.55.
- [345] E. Audusse, F. Bouchut, M.-O. Bristeau, R. Klein, and B. Perthame. A fast and stable well-balanced scheme with hydrostatic reconstruction for shallow water flows. *SIAM Journal on Scientific Computing*, 25(6):2050–2065, 2004. ISSN 1064-8275. doi: 10.1137/s1064827503431090.
- [346] B. van Leer. Towards the ultimate conservative difference scheme. II. Monotonicity and conservation combined in a second-order scheme. *Journal of Computational Physics*, 14:361–370, 1974.

- [347] S. Diot, S. Clain, and R. Loubère. Improved detection criteria for the Multi-dimensional Optimal Order Detection (MOOD) on unstructured meshes with very high-order polynomials. *Computers and Fluids*, 64:43–63, 2012. ISSN 00457930. doi: 10.1016/j.compfluid.2012.05.004. URL <http://dx.doi.org/10.1016/j.compfluid.2012.05.004>.
- [348] C. E. Synolakis, E. N. Bernard, and V. V. Titov. Criteria, and procedures for NOAA evaluation of tsunami numerical models. Technical report, National Oceanic and Atmospheric Administration, 2007.
- [349] S. Abadie, F. González, S. Grilli, J. Horrillo, B. Knight, D. Nicolsky, V. Roeber, F. Shi, E. Tolkova, Y. Yamazaki, J. Zhang, and L. Pahlke. Proceedings and results of the 2011 NTHMP model benchmarking workshop. Technical report, National Tsunami Hazard Mitigation Program, National Oceanic and Atmospheric Administration, 2012.
- [350] Z. Zhang, H. Qiang, and W. Gao. Coupling of smoothed particle hydrodynamics and finite element method for impact dynamics simulation. *Engineering Structures*, 33(1):255–264, 2011. ISSN 01410296. doi: 10.1016/j.engstruct.2010.10.020.
- [351] J. Douglas and H. Aochi. A survey of techniques for predicting earthquake ground motions for engineering purposes. *Surveys in Geophysics*, 29(3):187–220, 2008. ISSN 01693298. doi: 10.1007/s10712-008-9046-y.
- [352] M. Pagani, D. Monelli, G. Weatherill, L. Danciu, H. Crowley, V. Silva, P. Henshaw, L. Butler, M. Nastasi, L. Panzeri, M. Simionato, and D. Viganò. Openquake engine: An open hazard (and risk) software for the global earthquake model. *Seismological Research Letters*, 85(3):692–702, 2014. ISSN 19382057. doi: 10.1785/0220130087.
- [353] G. M. Atkinson and K. Assatourians. Implementation and validation of EXSIM (a stochastic finite-fault ground-motion simulation algorithm) on the SCEC broadband platform. *Seismological Research Letters*, 86(1):48–60, 2015. ISSN 19382057. doi: 10.1785/0220140097.
- [354] E. Yenier and G. M. Atkinson. Regionally adjustable generic ground-motion prediction equation based on equivalent point-source simulations: Application to central and eastern North America. *Bulletin of the Seismological Society of America*, 105(4):1989–2009, 2015. ISSN 19433573. doi: 10.1785/0120140332.
- [355] D. M. Boore. Stochastic simulation of high-frequency ground motions based on seismological models of the radiated spectra. *Bulletin of the Seismological Society of America*, 73:1865–1894, 1983. ISSN 00371106.
- [356] D. M. Boore. Simulation of ground motion using the stochastic method. *Pure and Applied Geophysics*, 160(3-4):635–676, 2003. doi: 10.1007/PL00012553.
- [357] J. N. Brune. Tectonic stress and the spectra of seismic shear waves from earthquakes. *Journal of Geophysical Research*, 75(26):4997–5009, 1970. ISSN 01480227. doi: 10.1029/JB075i026p04997. URL <http://doi.wiley.com/10.1029/JB075i026p04997>.

- [358] J. Solnes. *Stochastic Processes and Random Vibrations - theory and practice*. Wiley, first edit edition, 1997.
- [359] M. D. Paola, L. L. Mendola, and G. Navarra. Stochastic seismic analysis of mdof structures with nonlinear viscous dampers. *Journal of Structural Engineering*, 133(10):1475–1478, 2007. doi: 10.1061/(ASCE)0733-9445(2007)133:10(1475)CITATIONS.
- [360] F. T. Mckenna. *Object oriented finite element programming: frameworks for analysis, algorithms and parallel computing*. Phd thesis, University of California, Berkeley, 1997.
- [361] F. McKenna, M. H. Scott, and G. L. Fenves. Nonlinear finite-element analysis software architecture using object composition. *Journal of Computing in Civil Engineering*, 24(1):95–107, 2010. ISSN 0887-3801. doi: 10.1061/(asce)cp.1943-5487.0000002.
- [362] A. Preumont. *Twelve lectures on structural dynamics*, volume 198. Springer, Berlin, Germany, 2013. ISBN 9789400763821. doi: 10.1007/978-94-007-6383-8-1.
- [363] Z. Qiu, J. Lu, A. Elgamal, L. Su, N. Wang, and A. Almutairi. OpenSees three-dimensional computational modeling of ground structure systems and liquefaction scenarios. *CMES - Computer Modeling in Engineering and Sciences*, 120(3):629–656, 2019. ISSN 15261506. doi: 10.32604/cmes.2019.05759.
- [364] V. K. Papanikolaou. GiD+OpenSees interface : An integrated Finite Element Analysis platform, 2017.
- [365] L. W. Wotherspoon. Three dimensional pile finite element modelling using OpenSees. In *New Zealand Society for Earthquake Engineering Inc. - NZSEE Conference*, 2006. URL <http://www.nzsee.org.nz/db/2006/Paper26.pdf>.
- [366] A. M. Hassan. Winkler model for pile seismic analysis considering end constraints effects. *HBRC Journal*, 14(3):316–320, 2018. ISSN 1687-4048. doi: 10.1016/j.hbrcj.2017.02.001. URL <https://doi.org/10.1016/j.hbrcj.2017.02.001>.
- [367] M. M. Chiaramonte, P. Arduino, D. E. Lehman, and C. W. Roeder. Seismic analyses of conventional and improved marginal wharves. *Earthquake Engineering and Structural Dynamics*, 42:1435–1450, 2013. doi: 10.1002/eqe.2280. URL [http://www.stanford.edu/~sim\\$bakerjw/Publications/Baker\(2007\)Recordscaling,8PCEE.pdf%5Cnpapers2://publication/uuid/1498A307-A88B-4AAF-B3F7-E6B4B14F87C2](http://www.stanford.edu/~sim$bakerjw/Publications/Baker(2007)Recordscaling,8PCEE.pdf%5Cnpapers2://publication/uuid/1498A307-A88B-4AAF-B3F7-E6B4B14F87C2).
- [368] A. I. Panagiotidou, A. Vytiniotis, A. J. Whittle, and P. Candidate. Prediction of seismic response and damage mitigation for pile-supported wharf structures. In *XV Pan-American Conference on Soil Mechanics and Geotechnical Engineering*, 2015. ISBN 9781614996033. doi: 10.3233/978-1-61499-603-3-1184. URL <https://www.researchgate.net/publication/287202324>.

- [369] A. Shafieezadeh, R. DesRoches, S. D. Werner, and G. J. Rix. Seismic response of pile-supported container wharves. *TCLÉE 2009: Lifeline Earthquake Engineering in a Multihazard Environment*, 357(2004):83, 2009. doi: 10.1061/41050(357)83.
- [370] A. Shafieezadeh, R. DesRoches, G. J. Rix, and S. D. Werner. Seismic performance of pile-supported wharf structures considering soil-structure interaction in liquefied soil. *Earthquake Spectra*, 28(2):729–757, 2012. ISSN 87552930. doi: 10.1193/1.4000008.
- [371] L. Su, H. P. Wan, Y. Dong, D. M. Frangopol, and X. Z. Ling. Seismic fragility assessment of large-scale pile-supported wharf structures considering soil-pile interaction. *Engineering Structures*, 186(August 2018):270–281, 2019. ISSN 18737323. doi: 10.1016/j.engstruct.2019.02.022. URL <https://doi.org/10.1016/j.engstruct.2019.02.022>.
- [372] X. Lu, L. Xie, H. Guan, Y. Huang, and X. Lu. A shear wall element for nonlinear seismic analysis of super-tall buildings using OpenSees. *Finite Elements in Analysis and Design*, 98:14–25, 2015. ISSN 0168874X. doi: 10.1016/j.finel.2015.01.006. URL <http://dx.doi.org/10.1016/j.finel.2015.01.006>.
- [373] M. Shahnewaz, Y. Pan, M. Shahria Alam, and T. Tannert. Seismic fragility estimates for cross-laminated timber platform building. *Journal of Structural Engineering*, 146(12):04020256, 2020. ISSN 0733-9445. doi: 10.1061/(asce)st.1943-541x.0002834.
- [374] F. Vanin, A. Penna, and K. Beyer. Equivalent-frame modeling of two shaking table tests of masonry buildings accounting for their out-of-plane response. *Frontiers in Built Environment*, 6(April):1–18, 2020. ISSN 22973362. doi: 10.3389/fbuil.2020.00042.
- [375] S. V. Karafagka, S. D. Fotopoulou, and K. D. Pitilakis. Analytical tsunami fragility curves for seaport RC buildings and steel light frame warehouses. *Soil Dynamics and Earthquake Engineering*, 112(May):118–137, 2018. ISSN 02677261. doi: 10.1016/j.soildyn.2018.04.037. URL <https://doi.org/10.1016/j.soildyn.2018.04.037>.
- [376] X. G. Zeng, S. F. Jiang, X. C. Xu, and H. S. Huang. Numerical modeling of earthquake-damaged circular bridge columns repaired using combination of near-surface-mounted BFRP Bars with external BFRP sheets jacketing. *Materials*, 12(2), 2019. ISSN 19961944. doi: 10.3390/ma12020258.
- [377] Z. R. Feng, L. Su, H. P. Wan, Y. Luo, X. Z. Ling, and X. H. Wang. Three-dimensional finite element modelling for seismic response analysis of pile-supported bridges. *Structure and Infrastructure Engineering*, 15(12):1583–1596, 2019. ISSN 17448980. doi: 10.1080/15732479.2019.1625932. URL <https://doi.org/10.1080/15732479.2019.1625932>.
- [378] Y. Zhang, J. P. Conte, Z. Yang, A. Elgamal, J. Bielak, and G. Acero. Two-dimensional nonlinear earthquake response analysis of a bridge-foundation-ground system. *Earthquake Spectra*, 24(2): 343–386, 2008. ISSN 87552930. doi: 10.1193/1.2923925.

- [379] A. R. Barbosa, H. B. Mason, and K. Romney. SSI-Bridge: Soil-Bridge Interaction during long-duration earthquake motions. Technical Report Report No. 2012-OSU-0008, Oregon State University, Oregon, EUA, 2014.
- [380] L. Cressman. *Tsunami simulation using OpenSees: Validation of bridge response and exploration of shallow water flow*. Masters thesis, Oregon State University, 2015.
- [381] M. Zhu, I. Elkhetafi, and M. H. Scott. Validation of OpenSees for tsunami loading on bridge superstructures. *Journal of Bridge Engineering*, 23(4):1–10, 2018. ISSN 10840702. doi: 10.1061/(ASCE)BE.1943-5592.0001221.
- [382] T. J. Carey, H. B. Mason, A. R. Barbosa, and M. H. Scott. Multihazard earthquake and tsunami effects on soil-foundation-bridge systems. *Journal of Bridge Engineering*, 24(4), 2019. ISSN 10840702. doi: 10.1061/(ASCE)BE.1943-5592.0001353.
- [383] C. Reis, J. Figueiredo, S. Clain, R. Omira, M. A. Baptista, and J. M. Miranda. MUSCL vs MOOD techniques to solve the SWE in the framework of tsunami events. In *SYMCOMP 2017 - 3rd International Conference on Numerical and Symbolic Computation: Developments and Applications, Proceedings*, pages 189–204, Guimarães, Portugal, apr 2017. ISBN 9789899941038.
- [384] G. F. Carrier and H. P. Greenspan. Water waves of finite amplitude on a sloping beach. *Journal of Fluid Mechanics*, 4(1):97–109., 1958.
- [385] G. F. Carrier, T. T. Wu, and H. Yeh. Tsunami run-up and draw-down on a plane beach. *Journal of Fluid Mechanics*, 475(475):79–99, 2003. ISSN 00221120. doi: 10.1017/S0022112002002653.
- [386] J. F. Luis. Mirone: A multi-purpose tool for exploring grid data. *Computers and Geosciences*, 33(1):31–41, 2007. ISSN 00983004. doi: 10.1016/j.cageo.2006.05.005.
- [387] C. Altomare, J. M. Domínguez, A. J. C. Crespo, J. González-Cao, T. Suzuki, M. Gómez-Gesteira, and P. Troch. Long-crested wave generation and absorption for SPH-based DualSPHysics model. *Coastal Engineering*, 127(August 2016):37–54, 2017. ISSN 03783839. doi: 10.1016/j.coastaleng.2017.06.004.
- [388] K. M. Kleefsman, G. Fekken, A. Veldman, B. Iwanowski, and B. Buchner. A Volume-of-Fluid based simulation method for wave impact problems. *Journal of Computational Physics*, 206(1):363–393, 2005. ISSN 10902716. doi: 10.1016/j.jcp.2004.12.007.
- [389] Y. Tang, Y. Yin, K. Hill, V. Katiyar, A. Nasser, and T. Lai. Seismic risk assessment of Lisbon metropolitan area under a recurrence of the 1755 earthquake with tsunami inundation. In *15th World Conference on Earthquake Engineering (15WCEE)*, Lisbon, Portugal, 2012.
- [390] S. Ozawa, T. Nishimura, H. Suito, T. Kobayashi, M. Tobita, and T. Imakiire. Coseismic and postseismic slip of the 2011 magnitude-9 Tohoku-Oki earthquake. *Nature*, 475(7356):373–

- 377, 2011. ISSN 00280836. doi: 10.1038/nature10227. URL <http://dx.doi.org/10.1038/nature10227>.
- [391] Y. Yokota, K. Koketsu, Y. Fujii, K. Satake, S. Sakai, M. Shinohara, and T. Kanazawa. Joint inversion of strong motion, teleseismic, geodetic, and tsunami datasets for the rupture process of the 2011 Tohoku earthquake. *Geophysical Research Letters*, 38(24):1–5, 2011. ISSN 00948276. doi: 10.1029/2011GL050098.
- [392] N. Maercklin, G. Festa, S. Colombelli, and A. Zollo. Twin ruptures grew to build up the giant 2011 Tohoku, Japan, earthquake. *Scientific Reports*, 2, 2012. ISSN 20452322. doi: 10.1038/srep00709.
- [393] G. M. Atkinson and D. M. Boore. Empirical ground-motion relations for subduction-zone earthquakes and their application to Cascadia and other regions. *Bulletin of the Seismological Society of America*, 93(4):1703–1729, 2003. ISSN 00371106. doi: 10.1785/0120020156.
- [394] N. A. Abrahamson, W. J. Silva, and R. Kamai. Summary of the ASK14 ground motion relation for active crustal regions. *Earthquake Spectra*, 30(3):1025–1055, 2014. ISSN 87552930. doi: 10.1193/070913EQS198M.
- [395] D. M. Boore, J. P. Stewart, E. Seyhan, and G. M. Atkinson. NGA-West2 equations for predicting PGA, PGV, and 5shallow crustal earthquakes. *Earthquake Spectra*, 30(3):1057–1085, 2014. ISSN 87552930. doi: 10.1193/070113EQS184M.
- [396] K. W. Campbell and Y. Bozorgnia. NGA-West2 ground motion model for the average horizontal components of PGA, PGV, and 5 *Earthquake Spectra*, 30(3):1087–1114, 2014. ISSN 87552930. doi: 10.1193/062913EQS175M.
- [397] H. Si, S. Midorikawa, and T. Kishida. Development of NGA-sub ground-motion model of 5pseudo-spectral acceleration based on database for subduction earthquakes in Japan. *Earthquake Spectra*, 1(25), 2022. doi: 10.1177/87552930221090326.
- [398] H. Ghofrani, G. M. Atkinson, K. Goda, and K. Assatourians. Stochastic finite-fault simulations of the 2011 Tohoku, Japan, earthquake. *Bulletin of the Seismological Society of America*, 103(2 B): 1307–1320, 2013. ISSN 00371106. doi: 10.1785/0120120228.
- [399] Y. Y. Saurabh. Literature review on finite element meyhod. *International Journal of Enhanced Research in Science, Technology and Engineering*, 5(3):267–269, 2006. ISSN 02730979. doi: 10.1090/S0002-9904-1943-07818-4.
- [400] S. Park. *Understanding and mitigating tsunami risk for coastal structures and communities*. Phd thesis, Colorado State University, Fort Collins, Colorado, United States, 2011.
- [401] S. Popovics. A numerical approach to the complete stress-strain curve of concrete. *Cement and concrete research*, 3:583–599, 1973.

- [402] J. B. Mander, M. J. N. Priestley, and R. Park. Theoretical stress-strain model for confined concrete. *Journal of Structural Engineering*, 114(8):1804–1826, 1989.
- [403] F. C. Filippou, E. Popov, and V. Bertero. Effects of bond deterioration on hysteretic behavior of reinforced concrete joint (EERC 83-19). Technical report, Earthquake Engineering Research Center, University of California, Berkeley, Berkeley, California, 1983.
- [404] R. Carreño, K. H. Lotfizadeh, J. P. Conte, and J. I. Restrepo. Material model Parameters for the Giuffrè-Menegotto-Pinto uniaxial steel stress-strain model. *Journal of Structural Engineering*, 146(2):04019205, 2020. ISSN 0733-9445. doi: 10.1061/(asce)st.1943-541x.0002505.
- [405] R. von Mises. Methodik der festen korper im plastisch deformablen zustand. In *Nachrichten von der Koniglichen Gesellschaft der Wissenschaften zu Gottingen*, page 626. Niedersächsische Staats und Universitätsbibliothek Göttingen, Berlin, Germany, 1913.
- [406] D. Drucker and W. Prager. Soil mechanics and plastic analysis or limit design. *Quarterly of applied mathematics* 157-165., 10(2):157–165, 1952. ISSN 0033-569X. URL https://www.jstor.org/stable/43633942?seq=1#metadata_info_tab_contents.
- [407] H. Arnason, C. M. Petroff, and H. Yeh. Tsunami bore impingement onto a vertical column. *Journal of Disaster Research*, 4(6):391–403, 2009. ISSN 1881-2473. doi: 10.20965/jdr.2009.p0391.
- [408] R. H. Cross. Tsunami surge forces. *Journal of the waterways and harbors division*, 93(4):201–234, 1967.
- [409] T. S. Murty. *Seismic sea waves: Tsunamis*. Supply and Services Canada, Ottawa, Ontario, Canada, 1st editio edition, 1977. ISBN 0660005654. doi: 10.1038/132447c0.
- [410] J. Wienke and H. Oumeraci. Breaking wave impact force on a vertical and inclined slender pile - Theoretical and large-scale model investigations. *Coastal Engineering*, 52(5):435–462, 2005. ISSN 03783839. doi: 10.1016/j.coastaleng.2004.12.008.
- [411] I. N. Robertson, H. R. Riggs, K. Paczkowski, and A. Mohamed. Tsunami bore forces on walls. *Proceedings of the International Conference on Offshore Mechanics and Arctic Engineering - OMAE*, 1(January):395–403, 2011. doi: 10.1115/OMAE2011-49487.
- [412] T. Al-Faesly, D. Palermo, I. Nistor, and A. Cornett. Experimental modeling of extreme hydrodynamic forces on structural models. *International Journal of Protective Structures*, 2012. ISSN 20414196. doi: 10.1260/2041-4196.3.4.477.
- [413] S. Shafiei, B. W. Melville, and A. Y. Shamseldin. Instant tsunami bore pressure and force on a cylindrical structure. *Journal of Hydro-Environment Research*, 19:28–40, 2018. ISSN 15706443. doi: 10.1016/j.jher.2018.01.004.
- [414] J. R. Morison, M. P. O'Brien, J. W. Johnson, and S. A. Schaaf. The force exerted by surface waves on piles. *Journal of Petroleum Technology*, 2(05):149–154, 1950. ISSN 0149-2136. doi: 10.2118/950149-g.

- [415] H. Arnason. *Interactions between an incident bore and a free-standing coastal structure*. Phd thesis, University of Washington, 2005.
- [416] M. Potter, D. Wiggert, and B. Ramadan. *Mechanics of fluids*. Cengage Learn, 4th editio edition, 2011.
- [417] O. C. Blender. Blender - A 3D modelling and rendering package, 2018.
- [418] A. Vieira, O. García-Feal, J. M. Domínguez, A. J. C. Crespo, and M. Gómez-Gesteira. Graphical user interface for SPH codes: DesignSPPhysics. Universidad de Vigo, Vigo, Spain, 2017.
- [419] A. Apotsos, M. Buckley, G. Gelfenbaum, B. Jaffe, and D. Vatvani. Nearshore tsunami inundation model validation: Toward sediment transport applications. *Pure and Applied Geophysics*, 168(11): 2097–2119, 2011. ISSN 00334553. doi: 10.1007/s00024-011-0291-5.
- [420] A. Trimulyono and H. Hashimoto. Experimental validation of smoothed particle hydrodynamics on generation and propagation of water waves. *Journal of Marine Science and Engineering*, 7(1), 2019. ISSN 20771312. doi: 10.3390/jmse7010017.
- [421] E. Didier, D. R. C. B. Neves, R. Martins, and M. G. Neves. Modelling of hydrodynamics around an impermeable breakwater: Comparison between physical and SPH numerical modeling. *Revista de Engenharia Térmica*, 11(1-2):68, 2012. ISSN 1676-1790. doi: 10.5380/reterm.v11i1-2.62003.
- [422] I. N. Robertson. *Tsunami loads and effects. Guide to the tsunami design provisions of ASCE7-16*. American Society of Civil Engineers, Reston, Virginia, United States, 2020. ISBN 9780784414248.
- [423] S. Chen and W. Niu. On different calculation formulas of the pressure term in bi-phase SPH simulations. *AIP Advances*, 8(10), 2018. ISSN 21583226. doi: 10.1063/1.5052504. URL <http://dx.doi.org/10.1063/1.5052504>.
- [424] Pedro Bettencourt Correia. Estudo de impact ambiental da expansão do terminal de contentores (TXXI) do Porto de Sines (3 e 4 fases). Technical report, Nemus and Hidromod for APS S.A., Lisboa, 2014.
- [425] Pedro Bettencourt Correia. Estudo Prévio e Estudo de Impacte Ambiental do Terminal Vasco da Gama. Technical report, Consulmar, Nemus and Hidromod, Lisboa, 2018.
- [426] L. Matias, T. A. Cunha, A. Annunziato, M. A. Baptista, and F. Carrilho. Tsunamigenic earthquakes in the Gulf of Cadiz: fault model and recurrence. *Natural Hazards and Earth System Science*, 13(1):1–13, 2013. ISSN 15618633. doi: 10.5194/nhess-13-1-2013.
- [427] S. Custódio, N. A. Dias, F. Carrilho, E. Góngora, I. Del Rio, C. Marreiros, I. Morais, P. Alves, and L. Matias. Earthquakes in western Iberia: Improving the understanding of lithospheric deformation in a slowly deforming region. *Geophysical Journal International*, 203(1):127–145, 2015. ISSN 1365246X. doi: 10.1093/gji/ggv285.

- [428] A. C. Johnston. Seismic moment assessment of earthquakes in stable continental regions - III. New Madrid 1811-1812, Charleston 1886 and Lisbon 1755. *Geophysical Journal International*, 126:314–344, 1996.
- [429] Z. Zheng, X. Ma, Y. Ma, M. Perlin, and G. Dong. Numerical investigation of seismic-induced harbor oscillations. *Coastal Engineering*, 165(July 2020):103838, 2021. ISSN 03783839. doi: 10.1016/j.coastaleng.2020.103838. URL <https://doi.org/10.1016/j.coastaleng.2020.103838>.
- [430] V. S. Moreira. Seismotectonics of Portugal and its adjacent area in the Atlantic. *Tectonophysics*, 117(1-2):85–96, 1985. ISSN 00401951. doi: 10.1016/0040-1951(85)90238-0.
- [431] F. M. Rosas, J. C. Duarte, P. Terrinha, V. Valadares, and L. Matias. Morphotectonic characterization of major bathymetric lineaments in Gulf of Cadiz (Africa-Iberia plate boundary): Insights from analogue modelling experiments. *Marine Geology*, 261(1-4):33–47, 2009. ISSN 00253227. doi: 10.1016/j.margeo.2008.08.002.
- [432] T. A. Cunha, A. B. Watts, L. M. Pinheiro, and R. Myklebust. Seismic and gravity anomaly evidence of large-scale compressional deformation off SW Portugal. *Earth and Planetary Science Letters*, 293(1-2):171–179, 2010. ISSN 0012821X. doi: 10.1016/j.epsl.2010.01.047.
- [433] M. Bezzeghoud, J. F. Borges, and B. Caldeira. Seismicity and ground motion simulations of the SW Iberia Margin. In A. Silva, A. Reis, A. Fitas, J. Figueiredo, B. Caldeira, and M. Bezzeghoud, editors, *Jornadas de Física por ocasião da jubilação do Professor Rui Namorado Rosa*, pages 291–310. University of Évora, Évora, Portugal, 2010.
- [434] J. C. Duarte, F. M. Rosas, P. Terrinha, W. P. Schellart, D. Boutelier, M. A. Gutscher, and A. Ribeiro. Are subduction zones invading the Atlantic? Evidence from the southwest Iberia margin. *Geology*, 41(8):839–842, 2013. ISSN 00917613. doi: 10.1130/G34100.1.
- [435] P. Teves-Costa, J. Batlló, L. Matias, C. Catita, M. J. Jiménez, and M. García-Fernández. Maximum intensity maps (MIM) for Portugal mainland. *Journal of Seismology*, 23(3):417–440, 2019. ISSN 1573157X. doi: 10.1007/s10950-019-09814-5.
- [436] L. Somoza, T. Medialdea, P. Terrinha, A. Ramos, and J. T. Vázquez. Submarine active faults and morpho-tectonics around the Iberian Margins: Seismic and Tsunamis Hazards. *Frontiers in Earth Science*, 9(June):1–25, 2021. ISSN 22966463. doi: 10.3389/feart.2021.653639.
- [437] S. Martínez-Loriente, V. Sallarès, and E. Gràcia. The Horseshoe Abyssal plain thrust could be the source of the 1755 Lisbon earthquake and tsunami. *Communications Earth and Environment*, 2(1):1–9, 2021. ISSN 2662-4435. doi: 10.1038/s43247-021-00216-5. URL <http://dx.doi.org/10.1038/s43247-021-00216-5>.
- [438] C. S. Serra, S. Martínez-Loriente, E. Gràcia, R. Urgeles, L. Gómez de la Peña, F. E. Maesano, R. Basili, M. Volpe, F. Romano, A. Scala, A. Piatanesi, and S. Lorito. Sensitivity of tsunami scenarios to complex fault geometry and heterogeneous slip distribution: Case-studies for SW

- Iberia and NW Morocco. *Journal of Geophysical Research: Solid Earth*, 126(10):1–19, 2021. ISSN 21699356. doi: 10.1029/2021JB022127.
- [439] J. Milne. *Earthquakes and other Earth movements*. D. Appleton and Company, New York, EUA, the intern edition, 1886.
- [440] H. F. Reid. The Lisbon earthquake of November 1 1755. *Bulletin of the Seismological Society of America*, 4(2):53–80, 1914.
- [441] F. Machado. Contribuição para o estudo do terramoto de 1 de Novembro de 1755. *Revista da Faculdade de Ciências de Lisboa, 2ªa Série(Fasciculo 1)*:19–31, 1966.
- [442] A. Levret. The effects of the November 1, 1755 "Lisbon" earthquake in Morocco. *Tectonophysics*, 193(1-3):83–94, 1991. ISSN 00401951. doi: 10.1016/0040-1951(91)90190-4.
- [443] S. P. Vilanova, C. F. Nunes, and J. F. Fonseca. Lisbon 1755: A case of triggered onshore rupture? *Bulletin of the Seismological Society of America*, 93(5):2056–2068, 2003. ISSN 00371106. doi: 10.1785/0120020245.
- [444] M. A. Baptista, P. M. Miranda, J. M. Miranda, and L. A. Mendes-Victor. Rupture extent of the 1755 Lisbon earthquake inferred from numerical modeling of Tsunami data. *Physics and Chemistry of the Earth*, 21(1-2 SPEC. ISS.):65–70, 1996. ISSN 00791946. doi: 10.1016/s0079-1946(97)00011-6.
- [445] M. A. Baptista, P. Miranda, J. M. Miranda, L. M. Vitor, and L. A. Mendes-Victor. Constrains on the source of the 1755 Lisbon tsunami inferred from numerical modelling of historical data on the source of the 1755 Lisbon tsunamis. *Journal of Geodynamics*, 25(2):159–174, 1998. ISSN 02643707. doi: 10.1016/S0264-3707(97)00020-3.
- [446] M. A. Baptista, S. Heitor, J. M. Miranda, P. Miranda, and L. A. Mendes-Victor. The 1755 Lisbon tsunami; evaluation of the tsunami parameters. *Journal of Geodynamics*, 25(1-2):143–157, 1998. ISSN 02643707. doi: 10.1016/S0264-3707(97)00019-7. URL <http://linkinghub.elsevier.com/retrieve/pii/S0264370797000197>.
- [447] M. A. Baptista, J. M. Miranda, F. Chierici, and N. Zitellini. New study of the 1755 earthquake source based on multi-channel seismic survey data and tsunami modeling. *Natural Hazards and Earth System Science*, 3(5):333–340, feb 2003. ISSN 15618633.
- [448] N. Zitellini, L. A. Mendes, D. Cordoba, J. Danobeitia, R. Nicolich, G. Pellis, A. Ribeiro, R. Sartori, L. Torelli, R. Bartolomé, G. Bortoluzzi, A. Calafato, F. Carrilho, L. Casoni, E. Chierici, C. Corela, A. Correggiari, B. Delia Vedova, E. Gracia, P. Jornet, M. Landuzzi, M. Ligi, A. Magagnoli, G. Marozzi, L. Matias, D. Penitenti, P. Rodriguez, M. Rovere, P. Terrinha, L. Vigliotti, and A. Z. Ruiz. Source of 1755 lisbon earthquake and tsunami investigated. *Eos*, 82(26):285–291, 2001. ISSN 23249250. doi: 10.1029/EO082i026p00285-01.

- [449] P. Terrinha, L. M. Pinheiro, J. P. Henriët, L. Matias, M. Ivanov, J. H. Monteiro, A. Akhmetzhanov, A. Volkonskaya, T. A. Cunha, P. Shaskin, and M. Rovere. Tsunamigenic-seismogenic structures, neotectonics, sedimentary processes and slope instability on the southwest Portuguese Margin. *Marine Geology*, 195(1-4):55–73, 2003. ISSN 00253227. doi: 10.1016/S0025-3227(02)00682-5.
- [450] E. Gràcia, J. Danobeitia, J. Vergés, R. Bartolomé, and D. Córdoba. Crustal architecture and tectonic evolution of the Gulf of Cadiz (SW Iberian margin) at the convergence of the Eurasian and African plates. *Tectonics*, 22(4), 2003. ISSN 02787407. doi: 10.1029/2001tc901045.
- [451] E. Gràcia, R. Bartolomé, C. Lo Iacono, X. Moreno, S. Martínez Loriente, H. Perea, E. Masana, R. Pallàs, S. Díez, J. Dañobeitia, P. Terrinha, and N. Zitellini. Characterizing active faults and associated mass transport deposits in the South Iberian Margin (Alboran Sea and Gulf of Cadiz): On-fault and off-fault paleoseismic evidence. *Resúmenes de la 1ª Reunión Ibérica sobre Fallas Activas y Paleosismología*, pages 163–166, 2010.
- [452] M. A. Gutscher, J. Malod, J. P. Rehault, I. Contrucci, F. Klingelhoefer, L. A. Mendes-Victor, and W. Spakman. Evidence for active subduction beneath Gibraltar. *Geology*, 31(1):1071–1074, 2003. ISSN 19432682. doi: 10.1130/0091-7613-31.1.e22.
- [453] M. A. Gutscher, M. A. Baptista, and J. M. Miranda. The Gibraltar Arc seismogenic zone (part 2): Constraints on a shallow east dipping fault plane source for the 1755 Lisbon earthquake provided by tsunami modeling and seismic intensity. *Tectonophysics*, 426(1-2):153–166, 2006. ISSN 00401951. doi: 10.1016/j.tecto.2006.02.025.
- [454] A. Ribeiro, L. A. Mendes-Victor, J. M. L. C. Cabral, L. M. Matias, and P. A. G. Terrinha. The 1755 Lisbon earthquake and the beginning of closure of the Atlantic. *European Review*, 14(2):193–205, 2006. ISSN 10627987. doi: 10.1017/S1062798706000196.
- [455] R. Grandin, J. F. Borges, M. Bezzeghoud, B. Caldeira, and F. Carrilho. Simulations of strong ground motion in SW Iberia for the 1969 February 28 (Ms8.0) and the 1755 November 1 (M8.5) earthquakes - II. Strong ground motion simulations. *Geophysical Journal International*, 171(2): 807–822, 2007. ISSN 0956540X. doi: 10.1111/j.1365-246X.2007.03571.x.
- [456] R. M. Wood and A. Mignan. A phenomenological reconstruction of the Mw9 November 1st 1755 earthquake source. In L. M. Vitor, C. Sousa Oliveira, J. Azevedo, and A. Ribeiro, editors, *The 1755 Lisbon Earthquake: Revisited*, pages 121–146. Springer, Dordrecht, Netherlands, 2009. doi: 10.1007/978-1-4020-8609-0-8.
- [457] R. Barkan, U. S. ten Brink, and J. Lin. Far field tsunami simulations of the 1755 Lisbon earthquake: Implications for tsunami hazard to the U.S. East Coast and the Caribbean. *Marine Geology*, 264 (1-2):109–122, 2009. ISSN 00253227. doi: 10.1016/j.margeo.2008.10.010.
- [458] M. Wronna, R. Omira, and M. A. Baptista. Deterministic approach for multiple-source tsunami hazard assessment for Sines, Portugal. *Natural Hazards and Earth System Sciences*, 15(11): 2557–2568, 2015. ISSN 16849981. doi: 10.5194/nhess-15-2557-2015.

- [459] F. M. Rosas, J. C. Duarte, W. P. Schellart, R. Tomás, and P. Terrinha. Seismic potential of thrust-wrench tectonic interference between major active faults offshore SW Iberia: A new explanation for the 1755 Great Lisbon Earthquake? In J. C. Duarte and W. P. Schellart, editors, *Plate Boundaries and Natural Hazards, Geophysical Monograph*, chapter Chapter 9, pages 193–217. American Geophysical Union, first edit edition, 2016. ISBN 9781119054146. doi: 10.1002/9781119054146.ch9.
- [460] S. P. Vilanova, J. F. Fonseca, and C. S. Oliveira. Ground-motion models for seismic-hazard assessment in western iberia: Constraints from instrumental data and intensity observations. *Bulletin of the Seismological Society of America*, 102(1):169–184, 2012. ISSN 00371106. doi: 10.1785/0120110097.
- [461] V. Silva, H. Crowley, H. Varum, and R. Pinho. Seismic risk assessment for mainland Portugal. *Bulletin of Earthquake Engineering*, 13(2):429–457, 2014. ISSN 15731456. doi: 10.1007/s10518-014-9630-0.
- [462] V. Silva, M. Marques, J. M. Castro, and H. Varum. Development and application of a real-time loss estimation framework for Portugal. *Bulletin of Earthquake Engineering*, 13(9):2493–2516, 2015. ISSN 15731456. doi: 10.1007/s10518-015-9743-0.
- [463] G. M. Atkinson and D. M. Boore. Earthquake ground-motion prediction equations for eastern North America. *Bulletin of the Seismological Society of America*, 2006. ISSN 00371106. doi: 10.1785/0120050245.
- [464] S. Akkar and J. J. Bommer. Empirical equations for the prediction of PGA, PGV, and spectral accelerations in Europe, the mediterranean region, and the Middle East. *Seismological Research Letters*, 81(2):195–206, 2010. ISSN 08950695. doi: 10.1785/gssrl.81.2.195.
- [465] J. P. Stewart, J. Douglas, M. Javanbarg, Y. Bozorgnia, N. A. Abrahamson, D. M. Boore, K. W. Campbell, E. Delavaud, M. Erdik, and P. J. Stafford. Selection of ground motion prediction equations for the global earthquake model. *Earthquake Spectra*, 31(1):19–45, 2015. ISSN 87552930. doi: 10.1193/013013EQS017M.
- [466] G. M. Atkinson and D. M. Boore. Ground-motion relations for eastern north America. *Bulletin of the Seismological Society of America*, 85(5):1327–1342, 1995. ISSN 0037-1106, 1943-3573. doi: 10.1785/0120050245.
- [467] G. R. Toro, N. A. Abrahamson, and J. F. Schneider. Model of strong ground motions from earthquakes in central and eastern North America: Best estimates and uncertainties. *Seismological Research Letters*, 68(1):41–57, 1997. ISSN 00128287. doi: 10.1785/gssrl.68.1.41.
- [468] G. R. Toro. Modification of the Toro et al. (1997) attenuation equations for large magnitudes and short distances. Technical Report Risk Engineering Technical Report (2002), Risk Engineering, Inc., 2002.

- [469] K. W. Campbell. Prediction of strong ground motion using the hybrid empirical method and its use in the development of ground-motion (attenuation) relations in Eastern North America. *Bulletin of the Seismological Society of America*, 93(3):1012–1033, 2003. ISSN 00371106. doi: 10.1785/0120020002.
- [470] G. M. Atkinson and D. M. Boore. Modifications to existing ground-motion prediction equations in light of new data. *Bulletin of the Seismological Society of America*, 101(3):1121–1135, 2011. ISSN 00371106. doi: 10.1785/0120100270.
- [471] G. M. Atkinson. Ground-motion prediction equations for Eastern North America from a referenced empirical approach: Implications for epistemic uncertainty. *Bulletin of the Seismological Society of America*, 98(3):1304–1318, 2008. ISSN 00371106. doi: 10.1785/0120070199.
- [472] D. M. Boore and G. M. Atkinson. Ground-motion prediction equations for the average horizontal component of PGA, PGV, and 5 and 10.0 s. *Earthquake Spectra*, 24(1):99–138, 2008. ISSN 87552930. doi: 10.1193/1.2830434.
- [473] B. S. Chiou and R. R. Youngs. An NGA model for the average horizontal component of peak ground motion and response spectra. *Earthquake Spectra*, 24(1):173–215, 2008. ISSN 87552930. doi: 10.1193/1.2894832.
- [474] N. A. Abrahamson and W. Silva. Summary of the Abrahamson and Silva NGA ground-motion relations. *Earthquake Spectra*, 24(1):67–97, 2008. ISSN 87552930. doi: 10.1193/1.2924360.
- [475] G. M. Atkinson and M. Macias. Predicted ground motions for great interface earthquakes in the Cascadia Subduction zone. *Bulletin of the Seismological Society of America*, 99(3):1552–1578, 2009. ISSN 00371106. doi: 10.1785/0120080147.
- [476] D. Bindi, M. Massa, L. Lozano, G. Ameri, F. Pacor, R. Puglia, and P. Augliera. Pan-European ground-motion prediction equations for the average horizontal component of PGA, PGV, and 53.0 s using the RESORCE dataset. *Bulletin of Earthquake Engineering*, 12(1):391–430, 2014. ISSN 15731456. doi: 10.1007/s10518-013-9525-5.
- [477] S. Akkar, M. A. Sandikkaya, and J. J. Bommer. Empirical ground-motion models for point- and extended-source crustal earthquake scenarios in Europe and the Middle East. *Bulletin of Earthquake Engineering*, 12(1):359–387, 2014. ISSN 15731456. doi: 10.1007/s10518-013-9461-4.
- [478] N. A. Abrahamson, N. Gregor, and K. Addo. BC hydro ground motion prediction. *Earthquake S*, 32(1):23–44, 2016.
- [479] N. A. Abrahamson, N. Kuehn, Z. Gülerce, N. Gregor, Y. Bozorgnia, G. A. Parker, J. P. Stewart, B. Chiou, I. M. Idriss, K. Campbell, and R. Youngs. Update of the BC Hydro Subduction Ground-Motion Model using the NGA-Subduction Dataset. Technical report, Pacific Earthquake Engineering Research Center, Berkeley, California, 2018.

- [480] B. S. J. Chiou and R. R. Youngs. Update of the Chiou and Youngs NGA model for the average horizontal component of peak ground motion and response spectra. *Earthquake Spectra*, 30(3): 1117–1153, 2014. ISSN 87552930. doi: 10.1193/072813EQS219M.
- [481] C. Cauzzi, E. Faccioli, M. Vanini, and A. Bianchini. Updated predictive equations for broadband (0.01–10 s) horizontal response spectra and peak ground motions, based on a global dataset of digital acceleration records. *Bulletin of Earthquake Engineering*, 13(6):1587–1612, 2015. ISSN 15731456. doi: 10.1007/s10518-014-9685-y. URL <http://dx.doi.org/10.1007/s10518-014-9685-y>.
- [482] S. P. Vilanova, J. Narciso, J. P. Carvalho, I. Lopes, M. Quinta-Ferreira, C. C. Pinto, R. Moura, J. F. Borges, and E. S. Nemser. Developing a geologically-based Vs30 site-conditions model for Portugal: Methodology and assessment of the performance of proxies. *Bulletin of the Seismological Society of America*, 108(1):322–337, 2018. doi: 10.1785/0120170213.
- [483] M. D. Trifunac and A. G. Brady. On the correlation of seismic intensity scales with the peaks of recorded strong ground motion. *Bulletin of the Seismological Society of America*, 65(1):139–162, 1975.
- [484] C. Pro, E. Buforn, A. Udías, J. F. Borges, and C. Sousa Oliveira. Study of the PGV, strong motion and intensity distribution of the February 1969 (Ms 8.0) offshore Cape St. Vincent (Portugal) earthquake using synthetic ground velocities. *Pure and Applied Geophysics*, 177(4):1809–1829, 2020. ISSN 14209136. doi: 10.1007/s00024-019-02401-2.
- [485] L. Faenza and A. Michelini. Regression analysis of MCS intensity and ground motion parameters in Italy and its application in ShakeMap. *Geophysical Journal International*, 180(3):1138–1152, 2010. ISSN 0956540X. doi: 10.1111/j.1365-246X.2009.04467.x.
- [486] M. A. Zanini, L. Hofer, and F. Faleschini. Reversible ground motion-to-intensity conversion equations based on the EMS-98 scale. *Engineering Structures*, 180(March 2018):310–320, 2019. ISSN 18737323. doi: 10.1016/j.engstruct.2018.11.032. URL <https://doi.org/10.1016/j.engstruct.2018.11.032>.
- [487] A. A. Gomez-Capera, M. D’Amico, G. Lanzano, M. Locati, and M. Santulin. Relationships between ground motion parameters and macroseismic intensity for Italy. *Bulletin of Earthquake Engineering*, 18(11):5143–5164, 2020. ISSN 15731456. doi: 10.1007/s10518-020-00905-0.
- [488] T. Elmrabet, A. Levret, M. Ramdani, and B. Tadili. Historical seismicity in Morocco: Methodological aspects and cases of multidisciplinary evaluation. Technical report, Symposium on the seismicity seismotectonic and seismic risk of the Ibero-Maghrebian region, Madrid, Spain, 1990.
- [489] E. Buforn, C. López-Sánchez, L. Lozano, J. M. Martínez-Solares, S. Cesca, C. S. Oliveira, and A. Udías. Re-evaluation of seismic intensities and relocation of 1969 Saint Vincent Cape seismic sequence: A comparison with the 1755 Lisbon earthquake. *Pure and Applied Geophysics*, 177(4):1781–1800, 2020. ISSN 14209136. doi: 10.1007/s00024-019-02336-8.

- [490] J. J. Bommer, S. Scott, and S. K. Sarma. Hazard-consistent earthquake scenarios. *Soil Dynamics and Earthquake Engineering*, 19(4):219–231, 2000. doi: 10.1016/S0267-7261(00)00012-9.
- [491] P. G. Silva, J. Elez, R. Pérez-López, J. L. Giner-Robles, P. V. Gómez-Diego, E. Roquero, M. Á. Rodríguez-Pascua, and T. Bardají. The AD 1755 Lisbon earthquake-tsunami: Seismic source modelling from the analysis of ESI-07 environmental data. *Quaternary International*, 2021. ISSN 10406182. doi: 10.1016/j.quaint.2021.11.006.
- [492] A. Suppasri, I. Charvet, K. Imai, and F. Imamura. Fragility curves based on data from the 2011 Tohoku-oki Tsunami in Ishinomaki City, with discussion of parameters influencing building damage. *Earthquake Spectra*, 31(2):841–868, 2015. ISSN 87552930. doi: 10.1193/053013EQS138M.
- [493] J. Song, R. D. E. Risi, and K. Goda. Probabilistic tsunami loss estimation using momentum flux-based tsunami fragility functions. In *16th European Conference of Earthquake Engineering*, pages 1–12, Thessaloniki, Greece, 2018.
- [494] A. Ribeiro, J. Cabral, and L. Matias. Stress pattern in Portugal mainland and the adjacent Atlantic region West Iberia. *Tectonics*, 15(2):641–659, 1996. doi: 10.1029/95tc03683.
- [495] G. Zonno, A. Carvalho, G. Franceschina, A. Akinci, A. Campos-Costa, E. Coelho, G. Cultrera, F. Pacor, V. Pessina, and M. Cocco. Simulating earthquake scenarios using finite-fault model for the Metropolitan Area of Lisbon (MAL). In L. A. Mendes-Victor, C. S. Oliveira, J. Azevedo, and A. Ribeiro, editors, *250th Anniversary of the 1755 Lisbon Earthquake*. Springer Science and Business Media, Milan, Italy, 2005.
- [496] A. Carvalho, A. C. Costa, C. Sousa Oliveira, and C. S. Oliveira. A finite-fault modeling of the 1755 Lisbon earthquake sources. *Geotechnical, Geological and Earthquake Engineering*, 7 (December):433–454, 2009. ISSN 15736059. doi: 10.1007/978-1-4020-8609-0_28.
- [497] A. Carvalho, C. Reis, and D. Vales. Source and high-frequency decay parameters for the Azores region for stochastic finite-fault ground motion simulations. *Bulletin of Earthquake Engineering*, 14(7):1885–1902, 2016. ISSN 15731456. doi: 10.1007/s10518-015-9842-y.
- [498] K. A. Bani-Hani and A. I. Malkawi. A Multi-step approach to generate response-spectrum-compatible artificial earthquake accelerograms. *Soil Dynamics and Earthquake Engineering*, 97: 117–132, 2017. ISSN 02677261. doi: 10.1016/j.soildyn.2017.03.012. URL <http://dx.doi.org/10.1016/j.soildyn.2017.03.012>.
- [499] J. Vemuri, S. Kolluru, and S. Chopra. Surface level synthetic ground motions for M7.6 2001 Gujarat earthquake. *Geosciences (Switzerland)*, 8(12), 2018. ISSN 20763263. doi: 10.3390/geosciences8120429.
- [500] D. C. Sanchez, Y. B. Heredia, O. F. G. Matos, and M. L. Arias. Strong ground motion simulation by using signals from moderate earthquakes in the Oriente fault zone. *Mineria y Geología*, 37(3): 253–273, 2021.

- [501] I. M. I. Qeshta, M. J. Hashemi, M. R. Hashemi, R. J. Gravina, and S. Setunge. Development of fragility functions for rigid-frame bridges subjected to tsunami-induced hydrodynamic forces. *Structure and Infrastructure Engineering*, 0(0):1–18, 2021. ISSN 1573-2479. doi: 10.1080/15732479.2021.1892774. URL <https://doi.org/10.1080/15732479.2021.1892774>.
- [502] C. Petrone, T. Rossetto, K. Goda, and I. Eames. Tsunami analysis of structures: Comparison among different approaches. In *16th World Conference on Earthquake, 16WCEE*, page Paper No. 3706, Santiago, Chile, jan 2017.
- [503] T. Tomiczek, A. Wyman, H. Park, and D. T. Cox. Modified Goda equations to predict pressure distribution and horizontal forces for design of elevated coastal structures. *Journal of Waterway, Port, Coastal, and Ocean Engineering*, 145(6):1–16, 2019. ISSN 0733-950X. doi: 10.1061/(asce)ww.1943-5460.0000527.
- [504] Proman. Empreitada de construção para a expansão do Terminal XXI - Fase 2, 2013.
- [505] M. Pipa. *Ductilidade de elementos de betão armado sujeitos a acções cíclicas - Influência das características mecânicas das armaduras*. Phd, Instituto Superior Técnico, Laboratório Nacional de Engenharia Civil, 1993.
- [506] C. E. Synolakis and U. Kanoglu. The Fukushima accident was preventable. *Philosophical Transactions of the Royal Society A*, 373(2053), 2015.

Appendix A

Eulerian SW-FV benchmarking: Tohoku-oki, 2011 tsunami

The M_w 9.0 Tohoku-Oki earthquake occurred in 2011 March 11 along the Japan Trench, causing strong ground motions, a devastating tsunami and melt-down of three nuclear power plants along northeast Japan [151, 152, 319, 506]. During the tsunami, more than 250 instruments recorded waves elevation [297]. Fig. A.1 shows the location of some tide gauges, GPS wave gauges and Deep Ocean Assessment of Tsunami (DART) stations, that were used to benchmark the SW-FV tool. Fig. A.3 depicts the correlation between instrumentally-recorded data acquired along the Japanese territory and numerically solutions using SW-FV numerical tool.

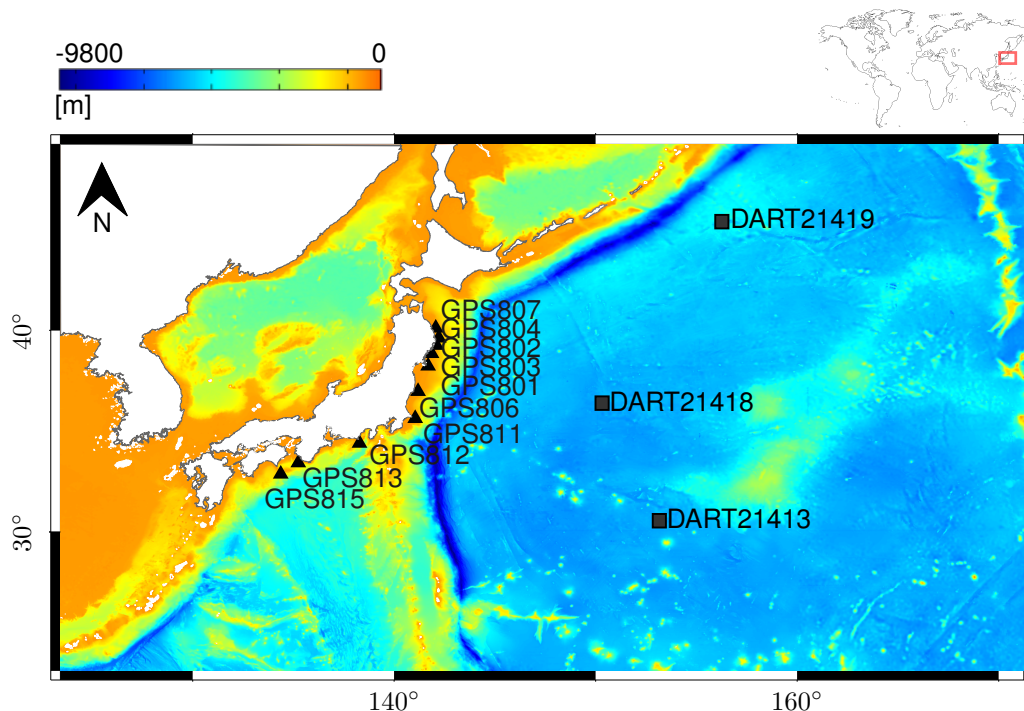
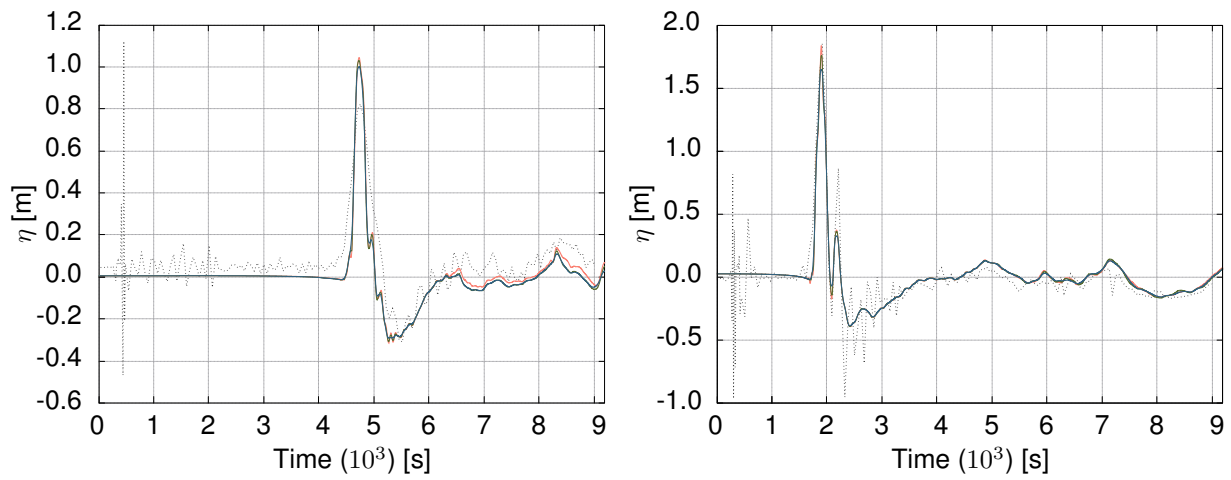
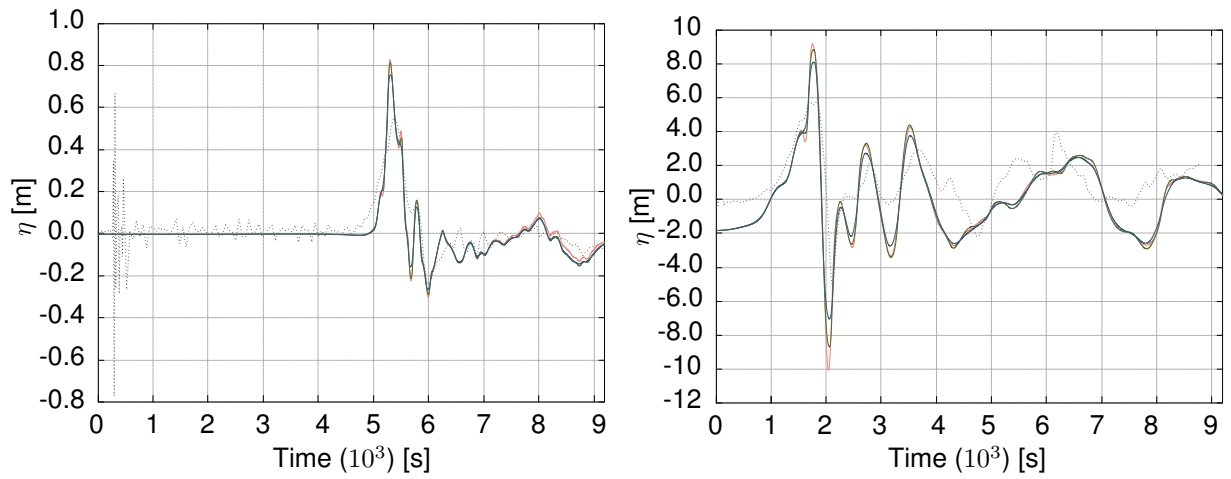


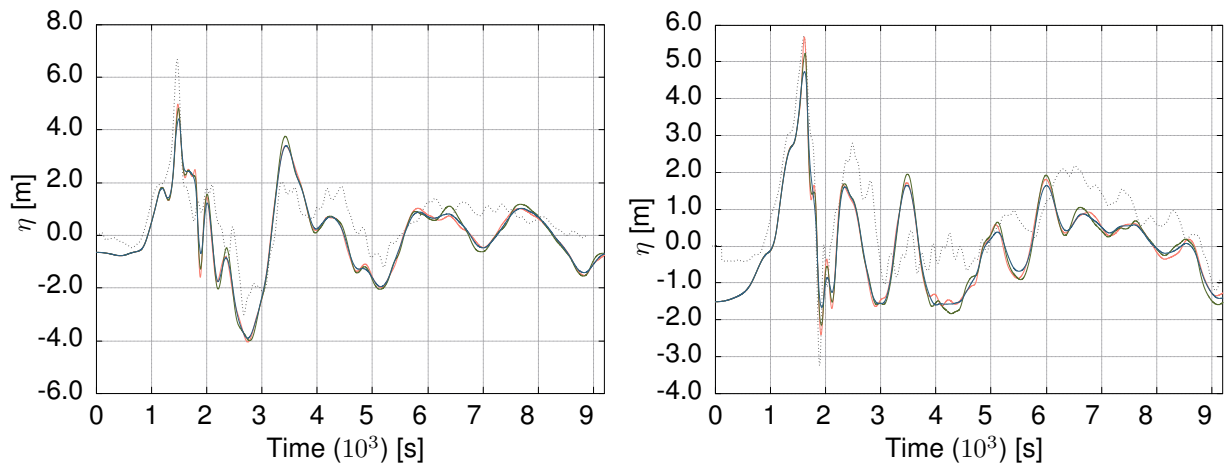
Figure A.1: Validation of Eulerian SW-FV scheme: Tohoku-Oki, 2011 tsunami. Location of ocean DART and coastal GPS buoys instruments.



(a) Left: oceanic DART21413 buoy and VG_{21413} solution. Right: oceanic DART21418 and VG_{21418} solution.



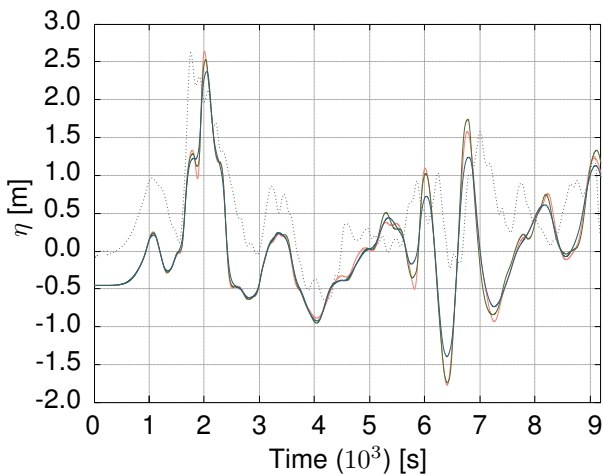
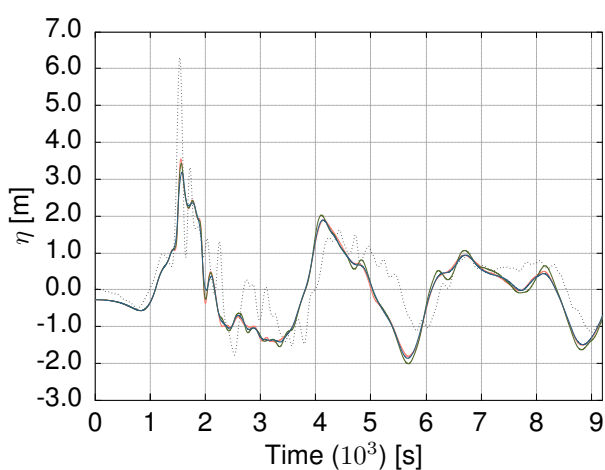
(b) Left: oceanic DART21419 buoy and VG_{21413} solution. Right: coastal GPS801 Central Miyagi and VG_{801} solution.



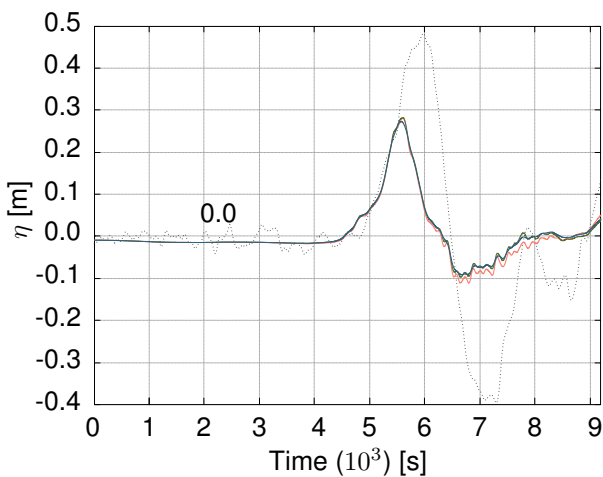
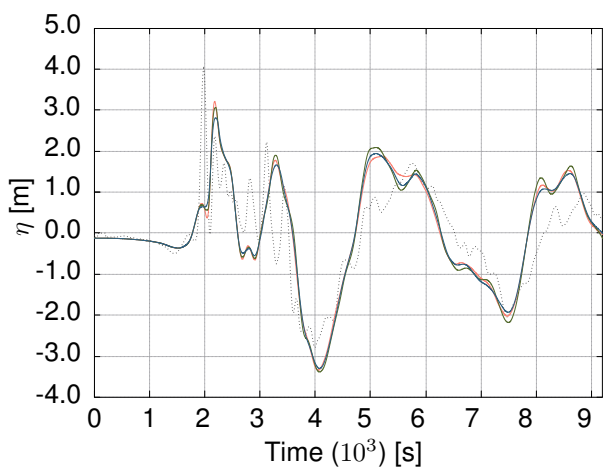
(c) Left: coastal GPS802 South Iwate and VG_{802} solution. Right: coastal GPS804 North Miyagi and VG_{804} solution.

KEY: Recorded — MOOD — MUSCL vanLeer — MUSCL minmod

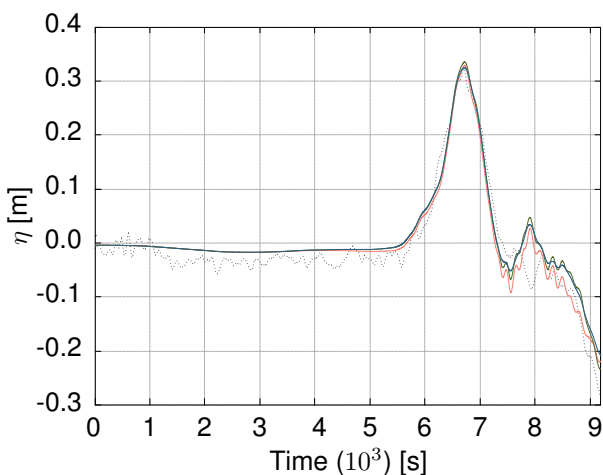
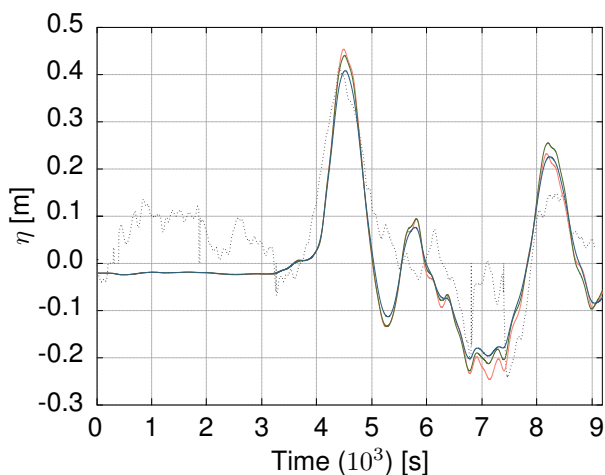
Figure A.2: Validation of Eulerian SW-FV scheme: correlation between instrumentally recorded data and numerical solutions computed at the correspondent VG using MUSCL, *minmod* and *vanLeer*, and MOOD techniques. Cont. →



(a) Left: coastal GPS805 Central Iwate and VG_{805} solution. Right: coastal GPS806 Fukushima and VG_{806} solution.



(b) Left: coastal GPS807 North Iwate and VG_{807} solution. Right: coastal GPS811 Mie-Owase and VG_{811} solution.



(c) Left: coastal GPS812 Shizuoka-Omaezaki and VG_{812} solution. Right: coastal GPS813 Southwest Wakayama and VG_{813} solution.

KEY: Recorded — MOOD — MUSCL vanLeer — MUSCL minmod

Figure A.3: Validation of Eulerian SW-FV scheme: correlation between instrumentally recorded data and numerical solutions computed at the correspondent VG using MUSCL, *minmod* and *vanLeer*, and MOOD techniques.

Appendix B

Coupled Eulerian-Lagrangian benchmarking: OSU experimental campaign

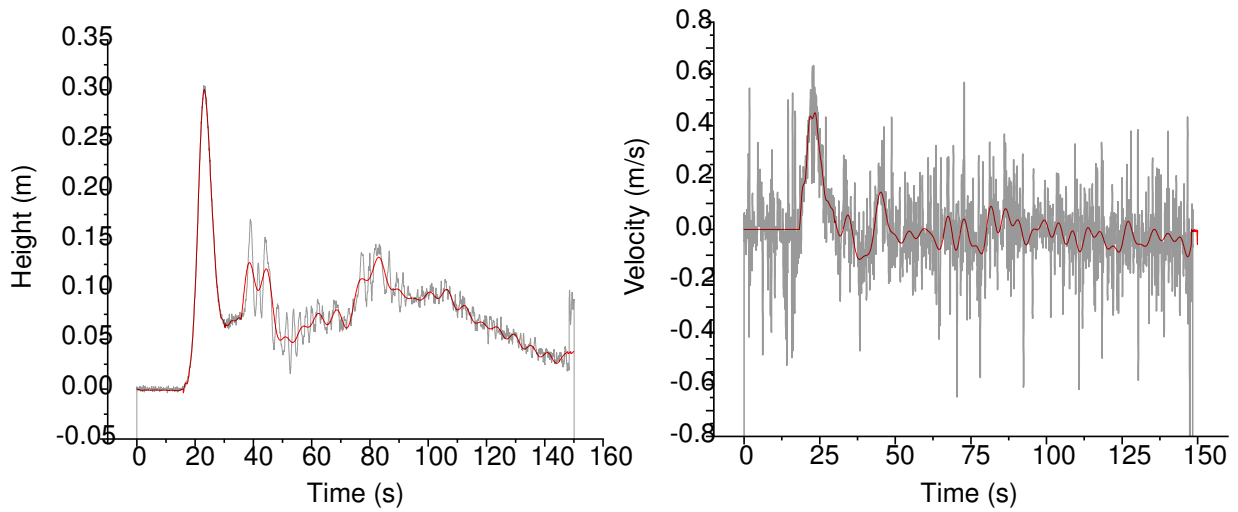
B.1 Instrumental setup

The instrumental configuration of the experimental campaign performed at the large wave flume of the Hinsdale Wave Research Laboratory, Oregon State University, is resumed in Table B.1. All locations of the instruments are with respect to the flume reference coordinate system.

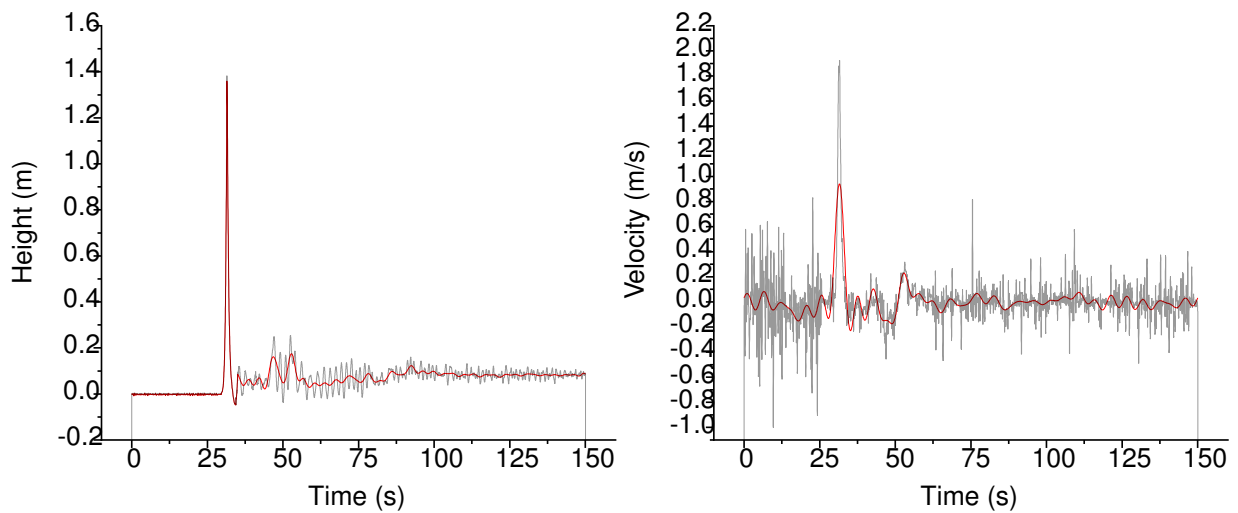
B.2 Measurement uncertainty

The tests and data acquisition were repeatedly trialed for each wave case. The average data concerning the waves elevation, pressures, and forces, present small deviations in the measurements acquired in the different trials. Conversely, the inherent difficulty of velocity data acquisition partially constrained the quality of the correlations that were possible due to the noise in the velocity records. To limit the uncertainty added to the validation process of the algorithms to assess hydrodynamic quantities and forces/pressures, flow height and velocity records were subjected to Fourier filters specifically design to preserve the main signal while eliminating the high frequencies aiming to assess the validity of the recorded data. Using both records, one with high quality aquisition and the other compromised with noise, is possible to correlate the general fitting between recorded and filtered data. Fig. B.1 shows the comparison between the average recorded and the filtered data revealing a general fitting of the time-series. However, observing the flow height correlations is identified an accentuated smoothing of the signal, i.e., applying filters might often lead to lose information detail on both flow height and velocity. Thus, it was considered preferable to maintain the use of unfiltered laboratorial records in the benchmark process. Therefore, the physical data considered is the average value of all

trials, complemented with the respective standard deviation.



(a) Flow height (left) and velocity (right) of the unbroken-wave case.



(b) Flow height (left) and velocity (right) of the broken-wave case.

Figure B.1: Experimental setup: considerations for the benchmarking. Correlation between recorded and filtered data.

The uncertainty in measurements of wave heights, pressure, and forces of test trails for the two unbroken- and broken-wave conditions were evaluated. The coefficients of variation, COVs, of maximum wave heights, pressure and wave-induced forces on the structure are presented in Table B.2.

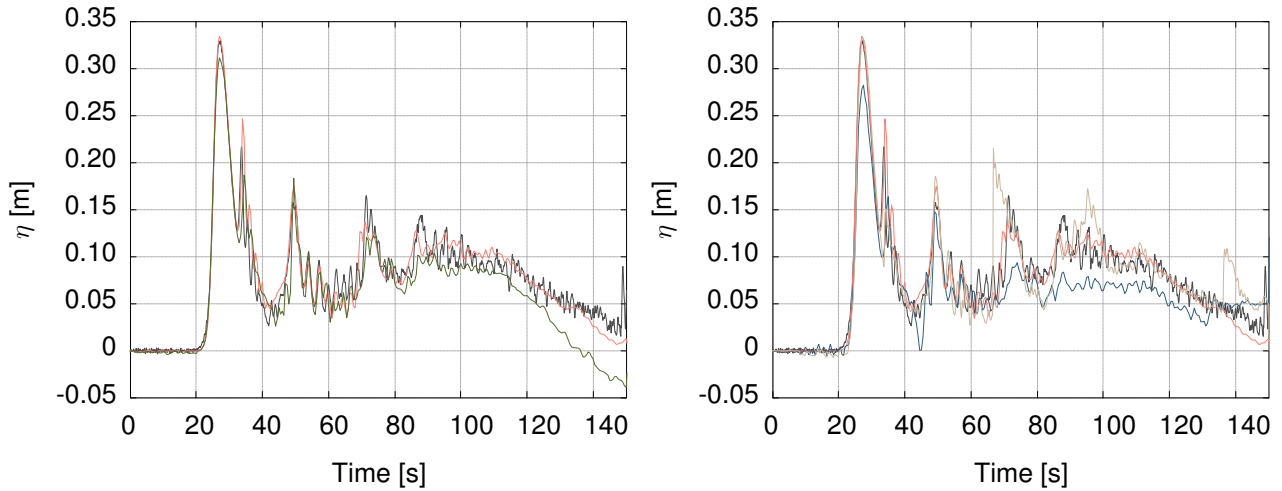
The experimentally acquired data is available in a repository [175] online in accordance with funder data retention policies. More information on the facility can be found at <https://wave.oregonstate.edu/large-wave-flume>.

B.3 Dirichlet boundary conditions

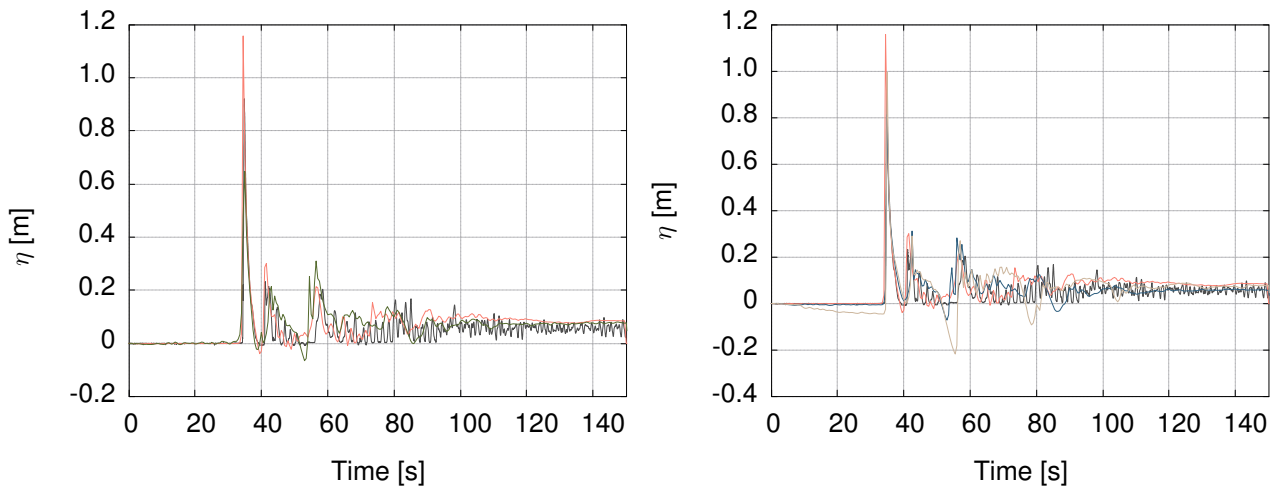
Three time-histories of the wave height and velocity were adopted to prescribe an open boundary condition at $x = 13\text{ m}$, corresponding to WG1 location in the experimental setup. The first one uses

the hydrodynamic quantities computed by NS-SPH stand-alone method to initialize the partial domain after $x = 13\text{ m}$. The second and the third BC are prescribed using data instrumentally recorded by WG1 and ADV1, and numerically estimated data using SW-FV method. The 2D partial NE-SPH domain was discretized into $\Delta p = 0.03\text{ m}$. The analysis was developed using solutions of free surface elevation in the flume, WG2, near the elevated structure, USWG1, and after the structure, USWG5.

Figs. B.2 to B.4 depict the correlation between the various solutions of free surface elevation.



(a) Simulation of the partial domain initiated by OBC using hydrodynamic quantities acquired from NS-SPH solution (left), and instrumentally-recorded data from the laboratorial campaign and SW-FV solution (right). Unbroken wave case.



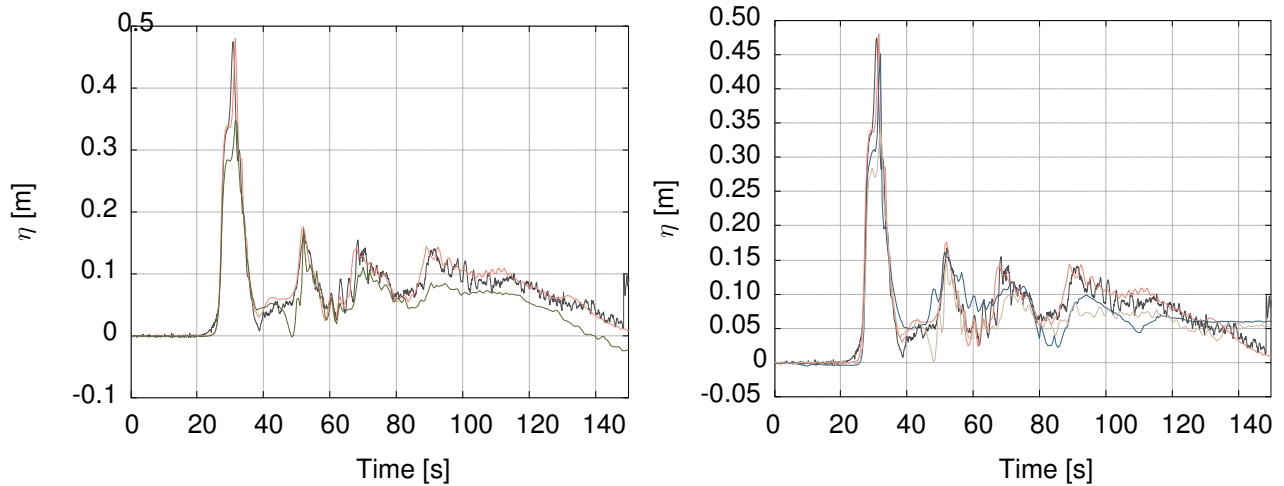
(b) Simulation of the partial domain initiated by OBC using hydrodynamic quantities acquired from NS-SPH solution (left), and instrumentally-recorded data from the laboratorial campaign and SW-FV solution (right). Broken wave case.

KEY: — Recorded — NS-SPH — SPH-SPH — Lab-SPH — FV-SPH

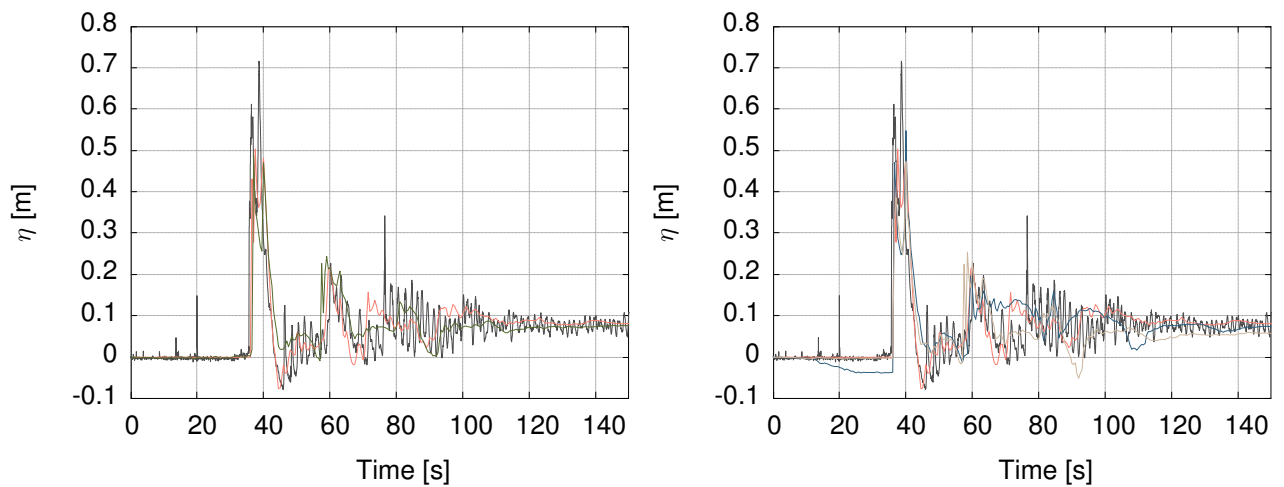
Figure B.2: Physical benchmarking. Influence of prescribing OBC to initiate partial domains of NS-SPH models. Free surface elevation in the flume, WG2, due to unbroken and broken waves.

The numerical solutions obtained from full and partial SPH models show that coupled models tend to undervalue the free surface elevation estimates. The correlation also highlights a cumulative loss along the simulation time, more evident in the solutions of the unbroken wave case.

The correlation of the solutions obtained from the coupled models using recorded and numerical SW-FV data, show the influence of the data used to prescribe the open boundary condition. The OBC



(a) Simulation of the partial domain initiated by OBC using hydrodynamic quantities acquired from NS-SPH solution (left), and instrumentally-recorded data from the laboratorial campaign and SW-FV solution (right). Unbroken wave case.

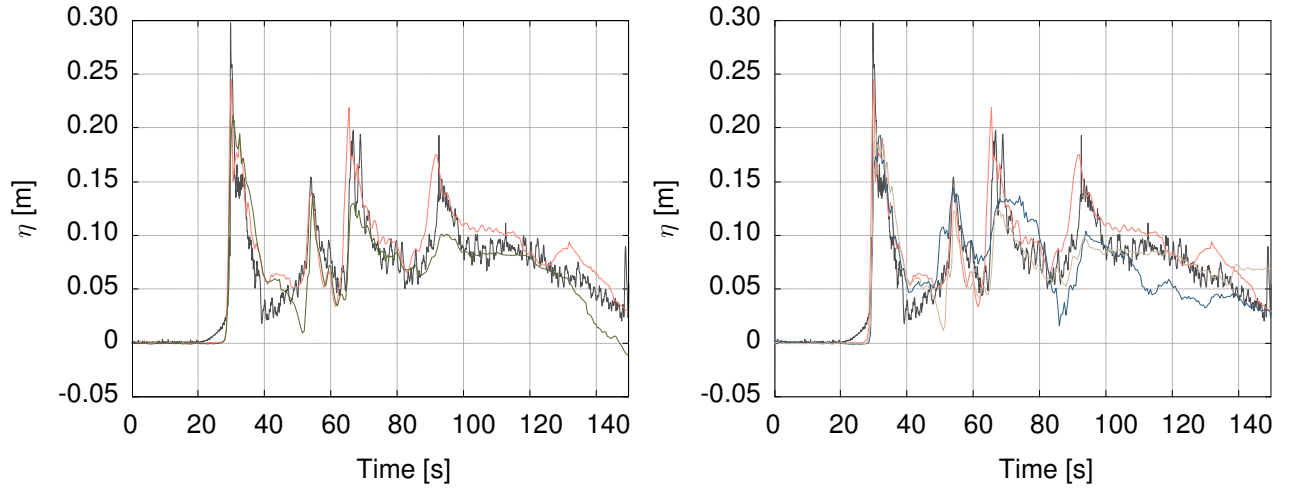


(b) Simulation of the partial domain initiated by OBC using hydrodynamic quantities acquired from NS-SPH solution (left), and instrumentally-recorded data from the laboratorial campaign and SW-FV solution (right). Broken wave case.

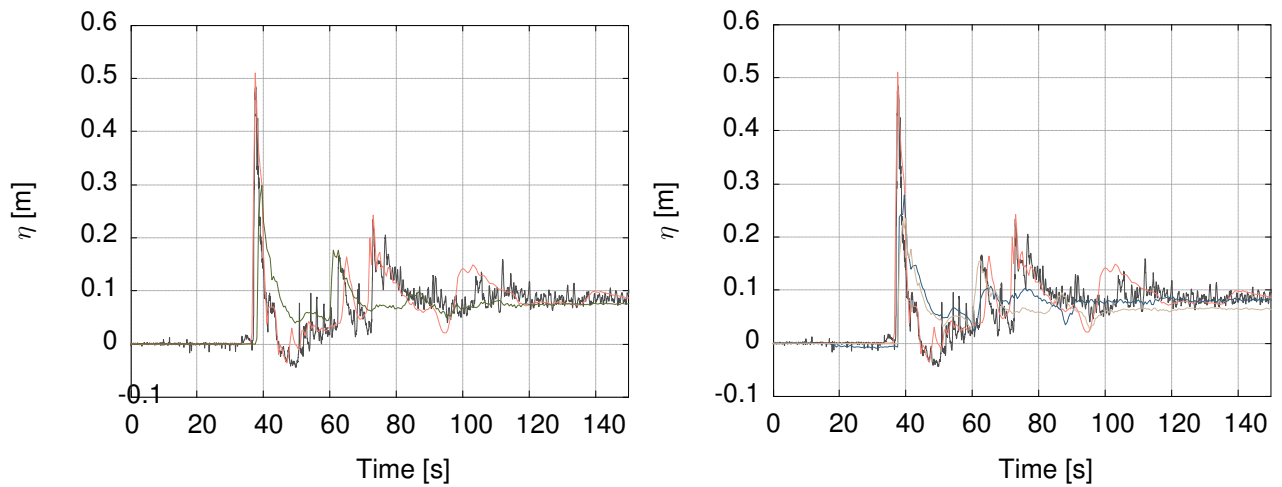
KEY: — Recorded — NS-SPH — SPH-SPH — Lab-SPH — FV-SPH

Figure B.3: Physical benchmarking. Influence of prescribing OBC to initiate partial domains of NS-SPH models. Free surface elevation near the elevated structure, USWG1, due to unbroken and broken waves.

using instrumentally recorded data from the laboratorial campaign promote the numerical solutions best fitting the free surface quantities measured by the WG and USWG sensors. Nonetheless, a disclaimer regarding the quality of the solutions is mandatory to show the coupled method potential. The Dirichlet boundary conditions are prescribed using hydrodynamic quantities, free surface and flow velocity. Since the acquisition of the flow velocity represented a challenging task during the laboratorial campaign (see standard deviations from the different trials of velocity acquisition represented in Fig. 5.13(b), Section 5.3), the quality of the solution is partially compromised due to the ADV1 input in the OBC. The second best solution was obtained from the model using the NS-SPH numerical quantities in the OBC, and finally, the solution using SW-FV data to prescribe the OBC. The lack of diffusion effects in FV represents an inherent constrain of the method. On the contrary, SPH considers the numeric diffusion and the physical viscosity in its formulation, leading to more accurate reproductions of the hydrodynamic effects. Moreover, the solution using the SW-FV data in the OBC is



(a) Simulation of the partial domain initiated by OBC using hydrodynamic quantities acquired from NS-SPH solution (left), and instrumentally-recorded data from the laboratorial campaign and SW-FV solution (right). Unbroken wave case.



(b) Simulation of the partial domain initiated by OBC using hydrodynamic quantities acquired from NS-SPH solution (left), and instrumentally-recorded data from the laboratorial campaign and SW-FV solution (right). Broken wave case.

KEY: — Recorded — NS-SPH — SPH-SPH — Lab-SPH — FV-SPH

Figure B.4: Physical benchmarking. Influence of prescribing OBC to initiate partial domains of NS-SPH models. Free surface elevation after the elevated structure, USWG5, due to unbroken and broken waves.

assembled by three sub-domains. The first part of the wave generation using a piston wave-maker is computed by NE-SPH ($x = [0, 2] m$), followed by a SW-FV sub-domain (until $x = 13 m$) and then is finalized returning to another sub-domain solved by SPH-NSE approach. As previously referred, the number of interpolations in the form of Dirichlet boundary condition influence the quality of the solution. The transference of information between SW-FV and NS-SPH is more adequate when the SPH satisfies the physical wave characteristics for the SWE system, i.e. long and deep waves.

In conclusion, the initialization of the NS-SPH model using an OBC can lead to a slight underestimation of the waves heights, and consequently, the pressure exerted against the structure. The analysis of the OBC influencing the quality of the solutions focused only on the free surface elevation estimates due to the challenging instrumental acquisition of velocity, which limited the validation of the velocity and its derivative quantities, such as hydrodynamic forces and pressures.

To provide a simultaneous accurate and fast solution, the implementation of the hybridization point

should balance distances: away from the influence of the reflected waves an the breaking-wave area, but as close as possible to the “complex flow” area, to decrease the SPH domain and, consequently, the computational costs (memory and time) of simulation.

The use of Dirichlet BC to subdivide numerical simulations into sub-domains solvable by numerical schemes with different levels of sophistication constitutes a potential technique to optimize the trade-offs between numerical accuracy and costs.

Table B.1: Experimental setup: instrumental setup.

| Description | Instrument | Location | | | Measurement |
|--------------------------------|------------|----------|--------|-------|--|
| | | x [m] | y [m] | z [m] | |
| Wave gauge 1 | WG1 | 14.169 | -1.388 | - | Free-surface level along the flume |
| Wave gauge 2 | WG2 | 32.443 | -1.379 | - | Free-surface level along the flume |
| Wave gauge 3 | WG3 | 36.099 | -1.368 | | Free-surface level along the flume |
| Ultrasasonic wave gauge 1 | USWG1 | 39.700 | -1.382 | 3.652 | Free-surface level near the structure |
| Ultrasasonic wave gauge 2 | USWG2 | 43.214 | -1.377 | 3.348 | Free-surface level near the structure |
| Ultrasasonic wave gauge 3 | USWG3 | 43.212 | -0.012 | 3.322 | Free-surface level near the structure |
| Ultrasasonic wave gauge 4 | USWG4 | 44.290 | -1.306 | 3.412 | Free-surface level near the structure |
| Ultrasasonic wave gauge 5 | USWG5 | 45.685 | -1.375 | 3.314 | Free-surface level after the structure |
| Ultrasasonic wave gauge 6 | USWG6 | 45.680 | -0.003 | 3.371 | Free-surface level after the structure |
| Load cell 1 | LC1 | 43.862 | -0.445 | 2.122 | Streamwise force in the columns |
| Load cell 2 | LC2 | 44.671 | 0.450 | 2.122 | Streamwise force in the columns |
| Load cell 3 | LC3 | 43.890 | -0.766 | 2.849 | Transverse force in the specimen |
| Load cell 4 | LC4 | 44.757 | -0.765 | 2.843 | Transverse force in the specimen |
| Load cell 5 | LC5 | 45.127 | -0.001 | 2.473 | Horizontal force in the specimen |
| Load cell 6 | LC6 | 43.840 | -0.426 | 2.662 | Vertical force in the specimen |
| Load cell 7 | LC7 | 43.841 | 0.433 | 2.663 | Vertical force in the specimen |
| Load cell 8 | LC8 | 44.710 | -0.426 | 2.662 | Vertical force in the specimen |
| Load cell 9 | LC9 | 44.711 | 0.433 | 2.663 | Vertical force in the specimen |
| Acoustic Doppler velocimeter 1 | ADV1 | 13.971 | -1.425 | 0.632 | Flow velocity in the flume |
| Acoustic Doppler velocimeter 2 | ADV2 | 35.895 | -1.418 | 1.539 | Flow velocity in the flume |
| Acoustic Doppler velocimeter 3 | ADV3 | 43.214 | -0.501 | 1.753 | Flow velocity around the structure |
| Acoustic Doppler velocimeter 4 | ADV4 | 43.221 | 0.494 | 1.753 | Flow velocity around the structure |
| Acoustic Doppler velocimeter 5 | ADV5 | 44.265 | -1.386 | 1.761 | Flow velocity around the structure |
| Acoustic Doppler velocimeter 6 | ADV6 | 44.264 | 1.375 | 1.758 | Flow velocity around the structure |
| Acoustic Doppler velocimeter 7 | ADV7 | 45.692 | -0.005 | 1.819 | Flow velocity around the structure |
| Pressure gauge 1 | PG1 | 43.761 | -0.350 | 2.057 | Horizontal pressure |
| Pressure gauge 2 | PG2 | 43.762 | -0.350 | 2.135 | Horizontal pressure |
| Pressure gauge 3 | PG3 | 43.762 | -0.350 | 2.287 | Horizontal pressure |
| Pressure gauge 4 | PG4 | 43.759 | 0.006 | 2.059 | Horizontal pressure |
| Pressure gauge 5 | PG5 | 43.759 | 0.005 | 2.288 | Horizontal pressure |
| Pressure gauge 6 | PG6 | 43.761 | -0.361 | 2.061 | Horizontal pressure |
| Pressure gauge 7 | PG7 | 43.760 | -0.361 | 2.137 | Horizontal pressure |
| Pressure gauge 8 | PG8 | 43.764 | -0.362 | 2.289 | Horizontal pressure |
| Pressure gauge 9 | PG9 | 44.139 | -0.502 | 2.059 | Vertical pressure |
| Pressure gauge 10 | PG10 | 44.139 | 0.507 | 2.059 | Vertical pressure |
| Pressure gauge 11 | PG11 | 44.139 | 0.028 | 2.002 | Vertical pressure |
| Pressure gauge 12 | PG12 | 44.393 | -0.502 | 2.059 | Vertical pressure |
| Pressure gauge 13 | PG13 | 44.393 | 0.507 | 2.059 | Vertical pressure |
| Pressure gauge 14 | PG14 | 44.765 | -0.001 | 2.018 | Vertical pressure |

Table B.2: Experimental setup: percentage of coefficients of variation of maximum measurements.

| Wave case | Wave gauge | | | Ultrasonic wave gauge | | | | | |
|-----------|------------------------------|------|------|-----------------------|-------|-------|-------|-------|-------|
| | WG1 | WG2 | WG3 | USWG1 | USWG2 | USWG3 | USWG4 | USWG5 | USWG6 |
| Unbroken | 1.7 | 0.5 | 0.4 | 2.5 | 1.5 | 2.3 | 1.4 | 0.7 | 1.9 |
| Broken | 1.3 | 2.3 | 13.6 | 10.2 | 26.7 | 75.7 | 77.2 | 7.9 | 8.4 |
| | Load cell | | | | | | | | |
| | LC1 | LC2 | LC3 | LC4 | LC5 | LC6 | LC7 | LC8 | LC9 |
| Unbroken | 3.7 | 4.7 | 2.3 | 3.0 | 1.6 | 2.5 | 2.8 | 0.5 | 1.1 |
| Broken | 17.0 | 21.0 | 10.9 | 13.6 | 6.1 | 11.4 | 15.0 | 7.8 | 11.7 |
| | Pressure gauges (horizontal) | | | | | | | | |
| | PG1 | PG2 | PG3 | PG4 | PG5 | PG6 | PG7 | PG8 | |
| Unbroken | 0.7 | 0.4 | 1.0 | 0.8 | 0.8 | 0.4 | 0.4 | 0.7 | |
| Broken | 21.4 | 14.2 | 14.7 | 12.9 | 18.1 | 20.4 | 16.4 | 14.1 | |
| | Pressure gauges (vertical) | | | | | | | | |
| | PG9 | PG10 | PG11 | PG12 | PG13 | PG14 | | | |
| Unbroken | 1.7 | 0.9 | 3.0 | 1.4 | 0.8 | 1.5 | | | |
| Broken | 36.8 | 35.1 | 23.4 | 33.1 | 31.4 | 21.7 | | | |

Appendix C

Sines: test-case

C.1 Container terminal of the Sines deep-water seaport

The current configuration of Terminal XXI is the result of two construction phases. The first adopted a closed-type constructive solution, on which the $\approx 300\text{ m}$ -long quay is supported by gravity RC blocks, while the second adopted an open-type solution, on which the quay is supported by piles driven into hard soil. The last $\approx 600\text{ m}$ -long wharf was constructed by Mota-Engil company and has been operational since 2017. Fig. C.1 depicts the photography of the current configuration (adapted from the site of the construction company <https://engenharia.mota-engil.pt/portfolio/ampliacao-do-terminal-de-sines>).

The combination of the current container configuration ($\approx 1\text{ km}$) with 10 “pós-panamáx” and “super pós-panamáx” cranes and 2 moving cranes, an adjacent storage area of 42 ha and hinterland connections make Sines port capable of handling an annual 2.3M TEU cargo. Fig. C.2 shows the contribution of Sines port to the global annual maritime traffic during 2021, highlighting the critical nature of the infrastructure, even within the pandemic sanitary conditions (www.marinetraffic.com/).

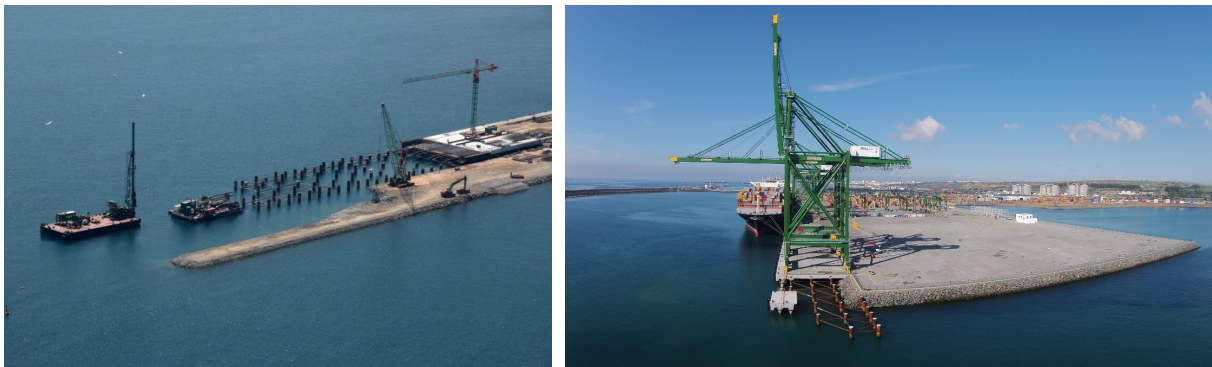


Figure C.1: Terminal XXI during construction works (left) and after conclusion (right).

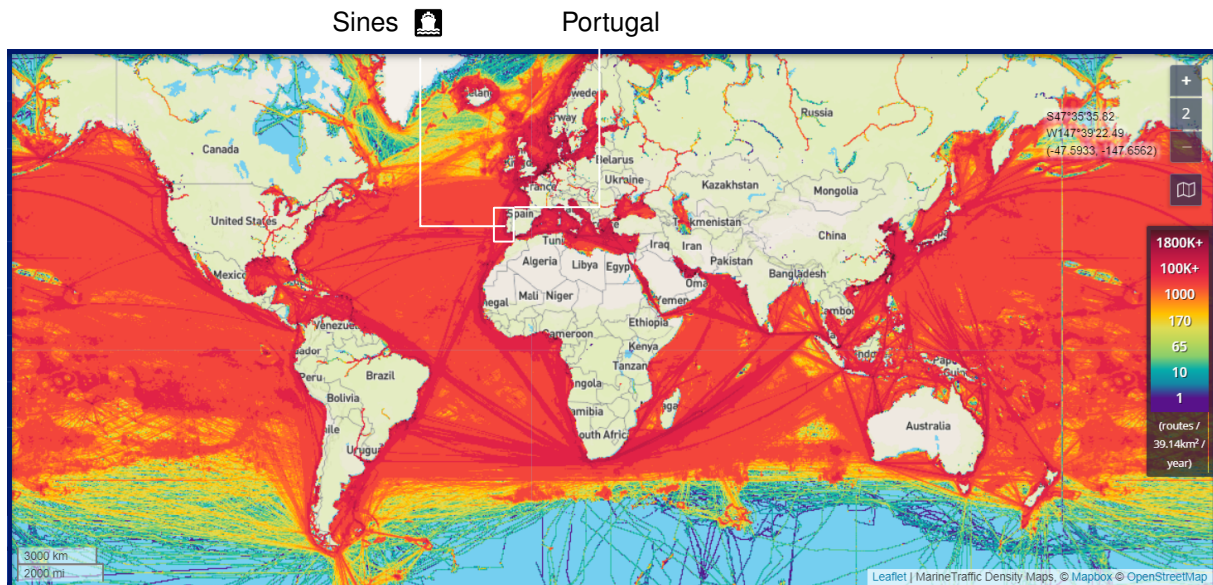


Figure C.2: Global maritime traffic, 2021.

C.2 Expansion of the Sines container terminal

Endeavouring to increase Sines cargo capacity, tenders, studies and design works are being developed by various key players, from technicians to stake-holders to politics. The expansion of the container terminal to almost 2 km of wharf length accompanied by the corresponding extension of the protection breakwater, an adjacent area of storage with 60 ha and add 9 super post-panamax cranes to support the work of the 10 existent ones. The long-term expansion planes predict the construction of a new modern wharf to serve as complementary container terminal, named after the historic Portuguese navigator Vasco da Gama, the first to link Europe and Asia by an ocean route, connecting the Atlantic and the Indian oceans and therefore, the West and the Orient. The 1375 m -long Vasco da Gama terminal will account with storage area of 30 ha and 10 berthing positions, each one equipped with the respective crane. Fig. C.3 depict content of the Sines expansion debated on the Portuguese Parliament (presentation by the President of the Administration board, Eng. Luis Cacho, 2014, available on <https://www.parlamento.pt/>, last access 12jun2022.). Fig. C.4 shows details of the Environmental Impact Assess developed by Nemus and Consulmar for Administração dos Portos de Sines e do Algarve S.A. regarding the third and fourth expansion phases of the cargo hub [424, 425]. Finally, Fig. C.5 resumes the presumable implementation of the seaport in Sines region accounting for the resultant of the third and fourth expansion phases planned for the infrastructure (personal communication and data provided by Administração dos Portos de Sines e do Algarve S.A.).

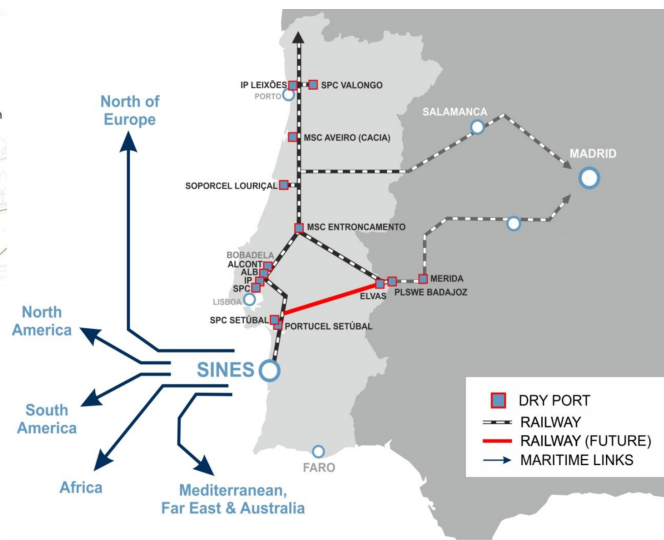
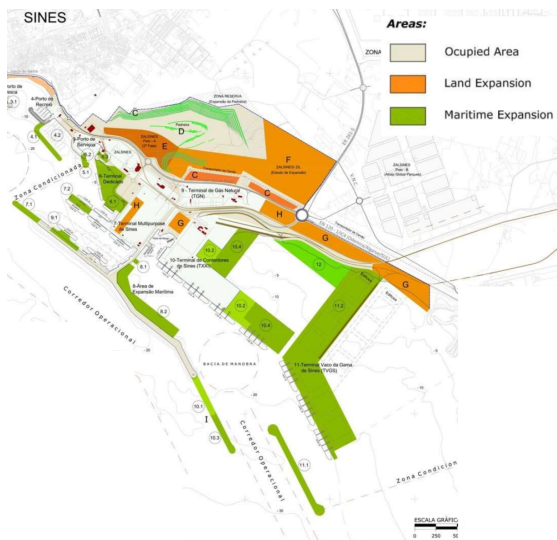


Figure C.3: Embryonic plans endeavouring the increase of Sines seaport cargo capacity. Adapted from the parliamentary session at the Portuguese Assembleia da República, in 2014.

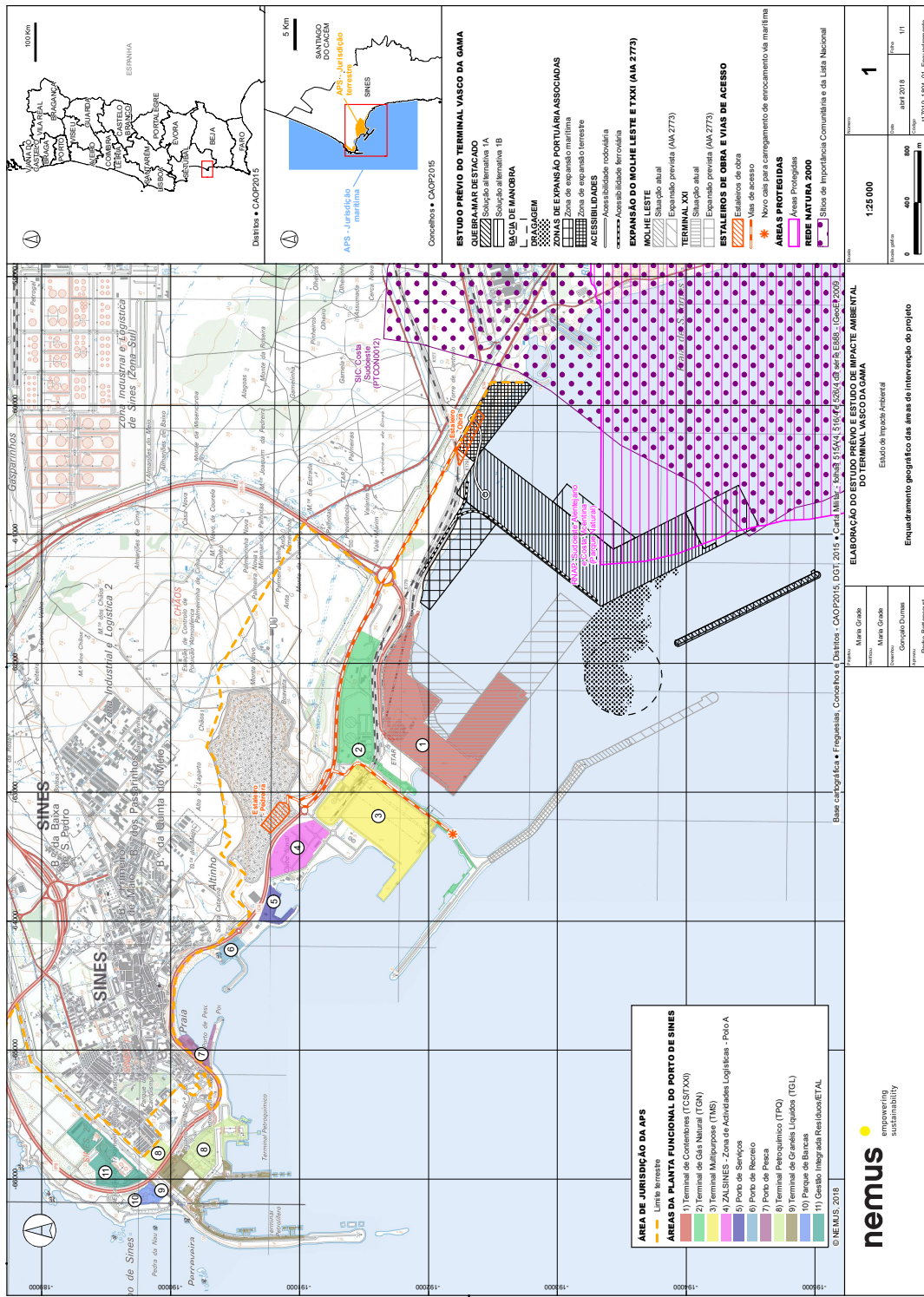


Figure C.4: Study of the environmental impact assessment for the third and fourth expansion stages of the Sines seaport cargo hub. Adapted from the Environmental Impact Assess developed by Nemus for Administração dos Portos de Sines e do Algarve S.A..

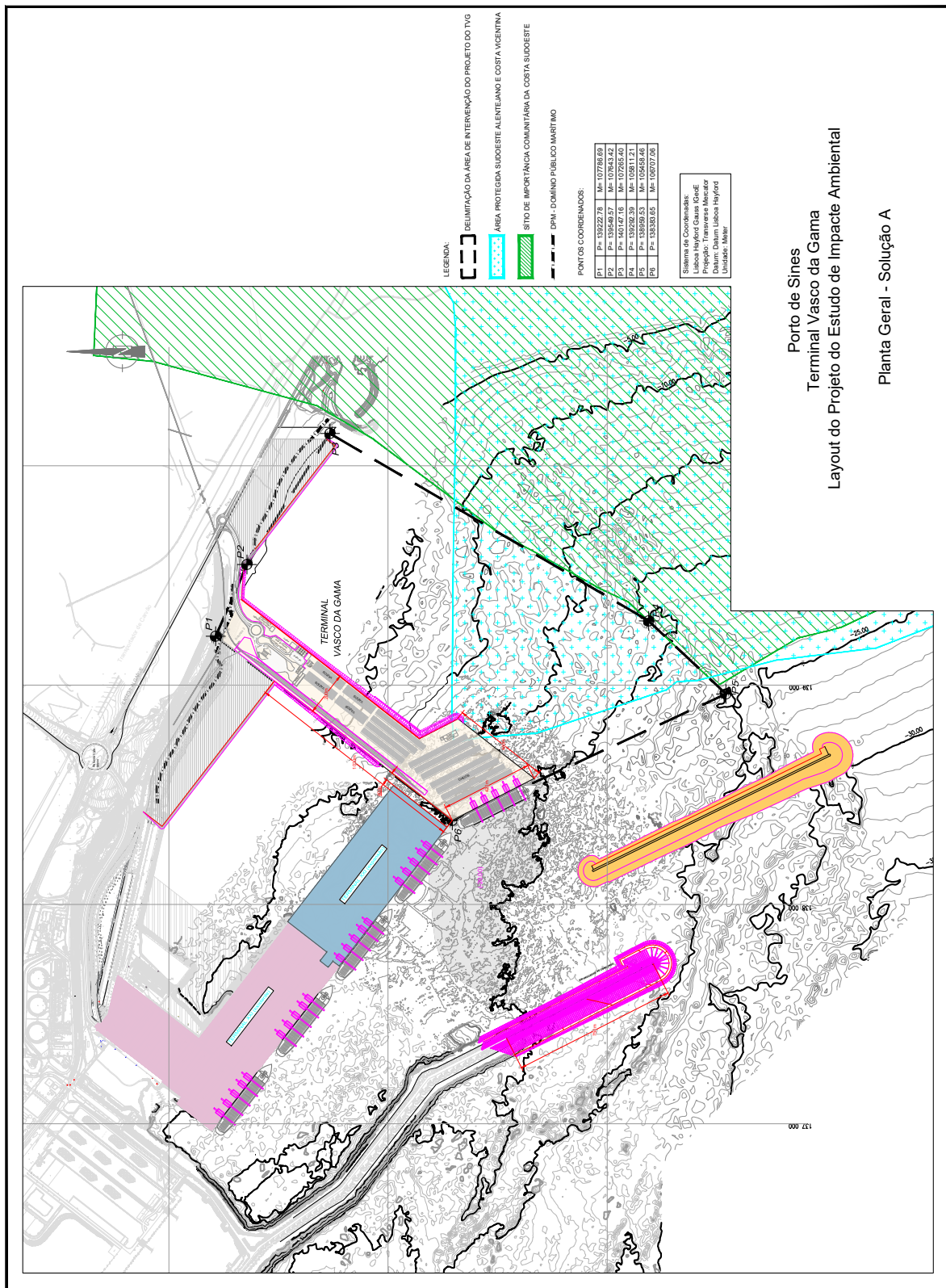


Figure C.5: Presumable design configuration for the third and fourth expansion stages of the Sines seaport cargo hub.

Appendix D

Sines: cascading seismic and tsunami multi-hazard

D.1 Parameters of tsunamigenic regional and local sources

Tables D.1 and D.2 summarize the $S_{candidate}$, respectively encompassing single or composite fault ruptures.

| Acronym | Ref. | D [km] | L [km] | W [km] | φ [°] | δ [°] | Θ [°] | λ [m] | μ [10 ¹⁰ Nm] | Mw |
|---------|--------------|--------|--------|--------|---------------|--------------|--------------|---------------|-----------------------------|------|
| GBF | [428] | 250 | 200 | 80 | 45 | 40 | 90 | 10 | 6.5 | 8.6 |
| | [455] | 250 | 170 | 100 | 60 | 40 | 90 | 13 | 6.0 | 8.7 |
| | [456] | 250 | 175 | 50 | 55 | 45 | 90 | 20 | 6.5 | 8.7 |
| | [22] | 250 | 127 | 60 | 233 | 35 | 90 | 8.3 | 3.0 | 8.1 |
| | [426] | 250 | 200 | 80 | 57 | 40 | 90 | 12 | 6.5 | 8.7 |
| | [458] | 250 | 200 | 80 | 53 | 35 | 90 | 10 | 4.5 | 8.5 |
| MPF | [448] | 150 | 100 | 70 | 22 | 20 | 90 | 15 | 3.0 | 8.3 |
| | [454] | 150 | 60 | 120 | 23 | 30 | 90 | 10 | 6.5 | 8.7 |
| | [456] | 150 | 150 | 50 | 10 | 25 | 60 | 20 | 4.0 | 8.6 |
| | [426]; [454] | 150 | 60 | 120 | 23 | 30 | 90 | 10 | 6.5 | 8.4 |
| | [426] | 150 | 60 | 120 | 23 | 45 | 90 | 10 | 6.5 | 8.4 |
| | [458] | 150 | 110 | 70 | 20.1 | 35 | 90 | 8 | 4.5 | 8.3 |
| CWF | [452, 453] | 280 | 15 | 180 | 210 | -11.0 | 79 | 15 | 3.0 | 8.8 |
| | [455] | 280 | 180 | 205 | 349 | 5 | 79 | 10 | 3.5 | 8.4 |
| | [456] | 280 | 200 | 200 | 350 | 25 | 79 | 20 | 4.0 | 8.9 |
| | [22] | 280 | 168 | 200 | 349 | 5 | 90 | 10 | 3.0 | 8.6 |
| | [458] | 280 | 170 | 200 | 349 | 5 | 90 | 20 | 3.0 | 8.8 |
| HSF | [454] | 240 | 175 | 140 | 39 | 45 | 90 | 10 | 6.5 | 8.7 |
| | [22] | 240 | 165 | 70 | 42.1 | 35 | 90 | 11 | 3.0 | 8.3 |
| | [426]; [454] | 240 | 80 | 175 | 39 | 45 | 90 | 10 | 6.5 | 8.74 |
| | [426] | 240 | 60 | 150 | 39 | 45 | 90 | 10 | 6.5 | 8.65 |
| | [458] | 240 | 165 | 70 | 42.1 | 35 | 90 | 15 | 4.5 | 8.5 |
| | [457] | 250 | 200 | 80 | 345 | 40 | 90 | 13 | 4.0 | 8.5 |
| SVF | [454] | 120 | 80 | 140 | 55 | 45 | 90 | 10 | 6.5 | 8.7 |
| PBF | [22] | 180 | 105 | 55 | 266.3 | 24 | 90 | 7 | 3.0 | 8.0 |
| WIS | [446] | 180 | 360 | 100 | 160 | 25 | 90 | 20 | 4.0 | 8.8 |
| | [456] | 180 | 250 | 150 | 350 | 25 | 60 | 20 | 4.0 | 8.9 |

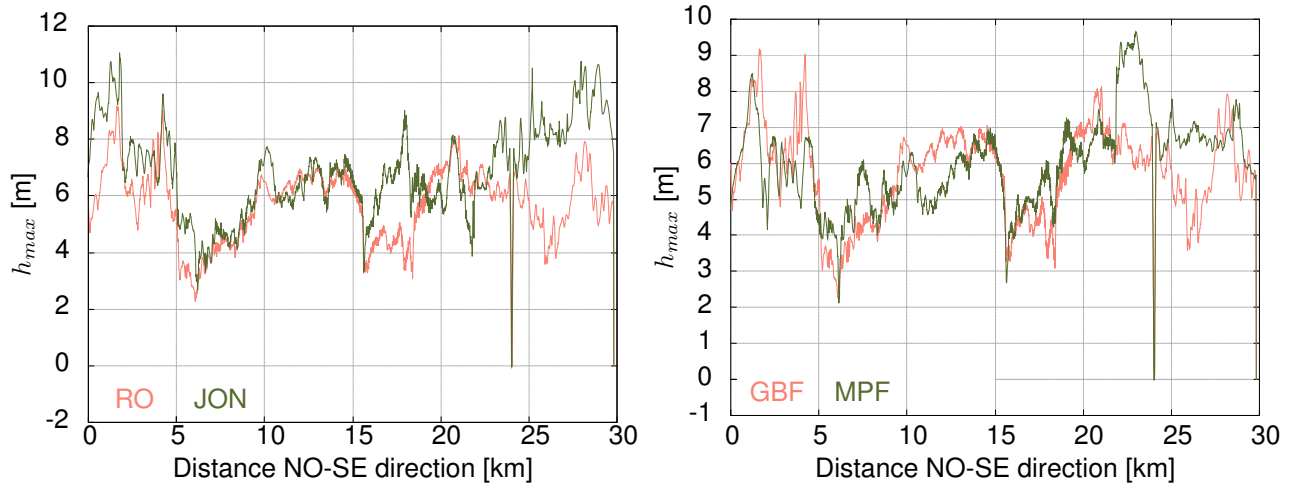
Table D.1: Fault parameters of the single tsunamigenic sources: distance from the source to the site, fault geometry (length and width), kinematics (strike, dip, rake and slip), soil rigidity and moment magnitude. A value of 5 km was assumed to model the depth to the top parameter.

| Acronym | Refs. | L [km] | W [km] | φ [°] | δ [°] | Θ [°] | λ [m] | μ [10 ¹⁰ Nm] | Mw |
|----------|--------------|------------|------------|---------------|--------------|--------------|---------------|-----------------------------|------|
| MPPSF | [449] | 120; 70 | 100 | 15 | 9 | 90 | 10 | 3.2 | 8.6 |
| | [455] | 200 | 70 | 20 | 15 | 60 | 10 | 3.5 | 8.4 |
| MPPBF | [447] | 95; 100 | 55 | 70; 21.7 | 45; 24 | 90 | 20 | 3.0 | 8.7 |
| MPHSF | [450, 451] | 50; 90 | 30 | 20; 36 | 25 | 90 | 8 | 3.0 | 8.7 |
| | [426]; [454] | 175; 60 | 140; 120 | 39; 23 | 45; 30 | 90 | 10 | 6.5 | 8.82 |
| | [426] | 210 | 120 | 39; 23 | 45 | 90 | 10 | 6.5 | 8.75 |
| | [458] | 165; 110 | 70; 70 | 42.1; 20.1 | 35 | 90 | 15; 8 | 4.5 | 8.75 |
| GBTVF | [443] | 120; 80 | 80 | 60; 38 | 40 | 90 | 12 | 6.5 | 8.7 |
| | [459] | 69; 73; 91 | 57; 61; 76 | 105; 74; 42 | 35 | 90 | 3.1; 3.3; 4.1 | 6.5 | 8.6 |
| HSCFSWIM | | 165 | 110 | 100; 73; 41 | 35 | 90 | 7.4 | 6.5 | 8.6 |
| | | 69; 73; 91 | 57; 61; 76 | 105; 74; 41 | 90; 70; 35 | 90 | 2.4; 2.5; 3.2 | 6.0 | 8.4 |
| | | 165 | 60.3 | 100; 73; 41 | 56 | 90 | 5.6 | 6.0 | 8.3 |

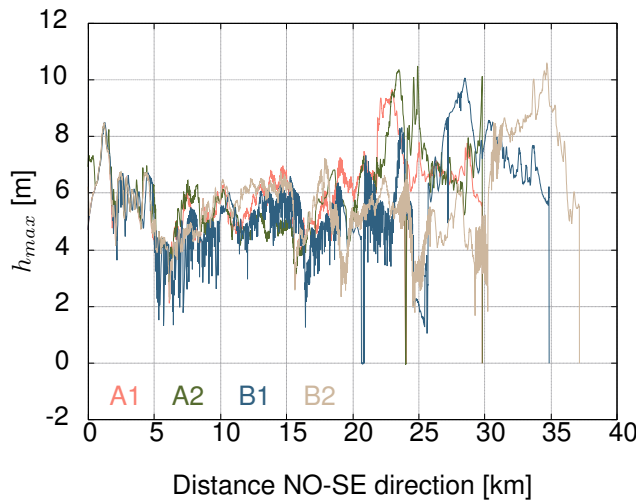
Table D.2: Fault parameters of the composed tsunamigenic sources: fault geometry (length and width), kinematics (strike, dip, rake and slip), soil rigidity and moment magnitude. A value of 5 km was assumed to model the depth to the top parameter

D.2 Influences on tsunami arrival

Fig. D.1 presents examples of h_{max} profiles calculated for 1) $S_{candidate}$ for the same source but using different proposal of rupture parameters, 2) $S_{candidate}$ whose waves are tendentiously orientated to north and south of coast of Sines, and 3) profiles of h_{max} calculated for the same $S_{candidate}$, but different coastal conditions.



(a) Influence of fault rupture on the H_{max} profiles, e.g. correlation of GBF solutions using source parameters proposed by Omira et al. 2009 [22] and Johnston 1996 [428] (left). Influence of the preferential waves orientation towards Sines coast considering Marquês de Pombal and Gorrige Bank faults [22] (right).



(b) Influence of coastal current and future configurations introduced in Fig. 6.6 on H_{max} profiles considering the same Gorrige Bank source [22].

Figure D.1: Peak tsunami hazard: physical and modeling sources of uncertainty influencing H_{max} profiles acquired at the dry-wet interface of Sines coast, $t = 0$ s.

Appendix E

Sines: successive structural response due to seismic and tsunami actions

E.1 Modal analysis

For the dynamic analysis purpose, the Rayleigh damping parameters need configuration based on modal analysis. Fig. E.1 depicts the first six modes of vibration of the soil-wharf system, for 2D models, with SP1 and SP1* configuration. The first two vibration modes were adopted when defining α and β parameters of the Rayleigh damping linear approach, $c = \alpha m + \beta k$.

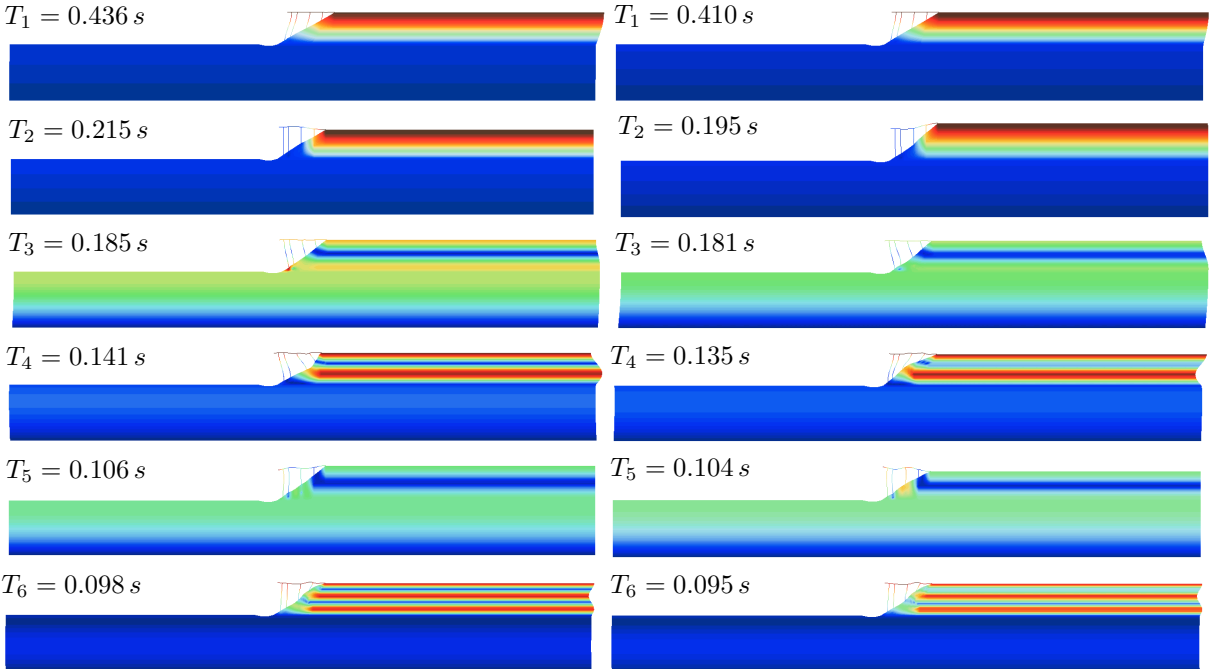


Figure E.1: Structural analysis: modal analysis of 2D soil-wharf system. Representation of the first six modal periods considering SP1 (left) and SP1* (right) configurations.

